Swansea University
Prifysgol Abertawe

Swansea University
College of Engineering

Tidal Energy and Coastal Models: Improved Turbine Simulation

EngD Thesis

Author:
Ross Gwenter

Supervisor's:
Prof. Ian Masters
Dr. Alison Williams

M2A
MATERIALS AND MANUFACTURING ACADEMY

ERDF
Llywodraeth Cymru
Welsh Government

Ewrop & Chymru: Buddsoddi yn eich dyfodol
Cronfa Datblygu Rhanbarthol Ewrop
Europe & Wales: Investing in your future
European Regional Development Fund

Declaration

This work has not previously been accepted in substance for any degree and is not being concurrently submitted in candidature for any degree.

Signed: ..
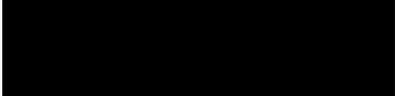
Date: ...7/7/22....

Statement 1

This thesis is the result of my own investigations, except where otherwise stated. Where correction services have been used, the extent and nature of the correction is clearly marked in a footnote(s). Other sources are acknowledged by footnotes giving explicit references. A bibliography is appended.

Signed: ..

Date: .....7/7/22..

Statement 2

I hereby give consent for my thesis, if accepted, to be availible for photocopying and for inter-libary loan, and for the title and summary to be made available to outside organisations.

Signed:
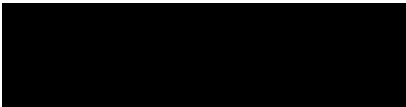
Date: ......7/7/22.

Statement 3

The universities ethical procedures have been followed and, where appropriate, that ethical approval has been granted.

Signed: ....

Date: 7/7/22

Abstract

Marine renewable energy is a continually growing topic of both commercial and academic research sectors. While not as developed as other renewable technologies such as those deployed within the wind sector, there is substantial technological crossover coupled with the inherent high energy density of water, that has helped push marine renewables into the wider renewable agenda. Thus, an ever expanding range of projects are in various stages of development.

As with all technological developments, there are a range of factors that can contribute to the rate of development or eventual success. One of the main difficulties, when looking at marine renewable technologies in a comparative view to other energy generation technologies, is that the operational environment is physically more complex: Energy must be supplied in diverse physical conditions, that temporally fluctuate with a range of time scales. The constant questions to the iteration to the local ecology. The increased operational fatigue of deployed devices. The financial risk associated within a recent sector.

This work presents the continual research related to the computational research development of different marine renewable technologies that were under development of several institutional bodies at the time of writing this document.

The scope has a wide envelopment as the nature of novel projects means that the project failure rate is high. Thus, forced through a combination of reasons related to financial, useful purpose and intellectual property, the research covers distinct projects.

Contents

II   Swansea Bay Tidal Lagoon   90

3   Far-Field Hydrodynamics   91

4   Near-Field Hydrodynamics   104

List of Figures

List of Tables

Nomenclature

Acronyms

$2D$	Two Dimensional
$3D$	Three Dimensional
ADV	Vectrino Acoustic Doppler velocimeter
$AIST$	The National Institute of Advanced Industrial Science and Technology
AOI	Area of Interest
$BEMT$	Blade Element Momentum Theory
CFD	Computational Fluid Dynamics
CFL	Courant-Friedrichs-Lewy condition
CHP	Combined Heat and Power
CSP	Concentrating Solar thermal Power
da	Depth Averaged
DS	Downstream
EMF	Electro Magnetic Frequency
FEA	Finite Element Analysis
$FENCH-GHG$	Full Energy Chain analysis of GreenHouse Gas
$GaAs$	Gallium Arsenide semiconductor
GAD	Generalised Actuator Disk
$GaInAs$	Gallium Indium Arsenide semiconductor
$GaInP$	Gallium Indium Phosphide semiconductor
$GaInPAs$	Gallium Indium Phosphide Arsenide semiconductor
GCI	Grid Convergence Index
GCI_{AR}	Asymptotic range of Grid Convergence

HAT	Horizontal Axis Turbines
HATST	Horizontal Axis Tidal Stream Turbines
HATST	Horizontal-Axis Tidal Stream Turbine
HOT	Higher Order Terms
HPC	High Performance Computing
Iθ	Inclined Scour Mattress
IAEA	International Atomic Energy Agency
LE	Trailing Edge
MCT	Marine Current Turbines
MRF	Moving Reference Frame
MS	Mesh Sensitivity
QTDT	Quadruple Turbine Draft Tube
R&D	Research and Development
RANS	Reynolds Averaged Navier-Stokes equations
RoR	Run-Of-River
RPA	Reflection Parameter Alpha
SBTL	Swansea Bay Tidal Lagoon
SLS	Selective Lazer Sintering
SM	Scour Mattress
SM	Sliding Mesh
STDT	Single Turbine Draft Tube
SWE	Shallow Water Equations
TDT	Turbine Housing Draft Tube
TE	Trailing Edge
TFEC	Total Final Energy Consumption
TH	Turbine Housing
TKE	Turbulent Kinetic Energy
VAWST	Vertical Axis Wind Stream Turbines
WSS	Wall Shear Stress

ZEF	Zone of Established Flow
ZFE	Zone of Flow Establishment

Parameters

α	Angle of Attack
α	angle of attack
$\dot{V}$	Volumetric flow rate $[m^3 s^{-1}]$
ε	Turbulent kinetic energy dissipation rate $[m^2 s^{-3}]$
ι_m	Mixing length
κ	Turbulent Kinetic Energy $[m^2 s^{-2}]$
λ	Characteristic Speed
ν_t	Turbulent viscosity $[m^2 s^{-1}]$
ρ	Density
τ	shear stress
τ_b	bed shear stress
$\vec{u}_1$	Velocity at Indicative Position Preceding Following Integer
$\vec{u}_2$	Velocity at Indicative Position Succeeding Previous Integer
$\vec{u}_x$	Velocity point along x-axial length
$\vec{u}_\infty$	Free-stream Velocity
$\vec{u}_{x \to \infty}$	Downstream Velocity towards Infinity
ζ	Free surface elevation above the reference plane
A_f	cross sectional flow area
A_s	wetted surface area
B_o	Initial Jet-flow width/width of gap
c	Speed of sound $[ms^{-1}]$
C_1	Model coefficient
C_2	Model coefficient
C_μ	Model coefficient for the turbulent viscosity
C_D	coefficient of Drag
C_d	discharge coefficient

C_L	coefficient of lift
d	averaged depth
D_ε	Effective diffusivity for ε
D_κ	Effective diffusivity for κ
D_H	Hydraulic diameter
F_s	Safety Factor
H	head difference, total depth
h	Measure of Grid Spacing
H_{min}	minimum head required to operate turbines
I	Turbulence intensity
M	Mach number
N_T	Total Number of Cells
P	Perimeter
P	Turbulent kinetic energy production rate $[m^2 s^{-3}]$
Q	flow rate
r_c	Refinement Ratio
Re	Reynolds number
Re_o	Reynolds number at the origin point
S_i	Source term
T	shear stress tensor
T_c	Simulation Clock-Time
u	scalar depth-averaged horizontal velocity
U_e	Velocity at boundary layer edge $[ms^{-1}]$
Z	Vertical co-ordinate in physical space

Variables

$\hat{n}$	unit normal vector
μ_l	Lamianr dynamic viscosity
μ_t	Turbulent dynamic viscosity
τ_w	Strength of vortex filament at origin

Γ	Strength of vortex filament
Γ_o	Strength of vortex filament at origin
$\vec{u}_o$	Velocity at origin
E	Solution Error
l	Characteristic eddy length
l_0	Integral length scale
L_{pc}	Potential core length
p	Order of Convergence
R	Convergence Ratio
u_i	$i_t h$ component of the velocity vector
u_*	Friction velocity
x_o	x-axial position of the virtual origin relative to the outlet
$x_{95}\%$	position of 95% depth averaged velocity magnitude reduction

A list of parameters, variables and acronyms, which are representational in this thesis are provided below. Where applicable, SI units are stated. If of derived units, then the SI base units will be stated. Certain parameters are modified in text with SI prefixes to denote that said parameter is scaled.

Part I

Preliminaries

Chapter 1

Introduction

1.1   Thesis Motivation

Over the later part of the 20th century and entering the 21st, there has been ever increasing amounts of evidence that human activity is influencing the climatic balance of our planet. This coupled with the security of supply are both constant sources of presentiment for the major problems humanity will face in the coming future.

Evidenced through shifts in the weather systems at global scales, where measured data taken from relevant sources has provided consistent and unilateral trends; that can only be explained through the realisation that the Earth's temperature has been increasing [160]. While the Earth's climate has also been shown to have fluctuated throughout its history, with evidence that temperatures have been both higher and lower than they are now [89]. There are two pressing notions that set the current predicament apart from the previous. They are that this is the first time human involvement has been largely credited. Secondly, that extinction events and climate change have been shown to have entwined relations; with the magnitude of the extinction period being directly proportional to the rate of habitat change [82]. Simultaneously, widespread pollution, which has largely the same causation as climate change, only acts to exasperate the situation even further [243].

The range of issues attributed climate change are not just a figment of current academic hypothesises, but are realisable at this current period of time. As mentioned above, evidential impacts have been shown in changes of the hydrosphere:

- Higher oceanic levels: polar/glacier melt water & thermal expansion
  - Resultant loss of low-lying coastal & island regions.
  - Mass population migration.
  - Reduced living space.

- Bleaching of coral reefs.
  - Mass disruption to marine ecosystem balance dependant on healthy coral.

- – Knock-on effect on global fisheries

- • Acidification from carbon dioxide absorption
    - – Implications for the ocean ecosystem.

- • Salinity of ocean water
    - – Implications for the ocean ecosystem.
    - – Lowers the freezing point, thus disrupting polar ice-cap formation

- • Ocean currents
    - – Knock-on effect on ocean current dependant weather.
    - – Large potential to shift continental climate types.

- • Hydrological cycles
    - – Floods
    - – Droughts
    - – Fires
    - – Implication on freshwater supplies
    - – Disrupted food supply

- • Increasing prevalence and intensity of storm systems
    - – Large financial burden
    - – Destruction of essential infrastructure.

Eustatic, thermosteric and halosteric ocean characteristics are some of the most pronounced and longest studied measures of climate change; directing scientific opinion to that of seawater levels have been rising at incremental rates over the past century [141][38]. An accelerated water level increase rate of 3.1 mm/yr was reported during the last decade - an increase from the $1 - 2$ mm/yr range reported in measurements taken from the previous decade before [38]. Such accelerated rise in water levels has led to the envisioned destruction of coastal communities, with current coastal defences becoming inundated leading to millions of lives and billions of GBP worth of property and infrastructure at risk.

Additional concerns revolving around consequential changes to the political landscape cannot be dismissed out of hand. The displacement of significant numbers of people will set up the inevitable consequence of having to find alternative places to settle. Many nations around the world just don't have the infrastructure in-place or spare habitable land to settle them. Many will be faced with no other option than to turn towards actions of desperation; potentially giving rise to large scale migration crisis, or seeking a better future through politically aggressive movements promises. The impact to resource networks could also lead to nation states taking military action and thus create conflict.

Various different analyses have suggested that the climate change is linked to the increasing atmospheric concentrations of greenhouse gasses. The fossil fuel dominated energy sector has contributed to carbon dioxide (greenhouse gas) concentrations in the atmosphere to increase by 30% from the onset of the 18th century industrial revolution [256]. A degree of credence is given that larger changes of climate change can be predicted in the future [271].

Industrialised society has existed and flourished from the extraction of finite fossil fuel resources to such a level that those societies became near wholly dependent on the supply of such resources. Instances such as the 1970's energy crisis; a period where major industrial countries faced withdrawal of a steady oil supply and elevated prices, brought the 1970's western way of life to a standstill and led to large subsequent recessions. The system was 'shocked' to such an extent, a complete revision of policy-making regarding the relationship to fossil fuels was enacted by governments. Alternative sources of energy became increasingly attractive prospects.

Currently worldwide, the birth rate has 'exploded' while simultaneously the average lifespan of a person has increased. The 'Third-world' developing nations are also going through large industrialisation advances making them 'thirsty' for resources. Collectivity, people's lifestyles have also changed and are increasingly resource heavy from the growing global affluence [256]. A situation is quickly developing where the supply cannot meet the demand, which sits at $\approx 105,000 TW_h/yr$ globally; leading to a prognosis of price instability. The effect of this is likely a repeat of the 1970's energy crisis unless the situation is addressed [203].

The United Kingdom has chosen to address the issues of climate change and security of supply by instigating policies intended on curbing the use and reliance on fossil fuels; which currently contribute to 88.3% of the $\approx 1500 TW_h/yr$,2019 total energy consumption [58, 107]. A goal of phasing out 40% of greenhouse gas emissions by 2030, and 80-95% by 2050 has been announced. The phase out framework revolves around ambitious, cost-effective and flexible approaches to be conducted in a manner that will maximise the economic opportunities within the country [59]. In line to meet the specified targets, the UK government has begun the process of closing 82% of existing fossil fuel based power station capacity by 2030. This coincides with the push to increase the electrification of public and private utilities; transport, heat pumps etc. These actions have lead to an increasing demand on the national grid, leading to a predicted 32GW power deficit [238]. The UK and surrounding territories possess significant renewable energy resources which can be captured and used to address this predicted energy deficit, allowing the UK to have a more secure energy supply and a smaller carbon footprint.

As such there has been ever growing social and political pressure toward increasing the utilization of renewable energy resources to meet current and future energy

demands. However, current renewable energy deployment and technology remain unable to generate electrical energy from the natural environment on a competitive basis to conventional fossil fuel and nuclear plant temporal capacities. Renewable energy concepts are continually restrained by the inability to generate energy at either on 'push of a button' or in some cases, even on a reliable basis. The restraints are often intrinsically tied in with a particular form of power generation. An example of which is wind energy generation, which can only generate when the wind blows. To counteract this facet, multiple commercially novel avenues are being explored to diversify the electrical supply from renewable resources and hence be better able to meet the demand.

1.2 Renewable Energy - Contextual Background

The 'raison d'être' for renewable energy is primarily to provide a substitute for the carbon-based, fossil fuel electrical power generation; thus combating a major contribution to the current climate change crisis. In recognition of the growing problem, there has been a rapid growth in several renewable energy technologies; allowing for a pragmatically feasible step away from the current fossil fuel based energy generation dependency [17, 64]. An important consideration of renewable energies is that there is no prefect renewable energy source - that each option has inherent characteristics with both positive and negative attributes, which limit the potential for a complete dependency on each type. Thus, a prudent approach would be to seek development of a broad range of options, which would increase the security of supply.

Figure 1.1 shows a spider-diagram listing all the accepted mainstream core forms of renewable energy. Each renewable type can be further broken down into more elaborated forms. Additionally, there are generation concepts that are not depicted, as they have not yet reached a stage of development where they are relevant to the current conversation. This section will cover a summative overview of current commercial renewable technologies, highlighting the basic working principles of each, their advantages and disadvantages, and a current update on the global generation capacity of each type.
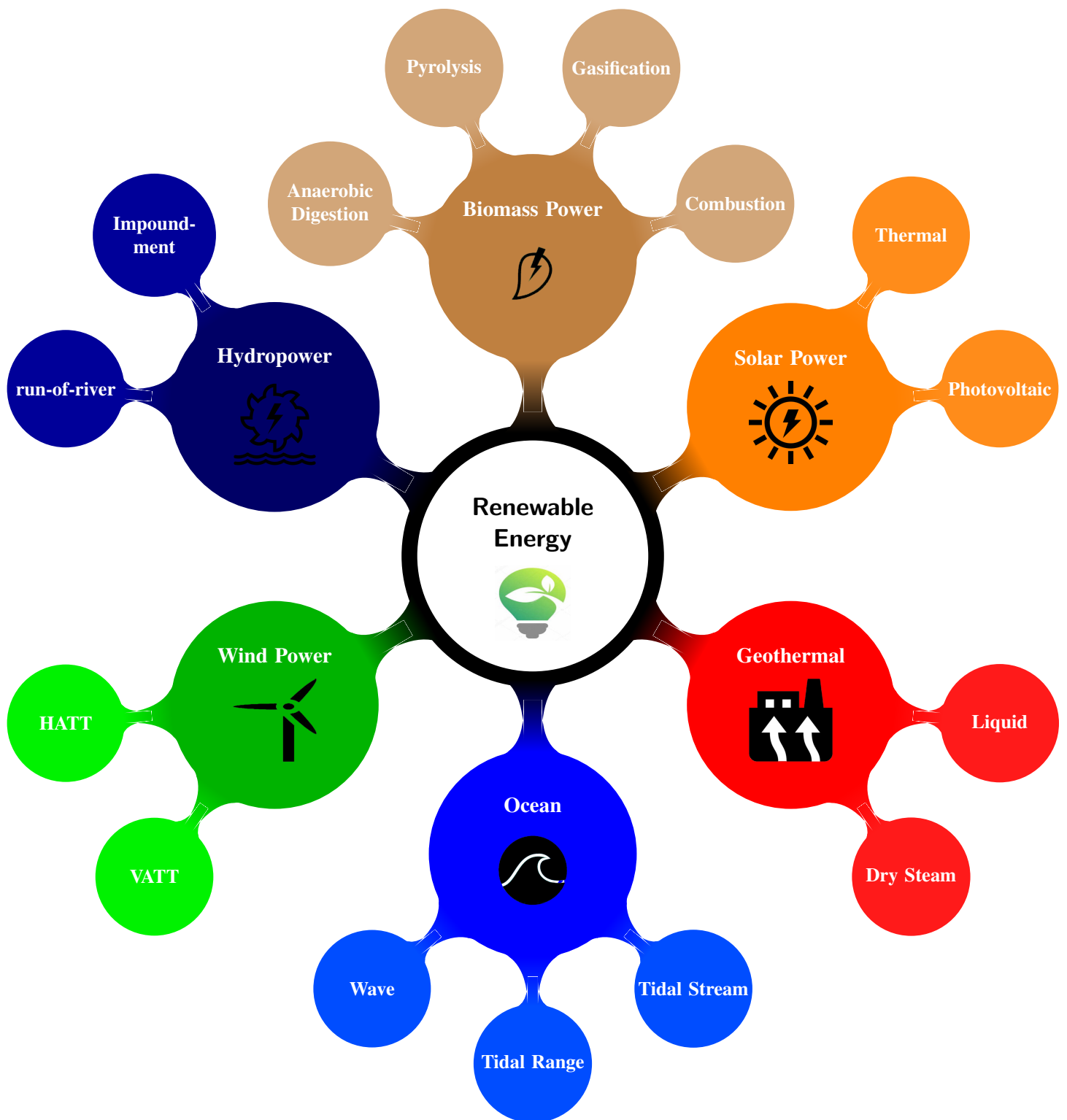
Figure 1.1: Infographic Spider Diagram of renewable energies

Solar Power

Solar Power is the direct utilization of the Suns incident rays onto Earth into usable energy. The main methods for harnessing such energy is the photovoltaic cells; made from semiconducting materials, which when a photon hits the cells an electron enters an excited, higher energy state, allowing the electron to be freed from its low-energy bounded state. The free electrons cross a one-way junction between dissimilar materials creating a positive and negative charge at either electrode - an electric potential. The intensity of the solar radiation incident on the cells is a direct function of the amount of energy produced by the cell.

Recently, advances have been made in the conversion efficiency of the cells. As of 2015, an efficiency of 46 % at 508-suns was achieved by AIST in Japan for a GaInP/GaAs//GaInAsP/GaInAs solar cells, presenting the highest independently confirmed efficiency recordings to-date [63].

The solar PV market increased by 25% in the 2014 period with an 50GW addition, lifting the global capacity to 227GW in 2015 [201].

The disadvantages of solar energy is the inability to generate during night time periods. The panels can still generate under cloudy weather, albeit at a reduced amount from the clouds blockage of the radiation intensity. The technology is also expensive and has a low power density. However, the prices of solar energy are dropping and subsequent large world wide growth of photovoltaic cells is predicted.

Another type of solar power is the CSP, which converts the solar radiation to thermal energy to boil water for steam powered electrical generators. To reach the temperatures needed to boil tanks of water, various methods can be used to concentrate the solar radiation into a thermal receiver; where temperatures in excess of $500^{\circ}C$ can be created. As of 2015, the total global capacity is 4.8GW [129, 201].

Geothermal

Geothermal energy generation taps into the Earth's innate thermal energy. Potential thermal extraction ranges from near surface hot water ($< 100C^{o}$) to deep hot rock many miles beneath the crusts surface.

The current prominent geothermal energy capture method is to drill into, regionally specific, naturally occurring 'hydrothermal convection' systems, where water in porous sections of the Earth's crust is forced through convection mechanisms into a cyclic process, powered from the heat supplied in the deeper parts of the crust. The drilling acts to lower the resistance to flow and thus improves the potential power capture. The steam produced from the heated water is funnelled to a turbine unit for electricity production [248].

Collectively around 315MW capacity was installed worldwide in 2015, which brought the global capacity to 13.2GW [201]. A further 700MW was installed during 2017 [202]. As of July 2019, thirty countries operate geothermal power plants, with the cumulative installed capacity of approximately 14.9 GW worldwide [6, 207].

Geothermal energy is hampered by the perpetually high development risk and high drilling costs [201]. Therefore, to be competitive to other renewable options, locational suitability is a major determinant - i.e. geographical "hot spots". Iceland is a geographically suitable nation, and as such, has been one of the leading nations in the development of geothermal energy generation. However, drilling related to

the geothermal power plants has been identified to induce seismicity - findings have shown the process to be a major factor in the onset of earthquakes, with the largest being M4 category on October 15, 2011 [123]. Additionally, it's been speculated that the drilling process has also been responsible for the release of methane and other toxic gasses. While the operational process can be considered very green, the installation process also contributes to the current climate crisis [126]. Despite the stated drawbacks, a huge theoretical potential exists. Aghahosseini *et al* [6] estimates that 200TW capacity is possible if economic and water stress constraints are excluded.

Biomass Energy

Biomass (plant material and animal waste) is considered a carbon net-neutral renewable energy resource. Like solar power, the original source of energy is the Sun; where incident rays are naturally converted through photosynthesis to form carbohydrates, which in turn are used by the plant as food to build biomass. Essentially, solar energy is converted into stored chemical energy which can then be combusted for energy.

When taking all forms of Biomass energy into account: heating,transport and energy; Biomass holds the highest share of the renewable energy resources - accounting for 12% or 45.2EJ of the total global energy consumption. When factoring for electrical energy generation, the global share was an estimated 6% resulting in 139GW in 2019. An increase of 8GW, 6.1% from 2018 and 9GW, 7.3% in 2017 [202, 203].

A situational advantage of Biomass energy is that since the energy is in a stored, stable state. Energy can be generated at a per-necessity basis to match the daily energy demand fluctuations. Therefore, energy losses associated with off-peak energy storage can be negated. Additionally, energy can be harnessed through Combined Heat and Power (CHP) plants; making use of what would be waste heat energy, giving greater energy efficiency.

Biomass struggles to compete with other forms of renewable energy because of the high costs compared to other renewable resources. The use of bioenergy has increased and helped some countries meet the rising consumer demand, while simultaneously meeting the environmental legislation. However, current political policy in some countries has hindered the resource development and has lead to uncertainty about the future markets constrained investment in developing capacity [201]. A contentious aspect of Biomass is that the combustion process, while not releasing Sulphur or Mercury into the environment, still releases Carbon Dioxide and Carbon Monoxide - both green house gasses. Biomass also requires large scale land use which can result in deforestation and damage to the local ecosystem from farming practices. Thus the success of the biomass energy generation rests in taking steps to mitigate environmental impacts with sustainable harvesting and use of land.

Wind Power

Wind Power harnesses the wind to turn turbines generating mechanical power. Historically, the mechanical power was used to turn grain stones and to pump water;

Nowadays, the mechanical power is directed through a shaft directly to an electrical generator or through a gearbox system before the electrical generator.

Wind power technologies have developed over time into what is now considered a mature technology. During 2015, 63GW installed capacity came online to make a global total of about 433GW. Since then, the capacity has increased by 10.7% per year on average, to 651Gw in 2019 [203].

Consistent instalment success and the maturation of wind power has lead to the technology to be generally seen as a reliable investment for stable returns and has seen corporations and private entities turn to it for low-cost power [201].

One of the major disadvantages of wind power is its dependency on the local weather systems - the catch being that the wind does not blow in phase with the energy demand. Thus, wind power can only exist to substitute the electrical supply in coordination with generation systems that are more reactive to the changes in demand.

An additional concern that is being put forward is the impact on residents in nearby areas to the turbine array fields. Initial complaints were directed towards cosmetic damages to the natural beauty of an area. In periods after instalment, there have been reports of consequential symptoms like constant migraines and tinnitus; symptoms which would alleviate once the person would leave the locale. Crichton *et al* [51] argues that the symptoms are nocebo in nature and that complaints directly coincide with increased media coverage. Negative coverage sets to form a 'blueprint' for what symptoms a person might expect, which reflects back as reported symptoms.

Hydro Power

Hydro-power is a term for electrical generation from harnessing dynamic water flow as the primary source of energy. Like wind energy, humans have harnessed water flow through rotating water wheels since the times of antiquity [263]. Modern day hydropower falls under two main categories being Impoundment and 'run-of-river' and mainly functions for electrical generation purposes. Additionally, like wind power, the length of time that hydropower technology has been around, has contributed to hydropower to be seen as a technologically mature renewable option.

The Impoundment type is the most common type of hydropower generation system. An impoundment system, also referred to as reservoir, utilizes a dam structure to store large quantities of river water in an upstream reservoir. The impounded water creates potential static head, which is extracted through releasing water flow through a penstock system, which leads to an electrical generation turbine. The run-of-river (RoR) variant harnesses the potential energy from dynamic flow without storing water. Typically, a proportion of a fast flowing river is diverted from the main body flow through a penstock system in series with a turbine generation system. After passing through the system, the is water directed back into the main body flow. Despite being defined as not storing water, the majority of ROR systems still do make use of smaller Dams or weirs to ensure an element of water level redundancy - so that enough water is continuously channelled into the penstock system. Without such, the plant is subject to fluctuating river levels born from weather systems [105, 239].

The smaller RoR reservoirs are often referred to as pondage rather than the larger reservoir description of the impoundmet type. The reservoir enables the system op-

eration to quickly attune its flow output, and consequentially electrical output, to the consumer demand. Without a substantial reservoir, ROR generation is limited to river systems where there is a constant year round minimal flow, and therefore constant electrical output. However, the scale of the pondage limits the degree to which the natural environment is altered. The river system will continue to exist under the pre-existing flood patterns. In comparison, larger reservoir types will flood and submerge large areas - destroying natural habitats for wildlife and potentially causing forced displacement of human settlements. Thus, ROR is often seen as the more environmentally friendly and potentially politically easier type. However, a large reservoir and flow control can greatly assist in flood management, a factor which also has been advertised in favour of impoundment type projects. Both types have been shown to disrupt fish migratory paths where formally present and the natural sediment transport. An example is the North American salmon. With environmentalism becoming more politically conscious, several dams have now been removed to restore the river system to its former natural state [105].

Hydropower currently stands as the renewable market that contributes to the largest global share at 1,150GW capacity, with a four-year average capacity growth of 21.5GW, though the capacity increase in 2015 was nearly double that of 2019 [203, 202, 201].

Ocean Energy

Despite the oceans covering a little over 2/3 of Earth's surface area, and holding vast amounts of energy, the ocean energy sector is the smallest sector out of the renewables in 2019. Ocean energy primarily exists in three distinct categories of Wave, Tidal Stream and Tidal Range. As of 2019, the global capacity stood around 535MW [203].

Wave energy is another renewable alternative, albeit at an earlier stage of development in comparison to wind. As such, a wide variety of wave energy capture systems at different stages of development are currently being developed, with no single method considered 'clear-cut' superior and in large scale commercial use [18, 112]. The wave resource is estimated to be 60TW worldwide with 3TW being released on the worlds coastline [258, 181] The main disadvantages in utilizing wave energy as a resource is its unpredictability.

Tidal stream involves inserting a tidal stream turbine into the tidally forced dynamic water flow to harness the energy. Due to its similarity in concept to wind energy, Tidal Stream technology is maturing with current designs following its wind 'cousin' with horizontal-axis turbines. In 2019, tidal stream contributed 45GWh. Recently tidal stream has benefited from increased interest in supporting development [203].

The Tidal Range type involves the construction of a lagoon or barrage breakwater; acting much in the same way to a dam, through impounding water to generate a potential static head. The difference being that the water level is forced by tidal movements rather than the collection of river water. The impounded water can then be harnessed through releasing over turbines.

Tidal range and tidal stream technologies have great potential to harness a predictable resource as a source for clean renewable energy. Consequent of the current climate, there is a considerable focus on the design and implementation of these

technologies [173].

Currently, two installed barrages exist which provide over 90% of the current installed capacity; La Rance (France) with 240MW capacity and the Sihwa plant (Republic of Korea) with a 254MW capacity [203, 202].

All Ocean Energy generation types have three unaminous negative environmental effects: the generation of EMF and noise from operation, the existence *in situ* can alter the natural habitat of local wildlife and also cause alterations to the marine environment. The degree of the potential impact will likely scale with the size of the generation system [60, 199].

The theoretical global tidal power resource has been estimated to be 3.7TW, which would be $\approx 30.8\%$ of the TFEC. 2.5TW of which is estimated to dissipate in shallow continental shelf waters. The remaining resource; 1.2TW, is dissipated in the deeper waters (1.0TW) and as friction in the solid Earth (0.2TW) [112, 198, 74, 20].

Renewable Summary

There has been considerable global reaction to the climate crisis that Earth is currently facing. What was initially speculation, has now been proven beyond all doubt. Nation states have previously proved to be fickle with policy change, but there are signs that the world is recognising the necessity for immediate change. During the 1990-2009 approximate period, many projects were specified in the KW. In the next decade, KW shifted to MW capacities [217]. At the close of 2019, 200GW of renewable energy was installed globally that year; which maintained the approximate 8% yearly growth seen in recent years. This brought the collective total installed capacity to 2,588GW, which accounts for 27.3% share of the global energy generation, with over 75% of yearly increased capacity coming from renewable sources [203].

Renewable technology capabilities have been projected as capable of supplying Earths growing energy demand, though their success is routed in a diversity of supply to counteract inherent limitations of each type.

1.3   Tidal Energy - State Of the Art Review

Research undertaken in this thesis includes both tidal range and tidal stream tidal models. Therefore in order to develop models that more accurately simulate marine renewable power plants, it is vital to understand the coastal marine characteristics and their mechanisms. Additionally, a key to successful implementation is learning from previous projects, current prospectus and accounting for future projections.

Tides can be described as periodic forcing of the global oceans; produced from gravitational interactions between the Earth and large celestial masses of the sun and the moon. The positions of which can be predicted indefinitely. The astronomical tidal oscillations may be partially disturbed by atmospheric disturbances, which are only predictable over a period of a couple of days. However, large atmospheric disturbances that cause any significant variation in the tidal ranges are rare. Thus a inherent quality of tidal energy is the comparably high level of predictability relating to the astronomical influences [2]. The high predictability is invaluable in

comparison to the less predictable renewable resources such as wind, wave and solar generation.

A major consideration for national grids is the surety of electrical supply to meet fluctuating demand. Energy sources such as gas and nuclear power plants can adjust their output in a *ad lib* manner, with flywheels accounting for immediate impromptu responses. Geothermal, Hydropower and Biomass power plants are the only renewable sources that can provide equivalent *ad lib* electrical generation. Solar, Wind and wave generation is subject to fluctuating weather patterns, so have to have incorporated energy storage systems for further control of supply. Tidal schemes provide a unique characteristic of being completely predictable, yet cannot meet electrical demand in a *ad lib* manner. However, the regularity and predictability of tidal generation can enable national grid operators to pre-emptively optimize supply from alternative sources to essentially 'fill in the gaps' to meet the demand.

The Crown Estate in 2012 [231] has produced theoretical tidal energy resource potential for the UK as stipulated in 1.1.

Table 1.1: Table summarising the tidal energy resource for the UK. [231, 58, 107]

Tidal Resource	Theoretical Tidal Energy (2012) [TW_h/yr]	Rated Capacity [GW]	Compared to UK Consumption [%]
Stream	95	32	6.3
Range (Barrage)	96	45	6.4
Range (Lagoon)	25	14	1.6

Predicted figures are not mutually exclusive. Locations which posses extractable resource potential will over-lap with each respective case.

1.3.1   Tidal Stream

As touched on in the Ocean Energy section above, Tidal stream energy refers to the extraction of energy from tidally forced dynamic water flow. The environmental impact of which is generally believed to be minimal and ideal trade-off considering the renewable benefits. The highest CO_2 emission for the SeaGen tidal stream turbine is released during the Materials and manufacturing stage; accounting for 80% [88, 69]. The remaining emissions are likely attributed those released during transportation and maintenance purposes.

There are several polluting aspects common to tidal stream designs, but these are comparably insignificant in comparison to other water based systems. Lubricating oils are present and can be leaked but otherwise designs keep them well contained. Anti-fouling paints are used, albeit limited to the most environmentally friendly; glass, copper, or PTFE based. The decommissioning process is competitively fast and leaves minor changes to the local environment.

The threat to marine life is often considered low, though this factor is often the cause of much concern among the technology's critics. The rotational velocity of hydro turbines, since producing energy form a denser flowing medium, is generally low in comparison to that of wind turbines, with designs performing tip velocities around $12ms^{-1}$. A typical tidal stream turbine will absorb $\approx 4KWm^{-2}$, if put in comparison to a ship's propeller which can exert $\approx 100KWm^{-2}$ on the water column, the effect is minute and less likely to be a threat in comparison to other said threats which are currently prevalent in the worlds ocean waters. A directly linked aspect is the underwater noise, which again is low in comparison other marine craft. The low speed also helps to reduce cavitation effects [88].

For tidal stream turbines to be functional, they are restricted to water flow rates in excess of the design minimum requirement. This functional limitation is the primary constituent to the main drawbacks of tidal stream technologies; being the limited number of potential sites with high flow rates for the turbines to be deployed. Open water tidal flow velocities are too slow; low velocity tidal concepts do exist, which would at first seem to address the issue providing access to a greater range of deployment zones. However, the crux of the issue comes down to the energy density and consequentially economic feasibility. The low velocity concepts have capacities rated in the kW, while the conventional turbines that are currently deployed are in the MW [69]. However, there are numerous places along the coastlines where the geometry of the landmass, in conjunction with the seabed, are able to constrict water flow and induce local acceleration's - as a product of continuity. Characteristic areas include; constrained channels, islands or headlands [79, 80]. These areas can commonly produce water velocities in excess of level required for feasible tidal stream generation.

Current operational commercial turbines require flow velocities in excess of $2ms^{-1}$, Though several axial-flow turbines in academic development are capable of operation in flow velocity's $< 2ms^{-1}$ [210].

It is often the case with sites which possess suitable flow velocities, that they are often situated in close vicinity to rocky coastal features which present a serious risk for water-craft. A 'flip-side' to that aspect is the same areas are generally avoided by other commercial craft; preferring to operate shipping lanes in less hazardous waters, and hence the installed turbines will not likely pose significant disturbance to potential shipping traffic. Though where the two are likely to be in close proximity, there is potential to design protruding features, which can be fitted with smart navigation aids or guidance lights. Thus, possibly provide a platform to enhance navigation in hazardous waters rather than being a hindrance.

There is also reasonable suggestion that if the array will pose a risk to shipping, which will subsequently be prevented from entering the area. To create fishing exclusion zones in the vicinity of the array, and provide a protected habitat for certain species.

Pentland Firth, UK, has been touted as one of the most promising sites for the tidal stream development with current estimates putting the power potential somewhere between 1-18GW [79, 70]. Though said estimates have been questioned and alternative sources have put the estimate around 1.9GW [3]. Other suitable sites around Anglesey, the Channel Islands, the Isle of Man and Pembrokeshire.

Current statistical data presents the axial-flow turbine concept (turbine rotational axis parallel to the fluid flow direction) as the preferred option to convert hydrody-

namic flow energy into mechanical energy, and as of 2016, axial-flow turbines currently makes up the majority of the worlds electricity production with a 90%; when combining the energy generation from fossil fuel, nuclear, geothermal, biomass, hydro and wind resources [146]. As of 2008, Marine Current Turbines (MCT) have inserted a SeaGen device into the waters off Strangford Lough, Northen Ireland. The device was the first commercial tidal turbine installed and connected national grid. The device has an rated power of 1.2MW and an expected operational lifespan of 20 years [69]. An example concept of the device is shown in figure 1.2 twin 16m diameter bladed rotors connected via a crossbeam which is able to be hoisted above the water line for maintenance.
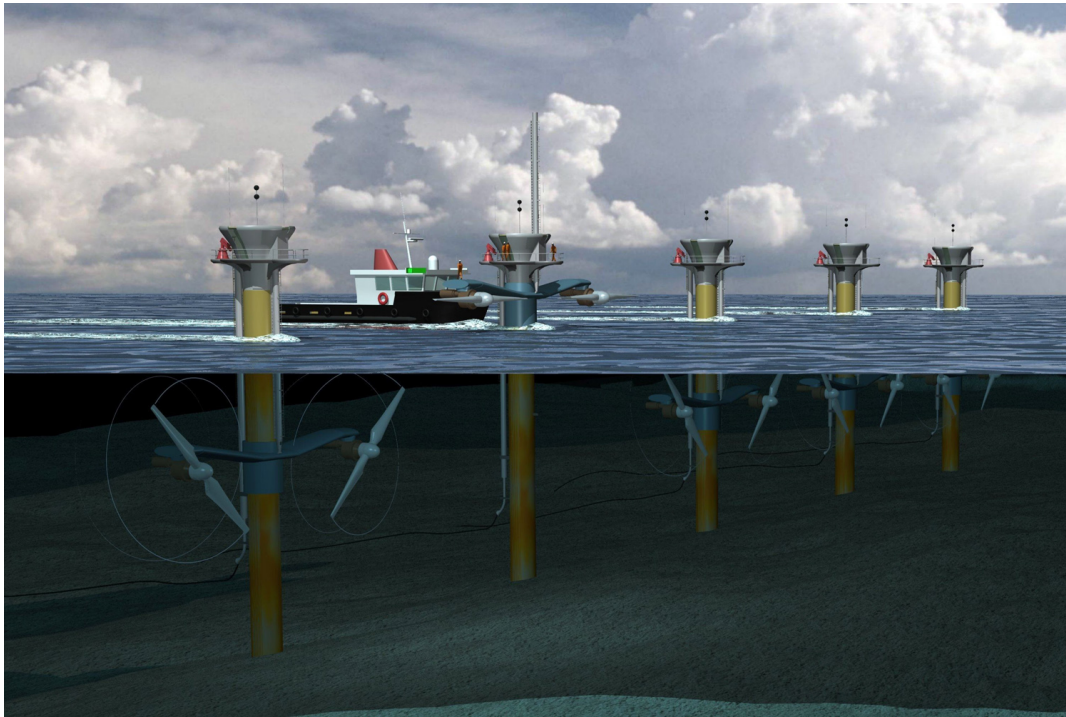
Figure 1.2: 1.2MW SeaGen array artistic impression [88]

The Implementation of turbines into the tidal stream will inevitably induce regions of reduced flow as a consequence of extracting the flow energy. localised regions of increased flow can also be formed from blockage effects [79, 187]. For tidal stream projects to be economically feasible, turbines will likely have to be situated in array formations. Fluctuations in the flow velocity perpetrated by the forward turbine rows will inevitably subject the subsequent turbines to different flow conditions. Thus also the performance of the turbine will be altered. Additionally, extracting more than 10-15% of the tidal stream energy for a given array will lead to a sharp diminution of the potential energy that can be extracted from the diminished flow velocity for each successive turbine in that array. If the performance of successive turbines in the array is reduced, the return on investment for each additional turbine will be significantly abated and potentially seen as a bad investment. Therefore, understanding the degree of which the flow regime is altered will be pivotal in developing array formations that are both financially attractive for investors and optimal for energy extraction from the water flow.

The incremental drop in extraction efficiency will have a bearing that produces a

seemingly self-regulating curtail on constructing arrays in excess of a critical point. Past such a point would bring the potential for greater environmental disruption while providing reduced returns for investors.

Altered flow regimes can also be considerable factors of influence on the natural sediment transport in the vicinity, potentially changing the morphology of sandbanks from their pre-existing states. Masters $et-al$ [153], noted the potential possibility of unforeseen damage to occur to the existing environmental state with turbine arrays installed. To avoid such occurrences, the current state of understanding must be improved. Since the Pentland Firth possesses a considerable portion of the UK's tidal stream resource, and currently in the process of deploying turbines. Martin-Short $et-al$ [149] argued that research into sediment transport around the Pentland Firth should be a priority to readdress of the current lack of knowledge.

Robins $etal$ [211] investigated smaller array deployments. He concluded that the effects of 10-50MW extraction was less than the natural variation. However an array size over 50MW could have a significant impact on the sediment transport. It was alluded to that the range of hydrodynamic, bathymetric and sedimentary properties between sites lead to the degree of impact being very much case specific. He also suggested that the implementation of 3D modelling could allow a accurate representation of energy being extracted from a select depth; allowing for more credible representation of the hydrodynamic effects. Neil $etal$ [170] showed that optimised positioning of turbine arrays could provide options, so that economically viable array capacities of 300MW could be situated over a headland sandbank, while mitigating impacts to the morphology of sandbanks.

1.3.2 Tidal Range

Ideas of harnessing the tidal range to benefit of society can be traced back as far as Roman era 'Britannia', with what is currently speculated to be a tidal-powered mill system [225]. Based on the same concept as modern tidal range systems. Utilizing the innate tidal flood flow to force water upstream, then create a hydraulic head through trapping the water on the ebb flow period. The water can then be released on requirement until the subsequent flood tide levels neutralise the hydraulic head. Like all early mechanical systems, the extracted energy was used to generate rotary motion; most likely applied to mill grinding stones, but could also be purposed for lumber, textile and mining operations [176, 113]. Modern energy requirements are vastly more complex than the formally required kinetic energy transformation. With the advent of electrical generation, and network grids; industry is no longer dependant on local energy resources. Thus, the modern era heavily utilizes electrical generation for its usefulness as a general utility energy resource. In line with modern requirements, the primary purpose of tidal range devices is for electrical generation, though secondary lateral purposes like flood prevention an estuarine road crossings are often featured.

The fundamental concept behind tidal range technology is artificially isolating a reservoir that is naturally subjected to a large tidal range, so that a hydraulic head can be produced between the natural tidal sea-levels and that of the reservoir. The flow of water is controlled through sluice gate operation, which act to create a substantial hydraulic head which can then be used to operate generation turbines. The current limitation to further commercialisation of tidal range schemes in the UK can

be largely attributed to the novelty aspect of such generation concepts. While the actual electrical generation aspect has a firm basis in mature and proven technology - tidal range concepts are thought to have a potentially significant impact on the local environment. A concern which is exasperated with the significant initial capital investment [272]. Few investors are willing to risk such capital on novel schemes.

While the potential power capacity of such schemes is proportional to the impounded volume of water, smaller schemes are being considered as they are more financially viable in the current political climate. Currently, several commercial enterprises are seeking a financially viable pathfinder project to validate the tidal range energy generation in the UK and thus pave the way for the larger higher capacity schemes. Previous coastal hydrodynamic research has consistently shown that tidal range impoundments can induce regional hydrodynamic regime alterations, with varying degrees on the sediment morphology, water quality and tidal water levels [268, 124]. Other factors will also contribute to the viability of tidal range schemes but are out of the scope of such work. Further reading on such factors can be found in C.Baker *et al* [24]. Therefore there exists an incentive to reduce the current uncertainties around tidal range schemes through giving possible insight into the potential environmental impacts.

There are three distinct generation cycles a tidal generation system can operate on. Flood-generation, Ebb-generation and two-way generation. Since an hydraulic head can be achieved on both the flood or ebb tides, generation can be also achieved on both tidal movements. Generation systems that achieve both are known as having bi-directional functionality. Each form of generation is outlined below, and A summative schematic diagram of each operational mode is shown in Figure 1.3.

- Ebb generation: water is channelled into a interior reservoir basin on the flood tide. On the high tide mark, sluice gates are closed so that an hydraulic head is formed between the reservoir and subsequent lowering sea-level. Some schemes utilize pumping for a short period to further increase the hydraulic head; with purpose of increasing the net power delivery. On the ebb tide, the turbine draft tube wicket gates are opened at the point where sufficient head to operate the turbines (H_{MIN}), then closed when the head drops below the head value again.

- Flood generation: On the onset of the flood tide, the wicket gates are kept closed until H_{MIN} is reached, then opened on the onset of which, providing generation until H_{MIN} level is reached. In contrast to Ebb generation, flood generation also occurs on both the flood and a part of the ebb tide periods. The sluice gates are once more opened after the sea-level equates to the reservoir level, allowing the reservoir to empty with the naturally receding tidal water levels. At the point where outward flow ceases from water level equilibrium, the sluice gates are closed. Pumping can then be utilised to further empty the reservoir so that greater hydraulic head can be achieved on generation.

- Bi-directional generation: Generational sequences on both the flood and ebb tides are similar to the flood and ebb only counterparts, though optimised for maximum net generation over both tide cycles. A consequence of which is that the tidal range within the interior is closer to the natural cyclic sea-level

16

range, and smaller power delivery for a single tidal period. The flood generation period begins after, scheme dependant, pumping and hold period. Since the reservoir is not emptied to the same degree as would be with flood-mode generation, the generation period is shorter and the sluice gates are opened closer to the post high-tide mark. After which occurs the pumping and holding periods until H_{MIN}, where the turbine draft tube wicket gates are opened for the generational period until H_{MIN} is reached on the turn of the tide.

A common trait with tidal stream is that emission profile is heavily profiled over the installation phase. Though the magnitude of the emissions is far larger. This is simply to do with the initial large amounts of construction materials such as steal and concrete; used to construct the breakwater, turbine housing and the turbines themselves [239]. However, tidal range projects have the potential to greatly surpass alternative tidal stream and wave proposals in renewable generation capacity and longevity. Thus over the long term potentially provide a smaller lifetime carbon footprint, greater generation capacity and longer lifespan.

While there are few established tidal energy projects where complete life emissions profiles can be established, parallels can be drawn with hydro power plants where more established profiles have been summarized. The larger structures involved with reservoirs can have substantially higher carbon footprints than the Run-of-river types.

The typical carbon footprint over life use is between $10 - 30 \, gCO2eq/kWh$, with a mean of $15gCO2eq/kWh$ and $< 5gCO2eq/kWh$ respectively for the two types, with [239, 262]. The run-of-river type often has some of the lowest carbon footprints of electrical generation methods, though the capacity capabilities of such projects are often smaller than their counterparts. The large footprint range for the reservoir type is due to the heavily weighted dependants on regional biomass characteristics and size of flooded area; alpine regions producing $< 0.5gCO2eq/kWh$ to peat soil regions reaching $30 - 41 \, gCO2eq/kWh$ [239, 91, 262]. When isolating emissions for the construction phase, carbon footprints range between $2 - 9 \, gCO2eq/kWh$ [239, 262]. Additionally, Van De Vate, reporting on the "Expert meetings on FENCH-GHG intercomparison" holded by the International Atomic Energy Agency (IAEA) states that hydropower probably has unrealistic assumptions for the emission profile from the reservoir [251]. IAEA provided recommendations for hydropower schemes to have 100 years operational lifespan[251, 91].

At the time of writing, it is unclear if there has been an investigation into whether potential tidal range schemes have the potential to release additional green house gas emissions related to biological decomposition. However, ebb-mode generation schemes that incorporate pumping sequences, exhibit higher water levels than the natural high tide water level. Thus will submerge additional land space, albeit temporarily, and possibly contributing to biological decomposition and release of green house gasses. Secondly, the bi-directional system would continually flood sections of land that would only naturally be flooded for cyclic intervals - altering the biomass' habitat and leading decomposition based green house gas release. Despite mentioning the possibility or biomass green house gas release from flooded land, the magnitude of such with respect to tidal range projects is far more comparable to the run-of-river schemes than that of large reservoirs. Therefore prudent speculation would draw closer comparisons to the run-of-river for operational emissions profiles and large impoundment structure types for construction emission profiles.
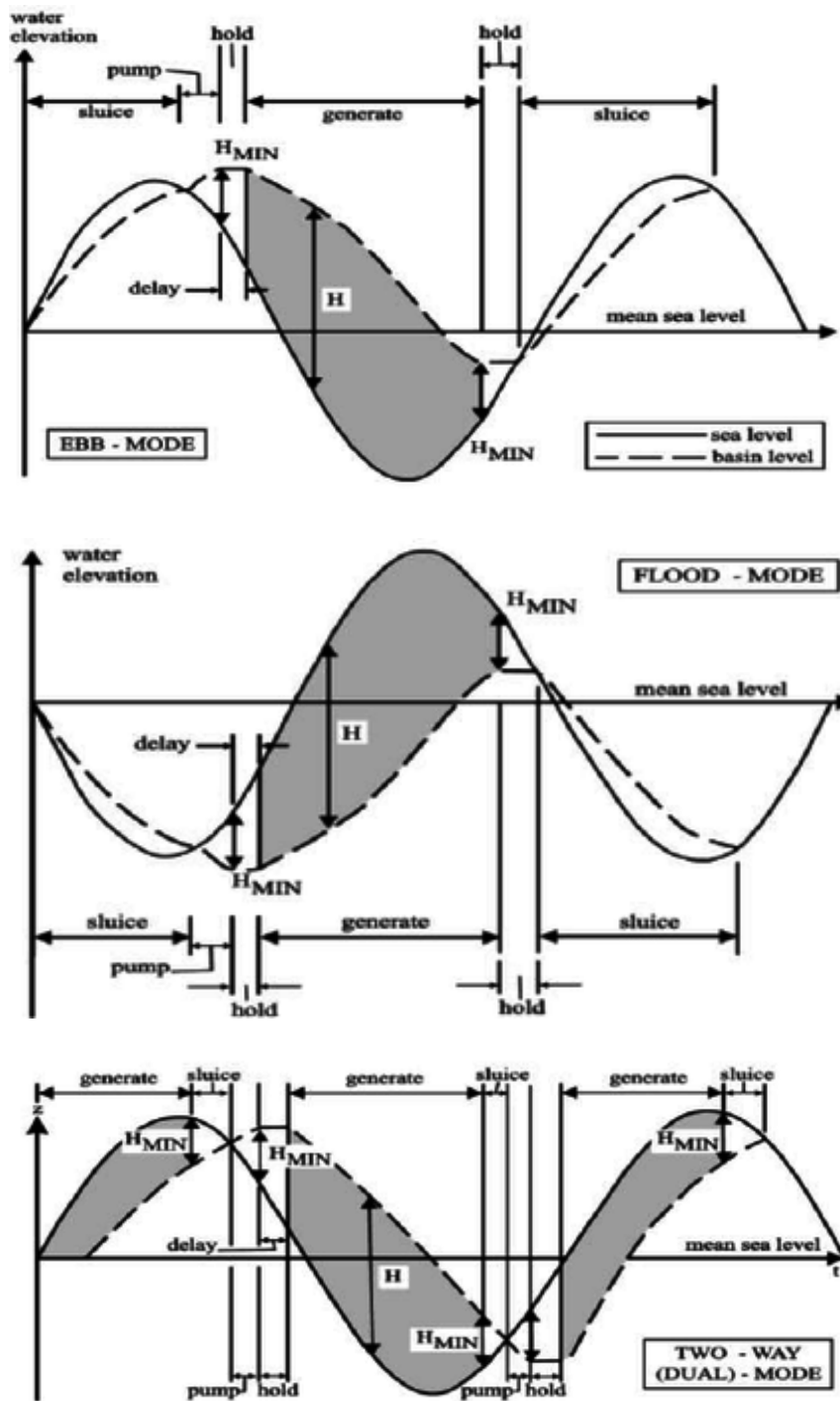
Figure 1.3: Graphical schematic of approximate modes of tidal range operation. The dashed line indicates the upstream reservoir water level, the solid line representing the tidal sea-levels. Energy generation capacity is proportional to the grey highlighted area. Ebb-mode is shown top, Flood-mode is shown middle, bi-directional is located bottom. [274]

When comparing to the Pelamis Wave Power device's life cycle assessment; which is speculated to be $24 - 30$ $gCO2e/kWh$ [234], and SeaGen tidal stream turbine 15 $gCO2/kWh$ with a life time speculation of 20 years [69]. It can be hypothesised that tidal range power schemes have the potential to supply large capacities for considerably longer operational life-terms, with emission profiles possibly lower than equivalent ocean energy resources.

Other advantages of Tidal Power, contrary to fossil fuel power plants, do not directly emit pollutants such as sulphuric dioxide and carbon dioxide from generation, which lead to acid rain, or any other waste products that need treatment. Neither is there any risk from large oil spills leading to disastrous consequences for the natural environment. Lastly, and with respect to nuclear - low predicted decommissioning costs, since the conventional structural demolishing methods can be applied without special treatment.

Figure 1.4: La Rance Tidal Barrage, France. Constructed in 1966 and capable of generating 240MW of electricity

In direct relation with the emission profile, tidal range projects posses large capital costs, that are disproportionately levied towards construction costs. The magnitude of the costs also depend on the size of the breakwater structure. A small tidal range project like La Rance was constructed between landmasses approximately 750m apart, requiring minimal breakwater construction and therefore lower capital cost [190].

Suitable locations for the tidal range schemes are often estuaries; which have natural large enclosed tidal areas. Under the natural state, the estuarine mud flats are cyclically exposed during the lower tide periods. If a tidal range structure would be installed, the water levels will be forced from the natural states. Creating a shock impact to the natural habitat for local and migratory birds; altering the exposure of the mud flats, thus disrupting the food resources usually depended on. Additionally,

Figure 1.5: Sihwa Lake Tidal Barrage, South Korea. Constructed in 2011 and capable of generating 254MW of electricity

several fish species can be prevented from migratory access [247, 124]. Installed structures can also alter the flow regimes, potentially creating increased flow rates which can lead to amplified erosion, shifting sand and mud banks; which can completely change the morphology of the area. Such cases can impact coastal shipping routes, where previous bathymetric charts would become outdated; forcing Hydrographic offices to re-map the local waterways to avoid cases of ship beaching.

However, the breakwaters can help to reduce flooding, allow greater access for water craft to harbours and the barrier can be used for additional developments; roads wind-turbines etc. For the tidal range projects to be feasible the impoundment barriers are large and take some extended time to construct. This factor develops concern for the environment where companies could rush the process; leading to a lack of environmental care in order to have the site operational and making money in as short a time period as is possible. Previously constructed sites like the La Rance in France had a substantial impact on the local environment. The long term reaction has been that a flourishing natural ecosystem has re-established itself. However, different from the natural ecosystem and slow to establish [247].

Several factors can seep into the development proposals of the tidal range schemes that can preclude development, even if the intended site characteristics theoretically suggest substantial generation potential. Environmental issues have played a particularly integral part in preventing large scale tidal range development plans from being approved [261].

Tidal Lagoons have several similarities to the tidal barrages, however, their structure does not use natural features to form an basin, but entirely consists of a man-made breakwater structure. The advantage with respect to estuarine barrages is the lower environmental footprint. With the concept being artificial, only limited by lo-

Table 1.2: Current Operational Tidal Range Schemes

Barrage Name, Country	Inauguration Date	Mean Tidal Range (m)	Submerged Area (Km^2)	Installed Capacity (MW)
La Rance, France	1966	7.9	43	240
Kislaya Guba, Russia	1968	2.4	2	0.4
Jiangxia, China	1980-1986	5.0	2	3.2
Annapolis Royal, Canada	1985	6.4	6	20
Sihwa Lake, South Korea	2011	7.8	23	254

cational tidal range; potential sites for schemes are more numerous. Thus, greater potential to 'cherry-pick' sites where there could be a lower environmental impact. The disadvantage being the higher capital costs in comparison to barrage schemes of similar power generation capacity [24].

The UK is home to some of the largest tidal ranges in the world. The largest single share being located in England and Wales, in the Severn estuary and Bristol channel, home to the second highest range in the world - producing tidal ranges over 12m [100]. If harnessed, a significant proportion of the national energy could be supplied from this predictable renewable resource [17, 210].

Eight sites have identified for possible large scale barrage installation, with a combined theoretical resource estimate of near 50TWh/yr. The locations were chosen as ideal sites since each location had the combination of a large tidal range, a geographic advantage; a large water basin could be created from a closed of 'bottle neck' in the natural landscape, and close proximity to main transmission grids. The sites; the river Severn, Solway Firth, Morecambe Bay, Wash, Humber, Thames, Mersey and Dee (in order of scale depreciation). Several smaller scale sites were also identified, though the sites suffer from a lack of economic advantage [24].

One proposed scheme is the Cardiff-Weston, Severn Estuary barrage. Speculated to have the potential installed capacity of 8.64GW and contribute 17TWh of electrical energy per year to the national grid [272]. When compared to predictive assessments of alternative tidal generation schemes in the Severn Estuary, the generation capacity can be over 50 times greater. Ahmadian *et al* [7] assessed the maximum available energy extraction in the same approximate location as the Cardiff-Weston barrage; with the highest estimated capacity being 154MW. Additionally, the estimated capacity is over 4.5 times larger than that of the theoretical maximum in the Pentland Firth [3].

The current global state of tidal range generation exists as five operational schemes Only France and South Korea having large capacity schemes (Table 1.2).

The largest is Sihwa Lake Tidal Power Station in South Korea, rated at 254MW. The scheme originated as a general purpose da constructed in 1994; holding a vast sum of water for irrigation and providing flood defences. Environmental concerns were raised when the water became too polluted to be safely used for irrigation purposes. A solution was found in a modifying the dam for a tidal range generation purpose, where toxic pollutants could be prevented from building-up with the additional bonus of generating clean renewable electricity each tidal cycle [23, 139].

The breakwater dyke is 12.7 km long and holds an 56.5km^2 lake. The turbine housing consists of 10, 7.5m, 25.4 MW 'bulb-type' turbines with a combined oper-

ational capacity of 254MW. The turbines are reported to be similar to the turbines installed in La Rance, France, but are modified for only flood-mode generation. Operating under flood-mode generational cycles has also allowed $173km^2$ of intertidal land to be reclaimed, which would otherwise be under water with other operational systems [23].

The Lake Sihwa Barrage has been considered an semi-successful project, with the initial objective of improving the water quality only being minimally improved, and has been noted as a clear example of how incorrect policies can lead to mismanagement of ecosystems and budgets [139]. However, the south Korean government are currently exploring the possibility of further sites such as the bays of Gerolim and Incheon [261].

The La Rance tidal barrage is the worlds first operational tidal range project, with construction having started in 1961 and becoming operational in 1966. The Barrage is a 720m long breakwater and holds back $22km^2$ of water. The turbine housing holds 24 bulb turbines, each rated at 10MW, giving an installed capacity OF 240MW [13]. At the time of construction, the barrage cost €95m, approximately €580m today [134].

The Barrage is operated with bi-directional as well as on-way operational cycles and can also use the turbines as pumps to improve the head difference [190] [13].

The design has several features which increase the barrages function beyond just power generation. A road along the length allows for the passing of up to 60,000 vehicles a day and a ship lock allows 20,000 boats a year to pass. The project has also proved to be a valuable tourist attraction and improved the local economy [134].

The project has been classified as a technical success, with as little as 1% production loss (as of 1993) with no major overhaul despite the severe operating conditions [90]. Environmentally the area is still a substantive habitat [134].

The Annapolis barrage, Canada, was constructed between 1980 and 1984 at the mouth of the Annapolis river, which flows into the bay of Fundy; which holds spring tides of 16m, the largest tidal range in the world [78].

The project was initiated as a pilot scheme to assess the potential of harnessing the tidal energy in the area and straflo turbine generation. Prior to the tidal plant installation, the estuary was closed of by a causeway intended to restrict the tidal flow further up river. The barrage traps $15km^2$ of water behind the causeway [19].

The plant is powered through ebb-only generation by a single 20MW Straflo turbine. The plant is also used for flow defence purposes as well as road way[19] [76]. The site has also been a noticeable source of attracting 40,000 tourists, engineers and investigators; interested in the technology for both a resource and investment [76].

Further development of tidal power in the bay of Fundy is currently being investigated. The two other potential sites for development are the Minas Basin and the Cumberland Basin [78] [216].

The Jiangixa barrage, China, was constructed between 1974 and 1985. The plant is China's largest, and the third largest in the world after La Rance and Annapolis [257]. The spring tidal range in the area is 8.39m [261].

The current installed system is comprised of 6 bulb turbines operating bi-directionally; producing an installed capacity of 3.9MW [257].

The Plant had considerable resources put into and advances in the industrialisation research, reliability, sediment reduction, protection form erosion, operating automation and optimal scheduling[257] .

The materials and technologies used in the project were entirely sourced form within China. The Project was also reported to of benefited the local environment and economy with improved fishing conditions [261][28].

The Kislaya Guba Barrage, Kola Peninsula Russia, was constructed between and 1968, then the USSR, to be the nations first tidal power plant. The project was took inspiration from the La Rance tidal barrage with the same bulb turbines, though adapted for being located in a harsher Arctic environment. The barrage is located between two cliff faces and is comprised of pre-fabricated sections that were assembled to span a narrow section of 40m. The tidal range in the area is 9-13m [46].

The Project was sanctioned to explore alternative energy resources to address the depleting natural resources of oil and gas. The size of the plant is the smallest in the world with a capacity of 1.2MW. The project has been regarded as a success and has lead to feasibility studies of larger sites in northern and eastern Russia. Two suggested sights are the Mezen Bay and Tugar Bay with installed capacities of 15GW and 6.8GW respectively[216][45].

Tidal range developments are a relatively newcomers to the renewable energy sphere, with only a handful schemes in place and in development. Tidal range generation has been hindered from greater development due to several holdbacks relating to costs and environmental footprint. Alternative concepts to the original barrage types, such as the lagoons, fences and reefs; have been put forward have been put forward to address environmental concerns, but have less attractive economic and capacity attributes [70].

Currently there is considerable developmental focus is on building a comprehensive basis, detailing the magnitude of the impact to the regional hydrodynamics of such schemes; which at this point, there is no widely accepted consensus. However, the potential to limit environmental impact has lead to an increasing interest in such lagoon developments; driving a recent rush in numerical analysis of such potential schemes. Thus, considerable focus of research is how tidal range structures will interact and potentially alter the natural environment, theoretical resourse potential and power plant optimization [172].

Angeloudis et al [17] simulated Tidal Lagoons in coastal models, with simulations involving the Swansea Cardiff and Newport lagoons in the Bristol channel and three Lagoons in north Wales. The models were discretised into an upstream and a downstream domain separated by a breakwater wall and open boundaries. The Turbine Housing (TH) (Figure 1.6) were described in the model through a source term in the open boundary related to a specific turbine performance hill chart and derivations of the orifice equations for both the turbines and the sluice gates respectfully. The flow is injected into the model across a single layer with zero rotation. The lack of any representation for the flow interaction with the scour matt at the base of the TH and the ensuing 3D turbulent mixing will likely produce a wake larger than what may be seen in both a physical model and the actual Lagoon turbine housing wake. An additional point concerning accuracy of the model is that the geometry of the turbines is not modelled. The flow out of the turbine is calculated by first principles (v=Q/A), with volumetric flow rates attained from hill charts used in [50], and the assumption that the TH draft tube is 7m in diameter along its entire length. The Swansea Bay Tidal Lagoon turbine housing design [240] is shown to have a turbine draft tube exit of 15m diameter. The water flow injected into the model is going to

be considerably higher than the actual water flows out of the turbine outlet.
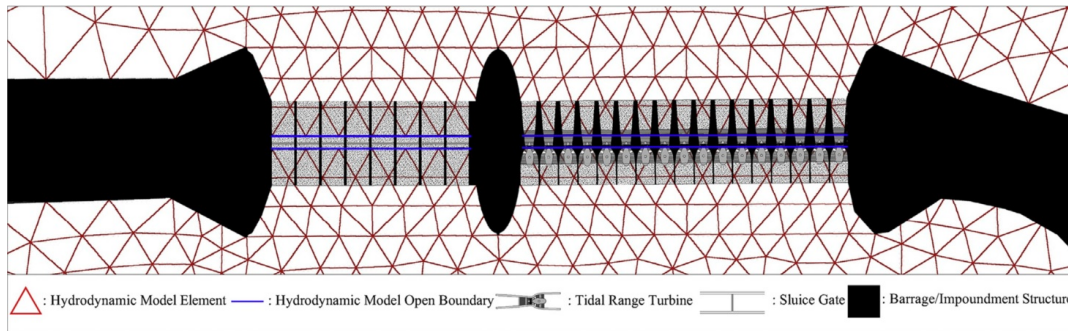
Figure 1.6: Overhead snap-shot of the Swansea Bay Turbine Housing geometry situated within a 2D model to simulate the effects of the released impounded water on both the flood and egbb tides. [17]

Jeffcoate et al [121, 119], completed a series of physical models which demonstrated the relationship of turbulent mixing and wake dissipation rate. The paper looked into how the velocity from a scale representation varies with depth and distance, and how well 3D software STAR-CCM+, produced by Siemens, replicated those results, when 2D depth depth-averaged modelling is justified and how the shear stresses on the bed varies along the downstream length through the 3D effects. The 3D simulation provided a reasonable similarity with the experimental results.

Socio-economic benefits through multiple use of space

Tidal impoundments are sometimes perceived as large monstrosities, completely disrupting the local aesthetics and providing little perceptible local benefit. While the generation of renewable energy is commonly regarded as a positive step forward and a worthwhile investment, there still can be an issue of reactionary response to development in the local area [53]. An artificially sheltered region, protected from waves and strong currents, can provide the basis for multiple commerce, environmental and recreational activities.

Tidal Lagoon Power put forth a report of the Swansea Bay Tidal Lagoon, with business propositions featured with proposed electricity production capacities [37]. Within Swansea, the existing visitor attractions bring in one million visitors each year.

From the 2015 Swansea bay visitor survey, the single leading draw to Swansea is outdoor recreational activities; of those surveyed, 59% cited they were influenced, and 35% said that the main draw to Swansea was the coastline/scenery available in the area, with 33% also listed low-level walking as the intended activity during their stay in Swansea. 57% listed the national waterfront museum as the specific draw to the Swansea city [144]. It could therefore be expected that a visitor centre located on the lagoon, with similar educational value as the museum could attract similar numbers. Other barrages such as the la Rance an attract a approximately 70,000 yearly [134]. Plans for boating centre, arts, cultural, sporting events are planed to take place and the breakwater to provide amenity value for walking, running, cycling and recreational fishing. Aqua culture spaces are also expected to be developed within the enclosed area. In conclusion, the intelligent multi-use of space can provide sustain-

able, long term benefits to the local population and help alleviate negative positions held against tidal range impoundments projects.

1.4 Scope of the Thesis

1.5 Raison d'Être

In 2012, Tidal Lagoon Power (TLP) proposed a series of ambitious lagoon projects along the Bristol Channel and Severn estuary, with an initial proposed path-finding project; the Swansea Bay Tidal Lagoon (SBTL). The SBTL consists of a 9.5Km U-shaped breakwater that is attached to the mainland at the Swansea docks and coastline adjacent to the Swansea University Bay Campus. A single turbine and sluice gate housing is located at the southern tip of the breakwater; fitted with bi-directional bulb turbines for both flood and ebb generation. The SBTL has an estimated 3-4 years construction time and £1.3 billion initial private capital investment. Once built, the SBTL has a 240 MW capacity, will produce electricity at similar consumer cost as nuclear power for the next 120 years [238] [189]. During operation, it is likely that dredging operations will need to be conducted to preserve the energy yield.

It is known that such schemes have numerous near and far fields effects on the marine hydrodynamic environment. The main cause of disruption is the potential for the tidal flow characteristics to be altered, creating shifts in the sediment transport regimes which were previously in equilibrium. These shifts can lead to both geomorphological and ecological changes along a coastline, therefore, consideration needs to be taken into account when converging on a final impoundment design and subsequent operation processes, such as the frequency of the dredging operations [124].

The proposed plan, schematically shown in Figure 1.7 is to install 16 conjoined, low-head, bi-directional Kalplan bulb turbines with wicket gates, and 8 sluice gates, into a structure of 410m in length and 45.5m wide. Each turbine will each be 7m in diameter. Greater detail of the lagoon design can be found through the design proposals from Tidal Lagoon Power [189].

Developments of low-head turbines have substantially opened up the potential of tidal range technology through allowing the resource to be extracted an numerous sites [46].

Large eddies and vortices are predicted to be induced by the high turbine density along a single section of the breakwater wall- for both the tidal ebb and flood, inside the tidal lagoon basin. These strong re-circulating currents are likely to re-deposit sediment, which may prompt sequential dredging operations [17]. If the turbines were spread around the perimeter of the lagoon, the likelihood of strong eddies forming is greatly reduced. This would likely come at a reduction of the lagoon commercial viability [210].

Hence the development of tidal range projects can be greatly assisted by the use of numerical models to simulate the coastal hydrodynamics around the hydraulic structures; allowing the project development teams to attain a greater understanding of the multiple interacting processes which will likely occur. Consequently, a con-
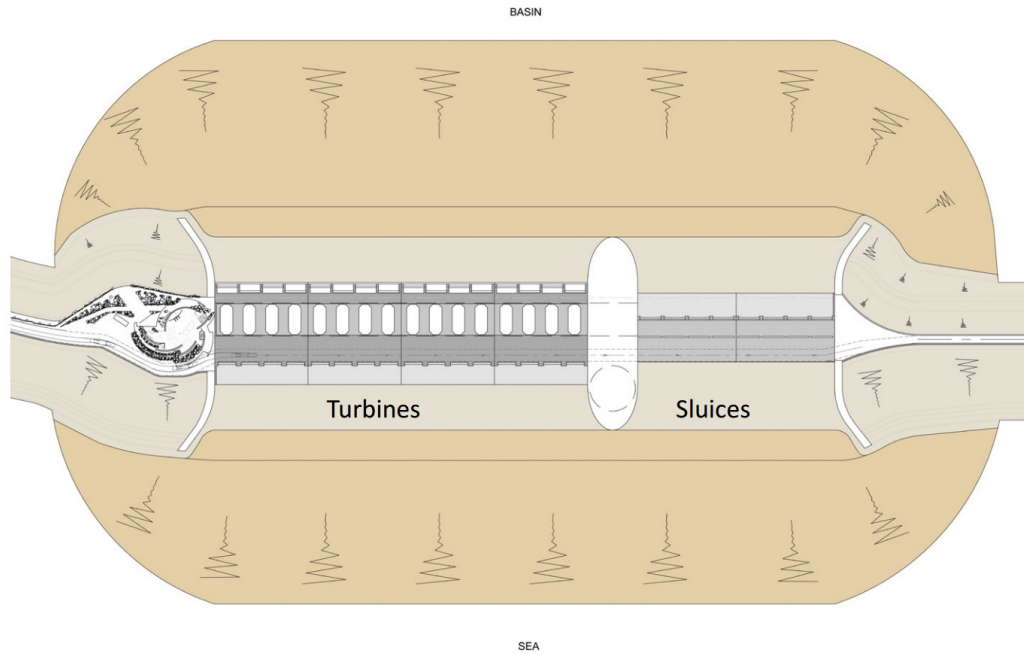
Figure 1.7: An to scale schematic diagram of the Swansea Bay Tidal Lagoon's turbine housing - as featured on the TLP proposed plan [189]

siderable amount of money can be saved and potentially catastrophic errors avoided.

The current coastal models implement 2D numerical models using the Shallow Water Equation's (SWE) over areas ranging a few kilometres to encompassing entire oceans, and simulated over extended time periods - a couple of weeks to years. An example of the current tidal 2D SWE models of the Swansea tidal Lagoon, constructed by Cardiff University can be seen in Figure 1.11a. The SWE are not apt at describing smaller details, such as features with dimensions of only a few meters or time periods of a few seconds, like the complex flows through hydraulic structures. Currently the hydraulic structures are implemented into the 2D with derivations of the orifice equation or hill charts, though those methods only provide an estimated approximation.

Computational Fluid Dynamics (CFD) can be used to provide substantially closer representation of the complex water flow through hydraulic structures and the subsequent wake. The small length scales common in CFD simulations enable high geometric detail simulations involving complex fluid-flow dynamics. CFD models are computationally intensive and impractical to use on as large models; with simulation times small - typically over a few seconds.

The project focused on improving the representation of the hydraulic structures by developing a nested multi-grid model. A CFD parametrised sub-grid model will accurately describe the complex flow through the hydraulic structures. The sub-grid model is then nested with a larger SWE model, which simulates the continuation of the flow and the far-field effects. The grids interact through an exchange in velocity information at the interface. The initial proposed strategy is to compute the CFD in advance and use this as lookup data in the SWE model to improve computational efficiency.

The numerical models were to be validated against known tidal data, laboratory experiments and the Swansea Lagoon path-finding project. However, Tidal Lagoon

(a) Flood generation cycle   **(b)** Ebb generation cycle
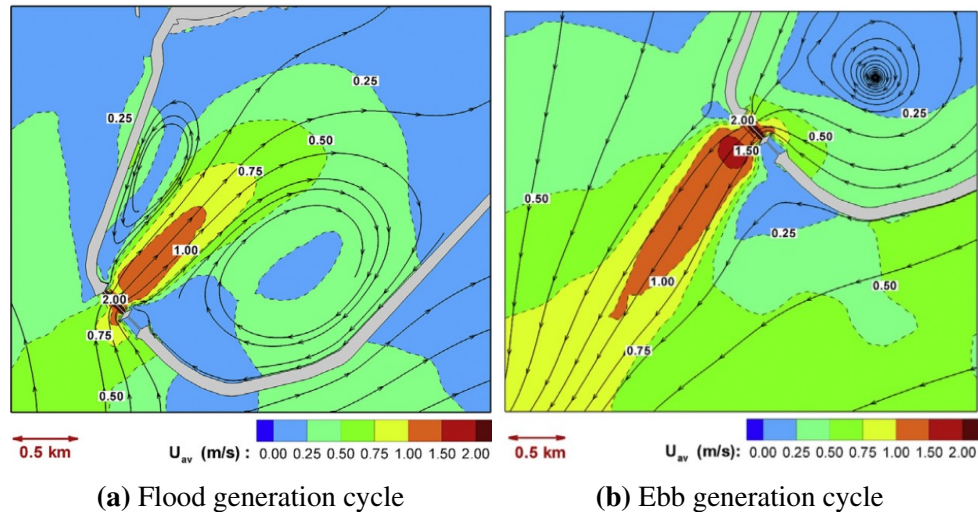
Figure 1.8: 2D Hydrodynamic modelling of the turbine wakes and the subsequent flow structures both inside and outside of the Swansea Bay Tidal lagoon breakwater [17].

Power Ltd were unable to come to an agreed energy strike price with the UK government; which lead the Swansea Bay Tidal Lagoon project to be shelved for the foreseeable future.

1.5.1 initial

This research covers two distinct project scopes. One in partnership to Tidal Lagoon Power Ltd; covering numerical modelling of the Swansea Bay Tidal Lagoon. The second revolves around developing CFD parameter based coefficient profiles; where the end game is for the GAD system to better represent realistic hydrodynamic characteristics of tidal stream turbines *in-situ*.

The main scope of this thesis is on the development of tidal lagoon power plants through improving the representation of the lagoons in SWE coastal models.

The development of tidal Lagoon projects are greatly assisted by the use of numerical models to simulate the coastal hydrodynamics around the impoundment structures, allowing the developer to attain a greater understanding of the processes which will likely occur, consequently, the developer can save a considerable amount of money and avoid potentially catastrophic errors. The current coastal models implement 2D numerical models using the SWE's over areas ranging a few kilometres to encompassing entire oceans, and simulated over time periods, a couple of weeks to years. An example of the current tidal 2D SWE models of the Swansea tidal Lagoon, constructed by Cardiff University can be seen in Figure:1.10. The SWE are not apt at describing smaller details, such as features with dimensions of only a few meters or time periods of a few seconds, like the complex flows through hydraulic structures. Currently the hydraulic structures are implemented into the 2D with derivations of the orifice equation or hill charts, though those methods only provide an estimated approximation. Without taking into account the complex 3D flow structure that will inevitably be present in the exit flow, an accurate prediction of the wake impact cannot be truly achieved and used to inform decision making regards

Figure 1.9: Schematic of the proposed Swansea Bay Tidal Lagoon. The turbine housing region is highlighted as the area of interest; with the area consisting of all the turbine draft tubes and sluice gates.

to policy.

CFD can be used to provide substantially closer representation of the complex water flow through hydraulic structures and the subsequent wake. A CFD model of three tidal stream turbine wakes are shown in Figure:1.11(a). The small mm sized cells allow for high detail, complex flow simulation with run times typically over a few seconds. CFD models are computationally intensive and impractical to use on as large models.

The project focuses on improving the representation of the hydraulic structures by building a nested multi-grid model. A CFD parametrised 'sub-grid' model will accurately describe the complex flow through the hydraulic structures. The 'sub-grid' model is then nested with a larger SWE model, which simulates the continuation of the flow and the far-field effects. The grids interact through an exchange in velocity information at the interface. Figure1.11(b) shows an initial trial of this approach, where the CFD model for Figure1.11(a) is the white spatial area nested in the SWE model. The initial proposed strategy is to compute the CFD in advance and use this as lookup data in the SWE model to improve computational efficiency. The numerical models built will be validated against known tidal data, laboratory experiments and eventually against the Swansea Lagoon path-finding project.

(a) Flood water flow rate 1 **(b)** Ebb water flow rate 2
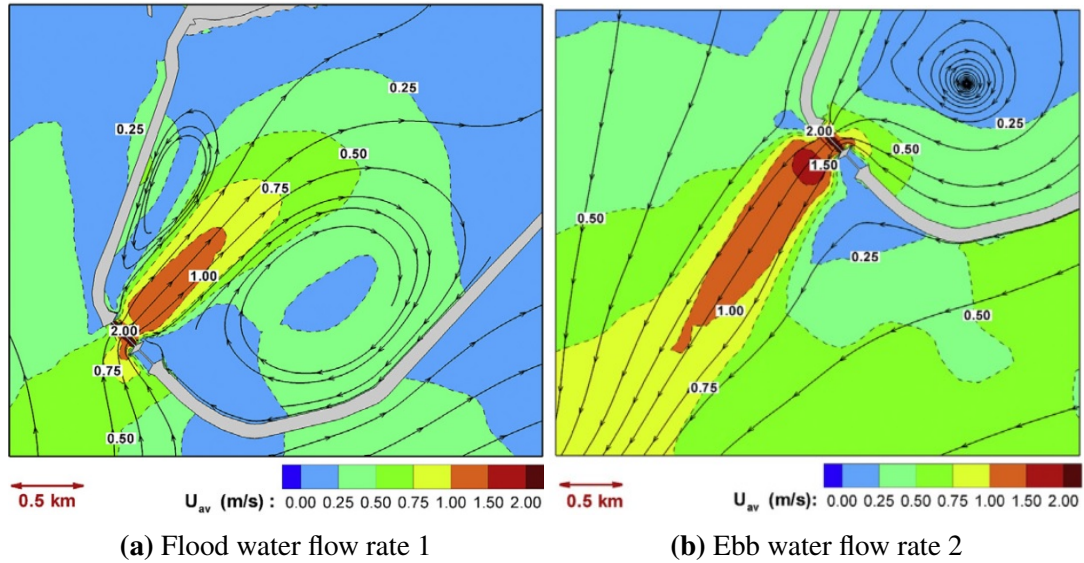
Figure 1.10: Cardiff University approximate model of the turbine wakes and the subsequent vortices of Swansea Bay Lagoon [17].

The CFD software to be used to model the turbine housing is open-source software, OpenFoam. The SWE software to be used for the coastal model is also open-source, Delft3D. The software choice was primarily selected for compatibility purposes with TLP.

1.5.2 SBTL Project Scope

This thesis part contains work centred around commercial and academic partnership, with Tidal Lagoon Power Ltd. The project was based on providing an academic numerical modelling perspective, to the otherwise industry-led development of the Swansea Bay Tidal Lagoon concept.

The main objective of the work presented in this section is to provide CFD analysis of the Swansea Bay tidal Lagoon over both larger and smaller scales. As such, this part will be split up into two distinct modelling sections of covering each respectively:

- Far-Field Modelling - Section 3
- Near-Field Modelling - Section 4

The Far-Field Modelling Section 3 covers the development of an 2D hydrodynamic ocean model to simulate the hydrodynamics' forced from Far-Field tidal movements. Emphasis is given to determining model artefacts than the near replication of the tidal velocities and tidal water levels. The aim is to form an initial single model which spans out beyond the continental shelf to achieve a boundary independent replication of the tidal flows. In doing so, produce reliable approximate tidal timings in Swansea bay and other possible locations around the UK. The model is set to be computationally light for simulating the expanse, yet retain refinement for the Severn Estuary to provide initial estimates to the local hydrodynamics. The temporal and spatial sea water assessment across the grid nodes can then be used to provide initial parameter data for boundary conditions Nearer-field CFD models.

29
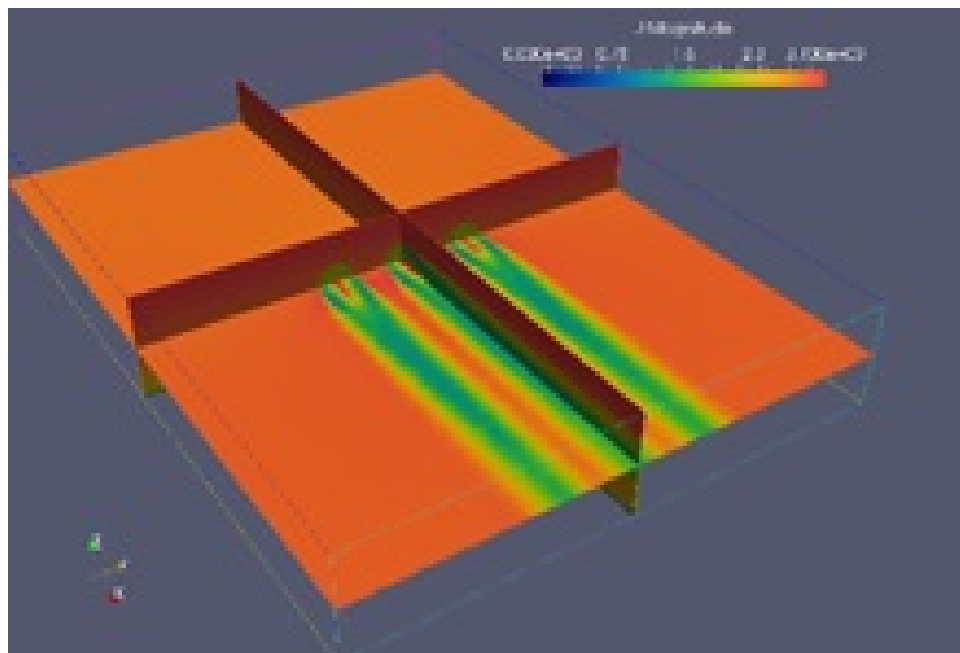
(a) 3D CFD
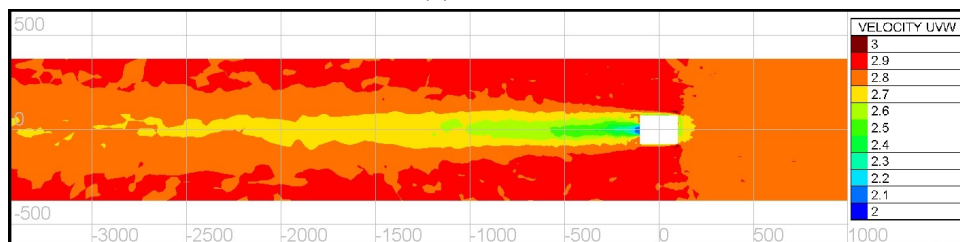
(b) SWE source term

Figure 1.11: Two distinct methods of implementing tidal stream turbines into CFD models.

The Near-Field Modelling Section 4 addresses the smaller scale 'Near-field', which can be arbitrarily considered to relate to areas within 20km of the feature of interest. Thus, will encompass the following sections:

- Simplified Turbine Draft Tube 3D analysis.
- Turbine Housing 3D analysis.
- Breakwater & Turbine Housing 3D analysis.
- Comparison between 2D & 3D turbulent cascades.

The Process is set-up to be sequentially developed with increasing complexity - so as to isolate how single geometric features influence the system. Firstly, the turbine draft tube flow is analysed in singularity, before being combined and then interacting with additional geometric features of the Swansea Bay Tidal Lagoon. The aim is to replicate the complex 3D hydrodynamics of the jet-jet profile that will likely exit from the Swansea Bay Tidal Lagoon into the near-field environment and analyse the interaction. The approximate downstream length required for the 3D turbulent velocity structures to dissipate, so that no concernable vertical velocity stratification is present, is also investigated. The findings enable the sub-grid domain sizes to be determined - where the downstream boundary is positioned for effective
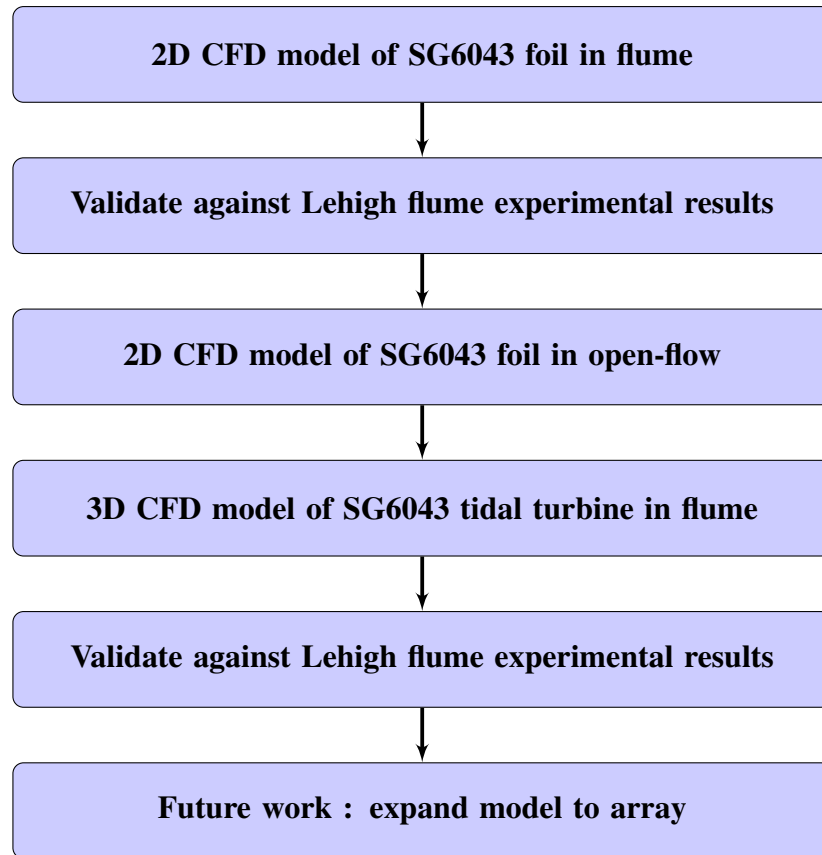
Figure 1.12: Breakdown of the Far-field model development milestones for building model.

parameter transfer between the 3D and 2D models. Additionally, the 2D model-equivalent geometric structures are modelled to analyse the equivalent downstream cascade and how capable the SWE model is of simulating jet-flow and the required mesh resolution to do so.

1.5.3 GAD Project Scope

The main objective of the research presented within Part III seeks to contribute to the development of Horizontal-Axis Tidal Stream Turbine (HATST) CFD analysis Methodology, through contributing to the development of the Generalised Actuator Disk (GAD)-CFD method. The Impact of which will work towards addressing the limitations currently faced with modelling HATST arrays, with current Computational Fluid Dynamics (CFD) solvers.

This investigation aims address said issue through establishing a comprehensive analysis of the hydrodynamical characteristics of the flow around the SG6043 hydrofoil at various Angles of Attack (AOA) when operating under flow conditions of various Reynolds numbers, Turbulence Intensities and foil surface roughness'.

The research will then be combined into the main body of GAD-CFD developmental research.

The work is split between two distinct modelling research bodies:

- 2D SG6043 Performance Parametrisation
- 3D GAD Flume Experimental Correlation

The 2D SG6043 Performance Parametrisation chapter will present research covering the performance analysis of the SG6043 foil profile through utilising 2D CFD techniques.

The SG6043 performance parameters will be validated against experimental flume data provided by Lehigh University.

The comprehensive mapping of lift (C_L) and drag (C_D) coefficient datasets for divergent fluid flow conditions can then be contributed to the GAD-CFD model.

The 3D GAD Flume Experimental Correlation chapter utilises the resultant coefficient data-set from the previous chapter through, inclusion into the GAD-CFD model. Where previous results can be compared to the updated version.

Chapter 2

Computational Modelling - Underlying Theories

2.1 Fundamentals of Numerical modelling

The previous chapter introduced the current climate situation and several approaches the engineering world can develop to help combat climate change; with heavy focus on tidal energy electrical generation. This chapter focuses on the computational modelling aspect of tidal energy electrical generation. Providing a brief introduction to basic concepts and methodology, before going into deeper areas relating to computational modelling applicable to both tidal range and tidal stream energy generation technologies.

2.1.1 Computational Method Background

CFD is the analysis of physical systems involving material of a fluid state, the transfer of heat and additional linked processes through use of computational software. While being a relatively new area, coming into use with the advancement of computer science capabilities through the 1980's and 1990's; There are corresponding 'teething' issues. In today's world CFD is increasingly becoming a go-to component in Research and Development (R&D) processes in both the industrial and academic worlds.

The continuous developmental aim of CFD research is to provide capabilities comparable to other means of scientific measurement, though bare distinct advantages. When such developmental capabilities mature, synchronous with the state of computational hardware progression, CFD will be able to create research scenarios previously unattainable to all but the most well-funded programs.

One such advantage of using simulations is to gain an insight onto physical characteristics and to record experimental data without investing in an expensive and time consuming full scale physical model. The absence of any type of model means a risk of developing a project/system with limited evidence on how it will behave, leading to potential outcomes that can be expensive, dangerous or time or consuming even all three.

Since the onset of what can be colloquially referred to as the digital revolution, with CFD and FEA methodologies coming into wide effect and acceptance in advanced engineering purposes; challenges that accompanied development tasks that once took extended periods and expertise in a specific field to complete were nullified. Engineering became less specialised and available to a larger base of people. Additionally, large data could be easily stored, transported, and accessed across the globe at a figurative 'click of a button'. To conclude the digital revolution drastically boosted productivity and capabilities, through efficiency and ease of access.

While the introduction of computational numerical methods has given the modern engineer a greater reach and capability, issues have been seen with general antipathetic nature of older generations stuck with older, proven methods. Additional concerns have also arisen regarding how these new systems, that are increasingly becoming common place in the commercial world, will be managed and the data secured.

The main industrial benefit for utilising computational simulations is that they reduce the requirement to build and test prototypes; a costly and time-consuming process. While simulations cannot ever fully replace prototypes as they require validation against a baseline, they can be used to tweak aspects of a design without pro-

ducing additional prototypes and provide greater insight on what effect those tweaks will have to the system.

The current state of the discipline often requires what is being simulated, to be simplified for a numerical result within the time restraints. Model simplifications are applied where there will be the greatest savings in terms of computational intensity, but with minimal influence on the research outcomes. The line of which is often difficult to substantiate by CFD methods alone. Thus, it is common for results with decreased realism and numerical uncertainties to be present. This limitation is systematically addressed through comparisons with other measured data produced through the application of more mature methods. Though, experimental and simulation data sometimes does not agree; this does not necessarily mean either is wrong. There are tolerances on measuring equipment, numerical error and simplification assumptions that will cause recorded data to deviate from the 'actual' true value. Data from simulations is more often used to provide insight on trends rather than accurate values.

Despite the current drawbacks, the use of and acceptance of CFD tools have become widespread, with several commercial and open-source CFD solvers available. The complexity of working with such tools has also lead to the availability of contractors, that are well versed with applying CFD solvers, and generating an accurate result within timescales required with fast paced commercial projects.

The CFD solvers available for research are continually refined with releases of updated versions and patches. Each successive release aims to further the CFD tool towards a conceptualised perfect scenario, where the solvers are able to truly mimic the physical complexity of the fluid dynamics around 3D, real world structures.

In current practice, CFD models cannot fully capture the full physics, rather the most dominant factors. Different solvers being better suited to model different physics creates a consistent scenario where there is next to always a trade-off when selecting a particular solver.

Experimental testing can be grouped into three distinct umbrella categories:

1. *in situ* deployments

2. Laboratory experiments

3. Computational experiments

Each of which could be placed on a conceptual continuum positioned respectively. On one end, the *in situ* deployments with typical characteristic traits of producing data with respect to the most true and often complex conditions. However, placing prototypes *in situ* is contemporarily the most resource expensive. Additionally, legality considerations also play a considerable role in how *in situ* testing is conducted. The other end of the spectrum lies the Computational experiments; with traits that almost antithetical. Thus, the determination of which research route to undertake will come down to where on the continuum will there be the most advantageous trade-off with the realism of data and the available resources at hand.

Therefore, the method for each experimental route must be refined to provide the most accurate and reliable data for the least resources possible.

While CFD experiments, by nature, are less financially expensive and time consuming than *in situ* deployments and Laboratory experiments. This does not mean

that expenses are an irrelevant aspect. Fully resolved geometries are often considered computationally expensive, and thus often impractical for the purpose at hand. There is a limit to where CFD could be perceived as a worthwhile investment at this current point in time. Contractors may not see the benefit of investing in research, that is of a lower accuracy and confidence than what can be achieved through other experimental routes. This unless there can be considerable resource savings and potential upscaling of features that cannot be achieved through any other experimental route.

Thus, simplification techniques are developed concurrently with the solvers to push the continuum to maximise the accuracy of results while reducing the computational expense.

2.1.2 Procedural Steps

The goal of numerical modelling is quintessentially that of mimicking real world phenomena. For this task to be accomplished, numerous successive actions must be taken, with each requiring the correct application of the former to have been completed. The process can be broken down into distinct procedural steps; discretely describing how to go from conception, construction, processing then post-processing to finally achieve the goal. The process is schematically shown in Figure 2.1 which has broken down the steps into distinct major sections, each with further sub-divisions.

The first step in the process is that of conception. The real world phenomena has to be identified, then the question of what can be gained from modelling the phenomena has to be made. This process concludes in defined objectives that will be required to reached in order to fulfil the purpose. The next stage is constructing a Conceptual model ie acquiring the necessary resources. The initial step is to undertake a formulation of relevant technicalities from available sources. This comes is the form of datasets and technical expertise and if necessary, from additional experimental investigation into the phenomena in question. The sourcing of technicalities should have revealed the relevant variables and parameters and thus can be tied together through mathematical formulation; based on either the fundamental theoretical laws or empirical principles. The outcome should result in the specification of the 'Governing Equations'. In the simplest case, will consist of single formula, but more generally should consist of a series of equations.

The geometric entity about which the physics is to be modelled requires the digitalisation of the object geometry. This is generally done through CAD software. The formulation of the 'governing equations' often reveals key insights into necessary geometric aspects. Often for simplification purposes, a complete rendering of geometry can be reduced to simplified forms, while still providing reasonably equivalent representation. This includes the spatial dimensional characterisation. For example, aerofoil performance can measured through 2D analysis of the cross-section rather than the 3D representation required for equivalent analysis with physical experimentation. The size of the domain is often dictated by the scale of the geometry that is intended to be modelled with. When simulating stresses through solid objects, the model domain is synonymous with that of the body geometry, which would be meshed. However, when modelling with fluids, the size and geometry of the model domain is antithesis to the object geometry. Thus, without additional boundary surfaces, the model domain would expand indefinitely. Typically through an iterative
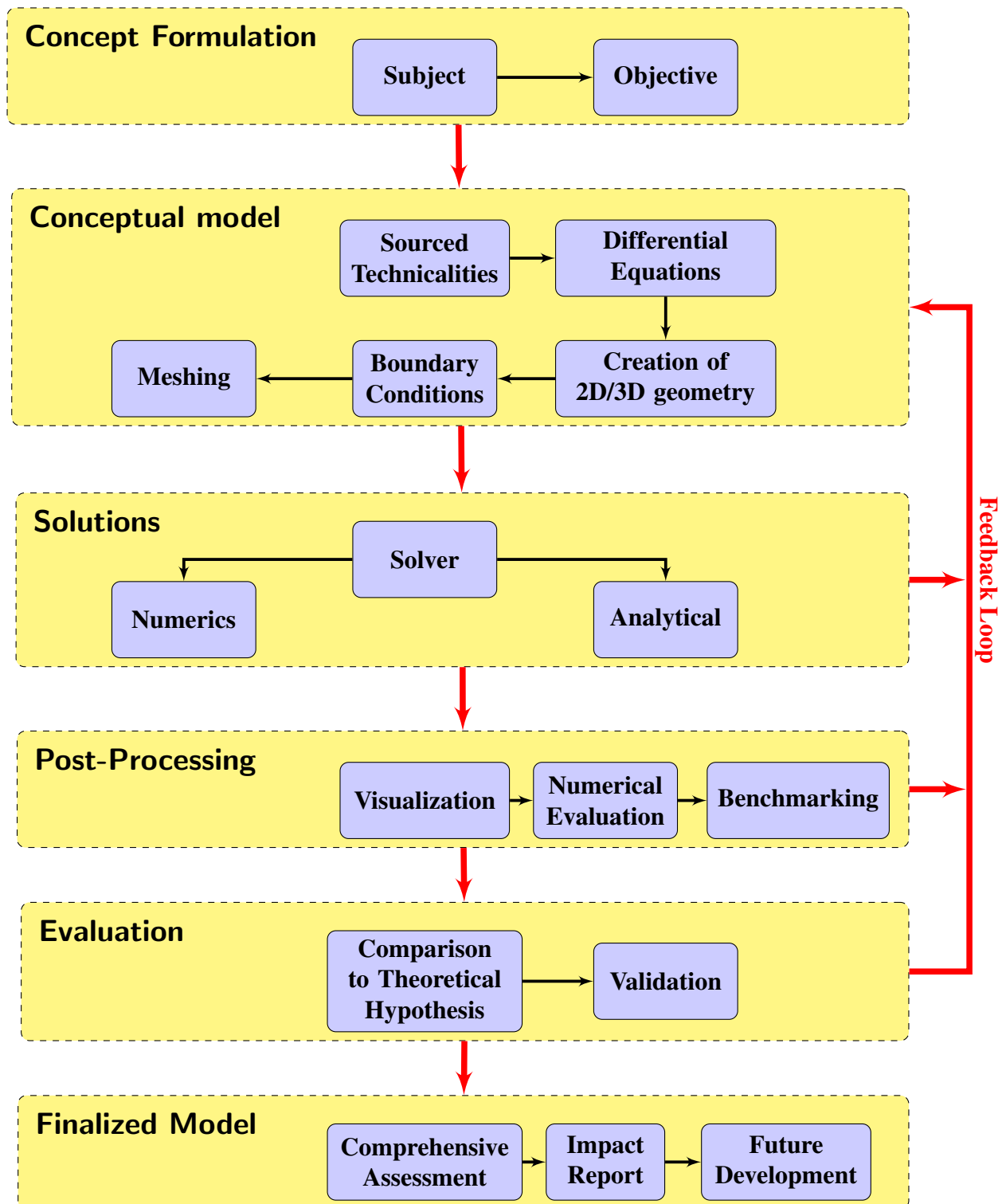
Figure 2.1: Breakdown of procedural steps required for the modelling process. Major sections are distinguished through yellow background and the process path dictated through red arrows. Each major section is further sub-divided into discrete considerations distinct from each other.

approach and a basis in sourced technicalities, the computational domain can be established. The boundary conditions can then be specified, accompanied by the initial conditions; thus completing the models mathematical formulation.

Lastly, the domain is most often discretized in to a grid or equivalently a mesh, but can be meshless and only requiring 'clouds' of points, upon which the governing partial differential equations are discretized. The process involves defining structures within the domain and forming a mesh of suitable quality. Often measured in terms of orthogonality, relative spacing and skewness. For optimization purposes, the mesh is typically refined and coarsened in accordance to areas of interest or regions where there will be significant variable gradients. Thus, the meshing process often is heavily weighted towards aspects like geometric bodies - which will alter the variable regime. Within CFD, additional considerations towards boundary layers are often made. Many solvers offer wall-functions, which predict the boundary layer over a cell, thus enable the mesh to be coarser near surfaces than what would would be needed if the boundary layer was to be fully resolved.

The differential equations are solved with computational solvers. For simple cases, solutions to the differential equations can be found with an analytical approach; where exact solutions can be calculated. However, for most problems the differential equations must be solved through using computational numerical solvers. These work to find an approximate solution under several tolerance parameters. Solvers are typically complicated, and in contrast to the analytical options, are typically implemented by the computational modelling software. Both commercial and open-source options exist to be utilised, each with considerations that offer potential suitability to individual cases. There is no single solver methodology; just multiple options that bear different principles.

Once computation has taken place, solutions from the solver must be converted into human understandable formats for interpretation. There is no set path to directly follow, however generating visual data can often provide a route to quickly assess the outcome of the simulation.

In practise, correct implementation is difficult to achieve. For example, the mesh often requires re-adjustments in order to ensure the accuracy of the results. Usually different grades of mesh are implemented over several feed-back loops, until the solutions reach a state of convergence.

Typically, the first feedback loop relates to how the software is implemented and involves testing the computation for errors in the output. Even if no errors are registered, smaller test cases can be set up to check if the output is correct. Typical methods of verifying the solution can from visual post-processing checks for any noticeable model artefact. Or simplified analytical solutions to provide ball park estimations. Testing solutions with other solvers can also be beneficial to the development of computational modelling as a whole. It is easy to get carried away with solutions that might appear correct when verified against other methods. However, other solvers working through alternative mechanisms can output similarly correct solutions. Objectively, neither solution is likely completely right or wrong; both being approximations. This process can typically be labelled as benchmarking. Since a numerical solution is found under tolerance parameters, often the model may require a calibration of those parameters to better suit the model to the application.

The solution then should be matched against the original set-out objectives and Hypothesis'. Should the objectives of the simulation be reached, the final step of

validating the data needs to be completed. Unless the solutions can be proved to be true, beyond reasonable doubt and research limitations; the data can carry little weight and be of limited use. The gold standard of validation is to replicate a real-world system to the utmost degree of accuracy. Typically from comparisons between computational and physical experimentally produced datasets. There are however limitations to degree in which the real world can be replicated - especially with complex systems. Thus there will always be aspects in which the model is insufficient compared to the real-world.

2.1.3 Simplification within Computational Modelling

As with every project, computational engineering projects are time, equipment and financially constrained. While simulations can greatly speed up the project development process and increase productivity, there are several constraints to the computational model development process:

- Unknown parameters.

- Unrealistic representation.

- validation.

In most cases, simulations can differ substantially from the experimental results, since there are errors in both the experimental measuring equipment and the numerical process. Simulations should be considered as an approximation tool to provide trends rather than accurate data. The reason for this comes down to assumptions made in the production of the model. The world around us has many highly complex processes that are very difficult to predict; as each aspect is dependent on multiple entwined factors. The magnitude and impact of each interacting factor in a very complex system is sometimes not always fully understood, which can inevitably lead to false modelling assumptions and ensuing deviations from reality. Additionally, complex processes are by rule of thumb computationally intensive. Essentially, only feasible when utilizing modern computational resources that are purposefully constructed to meet specifications for carrying out such tasks. For those reasons, simplifying assumptions and characteristics are often made when generating a simulation model.

Assumptions are made based on a relevancy order system, with the dominant relevant factors taking precedence over the minor. Additional factors can later be incorporated into a model to tailor the system to produce results of increased realism. Providing computational resources are available to account for the increased computational intensively that accompanies added factors. However, if the current assumptions are sufficient to address the goals of the simulation, additional complexity need not be added to increase the computational cost of the model.

Simplification of characteristics such as the geometry can be beneficial to developing and understanding phenomena that both numerical models and physical experimental models are trying to replicate. Simplicity allows repeatability and removes aspects of individuality that will be only present on a single specific case, thus providing a base in which the phenomena can studied in a generalised setting. Often

simplified geometry models of both numerical and physical are used in conjunction with each other for validation purposes.

Simplified models are used for engineering purposes where understanding interactions and their mechanisms are pivotal for concept development. One such is the effect of aerodynamic forces on road vehicles. The Ahmed body Figure 2.2 is commonly used as a simplified model to study such phenomena in the automobile industry [8, 140, 222, 226].
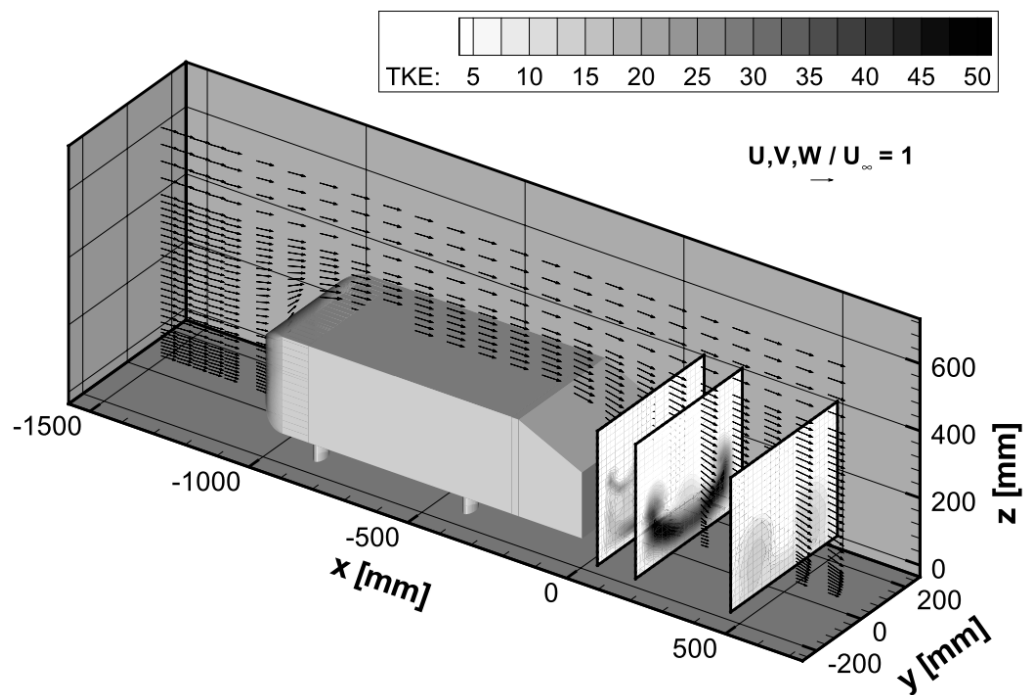
Figure 2.2: Example of a CFD TKE distribution along the Ahmed body [140]

Another is with how a fluid flow acts on a hydro/aerofoil structure. Continual development of such designs need to take advantage of advanced understanding of the complex interactions between the flow and geometry to improve the flow control and increase performance.

A common phenomenon studied when developing hydro/aerofoils is the vortex shedding phenomena; a dynamic oscillatory behaviour exhibited when a fluid passes around an object geometry. Cuboid and cylinders being simple shapes allow a generalised study of such phenomena, while each hydro/aerofoils design are bespoke by nature and often the geometry is a closely guarded commercial secret. There is little value of going down a specific route that cannot be widely applied or verified, while with simple geometry, the phenomena can be studied without complicating factors and a bench mark can be made.

Simplified, efficient models also owe existence due to the limited computational power available on a day-to-day basis for many projects existing in computational modelling. Large, full scale models may also not add further insight if uncertainties in boundary conditions are apparent. Simulations based research should not be assumed to be able to predict accurate absolute values, unless significant computational resources are expended, but can be usefully employed to provide enough accuracy and insight on trends at a significantly lower cost. Simplified models are

an extension of this principle, with further reductions in computational cost.

2.1.4 Computational Meshes Overview

The mesh or grid is a essential component of any computational simulation. The spatial domain under investigation is discretized during the construction of the conceptual model. Additionally, the mesh features in the post-processing stage, where during model visualisation, an over-layed mesh can aid in the understanding of the solution. Several different mesh constructions are categorised in computational modelling.

Computational meshes are categorised as either; regular (structured) or unstructured with a schematic example shown in Figure 2.3. The regular meshes are constructed by specifying the dimensions in a parametrisation of the global *xyz* coordinates.

The advantage of the regular structured mesh is that that the coordinates of the vertices are directly computed from the linear relationship between the parametrised and global coordinates and index 3D data arrays to store computed data. Performance wise, not requiring the storage of coordinate data and direct indexing, makes internal data acquisition very fast and reduces the memory load of the computed data.

The unstructured meshes are again a discretisation of the spatial domain through sets of irregular sized polygons. The usual polygon shape is either tetrahedron or hexahedron. The unstructured meshes vertex data and a connectivity list is required to describe each of the polygon cells thus continuously stored. In comparison to the regular meshes, more memory is required, and the grid cells often have large variance in size. The product of which is the ability to refine areas of the domain of high importance, such as areas which will likely exhibit complex flows, antipodally, can be coarsened in areas of lower importance or simplicity. Subsequently a mesh over a large domain can have a significant reduction of memory usage.

(a) *(b)*
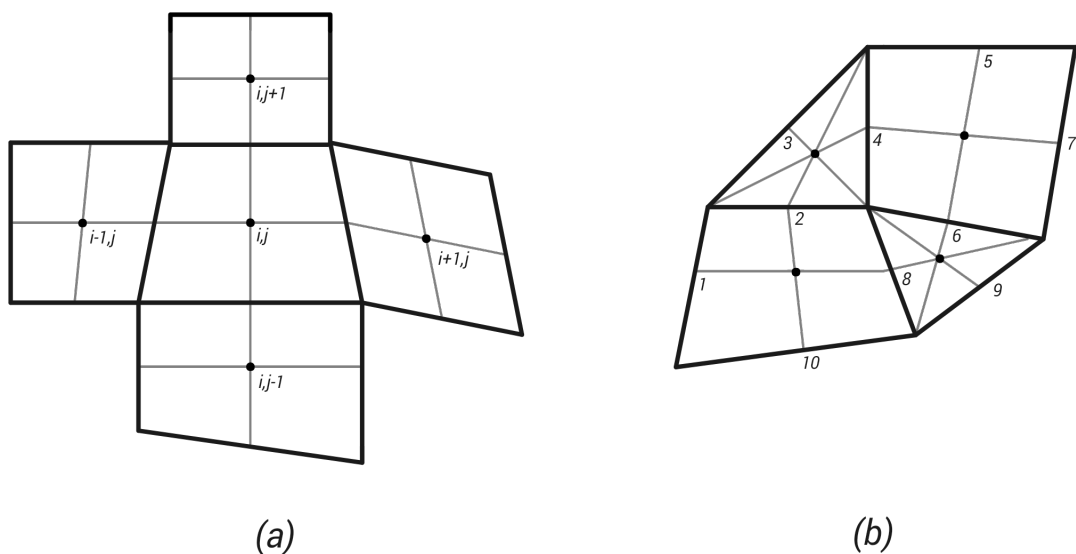
Figure 2.3: Schematic example of the differences between Structured (a) and Unstructured (b) meshes.

2.1.5   Mesh Sensitivity Studies

Mesh sensitivity or mesh convergence studies are where the functional length of elements is assessed to ensure that the results attained from an investigation are independent of mesh size. While this thesis is directly applicable to shallow water equation models and Computational Fluid Dynamics (CFD), the issue of mesh sensitivity is important in all computational analyses. The process can be briefly described as finding a point in which results converge when decreasing the length of the elements in a mesh.

The formal way of establishing the point of convergence is to express data collected from a critical result parameter in a specific location in a plot against a determined measure of mesh density. The number of convergence runs can vary from case to case, however a minimum of three simulations with varying mesh sizes will be required to formulate the convergence curve. Convergence is reached after a levelling of the curve indicating mesh independence [165].

Typically, the study is carried out with decreasing the mesh density with each sequential run, and comparing the results on the go. Additionally, with each successive refinement, all elements could be shortened by the same factor. Critical areas can sometimes have no effect of other areas of the model, and taking computational intensity into account, continually refining the mesh will increasingly prolong the simulation time. So, from a pragmatic standpoint, a model can be tested by refining in areas of interest, and retaining or coarsening the mesh elsewhere. This method also requires some consideration towards transition zones- coarse areas to fine areas. This concept can be extended if a model is only required to produce data in selected regions of interest. The role of elements elsewhere is to represent the complete geometry, or ensure coverage of all areas that be affected or be influenced by the simulation. These elements transmit the analysed results from each node throughout the wider interconnected network and synthesize with the refined elements in the areas of interest. These elements can be significantly larger providing the quality of the both roles is of reasonable quality and do not jeopardise the results.

It is frequent practice to vary the coarseness/refinement of the mesh in a model as the contrast; filling the entire model with small, high quality elements in a bid to improve the accuracy, is often found to be inefficient and unlikely to improve the accuracy in the model.

A common influence on the simulation results is the interaction with the boundaries. Refining the mesh around the boundaries will improve the representation of such affects. Commonly this area of consideration is referred as the geometry effect and distinct to mesh convergence, though the relation should be noted.

Analytical verification   Analytical methods for establishing spatial and temporal convergence definitions for CFD are derived from Roache [209, 208] and are based on Richardson's extrapolation [205] - which requires a critical global variable, to be taken against a mesh refinement measure $(f_1, f_2 ..., f_n)$.

The refinement ratio r_c defined as the ratio between consecutive refined mesh levels (N) or measure of grid spacing (h), where auxiliary grid generation parameters are uniformly maintained:

$$r_c = N_i/N_{i+1} = h_i/h_{i+1} \tag{2.1}$$

Where $1.1 < r_c < 2$ and is constant, to allow the discretization error to be differentiated from other error sources. The solutions attained corresponding to each N or h must be in the "asymptotic range of convergence". The order of convergence (p) associates the solution of error:

$$E = f(h)f_{exact} = Ch^p + HOT \tag{2.2}$$

Relating $f(h)$ a discrete value to the corresponding value that would result with a $h \rightarrow 0$, exemplifying the reduction of error corresponding to decreasing grid spacing. C is set as constant and HOT is representation of the Higher Order Terms; relating to the numerical algorithm. If the HOT are neglected, taking logarithms of equation 2.2 results in equation 2.2:

$$log(E) = log(C) + p \, log(h) \tag{2.3}$$

The gradient of the $(log(E))$ vs $(log(h))$ curve relates to the order of convergence:

$$p = \frac{ln(\varepsilon_{32}/\varepsilon_{21})}{ln(r_c)} \tag{2.4}$$

$$\varepsilon_{i+1} = f_{i+1,i} - f_i \tag{2.5}$$

As mentioned above, the accuracy of calculations is dependant on the measure of grid spacing being within the asymptotic range of convergence - which can be confirmed with the constant.

Roache introduced the $p^{th} order$ to the Richardson extrapolation to predict the $h \rightarrow 0$ value [209, 208, 175, 227, 109, 223]:

$$f_{h=0} \cong f_1 + (\frac{f_1 - f_2}{r_c^p - 1}) \tag{2.6}$$

The convergence ratio (R):

$$R = \frac{\varepsilon_{21}}{\varepsilon_{32}} \tag{2.7}$$

Can be used to evaluate the convergence conditions of the extrapolated value [227]:

1. Monotonic:$0 < R < 1$
2. Oscillatory:$R < 0$
3. Divergence:$R > 1$

Roache suggested the implementation of a standardised method in which grid convergence studies can be reported and accompanied with an error evaluation on the convergence solution. The Grid Convergence Index (GCI) is based on the fractional error derived from the generalisation of Richardson extrapolation [227, 223]. The GCI is calculated with a factor of safety of $F_s = 1.25$ for three or more grid comparisons.

$$GCI_{i+1,i} = \frac{F_s|\varepsilon_{i+1,i}|}{f_i(r_c^p 1)} \tag{2.8}$$

The solutions can again be checked to be residing within the asymptotic range of convergence:

$$GCI_{AR} = \frac{GCI_{23}}{r_c^p \cdot GCI_{12}} \approx 1 \qquad (2.9)$$

should the solutions be within the asymptotic range, then GCI_{AR} will either be equal or approximately equal to 1.

2.1.6 Validation

The accuracy of a CFD model and its solutions can be affected by errors and uncertainties in the numerical calculations which both originate in both the conceptual modelling and design. These errors need to be assessed and measured. The relevancy of computational methods in engineering is strongly tied to the credibility of the results that the simulations produce. Therefore the errors and uncertainties must be identified, measured and assessed, irrespective of the sources. Computational models built with an systematic approach to the reduction of errors and uncertainties will lead increasing greater accuracy and representation of the flows that are being modelled, developing greater confidence in the use of these techniques. The computational modelling researches have instigated a pragmatic approach to gain some idea of computer model accuracy and the errors on hand. Simply put, the models are put through verification and validation tests.

In circumstances where it is not actually possible to validate a numerical model through direct replication of the processes. Alternative approaches must be taken to attempt to provide some degree of credibility. One option is validate discrete parts of the system with the intention of then extrapolating the findings to the whole. Such a cases exist within the computational modelling of tidal energy generation - for both tidal range and tidal stream. Once such case is of the barrage and lagoon schemes currently being proposed. Current attempts to validate the hydrodynamic models include simulating the absence of any proposed structures in the intended region. Thus, several parameters that make up the tidal range models system will be valid, leaving only errors relating to the additional structures. Separately, the structures can be validated through scaled down approaches which aim to replicate the 3D flow fields, which then can be scaled up to the intended size. Investigations by P. Stansby et al [119, 120, 121] aimed to verify the 3D flow field close to a scaled barrage through experimental analysis, and determine the hydrodynamics effect on the local environment if such a barrage was installed.

A seven duct barrage model scaled to 1:143 was constructed from geometries given by the Department of Energy. The barrage was placed into a long flume and the ducts were positioned as to create a symmetric geometry along the flume centreline. The downstream velocity was measured using a two-component Vectrino acoustic Doppler velocimeter (ADV) set up on a gantry. The downstream water depth was set through an weir instalment adequate distance downstream from the barrage.

The experiment aimed to verify the numerical model to allow a greater measure of the hydrodynamics that what can be measured experimentally. The focus of the investigation was the bed shear stresses to acquire an enhanced perspective on sediment transport and mixing processes. The down-stream flow was also depth-averaged modelled using an in-house, 2DSWE, from comparison purposes, in which

the only empirical input is the horizontal mixing length and bed friction coefficient. The Jet swirl may not be incorporated in depth-averaged models and using an open duct will provide a near direct comparison.

2.2 Fluid Dynamic Phenomena and Numerical Method

2.2.1 Turbulence

Turbulence as a topic is vast, with textbook descriptions covering the basics to upper levels of expertise. This section aims to cover the relevant aspects that are pivotal to the production of this thesis.

Dynamic fluid flow domains are often subject to a categorical binary as being either laminar or turbulent. Laminar flow consists of un-interrupted stratified flow layers. In stark contrast, turbulent flow is chaotic by nature with rapidly fluctuating temporal flow parameters. The principal effect of turbulence is that of a mixing of the fluid which has corresponding repercussions ranging from increased rates of chemical reactions, greater dispersions of contained particles to aerodynamic performance resulting from momentum diffusion. It is difficult to produce a definitive numerical prediction, which presents a significant problem with turbulent flow being ubiquitous. Despite difficulty, statistical properties of the turbulent flow are reproducible [54].

Turbulent flow structures have been described as following irregular curved lines known commonly as eddies, though that description does not quite reveal the actual nature of turbulence. Rather, turbulent flow is a mass of intertwined flow structures of various dimensions that can rapidly change [101].

The turbulent flow structures are often described in terms of vorticity $\omega = \nabla \cdot \vec{u}$, which is in most cases, generated through fluid interaction with solid boundaries. Vorticity is generally categorised under two types, first being 'fast' which is a product of localised relative acceleration [101]. The second being born from tangential pressure over longer sections of fluid-solid interaction.

Since vorticity is mostly generated through interactions with solid geometry, we use a dimensionless parameter, the Reynolds number, which describes the state of fluid flow over a geometric surface pertaining to the relationship between inertia and viscous forces as shown in equation 2.10.

$$Re = \frac{\vec{u} \cdot L}{\nu} = \frac{\rho \cdot \vec{u} \cdot L}{\mu} \qquad (2.10)$$

Where the ratios presented were determined by Reynolds as the chiefly dominant factors when determining the onset of turbulence. The Characteristic length L and velocity $\vec{u}$ are representative quantities that do not affect the fundamental significance, just the numerical value. High $\vec{u}$ & L or low ν present an inertia dominated flow characterised by high Re values and turbulent flow criteria. Conversely, low Re present a viscous dominated, laminar flow regime.

Many engineering applications which work with fluids have a typical standardised convention as to what characteristic length variable and velocity should be used. For example, the internal diameter of a circular pipe is taken as the characteristic length and the mean flow velocity $\dot{V}/A_f$. Comparatively with aerofoil's, the

chord length and the ambient flow velocity [150]. The *raison d'être* of calculating Reynolds number is simply for comparing one flow regime against the other through corresponding lengths and velocities. Thus geometric similarity stands as an essential condition for gauging flow conditions. ie Different Re values will exist between the pipe and aerofoil examples mentioned prior.

Taking pipe flow as an example, lower Reynolds numbers $Re < 2000$, sometimes refereed to as the lower critical Reynolds number, result in a laminar flow categorisation. For $Re > 2300$, sometimes refereed to as the higher critical Reynolds number, beyond which the flow is classified as turbulent and for intermediary values as in a transitional state [154, 150]. It should be noted that laminar flow in pipes has been maintained past the higher critical Reynolds number, instilling a precedence that there is no upper limit at which the change from laminar to turbulent flow regimes exist. However, the lower Reynolds limit is considered to be more defined, and thus of higher importance [150].

Turbulence Scales and Cascade

Turbulent regimes can also be categorised under the scale of the eddies flow structures contained within the flow regime, often referred to as the eddy length scales. The smallest length scales are many orders of magnitude smaller than the largest with the largest being the same order of magnitude as the dimensions of the geometry: the characteristic length [267].

L.F. Richardson [205] introduced the concept of an energy dissipation cascade within turbulent flow. The idea speculates that each eddy within the turbulent flow, independent of length scale, is in itself subjected to inertial instabilities. The product of which is to continual break-up of a larger eddy flow structures into smaller and smaller vortices until a state is reached where the dissipation of kinetic energy due to viscosity is significant [218, 269, 204].

The variation in kinetic energy with eddy scale can be schematically illustrated as shown in Figure 2.4.

Turbulence at the largest scales can be categorised according to l, which possess the highest level of TKE per unit mass ($TKE = E(k)\delta k$). Kolmogorov [132, 131] hypothesised that eddies become isotropic when breaking up down the cascade, from typically anisotropic characteristics due to the modes of creation. Thus, $E(k)$ is then only a function of ε and length when Reynolds number is large. The product of his work was the 'five-thirds law' for the inertial sub-range:

$$E(\kappa) \sim \varepsilon^{\frac{2}{3}} \kappa^{-\frac{5}{3}} \tag{2.11}$$

Future experiments would produce data that would largely corroborate Kolmogorov's hypothesis [101].

2.2.2 Boundary Layers

The boundary layer phenomenon is an important consideration within field of fluid dynamics; which specifically concerns a volumetric layer adjacent to that of a boundary surface. Described kinematically, the fluid particles adjacent to a surface possess
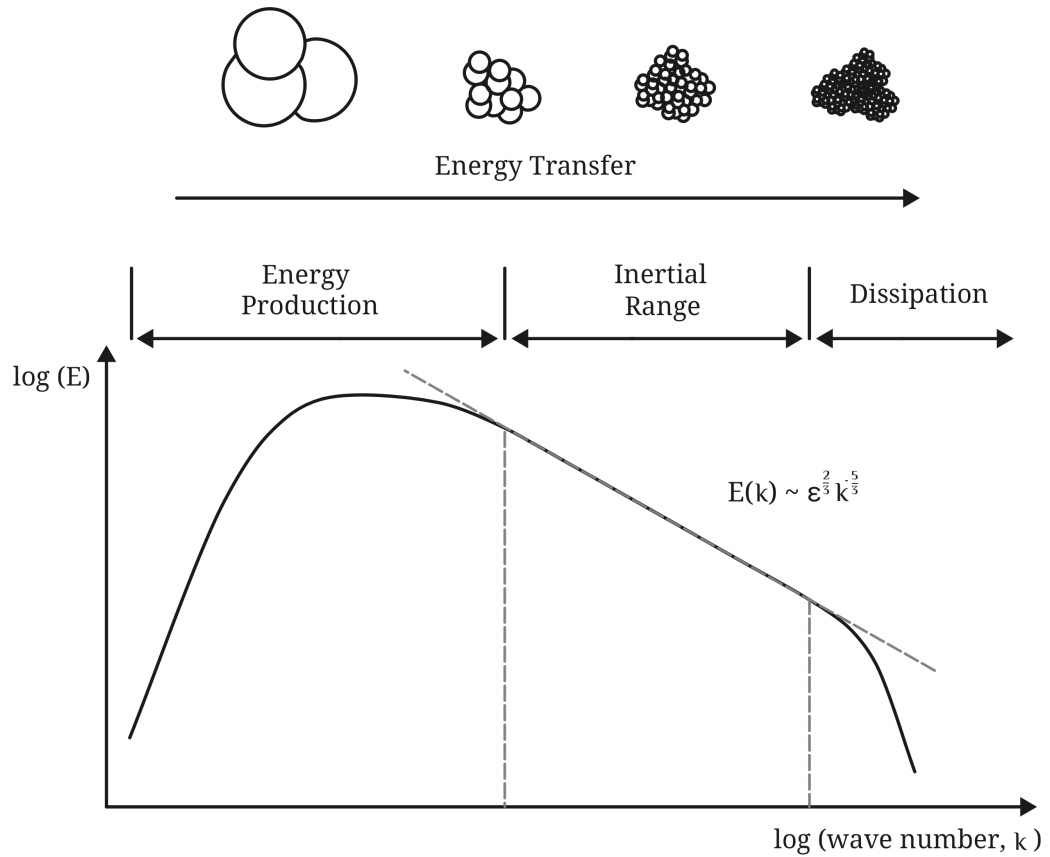
Figure 2.4: Schematic of the turbulent energy cascade spectrum.

zero respective velocity. Should ambient flow exist, a resultant velocity gradient will be formed between the near-wall and that of the ambient free-stream.

The boundary layer is conventionally designated under the formulation in equation 2.12:

$$u_{bl} \leq 0.99 \cdot u_{\infty} \tag{2.12}$$

Where the flow is 99% that of the ambient uniform average. Consequently, the perpendicular distance between the surface and the point where $u_e = 0.99 \cdot u_{\infty}$ is the boundary layer thickness. Figure 2.5 illustrated the concepts through application to the formation of a flat plate boundary layer.

The driving mechanisms are as consequence of inherent fluid viscosity and relative velocity difference between stratified layers of flow. Where viscous forces increasingly displace those of inertia as dominant with reducing perpendicular distance to the wall. This is in contrast to the main body of ambient fluid inviscid flow, where the velocity is uniform resulting in negligible viscous forces and dominated by inertia forces.

Additional considerations are also that of the flow conditions being either laminar or turbulence, with additional mention of the transitional period between the two states. The primary determinant of which is the Reynolds number (equation 2.10), with the characteristic length dimension taken from the point of initiation or fluid-surface contact, to a particular downstream length to which the Reynolds number is applied. The conventional standard for transition from laminar flow to that of

turbulence is $Re = 5 \times 10^5$ for flat-plate flow, though it should be noted that additional flow parameters of turbulence intensity and geometric aspects of surface roughness and non-linearity also feature into the point in which transition occurs.

Smooth Wall Boundary Layer
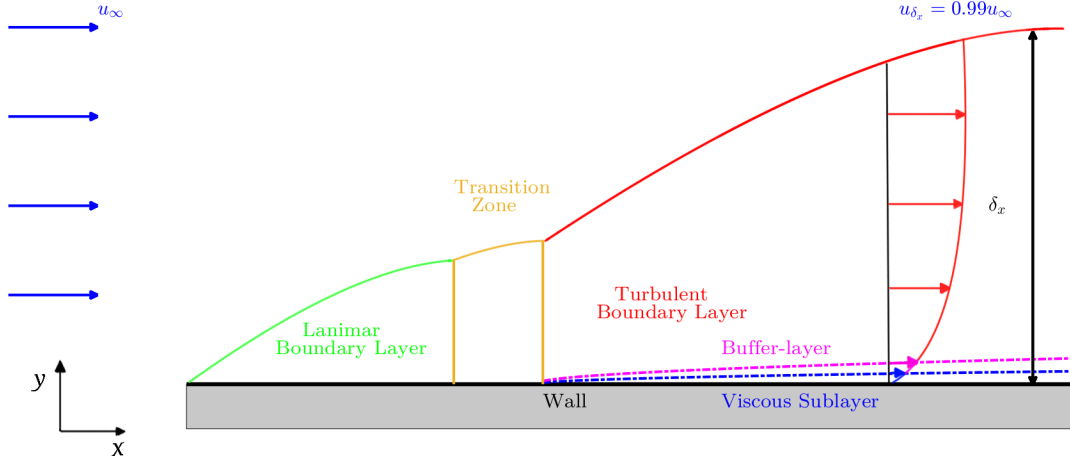
Figure 2.5: A schematic of a flat-plate boundary layer formation, formed from initial laminar flow.

At a point just before the formation of a boundary layer, the flow is effectively inviscid if the free-stream turbulence intensity is negated, with each particle possessing the same velocity u_∞. After initial contact with a *no-slip* surface, denoted as being $x = 0$, there is a finite fluid layer that effectively becomes stuck to the wall and completely losses all relative velocity. The same layer remains attached to the wall for the downstream length irrespective of the 'smoothness' or change in gradient. This characteristic condition of state holds true for near all but a select few cases with gasses at very low pressures [150]. An obvious dichotomy between the u_∞ and $u_{y=0}$ becomes present insinuating the presence of a velocity gradient $\delta\vec{u}/\delta y$. The first instances of viscous forces occur right at the interface between the finite fluid layer of $u_{y=0}$ and the adjacent, as described by Newton's 1687 shear stress equation 2.13 [176].

$$\tau = \mu \frac{\delta\vec{u}}{\delta y} \tag{2.13}$$

With increasing Δx, the shear stresses seamlessly propagates between stratified layers, with each corresponding layer subjected to a reducing velocity gradient until the velocity is asymptotic with the u_∞. The perpendicular distance from the wall where velocity is asymptotic u_e is approximated with equation 2.14, for when the flow condition is laminar.

$$\delta_{lam} \approx 5.2\sqrt{\frac{\nu x}{u_\infty}} = 5.0\frac{x}{\sqrt{Re_x}} \tag{2.14}$$

When $Re_x > 5 \times 10^5$ the flow condition transitions into that of turbulent flow. Understanding the quintessential difference between the two flow conditions as being

a departure away from stratification between flow layers. Induced mixing of fluid particles between flow layers effectively distributes the kinetic energy; altering the previous flow relationship governed in equation 2.13. The $u_{y=0}$ at the wall surface holds true. Thus a greater velocity gradient is formed adjacent to the surface (Figure 2.6).
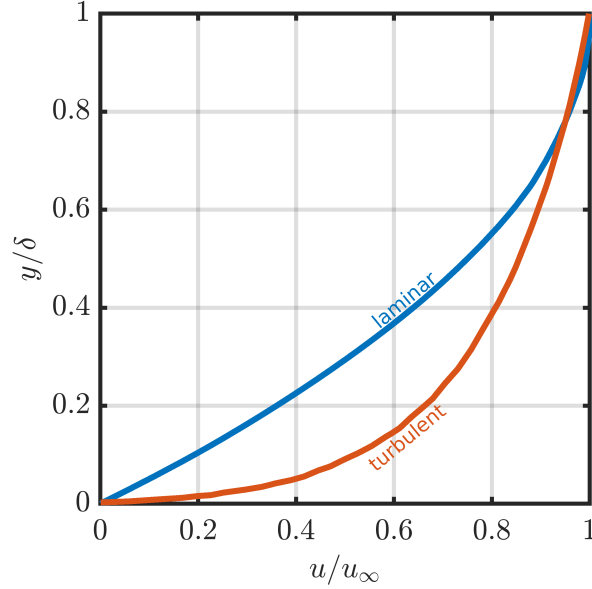
Figure 2.6: Comparison of velocity profiles between those of laminar boundary layer flow and turbulent.

The boundary layer thickness for turbulent zone is calculated through equation 2.15.

$$\delta_{turb} \approx 0.37 \frac{x}{Re_x^{1/5}} \tag{2.15}$$

Re calculated from the turbulent length scale *L* is always large for respective flows due to the dominance of the inertia forces over viscous.

If Reynolds number is taken with respect to perpendicular distance from the wall ($Re_y = \vec{u}y/v$), it can be seen that as $y \to 0$ $Re \to 0$. When $Re_y \approx 1$ the viscous forces will be of an equal order of magnitude to inertia forces at the wall. Thus the wall hydrodynamics can be considered to be not dependant on the inertia dominated free stream flow parameters, with the mean flow velocity depending on the perpendicular distance from the wall $u = f(y, \rho, \mu, \tau_w)$ [254].

Dimensionless analysis has been readily used to assist with the correlation of experimental data and has shown two important dimensionless numbers; the dimensionless velocity u^+ and the dimensionless wall distance y^+ [254], which can be shown as:

$$u^+ = \frac{u}{u_*} = f(\frac{\rho u_* y}{\mu}) = f(y^+) \tag{2.16}$$

Being the universal law of the wall, where the Friction velocity u_* is based through equation 2.17.

$$u_* = \sqrt{\frac{\tau_w}{\rho}} \qquad (2.17)$$

The high viscous effects adjacent to the wall inhibit turbulent motion which creates a permanent very thin layer which is referred to as the viscous sub-layer or sometimes also as the linear sub-layer as $u^+ = y^+$ as shown in Figure 2.7. The height of the viscous sub-layer is approximately stated to be when $y^+ < 5$.

With increasing perpendicular distance from the wall, the dominance of the viscous forces decreases leading to a departure from the $u^+ = y^+$ characteristic.

When $(30 < y^+ < 500)$ a new distinct zone exists, where both viscous and turbulent effects are both major parameters. Also, the shear stress can be assumed to be constant and of equal magnitude to the wall shear stress [254]. Within this zone a new relationship can be derived which is called the log-law of the wall:

$$u^+ = \frac{1}{k}ln(y^+) + B = \frac{1}{k}ln(Ey^+) \qquad (2.18)$$

where the Von Karman κ constant and *E&B* are numerical constants found through experimentation. being shown as $0.4, \approx 9.8$ and ≈ 5.5 respectively for smooth walls [254].
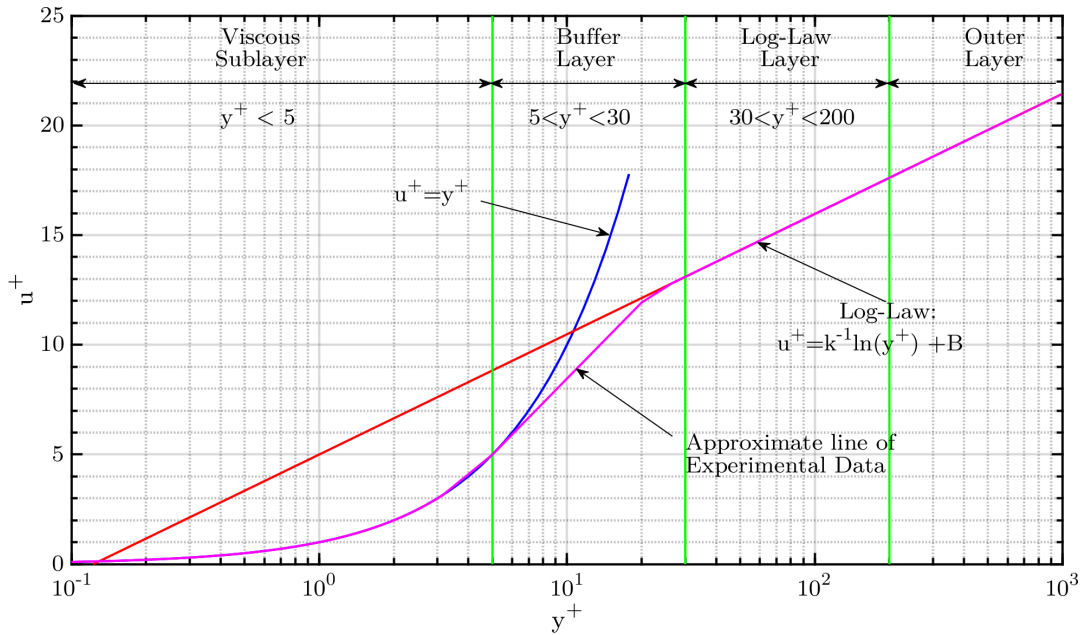
Figure 2.7: The universal 'law of the wall'. The $x-axis$ quantifies the dimensionless distance from the wall (y^+). The $y-axis$ quantifies the dimensionless velocity (u^+). The graph differentiates between profile zones for a turbulent boundary layer, that pertain different flow characteristics with perpendicular distance from the wall.

Pressure Gradient and Boundary Layer Separation

A developed turbulent boundary layer as discussed in Section 2.2.2, will shed vortices at the geometric end-point, or through the process of boundary layer separation when subjected to a non-zero pressure gradient.

Figure 2.8 illustrates a schematic example of boundary layer flow separation with a x being a curvilinear coordinate and y being perpendicular to the surface. Fundamentally flow will separate when the gradient $\delta\vec{u}/\delta y$ equals zero at the surface $y = 0$, as shown at S_3.
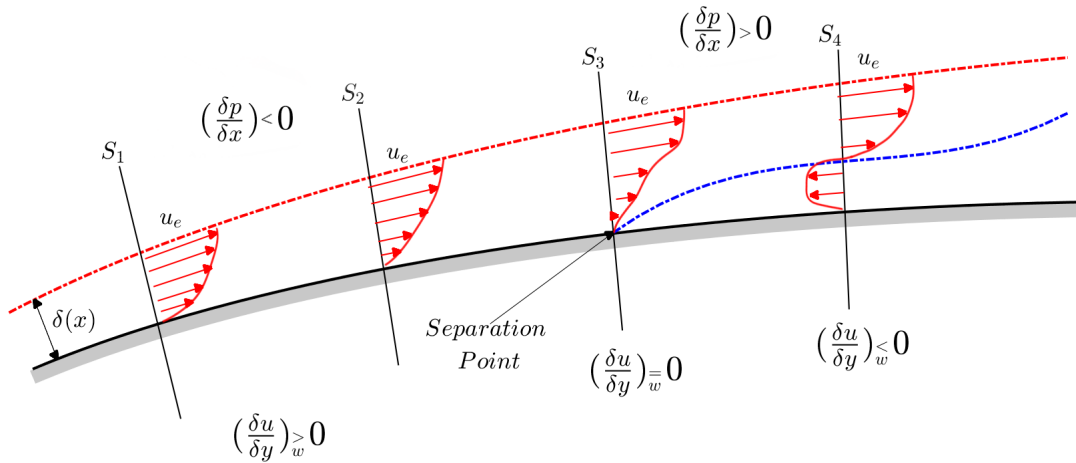
Figure 2.8: Schematic of boundary layer flow separation in the presence of an adverse pressure gradient. The system is described through x being a curvilinear coordinate and y being perpendicular to the surface.

In contrast to the formerly discussed flat-plate boundary layer in Section 2.2.2, flow over a curved surface will be subject to a non-uniform pressure distribution. Prior to S_1, flow will be deflected off the surface instigating some degree of transfer inertial kinetic energy into stagnation pressure. Thus, establishing a negative $\delta p/\delta x$ pressure gradient inducing flow acceleration. A consequence of which is further decreasing the static pressure along the x direction. Such pressure gradients are often referred to as 'favourable' [150, 104], since they counter act the viscous induced velocity reduction of the boundary layer, acting to stabilise the laminar boundary layer which in turn delays the transition point. A point will be reached (S_2) when the pressure is at a minimum and $\delta p/\delta x = 0$. After which, the pressure increases instilling a positive $\delta p/\delta x$ acting to oppose flow in the x-direction rather than drive, thus commonly referred to as an adverse pressure gradient. The deceleration effect is greater close to the surface where fluid inertia is lower compared to the outer section of the boundary layer. Thus under a uniform pressure, with respect to the cross-section, flow closest to the surface will decelerate to $\delta u/\delta y = 0$ before outer flow streamlines (S_3).

Downstream of which (S_4), the close to the surface flow will reverse and the outer streamlines will no longer be held to the surface. Referring to equation 2.13, the point in which $\vec{u}_x = 0$ will completely negate any shear stress between respective streamline layers. Said point stands as a dividing line between the forward and reversed flow and is referred to as the separation streamline.

Boundary layer separation can occur with both laminar and turbulent boundary layers under identical mechanisms. However, laminar flows are more susceptible since the velocity increase with distance from the surface is lower, mirroring the mechanism at (S_3) where lower inertia streamlines reverse earlier than those of higher inertia. Additionally, through mixing effects in a turbulent boundary layer,

more kinetic energy is transferred to the laminar viscous sublayer [150].

In summary, flow separation occurs with any wall attached flow where an adverse pressure gradient exists. Only differing in onset where the greater the adverse pressure gradient the earlier separation occurs.

2.2.3 Rough Surface Boundary Layer

Surface roughness in pipes has been shown through research carried out by G.Hagen and H.Darcy in the 1800s time period, to increase drag forces and blockage effects. Research relating to surface roughness has developed from said initial point, to a greater understanding of the mechanisms which take place that lead to observable reactions of heat and flow momentum transfer at the fluid-solid geometry interface [125].

As previously described in section 2.2.2, boundary layer initiation and propagation stages are often showcased through idealised conditions such as the flat-plate boundary layer with a smooth surface. Fluid flow over a surface is initially classified as being of laminar flow where streamlines flow parallel fashion to each other and the geometric surface. On the occurrence of streamline instability, the flow regime can be described as entering the laminar to turbulent transition state. However, many $in-situ$ engineering surfaces requiring analysis are rarely as geometrically simple nor smooth. Aspects like oxidisation, fouling, etc, regularly being a common facet in the hydrodynamical performance of a particular asset. The presence of surface roughness features can induce earlier onset of flow streamline instability very close to the surface. Effectively altering the flow regime to that which is termed as the roughness sublayer.

The degree of roughness in itself is a relative concept. Seemingly smooth surfaces at macroscopic length scales can be considered rough if viewed at microscopic scales. Trees and buildings can also be considered as features of surface roughness if considering the atmospheric boundary layer.

The presence of rough surface elements can have a considerable impact on how the surface will react with its environment; such as wear rates, friction coefficients and adhesion performance. Detection of surface irregularities can also provide valuable indications into the material performance as a mechanical component. A non-uniform structure under loading will develop stress concentrations which then may lead to fatigue nucleation sites.

Initially, an objects surface roughness is often determined during the manufacturing process, though this aspect will likely be reduced from the finishing processes, where the surface will likely undergo a polishing sequence. The smoothing capacity of which is dependant on material properties and the machining resources available during manufacture. For a given material, continually reducing the surface roughness will be an increasingly resource intensive process. Thus, coincidently increasingly monetarily expensive. This creates a optimum trade-off scenario; balancing the manufacturing process expenses against the performance requirements when in operation.

An objects surface roughness can also be altered when under operational conditions, and likely to a greater significance than during the production machining process. With respect to the thesis research topic, this may take the form of long-term degradation from weathering effects or possible collisions with objects in the
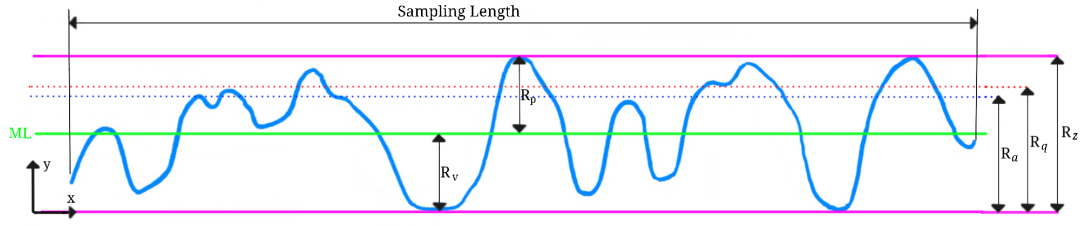
Figure 2.9: Schematic representation of surface roughness parameters (R_a,R_v,R_p,R_z&l_r)

local environment, like debris related to both human waste and naturally occurring objects like drift wood. There is also a considerable chance of collision with wildlife. Short-term instances of roughness can also feature; salt spray in the marine environment or possible icing if the turbine has been hosted out of the water for some time prior to a return to operation.

Roughness Parameters

An objects surface is usually systematically characterised through a parametrisation of collected measured data. The "Roughness" is then quantified through through measuring comparative surface texture deviations. Figure 2.9 shows a schematic of a surface roughness profile with visual representation of the surface roughness parameters (R_a,R_v,R_p,R_z&l_r) that are used to define the "roughness" of a surface.

The arithmetic average deviation(R_a) of the measured data is calculated through equation 2.19, which calculates the average distance between the median line of the surface profile and its peaks and valleys.

$$R_a = \frac{1}{n} \sum_{i=1}^{n} |y_i| \tag{2.19}$$

Equation 2.20 calculates the root mean square of the dataset.

$$R_q = \sqrt{\frac{1}{n} \sum_{i=1}^{n} y_i^2} \tag{2.20}$$

Equation 2.21 and Equation 2.22 calculates the maximum valley and peak distance from the median line respectively.

$$R_v = |\min_i y_i| \tag{2.21}$$

$$R_p = \min_i y_i \tag{2.22}$$

Equation 2.23 calculates the maximum peak to valley height of the measured surface.

$$R_z = R_v + R_p \tag{2.23}$$

Equation 2.24 calculates the skewness of the dataset.

$$R_{sk} = \frac{1}{nR_q^3} \sum_{i=1}^{n} y_i^3 \tag{2.24}$$

Equation 2.25 calculates the kurtosis of the data set.

$$R_{ku} = \frac{1}{nR_q^4} \sum_{i=1}^{n} y_i^4 \tag{2.25}$$

Flack and Schultz [84] stated that when R_q is used in tandem with skewness s_k or kurtosis k_u surface characterisation could be achieved. Additionally noting that single measures are incapable of apt descriptions of surface roughness.

R.Dirling [65] introduced a "*combinedsolidityandshapeparameter*" Λ for 2D roughness given in equation 2.26

$$\Lambda = \left(\frac{\psi}{k} \right) \left(\frac{A_f}{A_s} \right)^{4/3} \tag{2.26}$$

Where the solidity parameter is defined as the ratio of the average roughness element spacing ψ to the effective roughness height k. The shape parameter is the ratio of the frontal area of the roughness element A_f and the windward wetted surface area of a roughness element A_s.

Equivalent Sand Grain Roughness

Most forms of surface roughness by nature, are often of too high a level of geometric complexity to be accurately maintained for simulation purposes and replicated across different scales.

The basis for a standard roughness concept was first brought by Nikuradse [174], who used a sand-grain approach to provide data on the scaling formulations. The fundamental advancement of this approach was a standardisation to characterise roughness off a single length scale; being the diameter of a spherical sand-grain which is equatable to the roughness height k.

The sand grain roughness equivalence k_s principle revolves around relating two mutually distinct surfaces to equivalent roughness effects on the flow. The more similar a surface is to the Nikuradse sand grain roughness the higher the equivalency of the roughness height length scale. Antithetically, the greater the departure, the greater number of additional parameters that will be required to define the surface.

Figure 2.10 schematically presents a comparison between two different roughness types; one being the spherical sand grain, the other being a non-uniform rough surface. Both of which posses equivalent roughness heights k, however, both will impart different respective turbulent interactions with the flow.

To overcome this, a equivalent length scale was put forth by C.Colebrook and C.White [49], essentially equating a rough surface height k to an equivalent sand grain roughness height k_s.

Equivalent sand grain roughness has been expanded from pipe flows to other flow regimes and correlated against experimental data.

R.Boyle and M.Stripf [32] formed an equivalency shown in equation 2.27 from the statistics of the regular turbine geometry obtained from the blades after exposure to working conditions.

(a) Nikuradse Sand-Grain roughness elements. $k_s = k$

(b) Non-uniform roughness elements $k_s \neq k$
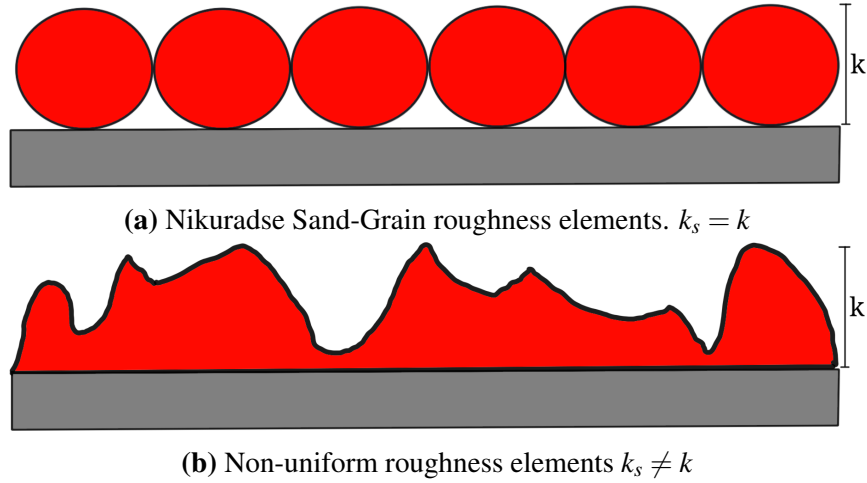
Figure 2.10: Schematic equivalency of sand-grain roughness and the more typical non-uniform surface roughness

$$k_s = 4.3R_q(1 + C_{sk}S_k) \tag{2.27}$$

where C_{sk} is a constant.

K.Flack and M.Schultz [84, 85] formed equation 2.28, a correlation relying solely on the root-mean-square roughness height R_q and the skewness S_k of the probability density function to form a approximation of the equivalent sand grain roughness k_s.

$$k_s = 4.43R_q(1 + s_k)^{1.37} \tag{2.28}$$

Roughness Ratio

As briefly touched on above, the concept of roughness is relative to the length scales in question. Relating surface roughness to a particular case on hand is a function of the roughness ratio 2.29.

$$\frac{k}{\delta} \tag{2.29}$$

Where the roughness height k relative to boundary layer height δ determines whether a particular geometric surface is dichotomised as either hydraulically rough or smooth. Though there is some degree of variance depending on the source [125]. This is likely a consequence of experimental roughness element variability and disagreement on acceptable degrees or error.

However, a gross generalisation can be formed as:

$$k \begin{cases} < \delta_v : Hydraulically \quad smooth \\ \approx \delta_v : Transitional \\ > \delta_v : Hydraulically \quad rough \end{cases} \tag{2.30}$$

Where elements of the roughness height are entirely enveloped in the viscous

sublayer, as shown in Figure 2.11, then the surface is classified as Hydraulically Smooth (HS). For such cases, the skin friction and the drag coefficient are equivalent to the idealistic completely smooth surface.
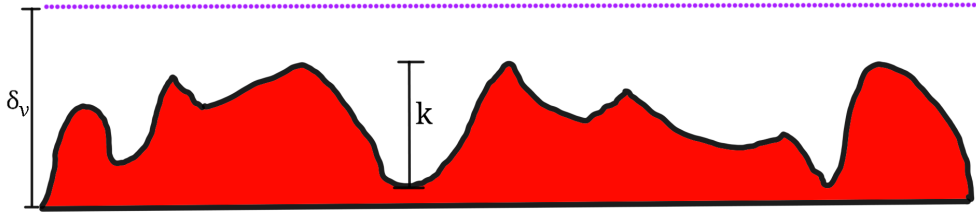
Figure 2.11: Schematic diagram presenting an hydro-dynamically smooth surface.

Antithetically the surface is classified as Hydraulically Rough (HR) if elements of the roughness height extends beyond the height of viscous sublayer. Figure 2.12 schematically presents roughness protruding from the viscous sublayer and the induced flow separation from the roughness peaks. In such cases the typical viscous sublayer characteristics are no longer present, having been replaced with an induced regime of turbulent streamline mixing, referred to as the Roughness Sublayer (RSL). For such regimes the skin friction and corresponding drag coefficient are substantially greater. The roughness sublayer extends to $\approx 2 - 5k$ out from the surface [197].
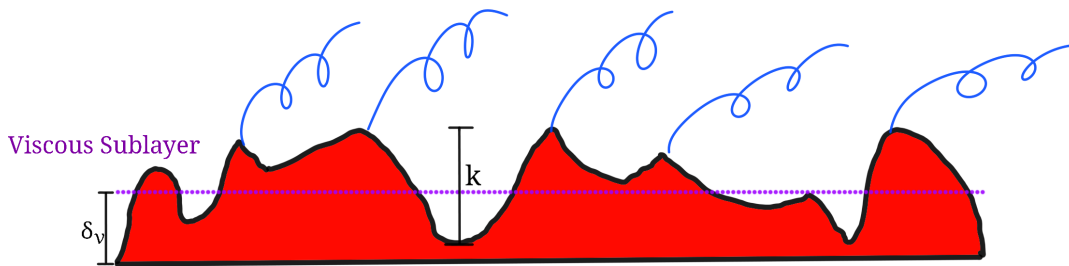
Figure 2.12: Schematic diagram presenting an hydro-dynamically rough surface.

When the roughness elements are approximately equal to the viscous sublayer height, the flow regime is refereed to as being transitional. The interaction between the fluid and the roughness elements is more complex with both viscous and turbulent forces present. With both contributing the resultant friction and drag coefficients. Within this region, the viscous sublayer height is decreased which has a corresponding effect of reducing the damping effects at the surface [125].

Experimental process has revealed that the degree of surface roughness imparts a characterised relationship the log-law or fully turbulent region that is dominated by inertia forces. The smooth wall scenario discussed in Section 2.3.3 is described through equation 2.18 and shown in Figure 2.7, features the dimensionless velocity profile u^+. Said profile features a consistent negative shift dependant on the magnitude of the roughness, as shown in Figure 2.13 [21]. The shift is credited as being a function of greater kinetic energy transfer into the roughness sublayer regime and is termed as the roughness function Δu^+. Thus the non-dimensional inertia dominant log-law region of the boundary layer is given by adapted equation 2.18 to equation 2.31:
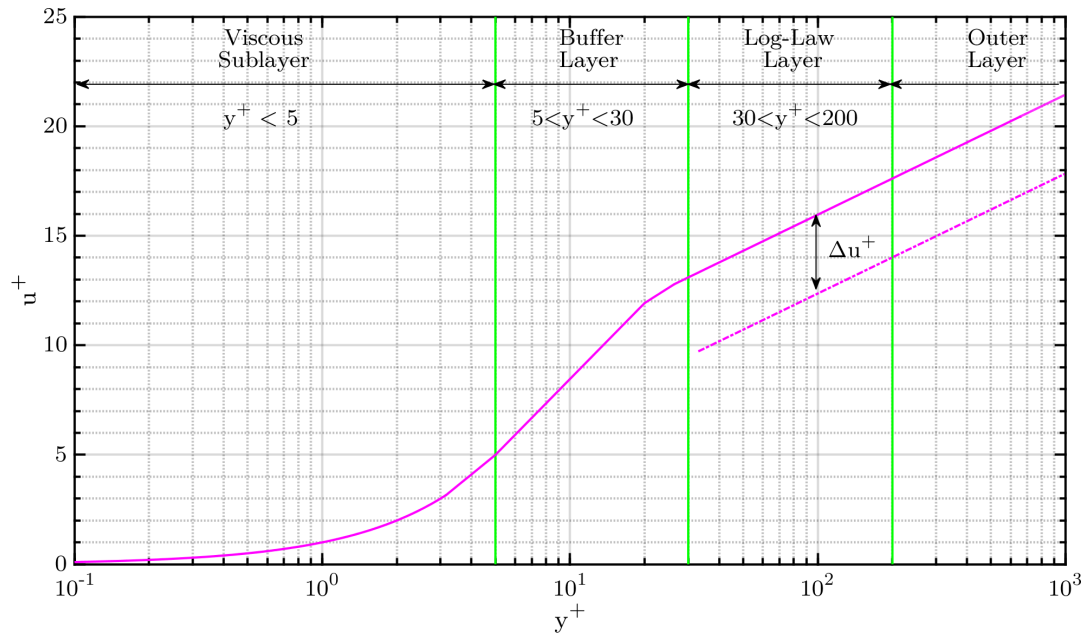
Figure 2.13: Comparative dimensionless velocity profiles between smooth and rough wall surface induced boundary layer in the log-law region of flow.

$$u^+ = \frac{1}{k}ln(Y^+) + B - \Delta u^+ \tag{2.31}$$

2.3 Computational Fluid Dynamic Modelling

The physical characteristics of the fluid dynamics are described through through fundamental equations, usually in an partial differential form. These equations are known as the governing equations of CFD. These equations are solved through software on high performance computers to produce numerical solutions.

- Continuity Equation - Conservation of Mass

- Momentum Equation - Conservation of Momentum

- Energy Equations - Conservation of Energy

The fluid dynamics equations which underpin the concept of fluid dynamics and used to model the flow using numerical solvers. A fluid in motion can be mathematically described by two scalar fields and a vector field. Both scalar and vector fields are spatial domain's that contain distinct discrete points, each representing a scalar or vector quantity. The points posses a single real value within a scalar field, conversely, the points within a vector field possess a tuple of real values.

The vector field of a fluid describes both the spatial and temporal characterised state of the fluid's velocity. The variables within the scaler field are required to fully quantify the fluid state. Commonly the two used are of pressure and density. Other accompanying quantized variables are directly derived during the simulation.

CFD solvers for both compressible and incompressible flow are not commonplace due to the differences in the governing equations of each. The following equations describe the governing equations of an incompressible viscous fluid; which features for the CFD models within this thesis.

The Navier-stokes equations describe the instantaneous motion of a fluid, through relations between the velocity, pressure, temperature, and density. The equations are derived from Newtons second law, the Law of motion:

$$F = \frac{d}{dt}(m\vec{u}) \tag{2.32}$$

with the assumption that the viscous stresses on the fluid are linearly proportional to the rate of deformation - a Newtonian fluid. Conservation of mass and energy equations, which includes the rate of heat transfer, can be coupled to provide a definition of a flowing fluid.

Fluid properties pertaining to those governed by the energy equations are not presented within this body of research, therefore will not be discussed further.

2.3.1 Conservation of Mass

Described through the "Eulerian approach" [193], where a control volume remains fixed in space. The fundamental principle in the conservation of mass is where:

Rate of which mass increases	**=**	**Net rate of mass flow**

resulting in the integral mass equation 2.33.

$$\frac{d}{dt} \iiint \rho \, dV = \oiint \rho \vec{u} \cdot \hat{n} \, dA \tag{2.33}$$

The conservation of mass of a fluid flowing through a fixed volume is mathematically described through the continuity equation 2.36.

Using Gauss's Theorem and moving the time derivative inside the integral results in equation 2.34.

$$\iiint \left[\frac{d\rho}{dt} + \nabla \cdot (\rho \vec{u}) \right] dV = 0 \tag{2.34}$$

∇ is the gradient operator which can be shown in longhand notation in equation 2.35.

$$\nabla = \frac{\delta}{\delta x} + \frac{\delta}{\delta y} + \frac{\delta}{\delta z} \tag{2.35}$$

Taking the control volume as being infinitesimal, the whole quantity must be zero at every point; resulting in the mass continuity equation 2.36

$$\frac{\delta \rho}{\delta t} + \nabla \cdot (\rho \vec{u}) = 0 \tag{2.36}$$

58

Incompressible Fluid An incompressible fluid can be defined as a fluid body that does not change volume; has a constant density ρ, when acted on by a change in pressure. Liquids such as water are often approximated as an incompressible fluid for pragmatic purposes. The derivative with respect to time and the density gradient are made redundant and are removed from the equation. Hence the continuity equation is reduced to:

$$\nabla \cdot \vec{u} = 0 \tag{2.37}$$

this equation with the conservation of mass equation 2.36, will describe a viscous incompressible fluid flow.

2.3.2 Conservation of Momentum

The derivation of the momentum equation is based on the first principle of Newton's second law, the law of motion (equation 2.32). Again under the 'Eulerian approach", where conservation of momentum of a fluid flowing through a fixed volume:

Rate of which momentum increases	**=**	Net sum of forces
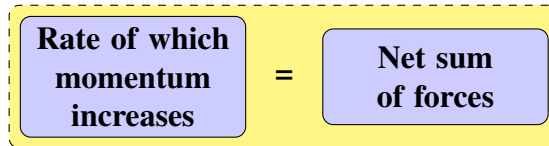
and mathematically described through the equation 2.38.

$$\frac{d\vec{p}}{dt} + \dot{\vec{p}}_{out} \dot{\vec{p}}_{in} = \vec{F} \tag{2.38}$$

Where $\vec{p}$ is the instantaneous momentum within the control volume. Represented as an integral as shown in equation 2.39. The $\dot{\vec{p}}_{out}$ term is the mass flow leaving the control volume, which carries momentum produced by $\vec{F}$ that $\vec{p}$ in itself does not account for. $\dot{\vec{p}}_{in}$ is mass flowing into the control volume, which is incorrectly accounted in $\vec{p}$ - thus is subtracted. Both terms can be evaluated as a surface integral of the momentum flux across the boundary area as shown in equation 2.40.

$$\vec{p}(t) = \iiint \rho \vec{u} dV \tag{2.39}$$

$$\dot{\vec{p}}_{out} - \dot{\vec{p}}_{in} = \oiint \rho (\vec{u} \cdot \hat{n}) \vec{u} dA \tag{2.40}$$

Applied Forces The right-hand side of equation 2.38, $\vec{F}$ represents the "body" or "surface" forces which act inside or on the surface respectfully. The two types can be distinguished as:

1. Body forces

    − Centrifugal force

    − Coriolis force

    − Electromagnetic force

  – Gravitational forces

2. Surface forces

  – Pressure forces

  – Viscous forces

Considering the gravitational, pressure and viscous forces. These forces can be defined according to equation 2.41, 2.42 and 2.43 respectively [12, 254].

$$\vec{F}_{Gravity} = \iiint \rho \vec{g} \, dV \tag{2.41}$$

$$\vec{F}_{Pressure} = \oiint (-P\hat{n}) \, dA \tag{2.42}$$

$$\vec{F}_{Viscous} = \oiint T \cdot \hat{n} \, dA \tag{2.43}$$

T, the shear stress tensor is shown in longhand notation in equation 2.44.

$$T = \begin{pmatrix} \tau_{xx} & \tau_{xy} & \tau_{xz} \\ \tau_{yx} & \tau_{yy} & \tau_{yz} \\ \tau_{zx} & \tau_{zy} & \tau_{zz} \end{pmatrix} \tag{2.44}$$

The viscous forces in the fluid can be seen to be caused by the τ in the fluid. Shear or dynamic viscosity is defined as the ratio between shear stress and shear rate. A Newtonian fluid μ is independent from shear rate, hence the τ is proportional to the rate of deformation [254]. The values of the nine shear stresses are shown in equations 2.45 to 2.50.

$$\tau_{xx} = 2\mu \frac{\delta u}{\delta x} + \lambda \nabla \cdot u \tag{2.45}$$

$$\tau_{yy} = 2\mu \frac{\delta u}{\delta y} + \lambda \nabla \cdot u \tag{2.46}$$

$$\tau_{zz} = 2\mu \frac{\delta u}{\delta z} + \lambda \nabla \cdot u \tag{2.47}$$

$$\tau_{xy} = \tau_{yx} = \mu \left(\frac{\delta u}{\delta y} + \frac{\delta v}{\delta x} \right) \tag{2.48}$$

$$\tau_{xz} = \tau_{zx} = \mu \left(\frac{\delta u}{\delta z} + \frac{\delta k}{\delta x} \right) \tag{2.49}$$

$$\tau_{yz} = \tau_{zy} = \mu \left(\frac{\delta v}{\delta z} + \frac{\delta k}{\delta y} \right) \tag{2.50}$$

λ is the second coefficient of viscosity, which relates the stresses to the volumetric deformation. In incompressible flows, λ drops out of the equation and is ignored [254].

Integral Momentum Equation

Substituting all the momentum (eq 2.39), momentum flow (eq 2.40) and force definitions (eq 2.41, 2.42 and 2.43) into newtons second law equation 2.38, will result in the integral momentum equation 2.51.

$$\frac{d}{dt}\iiint \rho\vec{u}dV + \oiint \rho(\vec{u}\cdot\hat{n})\vec{u}dA = \oiint(-P\hat{n})dA + \iiint \rho\vec{g}dV + \oiint T\cdot\hat{n}\,dA \quad (2.51)$$

Applied concurrently with the integral mass equation 2.33, problems of finite control volume can thus be solved.

Differential Momentum Equation

The integral momentum equation 2.51 can be converted into a volume integral through applying the Gradient Theorem 2.52[12].

$$\oiint(-P\hat{n})dA = \iiint \nabla P dV \quad (2.52)$$

Similarly the momentum flow surface integral can be converted into equation 2.53.

$$\oiint \rho(\vec{u}\cdot\hat{n})(u\hat{i}+v\hat{j}+w\hat{k})dA = \hat{i}\iiint \nabla\cdot(\rho\vec{u}u)dV \quad (2.53)$$

$$+\hat{j}\iiint \nabla\cdot(\rho\vec{u}v)dV \quad (2.54)$$

$$+\hat{k}\iiint \nabla\cdot(\rho\vec{u}w)dV \quad (2.55)$$

Thus the integral momentum equation 2.51 can be defined in terms of volume integrals in equation 2.56 [12].

$$\iiint\left[\frac{\delta(\rho u)}{\delta t}+\nabla\cdot(\rho u\vec{u})+\nabla P-\rho g-\nabla\cdot T\right]dV = 0 \quad (2.56)$$

Integrating over the infinitesimal control volume results in zero, the Navier-Stokes equation 2.57 is produced.

$$\frac{\delta\vec{u}}{\delta t}+\nabla\vec{u}\cdot\vec{u} = -\frac{1}{\rho}\nabla p+g+\nu\nabla^2\vec{u} \quad (2.57)$$

For incompressible Newtonian fluids $\frac{\delta\rho}{\delta t}=0$.

2.3.3 Numerical Turbulence Modelling

As discussed prior, the basic description of turbulence is that of a characteristic property of fluid flow, existing as induced eddies of various temporal and spatial length

scales. The mechanisms in which the fluid particles, interact with adjacent fluid particles and distinct objects are dynamic and complex. Within an engineering context, the impact of which the turbulent flow will interact with an object of interest is often of great importance. Thus, several computational numerical methods have been developed to capture the effects of turbulence. Each of which is an approximation based methodology optimised under imposed criteria. There are three main categories: [254]

- Direct Numerical Simulation (DNS)

- Large Eddy Simulation (LES)

- Reynolds-Averaged Navier-Stokes Equations (RANS)

DNS seeks to fully resolve all turbulent flow eddies, as well as the mean flow within scales reciprocal to the Komogorov length scales, and time-steps sufficiently minute enough to capture all velocity fluctuations. In order to fully resolve turbulence at such scales, a minimum of four cells would be required to fully resolve any eddy. This results in an important consequence for CFD, as the entire volumetric wake region will be required to captured, which inevitably corresponds to a significant total number of cells.

The simple reality of the situation is that the level of computational resource capacity required renders DNS completely unsuitable for the majority of commercial or academic projects [254].

However, a consequence of being unable to resolve turbulence at the smallest scales is that the mechanism for dissipating the kinetic energy is not simulated, which will lead to a "backed-up" over-prediction.

LES seeks to track the behaviour of the larger eddies. This is done through filtering out the smaller eddy length scales of the Navier-Stokes equations, thus leaving the larger eddies and the mean flow to fully resolve. The influence of the smaller eddies on the flow characteristic are introduced through a sub-grid scale source term. Diffusive schemes are used to model the dissipation of energy following a deemed realistic rate, for example, the "five-thirds" law shown in figure 2.4 and equation 2.11.

Good practice for mesh sizing with LES is to seek to resolve 80% of the turbulent kinetic energy, with the remainder modelled in the sub-grid. In practice, a cell size five times that of the intergral length scale, determined as the eddy length of the average kinetic energy of all the eddies, will generally suffice (Figure 2.14).

The computational demands to resolve the eddies to the degree required in LES are still high, though the method has been shown to be a beneficial tool when simulating flow around complex geometries [254].

RANS has a focus revolving around the mean fluid flow, with consideration on how the turbulence will affect the mean flow characteristic properties. Extra terms are added to the time averaged Navier-Stokes equations; The κ-ε and κ-ω turbulence models fall under this category. By rule of thumb, RANS based CFD is computationally modest for the simulation of accurate flow characteristics [254].

The RANS equations use Reynolds decomposition to separate the mean time averaged approximations and fluctuating quantities to the Navier-Stokes equations. Equation 2.58 shows the decomposition of velocity u:
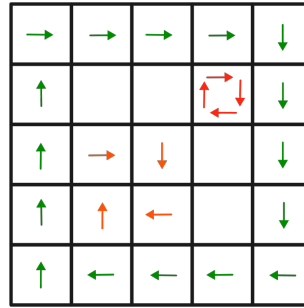
Figure 2.14: Schematic of mesh resolutions required to capture turbulence. sub-grid (red), minimum required to resolve an eddy (orange) and ideal resolution for 80% capture, $l_0/5$ (green).

$$u(x,y,z,t) = \overline{u(x,y,z)} + u'(x,y,z,t) \qquad (2.58)$$
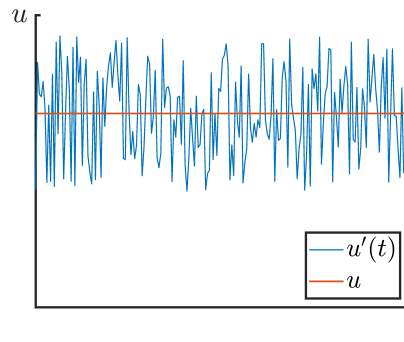
Figure 2.15: Schematic of the water level function given in Equation 2.97.

Where the $\overline{u}$ denotes the time average and the u' the fluctuations.

The RANS method has non-liner component terms, the Reynolds stresses. Therefore to solve these equations, a turbulence closure scheme is used, where assumptions as to the form of the stresses are simplified.

Selection of the turbulence methodology will often come down to reasons based on which method can produce acceptable accuracy of the results, weighted against the computational cost to simulate.

κ-ε Turbulence Model

The $\kappa - \varepsilon$ turbulence model; which is widely used for simulating turbulence on the mean flow at a sub-grid level, and is the most popular two-equation model [267]. The methods development sprung from efforts of Chou (1945) [48], Davidov (1961) and Harlow & Nakayama (1968), before being formalised by Jones and Launder(1972). However, most current researchers use the model presented in a 1974 paper by Launder and Spalding; who returned the closure coefficients [267].

The κ-ε turbulence model works through mechanisms of turbulent kinetic energy and is one of a derived family of two transport equation models with one solving k the turbulent kinetic energy and another ε governing the turbulent dissipation rate.

The κ-ε model transport equations are presented in equations 2.59 and 2.60, which govern the turbulent kinetic energy (κ) and the turbulent kinetic energy dissipation rate (ε).

$$\frac{\delta(\rho\kappa)}{\delta t} + \nabla\cdot(\rho\kappa\vec{u}) = \nabla\cdot\left[\left(v+\frac{v_t}{\sigma_\kappa}\right)\nabla\kappa\right] + P_\varepsilon - \rho\varepsilon \qquad (2.59)$$

$$\frac{\delta(\rho\varepsilon)}{\delta t} + \nabla\cdot(\rho\varepsilon\vec{u}) = \nabla\cdot\left[\left(v+\frac{v_t}{\sigma_\varepsilon}\right)\nabla\varepsilon\right] + \frac{C_1\varepsilon}{\kappa}(P+C_3\frac{2}{3}\kappa\nabla\cdot\vec{u}) - C_2\rho\frac{\varepsilon^2}{\kappa} \quad (2.60)$$

Where the given coefficients:

$$C_1 = 1.44, \quad C_2 = 1.92, \quad C_{3,RDT} = 0.0, \quad \sigma_\kappa = 1.0, \quad \sigma_\varepsilon = 1.3 \qquad (2.61)$$

are the closure constants for the classic κ-ε. The values were determined empirically through a extensive series of validation simulations of free shear flows [136, 254].

The dynamic turbulent viscosity v_t is calculated through the formulation (eqn 2.62) [136] :

$$v_t = C_u\frac{\kappa^2}{\varepsilon}, \quad C_\mu = 0.009 \qquad (2.62)$$

With the κ-ε model, the initial values and the boundary conditions must be specified for the subsequent solving of the respective equations, with the turbulent field requiring a fixed value condition at the inlets. The exact prescribed values can be subject to industry standards or found in published recommendations for a specific simulation being undertaken. However, the most common circumstance is to utilize a Prandtl mixing length based approach estimate through equation 2.63 and 2.64.

$$\kappa = \frac{3}{2}(I\cdot|\vec{u}|)^2 \qquad (2.63)$$

$$\varepsilon = \frac{C_\mu^{3/4}\cdot k^{3/2}}{l_m} \qquad (2.64)$$

where the specified turbulence intensity $I = \vec{u}'_{RMS}/|\vec{u}|$

The relationship is derived through and is representational quantity representing the macroscale of turbulence which is then defined in terms of κ and ε

The turbulent mixing length is circumstantially estimated as being $l = 0.07D$ for the centre axis of a pipe. For ducts and channels of non-circular cross-section, the hydraulic diameter $D = 4A/P$.

Turbulence is a function of the state of flow, should it's state change then it is necessary to account for such through varying l_m [254]. When considering simple flows, l_m can be determined through simple formulae presented in table 2.1

Table 2.1: Typical used mixing lengths for two-dimensional turbulent flows [213]

Flow	Mixing Length ι_m	L
Mixing layer	0.07L	layer width
Jet	0.09L	jet half width
Wake	0.16L	wake half width
Axisymmetric jet	0.075L	jet half width

The accuracy of the initial values for the internal flow domain is not deemed to be of critical importance since the simulation solution is dependant only for the initial few time-steps of the simulation. However, the simulation stability can become disaffected across the same initial time-steps, brought on by the flow boundary conditions instigating sharp pressure impulses [101]

The κ-ε was the first widely adopted CFD model for a variety of flows finding function in steady flow solutions with the time derivatives set to zero, and also in transient problems to capture unsteady hydrodynamics such as vortex's.

In summary, the κ-ε model is a comparably simple, with only initial and boundary conditions needing to be applied. Universally considered as being well established from it's extensive use in numerous industrial flows, and subsequently it's performance is well documented. However, it is known to be limited in high shear flow regimes with an over-prediction of turbulent kinetic energy at stagnation points. The model also requires near-wall treatment

With respect to low-Re formulations, damping functions are applied to the model coefficients C_μ, C_1 and C_2 so that the flow domain can be solved down to the viscous sub-layer ($y^+ < 5$). However, the κ-ω SST has supplanted the κ-ε model for such applications. Hence the κ-ε model now finding use in high-Re applications where adverse pressure gradients are not present.

The κ-ε turbulence model is an computationally efficient choice.

With respect to the free stream flow, the κ-ε model is not overly sensitive to the arbitrary variables imposed on the model boundary conditions [254].

κ-ω SST Turbulence Model

The κ-ω SST model is based on work done by Wilcox [265, 267, 264, 266], which uses the Turbulent Frequency ω as an alternative second variable. Both variables are used to compute the turbulent viscosity ν_t and close the RANS equations.

In diametric opposition to the κ-ε turbulence model, superiorly able to simulate the physics of the near-field boundary layer.

A hyperbolic variation (Equation 2.71), is applied across the grid cell that is adjacent to the model walls. It has been reported that the model, from an perspective of experimental implementation, is not overly sensitive to the exact implementation of the function [254].

The disadvantage of using such model is that the results have proved to be heavily dependent on the assumed free stream ω values. This can often, and in the case of this research, prove troublesome where the free stream turbulence variables are estimated through application of Equations (2.63 & 2.69) [254].

$$\frac{\delta(\rho\kappa)}{\delta t} = \nabla\cdot(\rho D_\kappa\nabla\kappa) + \rho G - \frac{2}{3}\rho\kappa(\nabla\cdot u) - \rho\beta^*\omega\kappa + S_\kappa \tag{2.65}$$

$$\frac{\delta(\rho\omega)}{\delta t} = \nabla\cdot(\rho D_\omega\nabla\omega) + \frac{\rho\gamma G}{\nu} - \frac{2}{3}\rho\gamma\omega(\nabla\cdot u) - \rho\beta\omega^2 - \rho(F_1-1)CD_{\kappa\omega} + S_\omega \tag{2.66}$$

$$\nu_t = a_1\frac{\kappa}{max(a_1\omega, b_1 F_{23}S)} \tag{2.67}$$

$$\alpha_{\kappa1} = 0.85, \quad \alpha_{\kappa2} = 1.0, \quad \alpha_{\omega1} = 0.5, \quad \alpha_{\omega2} = 0.856, \quad \beta_1 = 0.075, \quad \beta_2 = 0.0828,$$
$$\gamma_1 = 5/9, \quad \gamma_2 = 0.44, \quad \beta^* = 0.09, \quad a_1 = 0.31, \quad b_1 = 1.0, \quad c_1 = 10.0 \tag{2.68}$$

Initial Conditions

In the absence of $\kappa, \varepsilon \& \omega$ measurements, model development is directed through determining said variables by applying rough approximations for the inlet distributions.

The initial input κ patch variable is determined through Equation 2.63. With T_i being the turbulence intensity value and the reference velocity $|\vec{u}|$ [254].

The ω variable is thus determined through Equation (2.69), with the constant $C_\mu = 0.09$ [246].

$$\omega = \frac{\kappa^{0.5}}{C_\mu^{0.25}\cdot\iota_m} \tag{2.69}$$

The turbulence reference length (ι_m) is set from Equation 2.70 where the constant of 0.07 is set for conditions where no additional information is present [254].

$$\iota_m = 0.07L \tag{2.70}$$

$$\omega_P = \frac{6\upsilon}{\beta_1 y_P^2} \tag{2.71}$$

The κ-ω SST turbulence model put forward by Menter [158], was intended to blend the κ-ω & κ-ε turbulence models.

The resultant method has characteristics that has provided wide application within fields dealing well resolved, viscous flows with application of turbulence models being applied through the boundary layer [212, 34].

There has been some objection to the κ-ω SST turbulence model, with attention to the application of the arbitrary nature of the blending function, which could obscure some turbulence flow facets resulting in a critical model artefact.

comparability superior performance when predicting near-wall flow regimes such as those over foil blades.

Due to the importance of correct prediction of the flow adjacent to the foil surface The κ-ω SST model was determined to be the most applicable turbulence

model considering the study constraints and was adopted for all simulations within the GAD development Section.

Free-Stream Conditions

Free-Stream boundaries are where a fixed-pressure boundary condition is applied. At such boundaries both κ and ε are prescribed. For cases where the free-stream is assumed to be free of turbulence, κ and ε must be set to miniscule values. Equation (2.72) defines the eddy viscosity (μ_t) of the κ-ω model. As ω decreases to 0 at the wall surface, μ_t will increase indefinitely.

$$\mu_t = \rho \kappa / \omega \qquad (2.72)$$

Wall Modelling

Numerical Smooth Boundary Layer Model   The boundary layer in the near-wall region, as discussed prior in Section 2.2.2, features relatively large spatial velocity gradients. The correct modelling of which can be pivotal aspect as to whether the model produces accurate results.

This section solely discusses the application of wall modelling techniques employable with RANS turbulence models operating under the OpenFOAM framework.

There are two approaches that can be adopted for a RANS model prediction. Both of which rely on the dimensionless parametrisation of the boundary layer y^+ to determine the size of the first cell adjacent to the wall surface.

The first approach being to place cells within the viscous sub-layer ($y^+ < 5$) along the surface to fully capture the significant velocity gradient adjacent to the wall. Therefore across said cells, the velocity profile of the flow can be assumed to follow the linear relationship stipulated in equation 2.16. Such an approach is termed as the wall resolved approach or enhanced wall treatment [86].

It has been stated, that by a rule of thumb the first cell centroid be located at a y^+ of 1 for cell-centred solvers to reliably resolve the sub-layer when complex near-wall phenomena, such as adverse pressure gradient induced flow separation [86].

The downside to said approach is the potential for significant computational costs, which can potentially render a simulation unfeasible for very large spatial gradients and the required level of mesh refinement to sufficiently resolve them.

The other distinct methodology is the wall function approach, which provides approximate solutions for the boundary layer flow at a considerably lower computational cost. Wall functions work through taking advantage the log-law correlation (equation 2.18) with stable boundary layers, by using a distinct solver over the first cell from the wall surface which is placed in the logarithmic law region of flow ($30 < y^+ < 300$). Thus, requiring far fewer cells than it's contemporary. However, the wall function approach falls short of acceptable levels of deviation when simulating flows over surfaces of high curvature and or where flow separation and reattachment, such as described in Section 2.2.2, are present.

Additionally, the κ-ε family are not capable of modelling the near-wall region [86, 254]. However, The κ-ω family do not contain terms which are undefined at the wall, thus can be integrated to the wall without using wall functions. They are

also generally accurate and robust for a wide range of boundary layer flows with pressure gradients [86].

The turbulence model being used is this case is the κ-ω SST turbulence model. The SST stands for Shear Stress Transport and works through a blending function which acts to graduate the transition from the standard κ-ω model adjacent to the wall to a high Reynolds number version of the κ-ε turbulence model in the outer portion of the boundary layer. There is also an additional formulation of the turbulent viscosity, which accounts for the transport effects of the principal turbulent shear stress [86].

If the characteristic length, free stream velocity, kinematic viscosity are known and a y+ value has been selected, then the size of the first mesh cell can be calculated from the following equations and the Reynolds number equation 2.10:

The local skin friction can be calculated through equation 2.73; which is referred to as the 1/7 power law, suitable for Reynolds numbers in the range of $5 \times 10^5 < Re_x < 1x10^7$ in external flow conditions.

$$C_f = 0.0576Re^{0.2} \tag{2.73}$$

The wall shear stress can then be calculated the equation 2.74.

$$\tau_w = \frac{C_f \rho U_\infty^2}{2} \tag{2.74}$$

Then finally the height above the the surface through equation **??**

Numerical Implementation of Surface Roughness   With respect the the $\kappa\omega$ SST turbulence model considered within the scope of this thesis and related κ type models. There are two routes in which roughness effects can be accounted for. The choice of either route is largely dependant on limiting factors relating to the flow physics and the associated numerical cost. The two foremost being:

1. Modified Law-of-the-wall

2. Full Mesh Resolution

The first route is arguable the most common being that of modifications to the surface boundary conditions such as wall-functions. The second being fully resolved roughness geometry, which typically comes with substantially greater computational costs but is not limited in the capacity to predict adverse pressure gradients like the former.

As discussed in Section 2.3.3 contemporary modelling consideration for a fully resolved boundary layer, is for the first grid cell size to be y^+ 1. Depending on the type of surface roughness, the required cell sizes would be extremely minute and the computational cost required becoming unfeasible.

Other option's to model wall roughness do exist but are limited in either applicability or reliability.

Several approaches to compute rough surface interactions have been realised. However, the sand-grain method has proved its worth within research and industrial applications, through providing an simply orchestrated method, capable of reproducing the increased drag with only alterations to the numerical turbulence model.
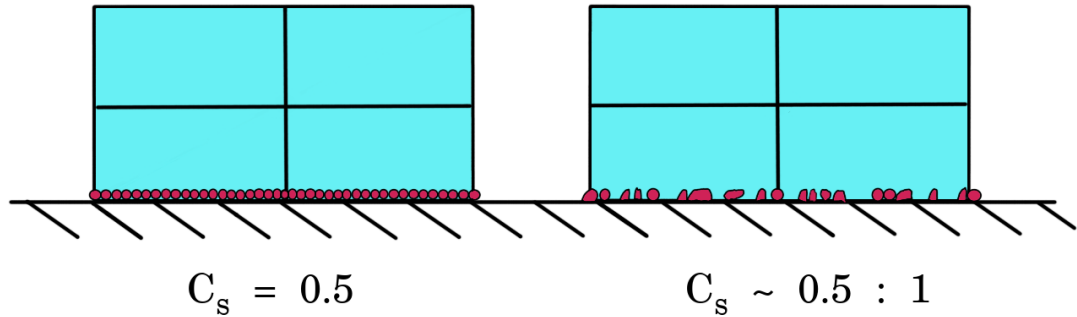
Figure 2.16: Schematic representation of of how OpenFOAM's nutRoughWallFunction incorporates surface roughness with respect to various C_s values and their impact on the red particle shape & spatial distribution. The left-hand side shows the when the C_s is set to the uniform 0.5 setting. The right-hand side provides a visual cue how values between 0.5 : 1 will alter the particle shape & spatial distribution.

The conventional method to address the concept of geometric roughness within a CFD model is to modify the standard Wall-Function source-code on how the Wall-functions which have been adapted for rough walls often have various parameters so that a closer approximation to various surfaces can be achieved - since most surfaces are not uniformly rough.

The utilised OpenFOAM wall-function describes the surface roughness representing a surface as a conceptual smooth substrate surface with superficial 'sand grains' simulating the roughness. κ_s represents the coefficient value of the roughness height- the conceptual (perpendicular) height of the 'sand grain' particles. A schematic diagram is shown in Figure 2.16, where C_s represents the coefficient value of the roughness constant - which describes the uniformity of particle shape and spatial distribution. C_s is limited to between 0.5-1, where 0.5 represents a completely spherical particle shape and 'shoulder to shoulder' spatial distribution. When between 0.5-1, the particle shape and spatial distribution increasingly diverge.

The wall-function is set similarly as the previously used wall functions, but with the inclusion of 'nutkRoughWallFunction' in the nut file with the constants κ_s and C_s specified.

OpenFoam has a wall function listed as nutkRoughWallFunction which utilises two constant variables to simulate the impact of a specified rough surface; being κ_s, the roughness height, and C_s, the roughness constant. The parametrisation of those variables in this investigation, alongside the case parameter notation is shown in Table 8.2. The surface roughness parametrisation is were selected with the intention to cover an envelope of equivalent roughness to the physical experimental foil against a smooth-wall representation, with additional scope to cover up to N.A.C.A standard surface roughness values; which act as a representation of the maximum surface roughness likely to be encountered with a turbine blade operation $in-situ$. As there is no direct definitive equivalence between the measured surface roughness and the roughness constant (C_s), the variable was adjusted for the centreline average roughness to gauge the impact of the constant.

The κ - ω SST turbulence model is considered both accurate and robust in the nearwall treatment which has contributed to it's regular feature in industrial use [157].

When setting the standard 'no-slip' wall boundary condition, all turbulent vari-

ables apart from ω are set uniformly to zero. ω within the viscous sublayer follows the equation:

$$\omega \to \frac{6\nu}{\beta_1 y^2} \quad when \quad y \to 0 \tag{2.75}$$

Wilcox' specified that equation 2.75 should be used to explicitly specify ω across the boundary layer mesh cells. Menter proposed a adjustment to equation 2.75 boundary layer relationship to:

$$\omega_{wall} = 10\frac{6\nu}{\beta_1 (\Delta y)^2} \quad at \quad y = 0 \tag{2.76}$$

Where Δy is the distance to the first cell node. Thus, negating the requirement to alter subsequent cell values into the flow domain, while still achieving equivalent levels of accuracy [159].

Wilcox (1988) also formulated rough wall treatment corrections to the model, with minor modifications to the standard ω_{wall} equation 2.75:

$$\omega_{wall} = \frac{u_\tau^2 S_R}{\nu} \qquad S_R = \begin{cases} \left(\dfrac{50}{k_s^+}\right)^2 & if \quad k_s^+ \leq 25 \\[2em] \dfrac{100}{k_s^+} & if \quad 25 \leq k_s^+ \leq 2000 \end{cases} \tag{2.77}$$

Effectively, in forcing a finite ω value onto the wall boundary, the degree in which turbulence is dissipated at the wall is reduced. Thusly, create conditions for higher momentum transfer and ensuing higher friction factors [21].

$$k_s^+ = \frac{k_s u_\tau}{\nu} \tag{2.78}$$

However, the velocity shift Δu^* is under-predicted for $K_s > 30$ as a consequence of the SST eddy viscosity limiter. While the SST eddy viscosity limiter is also active for smooth and small K_s surfaces, the diminutive magnitude of the near-wall turbulence reduces the impact. Hellsten and Laine [110] proposed a correction to inhibit the SST limiter through applying an additional coefficient:

$$F_3 = 1tanh\left[\left(\frac{150\nu}{\omega y^2}\right)^2\right] \tag{2.79}$$

The correction works by limiting the capacity of the SST eddy viscosity limiter close to the wall, yet not continue to inhibit inside the logarithmic region. However, the correction loses its capacity with $K_s > 1000$, though such surface conditions are beyond the scope of this thesis. Thus, the 1988 Wilcox' and 1998 Hellsten corrections in tandem are numerically adequate to simulate $k_s^+ < 25$ roughness lengths of $C_s = 0.5$ as those presented in Figure 2.17.

[111, 110, 21]
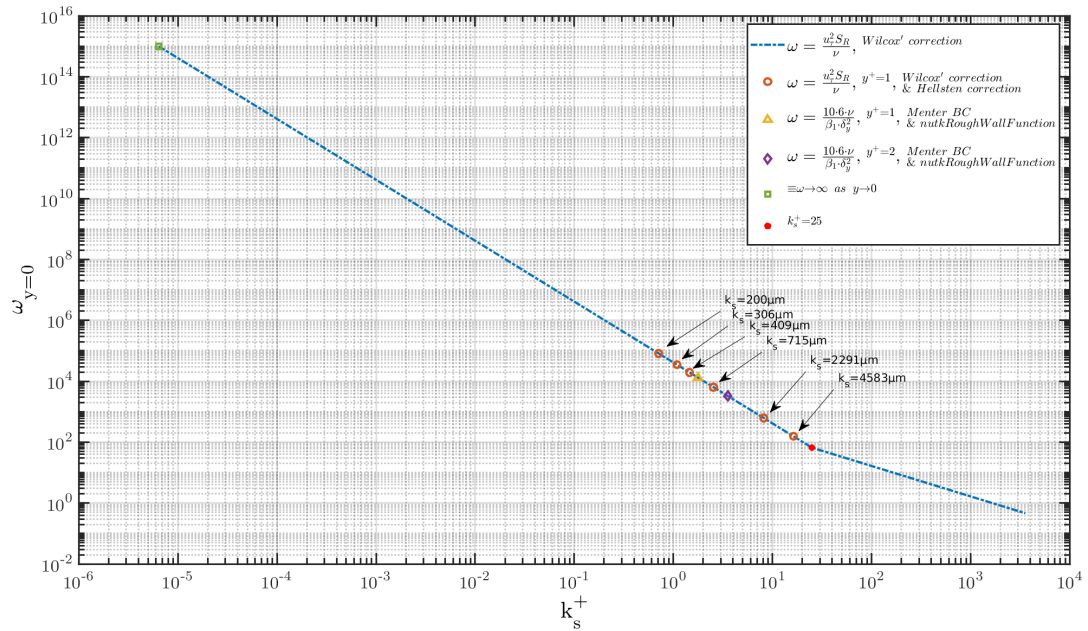
Figure 2.17: The imposed $\omega_{y=0}$ wall boundary condition, to differentiate equivalent k_s^+ representation between the boundary layer resolved Wilcox' correction, the *nutkRoughWallFunction* based with the Menter' correction and an unspecific high setting $\equiv \omega \to \infty$.

2.4 Discretisation Methods

The governing equations are expressed as spatial and temporally dependant, partial differential equations. The solution of which is computed after discrertising through a numerical method.

The numerical methods that are widely used to discretise the partial differential equations are:

- Finite Difference Method (FDM)

- Finite Element Method (FEM)

- Finite Volume Method (FVM)

2.4.1 Finite Volume Method

The finite volume method is a discretization scheme for a flow domain, with the integral equation form of the transport equations. The flow domain is discretised into diminutive volumetric spaces.

There are two main types of finite volume method; being the cell-centred and the cell-vertex finite volume methods. The main difference is illustrated in Figure2.18. The essential difference relates to where unknowns are integrated across. The cell-vertex integrates across the cell space between the vertices. It should be noted that the cell-vertex can be split up into two further sub-groups; being vertex-centred and the vertex itself. While the cell-centred is solely between the centre point of each cell. The difference in approaches
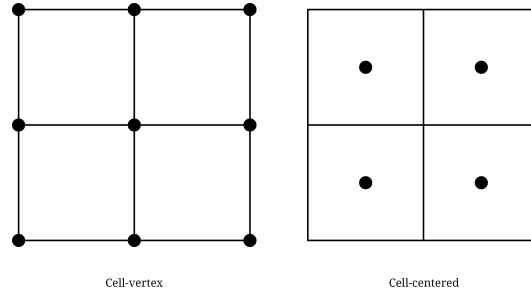
Figure 2.18: A schematic of the Cell-vertex (left) and the Cell-centred (right) variants of the finite volume method.

Consider the transport equation with scalar quantities represented through ϕ in terms of transient, convection, diffusion and source [52]:

$$\frac{\delta(\rho\phi)}{\delta t} + \nabla \cdot (\rho \vec{u} \phi) = \nabla \cdot (\Gamma_\phi \nabla(\phi)) + S_\phi \tag{2.80}$$

Equation 2.80 can be represented as a linear matrix equation in the form of:

$$\underline{\underline{A}}\vec{\phi} = \vec{b} \tag{2.81}$$

By making suitable approximations for each term. Where $\vec{\phi}$ is vector of the scalar quantity for a finite number that can approximated to within required levels of accuracy of the solution [52].

Each term is intergrated over the cell's control volume. However, if the system is transient, each term also is intergrated over with each time step Equation 2.82 [52].

$$\int_t^{t+\Delta t}\int_V \frac{\delta(\rho\phi)}{\delta t}dVdt + \int_t^{t+\Delta t}\int_V \nabla \cdot (\rho \vec{u}\phi)dVdt = \int_t^{t+\Delta t}\int_V \nabla \cdot (\Gamma_\phi \nabla(\phi))dVdt + \int_t^{t+\Delta t}\int_V S_\phi dVdt \tag{2.82}$$

Source Term

For parameters that cannot be described with terms applicable to convection, diffusion or temporal terms in the transport equation; yet are acting on the system are defined as source terms [52]. The Source term can be described as:

$$S_\phi = S_C - S_P\phi \tag{2.83}$$

Which is a linearised expression with the $S_P > 0$ to ensure that the diagonal dominance is maintained. In such format, the linearised source term can be discretised by integrating over the control volume [52].

$$V_P(S_C - S_P\phi_P) \tag{2.84}$$

72
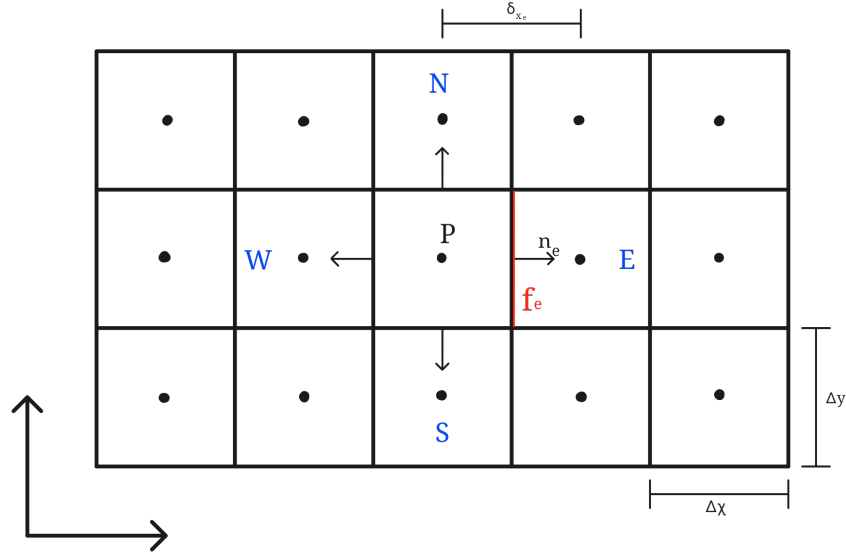
Figure 2.19: A schematic of the Cell-vertex (left) and the Cell-centred (right) variants of the finite volume method. P denotes the value at the centre of each element.

Diffusion Term

The diffusion term is discretised through applying the divergence theorem (Equation 2.85)

$$\int_V \nabla \cdot \vec{a} \, dV = \int_A \vec{a} \cdot \hat{n} \, dA \tag{2.85}$$

Which equates the integral of a divergence over the specific volume is equal to the fluxes through the face surface of the control volume [52]. Thus:

$$\int_V \nabla \cdot (\Gamma_\phi \nabla(\phi)) dV = \int_A (\Gamma_\phi \nabla(\phi)) \cdot \hat{n} \, dA \tag{2.86}$$

Equation 2.86 can be simplified if $\nabla(\phi) \cdot \hat{n}$ is recognised as being equal to the gradient of ϕ in the direction of the normal ϕ. Therefore, can be expressed as the sum of surface integrals over each surface face bounding the control volume [52].

$$\sum_f \int_f (\Gamma_\phi) \frac{\delta \phi}{\delta n} dA \tag{2.87}$$

In the case that the cell geometry is completely orthogonal; the line between both centre nodes will be parallel to the cell face normal.

$$\frac{\delta \phi}{\delta n} \simeq \frac{\phi_E - \phi_P}{\delta_{PE}} \tag{2.88}$$

where δ_{PE} is the separation between the nodal centres of P and E respectively. So the full discretised form can be shown as equation 2.89.

$$\sum_f (\Gamma_\phi)_f A_f \frac{\delta \phi}{\delta n} \tag{2.89}$$

Γ_ϕ is calculated on the face as equation 2.90

$$(\Gamma_\phi)_f = \alpha_f(\Gamma_\phi)_P + (1 - \alpha_f)(\Gamma_\phi)_E \qquad with \qquad \alpha_f = \frac{\delta_{Ef}}{\delta_{Ef} + \delta_{Pf}}$$

(2.90)

However, using the mean average has a severe drawback - if Γ_ϕ is equal to zero, there will be no flux whilst, yet, equation 2.90 will still output a non-zero solution. Another drawback is that if the $\Gamma_\phi)_E$ is diminutive with respect to $\Gamma_\phi)_P$, the low resistance to the flux between the center-point P and the interface in comparison to that of E and the face [52]. The harmonic interpolation equation 2.91 can instead be used

$$\Gamma_\phi)_f = \frac{\Gamma_\phi)_E \Gamma_\phi)_P}{\alpha_f(\Gamma_\phi)_P + (1 - \alpha_f)(\Gamma_\phi)_E}$$

(2.91)

which will output a zero value if either $\Gamma_\phi)_E$ or $\Gamma_\phi)_P$ are zero or $\Gamma_\phi)_P \gg \Gamma_\phi)_E$.

Convection Term

Like the diffusive term, the convection term is also transformed with the divergence theorem equation 2.85 into equation 2.92.

$$\int_V \nabla(\rho \vec{u} \phi) dV = \int_A \rho(\vec{u} \cdot \hat{n}) \phi dA$$

(2.92)

The surface intergral corresponds with the number of bounding faces over the control volume. The summation of which is given by equation 2.93.

$$\underset{\Sigma}{f} = (\rho \vec{u} \cdot \hat{n})_f \phi_f$$

(2.93)

ρ_f inherits the upwind element. Thus the following assumptions are held true in equation 2.94

$$\rho_f = \rho_P \qquad if(\vec{u} \cdot \hat{n})_f > 0.0 \, and \, \rho_f = \rho_A \qquad if(\vec{u} \cdot \hat{n})_f > 0.0$$

(2.94)

The Rhie-Chow interpolation method is used to calculate $(\vec{u} \cdot \hat{n})$ and ϕ is calculated at the cell face, as with the diffusion term [52].

Temporal Discretization

For unsteady flows, the time-dependant terms are also discretised and intergrated with respect to time along with the spatial. The time dependant term is shown in Equation 2.95

$$\frac{\delta \phi}{\delta t} = F(\phi)$$

(2.95)

Where $F(\phi)$ represents the sum of the spatial terms.

Courant-Friedrichs-Lewy (CFL) Condition

$$v = \frac{\delta x}{\lambda \Delta t} \tag{2.96}$$

Where λ is the characteristic speed, which becomes $\max |u|$ for incompressible flow, and $\max u + \sqrt{gh}$ for shallow water flow.

2.5 Solvers

The flow transport equations can be solved to calculate the convection of a scalar variable ϕ - if the magnitude and direction of the velocity field are known. However, there is no direct analytical solution. Thus, iterative numerical solvers are used.

2.5.1 SIMPLE Algorithm

The Semi-Implicit Method for Pressure Linked Equations (SIMPLE) algorithm is essentially a trial-and-error, iterative procedure for the calculation of pressure on a staggered grid arrangement [254]. The algorithm was created by Patankar and Spalding [183], and has become one of the most widely employed solvers for the Navier-Stokes equations.

A simplified flow chart of the sequence of operations in the SIMPLE CFD procedure is given in **Figure 2.20**.

Steady-state solvers have been successfully implemented in numerous CFD case procedures and are noted for the savings in computational effort. The SIMPLE algorithm is flawed with respect to accurate pressure corrections, however, the pressure corrections are determined to be satisfactory for correcting velocities [254, 185, 184].

2.5.2 SIMPLER Algorithm

Devised to address the pressure correction problem in the SIMPLE algorithm, the SIMPLER algorithm only uses the pressure corrections to correct velocities. The pressure is calculated though an additional discretised equation which was shown to be more effective [185]. Additionally, while the additional equation is applied, the number of calculations is increased by approximately 30%. However, convergence is achieved at a greater rate and a comparison between the methods has shown the SIMPLER to achieve reductions in computational intensity in the range of $30 - 50\%$ [11].

2.5.3 SIMPLEC Algorithm

The SIMPLEC (C-Consistent) is a related algorithm by Van Doormal and Raithby [252]. SIMPLEC has modifications to the momentum equations and subsequently omits terms from the velocity correction equations that become of lower significance.
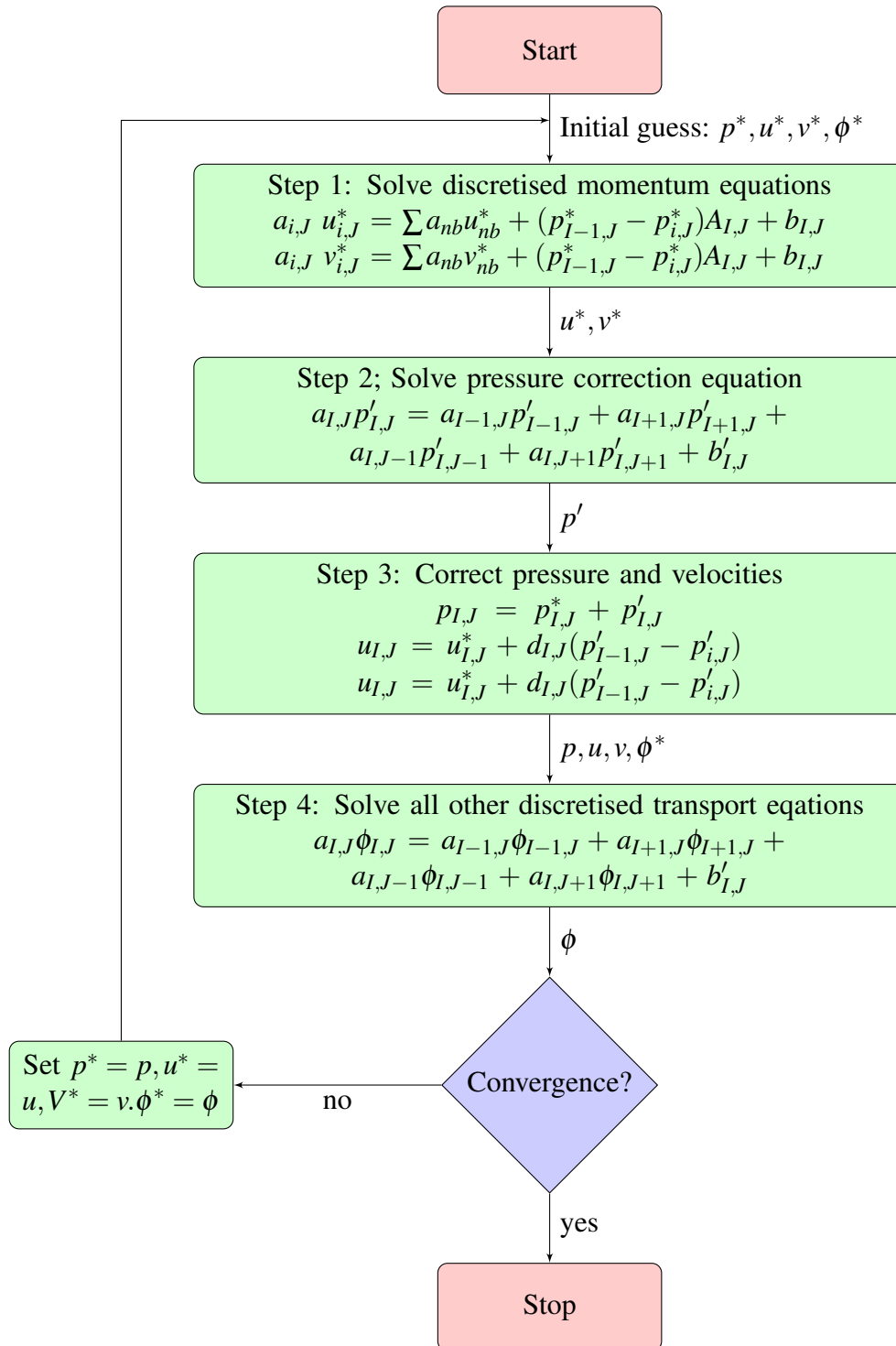
Figure 2.20: Simplified sequence of operations in the SIMPLE CFD procedure. [254]

The engineered purpose is to achieve faster convergence times than the SIMPLE algorithm with improvements of 30%. Additionally, the computational intensity is also lower than that of the SIMPLER algorithm since there is no additional discretised pressure equation to solve [252, 47, 276]. The sequence of operations for SIMPLEC is identical to those of the SIMPLE and can be followed in Figure 2.20.

2.5.4   PISO Algorithm

The PISO algorithm, standing for Pressure Implicit with Splitting of Operators. Formulated by Issa [117], could be summarised as an extension of the SIMPLE family; with a further corrective step to enhance the accuracy. Being a pressure-velocity formulation procedure intended to compute unsteady compressible flows, The PISO algorithm was successfully integrated into a iterative scheme for solving steady state problems [254].

The PISO algorithm solves the pressure correction equation twice the amount SIMPLE does. Therefore there is a corresponding storage requirement. Despite the implied higher computational intensity in comparison to SIMPLE, SIMPLER AND SIMPLEC; PISO has been found to perform surprisingly fast. In cases where the momentum equations were not coupled to a scalar variable, the robustness of convergence made possible time reductions by a factor of 2 [254, 117, 118].

2.5.5   Transient SIMPLE Algorithm

The SIMPLE algorithm can be adapted for solving transient problems, through the inclusion of transient terms in the discretised momentum equations. An additional Pressure correction is also required. When applied for transient flow simulations with implicit formulation, either of the SIMPLE family can be applied at each time step until convergence. Figure 2.21 illustrates the structure.

2.5.6   Transient PISO Algorithm

The transient PISO algorithm, it's original design adaption without iterative steps, utilises the 'splitting technique' to discretise equations and attain accurate temporal outputs [117]. The transient PISO method has also attained accurate results when time steps are set sufficiently small [117, 128].

2.5.7   Transient PIMPLE Algorithm

The PIMPLE algorithm is a intended hybridisation of the PISO and SIMPLE algorithms. While both PIMPLE and SIMPLE are iterative solvers, PIMPLE is used for transient cases whereas SIMPLE for steady state. PIMPLE can be described as recurring SIMPLE algorithm for each time step. The outer correctors are the iterations; once converged the next time step will commence until the solution is complete. PIMPLE has a advantage over PISO in that PIMPLE has a superior stability, especially with larger time steps and Courant numbers above 1, or when the simulation is inherently unstable.Iterative Solutions of the pressure and velocity are under-relaxed and continually iterate until a set limit of iterations or residual level [40, 102].
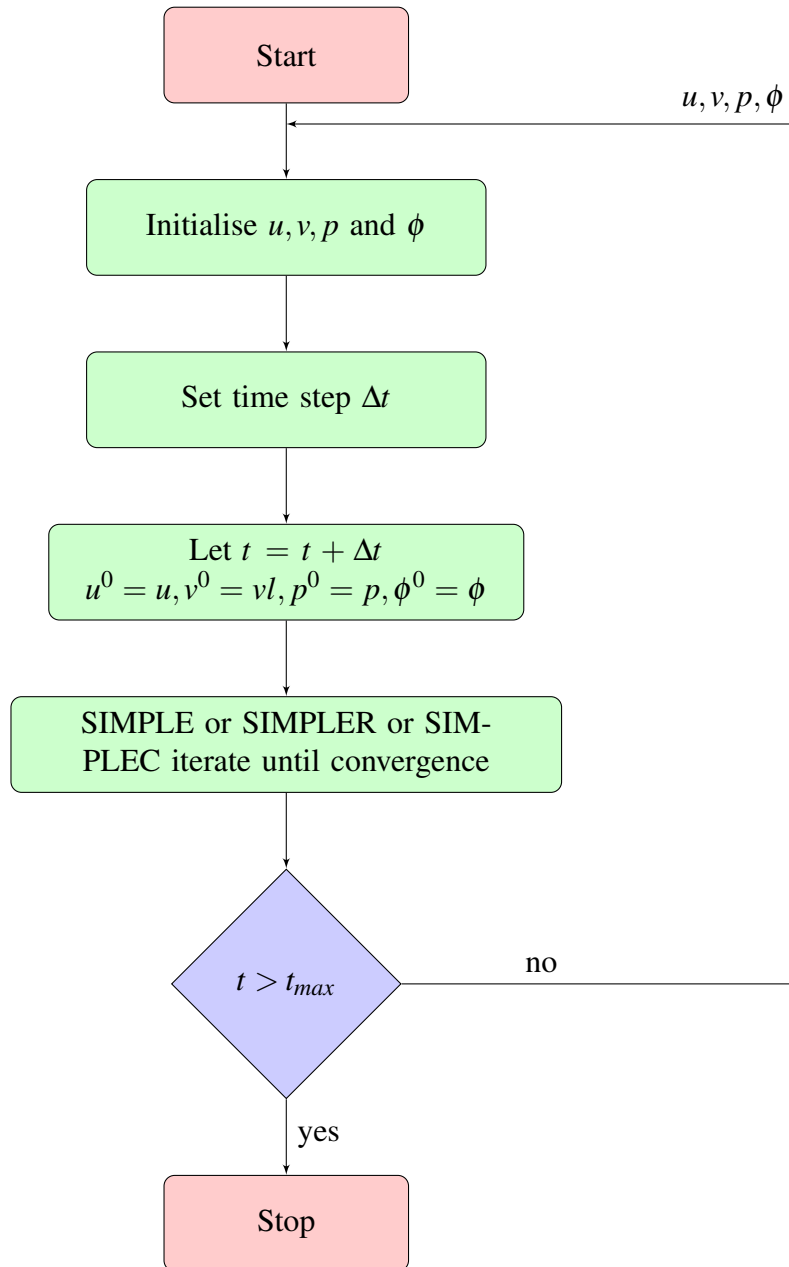
Figure 2.21: Simplified sequence of operations in the transient SIMPLE CFD procedure. [254]

2.5.8 Summary

In this section the relevant solvers have for modelling within this body of work have been briefly described. With respect to work conducted through modelling with OpenFOAM, the two primary solvers used are the SIMPLE [179] and PIMPLE [178] algorithms.

The SIMPLE algorithm is only suitable for solving steady-state solutions due to the pseudo-time stepping method, thus inadequate for simulating any transient hydrodynamics. Initially the SIMPLE algorithm was employed to find time efficient solutions to the TDT near-field. However, SIMPLE was substituted for the transient solver PIMPLE when the geometrical complexity was increased and "steady" were unable to be reached.

The SIMPLE algorithm was also employed to spin up the 2D foil parametrisation, essentially mapping a reasonable flow-field with, unsteady and viscous flow, which is more suitable for the transient solver 'pimpleFOAM'.

The GAD model simulations were conducted using SIMPLE for reasons of computational efficiency and that the simple domain geometry enable a "steady" solution to be reached.

2.6 Mathematical Modelling Categorization of Tidal Energy Extraction

Modelling in relation to developing tidal energy generation schemes spans utilization of a broad range of mathematical models to suit each specialized purpose. The development of tidal energy projects are greatly assisted with the implementation of numerical models of the hydrodynamics around the operational structures. These models vary in types from computationally un-intensive 0D and 1D models to the increasingly computationally intensive 2D to 3D models [192, 50, 4, 23, 191, 16, 14, 274, 272, 268, 81].

This section will cover a brief overview of how 0D and 1D models are used within tidal energy research before moving onto a more in-depth explanation of 2D and 3D modelling methods which will feature within this thesis.

The term 'model' can be used in a wide range of contexts, all denoting a designed representation of a phenomenon. Within this thesis, the term is explicitly used in a computational context of deterministic models. Within such, dimensions are referred using x y z and t notations for the three spacial and temporal dimensions respectively. The dimensional characteristics of a model are denoted through concise classification; of which is often given within the model name. Six classifications are used to indicate the dimensional state, namely:

1. Temporal numerical models.

   - Steady-state
   - Transient

2. Spatial numerical models.

   - 0-Dimensional (0D)

- 1-Dimensional (1D)

- 2-Dimensional (2D)

- 3-Dimensional (3D)

The presence of the temporal dimension would be denoted as being a 'transient' simulation, conversely, the absence of which is then classified as 'steady-state'. The steady-state approach is ideal for systems where internal convergence can be reached. Where temporal boundary conditions exist, the steady-state cannot be reached.

The number of spatial dimensions is denoted through numerical referencing: *D. The spatial dimensional requirement should be limited to where relevant spatial changes will occur.

It should be noted that increasing the number of spatial dimensions increases the system complexity and thus also the associated computational cost.

The simplest model variant is the 0D, where it is assumed there is an instantaneous transmission of inputs and outputs from a given system that the model represents.

With the 1D model, the spatial dimension is taken as the axial dimension. Thus can only provide rates of change along said dimension. The Steady-state model will output ordinary differential equations. If a temporal element is added, the output will be a partial differential equation. As a result, the selection of the model types is a judicious process.

All the discussed classifications of mathematical models can be situationally employed to replicate hydrodynamic environments. Utilizing these models allows for numerous aspects of tidal power or coastal processes to be studied and evaluated, allowing for the problems to be addressed.

2.6.1   0D Hydrodynamic Modelling

The 0D models are considered the least complex and computationally cheapest to operate out of the four types. The primary advantage of using lower fidelity models with respect to the 3D models is that they can often be simulated on lower performance computational systems and often on a single processor, where 3D models require considerably more computational effort, often employing cluster systems for the simulation to be feasible.

Revolving around the assumption that if a volume of fluid flows into a basin/reservoir, the fluid level will rise by an amount proportional to what was let in. The additional volume can de divided by the area of the basin to give the level increase. The level is also considered uniform across the basin/reservoir.

0D coastal impoundment models require the known tidal levels, the operational sequence, and a formulae to represent the hydraulic structures to a reasonable degree of accuracy, to simulate the overall performer of the impoundment concept. The hydraulic operation is often modelled using a water level time series as an input, dictated by the downstream temporal water level at the location. 0D modelling has been investigated in numerous literature sources and commonly deemed adequate under certain conditions. Limitations have been noted where 0D models can overestimate the power potential of schemes that have both a large intertidal region and

upstream surface area. An example of 0D tidal modelling can be found in papers by Angeloudis *et al* [16][14], who use the backwards-difference numerical model - which was developed according to the continuity equation, was refined according to principles of [4]:

$$A_s(Z)\frac{\delta Z}{\delta t} = Q(H) + Q_{alt} \tag{2.97}$$

Where (Z) represents basin water level and t time. The basin wetted surface area (A_s), in the absence of substantial wetting and drying, can be assumed constant. Which is not typically applicable a substantial number of tidal range projects. The limitation is particularly prevalent in estuarine environments with sizeable flood plains. The flow flux (Q) is a function of the total input from the sluice gates and turbines for a particular head (H). An additional term (Q_alt) is for alternative input sources such as rivers.
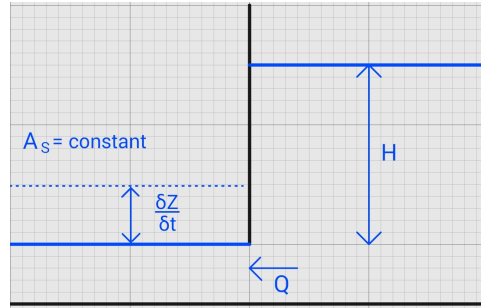
Figure 2.22: Schematic of the water level function given in Equation 2.97.

The approach used to calculate the flow driven through the hydraulic structures is the orifice equation:

$$Q = C_d A_f \sqrt{2gH} \tag{2.98}$$

Where the flow is driven through by a head difference through the sluice gate's cross-sectional area A_f is the flow area. The discharge coefficient C_d primarily dictates the regulation and specification of the flux, and is governed by specific mechanisms to aptly characterise the output flux to be more in-line with realistic measures from such hydraulic structures. An example case would be the decrease in value for a turbine with respect to a sluice gate of equivalent reference cross-sectional areas. Since the turbine bulb will act to restrict the flow and instigate an pressure drop. Another consideration that can be added to the model is accounting for the temporal element involved in the opening and closing of the sluice gates or turbine wicket gates during transitional periods. A ramp function term can be included into equation 2.98 to can govern the flow volume. Equation 2.99 and 2.100 express an example of such as a half sinusoidal or cosine for the opening and closing respectfully:

$$F_1(t) = sin\left(\frac{\pi t}{2T}\right), \ 0 < t \leq T \tag{2.99}$$

$$F_2(t) = cos\left(\frac{\pi t}{2T}\right), \ 0 < t \leq T \tag{2.100}$$

Where (T) is the transition time period and the function graphically represented

in Figure 2.23.
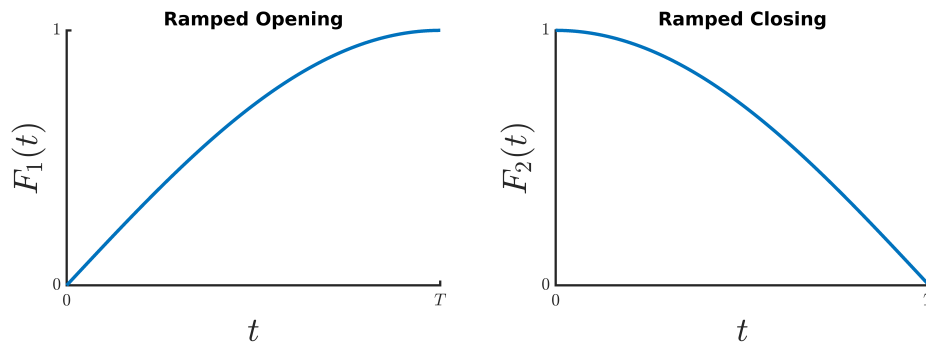
Figure 2.23: Ramp profile for a sinusoidal or cosine forced function for equations 2.99&2.100.

When modelling power generation, the discharge and power from each turbine can be calculated according to the manufacturers operational hill chart for a specific turbine design Figure 2.24.
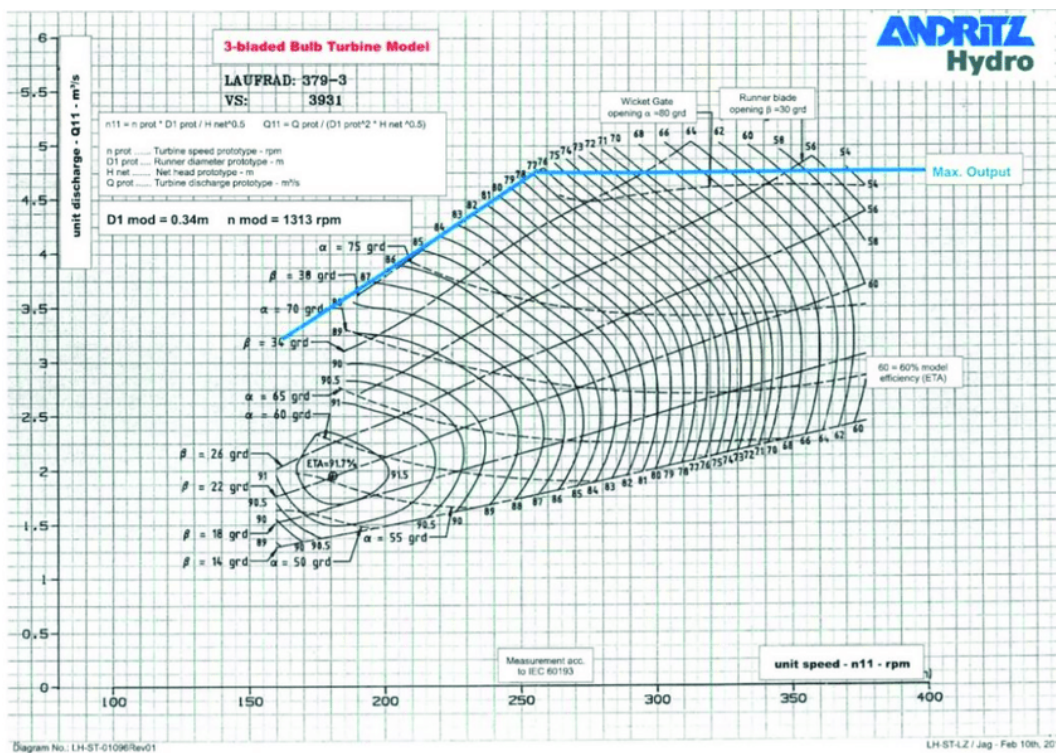
Figure 2.24: Turbine performance hill chart for a double regulated three bladed bulb unit. Blue line represents the maximum output. α the wicket gate angle. β the runner blade opening [5].

The hill chart is constructed from functions of the following equations 2.101,2.102 and 2.103 The unit speed (n_{11}) of a double regulated bulb unit (two modes of flow control being the wicket gates and the runner blade pitch) can be expressed as:

$$n_{11} = \frac{S_p \cdot D}{\sqrt{H}} \qquad (2.101)$$

D is the turbine diameter (m).

$$S_p = \frac{2 \cdot 60 \cdot f_g}{G_p} \tag{2.102}$$

Where S_p is the speed of the turbine, f_g is the national grid frequency, and the G_p is the number of generator poles.

The specific discharge Q_{11} is:

$$Q_{11} = \frac{Q}{D^2 \cdot \sqrt{H}} \tag{2.103}$$

The determination of the unit speed when the operating head is known can looked up against the line of maximum output in the hill chart. The related specific discharge and efficiencies (η) can then be determined.

Equation 2.103 then can be adapted to equation 2.104:

$$Q = Q_{11} \cdot D^2 \cdot \sqrt{H} \tag{2.104}$$

Thus, the power output from a turbine can be calculated through equation 2.105:

$$P = \rho g Q H \eta \tag{2.105}$$

Other efficiency losses such as the generator, transformer, gear box, drive train and frictional losses can also be accounted for.

2.6.2   1D Hydrodynamic Modelling

1D coastal models became necessary for tidal range modelling when considering locations with large spatial variation in tidal asymmetry along the lengths the domain. Large water impoundment structures are an example of which, where 1D models can be used to simulate some of the changes to the hydrodynamics without being as computationally intensive as the 2D or the 3D models. As of 2018, there are numerous examples of 1D modelling of the Severn tidal barrage [16, 171, 172]. Fundamentally being used as computationally efficient methods for qualitative assessments of the barrages scale of impact within the basin, and analysing the operating strategies for multiple scenarios. 1D models do have several inherent drawbacks stemming from inherent simplification related assumptions which can compromise the analysis if improperly used, and to a lesser extent are subject to large error bars within the data output from the models. One such facet that is difficult to 1D model is the natural tidal amplitude.

One example of such is the application of the 1D Saint-Venant equations 2.106 and 2.107 in the model presented by Angeloudis *et al* [15]:

$$\boxed{\text{rate of area change}} + \boxed{\text{input-output term}} = \boxed{\text{net lateral flow}}$$

$$\frac{\delta A_f}{\delta t} + \frac{\delta Q}{\delta x} = 0 \qquad (2.106)$$

| local acceleration | + | Convective acceleration | + | Pressure forcing | = | Friction force term |
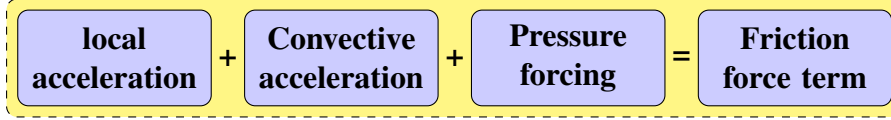
$$\frac{\delta u}{\delta t} + u\frac{\delta u}{\delta x} + g\frac{\delta \zeta}{\delta x} = -\frac{\tau_b}{\rho H} \qquad (2.107)$$

Where A_f is a function of the free surface elevation above the reference plane as according to Figure 2.25, and the frictional forces through a Manning formulation.
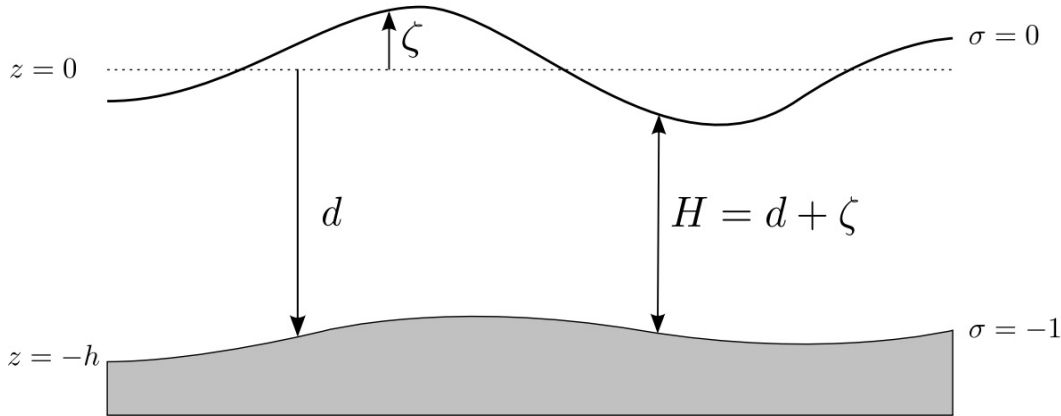
Figure 2.25: Schematic presentation of the numerical definition of the water level ζ, depth h and total depth H. [228]

2.6.3   2D & 3D hydrodynamic modelling

2D Shallow Water Equation   models are governed through derivations of the 3D model through depth-integrating. 2D models then can only hold true under conditions where the vertical dynamics are miniscule with respect to the horizontal dynamics and can thus be neglected. Thus, relating to tidal modelling, cannot replicate a breaking wave since the 3D effects are essential, but can simulate the tidal-wave since the wavelengths are long and small amplitude.

The 3D continuity equation is given by

$$\frac{\delta u}{\delta x} + \frac{\delta v}{\delta y} + \frac{\delta w}{\delta z} = 0 \qquad (2.108)$$

and the momentum equations are given by

$$\frac{\delta u}{\delta t} + \frac{\delta u}{\delta x} + \frac{\delta u}{\delta y} + \frac{\delta u}{\delta z} - fv = \frac{1}{\rho} \left(-\frac{\delta P}{\delta x} + \frac{\delta \tau_{xx}}{\delta x} + \frac{\delta \tau_{yx}}{\delta y} + \frac{\delta \tau_{zx}}{\delta z} \right) + M_x,$$

$$\frac{\delta v}{\delta t} + \frac{\delta v}{\delta x} + \frac{\delta v}{\delta y} + \frac{\delta v}{\delta z} - fv = \frac{1}{\rho} \left(-\frac{\delta P}{\delta x} + \frac{\delta \tau_{xy}}{\delta x} + \frac{\delta \tau_{yy}}{\delta y} + \frac{\delta \tau_{zy}}{\delta z} \right) + M_x, \quad (2.109)$$

$$\frac{\delta P}{\delta z} = -\rho g$$

Equation 2.109 describes the processes of acceleration, advection and the Coriolis effects on the left hand side. The right hand side describes the forces acting on the fluid due to pressure, shear-stresses and external forcing.

The fluid surface is subjected to boundary conditions but the spatial position is not known *a priori*. The primary assumption in SW-Theory is that Horizontal scales (wave length) are significantly larger than vertical scales (water height).

$$\underbrace{\frac{\delta u}{\delta x} + \frac{\delta v}{\delta y}}_{\substack{U \\ \approx \frac{U}{l}}} + \underbrace{\frac{\delta w}{\delta z}}_{\substack{w \\ \approx \frac{w}{h}}} = 0 \quad (2.110)$$

neglect vertical accelerations

$$\frac{\delta w}{\delta t} = 0 \quad (2.111)$$

Free-surface boundary condition

The corresponding boundary condition applied to the free surface is defined in equation 2.112 [143]

$$w \bigg|_{z=\eta} = \frac{\delta \eta}{\delta t} + u \frac{\delta \eta}{\delta x} + v \frac{\delta \eta}{\delta y}, \quad (2.112)$$

where η represents the free-surface elevation.

Bed boundary condition

The condition imposed at the sea-bed to fluid interface is where the momentum equation becomes [143].

$$w \bigg|_{z=\eta} = -\left(\frac{\delta h}{\delta t} + u \frac{\delta h}{\delta x} + v \frac{\delta h}{\delta y} \right), \quad (2.113)$$

$$\frac{v}{h} \frac{\delta u}{\delta z} \bigg|_{z=-h} = \frac{\tau_{bx}}{\rho}, \qquad \qquad \frac{v}{h} \frac{\delta v}{\delta z} \bigg|_{z=-h} = \frac{\tau_{by}}{\rho} \quad (2.114)$$

with $\tau_{bx}\&\tau_{by}$ being the components of the bed-stresses in the x and y directions respectfully $\tau_b = (\tau_{bx}, \tau_{by})$.

Depth-averaged   For 2D depth-averaged application, the shear-stresses at the bed surface from turbulent flow are governed by the quadratic friction law:

$$\tau_b = \frac{\rho g U}{C_{2D}^2} \tag{2.115}$$

The 2D-chezy coefficient C_{2D}^2 can be determined through:

$$C_{2D} = \frac{\sqrt[6]{H}}{n} \tag{2.116}$$

where H is the total water depth (m) and n is the manning coefficient ($m^{-1/3}s$).

2.6.4   Application to Coastal Models

Computational models at the foundation are fundamentally an equation or a series of equations that equate a quantity with other known quantities. With tidal models, the equations used are derived from Newtons laws of Motion and Gravitation, with conservation of mass, energy and angular momentum, to give the continuity, momentum and energy equation.

2-Dimensional (2D) models solve depth-intergrated Navier-Stokes equations, both momentum and continuity, to calculate water-levels and depth-averaged velocities in two spatial dimensions, can be used for larger spatial analysis on oceanic scales, such as shelf seas like the SEACAMS2 NW European Continental Sea model, . These large domain models are often very computationally intensive.

Tidal Modelling

Hydrodynamic modelling has its routes in developing shallow water shelf sea models, to form predictive methods for potentially catastrophic natural events such as storm surges- driven partially in the UK as a result of the devastating north sea flood in 1953 [61].

Papers [16][14] use the following 2D modelling method to produce the numerical simulations. The computational domains are discretised into triangular cells to form unstructured meshes for a cell-centred Finite Volume Method (FVM). Roe's approximate Riemann solver, including a Monotone Upstream Scheme for Conservation Laws (MUSCL); resolves the normal fluxes across cell interfaces, following a predictor-corrector time stepping algorithm to satisfy second-order accuracy in time and space. The boundary conditions (i.e. land, water level and discharge boundaries) are treated with an integrated thin film algorithm for wetting and drying processes in intertidal regions. The numerical model is based on a Total Variation Diminishing scheme; an explicit algorithm, therefore intrinsically stable while the CFL number is less than 1. As such, the predicted hydrodynamics are not susceptible to the generation of non-physical oscillations, therefore are suitable for modelling the high velocity flows produced through the turbine and sluice gates. Domain decomposition approaches are used to address the complexity of the processes, the upstream and

downstream of the hydraulic structures were separated and dynamically connected through specified open discharge boundaries. The representation of the hydrodynamic processes through the hydraulic structures is based on the supercritical flow boundary formulation, which preserves the flow area and momentum through the turbines and sluices. An assumption is made that no stratification of the tidal dynamics in the areas of interest. 3-D flow will exist in the flow from the hydraulic structures, however, from a regional perspective, will only be in the adjacent cells to the hydraulic structures. It was for this reason that a high-resolution 2-D model was used. The methodology was concluded with the model was based on the available boundary data and suitable for the assessment of the small lagoons. An accurate assessment is needed of the far-field effects when modelling larger scale impoundments with extended boundaries, providing credibility if the boundary conditions are not influenced. However, the author notes that the primary focus is the comparison of 0D & 2D power predictions and the selected boundary domain was sufficient.

Tidal Harmonics The dynamic gravitational interaction between the earth, sun and moon generate temporal and spatial forces acting on the Earth's Oceans. While the gravitational forces act as the driving force, other factors in combination ultimately determine the magnitude and phase of the tide at a particular point on the earths wetted surface. Tidal forcing can be subsequently discretised into several series of tidal forcings each named as a constituent sinusoidal tidal harmonic. The frequency of each harmonic constituent is determined by temporal astronomic conditions. However, the amplitude and phase is spatially dependant on specific location. For simplification purposes for implementation into coastal models, the principle forcing harmonics are utilised.

- M_2: Is the principal lunar semi-diurnal harmonic constituent. For tides around the UK, the M_2 constituent will be the single most significant. Directly responsible for the two tides per day with a period of 12 hours 24 minutes.

- S_2: Is the principal solar semi-diurnal harmonic constituent. When S_2 is in phase with M_2 a spring neap cycle occurs. The period is 24 hours.

- O_1, K_1: The two principle diurnal constituents. These, in combination, represent the effect of the moon on the declination of the tides.

- N_2, L_2:The two semi-diurnal lunar elliptic harmonics. These regulate the amplitude and frequency of M_2 in accordance to the variation in the moons orbital speed due to its elliptical orbit.

- M_4, MS_4:High frequency harmonics which usually a small fraction of the M_2 amplitudde. However, within coastal waters where the shallow waters can distorts the tide, they can typically possess larger amplitudes.

Bathymetry
Bathymetric data is a specific form of topography relating to that of the seabed surfaces in relation to a marine datum. The inclusion of which is an essential component in the understanding of the marine environment's hydrodynamics. Originally, ocean bathymetry was mapped in order for safe navigation through shallow channels. In

more recent times, additional marine dependencies such as ocean energy schemes installations and hydrodynamical simulations require high detail and up-to-date coastal terrain maps.

Original bathymetric data was collected through 'depth-sounding' - using a weighted rope of known length, which is cast over a ships side. This practice was time consuming since only a single point was measured at one time. Additionally, measurements were prone to distortions from the ship movements and water current loads along the rope length, which would move the line out from its true fall-line. Today most bathymetric data is collected from sonar or LIDAR systems [177].

Bathymetric data is referenced to tidal vertical datums. Often with deep water datasets, the Mean Sea Level (MSL) is the most common. However, it is common for bathymetric data around coastal areas to be referenced against other geographical datums, often depending on the locality of the dataset.

Drying & Flooding

Coastal regions such as estuaries and embayments posses attributes of being spatially large, shallow and relatively flat areas with deeper tributary channels. On flood tides, the entire area can be submerged. However, on the ebb tide, large areas are gradually exposed with only the lower streams that may remain submerged. Depending on the scales involved, should the model be of higher resolution and simulating nearer-field regions, the spatial area of the inter-tidal zone can be considerable. Thus, the accurate reproduction of the inter-tidal zones is a important feature of how a numerical model simulates the hydrodynamics.

In numerical models, the process of flooding and drying is represented by removing grid points from the flow domain when they become classified as 'dry'. Conversely, add grid points when 'wet'.

The 'depth' is specified at the vertices of each cell. The 'water-level point' of a cell is determined at the centre through either of several algorithms.

- MAX-option: $d_{m,n}^x = max(d_{m,n}, d_{m-1,n}, d_{m,n-1}, d_{m-1,n-1})$

- MEAN-option: $d_{m,n}^x = 0.25(d_{m,n}, d_{m-1,n}, d_{m,n-1}, d_{m-1,n-1})$

- MIN-option: $d_{m,n}^x = min(d_{m,n}, d_{m-1,n}, d_{m,n-1}, d_{m-1,n-1})$

- DP-option: $d_{m,n}^x = d_{m,n}$

Additionally, the value of the water depth is evaluated against specified thresholds; should the value drop below which, all four cell interfaces are then set to be 'dry'.

3D Software

OpenFOAM® is a open-source computational fluid dynamics (CFD) software suite. OpenFOAM's application revolves around complex fluid flows encompassing turbulence, heat transfer, chemical reactions, solid mechanics, acoustics and electromagnetics. There are professionally released revisions every six months, which have been bolstered with customer sponsored developments and additional contributions from the community. There is independent software testing carried out by

ESI-OpneCFD's application specialists, development partners and a selected customer base.

Part II

Swansea Bay Tidal Lagoon

Chapter 3

Far-Field Hydrodynamics

3.1 Summary

This section covers the development of an Delft3D model to simulate the hydro-dynamics' that are present in what would be the Far-Field hydrodynamic regime of coastal models. Emphasis is given to determining model artefacts than the near replication of the tidal velocities and tidal water levels. The aim was to form a single model which spans out beyond the continental shelf to achieve a boundary independent replication of the tidal flows in Swansea bay and other possible locations around the UK. The model is set to be computationally light for simulating the expanse, yet retain refinement for the Serven Estuary to provide initial estimates to the local hydrodynamics. The temporal and spatial sea water assessment across the grid nodes can then be used to provide initial parameter data for boundary conditions Nearer-field CFD models.

3.2 Introduction

This work focuses on the advancement of methodology for the representation of tidal generation schemes in coastal models. Thus looking to improve tidal range design and operation by looking to asses the schemes and their impact on the local hydrodynamic environment.

The purpose of this case is to determine the hydrodynamics around the Severn Estuary. In doing so, local water level and tidal velocities can be transferred to form a constituent to the CFD boundary conditions. Thus imposing far-field influences on the near-field hydrodynamics while retaining 3D hydrodynamic modelling capability.

2D Depth-Averaged Simulations with Delft3D

The Delft3D flow open-source software can simulate coastal flow hydrodynamics as well as sediment transport and other morphological processes. Delft3D-flow works through solving numerical problems through 2D depth-averaged shallow water equations (Section 2.6.3).
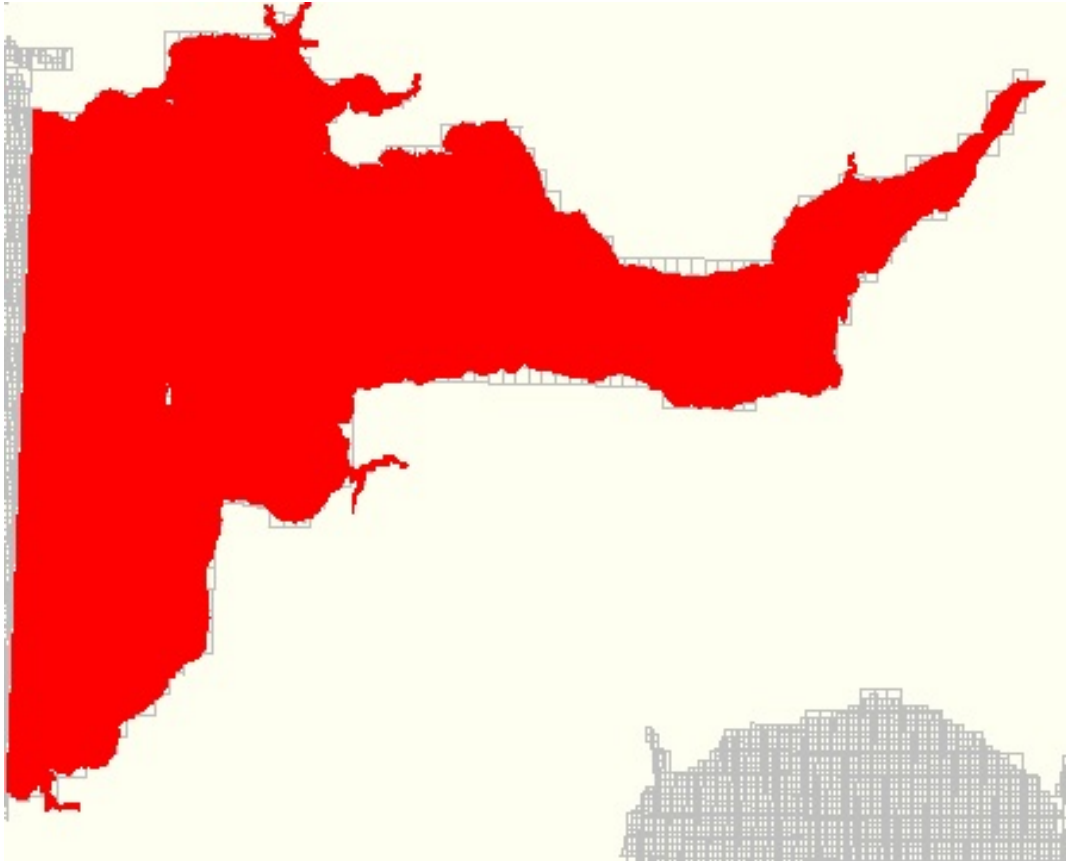
Figure 3.1: The model domain of the Bristol channel and Severn estuary (red Area). The encompassing grid meshes which the Bristol channel mesh is situated within are shown with distinctive differences in grid size. The plain area is the UK mainland situated above the highest high water mark.

The transport and deposition of sediments is usually calculated simultaneously, which creates a direct feedback relationship between the hydrodynamics and morphodynamics. However, this case works with lower detail bathymetry in combination with an interest in a shorter term analysis, therefore for simplification purposes, the transport part of delft3D-flow was not included. Delft3D-flow is also suited with a wet and drying algorithm. The grid cells are activated when water levels exceed a set flooding threshold. The same is true for the vice-versa [228].

3.3 Model Description

For coastal numerical models to adequately simulate the local hydrodynamic characteristics of a particular area, relevant field data must be collected and a standard coordinate system decided upon. The process is summarised in Figure 3.3.

The main methodologies to parametrise and force numerical models are through bathermetry data and boundary conditions. There are numerous online sources of bathymetry; GEBCO (global 1=2 arc-minute grid) and EMODnet (European 1=8 arc-minute grid).

It is not practical to use high detail geometric features away from the area of interest (AOI), as the proportion of water affected is local and not likely to influence
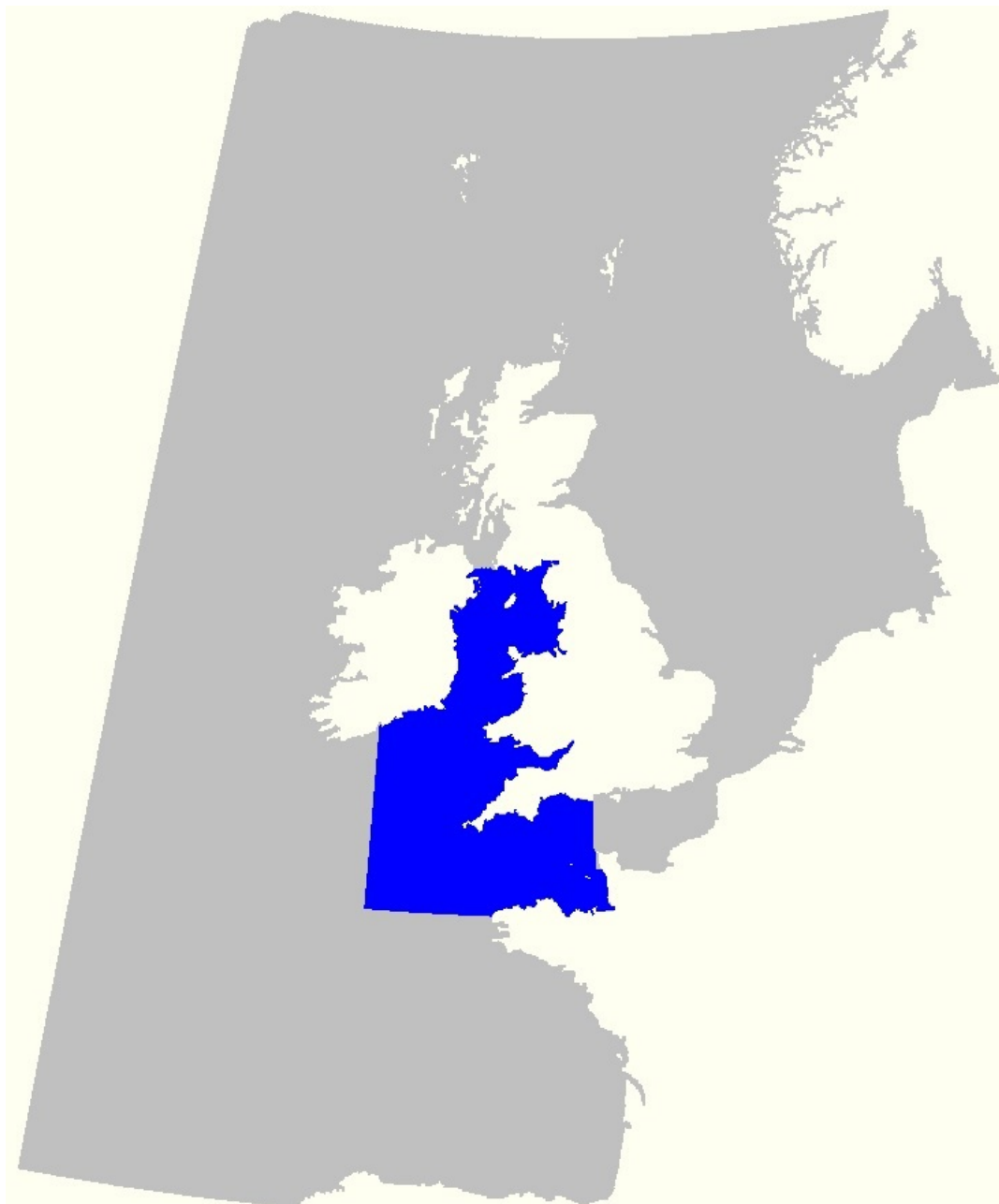
Figure 3.2: The model domains of both the NWECS model (grey) and the Welsh Waters (blue) grid.

the AOI.

3.3.1   Shoreline Geometry

A high-resolution geometric, hierarchically arranged closed polygon data-set from the World Vector Shorelines (WVS) [270] was used as the basis for the geographical positioning of landmasses with respect to bodies of water. The data-set is of the WGS 84 spherical coordinate system. The data-set was released under the GNU Lesser General Public licence. The WVS is capable of detailing the global shorelines at a scale of 1:250,000; capable of identifying 90% of features within 500meters circular
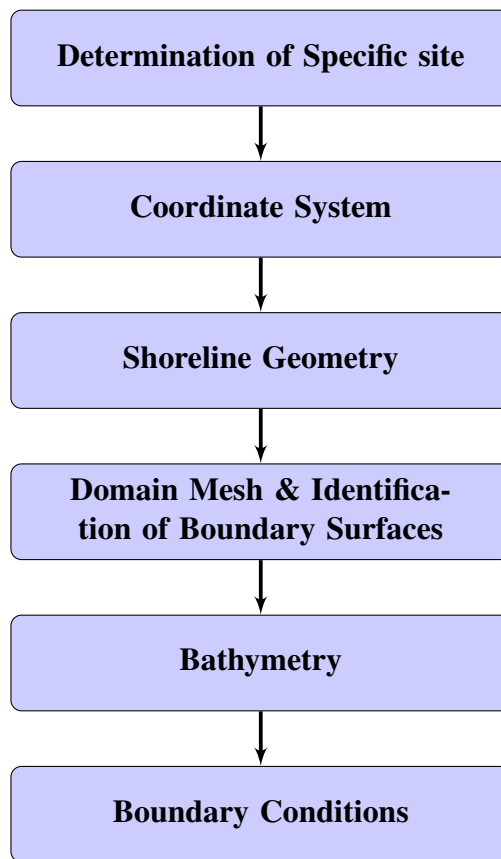
Figure 3.3: Breakdown of the Far-field model development milestones for building model.

Figure 3.4: UK Tide Gauge Network.
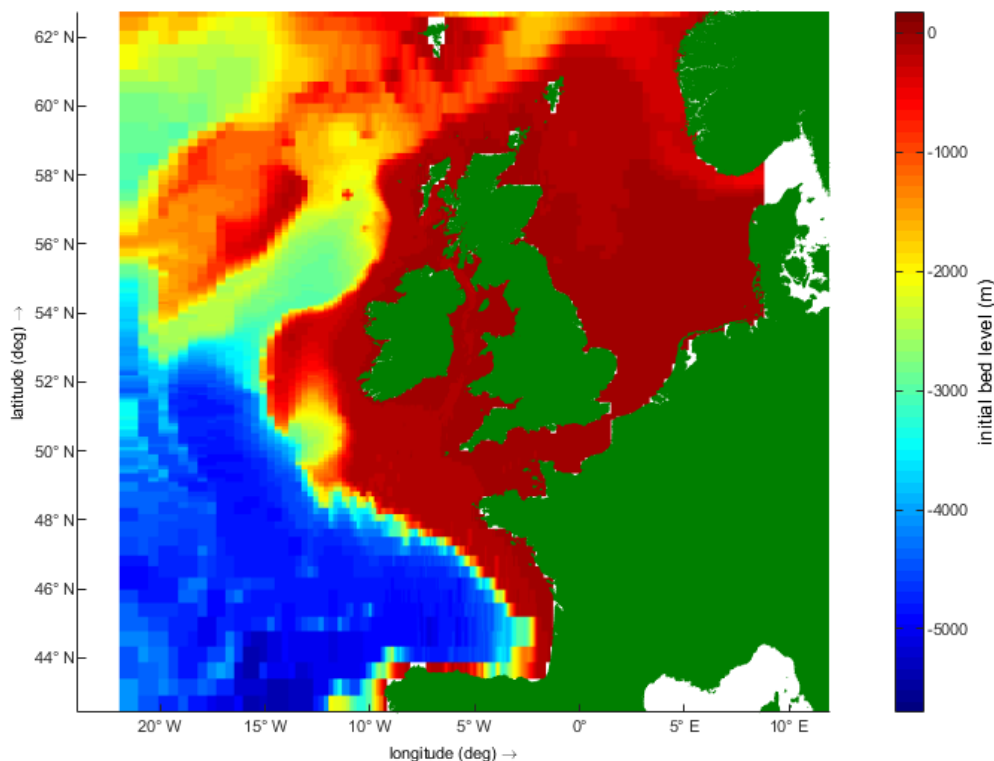
Figure 3.5: Bathymetric surface contour map for the NWES grid generated through interpolating GEBCO 08 bathymetry points with the grid nodes.

error of the true geogrpahic position with respect to the WGS datum. WVS is further described in the review by E.A. Soluri *et al* [224]

3.3.2 Mesh

The mesh was created with a Delft3D software feature called RGFGrid which is used for boundary fitted mesh generation [228]. The grid was set to be a structured grid with a quadrilateral cell for reasons of computational efficiency. The grid was initially generated with uniform cell sizes of 0.1 for Delta X and Delta Y. The mesh domain was initially set to extend between the Latitudinal and longitudinal limits of [41.026, -21.964] to [64.926, 12.636]. The initial grid was then superimposed upon the WVS boundaries. Cells were then cut following a condition that if a cell area contained landmass which constituted greater than 50%. Additionally, any cells that were isolated from the main body, such as for lakes, or located in the Mediterranean sea were also selectively deleted. Cell structures were then skewed towards the shoreline polygon.

The grid was then arbitrarily refined extending out from the approximate area of the Serven Estuary. Additionally, the mesh was de-refined along the outer boundaries. The grid was then smoothed out to reduce the abrupt refinement or coarsening of cells.

The final Grid consisted of a total 294954 cells with sizes ranging from [113373, 75582] meters at the [41.026, -21.968] Latitudinal and Longitudinal coordinate, to [137.44, 80.83] meters (**Figure 3.6**).

The Grid consists of four open boundaries where the tidal harmonic water level forcing is to be applied. The geometric identities of the open boundaries are shown in Table 3.1. The domain extends beyond the North-West European continental shelf for reasons of accurately capturing the tidal hydrodynamic movements over the UK coastal region. A.M. Davies *et al* [55] concluded that the most significant tidal constituents (Section 2.6.4) can be significantly affected by energy fluxes off the shelf edge.

3.3.3 Bathymetry

The bed surface was replicated through bathymetric data, being the bed surface relative to a sea level datum. The Bathymetric data used for this study was attained from publicly accessible sources. Different sources were sourced to account for the various degrees of refinement that would be required around the coastal region. The model comprised of GEBCO 08 bathymetry data, from the General Bathymetric Chart of the Oceans (GEBCO). Which is a continuous terrain model with a spa-

Table 3.1: Geometric identification of the NWECS domain Open Boundaries. Coordinates of the Northern hemisphere are indicated as positive. Likwise, coordinates of the Eastern hemisphere are also identified as such.

Name	Coordinates (λ, φ)	Type	Forcing
North	[-14.17,64.68]:[10.33,64.73]	Water Level	Astronomic
West	[-21.97,41.03]:[-21.98,63.83]	Water Level	Astronomic
South	[-21.97,41.03]:[-8.78,41.03]	Water Level	Astronomic
East	[8.81,58.45]:[8.81,57.04]	Water Level	Astronomic
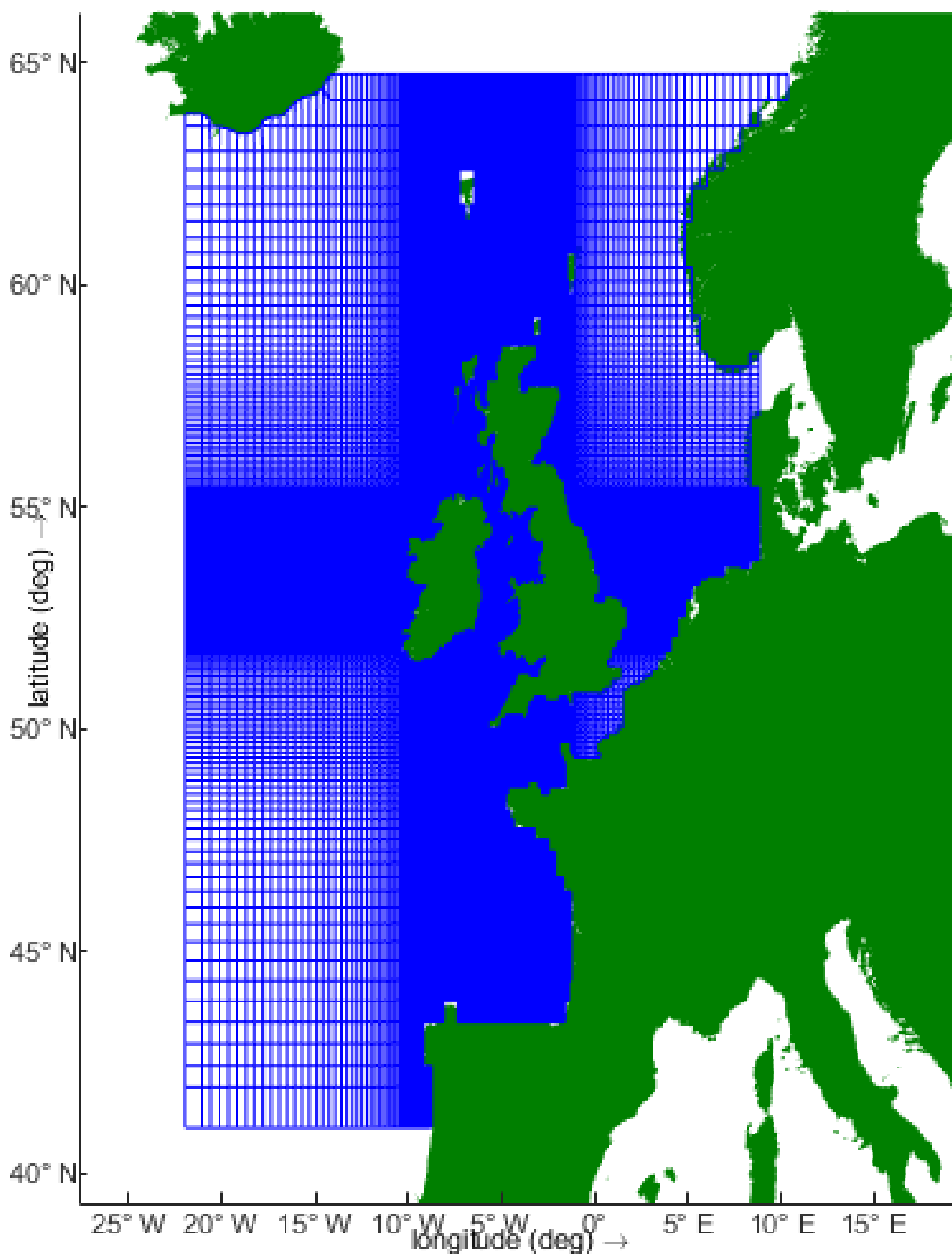
Figure 3.6: Domain of the North West European Continental Shelf (NWECS). Grid cells are blue in contrast to the open water and landmasses which are white and green respectively.

tial resolution 30 arc-seconds - approximately 926m, and tailored to provide global coverage rather than specific near-field features. Coastal areas close to areas of interest, are supplanted by additional high resolution bathymetric datasets for areas of higher refinement. The high resolution bathymetric datasets were sourced from within the UK Hydrographic Office (UKHO) online database, under the Open Government Licence v3.0. GEBCO's gridded bathymetry datasets are from the British Oceanographic Data Centre (BODC) data bank. GEBCO 08 is based on the World

Figure 3.7: Bathymetric surface generated through interpolating bathymetry points with the grid nodes.

Geodetic System 1984 (WGS84) coordinate system. The vertical coordinate system works from the global mean sea level (MSL) [87]. The high resolution data-sets were not of a uniform coordinate system. Thus, were converted under manipulation as described in A.1. Each data point is then interpolated to the grid centres to form a 2D bathymetry surface (**Figure 3.5**).

3.3.4 Boundary Conditions

The open boundary conditions were forced through water levels predicted from the TPXO 7.2 Global Inverse Tide Model. Further reading of the TPXO 7.2 Global Inverse Tide Model can be found from work produced by Egbert *et al*[75]. Only the M_2 and the S_2 tidal constituents were implemented - in isolation from the other tidal harmonic constituents. The advantage being that the computational time integration is significantly reduced [55]. The reflection parameter was set to $0s^2$ at each boundary. The MSL was used as the vertical datum and the initial condition was of 0 m water level. The uniform physical parameters were set as seen in **Table 3.2**. Additionally, the simulation tidal period time frames are shown in **Table 3.3**. The extent of the time frame was to ensure the model boundary forcing would settle. The simulation dates were used for the ease of access to what was at the time, current tidal gauge data.

The model is subjected to a Courant-Friedrichs-Lewy (CFL) constraint for model stability. As discussed in Section 2.4.1 and described through Equation 2.96. The select Cournant number condition imposed was $C \leq 0.9$.

$$\delta_t = (C \cdot \delta_x)/max_u \tag{3.1}$$

3.4 Results & Discussion

The NWCS Hydrographic model simulation was used to simulate tidal forced water levels across a period of 22 days Table 3.3. The simulation was carried out on the local system workstation: An Intel® Xeon(R) CPU E5-1650 v3 @ 3.50GHz×6 (12 threads). HPC systems were not utilised as currently Delft3D does not support multi-node execution. A spin-up time of 14 simulation days proved substantial for the model boundary to stabilise from the initial conditions Around the British Isles, both high and low tide points were clear and no clear visual artefact was present within the domain. Simulated water levels at Ordnance datum are presented in a colour contour plot of the NWCS model for the 18/11/2018 at 06:00:00 Figure 3.8. The specific

Table 3.2: The uniform physical parameters

Gravity (ms^{-1})	Water Density (kgm^{-3})	Roughness (Chezy) $(m^{0.5}s^{-1})$	Viscosity (m^2s)
9.81	1000	65	1

Table 3.3: Simulation time frames.

Simulation	Date	Time
Initiate	28/10/2017	00:00:00
Terminate	19/11/2017	00:00:00
Time Step	-	00:01:00

time was selected to coincide with the high tide at the mumbles tidal gauge on the last simulated day. This point was selected to compare the models ability to replicate the high tidal water levels that occur within Swansea Bay and thus accurately simulate the tidal forcing - which can then be used for the parametrisation of the near field models. Additionally, the final simulation time-steps are the least likely to affected by any residual instabilities that may still be present within the system.

Six sites from the UK National Tide Gauge Network were selected to act as validation sites to assess the accuracy of the water level data outputted from the hydrodynamic model. The sites were selected so that on the date specified, the various sites would provide comparison for different stages in the tidal cycle. Additionally, all but Dover will feature in the higher resolution models that will be nested within the NWCS mesh. The plots of Chart datum water level height at St Helier, Dover, Mumbles, Newlyn, Holyhead and Heysham are presented in Figure 3.9. Each covering a 24 hour period over the 18th of November 2017. Each plot presents both measured and astronomical tidal predictions at each site. The water levels given within the figure are of Chart Datum.

The approximations for each location are given in Table 3.4 alongside the measured levels from the tidal gauge network.

The NWCS hydrographic model shows good agreement with the measured tidal datasets. The tidal forcing are unanimously in phase and levels have a high similarity in actual ordnance datum water level. However, the hydrodynamic model appears to under predict the water level at the high tide points of Mumbles and St Helier. Conversely, the low tide points of Dover and Heysham do not outlay the estimated range. A possible reason for this occurrence could be a factor of the mesh resolution in those two areas. The actual bathymetry and geographical features likely do not get true representation with the length scales of the cells. It would be possible that the simulated features offer a greater resistance to flow, and thus simulate a lower maximum tidal level. Additionally, the models wetting function may also act as additional resistance to flow.

Table 3.4: Comparison of water level data taken from North West Continental shelf Hydrographic model and those recorded at teh UK National Tide Gauge Network select sites.

Location	SWE OD (≈Min)	SWE OD (≈Max)	CD (Recorded)	CD to OD (Difference)	OD (calculated)
St Helier	+03.00	+04.00	−05.88	+10.50	+04.62
Dover	−03.00	−02.00	−03.67	+01.25	−02.42
Mumbles	+03.00	+04.00	−05.00	+09.25	+04.25
Newlyn	+01.00	+02.00	−03.05	+04.75	+01.70
Holyhead	−01.00	+00.00	−03.05	+02.50	−00.55
Heysham	−04.00	−03.00	−04.90	+01.75	−03.15
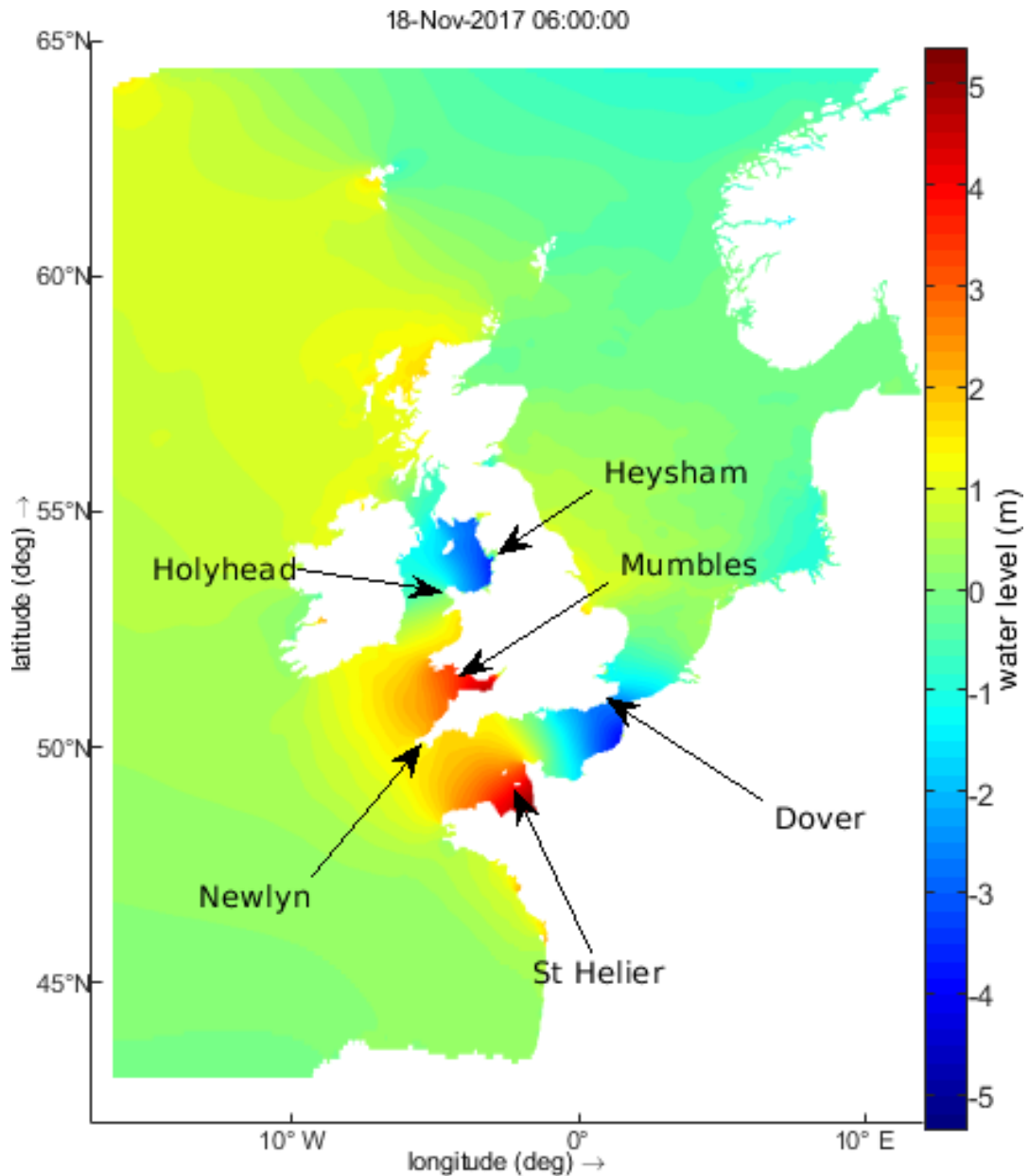
Figure 3.8: Water level height, with respect to the MSL across the NWECS domain. Dated for the 18/11/2017 at 06:00:00.The respective location of six sites from the UK National Tide Gauge Network are shown for referral to Figure 3.9.

3.5 Conclusion

The tidal regime over the North West Continental Shelf was simulated over a period of 22 days. The simulation took approximately 14 days until visible instabilities ceased from being present within the measured sections of the model. There was good agreement between the simulated water levels and those recorded at six location or the UK's National Tide Gauge Network, with respect to measured level and tidal forcing phase. However, the hydrographic model does appear to under predict the maximum tidal level. There are several possible hypothesised reasons as to why this is relating to either the mesh coarseness or wetting and drying functions. Since this feature has only currently been observed over two sites, further investigation

101

(a) St Helier

(b) Dover

(c) Mumbles

(d) Newlyn

(e) Holyhead

(f) Heysham

Figure 3.9: locational observable (blue) and astronomically predicted (red) real-time tidal level data from the UK National Tide Gauge Network [249]. The data was issued under an advisory status of not having been automated and unchecked. Times marked by vertical grid lines at 00:00, 04:00, 08:00, 12:00, 16:00, 20:00 GMT. Heights are in metres above chart datum.

could reveal if its an artefact of the two sites or a continuous issue within the model. In summary, further measurements and a fully post-processed dataset would act to clarify the current situation within the model. However, the general high agreement with measured data provides confidence that only several small tweaks would be required to solve any issues.

3.6 Future Work

The next stage in the process would be too further the progress with the nested models. The higher resolution mesh could possibly rectify the under prediction or the high tide currently observed with in the model, while also not significantly increasing the computational expense. After such, Lagoon or barrage representations could be implemented and tested to provide a bench mark for future development when incorporating the CFD parametrised sub-grid.

Chapter 4

Near-Field Hydrodynamics

This chapter addresses the RANS CFD modelling of the 'Near-field', which can be arbitrarily considered to relate to areas possessing the more complex 3D flow structures relevant to the operation of a tidal Lagoon.

The system being modelled can be summarily described as form of a combined low velocity water jets, which interacts with the bespoke geometry of the Swansea Bay Tidal Lagoon and surrounding Swansea Bay environment.

The aim is to develop a realistic CFD representation of the flow structures to enable developers of the Tidal Lagoon Project or equatable projects to gain a enhanced understanding onto how the Lagoon project would interact with the local environment.

To achieve said aim, the investigation of the SBTL will be split into separate investigative sections.

Section 4.2 seeks to study the near-turbine area that will feature the highest energy 3D flow structures, without incurring additional computational expense simulating areas with less stratified flow regimes in the wider bay area. With outcomes being the determination of appropriate degrees of mesh refinement.

Section 4.3 builds on the previous section with inclusion of additional features to further the production of a complete model of the Swansea Bay Tidal Lagoon through partial incorporation of extended sections of the breakwater wall and the sea bed slope. The model will be able to give some indication onto how much of the breakwater wall will need to be included in the CFD models to give an accurate depiction of the flow characteristics in the near field and the degree of downstream length to which 3D modelling is required. Direct real-world benefits from the production of the model would include insights into the altered sediment transport regime and possible risk to water transport and life from regions of high flow rate.

Section 4.4 works to study the generic, non-site specific facets in singularity, and in combination, to gauge a more universal future applicability.

4.1   Introduction

Characterization of 3D Fluid Phenomena

When characterising the flow regime exiting from the turbine draft tubes, an important consideration is the proper classification and thus distinction between flow phenomena. Thus, consideration must be made for the flow regime inside and downstream from the turbine draft tube, while applying diligence with respect to model assumptions.

Jet flows have been continuously researched, due to their vast presence in multiple applications ranging from aerospace to solvent mixers. With each case presented, the jet flow must be controlled for the application to the specific purpose, often in terms of jet speed and mass flow rate. Jet control falls under two classification; active, which refers to energised actuators for dynamic manipulation, or passive, for permanent or deployable features with no dynamic aspect during operation.

While jet flows can exceed supersonic velocities, the jets discussed below will deal with sub-sonic velocities of both jet initiation, evolution and fully developed flow, exiting from turbine draft tubes graphically described in [241]. The current literature does not seem to present a well structured description of the developing jet body from the initiation time, but rather one of the fully developed flow.

Accurate simulation of jets is often understood to be a onerous process, from the requirement to adequately apply the appropriate turbulence model for accurate large and small scale turbulence capture, coherent structures and nozzle exit conditions [127].

The various flow regions that form from a jet flow have been discussed in previous investigations [26, 92, 127] with earlier investigations looking to mathematically analyse, then progressively working to physical experimentation and numerical models.

105
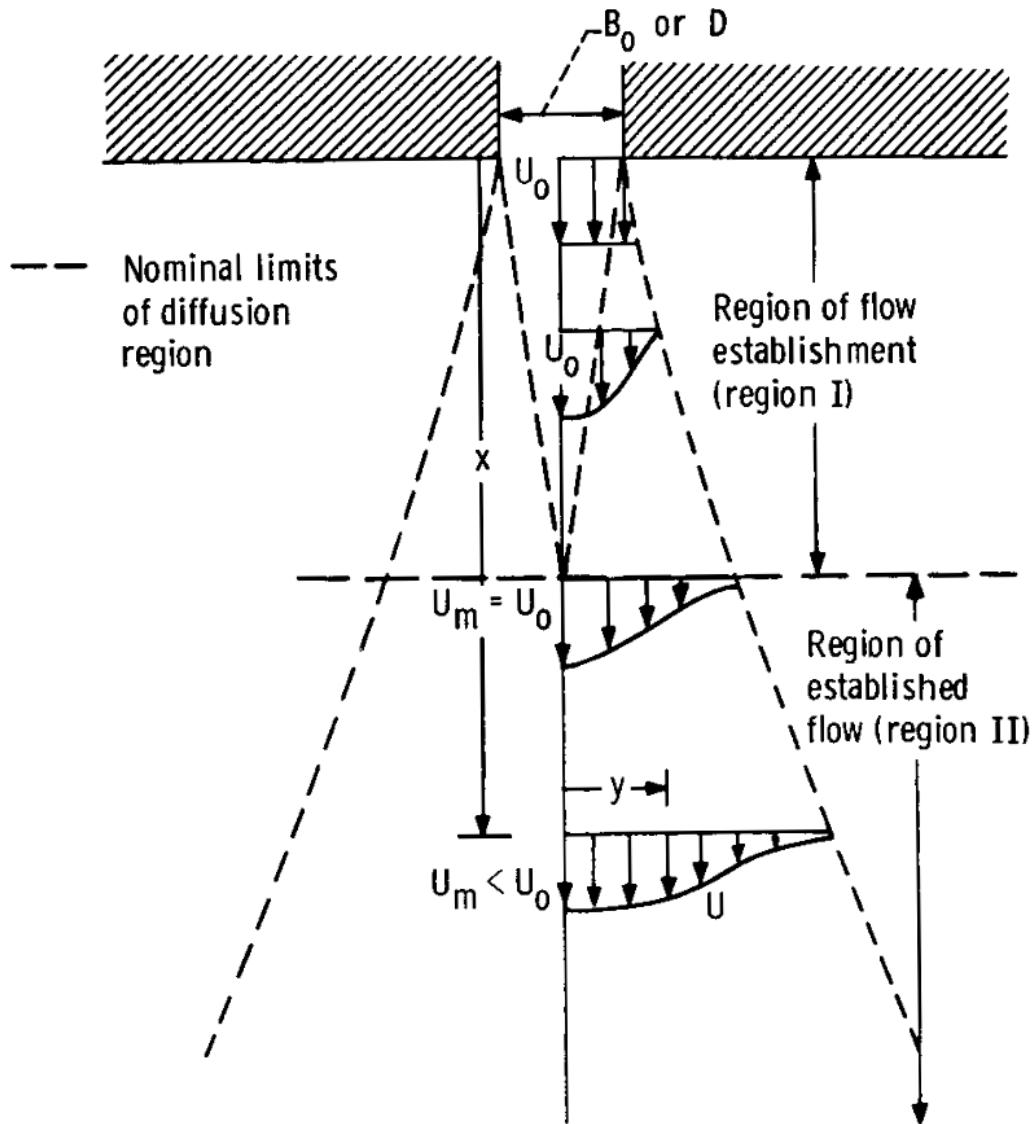
Figure 4.1: Schematic characterisation of jet flow diffusion [92].

Turbulent jet breakup is the phenomena of the disintegration of a jet flow due to turbulent forces acting on or from within the jet body.

Two separate distinctions of jet type exist relating to laminar or turbulent characteristics.

In the case of a water jet flow being injected into am ambient flow (4.1), several distinct flow regions can be identified. The first; Region 1 is where the flow is establishing. The region typically extends from the exit nozzle to the potential core end point. The potential core is defined as the central flow of the jet that is 'shielded' from ambient fluid by the outer region layer jet flow and thus retains the exit velocity. As such the flow maintains velocity in the axial direction, though narrows with increasing axial distance from the nozzle exit. Characteristics of Region 2 are that the jet flow is established and is characterised by the dissipation of the centreline jet velocity and spreading out of the 'top hat' velocity profile in transverse directions.

4.2 Swansea Bay Turbine Housing

4.2.1 Model Description

The CFD domain environment can be summarised as being that of several internal flow regimes of the TDT, entering into an external flow regime of what would be a representative of Swansea Bay.

All lagoon geometry is based from to-scale representation from engineering drawings available to the public at the National Infrastructure Planning website [242, 241, 240, 189]. The relevant images and method of geometric extraction is presented in Appendix B.

The domain is confined within a rectangular block with maximum and minimum bounding coordinates of [-38,-400,0]:[300 400 25]m as shown in Figure 4.2. Thus, spans a volume of 338x800x25m in the x,y and z directions respectfully. Of which the defining model geometry of the SBTL turbine housing was cut from with information held within a .stl file through the OpenFoam toolkit software 'snappy-HexMesh'.

The geometry was positioned so that the TDT outlet would be referenced as the origin point with respect to the x-axis normal plane, allowing for a downstream expanse of 300x800m. The inlet patch would be located on the x-normal plane at -38m. The TDT were set so that the midpoint would lie on the y-axis origin point so that the outlet flow would be central within the model domain. The base of the scour mattress will be at a depth of 25m in relation to the ceiling surface. After 50m in the x-direction, the scour mattress will incline with a gradient of 1 in 10, over a 120 meter distance in the same direction.

The height (z-axis) of 25m was used, which coincides with being just beyond the maximum tidal range that has been recorded [261], and the measured height of the breakwater/turbine housing structure which would be designed to contain 1 in 500 year storm surge high water levels [236].

Post scour mattress, the domain area is refereed to as the bed, which will have a depth of 13m in relation to the ceiling surface. The bathymetry of the bed is uniformly level, and therefore does not account for any interaction that might exist should any downstream features actually be present *in - situ* Swansea Bay.

The rough surface elements of both the breakwater and the scour mattress were not released at the time of construction due to stated commercial sensitivity listed by TLP. It was deemed to be impractical to devote time to generating estimations of such values, when the actual roughness could be later released by Tidal Lagoon Power.

The domain's downstream axial length (x-axis) was was arrived at through preliminary TDT analysis that found that the majority of the larger eddy structures were contained within 300m.

The sluice gates were not included as the energy generating operating sequence, i.e; when the turbines will be in use, the sluice gates wicket gates/ log gates will be closed. It is therefore not necessary or computation efficient to import geometry and mesh those areas.

Boundary Conditions

The domains initial fluid state is set with a kinematic viscosity equal to $1.5 \times 10^{-06} m^2 s^{-1}$ and set to a velocity of $0.1 ms^{-1}$ in the y-axis direction. The boundary conditions imposed of all domain patch/wall surfaces were set to accordance to those specified in Table 4.1.

The initial turbulent state of the domains bulk fluid is assumed to be equatable to that of typical marine background turbulence. At the time of writing, there has been no data found of background turbulence intensities within Swansea Bay at a location specifically equatable to where the Turbine housing would be located. Additionally, the presence of the lagoon structure will alter the previous typical tidal movements through blockage effects, which would likely result in a local increase. However, several studies into the background turbulence of tidal flow in areas suitable tidal stream turbines have been conducted in the UK and the USA. The summary of findings pointed to consistency over the tidal cycle and in the range 7-13%. Though it should be noted that said measurements were taken at depths typical for tidal stream turbines [137, 235, 161].An initial selected turbulence intensity I value of 7% was selected to be on the lower side of the aforementioned, acting as a compromise between the lower tidal flow velocity in Swansea Bay and no other available data.

Thus through applying equations 2.63 and 2.64 The kinetic energy κ and turbulence dissipation rate ε were set to $7.35 \times 10^{-05} m^2 s^{-2}$ and $1.1378 \times 10^{-07} m^2 s^{-3}$ respectively.

The inlet patch had a time independent, uniform plug inlet value which was held at 7 ms^{-1} across all 16 TDT's. With the absence of turbine data and thus likely swirl, a high estimate I was taken of 25%. Therefore the kinetic energy κ and turbulence dissipation rate ε were set to $4.59375 m^2 s^{-3}$ and $6.6034 m^2 s^{-2}$ respectively. The y-plus, y-minus and outlet boundaries were set to the inletOutlet OpenFOAM condition, where an time-independent, spatially uniform plug inlet of $0.1 ms^{-1}$ flow value was imposed along the y-axis direction. The inletOutlet is similar to the zeroGradient, however will switch to a fixedValue boundary condition if the velocity vector at the boundary acts in a oppositional direction (i.e. backward flow).

A zero-gradient (no-slip) condition was set on the solid surface geometry. The kinetic energy and dissipation rate were set to zero values. Wall functions are used to compute the boundary layer. The turbulence model used was the RNG κ-ε model.

Figure 4.2: CAD generated geometry of Domain boundaries for the Swansea Bay Tidal Lagoon. The boundaries are colour differentiated with the geometric surfaces, classified as walls (dark yellow). The downstream InletOutlet boundaries are shown individually as pink,red and blue respectively.

Table 4.1: This table displays a summary of each boundary condition specified at each listed boundary within the Turbine Housing model Figure 4.3.

Field		Velocity (ms^{-1})	κ (J/kg)	ε (J/kgs)	nut (Pas)	Pressure (Pa)
Initial State	Value:	uniform (0 0.1 0)	uniform 7.35×10^{-05}	uniform 3.6979×10^{-07}	uniform 0	uniform 0
Wall	Type:	noSlip	kqRWallFunction	epsilonWallFunction	nutkWallFunction	zeroGradient
	Value:	-	uniform 0	uniform 0	uniform 0	-
Inlet	Type:	fixedValue	fixedValue	fixedValue	calculated	zeroGradient
	Value:	uniform (7 0 0)	uniform 4.59375	uniform 6.6034	uniform 0	-
Outlets	Type:	fixedValue	fixedValue	fixedValue	calculated	zeroGradient
	inletValue:	uniform (0 0.1 0)	uniform 0.000009984	uniform 2.888982358	uniform 0	-
	Value:	uniform (0 0 0)	uniform 0	uniform 0	uniform 0	-
Ceiling	Type:	slip	slip	slip	slip	slip

Mesh Configuration

The mesh was constructed using a combination of OpenFoams's built-in toolbox utilities blockMesh and snappyHexMesh, defining the domain expanse base cell size then cutting the domain block and snapping the mesh to the geometry. The mesh is configured as being of hierarchical hexahedral type - structured to be refined through levelled subdivisions of the domain towards areas interest - the initial jet dissipation zone. Which envelopes the turbine draft tube exits and a volumetric area of 100x60x25m and refinement specified to level 3. This mesh grade levelling system is based on the number of times the base cell size was subdivided by 2 to reach the cell size in the specified region.

A hierarchical hexahedral mesh is useful for this type of domain due to large areas of straight flow needing relatively little refinement, and smaller turbulent regions such as the near draft tube exit region, which requires a significant level of refinement to fully capture the 3D flow behaviour [73].

The mesh was aimed to have higher refinement in and around the areas of interest, like around the turbine and downstream jet structure where complex flow structures are to be expected. Also have regions of coarser mesh, where relatively straight flow is present to reduce the computational intensity.

4.2.2 Results & Discussion

The simulations were carried out with the steady-state solver, SIMPLE. The cases were run for 1500 iterations without any case meeting the convergence criteria, indicating that system being simulated will likely have highly transient features and that the steady-state simulation may not be adequately suited for simulating the TDT output. The clock time for each case was also recorded and will be taking into account in the consideration process into which would the chosen mesh density. To ensure fairness of comparability, each case was decomposed in the same manner; using OpenFOAM's Scotch decomposerPar tool over 24 processors to match the 24 processors per node in HPC Wales's system. Using more cores than 24 will inevitably split the model processing over multiple nodes which can slow the computation.

Figure 4.4 presents an top-down perspective of the fine G-mesh case domain at
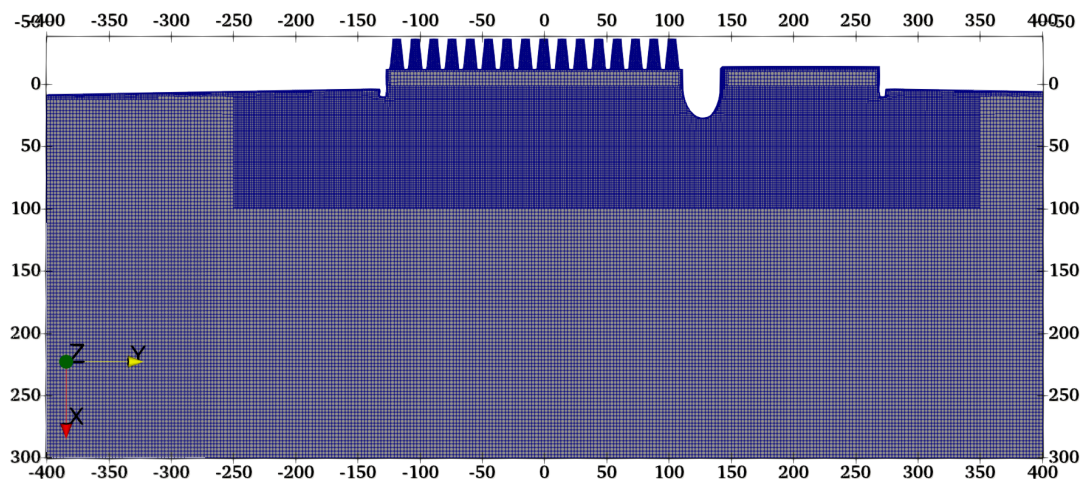
Figure 4.3: Overview of the domain's mesh configuration.
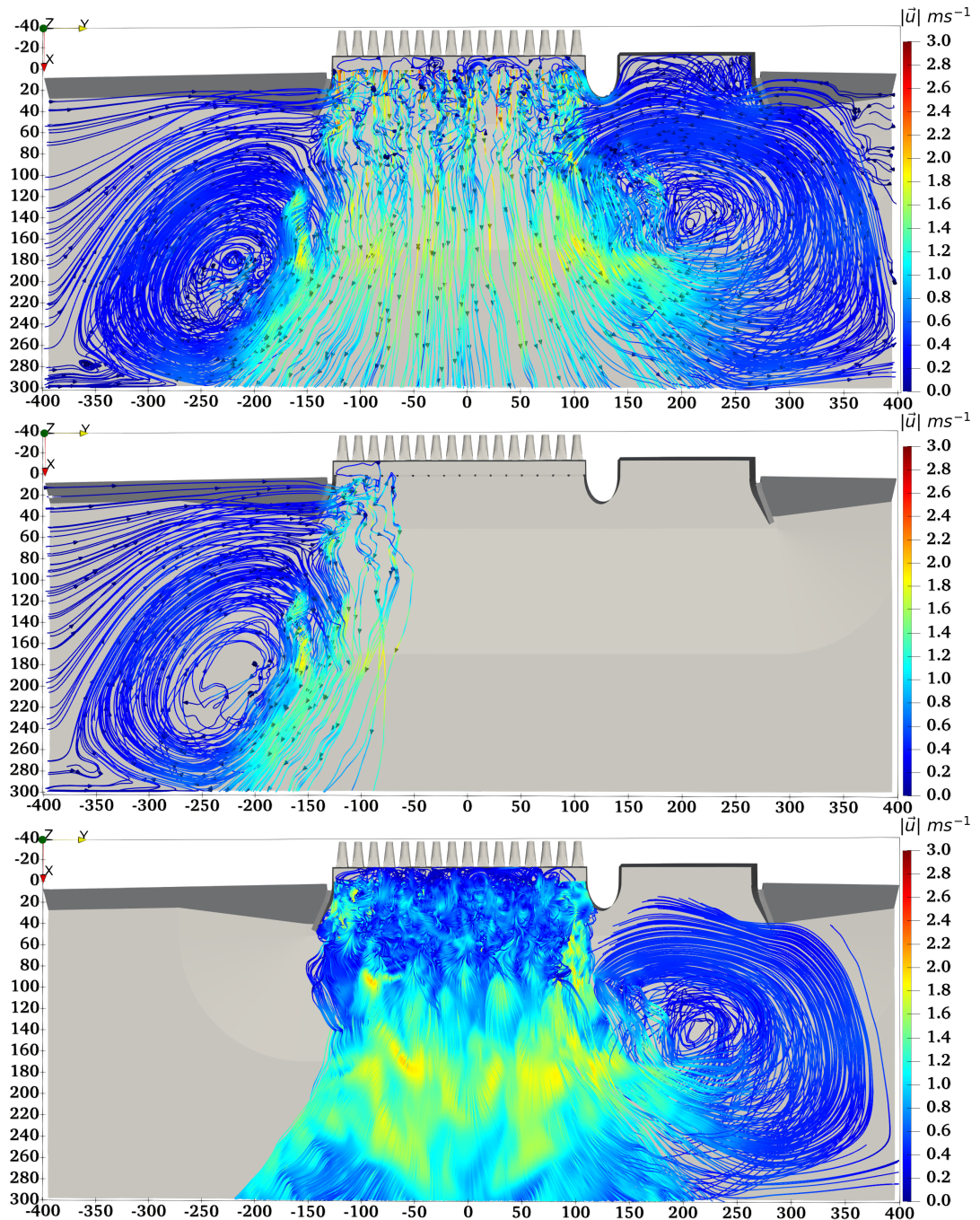
Figure 4.4: SBTL-TH near-field flow hydro-dynamics replicated with a $7ms^{-1}$ inlet flow rate and a $0.1ms^{-1}$ cross flow. Top image describes the entire flow field, middle the seeded cross-flow, and bottom the TDT seeded flow.
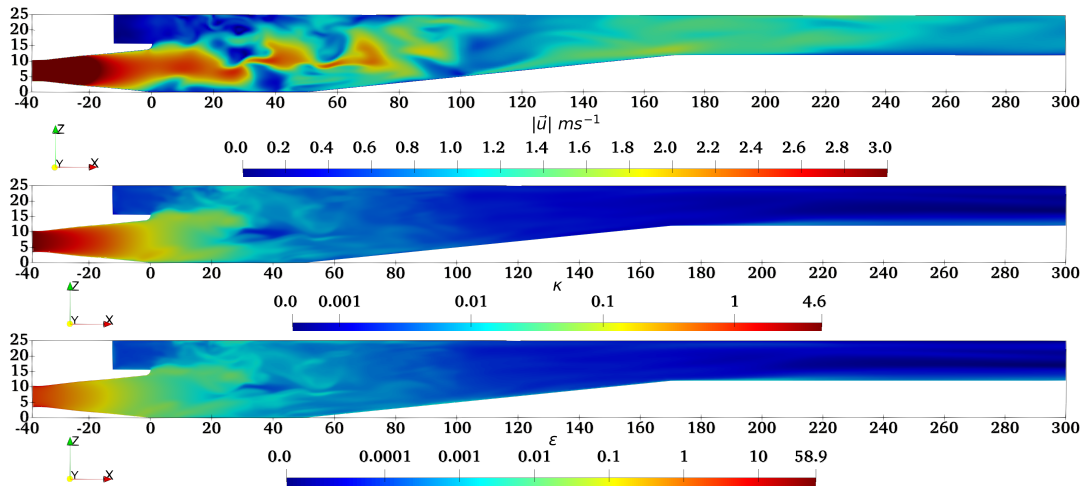
Figure 4.5: SBTL-TH near-field flow hydro-dynamics replicated with a $7ms^{-1}$ inlet flow rate and a $0.1ms^{-1}$ cross-flow. The flow field is presented as the xz-plane when y=0, for the velocity magnitude (top), $\log(\kappa)$ (middle) and $\log(\varepsilon)$ (bottom).
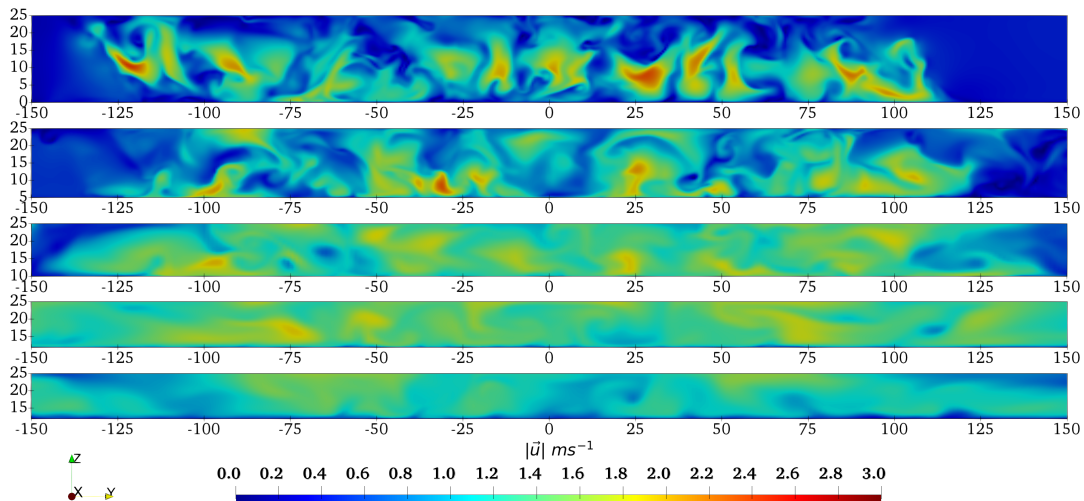
Figure 4.6: SBTL-TH near-field flow hydro-dynamics replicated with a $7ms^{-1}$ inlet flow rate and a $0.1ms^{-1}$ cross flow. The flow field is presented at 50m increments across the yz-plane.

112

1500 steady-state iterations with data visualised using velocity magnitude stream-lines scales from $0ms^{-1}$ (dark blue) to $> 3ms^{-1}$ (red). There appears to be considerable larger-than-grid turbulent eddy capture within 100m downstream of the turbine draft tubes exit. Past approximately $100m$, in regards to larger-than-grid turbulence criteria, the flow appears to steady as the larger eddies disperse to length scales below that which can be captured with the mesh resolution. Thus the flow becomes depicted within the RANS model as following relatively straight streamlines which continue to flow towards the Outlet boundary. It should be noted that $< 100m$ features the level 2 mesh refinement, which is capable of resolving eddies of length scale $> 1m$, while $> 100m$ the mesh cannot resolve $< 1.9m$ with the turbulence then modelled through the RANS $\kappa - \varepsilon$ RNG.

Figure 4.5 presents a downstream slice (y-normal plane) at $y = 0$, which corroborates the larger-than-grid eddy mixing before approximately $100m$ downstream and subsequent breakdown into smaller length scales before dissipation shown in the κ and ε plots. An interesting point of notice is the flow separation from the TDT bottom surface. Should the feature be a realistic representation of how the flow will behave, then the rough elements of the scour mattress would have reduced contribution to the breakup of the jet flow. However, considering the highly transient nature of the turbulence being depicted, the steady-state simulation is likely insufficient for correct capture. Thus the feature should be examined through a transient analysis and the magnitude of the effect on the system evaluated.

Two re-circulatory regions form along side the main flow body, though the relationship with the TDT exit flow is not symmetric. The shielded leeward side is substantially larger, filling most of the volume. Curiously, the flow appearing to be bounded by the outlet and y-plus boundaries, suggesting the nature of the feature may be that of a model artefact. Should the boundaries have been set further afield, it is likely that the recirculation would be larger. Additionally, it is likely that in a transient case it would be propagated downstream.

The re-circulatory current on the windward side appears to be compressed from the cross-flow and appears smaller, with the 'eye' situated 180m downstream compared to the leeward $140m$ and more oblong in shape. Additionally re-circled flow meets the main TDT flow further downstream, with flow from the cross-flow being funnelled behind and into the TDT flow adjacent to the outlet. Similarly to the leeward, the outlet boundary appears to contain flow.

Between the $-150m$ and $-200m$ y-axis mark on the windward and $100m$ to $140m$ on the leeward, horizontal entrainment vortexes can be seen, where the re-circulatory return streamlines interacts with the main flow body.

From the TDT outlet, the flow appears to transverse approximately $150m$ in both the y-plus and y-minus directions, in respect to initial main flow body until 150m downstream. After which, the flow appears to spread out to +200 meters in both the y-plus and y-minus directions. This corresponds with the outward dissipating pull of the re-circulatory flow streams which increased the dissipation of kinetic energy throughout the flow (Figure 4.6).

Flow acceleration can also be seen at the end of the scour mattress incline, which is likely as consequence of continuity with the fluid being squeezed through a smaller volumetric area. This acceleration effect could contribute to the steadying flow streamlines. The effect might be reduced if a model takes into account the bed surface slope.

Table 4.2: Displays the number of cells and Clock Time (hrs) for case in the mesh sensitivity study.

Model Case	V_p^{base} [m^3]	V_p^{L1} [m^3]	V_p^{L2} [m^3]	N	T_c [hrs]
	[m^3]	[m^3]	[m^3]		[hrs]
A-mesh	22.47	2.81	0.35	110×10^4	0.0956
B-mesh	11.65	1.46	0.18	211×10^4	0.17139
C-mesh	7.13	0.891	0.11	324×10^4	0.26611
D-mesh	4.56	0.57	0.07	494×10^4	0.34556
E-mesh	2.65	0.33	0.04	848×10^4	0.78972
F-mesh	1.55	0.19	0.02	119×10^5	1.11917
G-mesh	0.90	0.11	0.01	204×10^5	2.60528

Mesh Dependency

3D CFD analysis of the computational domain described in section 4.2.1 requires careful refinement in the TDT, and outlet areas along with the wall surfaces. The flow structure exiting the TDT will be transient and highly complex in nature and an accurate representation of which is required to ensure the downstream wake flow is neither over or under-predicted. The mesh structure is generated as per description in section 4.2.1. Table 4.2 shows seven progressive degrees of mesh refinement that were set through the global parameter of the base cell size and alphabetically labelled in sequential order - from coarsest (A) to densest (G).

Velocity Convergence

Three distinct points of (50 0 7), (100 0 16) and (200,200 12) were selected to cover the near-jet, the far-jet and the re-circulatory region. The velocity magnitude output was taken as the dependant variable of interest.

Figure 4.7 presents the resultant steady-state prediction for the velocity at said points. The first point at (50 0 7) being 50m downstream from the TDT outlet is located in a highly transient region of flow with larger-than-grid eddy structures. It can therefore expected that convergence will not be achieved through comparing the velocity magnitude at a single point. This would also be true if the simulation were to be transient. In such a case, a time-averaged approach would have been more appropriate with readings taken after an appropriate settling time. Position (100 0 16) and (200 200 12) are located in areas with flow that exhibits significantly less turbulent flow with no apparent larger-than-grid eddies being present. Particularly pertaining to the (100 0 16) point, the change in mesh refinement just before said point will likely contribute to the stability of the velocity magnitude measurement, since eddies $< 1.9m$ in length scale will not be resolved. Point (100 0 16) and point (200 200 16) achieve relative convergence with around 8 millions total cells (Mesh-E) and 2 million cells (Mesh-C) respectfully. The difference between the two can be attributed to proximity to the TDT outlets. Indicating that future mesh configurations should look to expand refined regions further downstream.
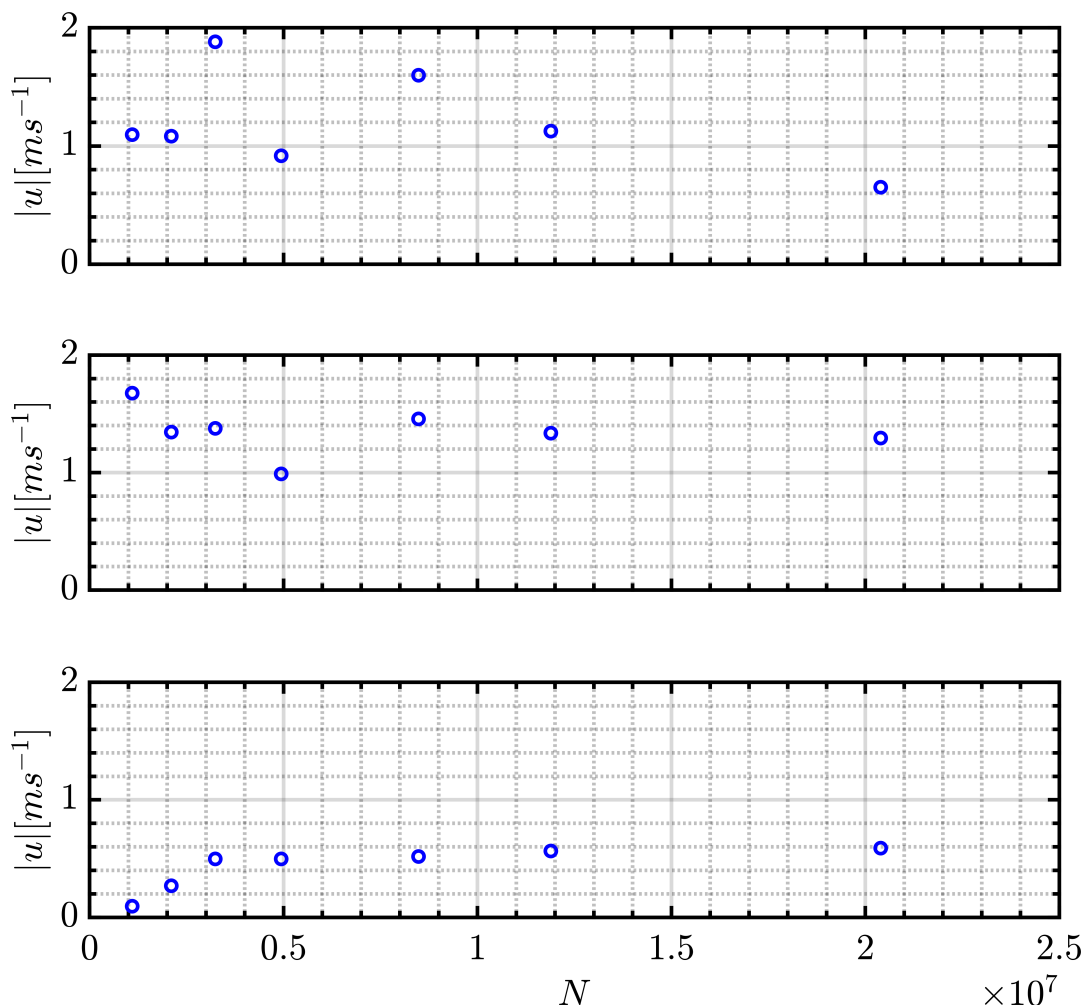
Figure 4.7: Velocity magnitude vs number of cells in domain at three distinct locations. top (50 0 7), middle(100 0 16) and bottom (200 200 12).

Table 4.3 summarises the order of accuracy and GCI of the the three points across meshes E,F and G with respect to the velocity magnitude. With respect to R, Pos_1 is just greater than 1, thus falls into the Divergence category. Pos_2 and Pos_3 both have values greater than zero but less than 1 so therefore are monotonic in convergence, possessing both an increasing and decreasing trend respectfully 4.8. The order of convergence was derived through a Bisection algorithm with bounding values of 0.025 and 2. Pos_1 and Pos_2 under such bounding conditions have an order of convergence contrasting against calculated $F_{h=0}$ values for each position. The error for Pos_1 is substantial, indicating a significant problem. While the error for the other two positions is relatively small with the order of convergence directly corresponding with the extrapolated relative error and the grid convergence index.

In summary, despite being in the most refined region within the domain, Pos_1 fails the analytical convergence tests. The likely reason being the convergence metric of using the velocity magnitude and the position being in the presence of transient larger-than-grid eddies while being a steady-state approximation. Conversely Pos_2 and Pos_3 can be argued to both pass the analytical convergence test depending on

the acceptable degrees of error. Additionally, a restructure of the mesh configuration would be advised; to extend the L1 border further downstream, encompassing both the *Pos₂* and *Pos₃* and to an extent that similar degrees of flow features are to be expected in a transient simulation. Thus, providing the required refinement in regions of interest without unnecessarily increasing refinement globally and accompanying increases in computational cost.
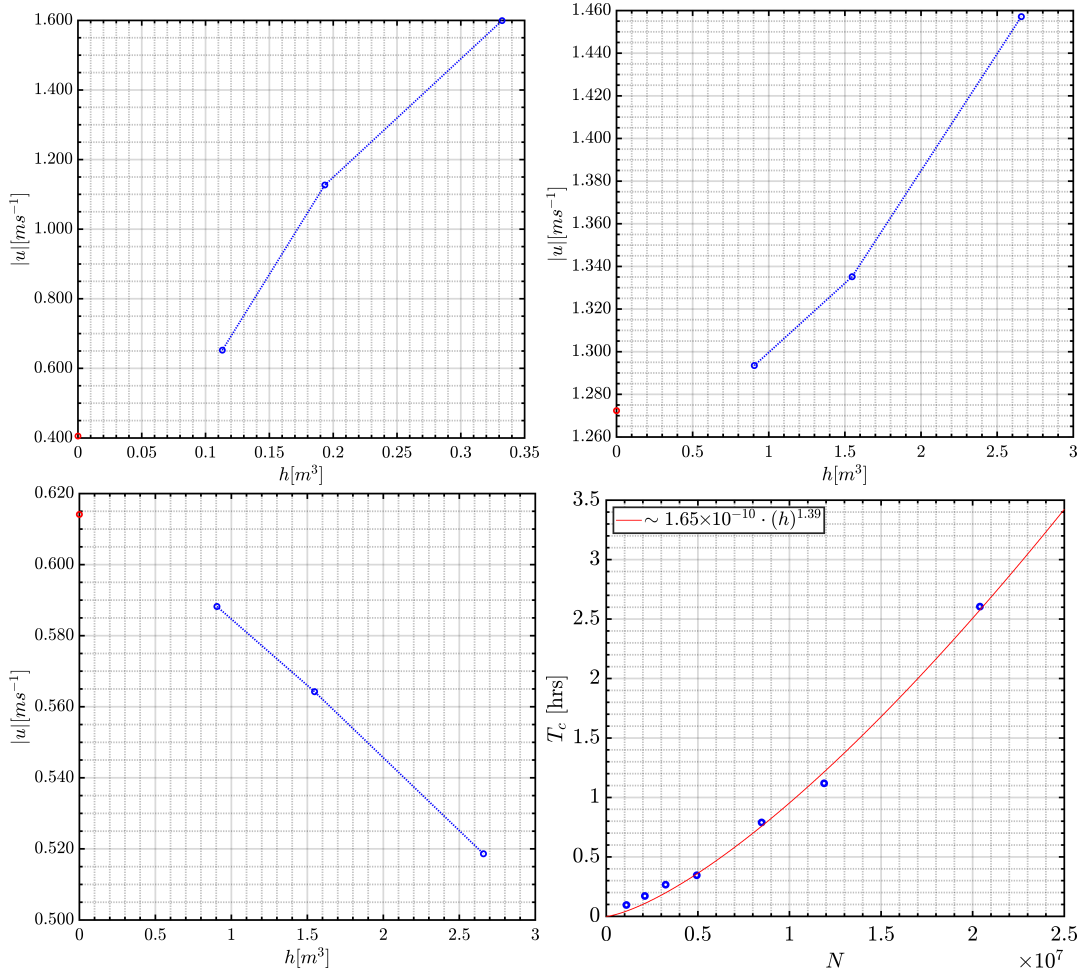
Figure 4.8: Respective spatial grid convergence graphs against the three grid resolutions (Mesh-E,F and G).

Table 4.3: The Order of accuracy and Grid Convergence Index (GCI) of three points accounting for the $|\vec{u}|$ at each respective point.

α	ε_{12}/f_1 [%]	ε_{23}/f_2 [%]	**R**	**p**	$\mathbf{f}_{h=0}$ [%]	**E1** [%]	**E2** [%]	**E3** [%]	$\mathbf{GCI}_{12}$ [%]	$\mathbf{GCI}_{23}$ [%]	$\mathbf{GCI}_{AR}$ [%]
Pos₁	73	41.94	1	2	0.41	60.83	177.89	294.44	47.28	138.26	1
Pos₂	3.2	9.13	0.3	2	1.27	1.66	4.94	14.53	2.05	6.07	1
Pos₃	4.1	8.08	0.5	1.2	0.61	4.22	8.12	15.55	5.51	10.6	1

Figure 4.8 shows the relationship between the number of cells and the clock time, also given in Table 4.2. The trend can be approximated as near linear, though

there is a slight increasing rate trend. The maximum computation time in the study is just over two and a half hours. In computing terms, the time-scales are minute. However the system was run with a steady-state solver, which will produce a result considerably faster than if a transient solver were to be used. The computation was conducted with 28 Intel(R) Xeon(R) CPU E5-2680 v4 @ 2.40GHz processing cores. Therefore, it is difficult to fully conclude at this stage whether further refinement to further reduce the extrapolated errors, would be worth the additional computational costs without a transient comparison. However, at the fulfilment of which, should a steady-state result provide an adequate assessment to produce valid conclusions, despite the acknowledgement of highly transient features, then the mesh can be refined to further degrees to approach the calculated $f_{h=0}$ and reduce error. Additional metrics such as the bed shear-stress could also have been used to asses suitable degrees of mesh refinement. As reasons relating to sediment transport and scour are driving factors in the construction of this work.

4.3 Full Breakwater & Turbine Housing Simulation (External Ebb)

4.3.1 Model Description

The purpose of this section was to further the production from section 4.2 of a complete model of the Swansea Bay Tidal Lagoon through partial incorporation of extended sections of the breakwater wall, local currents and rough sea bed slope. The model will be able to give some indication onto how much of the breakwater wall will need to be included in the CFD models and to give an accurate transient depiction of the flow characteristics in the near-field.

As mentioned prior, all lagoon geometry including novel facet of the breakwater wall was extracted from Engineering drawings available to the public at the NIP website [242, 241, 240, 189]. The relevant images and method of geometric extraction is also presented in Appendix B.

The model is constructed from a domain confined within a rectangular block of maximum and minimum coordinates of [-1000 -1500 0]:[2500 2000 25]m as shown in Figure 4.9. Thus the model extends over an volumetric area of 3500x340x25m in the x, y and z directions respectfully. The models solid surfaces, the turbine housing, breakwater and sea bed were initially completed as single set. The geometry was then split up into sections depending on the level of refinement required for each section when being meshed. IE. the turbine housing was isolated as this section will require the finest meshing to accurately simulate the features present.

A approximate declining downstream bed slope also featured in this model. Several water depth measurements were taken from bathymetric data (BODC [168]) along a line outwards from where the turbine housing would be located. The measurements were then averaged and used to form a average bed slope of 0.26 degrees.
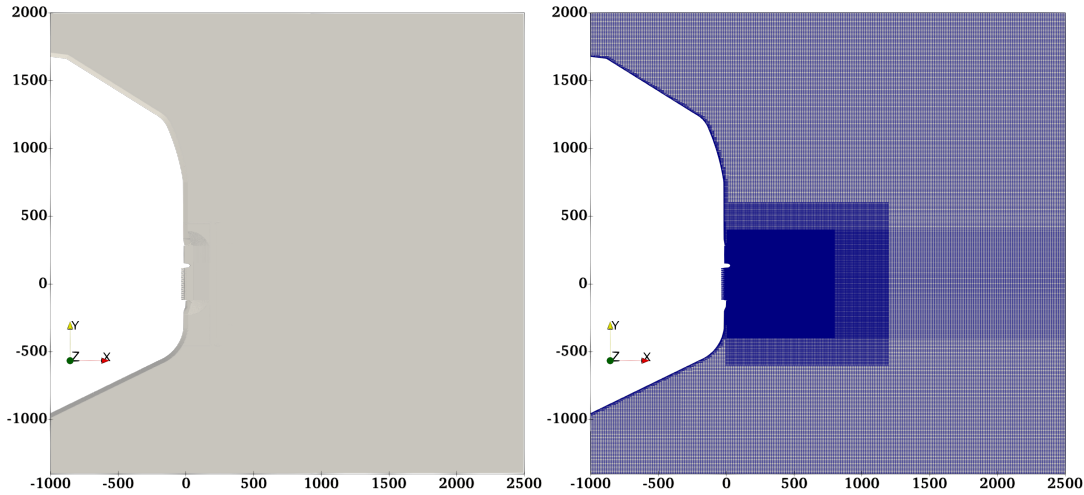
Figure 4.9: figure shows the stl surfaces of the model entire model geometry (left). Overview of domains mesh configuration (right).

Boundary Conditions

The domains initial fluid state was set with a kinematic viscosity of $1.5 \times 10^{-06} m^2 s^{-1}$ and a velocity set to 0.05 in the y-minus direction. The boundary conditions imposed on all the domain patch/wall surfaces were set to accordance with values specified in Table 4.4.

Approximate tidal velocities were taken from the delft 3D model discussed in Section 3.3 at the approximate locale of where the SBTL would be situated at a time where the maximum ebb flow was present in the simulation.

Like in section **??** the initial turbulent state is assumed to be equatable to that of a typical marine background turbulence. Therefore an initial selected turbulence intensity I value of 7% was selected to account for the lower tidal flow velocities present in the Swansea Bay region.

Thus through applying equations 2.63 and 2.64 The kinetic energy κ and turbulence dissipation rate ε were set to $6.615 \times 10^{-04} m^2 s^{-2}$ and $9.984 \times 10^{-06} m^2 s^{-3}$ respectively.

The inlet patch had a time independent, uniform plug inlet value which was held at 7 ms^{-1} across all 16 TDT's. With the absence of turbine data and thus likely swirl, a high estimate I was taken of 25%. Therefore the kinetic energy κ and turbulence dissipation rate ε were set to $4.59375 m^2 s^{-3}$ and $6.6034 m^2 s^{-2}$ respectively. The y-plus, y-minus and outlet boundaries were set to the inletOutlet OpenFOAM condition, where an time-independent, spatially uniform plug inlet of $0.1 ms^{-1}$ flow value was imposed along the y-axis direction. The inletOutlet is similar to the zeroGradient, however will switch to a fixedValue boundary condition if the velocity vector at the boundary acts in a oppositional direction (i.e. backward flow).

A zero-gradient (no-slip) condition was set on the solid surface geometry. The kinetic energy and dissipation rate were set to zero values. Wall functions are used to compute the boundary layer. The turbulence model used was the RNG κ-ε model.

Table 4.4: This table displays a summary of each boundary condition specified at each listed boundary within the SBTL full model presented in Figure 4.9.

Field		Velocity $[ms^{-1}]$	κ [J/kg]	ε [J/kgs]	nut [Pas]	Pressure [Pa]
Initial State	Value:	uniform (0 -0.05 0)	uniform 6.62×10^{-04}	uniform 9.98×10^{-06}	uniform 0	uniform 0
Wall	Type:	noSlip	kqRWallFunction	epsilonWallFunction	nutkWallFunction	zeroGradient
	Value:	-	uniform 0	uniform 0	uniform 0	-
Inlet	Type:	fixedValue	fixedValue	fixedValue	calculated	zeroGradient
	Value:	uniform (7 0 0)	uniform 4.59375	uniform 2.88898	uniform 0	-
Outlets	Type:	fixedValue	fixedValue	fixedValue	calculated	zeroGradient
	inletValue:	uniform (0 -0.05 0)	uniform 6.62×10^{-04}	uniform 9.98×10^{-06}	uniform 0	-
	Value:	uniform (0 0 0)	uniform 0	uniform 0	uniform 0	-
Ceiling	Type:	slip	slip	slip	slip	slip

Mesh Configuration

The mesh was structured to be densest around the geometric surfaces of the turbine housing and in adjacent areas where there is an expected high rate of change of either velocity, pressure or turbulence across the elements.

Using the blockMesh utility in the OpenFOAM toolbox, the mesh domain is configured as a hexahedral mesh over the extent of the domain. The model domain was initially divided up into several initial blocks. This was done to enable an input surface boundary within the model domain expanse. Several blocks needed to be constructed as each block attached an adjacent block needed to possess the same number of cells across the boundary. The subdivisions across each block are therefore; A[150 110 7], B[57 166 7], C[150 166 7], D[150 99 7], E[57 99 7] in *xyz*-directions respectfully.

The refinement of the mesh is achieved using the snappyHexMesh OpenFOAM toolbox utility. The finest meshed region is specified as level 3. This mesh grade levelling system is based on the number of times the base cell size was subdivided by 2 to reach the cell size in the specified region. The finest meshed zone is surrounded by three other zones, each sequentially enveloping the other and decreasing in specified level with the outermost zone being of the initial base cell size.

A hierarchical hexahedral mesh is useful for this type of domain due to large areas of straight flow needing relatively little refinement, and small regions of detail such as the near draft tube exit region, which requires a significant level of refinement to fully capture the 3D flow behaviour.

4.3.2   Results & Discussion

The simulation was carried out with the transient solver PIMPLE for a simulation run-time of 5000 seconds. An unfortunate outcome of data-loss prevented the simulation clocktime from being recorded. Though the domain was decomposed using OpenFOAM's scotch decomposePar tool over 84 processors totalling 3 nodes in HPC Wales Cluster system.

Figure 4.10 presents an top-down perspective of the domain at time points of 2500 and 5000 seconds, with data visualised using velocity magnitude streamlines scales from $0ms^{-1}$ (dark blue) to $> 1.5ms^{-1}$ (red) and complemented with velocity and pressure iso-surfaces.

At the initial phase of the simulation, the TDT injects fluid into the domain ambient flow, inducing substantial larger-than-grid turbulence that swells into a 'mushroom' shaped plume that advances ahead of the main fluid body. There are detectable amounts of disturbance in the ambient field up to $1500m$ downstream. As the plume progresses downstream, a high pressure front forms which forces flow in a perpendicular direction to that of the main body. The redirected flow is enters into a re-circulatory motion an fluid is entrained in the advancing main body flow. The full re-circulating eddy is formed when the front reaches 500m downstream. As the main body flow pushes further downstream, the re-circulatory eddies travel downstream, maintaining position relative to the front. Curiously, a stagnation point forms just off the y-plus side re-circulatory eddy, with cross-flow either diverted either ahead or behind the plume. While fluid that was being pushed forward by the higher pressure front, is then re-directed by the momentum of the cross-flow being directed ahead.
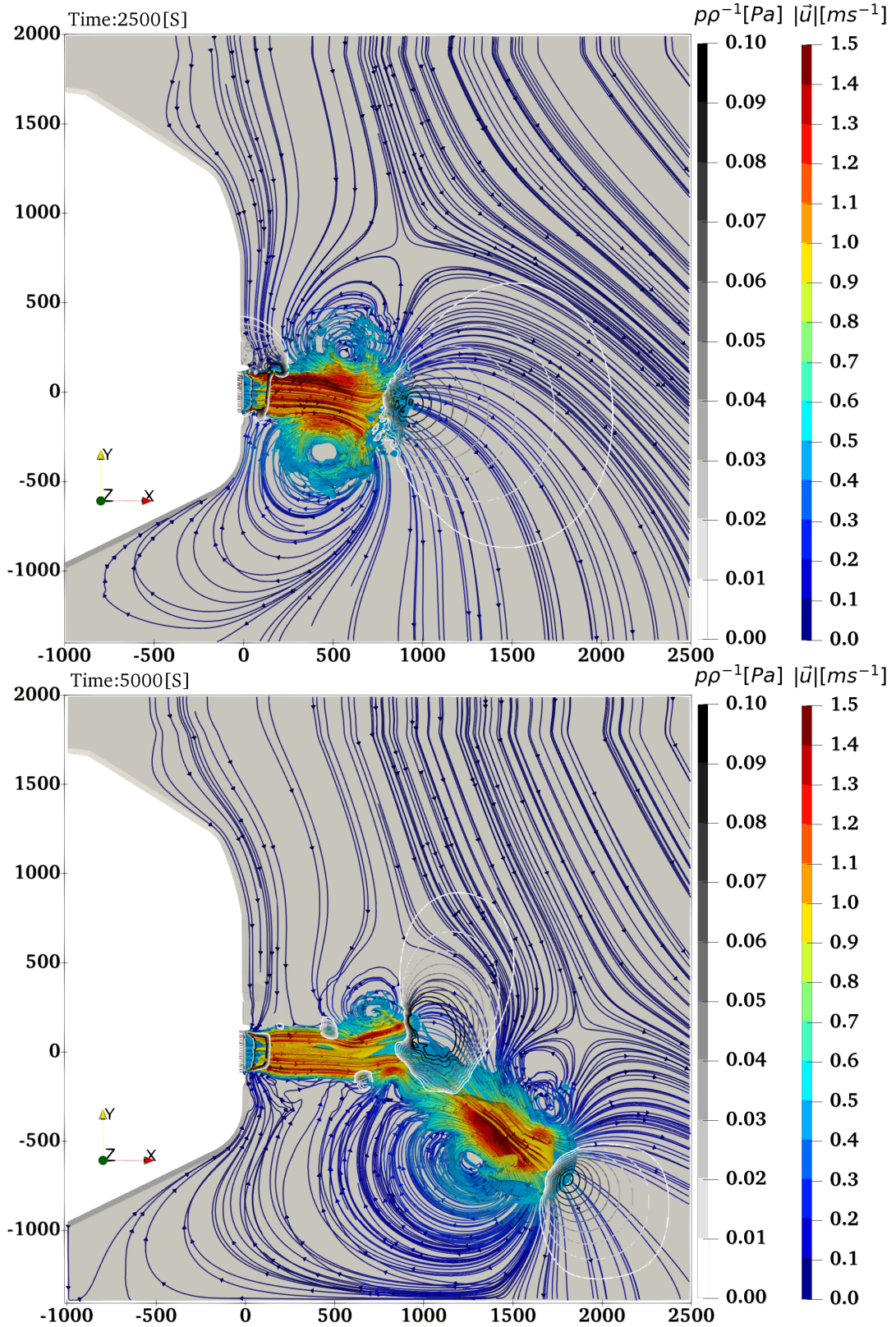
Figure 4.10: Velocity magnitude streamlines and pressure iso-surfaces at simulation time: 2500s (top) and 5000s (bottom)

At 2500*s* the jet-front has progressed approximately 1000m downstream and resembles the visage of the Swansea Bay Turbine Housing model, albeit unbounded
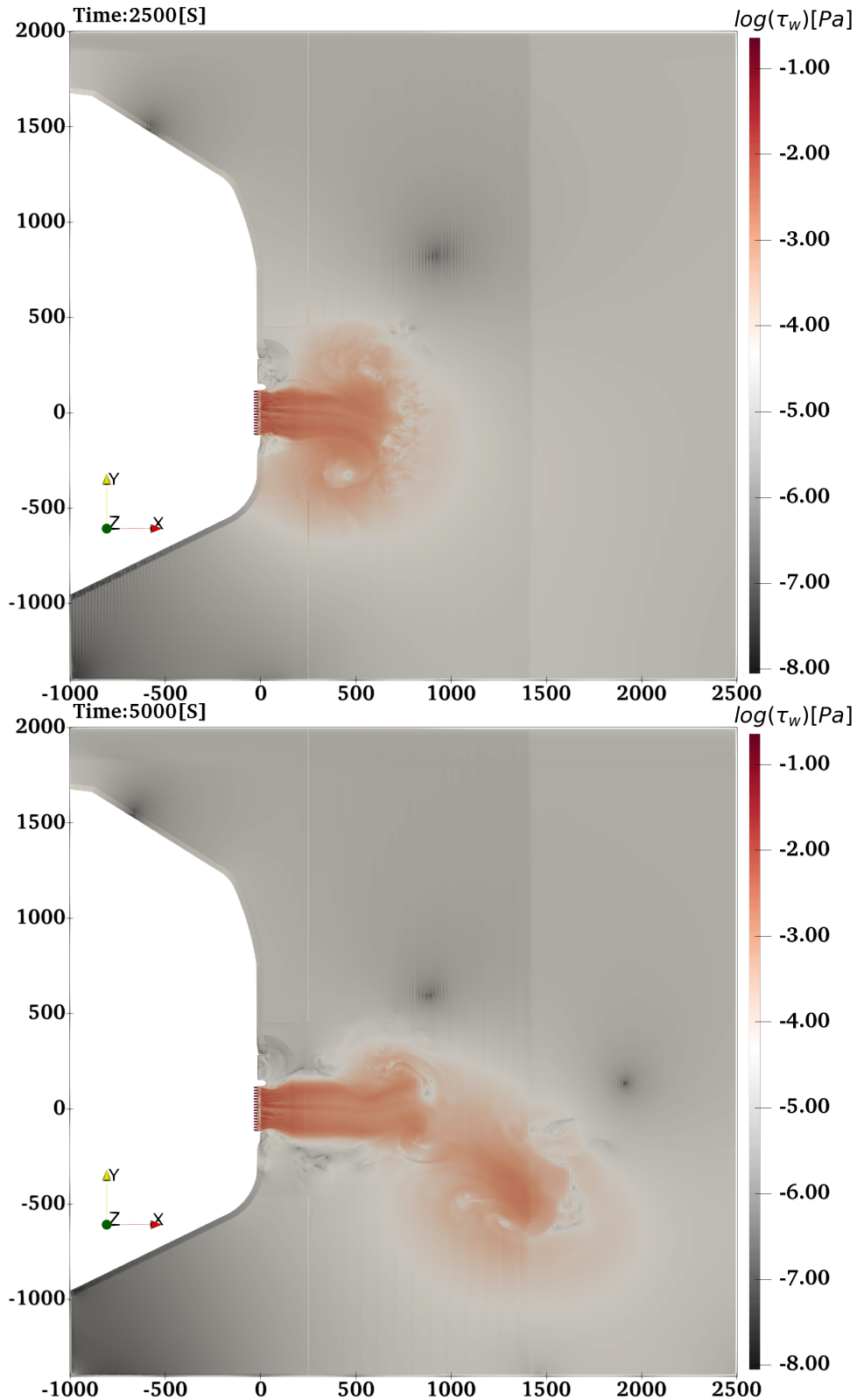
Figure 4.11: log Bed shear stress plot of the full Swansea Bay Tidal Lagoon model at simulation time: 2500s (top) and 5000s (bottom).

by the former domains boundaries. The cross-flow that is funnelled behind the re-circulatory flow and incident upon the main body flow adjacent to the outlet, begins to induce a point of high pressure. Which then grows with time as the main flow

body moves forward.

By the time the flow has reached 1500m downstream, the flow front centreline has deviated towards the y-minus by as much as 25°. Additionally, the high pressure zone induced by the cross-flow has acted to separate the main flow body. Resulting in a departed 'island' of higher flow velocities that continue to propagate downstream towards the domain boundary. The cross-flow induced high pressure then becomes the new pressure front for the flow behind.

Figure 4.11 depicts the shear stress that the flow exerts on the bed surface for time points of 2500s and 5000s. There is a direct correlation between areas of higher flow rates and those of higher bed shear stress. This will result in a strong likelihood that high degrees of scour will occur from sustained high flow over an area box of 750X400m downstream from the outlet. Scour can also occur in areas outside said zone from higher velocity flow, such as under the re-circulation eddies, though to a lesser degree due to the transient nature.

Low shear stress regions can been seen correlating with the points of flow stagnation, which occur on the outer edge of the windward re-circulating eddies. Over time, sediment is likely to collect and possibly form a sandbank that follows the outer edge of the main body flow.

Low shear regions can also be seen forming at the sides of the breakwater, which may suggest that there may be changes to the beach morphology.

4.3.3 Future Work

Future work will entail the addition of parameters for the scour mattress and the downstream bed gradients. Friction values for the sand bed will also be estimated. Thirdly, a time dependant water level parameter will be imposed to account for the tidal ranges. The Scour mattress can be tackled though three different approaches; a frictional value from recorded text book data, or implementing the scour mattress into the numerical model, and thirdly a specified resistance zone. The first method is least computationally intensive of the three methods. However, this method will not capture the realistic effects that a 3D macro-rough structure would have of the jet flow. The second Methodology is very computationally heavy, as the topography of the scour mattress will need to be finely meshed. The third methodology will be a trade-off between the previous two methodologies, where the zone will have flow resistance parameters equivalent to those expected from the scour mattress. The effect will be a 3D representation with a reduced computational cost. The current proposed mattress design and material is not available to the public, so a generic scour mattress design will be used in the model. Four possible selections of turbine mattress for scour protection in the Swansea Bay Tidal Lagoon are shown in Figure (4.12): Bag moulded concrete, Coarse non-uniform bolder, Gabion sections, Interlinked concrete mattresses. A further detail is also possible, use of a 'blade-box' region (entry region), large enough to encompass the expected rotor to be used in the Swansea Bay Tidal Lagoon. This could include swirl characteristics or could include a zero-flow area at the centre of each turbine to represent the turbine bulb. Finally, a proposed model of 16 turbines will need to include the geometry of the concrete walls at the ends of the turbine sections as shown in Figure (B.2).

Figure 4.12: Range of possible of scour mattress for respective tidal range projects. Ordered from the left: bag moulded concrete, coarse non-uniform bolder selection, gabion sections and interlinked concrete blocks.

4.4 Generic Turbine Draft Tube Interaction

This section seeks to breakdown the structure of the SBTL into smaller components. then conduct separate CFD analysis on each component in isolation. Since there was a restriction on time and resources, which prevented physical experimental validation from being incorporated into the investigation. Conducting such piecewise CFD analysis of generic, non-site specific facets in singularity, and in combination, can develop a greater understanding of tidal range systems for more universal future applicability and potential future validation.

This section covers the following areas:

- How the multiple jets from the turbine housing effect the jet expansion and length and assess the 3D characteristics inside the jet zone.

- Assess the bed shear across the scour mattress and beyond areas within the jet zone.

- Investigate the inclusion of additional turbine features such as the bulb within the TDT.

- Determine the expected difference, if any, between the depth-averaged models CFD.

4.4.1 Model Description

The computational domain is rectangular is shape and spans 600x120x30m in x, y and z directions respectfully. The magnitude of the downstream length was selected as overestimate of what jet lengths were likely to be observed being slightly over 42D. Additionally, the width was set with the intention to span an extent beyond reasonable jet/boundary interaction. The domain height is slightly exaggerated past what water levels are likely to be expected downstream of the barrage. This was done for planned model variants, testing the reaction of the model to various water levels. However, due to time constraints with the collapse of the TLP sponsor, such variants were not realised and thus out of the scope of this thesis.

For pragmatic simplification purposes, the turbine draft tube upstream of the turbine was not included in the models. The turbine draft tube expands from 7m circular diameter to a 14x14m square exit. Several cross-sectional measurements were taken along the turbine draft tube length to gauge the expansion rate and a linear interpolation approximation was used between each measurement.
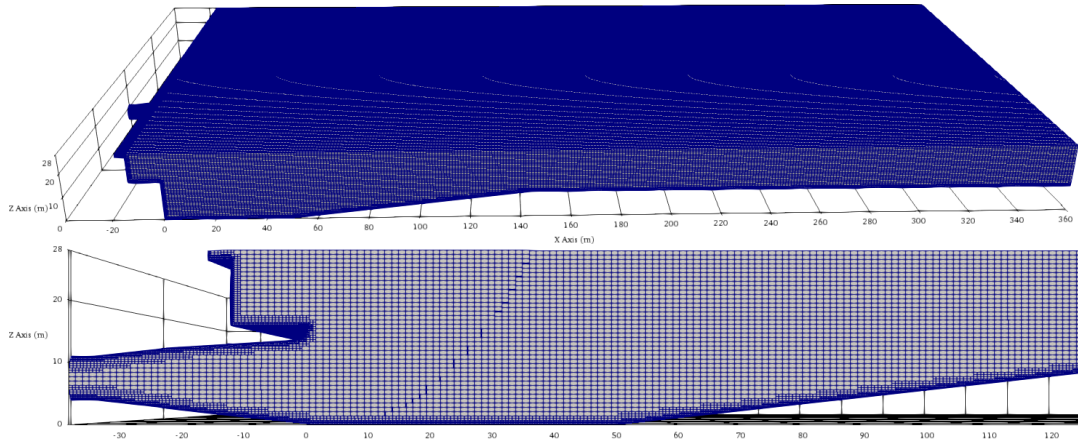
Figure 4.13: shows the Single Turbine draft tube with inclined bed model mesh.

Boundary Conditions

The domains initial fluid state is set with a kinematic viscosity equal to $1.5 \times 10^{-06} m^2 s^{-1}$. The boundary conditions imposed of all domain patch/wall surfaces were set to accordance to those specified in Table 4.1, with the exception of no cross-flow imposed on the outlet boundaries.

Through applying equations 2.63 and 2.64 with an assumption of $I = 7\%$, consistent with sections 4.2 and 4.3. The inlet kinetic energy κ and turbulence dissipation rate ε were set to $7.35 \times 10^{-05} m^2 s^{-2}$ and $1.1378 \times 10^{-07} m^2 s^{-3}$ respectively.

The inlet patch had a time independent, uniform plug inlet value which was held at 7 ms^{-1} across all TDT's. With the absence of turbine data and thus likely swirl, a high estimate I was taken of 25%. Therefore the kinetic energy κ and turbulence dissipation rate ε were set to $4.59375 m^2 s^{-3}$ and $6.6034 m^2 s^{-2}$ respectively. The y-plus, y-minus and outlet boundaries were set to the inletOutlet OpenFOAM condition.

A zero-gradient (no-slip) condition was set on the solid surface geometry. The kinetic energy and dissipation rate were set to zero values. Wall functions are used to compute the boundary layer. The turbulence model used was the RNG κ-ε model.

Mesh Configuration

The mesh was constructed using a combination of OpenFoams's built-in toolbox utilities blockMesh and snappyHexMesh, defining the domain expanse base cell size then cutting the domain block and snapping the mesh to the geometry. The mesh is configured as being of hierarchical hexahedral type structured to be refined through levelled subdivisions towards the wall surface cells. The base cell size was set with V_p equatable to the fine G-mesh grade in section 4.2.2. The meshed domain for the single TDT with incline slope is shown in Figure 4.13.
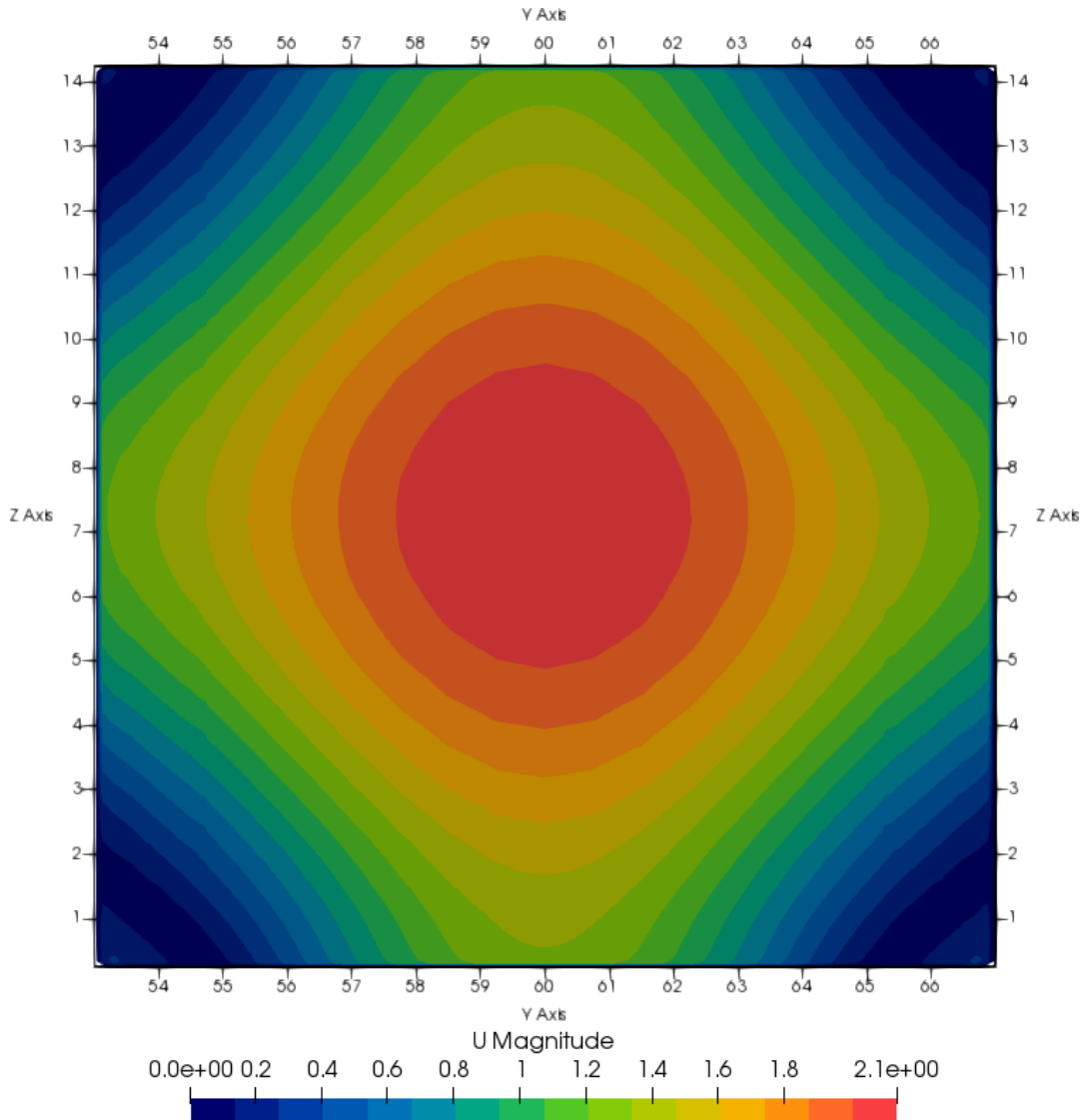
Figure 4.14: A velocity magnitude contour plot of flow profiles across the turbine draft tube exit.Taken as the plane normal to the x-axis at x=0

4.4.2 Results & Discussion

4.4.3 Single Turbine Draft tube

Turbine Draft Tube Exit Flow

Figure (4.14) shows the velocity magnitude (ms^{-1}) contour plot of the flow profile that exits from the turbine draft tube under the imposed inlet patch parameters. The turbine draft tube initially has a circular cross-section with an expanding diameter along the length. The tube cross-section shape then shifts to a square profile over 9.21m, while still expanding. These surface characteristics create a velocity profile which develops from a circular centre flow contour to one squarish in shape, and rotated 45 Degrees in comparison to the turbine draft tube surfaces. The flow is seemingly attracted to the turbine draft tube surfaces closest to the centre, which is mid-way along the sides.

The Coanda effect is described by Henri Coanda as: "the tendency of a jet of
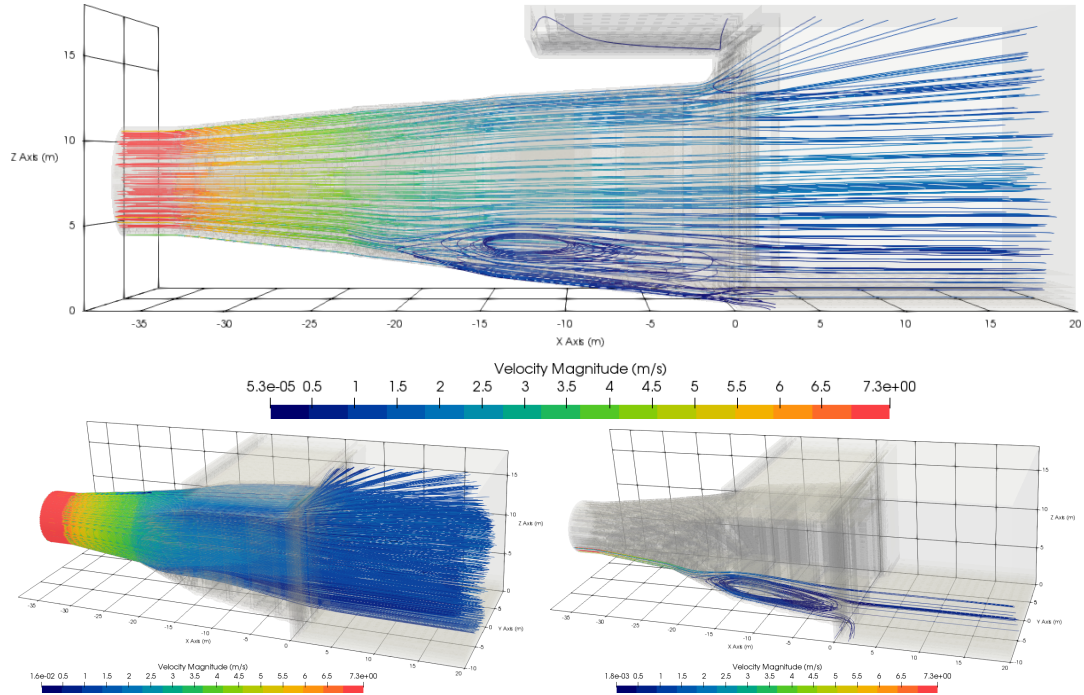
Figure 4.15: Velocity magnitude streamlines of the jet flow in the STDT

fluid emerging from an orifice to follow an adjacent flat or curved surface and to entrain fluid from the surroundings so that a region of lower pressure develops" [245]. The turbine draft tube expansion along the corner line is likely greater than which the Coanda effect can initiate, therefore flow separation maybe observed, with a low pressure vortex region in the corner as what is typical with conventional flow characteristics seen under the Coanda effect [135, 31]. What could be further evidence for small low-pressure velocity vortices is that there are velocity magnitude increases 1m from the corner point, with smaller, near zero velocity magnitude profiles between 1-2m from the corners, possibly being the vortices eye region (stagnation point). Further investigation into the corner through applying velocity profiles (streamlines) validated the hypothesis Figure 4.15.

The flow is injected into the model at $7ms^{-1}$. From the continuity equation:

$$\rho A_1 U_1 = \rho A_2 U_2 \tag{4.1}$$

Where ρ is the water density, $A_{1,2}$ are the cross-sectional areas for the tube in the inlet circular section and the square exit section respectfully. U1,2 is the velocity in the same section as the cross-sectional areas. The average exit velocity from the turbine draft tube is expected to be $1.37ms^{-1}$, 53% slower than the maximum velocity observed in the Figure (4.14) data contour plot. The continuity equation does not account for the development of the flow profile along the radial direction from the centre of the turbine draft tube. Hence, to obey the mass conservation law higher velocities are seen at the centre.

Velocity Magnitude Profile

A vertical plane and a horizontal plane, both of which intersect with the origin of the turbine draft tube inlet and extend the over the axial length of areas of interest, are
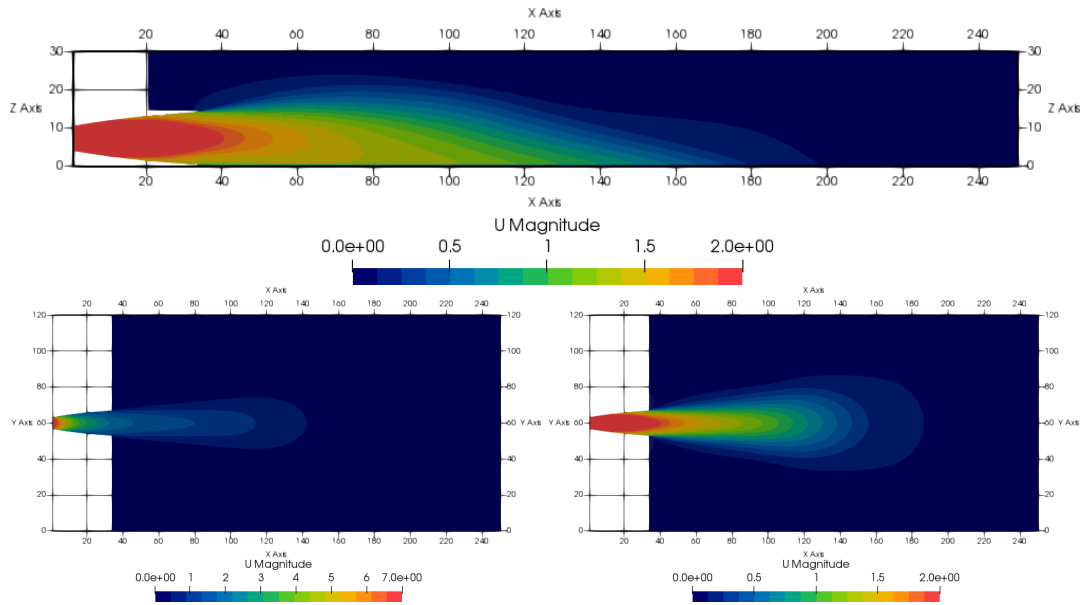
Figure 4.16: Rainbow velocity magnitude plots of the single turbine draft tube jet flow. A y-normal profile slice with a limited velocity range (top). A z-normal slice with the full velocity range (bottom left). A z-normal slice with the limited velocity range (bottom right).

used to display velocity magnitude to attain an overall perspective on the velocity profiles in the jet produced from the turbine draft tube. Figure 4.16 shows the domain sectioned along the vertical plane cross-section. The inlet velocity parameter was set to $7ms^{-1}$, uniformly across the entire inlet patch. The flow along the tube develops from the assumed irrotational, uniform velocity profile at the inlet into the cone shaped velocity profile resembling more developed jet flow profiles, with decreased flow velocity around the edges from the formation of a boundary layer and the highest velocities along the centre flow (inviscid core).

After exiting the tube, the jet expands while simultaneously decreasing in velocity as the turbine draft tube jet diffuses into the ambient fluid. Initially the centre flow of the jet has the highest velocity density. However, 20m after exiting the turbine draft tube when the jet flow velocity has reduced to $\approx 1.5ms^{-1}$, the contours plot shows the typical bell-shape velocity profile deviates from the axial centreline of the turbine draft tube (parallel to the wall); following a downward trajectory towards the bed surface. The top of the jet is clearly diffusing into the stationary water above the outlet. At 65m from the turbine draft tube exit the profile peak velocity has reduced to $\approx 1.3ms^{-1}$ along the bed surface. The velocity profile has altered to resemble a flame shape, though cut along the line of symmetry along the bed surface. As the jet velocity further reduces, the jet profile expands beyond the width of the turbine draft tube. The flame profile gradually gets 'bulbous' with decreasing velocity and the shear boundary layer gradient steepens towards the peak of the velocity profile. Once the jet flow has further reduced to $\approx 0.1ms^{-1}$ the contour profile bulges at the peak producing a steeper shear boundary before intersecting with the bed surface. At the widest extent, in the vertical direction; the width of the jet is 25m, 11m of which is above the turbine draft tube exit. The jet dissipates after 198m at which the velocity profile is $< 0.1ms^{-1}$. Note that flows $\sim 0.1ms^{-1}$ are probably at the error limits of the model and should not be treated as significant.

The profile part follows what could be described as a wall-jet, a shear flow created from a high energy and momentum fluid injected from a nozzle along a wall into an ambient fluid that is either stagnant or flowing at a comparatively low velocity in the same direction as the injected fluid. The injected flow forms the typical boundary layer along the wall with an additional free shear boundary layer between the injected fluid and the ambient fluid. The two layers have different turbulence characteristics and strongly interact with each other in the jet flow axial direction to determine the development of the wall jet [25, 56, 77].

The downward pull of the velocity profile could additionally be attributed to the Coanda effect. This is where the jet flow pulls and entrains water from the ambient into the jet flow, creating further low pressure either side of the flow. The bed prevents fluid from moving into the created low pressure region as fast as on the open side, therefore higher pressure on the open side pushes the jet flow into the low pressure region and hence the flow attaches to the bed surface [31].

Figure 4.16 shows the domain sectioned along the horizontal plane cross-section, providing an alternative perspective of the jet flow and its characteristics. Direct comparison can be drawn with the velocity profile peaks between the horizontal and the vertical cross-section velocity plots in respect to jet deceleration rate. However, the expansion profile of the jet differs from the vertical sectional perspective. The jet is symmetrical along the turbine draft tube central axis. The profile shape, initially bell-shaped at the inlet changes to flame-shaped at he turbine draft tube exit, before expanding and gradually changing to a tear-shaped profile over the wave length. The profile is in stark contrast to the vertical section, which displays a flame-profile that gradually displays jet expansion at the base of the jet before narrowing along the length. The jet expands across ≈60m at the widest point with a velocity of $\approx 0.1ms^{-1}$. It is likely the jet could be wider at different depths, since from mentioned above, the Coanda effect will pull the jet flow to the bed, there the innate flow momentum will cause further jet expansion until the energy is dissipated.

Figure 4.17 shows the velocity magnitude along the turbine draft tube axial centreline. The flow velocity decreases at decreasing rate along the turbine draft tube. After exiting the tube, there is no clear direct indication of any effect on the centre flow velocity. The rate of decreasing flow after the first 15m can be linearly approximated to $0.292ms^{-1}/m$ and $0.058ms^{-1}/m$ to 32m (turbine draft tube length). Between 50 and 100m (18-68m from tube exit), the rate of decreasing flow reduces, before increasing through 100-170m section (68-138m from tube exit). The flow rate then acts to flatten out to the ambient flow rate. The shift is deceleration rate coincides with Coanda effect, where the jet flow is pushed to the bed surface and attaches itself. As the Graph data is taken from a single line along the turbine draft tube central axis, the shift in jet peak velocity trajectory from that line due to the Coanda effect would intuitively lead to a steeper deceleration gradient. However, the opposite is seen. In that section, the jet flow velocity appears to be sheltered by the open side shear boundary layer between the jet flow and the ambient fluid maintaining velocity over an extended distance. The gradient then steepens again as the line passes through the suspected boundary layer flow before coming to rest in the ambient fluid region.
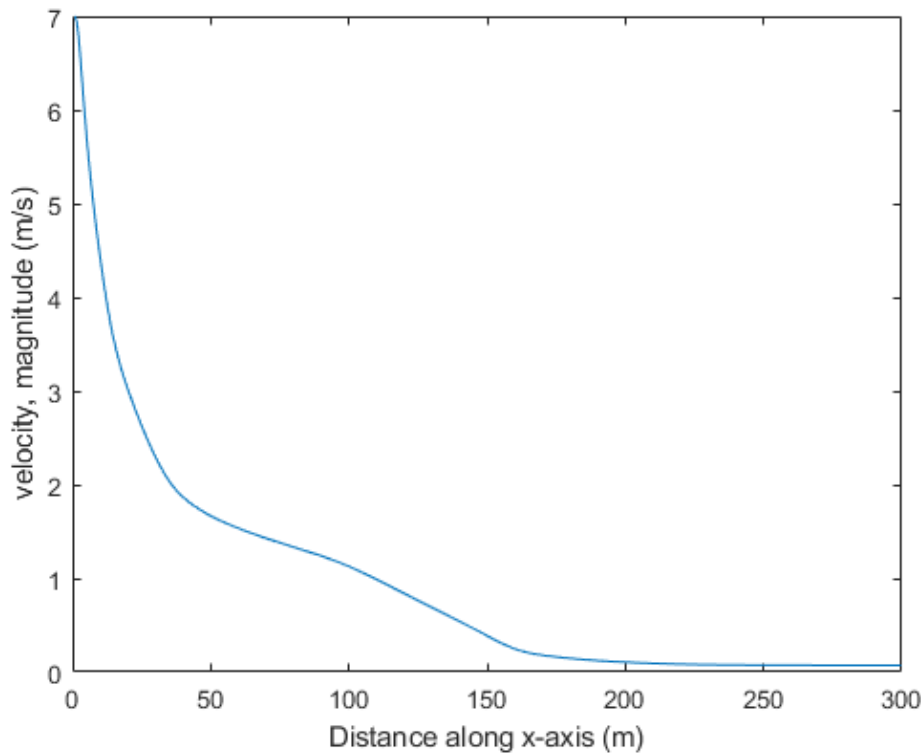
Figure 4.17: The velocity magnitude along the turbine draft tube centreline for the length of the x-axis.

Turbulent Kinetic energy (κ) profile

The turbulent kinetic energy (κ) inside the domain is shown in Figure 4.18. Again the κ profile characteristic is sectioned in to horizontal and vertical planes with the same dimensions as the velocity plots in Figure 4.16. The greatest turbulence intensity, as expected, is inside the turbine draft tube, in what is described as a hydrodynamic entry region. The κ contour plot follows a curved trajectory, following the approximate path of the assumed open side shear boundary layer. From 140m to 200m the κ value is $\approx < 0.07 J/kg$ but maintained until the 200m mark. The κ values in this region are higher outside the relatively higher velocity jet along the bed surface. This likely indicates some low energy turbulent mixing of the jet and ambient fluid before complete dissipation of the jet.

Figure 4.18 provides the horizontal perspective of the turbulent kinetic energy, 7m from the bed surface. The κ-values and contour density follows the boundary layer, appearing to initially flank the centreline before the jet flow drops from the Coanda effect. The increase in κ seen at x=110 occurs when the edge of the jet passes through this centreline plane. As with the vertical section contour plot, from 140m to 200m the κ value is $\approx < 0.07 J/kg$ until the 200m mark.

Bed Shear Stress

The Bed shear determines the sediment transport rates downstream of the barrage and hence the level of scour that will likely be seen. The ambient channel flow was near stagnant in the model used. In realistic circumstances, there will be a
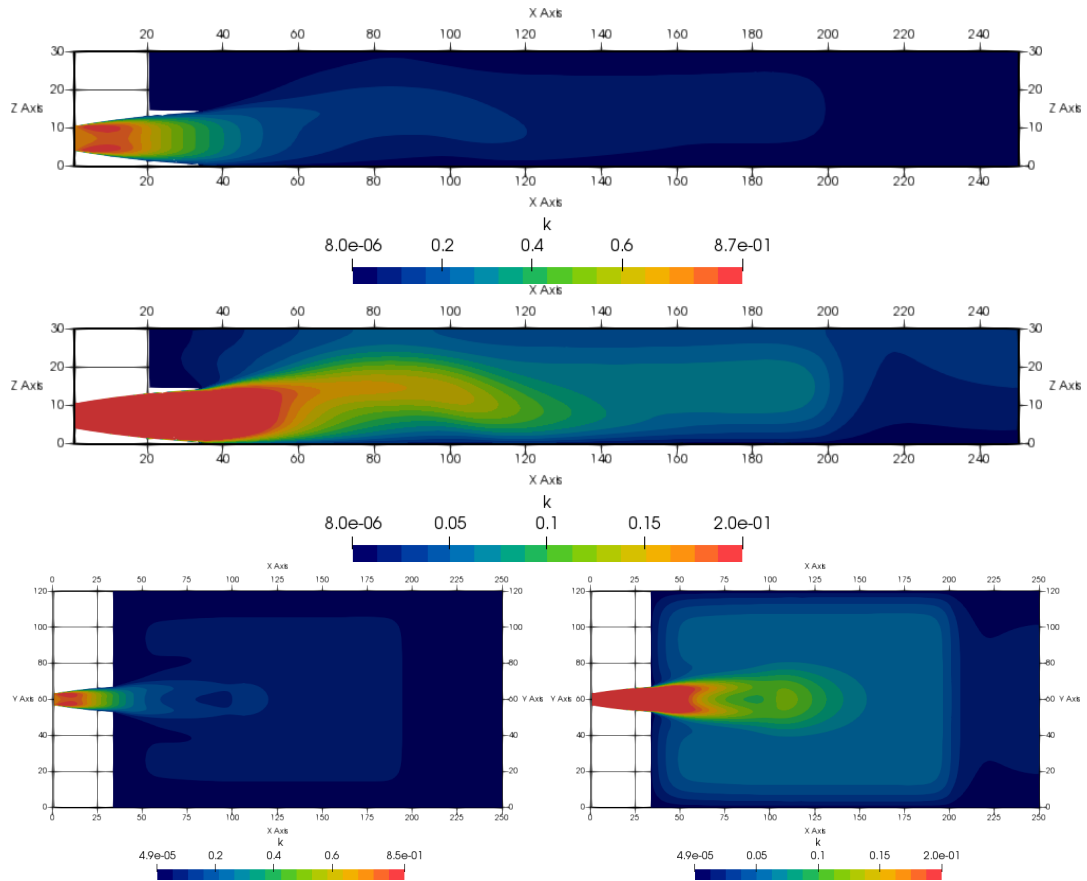
Figure 4.18: A rainbow κ plot extending the length of the jet flow. Top image is of the full κ data range. The second image shows the colour contours of a reduced limited data range to provide greater detail of the κ characteristics in the near field jet region outside of the turbine draft tube. Both plot is a section cut of the y-normal extending from the turbine draft tube midpoint. The bottom left is a full κ range and the bottom right is a limited section cut of the z-normal extending from the turbine draft tube midpoint.

small flow velocity from the tidal forces, this will have some small bearing on the ambient bed shear stress levels. Though it is expected that the bed shear stress will be considerably magnified above the ambient channel bed shear stress levels.

The magnitudes of the bed shear stresses are shown in Figure 4.19 not found for the entire length of the downstream bed surface. Data for the wall shear stress on the turbine draft tube and turbine housing wall was not included. The bed shear stress values were attained from the 3D CFD flow, Reynolds stress on the bottom surface. The bed surface is assumed to be uniform along its entire length and is set to zero slip. The bed shear stress reaches magnitudes of 0.0064 Pa in the region adjacent to the turbine draft tube exit that will be covered by the scour mattress, which extends out to $\approx 85m$ mark, where bed shear stress values of $\approx > 0.004$ pacals are found. Shear stresses of 0.001 Pa were shown at 175m away from the turbine draft tube exit. The bed shear stress contour lines mimic those of the horizontal velocity magnitude plots in Figure 4.16.
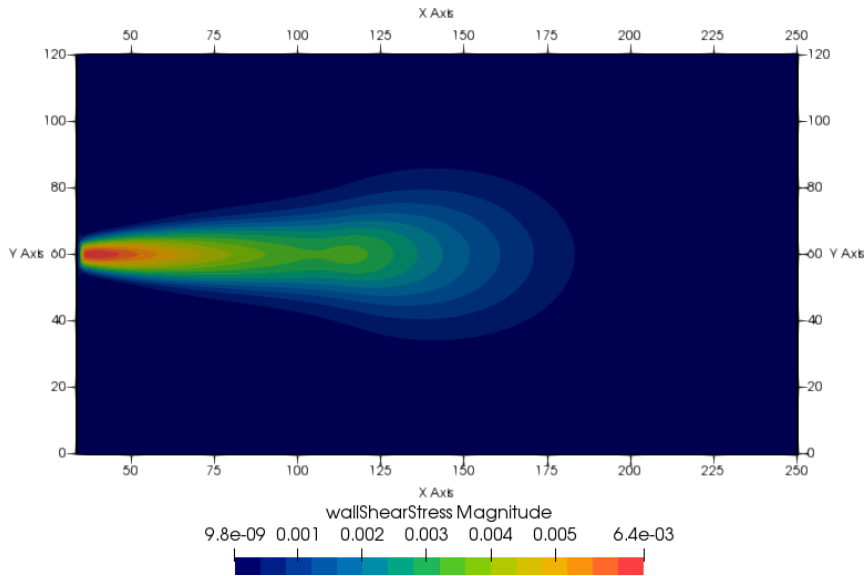
Figure 4.19: A Shear Stress magnitude (pascal) profile plot on the bed surface extending along the x-axis.

Analysis of Jet-jet Duality Profile

Following previous work [92] in and categorising the jet flow this chapter aims to investigate the jet flow from a near-field perspective of a single draft tube exit that has been numerical generated. Additionally, mapping the evolutional flow characteristics present from the model initiation to fully developed flow profiles and determine the temporal aspects to the case. While the case has not been validated with any physical experimentation, and the case is unique in respect to flow velocities and geometry, some trust can be attained through lose comparison to other experiments. The size and shape of the potential core is highlighted through applying an isosurface of the velocity magnitude values in the plot. The average outlet flow from the turbine draft tube is approximately $2ms^{-1}$, with the same geometry, mesh and parameters imposed as with the 1TDT case generic model.

Within 32 seconds the jet flow front has passed from the turbine draft tube exit (equivalent nozzle) and travelled 10 meters downstream in the x-axial direction **Figure 4.20**. The potential core is preceded by a turbulent high mixing front, the shape of which resembles a bowler hat, with the potential core being the crown, surrounded by the turbulent front being the rounded rim. The turbulent front expends radially as well as in thickness with axial distance downstream until the jet-jet transitional zone is reached. The potential core at this point is flat with a squarish shape from the perspective displayed in the figure.

The ambient flow at that time stage has little interaction with the jet body, though there is flow deflection with an over-topping flow between the wall surface and the turbulent front, with signs of entrainment.

At a later time stage of 371 seconds **Figure 4.21**, flow velocities equivalent to the exit velocity can be seen 180m downstream. The $2ms^{-1}$ iso-surface resembles a thin water stream falling under gravity with drop formation. The iso-surface profile narrows after 15m while simultaneously the flow shifts in the Z-plus direction, touching the surface ceiling at 60m downstream. After the initial narrowing effect the shape remains consistent until the break-up stage after 70m downstream. The

shape becomes amorphous and separates from a continuous core.

The ambient flow streamlines show flow over-topping near the draft tube exit, and then forming vertical counter rotating vortex before becoming entrained near the bed floor surface. There is also a strong likely hood that some flow will be entrained along the length of the vortex. Further along in the low-pressure shielded zone, large eddy formation is seen. Along the other side of the jet flow, the ambient flow is deflected and forms horizontal a vortex adjacent and parallel to jet main body flow.

At 531 seconds, the iso-surface has thinned further along its length and shows deflection bending towards the Y-plus direction. There is still a break-up effect, however the higher velocity areas are smaller and the shape is more continually spheroid. The flow characteristics remain consistent within the low pressure region.

After 711 seconds, the flow near stabilises with the typical potential core shape as described in [92]. No more velocity peaks above $2ms^{-1}$ appear downstream. The apex of the potential core is approximately 65 meters. The length of the potential core slowly decreases to approximately 55 meters after 1571 seconds, where it remains consistent indefinitely.

In summary, the jet flow when fully evolved showed similarity to the literature descriptions of jet flow potential core. The near straight characteristic of the potential core in the fully evolved flow indicates that's there is unlikely to be amalgamation of the potential cores of the jet flow. However, it is likely that the shielding effects of the outside jets will likely increase the length of the potential core. Under the parameters, several coherent structures develop along the jet flow such as the over-topping flow, and the horizontal axial votex.
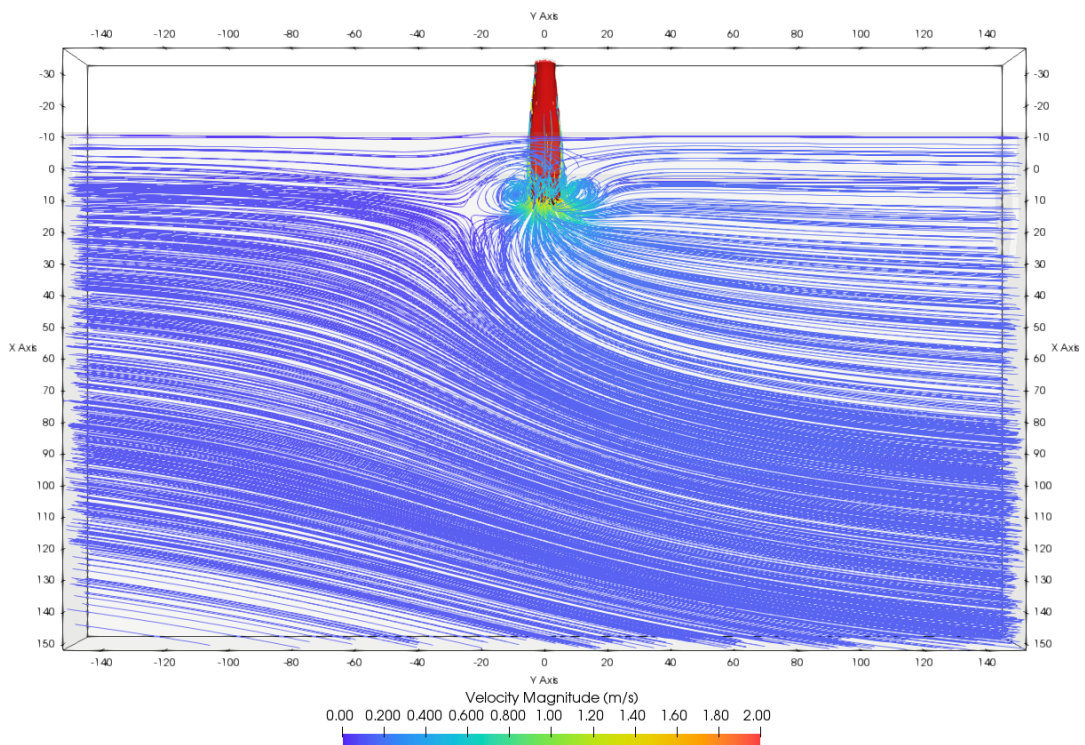
Figure 4.20: 1TDT case generic model to illustrate the potential core formation. Figure shows the potential core at 32 seconds after simulation initialisation
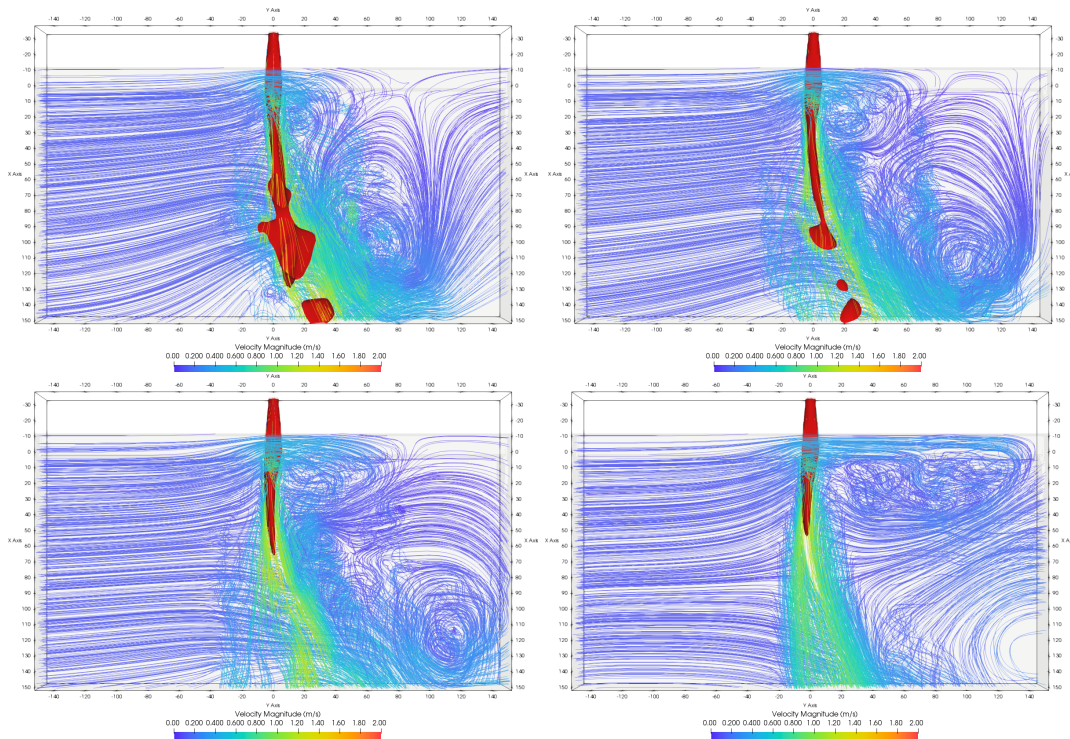
Figure 4.21: 1TDT case generic model to illustrate the potential core formation. Figure shows the potential core at 371 (top left), 531 (top right), 711 (bottom left) and 1571 (bottom right) seconds after simulation initialisation respectfully.
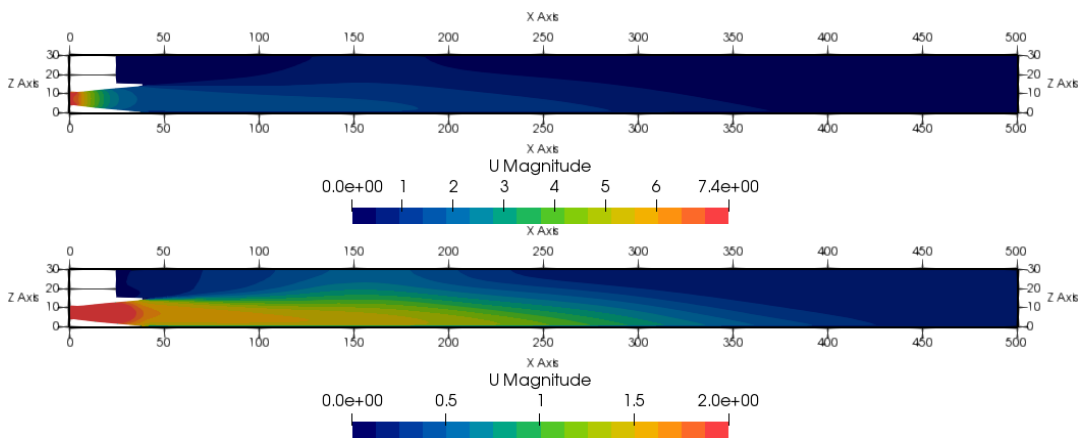
Figure 4.22: A rainbow velocity magnitude plot of the turbine draft tube jet flow. The top image is the full recorded velocity range. The bottom image shows the colour contours of a limited data range to provide greater detail of the velocity characteristics in the near field jet region outside of the turbine draft tube. The plot is a section cut of the y-normal extending from the turbine draft tube midpoint.

4.4.4 Quadruple Turbine Draft Tube

Velocity Magnitude Profile

Velocity magnitude data was taken from a vertical plane and horizontal plane, both of which intersect with the origin of the turbine draft tube inlet and extend the over the axial length of areas of interest, were used to display the extracted data set to
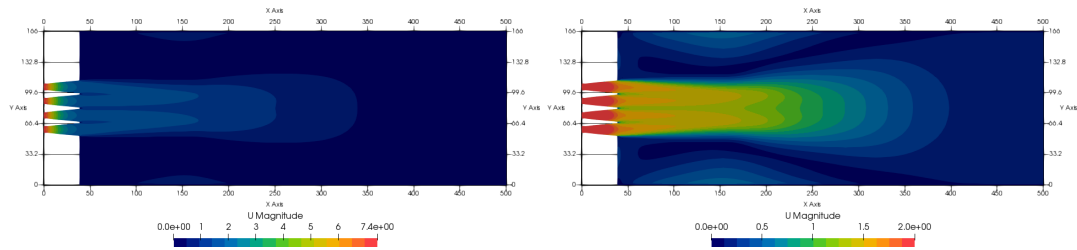
Figure 4.23: A rainbow velocity magnitude plot of the turbine draft tube jet flow. The left image is the full recorded velocity range. The right image shows the colour contours of a limited data range to provide greater detail of the velocity characteristics in the near field jet region outside of the turbine draft tube. The plot is a section cut of the z-normal extending from the turbine draft tube midpoint.

attain an encompassing perspective on the velocity flows profiles. Figure 4.22 shows the domain sectioned along the vertical plane cross-section of an inner turbine draft tube and downstream length. The inlet velocity parameter was set to $7ms^{-1}$, uniformly across the four inlet patches. The flow in the turbine draft tubes forms in the same way as what is described for the single turbine draft tube velocity profile characteristics.

After exiting the tube, the jet expands while simultaneously decreasing in velocity as the turbine draft tube jet diffuses into the ambient fluid. Like the section before, the Coanda effect attaches the flow to the bed surface in a similar location as in the single turbine model. There is a substantial cumulative effect of the quad grouping on factors such as the jet length and expansion. jet velocities of $\approx 0.1ms^{-1}$ extend 430m along the bed surface, when compared to the single turbine case this is $\approx 117\%$ increase in jet length. Like the single turbine flow, the jet transforms into a flame-shaped profile. The jet also expands to the water surface where velocities as high as $0.5ms^{-1}$ are observed between 35-200m downstream of the turbine draft tube exit.

Figure 4.23 shows the domain sectioned along the horizontal plane cross-section, providing an alternative perspective of the jet flow and its characteristics. Again, a direct comparison can be drawn with the velocity profile peaks between the horizontal and the vertical cross-section velocity plots in respect to jet deceleration rate. The expansion profile of the jet differs from the vertical sectional perspective. The jet profiles are no longer symmetrical along the turbine draft tube central axis. Instead there is jet grouping, with the outside jet and the nearest inside jet amalgamating a short length downstream. At 135m downstream, there are two velocity peaks with velocities around $1.5ms^{-1}$. The twin jet profiles further amalgamate, combining into a single head 235m downstream, with velocities around $1ms^{-1}$. Once the jets have combined the condensing effect disappears and the combined jet profile expands. Between the 50-200m mark, the velocity contours have a comparatively low density suggesting that there is again boundary layer shielding allowing the jet velocities less resistive forces inhibiting expansion. The outer two jet profiles likely guard the central jets, effectively removing shear forces from those jets. The horizontal jet expansion is difficult to determine with model. There appears to be interaction from the walls leading to unexpected distortions. It is possible that recirculation regions have formed at the side walls where velocity contours have congregated around the 150m mark. The $0.1ms^{-1}$ jet velocity extent is 400m at 7m above the bed. Future
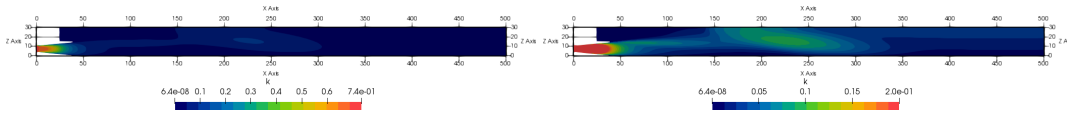
Figure 4.24: A rainbow κ (turbulent kinetic energy J/kg) magnitude plot extending the length of the jet flow. Top image is of the full κ data range. The bottom image shows the colour contours of a reduced limited data range to provide greater detail of the κ characteristics in the near field jet region outside of the turbine draft tube. The plot is a section cut of the y-normal extending from the turbine draft tube midpoint.
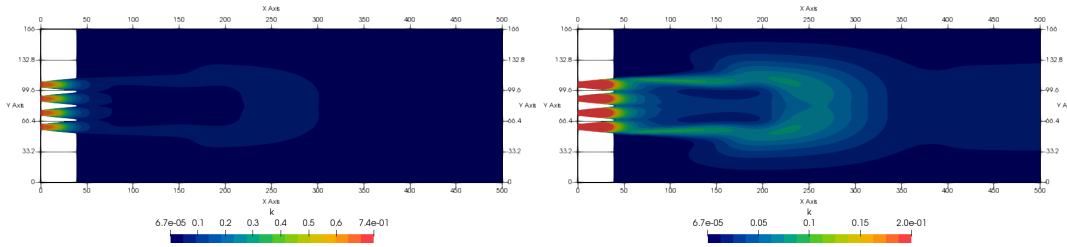
Figure 4.25: A rainbow κ (turbulent kinetic energy J/kg) magnitude plot extending the length of the jet flow. Left image is of the full κ data range. The right image shows the colour contours of a reduced limited data range to provide greater detail of the κ characteristics in the near field jet region outside of the turbine draft tube. The plot is a section cut of the z-normal extending from the turbine draft tube midpoint.

models will need to include a larger width to reduce this side wall interactions, with additional streamlines to gauge the resultant flow direction.

Turbulent Kinetic Energy (κ) Profile

The turbulent kinetic energy (κ) inside the domain is shown in Figure 4.24 and Figure 4.24. Again, the κ profile characteristic is sectioned in to horizontal and vertical planes with the same dimensions as the velocity plots in Figure 4.22 and Figure 4.23.

The κ contour plot again follows a curved trajectory, following the approximate path of the assumed open side shear boundary layer. However, there is increased κ-values around the surface region. Additionally, there is a long oval contour peak between 200-250m mark with κ-values of $\approx$0.1 J/kg. This peak region corresponds with significant dissipation of the velocity, further work is required to establish if this is an error caused by convergence issues or if this is a genuine flow feature. For computational intensity reasons, the mesh was coarsened along the jet region for allocation to the additional turbine draft tubes in this model. Expectedly there was no sudden drop in κ-values from sudden changes to mesh densities. Figure (4.24) provides the horizontal perspective of the turbulent kinetic energy, 7m from the bed surface. The κ-values and contour density follows the outer shear boundary layer, initially flanking the centreline before re-joining after $\approx$200m mark. There is a low κ-value encapsulated region where κ-values of ¡0.2J/kg exist between 70-220m mark along the x-axis and 62-102m mark along the y-axis. This coincides with the 'boundary layer shielded' region in the velocity magnitude plots shown in Figure (4.23), which adds validation to that hypothesis that the inside jets are protected from the turbulent shear mixing with the ambient fluid.
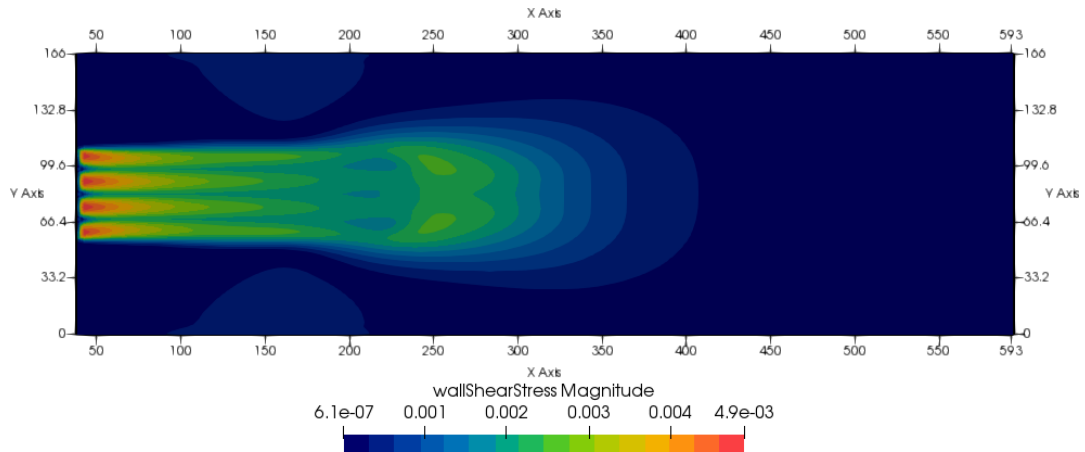
Figure 4.26: A rainbow shear stress magnitude plot of the domain bottom bed produced from the jet flow exiting from the turbine draft tube.

Bed Shear Stresses

The magnitudes of the bed shear stresses are shown in the data plot in Figure (4.26) for the entire length of the downstream bed surface. Data for the wall shear stress on the turbine draft tube and turbine housing wall was again not included. The bed surface parameters were kept the same as those for the single turbine draft tube model. The bed shear stress reaches magnitudes of 0.0049 Pa in the region adjacent to the turbine draft tube exit that will be covered by the scour mattress, which extends out to ≈ 85m mark, where bed shear stress values of $\approx > 0.0035$ Pa are found. Shear stresses of 0.001 Pa were shown at ≈ 360m away from the turbine draft tube exit. The bed shear stress contour lines mimic those of the horizontal velocity magnitude plots in Figure (4.23).

4.4.5 Single Turbine Draft Tube & TDT Exit Lip

Velocity Magnitude Profile

Velocity magnitude data was taken from a vertical plane and a horizontal plane, both of which intersect with the origin of the turbine draft tube inlet and extend the over the axial length of areas of interest, were used to display the extracted data set to attain an encompassing perspective on the velocity flows profiles, in the jet produced from the turbine draft tube flow.

Figure 4.27 shows the domain sectioned along the vertical plane cross-section. The inlet velocity parameter was set to $7ms^{-1}$, uniformly across the four inlet patches. The flow in the turbine draft tubes forms in the same way as what is described for the single turbine draft tube velocity profile characteristics. After exiting the tube, the jet expands while simultaneously decreasing in velocity as the turbine draft tube jet diffuses into the ambient fluid. Like the section before, the Coanda effect attaches the flow to the bed surface. Like the single turbine flow, the jet transforms into a flame-shaped profile. The jet also expands to the water surface at a greater rate than the previous two models, where velocities as high as $0.5ms^{-1}$ are observed between 35-200m downstream of the turbine draft tube exit. The velocity contours also show a shift towards the surface. The exaggerated jet expansion in comparison to the first
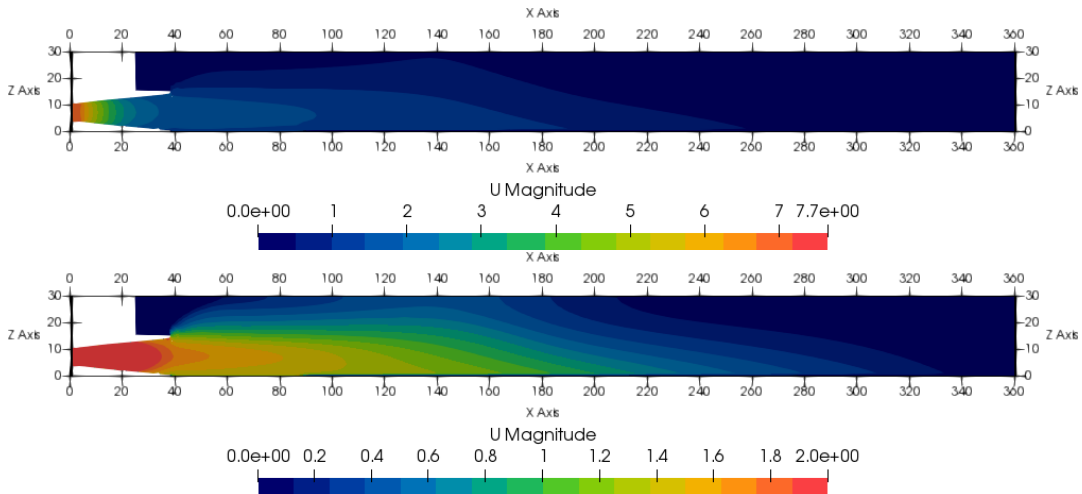
Figure 4.27: A rainbow velocity magnitude plot of the turbine draft tube jet flow. The left image is the full recorded velocity range. The right image shows the colour contours of a limited data range to provide greater detail of the velocity characteristics in the near field jet region outside of the turbine draft tube. The plot is a section cut of the y-normal extending from the turbine draft tube midpoint.
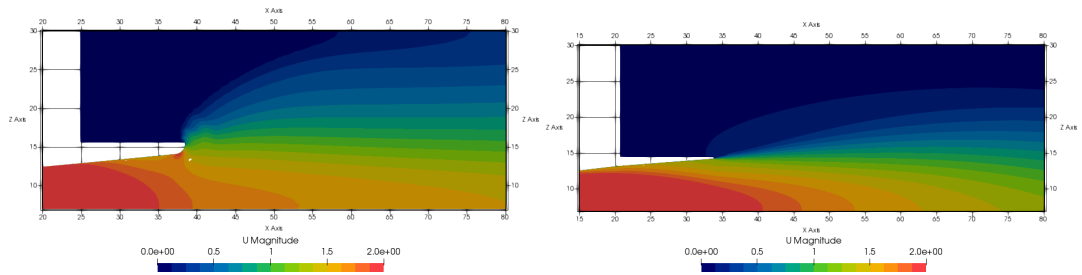
Figure 4.28: A rainbow velocity magnitude plot of the turbine draft tube jet flow around the upper draft tube exit surface lip. The left image is the STDT+EL model (refined geometry). The right image is the original STDT model (original geometry).
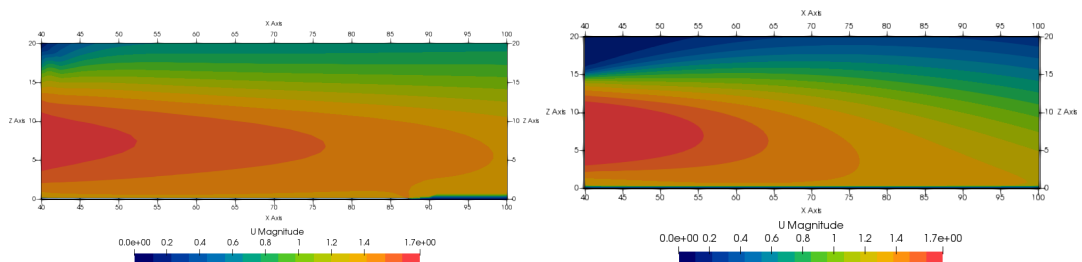
Figure 4.29: A rainbow velocity magnitude plot of the turbine draft tube jet flow around the Scour Mattress region. The left image is the original STDT model (original geometry). The right Image is the STDT+EL model geometry.

single turbine draft tube model could be put down to the modified upper lip of the turbine draft tube exit. The once abrupt square corner has been rounded off. The new surface profile will likely aid conditions necessary for the Coanda effect to take place, shifting the jet trajectory vertically upwards. This presents a scenario where the Coanda effect is intentionally applied to the jet flow at two opposing points. The likely intention is to aid the jet dispersion by creating conditions for greater initial
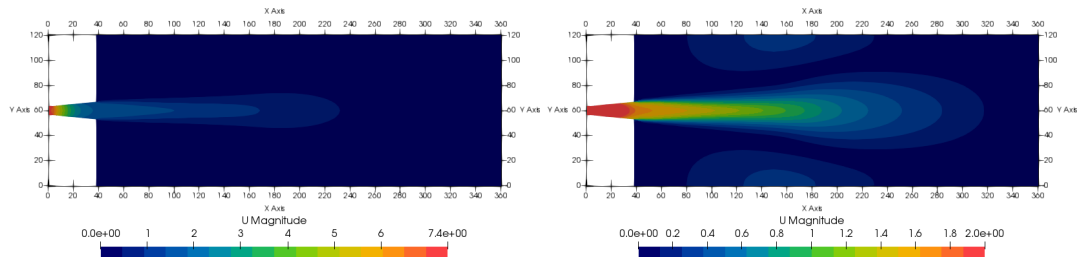
Figure 4.30: A rainbow velocity magnitude plot of the turbine draft tube jet flow. The left image is the full recorded velocity range. The right image shows the colour contours of a limited data range to provide greater detail of the velocity characteristics in the near field jet region outside of the turbine draft tube. The plot is a section cut of the z-normal extending from the turbine draft tube midpoint.

jet expansion in order to disperse the jet energy over a shorter downstream distance. The primary advantage of which would be that majority of the energy will be dispersed over the scour mattress region, therefore reducing the scour effects on the sand bed further downstream and shortening the jet dispersion length. A zoomed-in comparison between velocity magnitude contours from the original geometry of the STDT model and the STDT+EL geometry are shown in Figure 4.28. A high velocity contour patch can be seen just before the fillet edge. There is no apparent geometry feature or flow behavioural characteristic that can be attributed to this effect at this point in time. A recurring trend through the analysis of the results is the requirement of streamline to better gauge the exact flow behaviour. Additionally, since the velocities are shown at a reduced range and the feature is close to, for what is relative to this mode, a sharp feature. The mesh in that region could be insufficient or the mesh size change could lead to interpolation errors. An investigative route could be taken through taking data points from cell centres instead of the nodes. If the contours show some deviation, cell-centre analysis will show more blocky characteristics where interpolation errors between different cell sizes are present. The cell sizes can then be refined it those areas (providing they are of interest) until the interpolation errors reduce. The flow following the curved surface separates into three small peaks, with the peaks size decreasing with the longer that the flow streams remain attached to the surface. A likely result from the gradual reductive effect from the surface friction and fluid viscosity. The $0.125ms^{-1}$ and the $0.25ms^{-1}$ contours extending from the 20m mark follow consistent curved trajectory until about the 27-28m mark. At which point the contour lines then shift towards the water surface. A possible reason for this characteristic could be due to the head pressure decrease's towards the surface, and the effect becomes macro-noticeable around 3m below the water surface. At 65m from the turbine draft tube exit, the profile peak velocity has reduced to $\approx 1.4ms^{-1}$ along the bed surface. At ≈ 300m form the turbine draft tube exit, the jet velocity magnitude has reduced to $0.1ms^{-1}$.

A zoomed-in comparison between velocity magnitude contours along the scour mattress region from the original geometry of the STDT model and the STDT+EL model geometry are shown in Figure 4.29. As mentioned above in the STDT model the bed was set to a zero-slip surface. The STDT+EL had an incorporated scour mattress representation, where the surface had a defined friction factor and a raised profile. The scour mattress was an initial attempt to path-find how the feature should
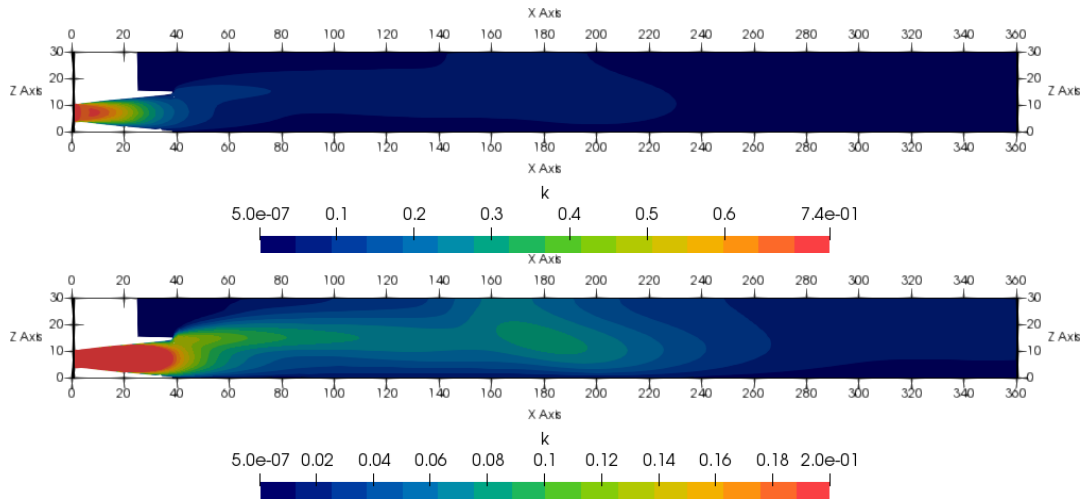
Figure 4.31: A rainbow κ (turbulent kinetic energy J/kg) magnitude plot extending the length of the jet flow. The plot is a section cut of the y-normal extending from the turbine draft tube midpoint.

be implemented in future iterations. The result seen in the STDT+EL velocity plot (middle image), shows that there flow velocity at the scour mattress representational surface (40-87m) is faster than the velocities seen further along the bed (+87m). It should be noted that the effect from the frictional value will be less than the equivalent effect from a zero-slip surface, which explains that effect. A more realistic representation of the scour mattress would impose a greater frictional effect on the flow that the bed surface. The Coanda effect also appears towards the raised scour mattress lip, where the flow is pulled down to the bed. Again streamlines are needed to fully gauge whether this is the case. Another instance that involves the Coanda effect is that the lower frictional value appears to have some degree on decreasing the flow attachment to the bed surface, since the flow contours in the STDT model, deviate from the initial trajectory path at an increased rate in comparison to the STDT+EL model. The other noticeable changes of the velocity contour shape profiles could be attributed to the modifications in the geometry between the two models, as discussed above.

Figure 4.30 shows the domain sectioned along the horizontal plane cross-section, providing an alternative perspective of the jet flow and its characteristics. Direct comparison can be drawn with the velocity profile peaks between the horizontal and the vertical cross-section velocity plots in respect to jet deceleration rate. However, again, the expansion profile of the jet differs from the vertical sectional perspective. The jet is symmetrical along the turbine draft tube central axis. The profile shape, initially bell-shaped at the inlet changes to flame-shaped at the turbine draft tube exit, before expanding and gradually changing to a tear-shaped profile over the wave length. Again, there appears to be interaction from the walls leading to possible recirculation currents centred around the 150m mark. As mentioned before future models will need to include a larger width to reduce this side wall interactions, with additional streamlines to gauge the resultant flow direction.
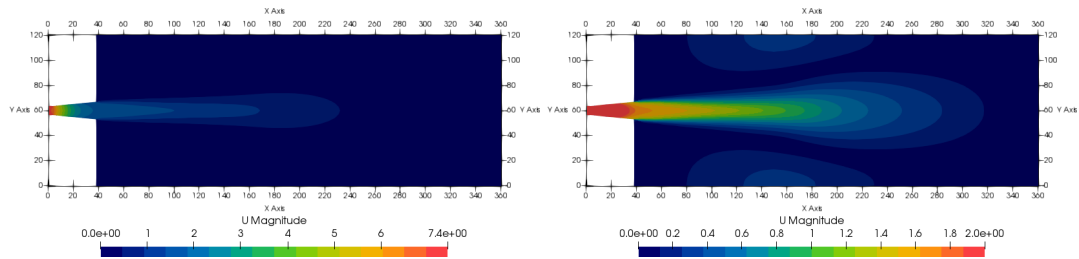
Figure 4.32: A rainbow κ magnitude plot extending the length of the jet flow. Left image is of the full κ data range. The right image shows the colour contours of a reduced limited data range to provide greater detail of the κ characteristics in the near field jet region outside of the turbine draft tube. The plot is a section cut of the z-normal extending from the turbine draft tube midpoint.
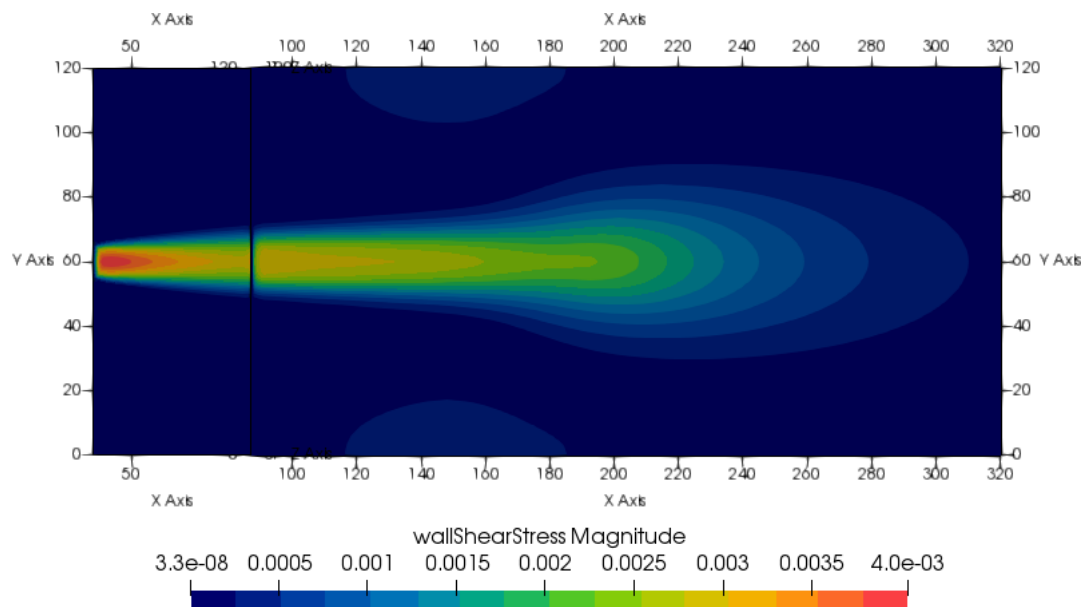
Figure 4.33: A Shear Stress magnitude (pascal) profile plot on the bed surface extending along the x-axis.

Turbulent Kinetic Energy (κ) Profile

The turbulent kinetic energy (κ) inside the domain is shown in Figure 4.31 and Figure 4.32. Again, the κ profile characteristic is sectioned in to horizontal and vertical planes with the same dimensions as the velocity plots in Figure 4.27 and Figure 4.30. The greatest turbulence intensity, as expected is inside the turbine draft tube which has been described in previous sections. The κ contour plot follows a curved trajectory, following the approximate path of the assumed open side shear boundary layer. Figure 4.32 provides the horizontal perspective of the turbulent kinetic energy, 7m from the bed surface. The κ-values and contour density follows the boundary layer, appearing to initially flank the centreline before the jet flow drops from the Coanda effect.
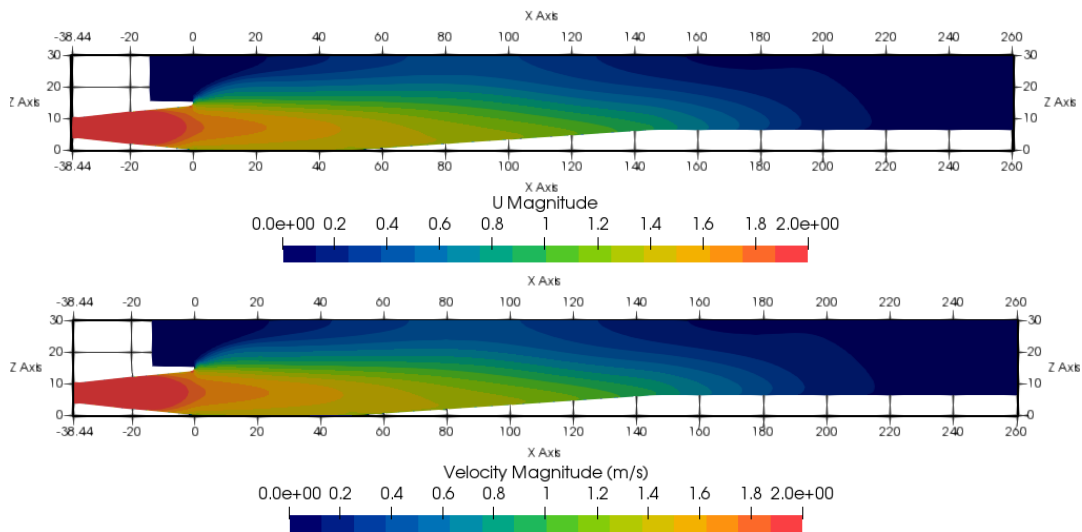
Figure 4.34: A rainbow velocity magnitude plot of the turbine draft tube jet flow. The top image is the full recorded velocity range. The bottom image shows the colour contours of a limited data range to provide greater detail of the velocity characteristics in the near field jet region outside of the turbine draft tube. The plot is a section cut of the y-normal extending from the turbine draft tube midpoint.

Bed Shear Stresses

The magnitudes of the bed shear stresses are shown in the data plot in Figure 4.33 for the entire length of the downstream bed surface and the new additional scour mattress section; represented from the origin mark to the red line 85m along the x-axis. Data for the wall shear stress on the turbine draft tube and turbine housing wall was not included. The bed shear stress values were attained from the 3D CFD flow, Reynolds stress on the bottom surface. The bed surface is assumed to be uniform along its entire length and is set to zero slip. The bed shear stress reaches magnitudes of 0.004 Pa in the region adjacent to the turbine draft tube exit that will be covered by the scour mattress. where bed shear stress values of $\approx> 0.003$ Pa are found. Shear stresses of 0.001 Pa were shown at 300m away from the turbine draft tube exit. The bed shear stress contour lines mimic those of the horizontal velocity magnitude plots in Figure 4.30.

4.4.6 Single Turbine Draft Tube & inclined Scour Mattress

Velocity Magnitude Profile

This model underwent modifications to create an inclined downstream bed in order to produce a closer copy of the anticipated actual downstream topography displayed in Figure B.2. Velocity magnitude data was taken from nodal values after numerical stabilisation. A vertical plane and a horizontal plane, both of which intersect with the origin of the turbine draft tube inlet and extend the over the axial length of areas of interest, were used to display the extracted data set to attain an encompassing perspective on the velocity flows profiles. Figure 4.34 shows the domain sectioned along the vertical plane cross-section. The inlet velocity parameter was
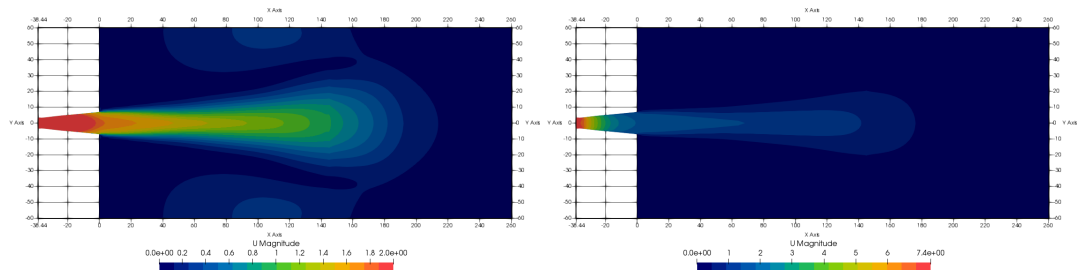
Figure 4.35: A rainbow velocity magnitude plot of the turbine draft tube jet flow. The left image is the full recorded velocity range. The right image shows the colour contours of a limited data range to provide greater detail of the velocity characteristics in the near field jet region outside of the turbine draft tube. The plot is a section cut of the z-normal extending from the turbine draft tube midpoint.

set to $7ms^{-1}$, uniformly across the four inlet patches. The flow in the turbine draft tubes forms in the same way as described for the single turbine draft tube velocity profile characteristics. After exiting the tube, the jet expands while simultaneously decreasing in velocity as the turbine draft tube jet diffuses into the ambient fluid. Like the section before, the Coanda effect still appears to be present and the flow attaches the flow to the bed surface. However, the magnitude of this effect is not as noticeable due the inclining bed rising to meet the jet flow. Gradually developing the model through single adjustments has potentially provided opportunistic insight into the jet flow behaviour that could otherwise have been missed if the model was built with complete geometry in the initial simulations. As with all previous jet flows, the jet transforms into a flame-shaped profile on exiting from the turbine draft tube. The jet also expands to meet the water surface at a similar rate to what was observed in the STDT flat-bed model while displaying what is seemingly similar flow pattern behaviour. The velocity contours also show a shift towards the surface. The exaggerated jet expansion above the outlet in comparison to the first single turbine draft tube model could put down to the same chamfered edge as listed in Section 3.3.1. The shape of the downstream jet departs from the STDT+ SM seen in Figure 4.27 after the jet profile starts to taper. The STDT+Iθ has a chunkier low jet velocity profile, just before dissipation into the ambient fluid. Though if a comparison is made in regards to the thickness of the jet at comparable distances downstream, the STDT+ SM flow has just begun to taper when the STDT+Iθ has near dissipated into ambient. This coincides with jet length reduction of approximately 125m or 37%. A clear conclusion can be drawn, that additional inclined slope in the model has the capacity to substantially reduce jet lengths downstream. At 75m from the turbine draft tube exit, the profile peak velocity has reduced to $\approx 1.4ms^{-1}$ along the bed surface. At ≈ 215m from the turbine draft tube exit, the jet velocity magnitude has reduced to $0.1ms^{-1}$. Attention should be drawn to the difference in jet flow velocity magnitudes within 100m of the turbine exit in both the STDT+ SM and STDT+Iθ. Comparing Figure 4.27 and Figure 4.34, in the region between 30 and 50m downstream of the draft tube exit, the velocity profile in the presence of the sloped bed is different, even in this region before the start of the bed slope. This difference is unexpected as the inclined bed should not effect the flow in this region. Either this is a genuine result, or could suggest that the models may not have converged entirely. Figure 4.35 shows the domain sectioned along the horizontal plane cross-section, providing
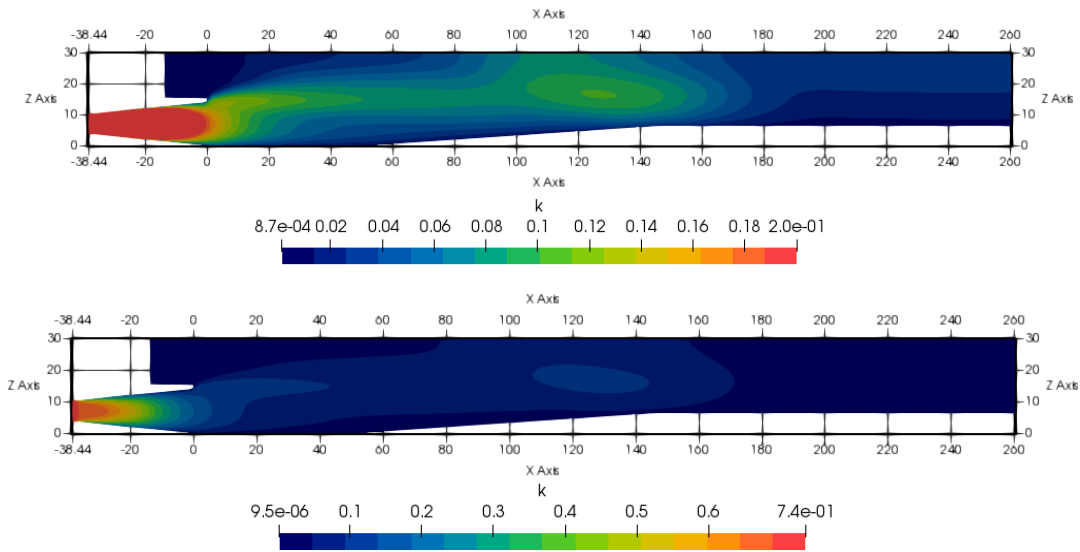
Figure 4.36: A rainbow κ magnitude plot extending the length of the jet flow. Top image is of the full κ data range. The bottom image shows the colour contours of a reduced limited data range to provide greater detail of the κ characteristics in the near field jet region outside of the turbine draft tube. The plot is a section cut of the y-normal extending from the turbine draft tube midpoint.
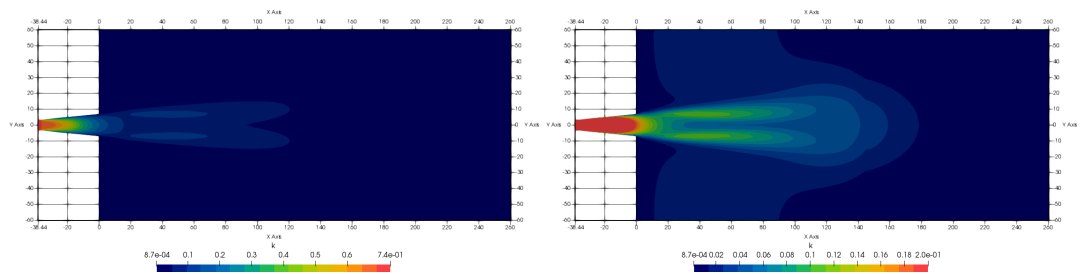

Figure 4.37: A rainbow κ magnitude plot extending the length of the jet flow. Left image is of the full κ data range. The right image shows the colour contours of a reduced limited data range to provide greater detail of the κ characteristics in the near field jet region outside of the turbine draft tube. The plot is a section cut of the z-normal extending from the turbine draft tube midpoint.

an alternative perspective of the jet flow and its characteristics. Direct comparison can be drawn with the velocity profile peaks between the horizontal and the vertical cross-section velocity plots in respect to jet deceleration rate. However, again, the expansion profile of the jet differs from the vertical sectional perspective. The jet is symmetrical along the turbine draft tube central axis. The profile shape, initially bell-shaped at the inlet changes to flame-shaped at the turbine draft tube exit, before expanding and gradually changing to a tear-shaped profile over the jet length.

Turbulent Kinetic Energy (κ) Profile

The turbulent kinetic energy (κ) inside the domain is shown in Figure 4.36 and Figure 4.37. Again, the κ profile characteristic is sectioned into horizontal and vertical planes with the same dimensions as the velocity plots in Figure 4.34 and Figure 4.35. The greatest turbulence intensity, as expected is inside the turbine draft tube which
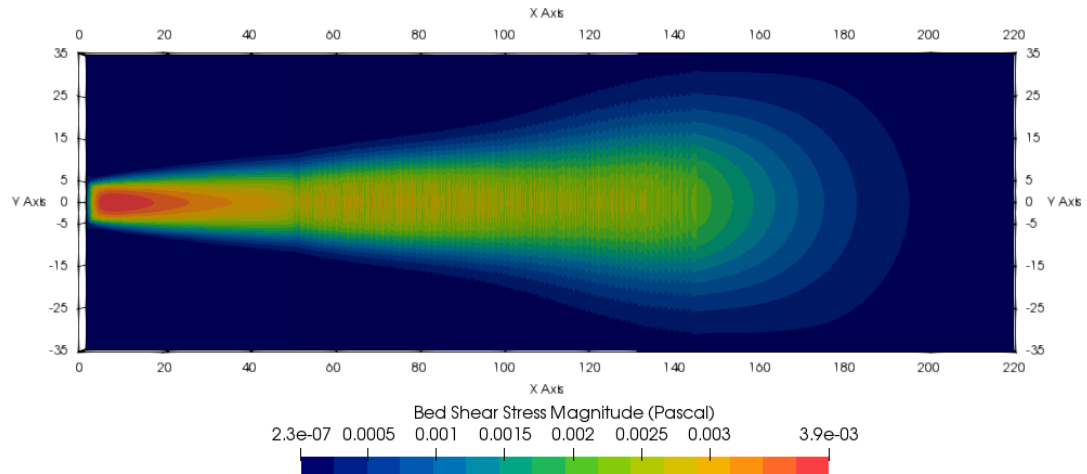
Figure 4.38: A Shear Stress magnitude (pascal) profile plot on the bed surface extending along the x-axis.

has been described in previous sections. The κ contour plot follows a curved trajectory, following the approximate path of the assumed open side shear boundary layer. There appears to exist greater turbulent kinetic energy downstream than the STDT+ SM model. This is likely from the flow being pushed upwards from the inclined bed.

Figure 4.37 provides the horizontal perspective of the turbulent kinetic energy, 7m from the bed surface. The κ-values and contour density follows the boundary layer as with the previous simulations. The inclined slope appears to increase the turbulent kinetic energy of the fluid that encapsulates the jet to a greater extent than seen in the STDT+ SM model. The slope could potentially increase mixing at the top edge of the jet or could also help the formation of eddies as the flow would face greater resistance when flowing downstream.

Bed Shear Stresses

The magnitudes of the bed shear stresses are shown in the data plot in Figure 4.38 for the entire length of the downstream bed surface. Data for the wall shear stress on the turbine draft tube and turbine housing wall was not included. The bed shear stress values were attained from the 3D CFD flow, Reynolds stress on the bottom surface. The bed surface is assumed to be uniform along its entire length and is set to zero slip. Though as described in Section 2.4.4, the bed surface was inclined in comparison to the scour mattress and further on downstream. The bed shear stress reaches magnitudes of 0.0039 Pa in the region adjacent to the turbine draft tube exit that will be covered by the scour mattress, where bed shear stress values of $\approx> 0.003$ Pa are found. Along the Incline section. The shear stress contours are fuzzy and there is not a clear distinction as the stress changes along the length. This is a limitation of the visualisation software. However, the stress profile across the width is easier to distinguish. Shear stresses of 0.001 Pa were shown at 190m away from the turbine draft tube exit. The bed shear stress contour lines mimic those of the horizontal velocity magnitude plots in Figure 4.38. In comparison to Figure 4.33 and the STDT+ SM model, the shear stress profile shape is wider which like the velocity magnitude plot can be attributed to an 'impact splash spread' as the jet flow hits a immovable surface and spreads out.

4.5 Inclusion of The Turbine Bulb

The purpose of this investigation is to determine whether the decision to not include the bulb of the bulb turbine in the lagoon and barrage models was valid. The initial assumption is that the feature would not have too much of a bearing on the characteristics and magnitude of the downstream jet, which is the main focus of this work. A second factor was the additional refinement that would be needed in the region which would add to the computational cost.

In previous investigations with the geometry of the Swansea Bay Tidal Lagoon turbine draft tubes, it was common to see flow separation where the streamlines would separate from the turbine draft tube surfaces before the exit. Additionally the flow leaving from the turbine draft tube was relatively laminar from a larger than grid turbulent perspective, and formed a high velocity potential core. A feature which is common with Jet flows. With only larger that grid turbulence becoming present in the near field region to the draft tube exits.

It will be of the projects and the environments best interest for the jet to have as high a jet dissipation rate as possible. Thus creating conditions where the flow does not separate from the turbine draft tube surfaces will lead higher flow rates over the rough scour mattress, helping to dissipate the energy.

If the bulb feature does produce such characteristics, then not including the feature could lead to an over prediction of jet flow magnitudes and leading to further ambiguity within the project. Additionally the bulb feature could act to disrupt the formation of a potential core; creating a more definitively correct wake flow: a region of re-circulatory/turbulent flow behind a blunt body where the flow has separated from said body.

Two model domains were created with identical characteristics apart from the inclusion of bulb features in one of the models. Other typical features such as the scour mattress were not included as they would impart the same reaction on both models. Hence, they were not necessary in determining how the bulb feature alters the flow characteristics through the turbine draft tube. A quadruple configuration was used to for the potential for the flow characteristics to vary from the outer TDT to the inner shielded TDT's.

A plug inlet velocity flow condition was imposed across all turbine draft tube cross-sectional surfaces. As the cross sectional area changes between model inlets varies with the addition of the bulb feature, the plug inlet velocity magnitudes were altered according to continuity so the same flow rate was present exiting from the TDT.

An inlet plug value of $16.34ms^{-1}$ was determined through applying the continuity equation for the expected maximum average discharge of $3ms^{-1}$ for the model without the bulb feature and $18.74ms^{-1}$ for the model with the bulb feature.

Both simulations were set up and run concurrently on the same cluster. During the set up, a human error was made where the plug input values were mixed up between the two models. Thus the model without the Bulb feature had a higher input velocity than the model with the bulb feature inserted into the model. This mix up has effectively lead to the model without the bulb having an volumetric input rate of $547.34m^3s^{-1}$ and $722.74m^3s^{-1}$ for the models with and without the bulb feature respectfully. A 25 percent difference between the two volumetric flow rate inputs. As such, a close comparison between the flow characteristics will not be of much
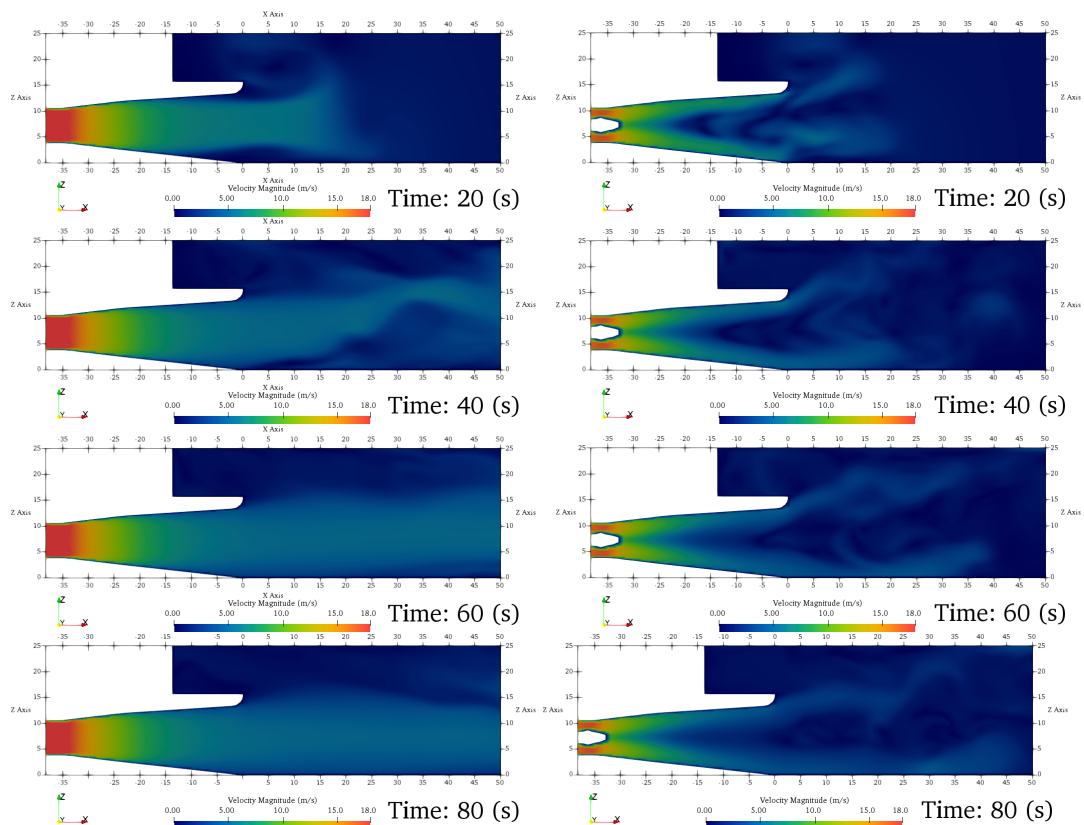
Figure 4.39: Temporal velocity magnitude (ms^{-1}) contours along a TDT (with the bulb feature incorporated) central splice line

point. However, the flow characteristics can still reveal trends which could help determine the validity of incorporating the bulb feature into further models.

Figure 4.39 shows the model without the bulb feature exhibited the same flow characteristics previously seen with other models. The input flow decelerates sharply for the first 15m along the TDT before forming a potential core where velocity is maintained. Additionally, flow separation from both the bottom and upper surfaces is present in the initial stages on the simulation. After the flow exits from the TDT, a turbulent front is formed which propagates ahead of the potential core. A vortex can also be seen along the upper edge of the jet flow.

After 33 seconds, the jet has travelled downstream but the near field is shown to be highly turbulent with the potential core being disrupted after approximately 15m downstream of the TDT exit. The main flow undergoes a cyclic motion of a sort of eddy shedding and shows no wall attachment to the bed surface.

At later time stages after around 60 seconds, the potential core has reformed and momentum is conserve. The eddy shedding in the region has stopped and the flow has developed wall attachment characteristics. A lower velocity layer can be seen adjacent to the bed surface from the interaction with the beds wall function, however the flow does travel along the bed, and will likely be subject to increased dissipation if realistic roughness values of the bed and scour mattress were to be used.

The implementation on the bulb feature leads to a substantial alteration to the flow characteristics. Figure 4.39 shows four time shots over 80 a second range, detailing the stages of jet development and allowing a direct comparison with the model without the bulb feature.

147

The flow is initially forced along the draft tube surfaces with a lower velocity re-circulatory region forming is the centre of the TDT. Wall attachment is observed along the upper surface leading the presence of the coandă effect off the top filleted lip. Outside the TDT exit the flow is split with both showing eddy shedding characteristics. It should be noted that the water depth in the model is far greater than that of the actual operating water level. Thus the wall attachment leading to the coandă effect around the fillet, will direct the flow to the surface where white water dissipation will likely result.

The simulation with the bulb feature does not appear to settle through the time steps with the same characteristics present through all recorded time steps. This could possibly mean that that the system has yet to settle and may do so if the simulation was run over a longer period.

Since there is continual wall attachment along the bottom surface for the duration of the simulation, this could indicate that a greater proportion of jet energy can be dissipated against the scour mattress. Additionally the extended period of time before the system settles indicates to more energy being dispersed in the near jet region than if the bulb feature was not there.

A further point is that with the previous inclusion of the scour mattress, a blockage effect developed which lead to the potential core being lifted up from the bed. A further investigation will be needed, but the bulb feature could help overcome this and continue to force the flow the scour mattress surface aiding with the dissipation.

The flow around the bulb feature in the model has 'blocky' characteristics which indicate that the mesh around the bulb feature in not fine enough to accurately capture the flow. However as previously argued, its unknown if further refinement would have an substantial consequential effect of the magnitude of the down stream jet for the additional computational cost required to refine the mesh further.

A further investigation could also look at the velocity magnitude distribution across the TDT exit. In previous investigations, the greater cross-sectional expansion in the corners led to vortex formations within the corners of the TDT exit with the inclusion of a scour mattress. It is still unknown whether these features will still exist with the adjustment to the flow regime when the bulb feature is used.

4.5.1 Conclusion

Computational modelling methodologies have always revolved around three issues; the numerical data, computational resources and validation. Three models have been presented in this report to outline the methodology, representing sequential stages of development towards the formation of a CFD model of the Tidal Lagoon Housing System that has been proposed to be constructed in the Swansea Bay area. Within each of the models three primary issues were addressed in the investigation:

- 1. How the multiple jets from the turbine housing effect the jet expansion and length and assess the 3D characteristics inside the jet zone.

- 2. Assess the bed shear across the scour mattress and beyond areas within the jet zone.

- 3. Determine the expected difference, if any, between the depth-averaged SWE models and CFD models.

All models presented in this report are for preliminary purposes, hence were tailored to be computationally economical and the data produced was not intended to carry weight, but to shed light on possible interactions of fluid flow interaction with stationary surfaces in the local environment. While the flow characteristics are not validated by any physical experiments, the flow profiles are relatable to what is seen in other investigations such as those carried out by Jeffcoate et al [121], and features characteristics of fluid flow that are commonly described in literature, such as the Coanda effect; which is suspected to have been utilized in the design to aid the initial jet expansion and shorten the downstream jet dissipation length. The jets appear to form a shear boundary layer between the jet flow and the near stagnant ambient fluid in the downstream region. The jet boundary layer zones contain the highest turbulent kinetic energy of the flow, outside of the turbine draft tubes. They also act as shield layer to the main jet body. When multiple jets are present, the two inside jet jets are protected by the outer jets from the shearing effects of ambient fluid interaction. This aspect is thought to lead to increased momentum conservation within the jet, resulting in longer jet lengths. An inclined gradient in the bed surface can have a substantial impact on the jet expansion rate and also the jet dissipation rate.

Despite comparative errors in the input flow rates. The inclusion of the bulb feature has a significant effect on the flow characteristic through the TDT and the near jet region. The flow appears to exhibit a higher degree of wall attachment which will aid in the dispersion of the jet through either being re-directed through the coanda effect towards the surface or along the rougher surface of the scour mattress. Both will likely aid in the overall jet dissipation. Additionally, there is no evidence of a formation of a potential core which is often attributed to conserving the momentum of flow. Further investigation into whether the blockage effect caused by the sour mattress will still lift the flow body if the bulb feature is present will need to be undertaken. From what can be attained from this investigation, there is probable cause to include the bulb feature in successive lagoon or barrage models.

Chapter 5

Delft Near-Field Hydrodynamics

5.1 Assessment of comparable flow regimes between Shallow Water Equation & Navier-Stokes Equation

5.1.1 Introduction

Inline with the *raison d'etre* of this thesis, the extent to which the 3D sub-grid domain would be required to extend downstream from the turbine housing before transitioning into the 2D shallow-water equation model needs to be determined. While Delft3D-FLOW has been widely validated for flow regimes, particularly those existing around coastal regions. The extent of Delft3D's capabilities of simulating high velocity gradient flow regimes such as those typical in jet-type flow regimes emanating from tidal lagoon turbine housing has not yet been fully investigated. Secondly, the corresponding computational cost benchmark required to replicate the high velocity gradient flows for respective length scales would also need to be determined. Insufficient consideration into the optimisation of computational model expense could reduce the product feasibility and thus reduce the potential research impact.

In this section, a model set up of an simplified high velocity gradient flow system to investigate Delft3D-FLOW's capacity is presented. Rather than seek to reproduce site-specific geometric conditions, which could limit the versatility with respect to wider applicability, determining a qualitative assessment on model parametrisations for flow velocity gradients and replication of hydrodynamic phenomena associated with respective turbulent length scales are of primary interest. The product of which would be to lay the foundation for establishing respective computationally optimised limitations on the 2D-SWE model, to which a 2D-3D sub-grid interface can then be implemented for accurate simulation of higher complexity flow hydrodynamics.

5.1.2 Model Description

Domain Characteristics

The model flow system can be surmised as being that of a jet-type flow regime covering both the first and second associated regions, discussed prior in Section 4.1 and 4.4.3. The domain which is schematically depicted in Figure 5.1 consists of a theoretical open rectangular 2D flow channel defined through maximum and minimum bounding coordinates of [-7.5, -7.5] : [37.5, 7.5]km with respect to the x,y Cartesian coordinate system. A infinitely thin dam-wall located 7.5km downstream partitions the domain into an upstream and downstream sections. A gap in the thin dam-wall located between [0,-0.3]:[0,0.3]km with respect to xy-coordinates, acts to constrict the channel width to produce corresponding flow convergence, jet flow, flow separation, recirculation, entrainment and downstream dissipation. Steady-state jet-type flows conditions can then be established through a constant elevation head differential between respective partitions.

The 15km domain width was made to be of an order 12 times the size of the dam wall gap, for purposes of isolating the jet-type flow regime from any boundary effects.

The forcing boundary condition was a time series water level. Post stabilisation, a steady inflow would enter the system in the upstream reservoir, approximately equivalent to the flow through the channel, and retaining a steady head difference between he upstream and downstream in the system. Over an extended time period, the basin would eventually fill. This would allow the mesh to be tested over a range of head differences and consequential jets produced through the hydraulic structures. A secondary investigative area was the flow over a corner section; monitoring behaviour of expected features such as corner eddies, recirculation regions, shear and boundary layers.
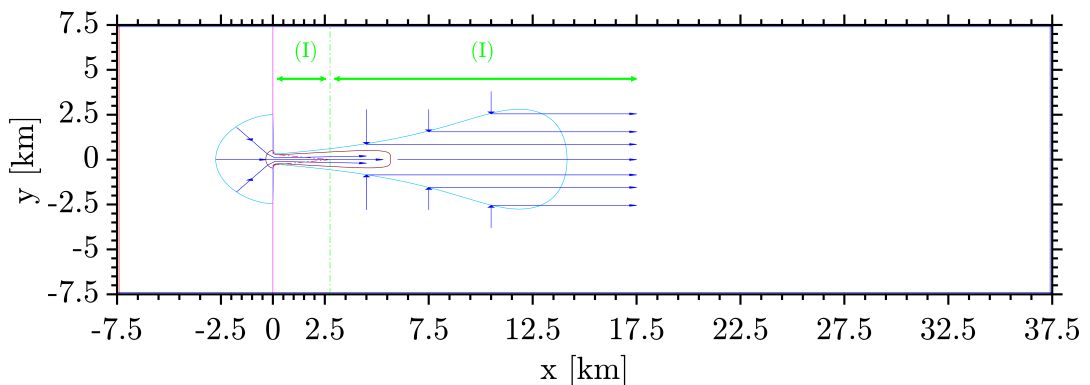
Figure 5.1: Schematic depiction of the full jet-flow test domain. A thin dam-wall partitions upstream and downstream sections apart from a 600m gap located between [0,-0.3]:[0,0.3]km with respect to xy-coordinates. A differential elevation head between respective sections induces flow acceleration through the gap leading to formation of a jet-type flow regime in the down stream section. Flow structures such as the potential core during that of flow establishment (Region (I)), and those of dissipation during the established developed flow (Region (II)) are presented in addition to entrainment streamlines.

The initial basis for the gap size of 600M resulted from uncertainty in the Swansea

Bay Tidal Lagoon turbine housing design and size due to conflicting media presented by Tidal Lagoon Power Ltd [237], where the turbine housing is clearly depicted as being 550m in length and consisting of an unbroken chain of turbine draft tubes and sluice gates. Finalised designs were later made available and presented in Section 4.4.1 Figure B.2. A larger size of 600m was chosen to simplify the division in cell sizes for this investigation. Since the primary directive of the investigation is that of jet flow capacity benchmark, the departure from the later design is of a lesser degree of consequence than determining a benchmark standard for how Delft3D handles jet flow velocity gradients.

The dam wall was constructed with Delft3D's "Thin dams" domain input parametrisation feature. Existing as an infinitely thin geometric objects, which are defined at the grid velocity points through setting flow velocity to zero between adjacent cells without altering the total wet surface of the volume of the model. The Thin dam feature was used because of it's likely implementation in models to represent the tidal lagoon structures, which would exist within the model with sub-grid geometric definitions; yet still evidently alter local hydrodynamics.

Boundary Conditions

The flow system was forced through a water level boundary condition shown in (eqn 5.1), set to a height of 1m above the reference water level taken as 0m. Though to reduce reflections of boundaries and hasten the model stabilisation after initiation, the input forcing was set as a ramped function, which would gradually raise the water level over a simulation-time 4 hour period to a height of 1m. The system was set with a uniform bathymetry of 10m below the reference water level.

$$\zeta = F_\zeta(t) + \delta_{atm} \tag{5.1}$$

The two side boundaries conditions were set as open discharge boundaries (eqn 5.2) with a flow value of zero along the entire length. The downstream outlet boundary was set as a water level uniformly maintained at the system reference water level.

$$Q = F_Q(t) \tag{5.2}$$

There was no system in Delft3D-FLOW that could enable the system to initiate with two separate water levels in separate but linked domains in delft3D-Flow module. The system initiates with a uniform reference water level. Thus, differential elevation head could only be achieved through forcing open boundaries acting on the system. Initial model instability induces reflection off solid boundaries such as the thin dam walls. However, the system would stabilize after a small-time period. Additionally, the boundaries were given a RPA of 100 to reduce the reflection effect.

The simulations were initially run over a two day period with varying time steps according to the CFL condition required for each mesh - of which a the CFL was limited to below that of 1. Additional Processes with constituents of; salinity, temperature, pollutants & tracers and sediments were completely excluded from the system, as was Physical processes of wind, wave and secondary flow.

The Physical parameters were kept at initial Delft3D-FLOW set system values. These consisted of Hydrodynamic constants; Gravity and water density, which were kept at 9.81 ms^{-2} and 1000 kgm^{-3} respectfully. Roughness was calculated from

the Chezy formula, with uniform value of 65 in both U and V. The background horizontal viscosity/diffusivity was also uniform at 1 m^2s^{-1}. The inbuilt function for 2D turbulence was not applied to the system.

Numerical parameters were also kept at standard values. Despite not being relevant in this particular case, the drying and flooding state was checked at the Grid cell centres and faces. The depth at the grid cell faces was judged by the mean. The threshold depth, Marginal depth, Smoothing time and Advection scheme for momentum were 0.1 m, -999m, 60m and cyclic for each numerical parameter respectfully.

Mesh Analysis

A range of mesh sizes featuring uniform element lengths between 300m and 25m with a constant aspect ratio of 1:1 was investigated. Smaller grid sizes were also considered. However, the computational intensity is very high and impractical to fully analyse variations in model's parameters with mesh sizes below 25m. Table 5.1 relates the mesh number to the total number of cells and the respective simulation clock times. The investigation was carried on a single core of an Intel® Xeon(R) CPU E5-1650 v3 @ 3.50GHz with a capacity of 62.7GB.

Table 5.1: Displays the element lengths, number of cells and simulation clock time.

Model Case	Element Length [m]	Total Number of Cells	Clock Time [hrs]
A-mesh	300	7500	0.014
B-mesh	150	30000	0.107
C-mesh	100	67500	0.305
D-mesh	75	120000	0.907
E-mesh	50	270000	4.251
F-mesh	25	1080000	32.414

5.1.3   Results & Discussion

Flow Visualisation

Figure 5.2-5.7 detail the depth averaged velocity magnitudes of the fully developed and stabilised steady-state jet-type flow regime for each case. A singular jet-type flow field exhibiting two distinct regions of flow; being the initial high velocity concentration and the latter diffusion. The centreline axis around y=0 acts as an axis of symmetry where lateral dispersions are identical across all time-frames.

The water level across the gap was measured to be 0.6m above the domain reference water level, thus existing as 10.6m in total depth. The Reynolds number of the jet flow (Table 5.2), with the turbulence reference length taken as the gaps hydraulic diameter and the flow velocity the mean average across the gap width, establishes the

jet-type flow firmly as that of highly turbulent being significantly beyond the laminar 2000 boundary [83]. Thus associated with a high dissipation rate and a shorter potential core from enhanced shear layer mixing spreading the jet.
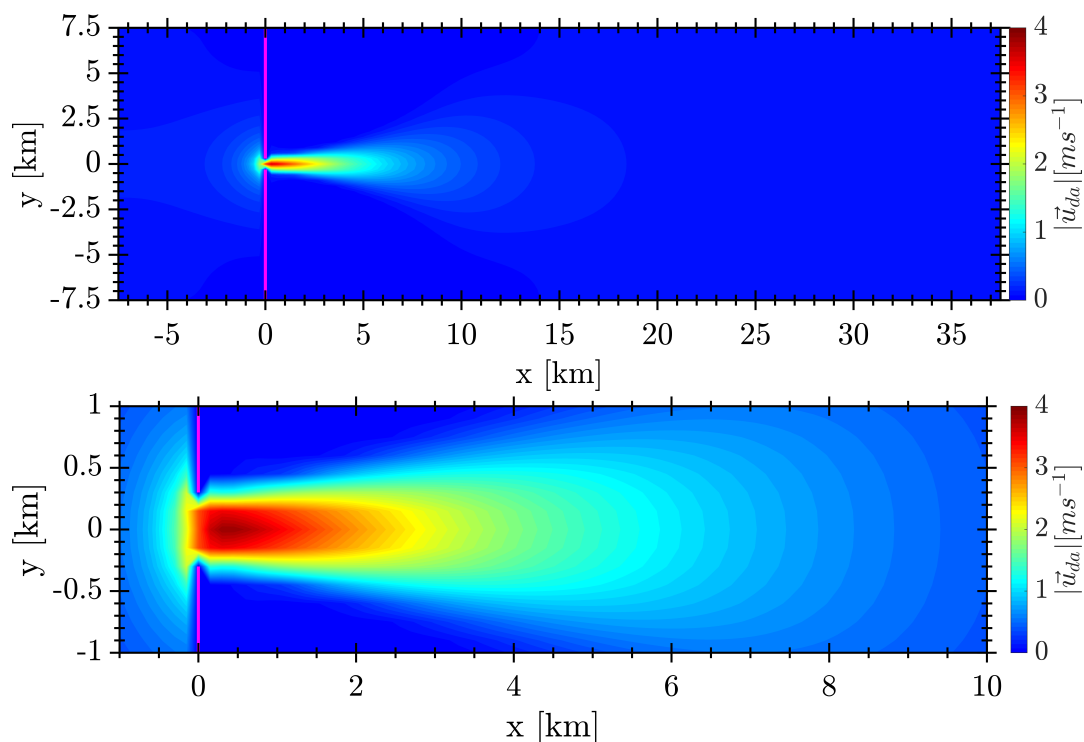
Figure 5.2: Depth averaged velocity magnitude contours of the flow simulated using the Mesh-A

The upstream fluid encapsulating the gap accelerates with depreciating radial distance in a manner that corresponds to fluid within the Schwarz-Christoffel mapping [62], which corresponds to the change in water level approaching the gap. The gap acts as a flow field constriction leading to subsequent development of flow convergence, high velocity potential core, before undergoing dispersion.

The flow continues to converge past the infinitely thin dam-wall, accelerating under the principle of continuity to that of the domain maximum flow velocity and form a *vena contracta*. There is a degree of continual separation between grid resolutions where the higher resolution depicts 'velocity overshoots' from streamlines directly forced around the thin-wall dams. Where as the coarser (A-D) increasingly fail to capture such until only a singular high-velocity point is depicted. Additionally, apart from the acceleration beyond the gap, the existence of the *vena contracta* is masked through the contour interpolation with the jet flow appearing to exist at the same width as the gap. Interpolation distortions can also be seen adjacent to the thin-wall dams, which exist as impermeable points holding velocity at zero. However, the distortion is limited to across the adjacent cell, with the near wall flow steams observed to continue without obvious deviation as to what would be otherwise be expected. The reason being is of the cell-centred holding of flow velocity, whereas the figures present vertices interpolations across cells.

The velocity gradient across the jet width (Figure 5.10), within the ZFE is also deterministic to the capture of the *vena contracta* and 'velocity overshoots', with the coarser grids bell curve becoming increasingly broad from the higher initial high-

velocity streamlines existing on the periphery. It is likely that should the gap width have been reduced, the high-velocity streamlines would likely converge at an earlier
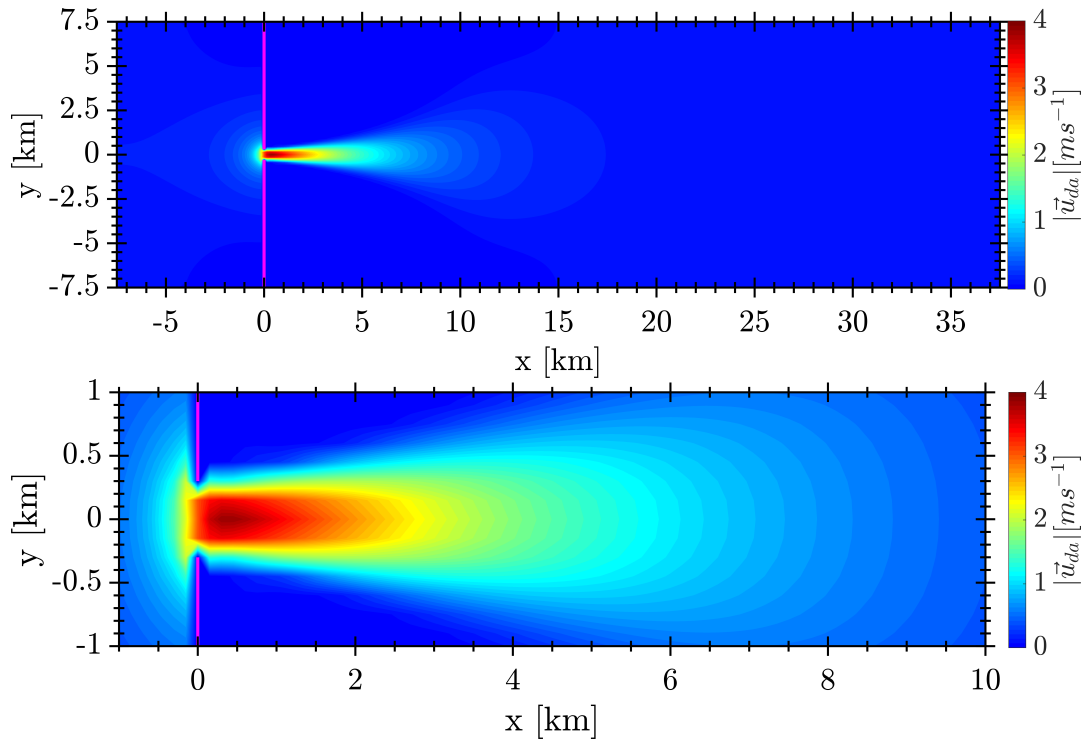
Figure 5.3: Depth averaged velocity magnitude contours of the flow simulated using the Mesh-B
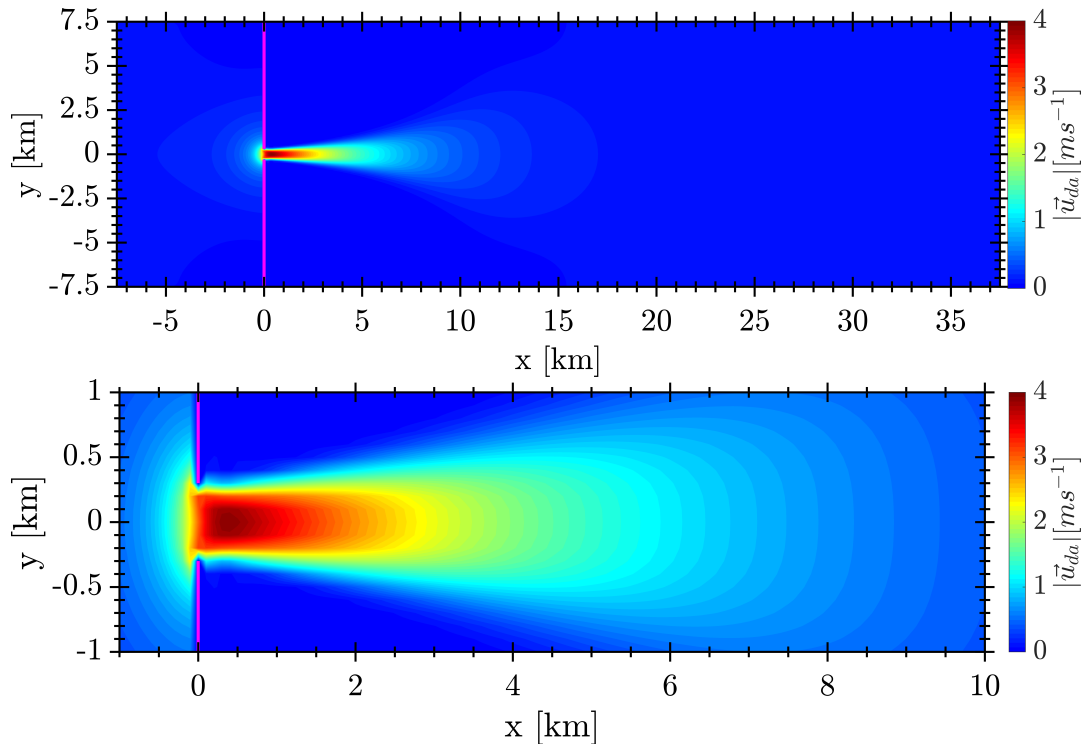
Figure 5.4: Depth averaged velocity magnitude contours of the flow simulated using the Mesh-C

point leading substantially higher maximum velocity values.

The inability to properly simulate the reduced flow cross-section and hence higher
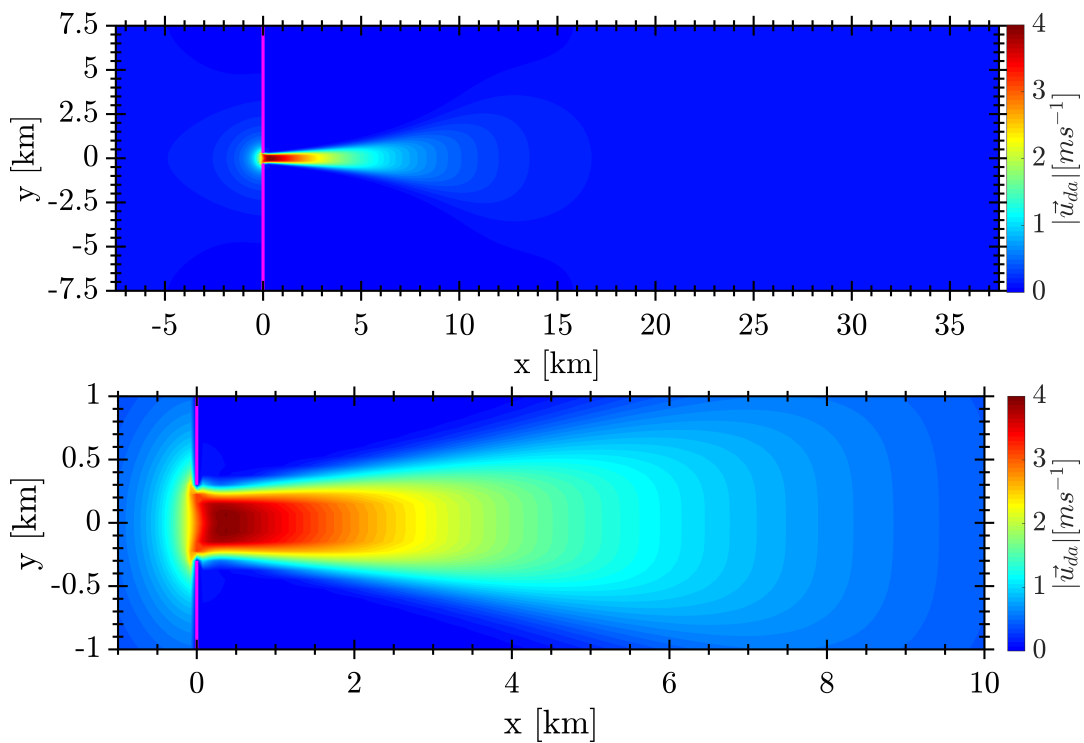
Figure 5.5: Depth averaged velocity magnitude contours of the flow simulated using the Mesh-D
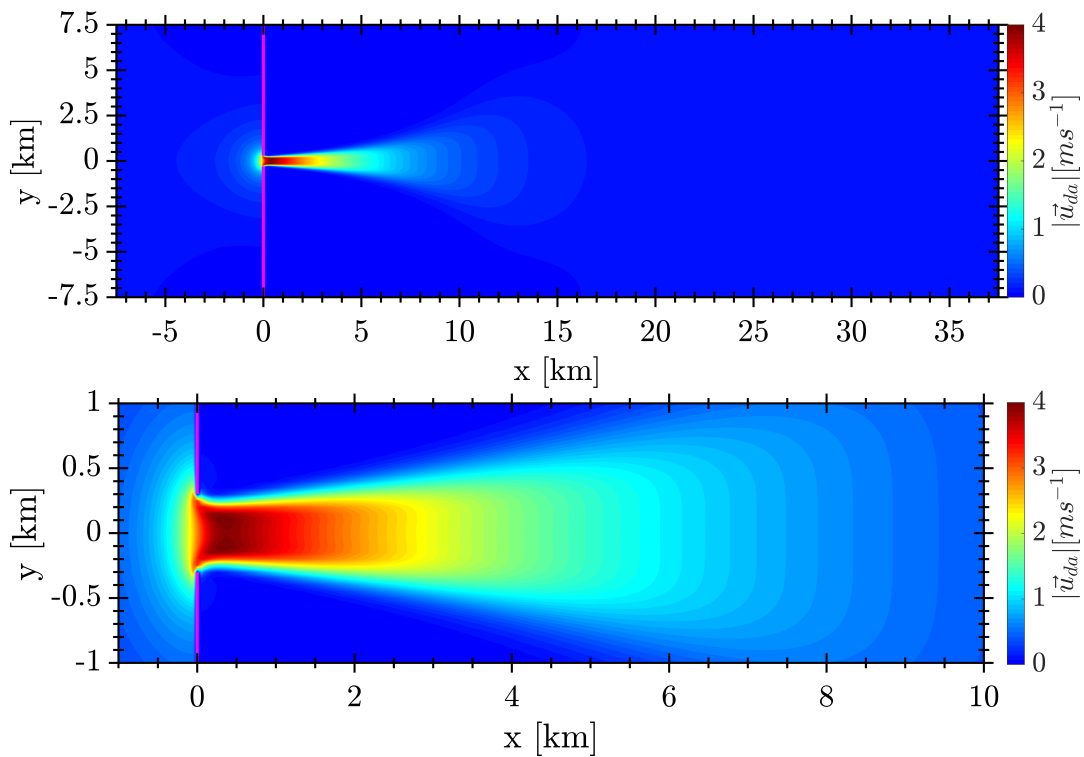
Figure 5.6: Depth averaged velocity magnitude contours of the flow simulated using the Mesh-E

flow velocities leads to a reduced maximum flow velocity along the jet centreline (Figure 5.8). Where the flow is also shown to undergo acceleration increasingly premature before the gap and maintain consistent higher velocity levels downstream after the flow enters into ZEF, indicating a reduced dissipative capacity. The reduction in dissipative capacity is additionally demonstrated with flow velocities been shown to reduce to less than 95% of the maximum after $26B_o$ for case A, then sequentially $24.8B_o$, $24.3B_o$, $24.1B_o$, $23.9B_o$ and $23.7B_o$ past the gap in the wall for case F. Though it must be noted the over simplification of the model in use leading to a gross over prediction of the jet downstream length.

Other than the steady decrement of the surface level elevation of the flow through the gap, no significant rise indicating the presence of a hydraulic jump is present. The presence of which would result in greater deceleration and strong lateral spreading of the downstream flow [233, 232]. Additionally, no quasi-periodic vortex structures are shown to emanate off the jet flow boundary with the ambient flow field.

For 'simple' round jets, the 'potential core' has been described as being flow of velocity equal to that of the jet exit within the ZFE, with termination marking the onset of transition into the ZEF. As such, respective authors have specified definitions based on the axial position as to when the centreline velocity drops below that of the exit velocity or specifically to various degrees of percentage decrease [**jianchun2010**, 95, 163, 92, 22, 215]. However, such cases don't feature ubiquity in engineering environments with only smooth contraction nozzles injecting flow featuring a completely uniform velocity [122].

While non-circular jets have been investigated extensively owing to the vast array of applications, their trajectory is not yet fully understood. Much of the surrounding research can often be obscure from the diver se input from the respective applicable
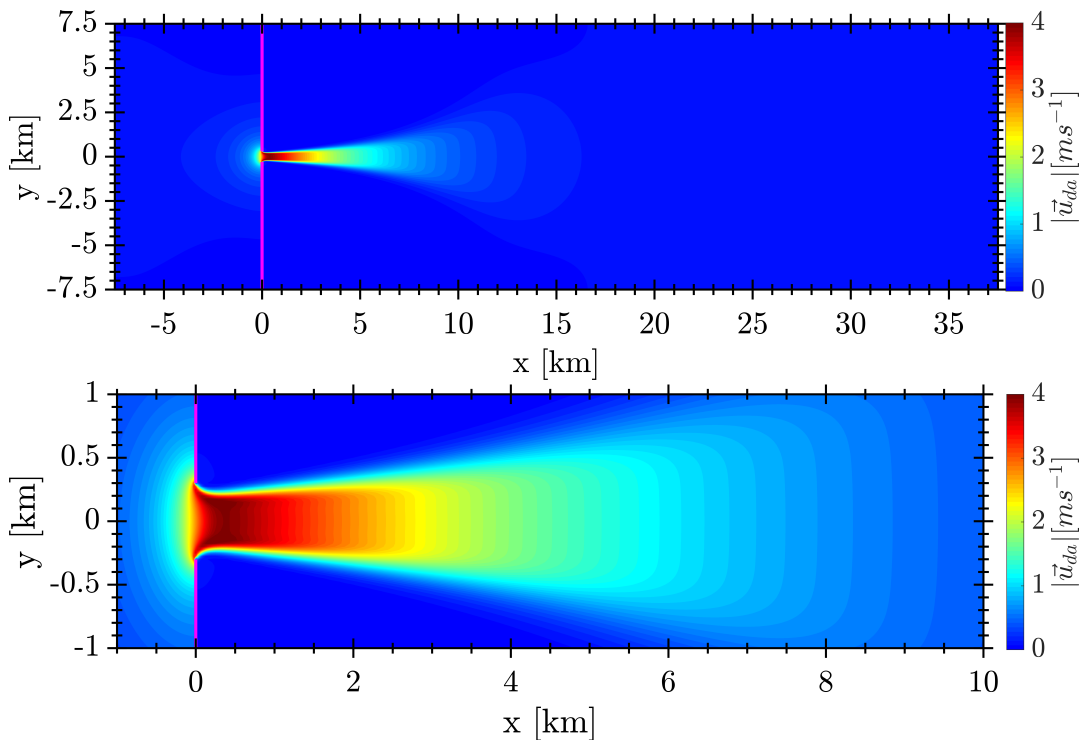
Figure 5.7: Depth averaged velocity magnitude contours of the flow simulated using the Mesh-F

fields [244, 122]. While the fundamental principles of what constitutes as that of the potential core; being the with high-velocity shear flow presenting as a "top-hat profile", there is not a definitive consensus in literature as to what exact criterion pertaining to the length of the potential core.

An alternative indirect method to determine both the potential core length and the virtual origin from the centreline axial velocity decay in the ZEF has also widely featured in literature [115, 180, 83, 273, 133, 108]. Turbulent jet flow reaches equilibrium until after several diameters downstream of the orifice where a steady-state of decay can be determined[83]. The exact number changes with respect to several parameters but is often listed around 6-10 diameters downstream [180]. The jet presents "self-similar" mean velocity and concentration profiles, where at any cross section, the time-averaged velocity can be expressed in terms of the jet centreline and a measure of width [83].

Fundamentally based on the round 'simple-jet' entering into a stagnant ambient field, equation 5.3 describes the centreline velocity decay rate within the ZEF for round jets as that of a power law behaviour x^{-1}.

$$\frac{u_m}{U_o} = \frac{K_1}{(x - x_0)/B_o} \tag{5.3}$$

The virtual origin is defined as the point at which the flow becomes self-similar in behaviour, which is equivalent to any respective jet flow in question and can be calculated as the distance between the jet exit x_o and that of the x-intercept 5.4 [115, 83, 180].

$$L_{pc} = K_1 B_o + x_o \tag{5.4}$$

However, its been shown that round the centreline velocity can decay in a manner other than that of x^{-1}, though is taken as a standard measure of such [43, 273].

The potential core length and virtual origin of planar jets can be determined similarly, albeit the axisymmetric flow for submerged rectangular jets occurs after the two shear layers from the short edges meet at the end of ZFE [133]. Thus the self-similar ZEF is described through equation 5.5.

$$\frac{u_m}{U_o} = \frac{K_1}{((x - x_0)/B_o)^{-0.5}} \tag{5.5}$$

which dictates the centreline velocity decay as that of a power law behaviour $x^{-0.5}$ [54, 92, 133, 260].

Considering the jet-type flow within this investigation, the initial conditions are distinct from the majority of literature, with presence of a free surface and being of a significantly larger geometric scale. Additionally, the presence of the *vena-contracta*, instigated by the effective 'sharp-edged orifice' of the infinitely thin-walled dam complicates numerical estimation with the point of maximum velocity, atypically with respect to most jet flows, occurring downstream from the exit at a point where the coaxial velocity overshoots coalesce [133, 94]. In this case, the term 'potential core', as it is often applied does not hold true. However, the ZFE still exhibits a high-velocity shear flow profile with an un-mixed core. Since all jet flows will theoretically asymptotically approach the self-similarity state of flow, and the rate of centreline velocity decay being indicative of jet spreading and mixing. The
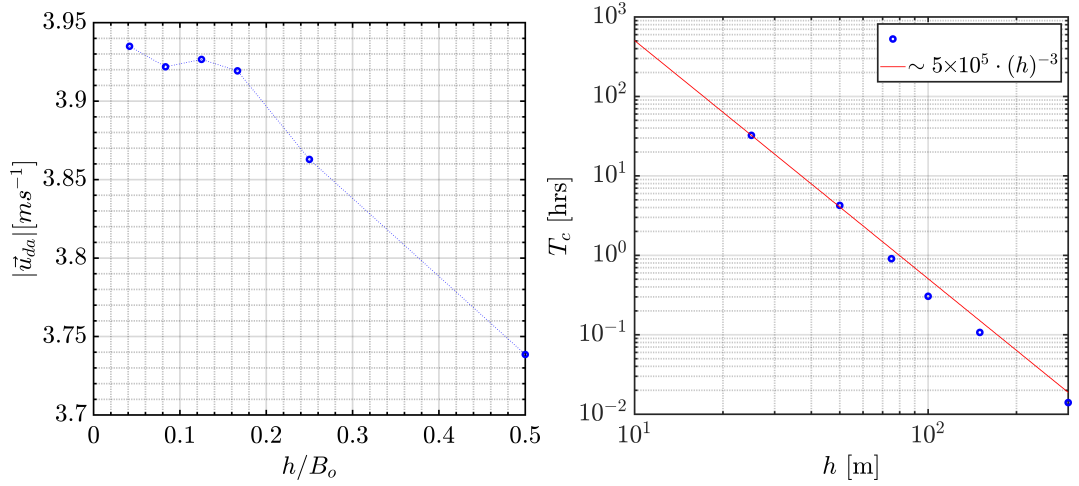
Figure 5.8: The maximum depth averaged velocity magnitude value (m/s) for each mesh.

indirect determination of the potential core length and point of virtual origin provides greater insight in how the initial development of the jet is interacting with the environment.

Therefore, within this investigation the high-velocity shear flow in the ZFE is termed synonymous with the 'potential core'.

Within this investigation the potential core length was determined through plotting the ratio between the maximum y-axial depth averaged velocity magnitude to the centreline depth averaged velocity magnitude $|\vec{u}_{max}\vec{u}_m^{-1}|$ vs the non-dimensional distance xB_o^{-1} as shown in Figure 5.9. The data was fitted with a inverse power law function of $K(xB_o^{-1})^m$, where m denotes the log gradient. Where said line intercepts $|\vec{u}_{max}\vec{u}_m^{-1}| = 1$, is determined as the potential cores termination position. The position of the virtual origin is determined through equation 5.4. The resultant y-axial centreline depth averaged velocity magnitude characteristics of the jet for various mesh cases are listed in Table 5.2.

Table 5.2: y-axial centreline depth averaged velocity magnitude characteristics of the jet for various mesh cases.

Case	$\mathbf{Re}_o$	$\mathbf{K}_1$	$\mathbf{x}_o\mathbf{B}_o^{-1}$	$\mathbf{L}_{pc}\mathbf{B}_o^{-1}$	$\mathbf{x}_{95\%}\mathbf{B}_o^{-1}$
F-Mesh	1.14E+08	0.428	6.108	6.536	23.667
E-Mesh	1.05E+08	0.436	5.992	6.428	23.917
D-Mesh	9.67E+07	0.444	5.858	6.302	24.125
C-Mesh	8.89E+07	0.452	5.742	6.193	24.333
B-Mesh	7.48E+07	0.464	5.576	6.040	24.750
A-Mesh	4.44E+07	0.497	5.111	5.607	26.000

The across-width data profiles Figure **??**, also displayed blocky characteristics for coarser sizes and sequential smoother profiles for each refinement in mesh size. Apart from precise velocity data at a point, this data set has also shown that there is an increased velocity profile at the corners of the thin wall dam compared to the channel centre. This characteristic was present in mesh sizes below 100m. A further
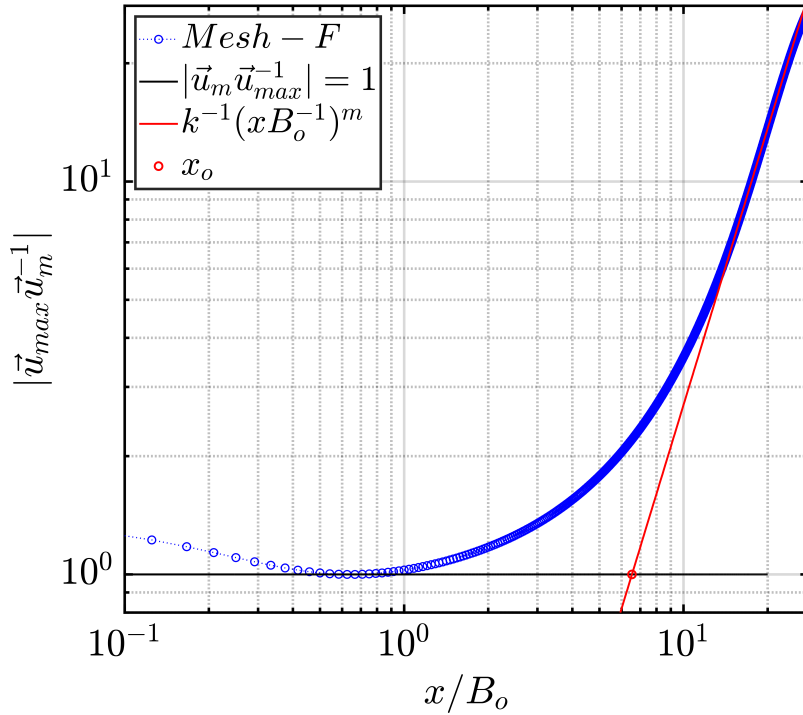
Figure 5.9: log-log centreline profile for the inverse jet non-dimensional axial depth averaged velocity magnitude. Fitted ZEF decay line $K^{-1}(xB_o^{-1})^m$ (red), and $|\vec{u}_{max}\vec{u}_m^{-1}| = 1$ (black).

point should be noted; like the maximum depth averaged velocity magnitude value in Figure **??** & **??**, there is consistent increase in the maximum velocity for each successive mesh refinement. The 'U' velocity profile also changes; becoming more pronounced as element size decreases, with sharper velocity 'spike'. This gives some indication that the high velocity areas at the intersection between the flow and the thin wall dam, is not entirely being captured by the meshes used. This can be considered as an axiom as the 'sharp or abrupt' edge assumption of the thin wall dam will lead to high turbulence, which meshes of 25m (smallest grid size) will be too large to capture.

Analytical verification

Table 5.3 summarises the order of accuracy and GCI of three grid resolutions, being Mesh-F, Mesh-E and Mesh-C which posses a uniform refinement ratio between each and are denoted through subscripts respective of ascending order. The refinement ratio(r_c) was selected as 2, which while within limits stated in literature, is at the maximum [209, 208, 39, 250].

Each tested across five non-dimensional dependant variables of interest, being the Reynolds number across the gap, the decay constant for the jet centreline velocity, the position of the virtual origin, the length of the potential core and the position of 95% depth averaged velocity magnitude reduction. All variables are of the mean values over the final simulation time-steps after a statistically steady flow regime had been achieved.

As listed in Table 5.11, across the board there is a significant reduction in GCI value for the successive grid refinements ($GCI_{12} < GCI_{23}$), with percentage de-
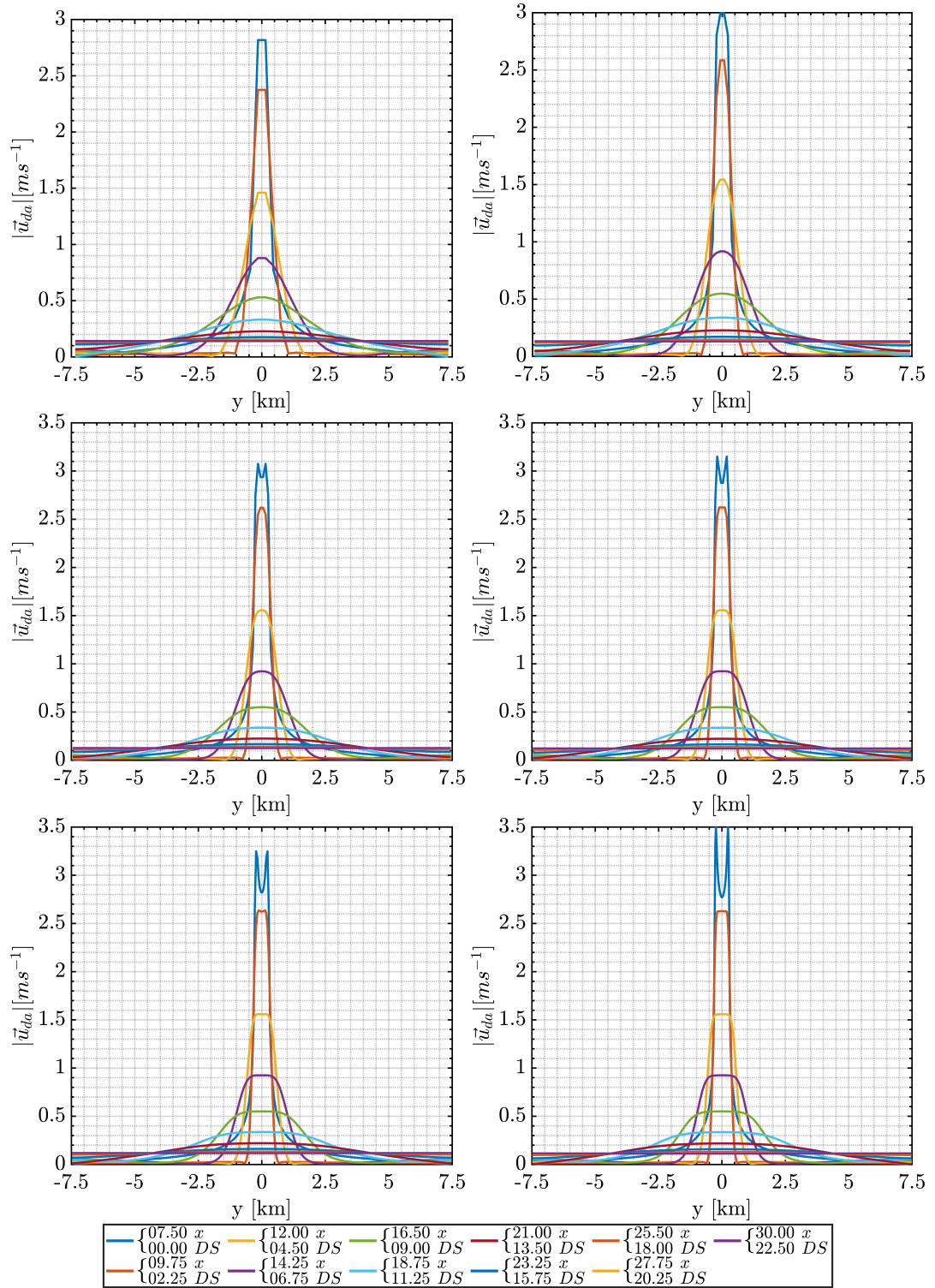
Figure 5.10: Graphs of depth averaged Velocity magnitudes taken across the domain width at set distances from the gap listed in the legend. Element lengths of 300m (top left) 150m (top right), 100m (middle left), 75m (middle right), 50m (bottom left), 25m (bottom right) with corresponding parameters presented in table 5.1.

creases of 47.8%, 49% 54.5%, 54.8% and 39.2%. Thus the GCI valve for the finer grid (CGI_{12}) can be considered relatively low with respect to the coarser grid index (CGI_{32}), indicating a significant reduction in the grid dependency. However, the

Reynolds number $CGI_{12}(Re_o)$ is 13%, down from 25% from the $CGI_{23}(Re_o)$ which is a significant error band. Whereas the remaining $CGI_{12} < 2.5\%$. However, the error bands considerably larger than what has been reported in literature as being of an acceptable range [221, 250, 109, 227] With respect to the convergence ratio (R), all cases are evaluated to be of monotonic convergence $0 < R < 1$, thus each case will have a reasonable prediction of the zero-grid spacing $h \to 0$ value.
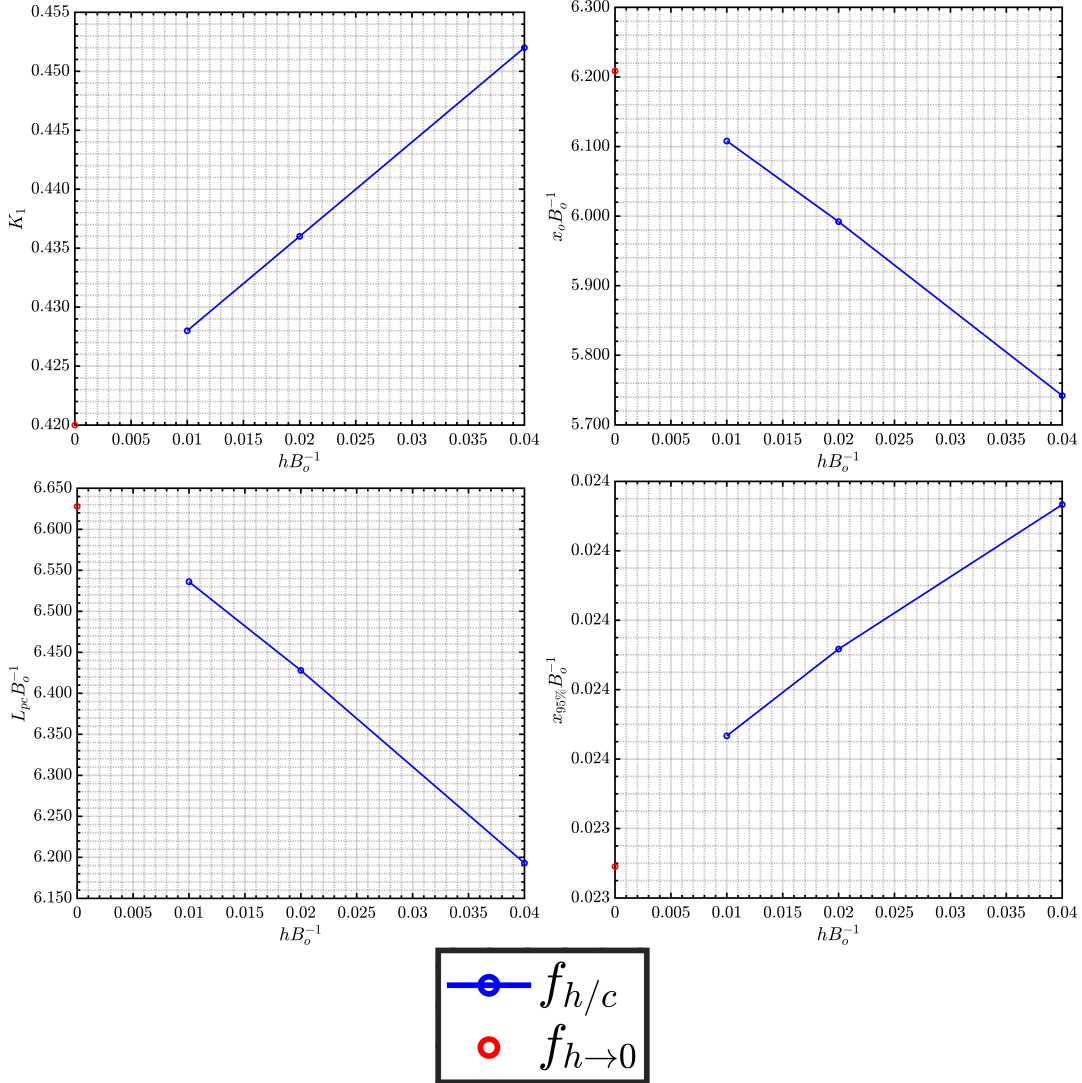
Figure 5.11: Respective spatial grid convergence graphs against the three grid resolutions (Mesh-C,E and F) normalised by the extrapolated value and the Richardson extrapolation estimate.

5.2 Conclusion

Considering the interest of this body of work is fundamentally to enhance the hydrodynamic representation of tidal range structures, we are primarily interested in the replication across the entire downstream length. Since the initial high-velocity shear flow is primarily dictated through the initial conditions, being that of the ge-

Table 5.3: The Order of accuracy and Grid Convergence Index (GCI) of Mesh-F, Mesh-E and Mesh-C.

Variable	Re_o	K_1	$\mathbf{x}_o\mathbf{B}_o^{-1}$	$\mathbf{L}_{pc}\mathbf{B}_o^{-1}$	$\mathbf{x}_{95\%}\mathbf{B}_o^{-1}$
ε_{12}	-9.20E+06	8.00E-03	-1.16E-01	-1.08E-01	2.50E-01
ε_{23}	-1.62E+07	1.60E-02	-2.50E-01	-2.35E-01	4.16E-01
R	0.57	0.50	0.46	0.46	0.60
p	0.82	1.00	1.11	1.12	0.73
$\mathbf{f}_{h=0}$	1.26E+08	0.42	6.21	6.63	23.29
$\mathbf{E}_{0\to1}[\%]$	9.55	1.90	1.62	1.39	1.62
$\mathbf{E}_{0\to2}[\%]$	16.83	3.81	3.49	3.02	2.69
$\mathbf{E}_{0\to3}[\%]$	16.83	3.81	3.49	3.02	2.69
$\mathbf{GCI}_{12}[\%]$	13.20	2.34	2.06	1.76	1.99
$\mathbf{GCI}_{23}[\%]$	25.30	4.59	4.51	3.89	3.27
$\mathbf{GCI}_{AR}[\%]$	1.0875	0.9817	1.0194	1.0168	0.9895

ometry and that of the mass and momentum fluxes, the capture of such is of primary importance [83].

Refining the mesh past 75m is not a pragmatic choice, as the additional computation time weighs heavily against any presumed increase in accuracy that corresponds with a further refined mesh, especially considering the assumptions made in the MS analysis. The analysis was completed with grid sizes of 300m, 150m, 100m, 75m, 50m and 25m. Only two cells span the 600m gap in the thin wall dam for the 300m cell size model; making realistic simulation of the flow through the gap impossible as the general rule is to have three cells across a gap for fluid flow representation.

the replication of geometry as thin-wall dams can lead to improper replication relatable to that of a sharp edge orifice With grid sizes below 25m, computational time becomes increasingly costly and unworkable. Additionally, large hard-disk memory space is required for very large file sizes.

5.2.1 Further Development

The second stage had hydraulic structures represented by the Porous plate functions build into Delft3D-flow. Further work could entail possible derivations of the orifice equations or source terms from TLP data to produce more realistic representations that are currently available. Additional turbulence terms can be added after the preliminary stages.

Further work will entail a replication of the SLTH submitted to PIN Figure 21, where characteristics of the designs will be used as the base for the simulation in both the SWE and CFD future models. With access the current blueprints in the public domain, and council from TLP, continuation with current model used in the MS analysis is not required. A further two MS-style studies will be conducted. Firstly, the TH will be represented using time based, discharge functions that are available in the delft code. TLP will supply adjusted discharge data from the source company for IP related reasons. Secondly, the initial SWE-CFD coupling attempt will be carried out within a simplified model design, before being nested into a large coastal

model. All previous MS models had a uniform bathymetry. A further modification could be the implementation of a sloped bathymetry and scour pad around the TH. Additionally turbulence terms need to be investigated and implemented in to the model.

Part III

Generalised Actuator Disk
Development Model

Chapter 6

Introduction

6.1 Raison d'Être

Ocean tidal currents harbour enormous amounts of kinetic energy and are becoming increasingly recognised as a potential energy resource to be exploited for renewable electrical generation. Fundamentally akin to wind energy, though disparate in operational fluid medium. Tidal energy possesses an intrinsic advantage of a significantly higher energy density than its wind energy cousin, routed in water bearing a density greater than air by a factor of approximately 800. Coupled with an additional advantage of being highly predictable; addressing the common criticism of other renewable options. National electrical grids can effectively plan for daily operations with surety baseline supply systems. As such, tidal energy has the potential to be a mainstay component in future electrical energy supply.

Tidal stream energy generation has developed over the past two decades to where pre-commercial turbine prototypes are now commonplace [155, 7].

Commercial success of such projects over the subsequent decades will be dependant on the effective cost when employing tidal-stream turbines *in-situ*. Essentially, how the industry maximises and sustains asset performance in its given operational environments, while minimizing capital and maintenance costs.

A considerable number of barriers to the developmental progression revolve around operating lifespan in the relatively harsh marine environment, being:

- Corrosion

- High loading related structural fatigue

- Cavitation

- Maintenance

Each of which fundamentally requires substantial prototype testing while *in-situ* or in closely-replicated environments, to form a complete qualitative assessment of device performance. Not only to be a functioning component of the future electrical supply system, but to increase shareholder surety of financial return, which in turn paves the way for large scale device deployment.

Additionally, there is a lack of a complete comprehensive understanding of how the various operational conditions will affect a devices generational performance. The impact that various Reynolds numbers and Turbulence Intensities have on foil

performance and structural fatigue is noted to be a developing sphere of high-impact research. Turbulent flow, incident onto a foil, by nature, will exert uneven pressure temporally and spatially across a surface - which has been shown to have a considerable negative influence on the rate structural fatigue and that of operational performance [155, 93, 164, 30, 29]. A facet that is compounded when multiple devices are deployed in arrays for greater capture of a tidal stream resource in a particular locale. This in turn contributes a myriad of questions ranging from those relating to environmental impacts to optimal array performance.

For instance, the kinetic energy extracted from the flow will lead to a downstream velocity deficit. The available power is related to the velocity by the following expression:

$$P = \frac{1}{2}\rho C_p A u^3 \tag{6.1}$$

Where ρ is fluid density, A is the turbine cross-sectional area and V is the fluid velocity.

C_P is the power coefficient which takes into account Betz' law - which effectively limits the maximum power coefficient to $C_{P,max} = 0.593$ in a similar manner as the Carnot cycle efficiency. The limit is imposed since to data there has been no turbine design that has been capable of exceeding said limit. The reason is simply down to the principles of conservation of mass and momentum. With respect to fluid flow passing through a respective turbines swept area, the turbine blades will extract some of the kinetic energy within the airflow, thus reducing the downstream flow velocity. For a fluid of constant density, the cross-sectional area varies inversely with velocity. So should a constant control volume, bounded within a stream tube which must pass through the swept-area be assumed. The airflow through the turbine must distribute to a wider area downstream for the mass flow rate to remain constant and continuity to be preserved.

The presence of the turbine causes a blockage effect on the approaching incident airstreams leading to a flow to isentropically convert some of it's kinetic energy into static pressure. The higher pressure consequently causes a gradual upstream reduction in velocity to become below that of the surrounding free-stream. Thus for a constant mass flow through the swept area, the stream tube must initially exist upstream with a smaller cross section than that of the swept area - which then expands with reducing velocity. The presence of the two aforementioned hydrodynamic reactions effectively creates a gradual increase in the cross-sectional area.

Through the swept area, the velocity drop coincides with a stepped pressure drop. Thus, downstream the flow exists at a reduced velocity and pressure in a wake flow regime. Downstream, the below atmospheric static pressure increases towards that of atmospheric to achieve equilibrium. Flow velocity must then further decrease to maintain continuity. The resultant far-field conditions are that of equatable upstream and downstream pressures, though a reduction of kinetic energy proportional to that extracted by the turbines.

To gauge how the mechanisms described above universally pertain to all HAT, we take the case of a theoretical ideal HAT. So consider the turbine and the swept area as a theoretical actuator disk equivalent to an infinite number of blades. Additionally for simplification purposes hold assumptions that there is a constant homogeneous steady-state flow in the absence of any frictional and viscous forces. The force acting on the disk is equatable to equation 6.2 applying the law of conservation of 1D linear

momentum.

$$F_t = \dot{m}(\vec{u}_\infty - \vec{u}_{x\to\infty}) \tag{6.2}$$

simultaneously taking net forces either side of the actuator disk:

$$F_t = A(P_1 - P_2) \tag{6.3}$$

Using Bernoulli's formula for both upstream and downstream lengths, the pressures either side of the actuator disk can be substituted for:

$$F_t = \frac{1}{2}\rho A(\vec{u}_\infty^2 - \vec{u}_{x\to\infty}^2) \tag{6.4}$$

Equating equation 6.2 and 6.4 and recognising that $\dot{m} = \rho A \vec{u}_1$:

$$\vec{u}_1 = \frac{1}{2}(\vec{u}_\infty - \vec{u}_{x\to\infty}) \tag{6.5}$$

It can thus be seen that the flow velocity just past the disk is the average of the upstream and downstream flow velocities. A axial induction factor (a) is used to account for the velocity variation across the actuator disk.

$$\vec{u}_1 = \vec{u}_\infty(1 - a) \tag{6.6}$$

thus

$$\vec{u}_{x\to\infty} = \vec{u}_\infty(1 - 2a) \tag{6.7}$$

Which implies that half the axial velocity loss takes place upstream of the actuator disk.

The power taken out of the flow is the product of the thrust force and the velocity at the disk. If equations 6.6 and 6.7 were then to be substituted in

$$P = \frac{1}{2}A\rho\vec{u}^3 4a(1 - a)^2 \tag{6.8}$$

The power coefficient :

$$C_P = \frac{P}{\frac{1}{2}A\rho\vec{u}^3} = \frac{Rotor\ power}{Power\ in\ the\ wind} \tag{6.9}$$

$$C_P = 4a(1 - a)^2 \tag{6.10}$$

With the maximum C_P being the derivative of the power coefficient with respect to the induction factor equation 6.11:

$$\frac{dC_P}{da} = 4(1 - a)(1 - 3a) = 0 \tag{6.11}$$

the induction factor $a = \frac{1}{3}$. Hence we have:

168

$$C_{P,max} = \frac{16}{27} = 0.5926 \qquad (6.12)$$

which is know as the Lanchester-Betz limit [35, 36, 148].

It can thus clearly be stated that the downstream velocity deficit will negatively impact the performance of successive downstream turbines. Reducing the total potential power that would be generated if each turbine would otherwise be operating in isolation. The degree of which each turbine is affected is less easily predicted when taking into account the hydrodynamic reaction from the turbine blades and hub, which will induce complex turbulent wake flow features, alongside local accelerations induced through blockage effects [188, 196, 79]. Effectively, array implementation will inevitably lead to changes from the initial flow regime, with successive downstream devices operating in altered and increasingly complex flow field that cannot easily be predicted. Thus, it is difficult to estimate the overall performance of a project, adapt designs and optimise array positioning to maximise performance and increase the overall array efficiency.

As discussed in Section 2.1.1, computational methods in research and engineering application, has the potential for system investigative capabilities beyond that of conventional methods, while operating at a fraction of the cost and time. Prototype deployment can provide a solid baseline for model validation purposes, where the systems within the model domain can then be systematically altered for alternative situations. Simulating, an actual prototype turbine in *in situ*, albeit operating in an array formation is a case in point.

A caveat of numerical methods, is the inherent limitation to available computational power. Model's of complex systems are often be described as 'computationally-intensive', when simulation time periods are substantial enough to be approaching feasible limits. Though, with respect to both situational access and current technological limitations, what is considered "computationally-intensive" is relative. Often, model systems are selectively simplified to reduce complexity and subsequently simulation times, albeit still achieve effective developmental insight.

Computational power will increase in time with technological development, as will computational benchmarks. What is currently considered as 'intensive' will become less so, and what is now deemed unfeasible will become possible. However, consideration into model simplifications will in all likelihood become an ever-present aspect in developmental computational research.

Currently, typical CFD approaches with fully resolved turbine geometry are considered extremely computationally expensive. A situation that is exasperated when considering the necessity for modelling turbines in arrays, which renders much needed research next to unfeasible for any party without access to HPC resources.

Thus, computationally efficient approaches are necessitated, if computational methods are to play an active role alongside the $in-situ$ prototype testing.

CFD approaches for modelling the dynamics between the flow field and the rotating fully resolved geometry of turbine blades, which both impart reactionary forces upon each other, are restricted to either of two methods.

The Sliding-Mesh (SM), schematically depicted in Figure **??** approach separates the domain between the rotational zone, which encompass the turbine rotor geometry and the outlying stationary zone, with a non-conformal interface between the two zones.

(a) SM   **(b)** MRF
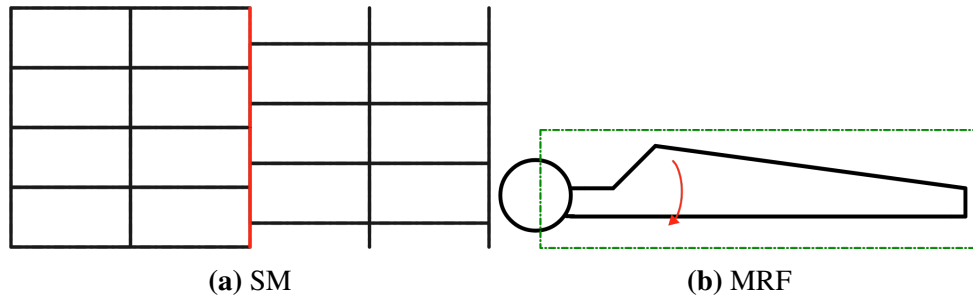
Figure 6.1: Schematic of SM (a) and the MRF (b) mesh concepts. The SM features a non-conformal interface separating the two zones. The MRF features a frame containing the blade that rotates with the blade.

For such application, the incompressible unsteady Navier-Stokes equation shown in 2.57 are solved after a minute incremental rotation of each sub-grid on the onset of each time-step. Considering the simulation is often initiated in the absence of a good initial condition, the simulation has to be ran for a significant simulation time period over several rotor rotations, until a state of convergence can be reached. Compounded with the number of minute time-steps required for each rotation and the solving of the unsteady Navier-Stokes equations, the SM method has a notable computational-intensive markup. Another issue that typically arises, is at the interface between the rotating sub-grid and the main-grid, where the two meshes are not conformal with each other. Thus, CFD software often has to incorporate additional interpolation algorithms to account for the interface discontinuity which can increase the instability within the model.

The other method is the Moving Reference Frame (MRF), which in contrast to the sliding mesh approach, has a stationary mesh. The principle is to consider a reference frame around each rotor attributed with a rotational velocity with respect to the outlying stationary frame. The velocity within the frame is solved using the moving reference frame equations. The resultant flow field is equivalent to the rotor having been frozen in time, with respect to a particular position. Hence why the approach is sometimes refereed to as the "frozen rotor approach".

The stationary mesh allows for a steady-state solution, which is considerably less computationally-intensive that the transient SM approach. If full consideration of the temporal flow field is required, multiple cases of the MRF approach with varying rotor position could be used as substitute, since the computation clock-time by an order of magnitude lower than the SM approach [162]. The MRF approach can provide a computationally efficient initial condition flow-field for the transient SM - effectively reducing the computational-intensity if the SM approach was used singularly. There are reported difficulties with the MRF approach with it being reported that there are pressure discontinuities at the interface [152].

More computationally-efficient approaches do away with simulating the geometry of the blade for a representative source term approaches using actuator disk, actuator lines or blade element disk approaches.

The least computationally heavy is the Blade Element Momentum Theory (BEMT), which is an analytical method that uses recorded aerofoil data such as the lift and drag coefficient profiles to assess turbine performance. The method by itself is a combination of the Blade Element (BE) and Momentum Theory (MT), where knowl-

edge of both is widely dispersed and often taught in engineering degree syllabus'. A full description can be found in [35, 36]. BEMT based codes have been widely used within the wind energy industry and readily found to be in good agreement with measured data, though can situationally lack accuracy [229, 66, 67]. On the back of such success, code tailored for tidal turbine applications has been developed and validated [151, 44, 182].

BEMT is often coupled with CFD approaches, since as a stand-alone, BEMT is not conducive to turbine array simulation. The inability to capture viscous and compressible physics renders BEMT unable to accurately model complex 3D wake flow features. Thus, limiting the capacity to model the entire downstream flow-field and in applications involving turbine array and environmental interactions [151].

I.Masters et al [152], reviewed and compared results from several in-house models of Horizontal Axis Tidal Turbines (HATT) at different spatial scales to demonstrate the similarities between Blade Element Momentum – Computational Fluid Dynamics (BEM-CFD), Blade-Resolved Geometry CFD (BRG-CFD) and BEMT approaches.

Comparisons between computational time proved that the simplified BEMT model could produce results from a TSR sweep within minutes using a standard desktop. In comparison, the BEM-CFD model would take around 5 days when running on a 32-core cluster.

Validation experiments showed that the BEMT, BEM-CFD and BRG-CFD were capable of producing repeatable results of reasonable accuracy to laboratory conditions flows. BEM-CFD was shown to capture the wake dynamics when compared to the experimental and BRG-CFD results. Direct comparisons between BEMT and BEM-CFD showed a reasonable similarity with peak Coefficient of Power (C_p) differing by 5.4%. However, realistic flow representation has a high uncertainty directly linked to the physical geometry and characterisation of the boundary conditions.

The Generalised Actuator disk (GAD) method introduced in [71] by Edmunds *etal*, is a direct successor to the BEM-CFD model presented in [151]. Seeking to address the limitations of its predecessor, significant improvements have been made to the prediction of power and thrust across a wide range of rotor operational conditions and to the accuracy of the downstream wake characterisation. As with the BEM-CFD model, the GAD system replicates the turbine through source term representation of the rotor. With additional modifications to the distribution of the downwash, which corrects losses along the foil. Ability to incorporate variable foil cross-sections along blade length. The capacity to account for dynamic changes to the systems Reynolds number and corrections for the tip radius. The accuracy of outputted results relies on correct lift and drag coefficient data to be implemented. Currently, there is no wide-ranging coefficient data for many foils, which comprehensively maps the coefficient change with varying free-stream turbulence and Reynolds numbers. Without consideration of which, the GAD system cannot account for the changes to the stall characteristics and those of the post-stall. Thus, currently the GAD method is limited in potential application capacity.

In summary, for competitive commercial success to be achieved, the industry requires a greater mapping of just how tidal-stream turbines will perform when operating *in situ*. To achieve this in sufficient time with minimal costs, computational methods become an increasingly attractive tool for developers to utilise. Developing further versatility within numerical modelling can allow developers the ability

to optimise simulations with respect to length scales and accuracy, without incurring unfeasible computational costs.

6.2 Generalised Actuator Disk Development

The GAD-CFD model is being developed through collaborative efforts between the Marine Energy Research Group (MERG) based at Swansea University, and the Mechanical Engineering & Mechanics department at Lehigh University, USA, and the South-east National Marine Renewable Energy Center, USA [71].

The coefficients will then be applied to the following Navier-Stokes equations representing the disk rotor characteristics through the inclusion of an additional source term (S_i):

$$\nabla \cdot (\rho \vec{u}) = 0 \tag{6.13}$$

$$\nabla \cdot (\rho \vec{u} u_i) = -\frac{\delta p}{\delta x_i} + \nabla \cdot ([\mu_l + \mu_t] \nabla [\rho u_i]) + S_i \tag{6.14}$$

Where ρ is the density, $\vec{u}$ is the water velocity vector, u_i is the ith component of the velocity vector, μ_l and μ_t are the laminar and turbulent dynamic viscosities respectfully. A complete breakdown of the governing equations of the GAD-CFD model is presented in [71].

6.2.1 GAD Implementation

The GAD-CFD approach works through designating each cell in a specified disk/blade sweep box with a local flow velocity. Thus, features like boundary layer shear flows can be accounted for within the model. Blade specific design features such as the chord and twist are also definable characteristics, which can additionally be set with respect to radial variation.

The GAD-CFD model works through an additional source term to the Navier-Stokes equations for mass and momentum, which acts as a representative of the disk rotor.

The GAD system is used in conjunction with the $\kappa - \varepsilon$ RNG turbulence model, which has been shown to be capable of producing results with high similarity to experimental data [71].

The hydrofoil properties are determined at incremental points along the radial length. Then they are averaged over 2π radians. At each incremental point along the radial expanse, the lift force vector is set perpendicular to the effective flow direction, which drag being perpendicular to lift, is thus set in parallel albeit opposite direction. A schematic that shows a discretization of the physics involved. The lift and drag forces are linked to the respective lift and drag coefficients through the following relationships:

$$F_L = 0.5\rho |u_R|^2 c C_L \tag{6.15}$$

$$F_D = 0.5\rho |u_R|^2 c C_D \tag{6.16}$$
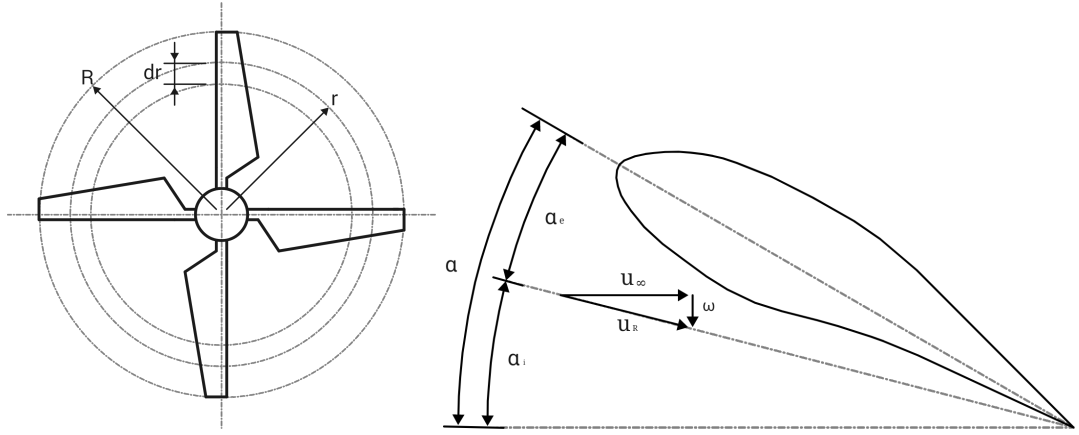
Figure 6.2: Schematic of foil component discretization.
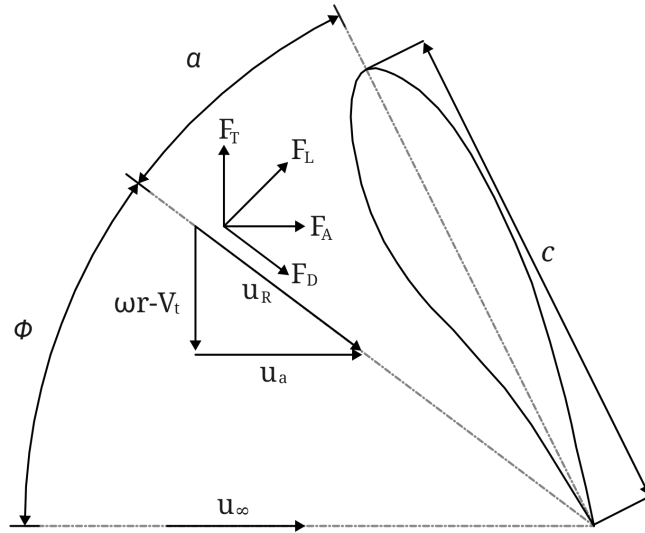
Figure 6.3: Schematic of foil component discretization.

where F_L and F_D are the lift and drag forces, ρ is the fluid density, u_R is the resultant velocity, c is chord length, and C_L, C_D being the being the lift and drag coefficients.

The fluid flow acts upon each element through axial (F_A) and tangential forces (F_T). As shown in equations 6.16 and 6.15, the lift and drag forces are dependant on their respective coefficients as functions of the Reynolds number and the effective angle of attack.

The axial and tangential forces acting on the foil section are defined as:

$$F_A = F_L sin\phi + F_D cos\phi \tag{6.17}$$

$$F_T = F_L cos\phi + F_D sin\phi \tag{6.18}$$

ϕ is representative of the flow inclination angle, which can be defined though:

$$\phi = tan^{-1}((\omega r - u_t)/u_a) \tag{6.19}$$

Where u_t and u_a are the respective tangential and axial velocities, and ω is angu-

lar velocity.

Thus, the source term can be defined through substituting equations 6.16 and 6.15 into equation 6.17. When taking into account the variation across the radial length, the equation becomes as follows:

$$S_a = dF_A = 0.5\rho|u_R|^2 c(C_L sin\phi + C_D cos\phi)dr \tag{6.20}$$

$$S_t = dF_T = 0.5\rho|u_R|^2 c(C_L cos\phi + C_D sin\phi)dr \tag{6.21}$$

where:

$$|u_R|^2 = u_a^2 + (\omega r - u_t)^2 \tag{6.22}$$

An extended downwash distribution method

The GAD system is adapted to better account for the effect of tip losses on the flow field through introducing an additional source term which represents the tip vortex induced downwash velocity ω, which acts to represent the downwash induced from the tip vortex. The force vector from the downwash is proportional to the S_a and S_t forces, with a distribution function E(r). Thus, a weighted response can be calculated, where: E(r) $\in [0, ..., 1]$ will return a value between one and zero for a given radius between the root and the tip respectively. The resultant force can thus be determined by:

$$S_u = dF_u = 0.5\rho|\omega|^2 cdr \tag{6.23}$$

Where dF_u represents an additional force vector to achieve representative flow deflection. Thus correcting the ω at the trailing edge.

The elliptical downwash distribution is described by M.Edmunds *et al* [72]. The method was deemed as reasonable approximation for a tapered wing. The method is however made redundant if the wing section is comprised of various aerofoil cross-sections, as shown in Figure 6.6, which is common place in commercial applications. Therefore an adapted distribution method must be developed so that a computationally cost effective solution can be found.

Thus, the Generalised Actuator Disk (GAD) method was developed to address such shortcomings through utilisation of the geometry in the downwash distribution function with the intention of achieving a more accurate representation. The full method is described by M.Edmunds *et al* [71], while a brief description of the methodology output terms is given below.

The downwash distribution function can be combined with the predicted axial and tangential forces given in equation 6.20 and 6.21 respectfully:

$$S_u \hat{u}_{\omega i} \equiv E(r)(S_a \hat{u}_{ai} + S_t \hat{u}_{ti}) \tag{6.24}$$

thus the source term S_i included in equation 6.14:

$$S_i = S_a \hat{u}_{ai} + S_t \hat{u}_{ti} + (S_a \hat{u}_{ai} + S_t \hat{u}_{ti})E(r) \tag{6.25}$$

The above formulation is then used to determine the power and thrust through
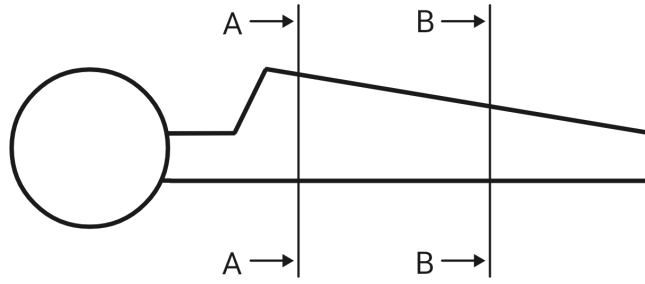
Figure 6.4: Schematic of turbine blade section discretization along the radial length.
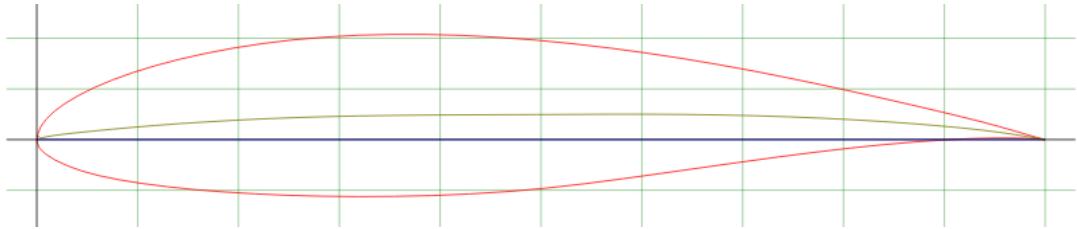
Figure 6.5: Example of Section A - A root foil profile - SG6040
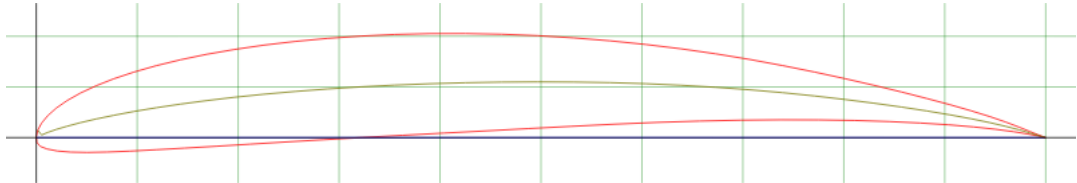
Figure 6.6: Example of Section B - A mid-span foil profile - SG6043

equations 6.26 and 6.27 respectfully.

$$Thrust = \sum_{i=0}^{n} S_a \hat{u}_{ai} Vol_i \rho \tag{6.26}$$

$$Power = \sum_{i=0}^{n} S_t \hat{u}_{ai} Vol_i \rho r \omega \tag{6.27}$$

Thus, the source term can be described as a three tuple in Cartesian space representing the change in kinetic energy per unit volume, with the scalar terms S_a, S_t and S_u representing the magnitudes in the axial and tangential directions and the additional downwash force. $\hat{u}_a$ and $\hat{u}_t$ are the respective axial, tangential and unit vectors, which define a plane that $\hat{u}_\omega$, the unit vector normal to $\alpha F_L = 0$ resides on.

Chapter 7

2D SG6043 Performance Parameterisation

7.1 Introduction

This chapter covers research into the performance parametrisation of the SG6043 foil profile operating under 2D flow conditions. The fundamental aim is to develop a comprehensive mapping of independent lift and drag coefficient profiles for various flow conditions attributed to variations of:

- Reynolds number
- Turbulence Intensity
- Surface roughness

The product of which can then be incorporated into the computationally efficient GAD model - addressing some of the possible improvements listed in [71]. With consideration to the scope of this thesis, the capacity to comprehensively map coefficient profiles is limited. However, select testing of variables can render optimal workload analysis to assess the impact distributions. The Taguchi method, also referred to as the Design of Experiments coupled with Analysis of Variances, is a time-efficient manner to determine the weighting of variables under experimental consideration so that the resultant experimental data can yield valid and objective conclusions [186]. With increasing consideration towards resource allocation in engineering applications, the Taguchi method is receiving resultant attention and expanded from initial manufacturing optimising applications to become widely utilised [147]. With success in related instances including; Hu and Rao [114] with maximising HATT performance, Chen et al [47] and Wang *et al* [259] with optimising Vertical Axis Wind Turbine (VAWT) performance. The range of parameters should typically be between the extremum of measured data collected *in situ*. Coincidentally, since the success of a tidal stream deployment being directly linked to the operational conditions - to which the design can be tailored towards for optimum performance and reliability. The locational characterisation that the prototypes will be operating under is also of paramount importance. Several studies [235, 161, 137] have hence been undertaken to map out regional tidal flow characteristics over extended

176

periods of time. The work focuses on the cyclical mean flow and turbulence intensity which collectively is grouped as the Free Stream Turbulence (FST). Lawrence *et al*'s [137] collected data across studies produced in the Uk and the US, show a prevailing levels of turbulence intensity over the tidal cycles. The turbulence intensity was shown to be around 12-13%, with "slight" variations, when taken from the direction of the bulk flow on both the flood and ebb tides. Slightly lower turbulence intensity values were recorded at 9-10% and 7-8% for the transverse and vertical directions respectfully. J. Thomson *et al* [235] similarly recorded Ti at 10% relative to rotor hub heights. Though recorded Ti of approximately 1% to 20%. Additionally noting that large scale anisotropic eddies dominated the Turbulent Kinetic Energy (TKE) spectra, and suggesting that proximity to headlands becoming a considerable determinant when present. Consideration to possible data bias towards current favourable prospective locations must also be noted. Should mainstream success become realised, locations with less favourable conditions will likely become potential considerations for further development. For such cases, it would be prudent to consider wider margins of expected flow conditions.

Another consideration when setting out the experimental design, is the requirement of passing the simulated data through validation evaluation processes to be considered reliable. Thus, simulated parameters must align with those of the intended validation experiment. Should results not show acceptable agreement, simulations of wider parameters that preceded the validation assessment would effectively be a summation of wasted computational resource.

With respect to this thesis, a prior arrangement with Lehigh University was made to provide flume experimental data for validation purposes. A complete experimental description and discussion of data is presented in Section 7.1.2. As a result of the order of acquirement, the simulated parameters within this section are mirrored from those of Lehigh University. Additionally, the foil cross-section was also pre-determined.

With respect to CFD modelling, to achieve independent lift and drag coefficient characterisation without additional interference, the archetypical modelling approach would be to set domain boundaries beyond the range of which interaction with the model geometry is possible. However, since the provided validation data is a product of a laboratory water flume, boundary independent CFD simulation cannot be justifiably validated against a flume experiment; not without addressing questions surrounding the typical blockage effects and boundary layer flow that will undoubtedly be present. Thus, to achieve the project aims, an experimental roadmap revolving around three successive sections is was required:

1. a 2D Flume-Flow parametrisation of the SG6043 foil is required to provide a solid grounding against experimental data. The geometry of which will be directly equatable to that present within the Lehigh flume experiment. Additionally, confidence in the within the simulated results can be demonstrated with an mesh dependence study.

2. Simulated results can then be directly compared to the flume experiment results and provide valid basis for the model.

3. The flume wall boundaries can be removed to attain boundary independent performance data for the SG6043 foil; to be used within the GAD simulation.

7.1.1   Surface Roughness Dependence

Surface Roughness refers to quantifying surfaces textures through measuring comparative surface deviations. In engineering, the concept of roughness is relative to the length scales in question. When comparable, surface roughness can have a considerable impact on how the surface will react with its environment; such as wear rates, friction coefficients and adhesion performance. Detection of surface irregularities can also provide valuable indications into the material performance as a mechanical component. A non-uniform structure under loading will develop stress concentrations which then may lead to fatigue nucleation sites.

Initially, an objects surface roughness is often determined during the manufacturing process, though this aspect will likely be reduced from the finishing processes, where the surface will likely undergo a polishing sequence. The smoothing capacity of which is dependant on material properties and the machining resources available during manufacture. For a given material, continually reducing the surface roughness will be an increasingly resource intensive process. Thus, coincidently increasingly monetarily expensive. This creates a optimum trade-off scenario; balancing the manufacturing process expenses against the performance requirements when in operation.

An objects surface roughness can also be altered, and likely to a greater significance than machining, when under operational conditions. With respect to the research topic, this may take the form of long-term degradation from weathering effects or possible collisions with objects in the local environment. With respect to the marine environment, this could be debris related to both human waste and naturally occurring objects like drift wood. There is also a considerable chance of collision with wildlife. A short-term instance could be from salt spray or ice if the turbine has been hosted out of the water for some time prior to a return to operation.

Surface roughness has been long linked to having consequential outcomes on how well a aerofoil has performed during application. The aerospace industry is well aware of the potential outcomes of icing on a planes wings, with numerous instances being attributed [116]. A common mechanism for these occurrences is the onset of stall which would not have occurred without the icing altering the flow dynamics over the wing.

It can be thus said; the potential importance of surface roughness having an impact on the flow regime cannot be understated, especially with the prevalence of degrees of surface roughness that will likely be present during turbine operation while *in situ*.

Despite instances where there has been a direct link between surface roughness and aerofoil performance, the subject is not completely mapped out; Aspects like the process of boundary layer separation in the presence of surface roughness is not fully understood [1].

P.Giguere *et al* [96] talks about how when operating below the stall-point, leading-edge roughness is not a critical factor in aerofoil performance(further mention of Tangler and Somers, 1995; Tangler, 1997). His results indicate how aerofoil design can have a substantial influence to how the aerofoil performance is influenced by surface roughness; that sensitivity increases to the design C_L. He also reported potential benefits for the SG6043 aerofoil to have leading-edge roughness - having shown the best energy capture when present.

W. Chakroun *et al* [41] results have shown that surface roughness has a substantial effect on the drag and lift performance. He simulated the NACA 0012 aerofoil and found the influence of surface roughness to be greatest between an angle of attack of -10° and $+10^o$. His results also align with P.Giguere *et al* in that the location of the surface roughness has a considerable bearing on performance. A leading-edge roughness was shown to produce a maximum drag, where the trailing-edge showed the minimum. Additionally, surface roughness was shown to delay the stall angle and increase the lift generated while in the stall region. His results also showed that a rough surface can induce turbulent boundary layer formation where a laminar boundary layer would form if the surface was smooth.

The impact of locational roughness can be attributed to the interaction to an accelerating flow. When a rough surface is present, the boundary layer becomes thinner and the skin friction increases. Thus, a larger non-dimensional roughness element and roughness effect[1, 42]. This ties in with the accelerating flow at an aerofoil's leading edge during optimum angles of attack.

7.1.2 Validation background

As previously touched upon before, the experimental coefficient of lift C_L and coefficient of drag C_D data of the SG6043 foil was recorded in a re-circulatory water flume at Lehigh University.

The flume cross-section was measured to possess a cross-sectional dimension of 0.61mX0.61m and a length of 1.68m, and was able to generate water flow velocities between 0.03m/s and 0.94m/s, with an accuracy of $\pm 2\%$ [73].

A.Lawrence *et al* [137] for Lehigh University produced work on the FST using the same equipment and likely the same methodology that was used to generate the Lift & Drag coefficients with the SG6043 foil in the experimental flume. The FST turbulence conditions are generated through the application of an active-grid turbulence generator located at the entrance to the test section. The device has 10 rotating axels (5 arranged horizontally and vertically respectively). Six flat square plates are attached along the axel. All are equally spaced and connected to the axel so that the diagonal lines will be parallel and perpendicular to the vertical and horizontal respectfully. Each square plate fits between the adjacent and collectively they form a grid of rotating plates *in situ*. Which when the axels are rotated, will stir the water around different planes of rotation. Thus creating a governable average FST of the flow passing through the grid. The FST characterisation is determined though setting the grid rotation parameters to a specific operation. Each axel in the grid is controlled through the application of multiple, in sync stepper motors with specific electronic inputs composed through operational software (LabVIEW).

A unanimous SG6043, zero-twist blade section of constant chord length (0.0762m) - with no further stated adjustments to the SG6043 foil profile thickness or other parameters past the limitations of the manufacturing process; a Selective Laser Sintering (SLS) process of four sections, which were later mated at the cross-sectional surfaces and fastened through connecting rods of presumably steel [138]. The blade section was suspended from parallel support frame rails situated above the flume test section. The blade length was connected in series to the frame through a tri-axial load cell to measure the resultant reactionary load to the flow variables set on a active grid turbulence generator. Then with an Aluminium frame adapter which enabled α to be
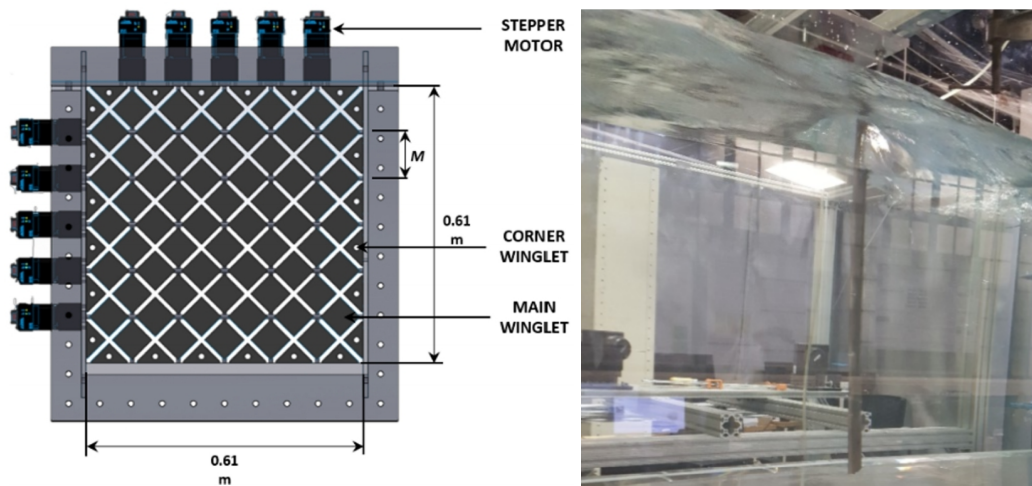
Figure 7.1: (left) Computer generated graphic of Lehigh Universities active grid turbulence generator [255, 137]. (right) SG6043 blade section immersed in Lehigh University's flume tank.

investigated across a range of -40° to -40°. The Free Stream Turbulence FST was measured through prior insertion of a Acoustic Doppler Velocimeter (ADV) device in-place of the blade.

The blade length extended through the flume tank water flow free surface to 2.667mm from the flume tanks bottom surface 7.1. The total submerged length was given as 596.9mm, which is assumed to be measured under still conditions without the distortion of the bow wave which will form on the free surface. The creation of the bow wave could be a possible feature which could have some bearing of the load measurements recorded by the 3-axis load cell. Since the experimental post-processing results are based on the foil blade being 596.9mm, it might not have been accounted for that the bow wave would effectively create a situation where water will be flowing over the foil blade at levels $\neq$ to the still water measurement. The adapter allows the foil to be rotated so that various angles of attack can be recorded, and the 3-axis load cell measures the loads acting on the foil blade. After each case scenario, the sensor was reset to reduce that chance of a miss-calibration affecting the accuracy of experimental results. It is also assumed that the foil blade is rotated about its mid-chord length so that an even distance between the walls is maintained.

Surface Roughness data was supplied by Lehigh University on the hydrofoil test subject experimented upon in the water flume. The supplied data consisted of 12 positions selected over the hydrofoil upper surface area. The precise location of the measurement sites was not provided. However, the 12 positions were systematically positioned so that surface roughness data was collected along the foil chord length; at the leading edge, mid-point and trailing edge locations. The positions were also taken along the blade length so that an equal span would be captured. The resultant surface roughness variables for the experimental flume hydrofoil, having been averaged across all 12 sites are shown in Table 7.1. Where R_a is the centre-lined average roughness, R_z is the maximum deviation from the center-line, R_q is the root mean square of the surface roughness, S_k is the skewness and K_u is the Kurtosis.

The resultant data in Table 7.1 indicate that the foil surface is relatively smooth, where there equal magnitudes of the peaks and the valleys. The peaks are calculated

Table 7.1: Summary table of the Surface Roughness parameters.

Parameter Notation	Value $[\mu m]$
R_a	23.36266
R_z	172.8892
R_q	31.20592
S_k	0.59827
K_u	3.587884

to be lepokurtic, where the peaks are averaged as slender with a longer tail. There is also a positive skew which may be a function of the blade geometry.

Review of Flume Validation Data

A continuation from the experimental background reported earlier in this section. Data was supplied from Lehigh University in two distinct batches.

The initial sets of Lift & Drag coefficient data supplied consisted of three dif-
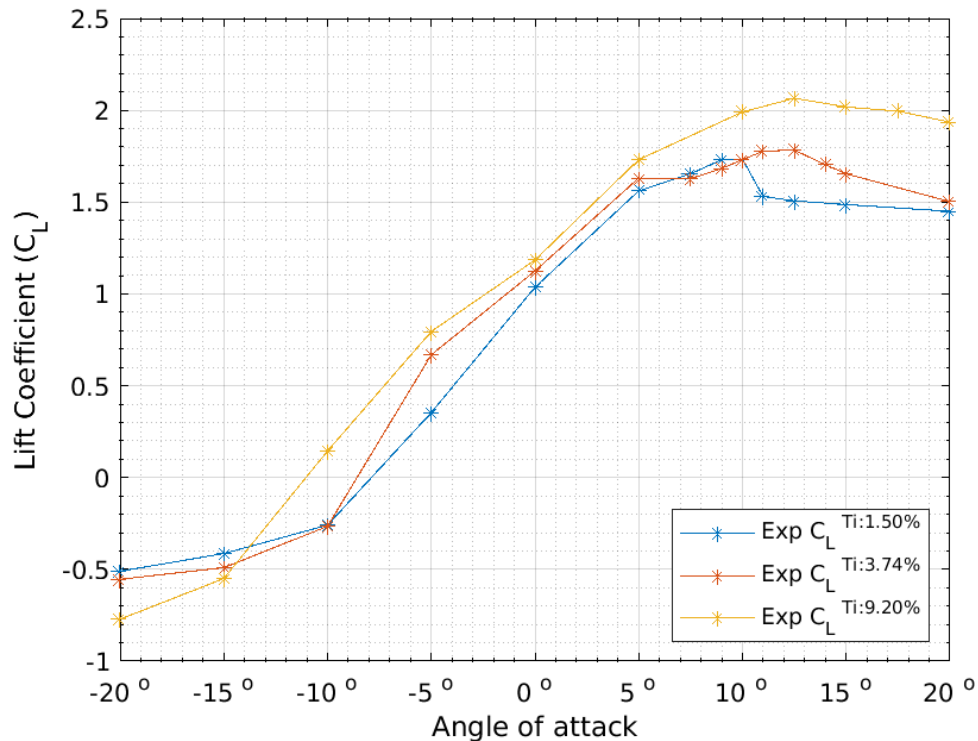
Figure 7.2: C_L plot depicting the relationship with the angle of attack and Turbulence Intensity of the flow-field, with respect to a **Reynolds Number of 6.3X10^4**. The experimental foil used for this data collection had a chord length of 0.0762m and the flume flow velocity was 0.82m/s. The tabulated experimental data can be found located in the Appendix Figures D.1,D.2&D.3.
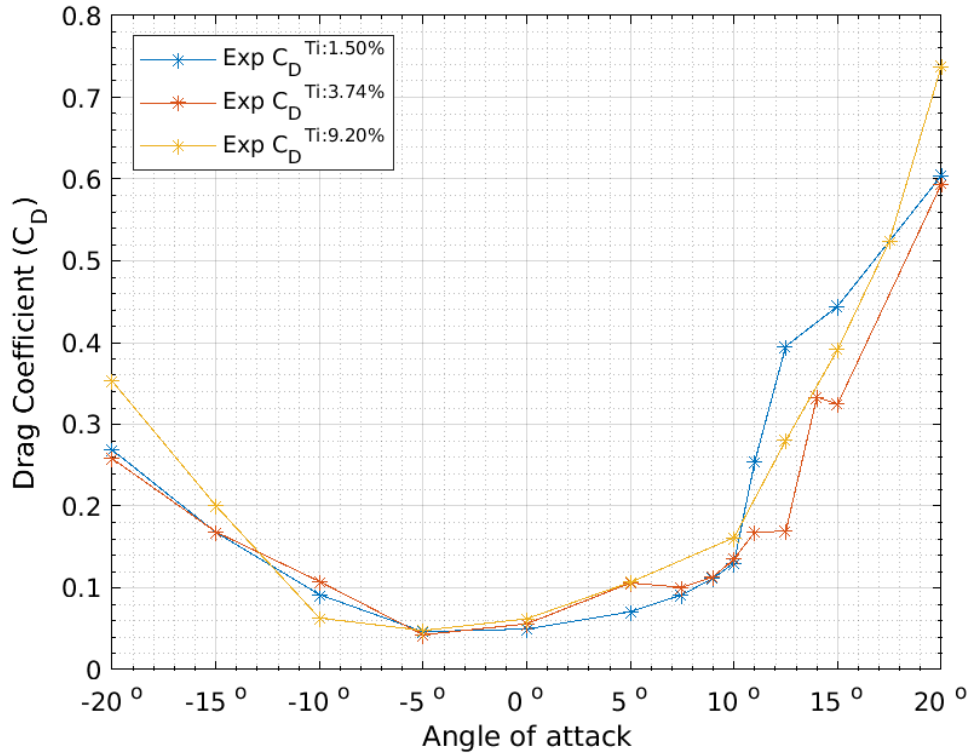
Figure 7.3: Drag Coefficient plot depicting the relationship with the angle of attack and Turbulence Intensity of the flow-field, with respect to a **Reynolds Number of 6.3X10^4**. The experimental foil used for this data collection had a chord length of 0.0762m and the flume flow velocity was 0.82m/s. The tabulated experimental data can be found located in the Appendix Figures D.1,D.2&D.3.

ferent FST conditions of 1.50%, 3.74% and 9.20% where the Reynolds Number was kept consistently at 63K - with the characteristic length taken as that of the chord length and the flow velocity as $0.82ms^{-1}$.

The resultant reactional forces on the foil blade were recorded through the tri-axis load cell, and recorded across a sweeping operational range of -40° to 40° with respect to the angle of the chord line to the prevailing flow direction.

The lift and drag coefficient dataset was supplied as presented in Appendix **??**. There are two publicly available documents presenting work that directly reports on the coefficient data provided, either in its entirety or in part. The 1.50% and 3.74% FST conditions were discussed in [137], along side an additional 7.30% series. A.Lawrence *et al* reported elevated levels of FST had a negative influence on the measured lift and thus calculated C_L, which was consistent across majority of α positions tested. Concurrently, the flow separation was observed to be delayed at equivalent α. This is starkly contrasted with the C_L data presented in Figure 7.2, where an antithetical observation can be made. The 9.20% data series popped up in A. Lawrences' thesis [138] alongside 1.5%,3.74% and 6.65% series. A general trend of increasing C_L with increasing Ti was reported. However, against the general trend, the 6.65% series was shown to have the highest recorded C_L out of the presented series. Comparing the two 7.30% and the 6.65% FST conditions from the respective [137, 138] documents, the contrasting C_L values could possibly indicate the presence
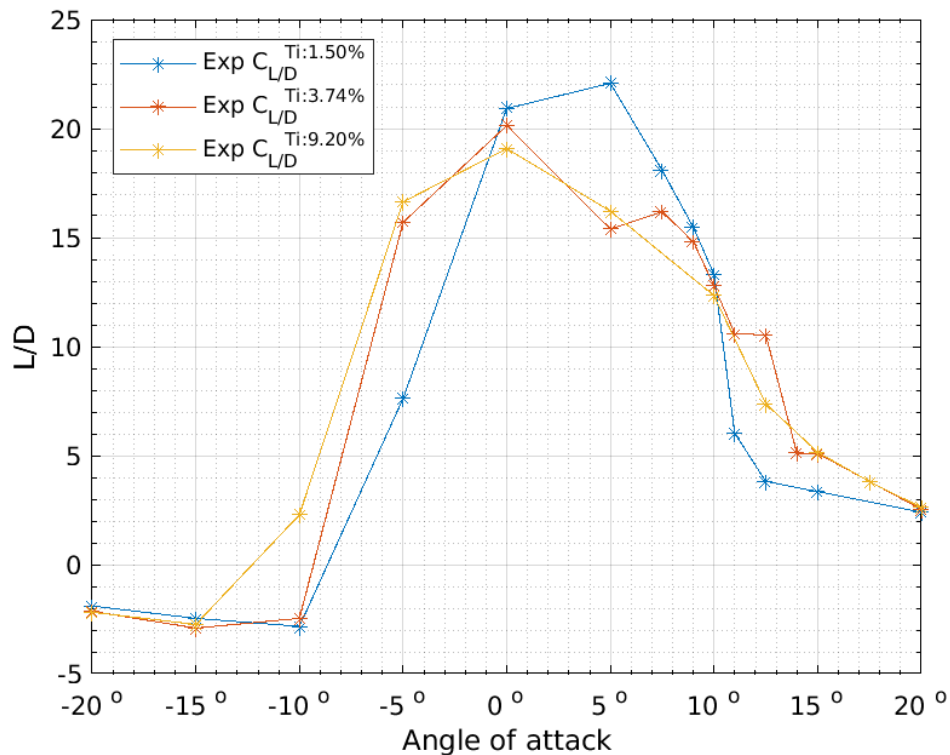
Figure 7.4: Lift/Drag Coefficient ratio plot depicting the relationship with the angle of attack and Turbulence Intensity of the flow-field, with respect to a **Reynolds Number of 6.3X10^4**. The experimental foil used for this data collection had a chord length of 0.0762m and the flume flow velocity was 0.82m/s. The tabulated experimental data can be found located in the Appendix Figures D.1,D.2&D.3.

of substantial experimental errors. The exclusion of either the 7.30% and the 6.65% data sets from those supplied for validation purposes by Lehigh University, suggest the accuracy of such were subject to question internally and removed. The absence of a cross-examination between the measured load readings and any observed flow-phenomena within the documents prevents any further attempts to understand how such measurements came about. Assuming the all cases were subject to the same experimental procedure, the lack of definitive explanation can contribute to a level of uncertainty with respect to the validity of the coefficient data set. However, the standard deviation of C_L values was presented for 1.50%, 3.74% and 7.30% in [137], with the latter being substantially higher than the former two across both stable and unstable α ranges; suggesting the problem may be only isolated to individual cases for undisclosed reasons.

Considering the coefficient data on hand; It can be seen in Figure 7.2 that the higher 9.20% T_i case produces a constant, lower C_L when the foil is operating with α less than -15°. However, after -15°, produces a constantly higher C_L value. Additionally, the higher T_i series can be seen to induce delayed-stall characteristics with both the 9.20% and 3.74% increasing the point of maximum lift from 10° to 12.5^o. However, the latter's C_L values converge with the 1.50% case around an α of 20°, while the former continually produces greater lift with respect to a non-linear relationship.

The corresponding drag coefficient series is shown in Figure 7.3. A relationship mirroring the non-linearity observed with the C_L-T_i relationship, at greater α with respect to both positive and negative angles, albeit with constant polarity in the drag case, can be observed. The 9.20% case is shown to reach a low drag state at 10° before the other series - which all converge upon an α of -5°. The data-set is too coarse, with a point separation of 5°, to depict the relationship to a greater degree. Along the α within the contemporary 'near-linear' range, the drag is increases at a greater rate with increasing T_i. Each series is shown to undergo rapid increases in drag past 10°. The 1.50% case appears to have the greatest initial increase in drag after 10°, however a direct trend is not observed with the higher 9.20% case possessing a greater gradient. Across both the lift and drag coefficient datasets the 3.74% case appears less smooth, which is particularly noticeable along the 'near-linear', pre-stall sections, which are typically subject to the most stable flow conditions. Conversely the lower 1.5% case appears the smoothest. As discussed above, the absence of additional information into the flow characteristics for each case renders the formation of a conclusion impossible. However, considering the general trend of increasing point instability with increasing T_i, the explanation may reside with the characterisation of the turbulent flow-field produced by the active grid and that of turbulent length scales. Considering the greatest instability was shown to be the 7.30% in [137], the relationship between T_i and the measured load instability cannot be linear. Since the turbulent flow-field with inevitably interact with the blade section in a non-uniform manner, could the T_i cases cause cyclic vibrations, which approach the blade sections residual frequency at 6.65%. Another angle that can be approached is if the turbulence scale is actually greater than that of the blade where, higher velocity flow misses the blade section.

The direct lift/drag coefficient ratio relationship is shown in Figure 7.4. The lower T_i, 1.50% case has the highest overall lift/drag ratio of 22.07 at an α position of 5°. Compared to the higher T_i cases of 3.74% and 9.20%, which present their respective peak lift/drag ratio of 20.13 and 19.08 respectively, at a lower α of 0°. Additionally, the 1.50% case possessed a higher lift/drag ratio of 20.12 at an α of 0° with a profile shape that could be described as more leptokurtic that the other cases. All series can be described as possessing a negatively skewed distribution. In contrast to the individual lift and drag profiles, the 3.74% and 9.20% series have a closer relationship.

The following set of supplied data consisted of lift & drag coefficient data incrementally measured over a -40° to $+40^o$ α range, with two different flow conditions parametrisations of FST and Reynolds Number; being 2.2% and 12.6% for the former and $13k, 43k, 73k, 23k and 63k$ for the latter. Higher resolution point sampling of -2.5^o for α positions between 5° and 20°, was used to capture the highly relevant sudden stall characteristics. No other instances of the experiment were divulged. Therefore it is assumed that the experimental methodology was consistent with that used to produce the prior dataset. Additionally, the absence of comparative flow-field representation limits the surety of characteristic trend diagnostics.

The C_L of each test condition is shown in Figure 7.5. In contrast to the previously received SG6043 C_L profile's as a function of α - typically being that of a single sigmoid-type curve in the pre-stall region and post-stall characterised by a T_i dependant damped trend. The expanded parametrisation with respect to both Reynolds number and T_i introduce additional non-linear characteristic features. Additionally,

there is disparities in the coefficient magnitudes and phase alignment between respective sets.

Fore example, if directly comparing flow conditions with a Reynolds number of 63k. The 1.5% and 3.74% cases have a maximum C_L of 1.73 and 1.78 at α of 10° and 12.5^o respectively; where as the 2.2% case has 1.26 at an α of 15°. The relationship between C_L magnitude and α position is not likely of a linear fashion. However, for simplification purposes, a linear interpolation between the 1.5% and 3.74% points from the initial data can approximate a expected maximum C_L of 1.75 at an α of 10.8, which is a higher than the measured by a factor of 1.38 and between $4 - 5^o$ out of phase.

Continual reduction of the Reynolds number below $63k$, with respect to measured data, wile maintaining a low $T_i = 2.2\%$ parameter, alters the negative α characteristic C_L profile. Whereas with $Re > 63K$ parameter condition, there is characteristic similarity with the higher $T_i = 12.6$ parametrisation, albeit the lower $T_i = 2.2\%$ parametrisation possesses a rougher profile and a comparatively delayed entry into the near-linear stage - the degree of which is likely exacerbated due to the coarseness of measured intervals. Additionally, there is similarity with the initial dataset trend
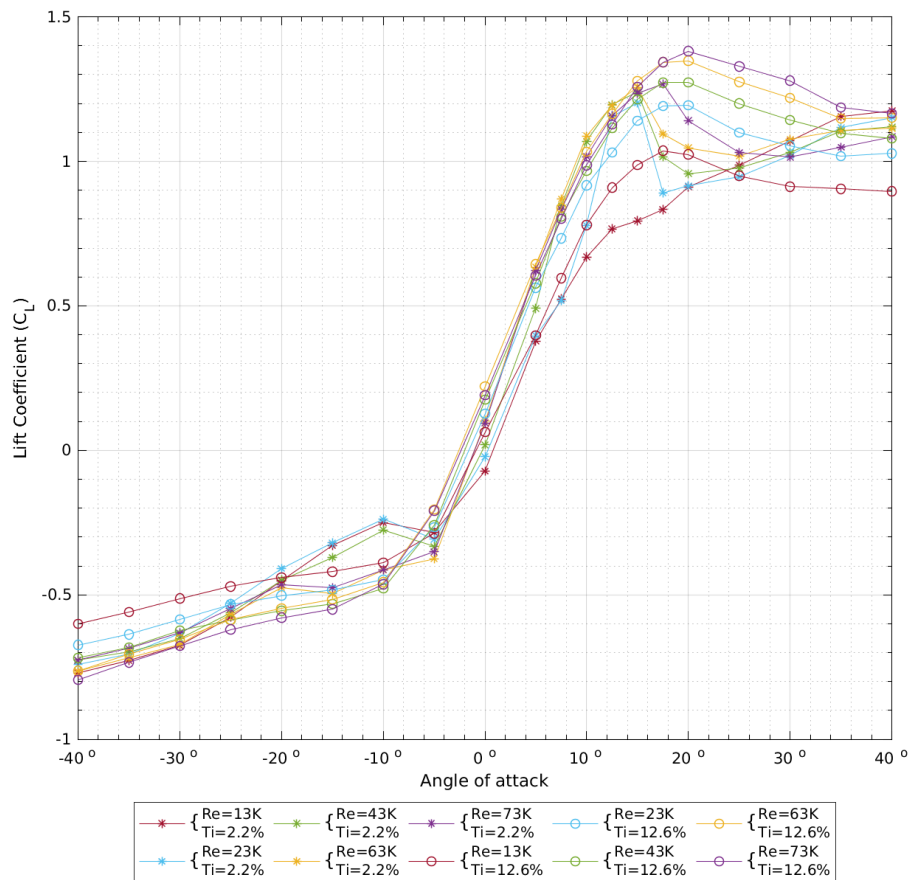
Figure 7.5: Combined C_L chart depicting the relationship with the angle of attack. The tabulated experimental data can be found located in the Appendix Figures
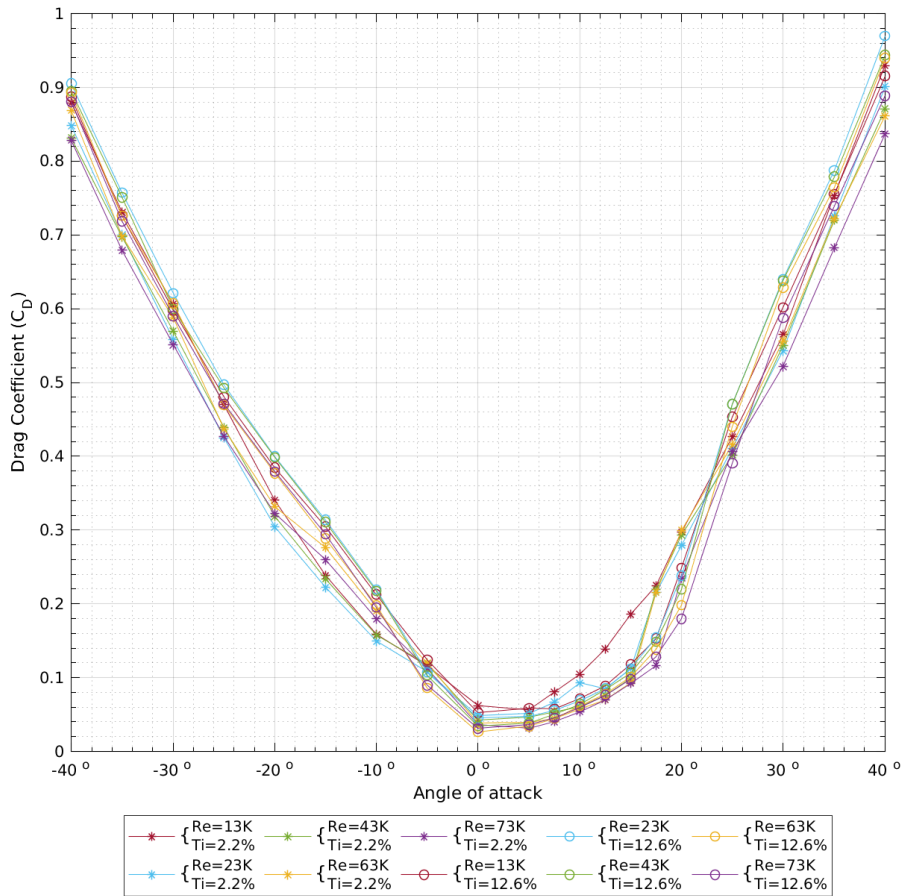
Figure 7.6: Combined Drag Coefficient chart depicting the relationship with the angle of attack. The tabulated experimental data can be found located in the Appendix Figures

where the higher T_i parameter conditions result in lower C_L values.

When flow conditions are set to $Re < 63k$ and $T_i = 2.2\%$, the respective section transitions to an S-shaped profile, with a constant local maxima at an α of -10°. However, the profile trends to characteristic convergence with the higher $Re > 63k$ series, adjacent to the inflexion point. After which, a general trend of slightly higher C_L values for higher Re is formed, though the $Re = 63k$ case stands anomalous against said trend. It should be noted that higher instabilities are common outside the near-linear region, which could cause a disruption to general trends should the effect magnitude be small. Conversely, the trend is reversed with respect to the higher $T_i = 12.6\%$, with the C_L increasing with an increasing rate as Re decreases, suggesting that FST becomes an increasingly dominant factor for low Re conditions in the negative α region. As product of both trends, a resultant point of interception between the higher and lower T_i series occurs, coincidentally at the point of inflexion - which shifts to a smaller negative α with decreasing Re.

A possible indication of an isolated fluid flow phenomenon is present with the $Re = 13k$ and $T_i = 12.6\%$ parametrisation at an α of -10° - where a delayed entry
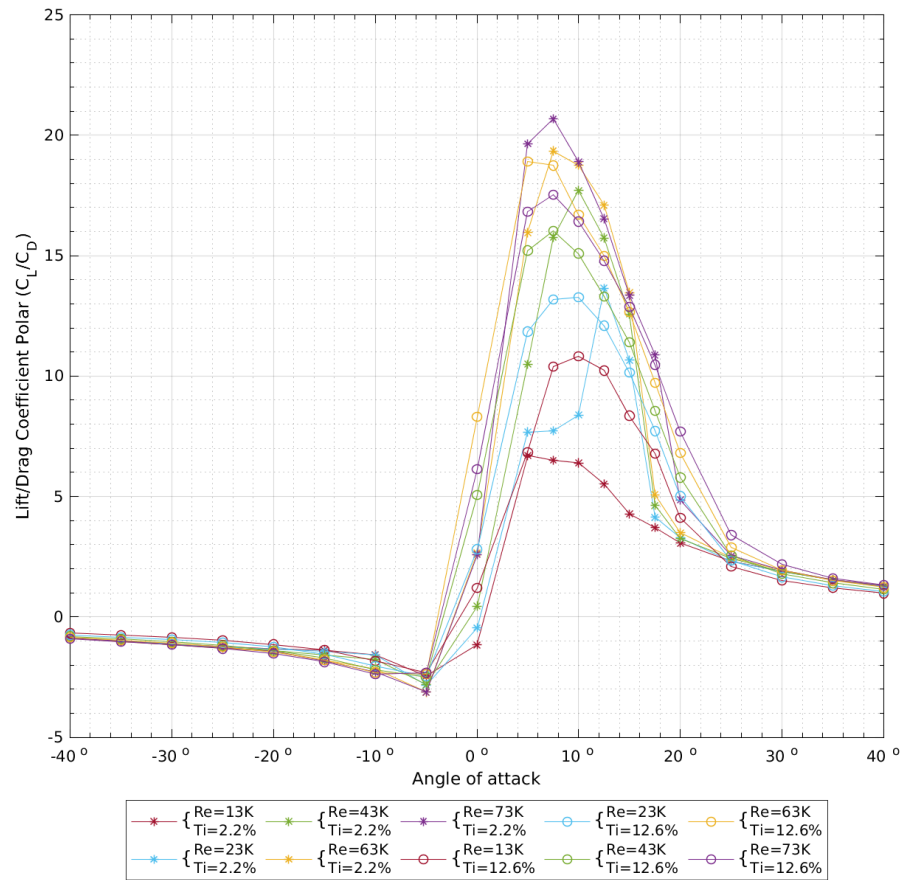
Figure 7.7: Combined Lift/Drag Coefficient chart depicting the relationship with the angle of attack. The tabulated experimental data can be found located in the Appendix Figures

into the near-linear region is present in addition to a higher comparative C_L with respect to other cases, where there is a unanimous entry into the near-linear region and close convergence at the same α.

Across the near-linear, stall-approach, stall and the post-stall region, the generally characterisation is that increasing Re and T_i parametrisation induces higher C_L values, though the $Re = 63K$ parameter is shown to be slightly above the $Re = 73k$ in all but the maximum C_L.

Increasing Re with the higher $T_i = 12.6\%$ parametrisation acts to increase the C_L at a decreasing rate; a facet not present with the lower $Ti = 2.2\%$ parameter. Additionally, entry into the stall-approach region is unanimous at an α of 10°, where the C_L begin to curve to a plateau and the point of maximum lift at 20°.

The lower $T_i = 2.2\%$ parametrisation equivalent, results in a more convoluted relationship. The transition into the stall-approach region for the higher $Re => 43$ is likewise at 10°. The point of maximum lift is 5° lower at 15°, apart from the $Re = 73k$ case where a slight comparative stall-delay is present at 17.5^o. In contrast to the general characterisation mentioned above, the near-linear region is steeper than

the higher $T_I = 12.6\%$ cases - which results in an intercept approaching the end of the near-linear region, and a small period of slightly higher C_L values. The gradient is reduced at a greater rate during the stall approach resulting in another intercept resulting in lower maximum lift.

The $Re = 13k$ and $Re = 23k$ cases displays an atypical transition characteristics. At 5° there is a slight kink, suggesting a transition from the near-linear region. However at 7.5^o, the $Re = 23k$ case again corners into a steeper gradient; until a small stall-approach plateau at 12.5^o, before maximum lift and stall point at 15°. The $Re = 13k$ case increases linearly to 12.5^o, where the gradient decreases, but the C_L continues in a near-linear manner in the absence of a stall and subsequent post-stall damped trend.

With respect to the parameters excluding the aforementioned, the post-stall region exhibits 'damped-trend' characteristics, with an contrasting relationship between the higher $T_i = 12.6\%$ and the lower $T_i = 2.2\%$ and that of increasing Re, with a behavioural analogy of an increasing over-damped and under-damped 'damping-factor' respectively - though with an attached caveat that the analogy holds to a single oscillation.

The corresponding drag coefficient profiles are shown in 7.6. A consistent trend can be observed with α between -40° to -5° and 25° to 40°, where the higher T_i consistently produces higher C_D with respect to equivalent Re. Though at an $Re = 13k$ and α less that -25° and greater than 35°, there appears to be no significant separation of data points. Additionally, there is no apparent dependence with respect to increasing Re. Although the higher $Re = 73k$ consistently results in comparatively lower C_D with angles of attack greater than $\pm20^o$. Within -5° to 20° range, there is a clearer general relationship with increasing Re and decreasing C_D. Additionally, the magnitude of Re also affects T_i dependency, with lower magnitudes inducing departing characteristics with earlier rapid C_D increase, and higher magnitudes acting in a antithetical 'buffering' manner. Otherwise, lower T_i parameters continually depict a clear and sudden 'cornered' entry into a rapid C_D increase. Whereas the higher T_i have a smoother continual gradient increase. However, at an α of 20°, coinciding with the point of maximum lift, there is a marked departure in the rate of gradient increase across the series, with decreasing Re leading to greater increases in C_D. The sudden 'corner' characteristic oof the lower T_i also directly correlates with the point of maximum lift.

The direct lift/drag coefficient ratio relationship is shown in Figure 7.7. The lower $T_i = 2.2\%$ and highest Re of $73k$ possesses the highest overall lift/drag ratio of 20.68 at an α position of 7.5^o. The lowest being 0.38 at an α of 5° - being diametrically opposed with respect for Re, albeit also the lower $T_i = 2.2\%$. The point of maximum lift/drag ratio increases in α with decreasing Re with exception to that of the $Re = 23k$ and $T_i = 2.2\%$ which corresponds to the a-typicality of both the C_L and C_D curves. The typical profile shape becomes more leptokurtic-shaped on increasing Re and conversely platykurtic-shaped when decreasing. However, the $Re = 23k$ and $T_i = 2.2\%$ condition stands in contrast the typical bell-curve with a stepped feature before a sharp increase to a maxima. The stepped feature corresponds to the kink in both the C_L and the C_D curves between 5° and 10°.

7.2 SG6043 Foil

An Aerofoil (Airfoil in American English) is the term for the cross-sectional profile of a geometric body, such as an aeroplane wing or propeller, that interacts with the air flow to produce dynamic reactionary lift and drag forces; with the lift force vector acting in perpendicular orientation to the bulk fluid flow and the drag parallel. The origin of the term is based in the initial widespread application within the aeronautical industry, with the working fluid being air - hence the aero or air prefix. Dimensionless analysis revealed similarity in fluid flows around geometric shapes; despite differing physical properties of density and viscosity, should the flow have equivalent dimensionless Reynolds and Euler numbers (Note: certain cases require additional dimensionless analysis). Aerofoil profiles that might have initially be designed for uses with air as the working fluid medium, can be scaled to applications in other fluid mediums such as water and theoretically vice-versa – providing operation and equivalent Reynolds numbers. There are however practical limits to what can be scaled since water is approximately 1000 times denser than 1 atmospheric air and is not as compressible. This can present a nomenclature or prefix issue when discussing a 2D cross-sectional profile which can feature in either. Typically, the determination of aero or hydro prefix is given for the operational environment a certain wing or turbine blade is intended to operate within – often easily differentiated by the scale and other design characteristics. This situation is true within this body of research when discussing the SG6043 'aerofoil' profile; initially designed for wind turbine applications, but recently found additional application in marine tidal stream turbines. To avoid confusion with prefix terms, when referring to the 2D cross-sectional profile, the term 'foil' will be used. The aero or hydro prefixes will only feature when discussing 3D sections scaled to operation in the respective environment.

7.2.1 Background

The SG6043 cross-section originated as a family group of aerofoils labelled as SG604X, which were designed for smaller scale, variable-speed, horizontal-axis wind turbines (HAWT) with rated power between 1-5kw. The design objective for this particular foil curve group was to achieve a high lift-to-drag ratio with less design priority given to operation over a wide range of conditions [220]. Figure 7.8 compares the SG6043 and other foils of the SG604X family against other foils designed for HAWT's at a Reynolds number of 300,000.

For the particular design purpose, the SG6043 foil has the highest design C_L for any given Reynolds number with fixed transition [96]. Additionally, the lift-to-drag ratio characteristic is essentially independent of the Reynolds number [96]. Thus, a rough leading edge will likely yield superior energy capture. The high design C_L also contributes to Reynolds number being a significant factor [96]. The SG6043 foil design objectives are listed as a C_L of 1.2 at a design Re of 250,000.

With respect to NACA foils which are often common place in many applications, foils pertaining to the 'Selig' type are generally regarded as superior. NACA foils were designed at a time when substantially less was known about the complex fluid dynamics at lower Re [145].
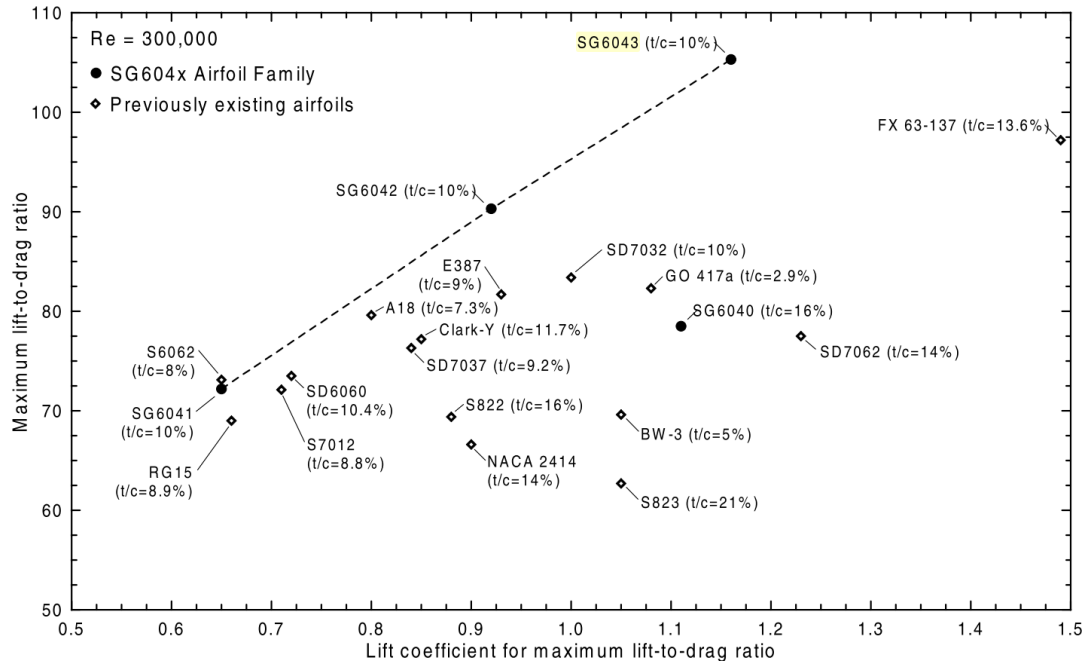
Figure 7.8: Maximum L/D values Vs C_L for various foils designed for HAWT [145]. The Reynolds number was set to 300,000 for all cases. The SG604X family is shown marked by · and connected through a linear relationship with respect to the graphs axis with a t/c of 10%.

7.2.2 Geometric Parametrisation

Foil geometry is typically received in coordinate format of both the upper and lower surfaces in addition to several parameters such as: maximum thickness, position of maximum thickness, maximum camber, position of maximum camber and nose radius. The geometric parameter characterisation identifies a particular foil to that of a foil section family, relatable geometries and intended operational conditions.

There is often some ambiguity with respect to machine tolerances and adherence to standardised geometric reference [219]. This can present itself a general discrepancy from the actual coordinates across both the upper and lower foil surfaces, or in the case where a foils TE is sharper than the machining capability, an altered cusp geometry is often required. Depending on the degree of departure, comparative data may not actually be representative of the true foil performance. The location and variance has a considerable effect on whether the error is critical. Differences at the TE have a similar behavioural impact to that of camber, affecting effective lift range. The upper surface can be substantially more dependant with the development separation bubbles and bubble drag. A uniform difference can be more indicative of the intended foil profile characteristics than if more erratic surface deviations are present, which may lead to more significant departures [145].

It should be noted that the degree of discrepancy that the counterpart SG6043 foil blade manufactured at Lehigh University has not been provided. Though there is a strong likelihood that there some deviation, particularly at the TE.

Another potential cause for geometric discrepancy is related to the meshing process. There is often disparity between different geometric interceptions of the upper an lower surfaces during the meshing process [109]. An example of TE variations
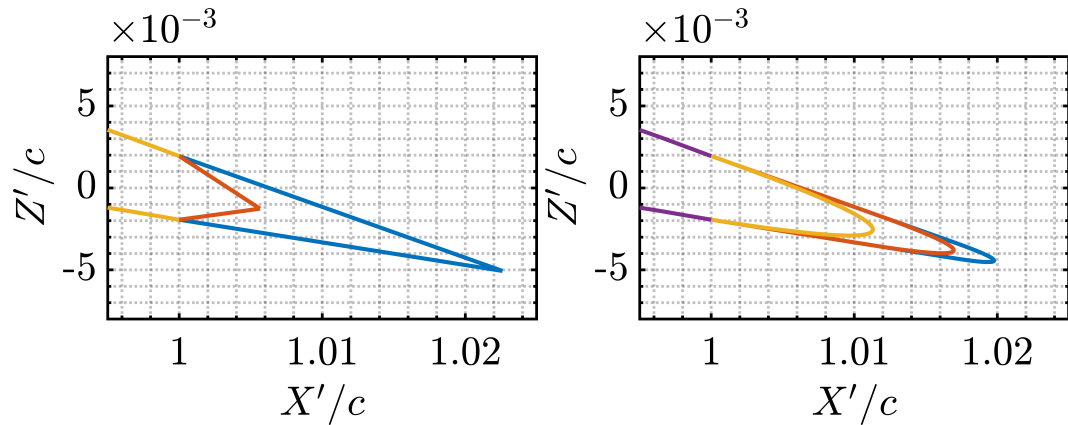
Figure 7.9: Different *TE* geometry variations, A sharp intercept point (left), A Bezier curve end (right).

are shown in Figure 7.9.

With respect to the case on hand, the SG6043 foil geometry used within this investigation is based on an normalized, 81 indexed xyz-coordinate set from a free online resource: Wind&Wet.com [68], which fetched the coordinate dat file from the University of Illinois airfoil coordinate database [219].

The coordinate resolution is too coarse for sections of high curvature, such as the *LE*, to accurately predict the onset of the boundary layer formation. Unlike the NACA series - which are generated through analytical equations and cosine increment spacing for closer groupings of coordinate points. The coordinate points constitute the fundamental SG6043 design characteristics. Thus, a cubic-spline based interpolation approach was used to construct high resolution smooth surfaces in areas of higher curvature featuring the discrete coordinate points as knot control points.

Despite methodological design to reduce deviations from intended shape. Interpolation, by nature of being a method to predict new points from existing discrete points, carries estimation error. Thus, geometric parameter analysis is required to establish similarity between officially stated SG6043 geometric standards and the fitted SG6043 spline surface.

An additional facet to consider is that the SG6043 foil section possesses a inherently highly cambered profile - where the forward most point, with respect to x-axis length, is distinct from the point of maximum curvature. Two separate definitions of the *LE* exist within literature. While the flow dynamics are independent of the definition, a standardised reference frame must be set for comparative purposes.

The fundamental geometric parameter terminology of a foil cross-section and descriptions are listed below as:

- **Leading Edge** (*LE*)
  Defined as either the forward-most point of a foil or the point of maximum curvature for foils featuring a high camber. The term is functionally polysemy, referring to either a discrete point which splits the upper and lower surfaces, or a section along a foils surface where the onset of boundary layer formation occurs [195, 148].

- **Trailing Edge** (*TE*)
  The *TE* is the aft-point of a foil section, being the furthest point from the *LE*.

Additionally, like the *LE*, is a junction between the upper and lower surfaces, and also has a polysemy functionality, with supplementary meaning towards the adjacent foil surfaces either-side of the point [148].

- **Chord Line** (*CL*)
  A single imaginary straight line existing along the shortest distance between the *LE* and *TE* - taken with respect to the '*point*' associated meaning [148].

- **Mean Camber Line** (*MCL*)
  A imaginary locus line constructed equidistant between the upper and lower surfaces [148].

- **Maximum Camber** (*MC*)
  Sometimes referred to as "camber", is the greatest separation between the *MCL* and the *CL*. MC has a strong influence on the lift generation properties of a foil - essentially the MC utilises the Coandă effect to alter the flow direction leaving the trailing edge (downwash). Consequentially, acting to increase the vertical lift force through Newton's third law of "for every action there is an equal and opposite reaction". As a general design principle, the greater the *MC* the greater the maximum lift achieved. Though at the same time drag is increased [104, 253, 130] .

- **Maximum Thickness** (*MT*)
  The greatest difference between the upper and lower surfaces, measured perpendicular to that of the *CL*. The greater the *MT*, the greater the α in which a stall will occur [104, 148].

- **Leading Edge Radius** (*LE$_r$*)
  The radius of an imaginary circle that fits the curvature of the leading edge. A determinant in the maximum lift of a foil. The general rule is; if the *LE$_r$* is increased, a greater lift at higher α can be achieved. The *LE$_r$* also has a significant effect on stall characteristics corresponding to an delayed flow separation mechanism. In contrast, a small *LE$_r$* incites flow separation closer the the LE; resulting in increasingly abrupt stall characteristics, whereas the aforementioned can increase stall delay and reduce post-stall lift drop-off. Additionally, the *LE$_r$* contributes to the induced drag, though considered a smaller variable with respect to the rest of the foil geometry [104, 214, 99].

The *LE*, defined as the point of maximum curvature, is calculated through applying the law of sines in relation to the circumcircle through three adjacent points along the SG6043 spline (x1,y1), (x2,y2), and (x3,y3):

$$\frac{a}{sinA} = \frac{b}{sinB} = \frac{c}{sinC} = 2R \qquad (7.1)$$

where

$$a = \sqrt{(x1-x2)^2 + (y1-y2)^2}$$
$$b = \sqrt{(x2-x3)^2 + (y2-y3)^2} \qquad (7.2)$$
$$c = \sqrt{(x3-x1)^2 + (y3-y1)^2}$$

and that to the area of the triangle

$$A = \frac{1}{2} a \cdot b \cdot \frac{c}{2R} = \frac{a \cdot b \cdot c}{4R} \qquad (7.3)$$

Then implying Heron's formula for the area:

$$A = \sqrt{s(s-a)(s-b)(s-c)} \qquad (7.4)$$

where s stands as the semi-perimeter of a triangle:

$$s = \frac{a+b+c}{2} \qquad (7.5)$$

to solve for the radius of curvature:

$$R = \frac{a \cdot b \cdot c}{4 \cdot R} \qquad (7.6)$$

and relation to maximum curvature:

$$K = \frac{1}{R} \qquad (7.7)$$

Figure 7.10 depicts the identified Leading-edge point through the maximum curvature definition; alongside the LE_r.

The original SG6043 foil geometric source [219] is noted to be of "Selig format", meaning an x,y coordinate format with points between 0 and 1; starting from the TE, to the LE along the upper surface, then back along the lower surface to the TE [103]. With respect to the preceding description, the "Selig format" implies that the LE is located precisely at the $[0,0]$ coordinate - thus takes the 'forward-most point' as the LE definition. However, considering there was no definitive coordinate point specifically at [0,0], the LE-point was thus estimated through the interpolation method, and being subject to the geometric errors in the surface generation.

A visual comparison between the geometric identities is shown in Figure 7.11. As mentioned previously, the SG6043 foil can have two distinct LE points depending on which of the two distinct LE definitions - subsequently propagate a knock-on effect to other geometric parameters of the CL, MCL, MC, MT and the LE_r. With respect to how the LE definition affects the α, the difference is a negligible $\approx 0.05^o$ for the forward-most edge LE definition, and 0.26^o for the Maximum curvature definition; where still small, might cause some variation in a C_L or C_D reading for a respective α, especially where changes in the flow regime are rapidly evolving. The MT parameter varies little since both the upper and lower surfaces have similar gradients at the thickest section. However, the MC has a larger separation - effectively forced by the slight shift in the MCL coinciding in a region where the surface gradients are
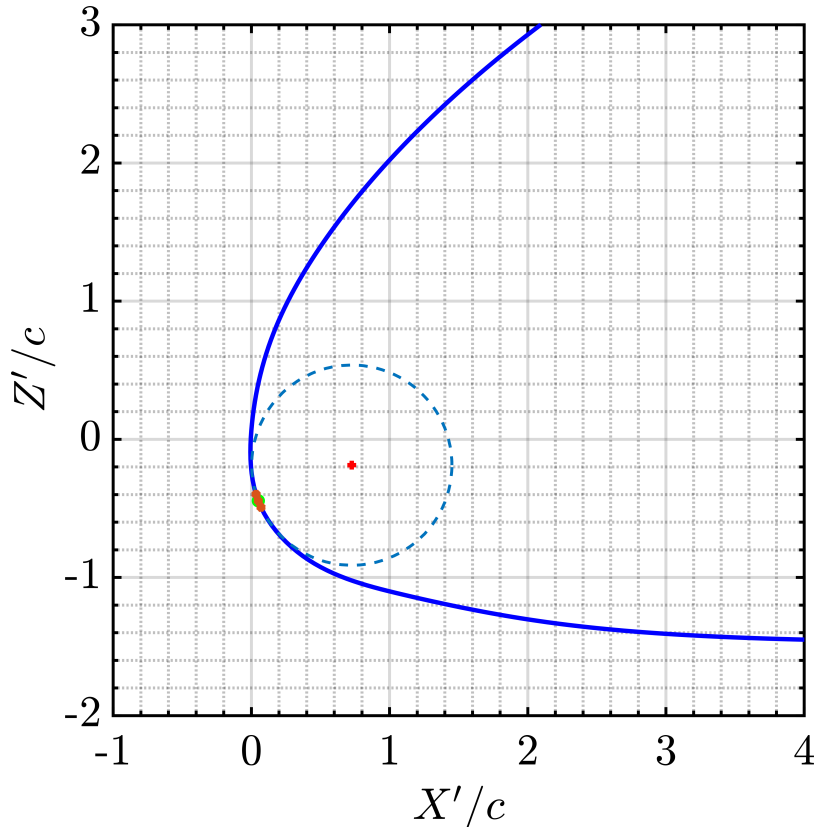
Figure 7.10: A schematic displaying key points in the determination of the point of maximum curvature and the leading edge radius for when the Leading edge is defined as being of such. A sectioned cut of the SG6043 spline nose section (dark blue) is intercepted by an imaginary circle of minimum radius(light blue) and origin point (red cross), at three points (orange star) which act to define the circle at the point of maximum curvature (green circle).

changing, though still only difference of 0.19% in magnitude and 1.24% in position. The greatest difference is in the LE_r parameter where the Max-curvature LE definition has a comparatively small magnitude of 0.724% compared to the Forward-most definition being 1.528% - a 111.05% increase.

The sum of the differences are displayed in table 7.2. The original source papers of the SG6043 foil [96, 145] presents the coordinate profile along with the prescribed thickness of 10% and camber of 5.5%, with no mention of the chord wise position or any other geometric identities. Similarly, lecture notes [220] do not offer any further insight into a definitive geometric identity. Günel *et al* [106] states source referenced maximum thickness and maximum camber, though also a LE_r of 1.7% - which closer matches to the Forward-most edge definition with respect to both LE_r and *MC*. Curiously, online database *'airfoiltools.com'* [10], states a maximum thickness of 10% at 32.1% of the chord-wise length and a maximum camber of 5.1% at 53.3%. The coordinate data source is claimed to be [103, 219], though interestingly, the stated camber is different from the original source. Additionally, with no clear documented source, it is likely that the chord-wise positions were independently calculated. Göçmen *et al* [97] states the thickness of 10% at 32.3% of the chord-wise length and a maximum camber of 5.45% at 48.8%, though does not provide any reference to the coordinate data source or geometric identities, though the maximum

camber is close to that stated from the original source. Yin Htay Aung *et al* [275] states the thickness of 10.01% at 32.3% of the chord-wise length and a maximum camber of 5.49% at 48.8%, with reference to a online source: Profili [194]. While both *LE* definitions may hold respective validity, the Forward-most is seemingly most prevalent within research for the SG6043 profile. The Max-curvature definition may reserved for foil profiles with a significant departure with respect to the camber profile.

Table 7.2: Summary table of the SG6043 geometric parameters with respect to alternative reference points.

Version	Leading-Edge Radius (LE_r)	Maximum Thickness (MT)	Maximum Camber (MC)
Max-Curvature	0.724%	10.01%@32.45%	5.73%@48.84%
Forward-most Edge	1.528%	10.02%@32.43%	5.54%@50.08%
Selig/Giguere [96]	N/A	10.00%@N/A	5.50%@N/A
Gunel *et al* **[106]**	1.7%	10.00%@N/A	5.50%@N/A
Goçmen *et al* **[97]**	N/A	10.00%@32.30%	5.45%@48.80%
Yin Htay Aung *et al* **[275]**	N/A	10.01%@32.30%	5.49%@48.80%

7.3   Numerical System

From a fluid dynamics perspective, flow characterisation around a geometric singularity is significantly less complex than flow phenomena induced through proximity interactions between multiple geometric bodies.

With respect to the case on hand, the foil exits in relative isolation, making the case highly predictable and thus able to be easily optimised with respect to mesh refinement and correct numerical requirements.

The flow-field domain can be broken down into four distinct elements of consideration for numerical representation.

1. The ambient flow-field

2. The flume wall boundary Layer's

3. The foil boundary layer's

4. The downstream wake flow field

Each of which is schematically presented in Figure 7.12; detailing the spatial relationship between each and corresponding domain boundary acting as a interrelated whole.

The consideration for the ambient flow field primarily relates to the parametrisation of the inlet boundary conditions; which defines the convective terms and acts as the forcing function for the fluid within the domain. Essentially, instigating a
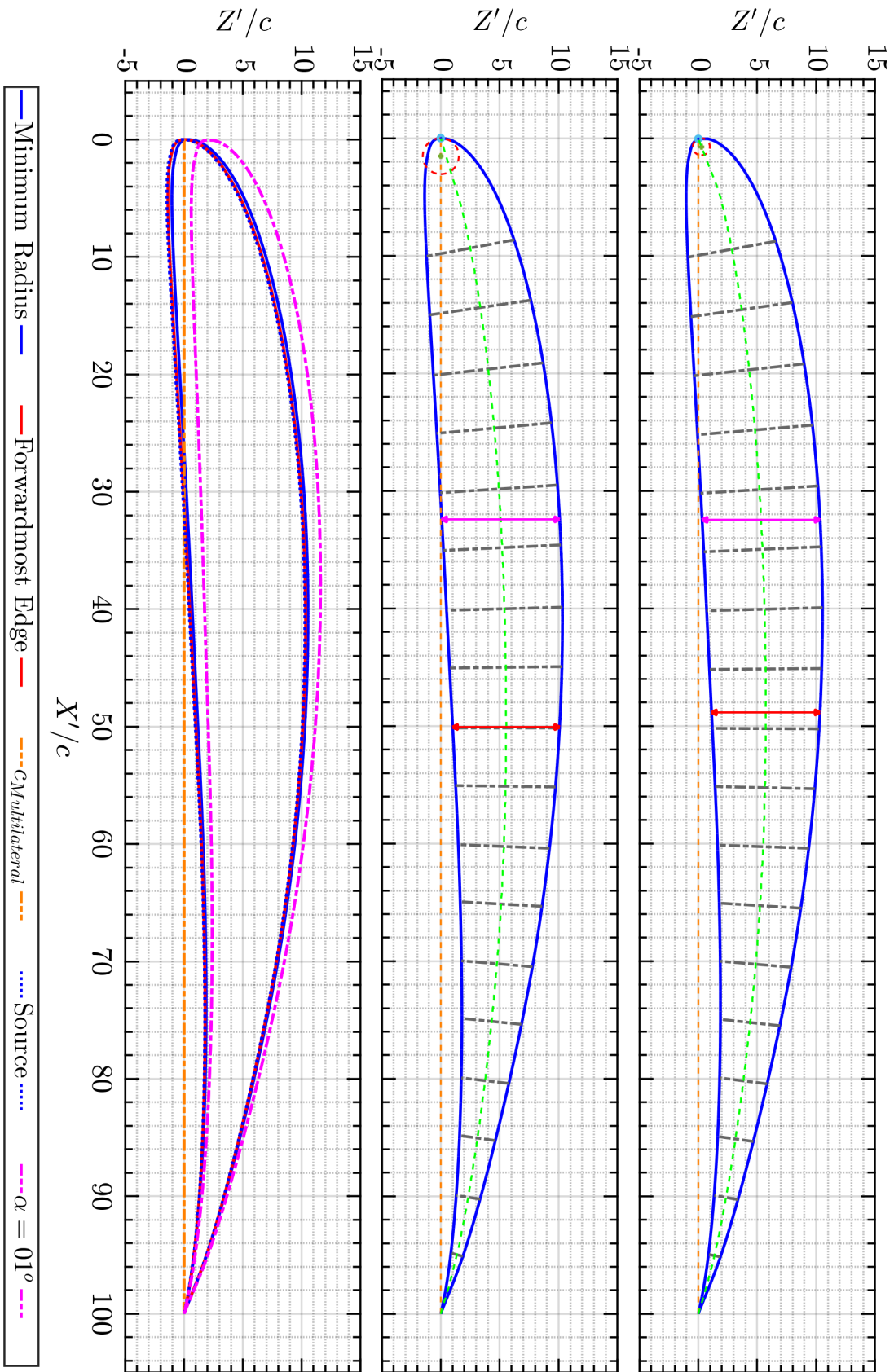
Figure 7.11: Comparison between the SG6043 geometric parameters when taking the LE as the minimum radius (top), or of the forwardmost edge (middle). Then the profiles superimposed and compared to the source coordinates and at $\alpha = 1^o$.
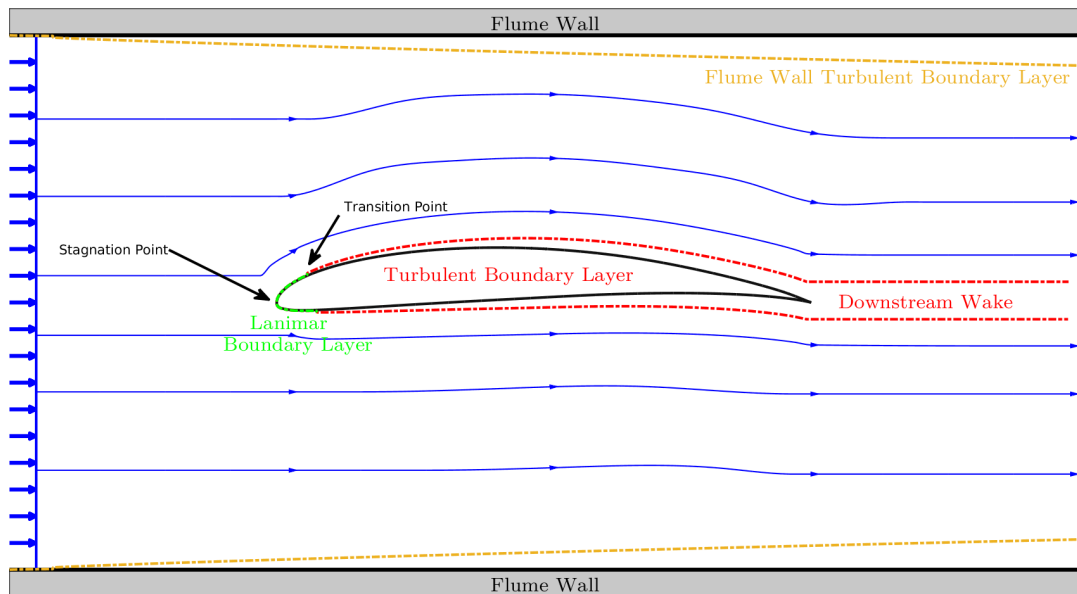
Figure 7.12: Schematic diagram of the Flume flow domain.
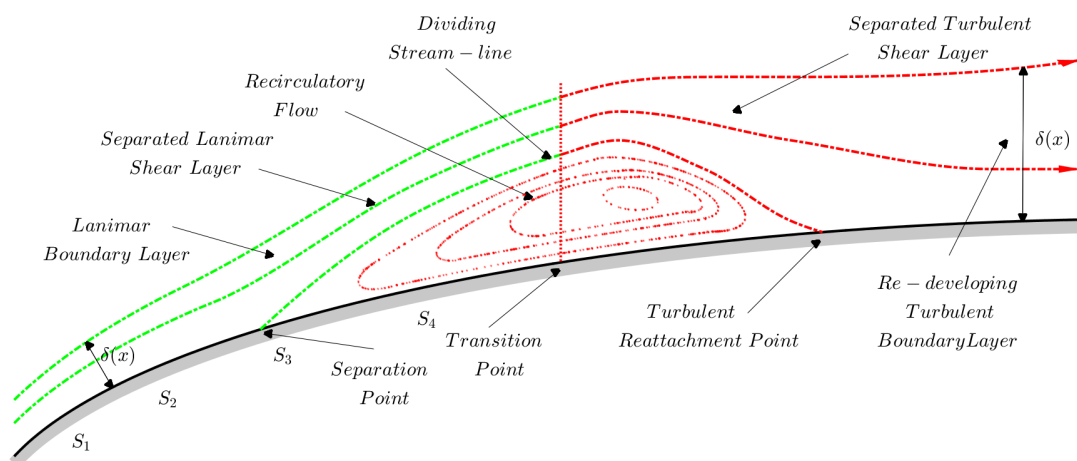
Figure 7.13: Schematic diagram of the Flume flow domain.

flow-medium, which acts as the initial propagator for all hydrodynamic phenomenon generated within the domain.

One of such is the 'flat plate' type boundary layer formation along the flume wall, inducing departure from the ambient flow characteristics. Additionally, considering proximity to the foil, of which when rotated will reduce the effective cross-section of the flow domain - inevitably inducing blockage characteristics forced by the principle of continuity.

The flow incident onto the foil LE will form a instant stagnation point, where the flow field will be bilaterally separated between two nonsymmetrical geometric surfaces before eventual surface detachment. At which point the flow will constitute part of the downstream flow field. Therefore, two distinct surface interfaces will be present, differing with respective viscous-inviscid flow field dynamics and corresponding pressure distributions. The relationship becomes more complex simulating at higher angles of attack. The larger eddies that form will act to disrupt the bulk-mean uniformity of the wake flow and generate multiple interfaces between fluid

197

bodies that are characteristically distinct. Resulting in a corresponding increase in computational complexity of the case. However, this aspect can be relatively trivialised. The downstream flow only needs to be bulk simulated so that no downstream model artefact will affect the flow over the foil surfaces. Thus, downstream mesh coarsening can act to counteract the inherent computational cost of simulating the increasing complexity of interacting turbulent mixing layers.

It can hence be understood that the majority of the model domain will consist of the mean fluid flow, which RANS model are efficient at simulating. With respect to the primary objectives of this research - to further the capacity of a numerically efficient turbine simulation. This section contributes to a part of that simulation system's effective numerical cost. Excessive simulation time to attain performance criteria for each foil section, will act to diminish the practicality of the GAD model and thus the potential research and industrial prospects. Thus,

Accurate prediction of the foil lift and drag coefficients is fundamentally dependant on accurate representation of the boundary layer along foil surfaces [159].

Unlike typical flat-plate boundary layer formations, an adverse pressure gradient is a common feature along foil upper surfaces. The dynamics of the viscous-inviscid fluid interaction largely dictate the pressure distributions and thus fluid dynamic character. Manifestations of which can feature as a LE bubble or TE separation. The dynamic propagation of either along the foil surface can define stall characteristics between delayed stall states an those of sudden stall. Therefore it is also of utmost importance that the precise location of flow separation can be simulated, along with the corresponding displacement effects [159].

Additionally, the inclusion of the SST eddy viscosity limiter eliminates unrealistic eddy-viscosity build up at an foil's LE stagnation point [159].

Thus, the $\kappa - \omega$ SST turbulence model was selected for being the best fit out of the mainstream RANS methods, as its superiorly able to simulate the physics of the boundary layer while being of modest computational cost. Section 2.3.3 discusses the $\kappa - \omega$ SST turbulence model in greater detail.

OpenFOAM ("**Open**-source **F**ield **O**peration **A**nd **M**anipulation") software suite, version 4.1, was selected to numerically investigate the SG6043 foil Performance under various flow parametrisations instigated through altering variables related to the Reynolds number, Turbulence intensity and geometrically attributed entities such as surface roughness. OpenFOAM currently does not support fully 2D grid simulations, forcing simulations to conducted across grids of a single cell width. The foil is simulated within a dynamic fluid body without any interaction with distinct features. Thus, the model only has to deal with a singular entity and how the fluid flow will react.

A full SG6043 foil performance parametrisation requires operational analysis over a complete range of α's. A consequence of operating at higher α, will inevitably instigate transient phenomena such as vortex shedding which would subsequently deny convergence to a single steady-state solution. The transient solver 'pimpleFOAM' operates under the assumption that the flow field is incompressible, unsteady and of viscous flow. Initial conditions within the flow-field cannot be set as such. The solver would thus be forced to use a fictitious value for the velocity, pressure and the turbulent flow field; consequently instigating increased instability within the model, which would delay convergence of flow conditions.

A 'hybridisation' method, initially utilising the steady-state solver 'SIMPLE' to

instigate the initial guess - essentially mapping a reasonable flow-field with, unsteady and viscous flow, which is more suitable for the transient solver 'pimpleFOAM'. This methodology is tailored for the $\kappa - \varepsilon$ SST turbulence model; which is non-linear and has greater difficulty to reach a converged state. Additionally the model has been shown to be sensitive to the initial guess of the solution. The mapped fields would provide a further iterated improvement to the initial guessed solution, hence providing an effective computationally efficient method for working with the $\kappa - \varepsilon$ SST turbulence model and fully developed stream-flows.

7.4 Flume-flow Parametrisation

7.4.1 Flume Model Description

An independent performance parametrisation of the SG6043 foil would necessitate, an external flow regime without there being any question of reactionary flow dynamics from adjacent surfaces - which would interact with the formation of the boundary layer over the foil surfaces. However, conducting a parametrisation study within the confines of parallel flume wall surfaces, will inevitably bring such interaction into question. Thus, the computational flow domain in this case should be considered that of internal flow.

The defining geometry is that of the SG6043 foil cross-section which is positioned so that the domain point of origin intercepts with the chord-wise mid-point of which also acts as the axis of rotation.

The domain bounds were $0.61m$ X $0.61m$, constrained by experimental flume dimensions and the SG6043 cross-section blade of a reported 0.0762m chord length.

In relation to the *Raison D'etre* of this investigation, as discussed in Section 6.1, dimensions were normalised with respect to the chord length as 1m, to 'normalise' the turbulence length scales for eventual application into the GAD methodology. The thickness was set to be "normal thickness" ($t/c = 10\%$), for respective chord length according to the Selig format [220]. All geometric entities set for the SG6043 foil profile were set in accordance to those defined under they 'Forward-most' edge definition outlines in section 7.2.2

Thus, the 2D flume cross-section was scaled inline with the chord length:

$$normalised \ fume \ width = \frac{orginal \ fume \ width \cdot normalised \ chord \ length}{orginal \ chord \ length}$$

(7.8)

$$normalised \ fume \ width = \frac{0.61 \cdot 1}{0.0762} = 8.005m$$ (7.9)

In total, within the confines of the representational flume walls, the domain is constructed as a single rectangular block of maximum and minimum bounding coordinate points of $[-4.0025, -5.4e - 05, -4.0025]$ to $[5.6035, 5.4e - 05, 4.0025]$.

The SG6043 profile was not modified through a blunting or truncating of the TE and exists as being of a sharp taper of finite thickness.

Initial & Boundary Conditions

The initial fluid state is set with a kinematic viscosity (v) equal $1.3065 \times^{-06}$ $m^2 s^{-1}$, which is approximately equivalent to air temperatures of 281 degrees Kelvin [9]. With velocities ranging according to table 7.3. The foil chord length remains consistently 1m and is treated as the systems characteristic length. The boundary conditions imposed throughout the domain on all patch surfaces were set in accordance to those specified in Table 7.4.

Table 7.3: Table summarising the equivalent Inlet Velocity to the Reynold numbers with respect to the 1m turbulent length scale dictated by the chord length.

Reynolds Number	Inlet Velocity [m/s]
43k	0.056179
50k	0.065325
63k	0.082309
73k	0.095374

With respect to the domains initial condition state, the fluid was forced to be consistent with parameters specified on the inlet boundary. Thus, the fluid is injected as a uniform plug velocity flow condition at said boundary, with continuity being preserved with flow exiting out of the domain through the 'Outlet' patch.

The κ and ω are set similarly, with values according to case profile as stipulated in Table7.3. The flume walls are represented through solid wall patches and fixed the flow velocity to $0.0ms^{-1}$. The fluid velocity is calculated at the adjacent cell-centre, which exists at a y+ criteria of $30 < y^+ < 200$. through application of wall functions which estimate the un-resolved boundary layer. The XZ-Boundary planes existing at both the maximum and minimum Y-axis values was set as empty which represent directions that are not solved during said cases. The Courant number is set to dynamically change with the simulation requirements but is limited to not exceed 0.9.

Mesh Configuration

The sharp TE of the SG6043 profile coffers inherent limitations for typical unstructured or Cartesian girds. While there is an optimal distribution of refined cells making a more efficient mesh type, the cells at the TE are often skewed - which is a critical limitation with viscous flow and computation of accurate performance coefficients. The C-type mesh addresses the mesh quality issue present in conjunction with a foil profile that has a sharp finite-thickness TE; with the cells at that point remaining un-skewed and of a collective higher quality. Additionally, the C-mesh type can capture the LE without point singularities and therefore clustered cells.

Although an often-cited disadvantage of using the C-type mesh configuration is the inherent characteristic of continued downstream cell propagation past the trailing edge, at the same refinement level as the boundary layer. Although at low α, there is a beneficial aspect, as the extra refinement can aid in the capture of the downstream

Table 7.4: This table displays a summary of each boundary condition specified of every boundary within the 2D flume model.

Field		Velocity (m/s)	κ (J/kg)	ω (J/kgs)	nut (Pas)	Pressure (Pa)
Initial State	Value:	uniform (* 0 0)	uniform **	uniform ***	uniform 0	uniform 0
SG6043	Type:	FixedValue	FixedValue	FixedValue	calculated	zeroGradient
	Value:	uniform (0 0 0)	uniform 1e-15	uniform 1e15	uniform 0	-
Flume-wall	Type:	FixedValue	kqRWallFunction	omegaWallFunction	nutkWallFunction	zeroGradient
	Value:	uniform (0 0 0)	uniform 0	uniform 0	uniform 0	-
Inlet	Type:	inletOutlet	inletOutlet	inletOutlet	calculated	outletInlet
	Value:	uniform (* 0 0)	uniform **/0	uniform ***/0	uniform 0	uniform 0/0
Outlet	Type:	inletOutlet	inletOutlet	inletOutlet	calculated	outletInlet
	Value:	uniform (* 0 0)	uniform **/0	uniform ***/0	uniform 0	uniform 0/0
XZ-Boundary Planes	Type:	empty	empty	empty	empty	empty

* : Denotes case dependant velocity value which can be looked up in table 7.3

** : Denotes case dependant κ value.

*** : Denotes case dependant ω value.

shear layer [230]. This facet, however, is only true for a small number of the simulation runs as the α will range from -8 to 20 degrees. Thus, will add non-functional load to the simulation which results in a less efficient simulation. However, as the research is focused on determining accurate predictions of the C_L and C_D coefficients of the foil, the physics of the downstream section is less of a priority, with the mesh only having to be fine enough that model artefacts are not created which disrupt the foil coefficient prediction.

OpenFOAM does not offer any utility to automatically construct C-mesh type systems. However, OpenFOAM's built in 'blockMesh' utility can be used in tandem with in-house developed, Matlab based software utility; which automatically tailor's C-type mesh parameters for a series of tested foil cross-sections. Albeit, the utility does possesses untested unilateral foil cross-section meshing capability. A description of which is presented in the Appendix E.

Additionally, the meshing utility possesses capabilities to intermediate between the C-type mesh constructed around the foil cross-section and the flume-wall surfaces. The foil cross-section can be rotated across an α sweep without significant skewness being forced across interactant cells - achieved through dynamic coupling of cell block vertices, rotating synchronously without significant distortion beyond set quality limits.

The mesh configuration is structured to be refined through calculated grading systems towards hydraulic structures; such as the SG6043 foil and the flume wall surfaces. The degree of grading refinement is dictated by necessity 7.14. The SG6043 cross-section geometry possess a surface cell size $< y^+ = 1$ in accordance to fully resolve the formation and propagation of the boundary layer - being an essential component for accurate lift and drag coefficient prediction. In contrast, the flume-wall surfaces interact with the fluid as a 'flat-plate' with corresponding boundary layer development and propagation properties - existing without adverse pressure gradients. Thus, possess adjacent cell sizes of $y^+ \approx 100$, existing within wall function criteria of $30 < y^+ < 200$.

A disadvantage of using the C-type mesh is that there are areas of high refinement along the downstream length which will not cover areas of dynamic flow for the majority of the α that will be tested. A possible avenue in which to go down could be to address this aspect. Like for the frontal section, where the mesh blocks were spherical, the downstream blocks labelled E & F as shown in Figure ?? could also be set as spherical, thus distributing the refined cells across a wider span and giving an more optimal cell count for a wider range of α's, as will be the requirement for the mesh when producing the lift and drag coefficient library.

Possible limitations of going down this meshing route can include the increased complexity when generating the cells so that they are not skewed. If the mesh cannot be constructed with reasonable skewness, then the computational efficiency advantage would be negated as the quality of the solution will become impeded.

Mesh Dependency

In the context of simulation reliability, the quality of the conceptual model must be verified through estimating the numerical error or uncertainty of a research dependant solution [208, 175].

Within the confines of this investigation, the two dependant variables of interest
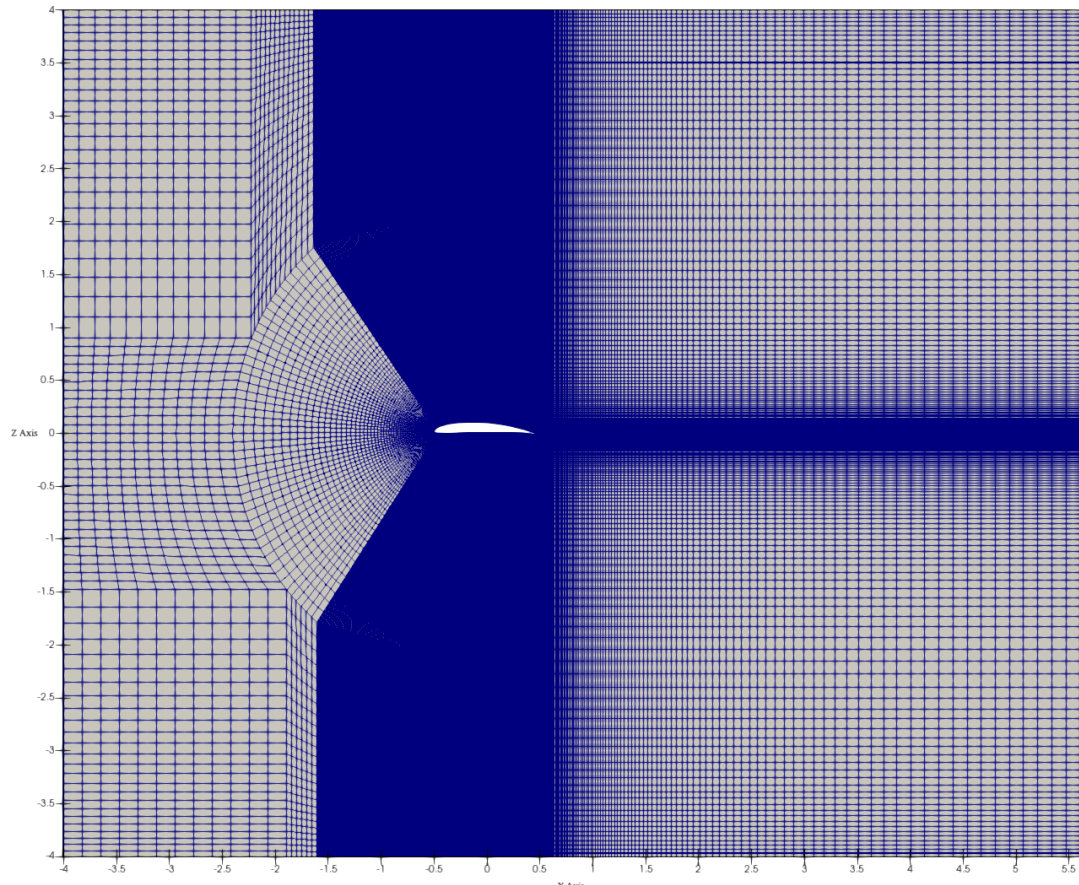
Figure 7.14: First Angle view of the Flume-Flow mesh domain. The SG6043 foil is set at two degrees α with its centre-point set as the model origin. The mesh was generated through a in-house mesh parameter generation tool and OpenFOAM's 'blockMesh' utility. Note the refinement towards the SG6043 foil and the upper and lower boundary walls. The mesh was refined so that there would be a $y^+ < 1$ for the first surface cell-centre - OpenFOAM solver via a cell-center approach.

are the lift and drag coefficients. Outside of the dependency on the ambient flow parametrisation, the accuracy of predicted solutions pertain to the correct representation of flow phenomena adjacent to the foil geometry; primarily relating to that of the boundary layer. The Numerical system prescribed in 7.3

The surface-cell height, perpendicular to the surface is determined through accordance to the imposed $y^+ < 1$ criteria - thus testing the cell expansion dependency in said direction is inconsequential. However, the parallel length of each cell along the foil is not governed by such criteria; just by the capability to accurately capture the boundary layer physics. When the foil is at low angles of attack and the flow existing in a laminar state, the variation in the length of each cell is likely to be of lower importance. However, the situation changes when encountering changes in the state of the boundary layer; such as the flow separation phenomenon. For such cases, the correct capture of the physics is of paramount importance for the accuracy of the resultant coefficients.

2D CFD analysis of the computational domain described in 7.4.1 requires refinement in two distinct regions of the domain; being the spatial area around the foil geometry and the flume-wall surfaces. Both of which require transient numerical
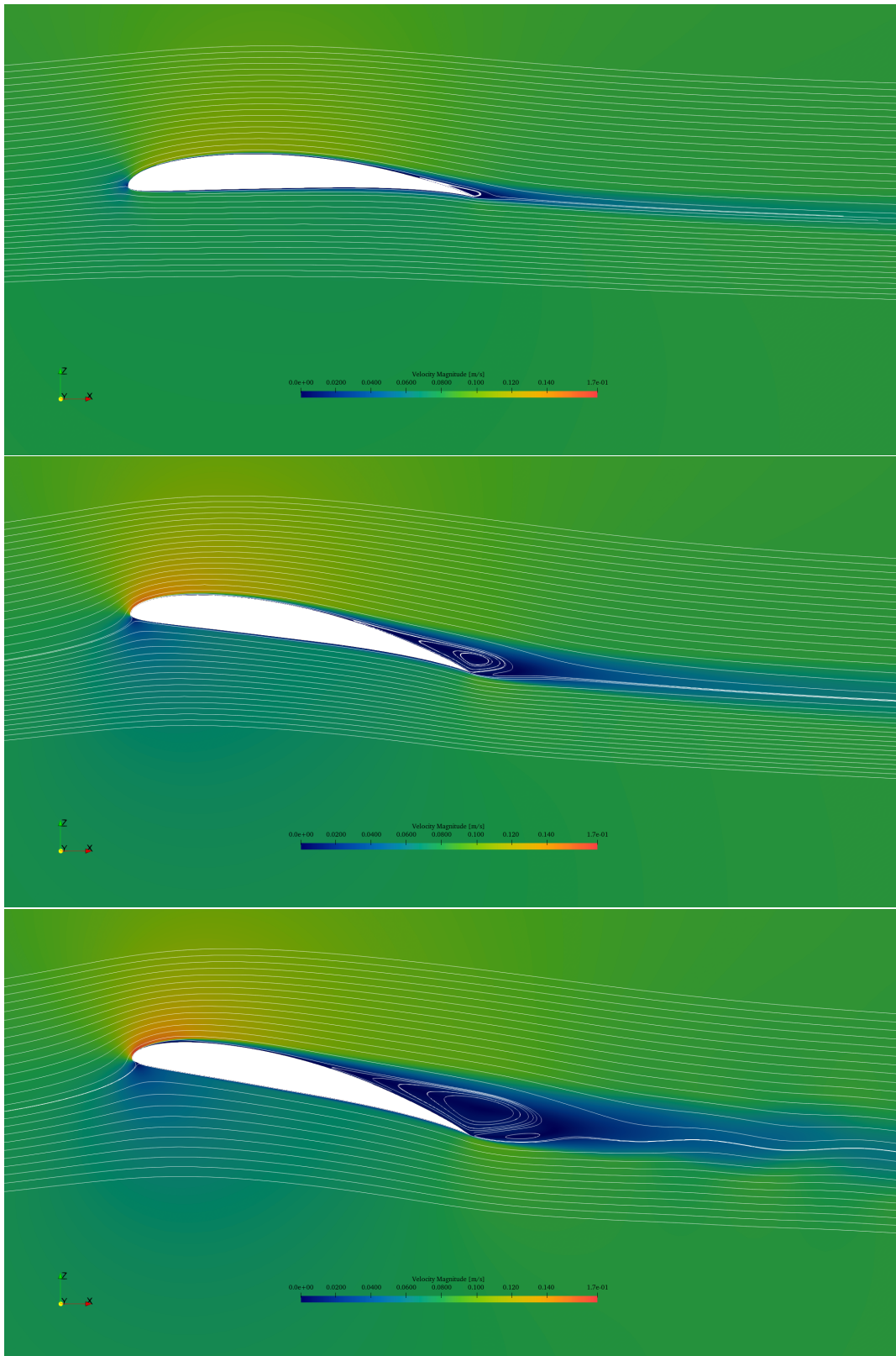
Figure 7.15: Velocity Magnitude [m/s] supplemented with velocity streamlines of α +02 (top) +10 (middle) +13 (bottom). FCBA case with 600 cells along circumference of foil.

prediction of the boundary layer along each geometric 'wall' surface. The downstream wake structure, particularly at higher α, will be complex in nature. However, complete representation of which is not necessary for the purposes of this coefficient performance study; the only downstream consideration would be to ensure the fluid to be able to flush out the domain without the onset of model artefacts.

The mesh structure is generated as per described method in section 7.4.1, for $\alpha = [+02, +10, +13]$. The select α positions cover flow conditions of the near-linear lift region, the transition to plateau, and the approximate stall point. Both the C_L and C_D are selected as critical global variables, where the accurate prediction of which is fundamental measure of success; to be taken against a mesh refinement measure of the number of cells on the circumference of the SG6043 section geometry surface. The range of refinement and corresponding total number of grid cells is presented in table 7.5.
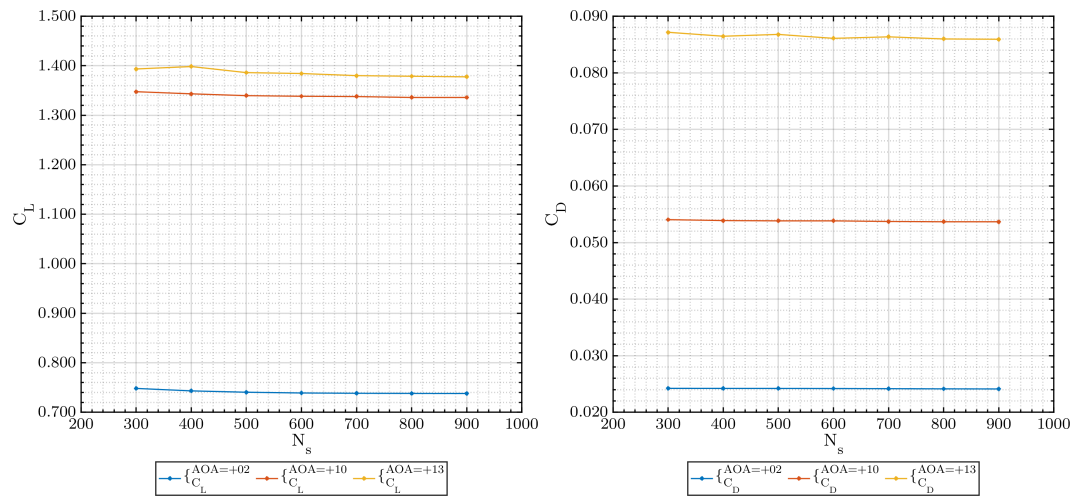
Figure 7.16: Details a combined series plots of Lift C_L & Drag C_D Coefficients relating to foil α positions of +02 (blue),+10 (orange) & +13 (yellow) against the number of cells along the foil. Each foil has a smooth surface ($K_s = 0\mu m$) and a 1m chord length. Additionally, all cases were run with a Reynolds Number of 63K and a Turbulence Intensity (T_i) of 1.5%.

Table 7.5: Summary table attributing the number of cells along foil surface to that of the total number of cells.

Number of cells along foil	Total number of grid cells
300	67780
400	80728
500	93900
600	119783
700	106841
800	132968
900	145903

205

Flow Visualisation Figure 7.16 presents the resultant converged coefficients for the flume conditions of $Ti = 1.5\%$ and a $Re = 63k$ case.

With respect to the $\alpha = +02$ & $\alpha = +10$, convergence can be seen at 500 cells for the C_L C_L; while the point of convergence with respect to the drag coefficient C_D appears to be below 300 cells.

The $\alpha = +13$ case provides less conclusive convergence with respect to the number of circumference cells for the Drag coefficient C_D. However, convergence within acceptance limits can be seen past 600 circumference cells for the C_L C_L. When comparing against flow characteristics depicted in Figure 7.15 - which presents the velocity magnitude colour contours with supplementary directional streamlines. It can be seen that the across all cases there is boundary layer separation giving way to an inverse velocity gradient; where the flow separation is initiated at an earlier point along the foil upper surface with increasing α. Additionally, the size of the induced eddies also increase with respect to α. However, a distinguishing flow characteristic is present for the $\alpha = +13$; which is that the eddies appear to shed from the upper surface, which will as consequence, imply greater temporal flow velocity variation along the surface. Such instabilities might prevent consistent determination of coefficient irrespective of circumference cell count. With respect to α positions where the flow characteristics are steady, i.e. before the onset of eddy shedding - the system appears less sensitive to circumference cell count. It can be speculated that after 500 circumference cells, the cell lengths are diminutive to the steady eddy turbulent length scales present and appears to adequate capture of the flow physics.

Analytical Verification Table 7.6 and 7.7 summarises the order of accuracy and Grid Convergence Index (GCI) of three critical global variables accounting for the C_L and CD_D across three angles of attack. Subscripts denote the cases of 900, 600 and 400 foil surface cells, respective to ascending order. All variables are of mean values over final simulation time-steps once a statistically steady flow regime was observed across the coefficient time-series and observed flow conditions. With respect to the R, all C_L are evaluated to be of monotonic convergence with each coefficient time series possessing a decreasing concave-up trend.

The C_D variables have contrasting R; the $\alpha = +13^o$ case returns to a monotonic convergence criteria. However, $\alpha = +2^o$ shows a divergence condition of 3.57 and the $\alpha = +10^o$ a very large divergence of 49.25. The determination can be attributed to the fine, medium and coarse selection of 900, 600 and 400 cell respectfully, forming a convex profile. Whereas a comparative profile featuring the collective grids as presented in Table 7.5 and in Figure 7.21 is indicative of a monotonic nature.

With respect to the aforementioned, a divergent condition will instigate a negative p and thus an erroneous prediction of the zero-grid spacing $h \to 0$ value. However, checking against the asymptotic range of convergence condition shown in equation 2.9. The close proximity of 0.9986 and 0.9982 to 1 indicates the respective grid solutions are well within the asymptotic range of convergence. Thus, the equation 2.4 can be modified by reversing the polarity; resulting in more reasonable corresponding estimate for $f_{h\to 0}$ being 0.02409 and 0.05365 for the respective α. The p was calculated to be of a significant 3.6 and 9.6 for $\alpha = 2^o$ and $\alpha = 10^o$ respectively. However, the minute $\varepsilon_{12\$23}$ denigrate the corresponding p. Interestingly, the GCI_23 are an order of magnitude smaller than those of GCI_12; acting reciprocally the ratio between $\varepsilon_{12\$23}$ and the magnitude of the respective p.

The $\alpha = 10^0 \& 13^o$ for the C_L and $\alpha = 13$ for the C_D both have an order of convergence of $\approx 2^{nd} order$.

There is a reduction in GCI values across the three successive grids .

All solutions for both the C_L and C_D tested were found to be comfortably within in the asymptotic range of convergence.
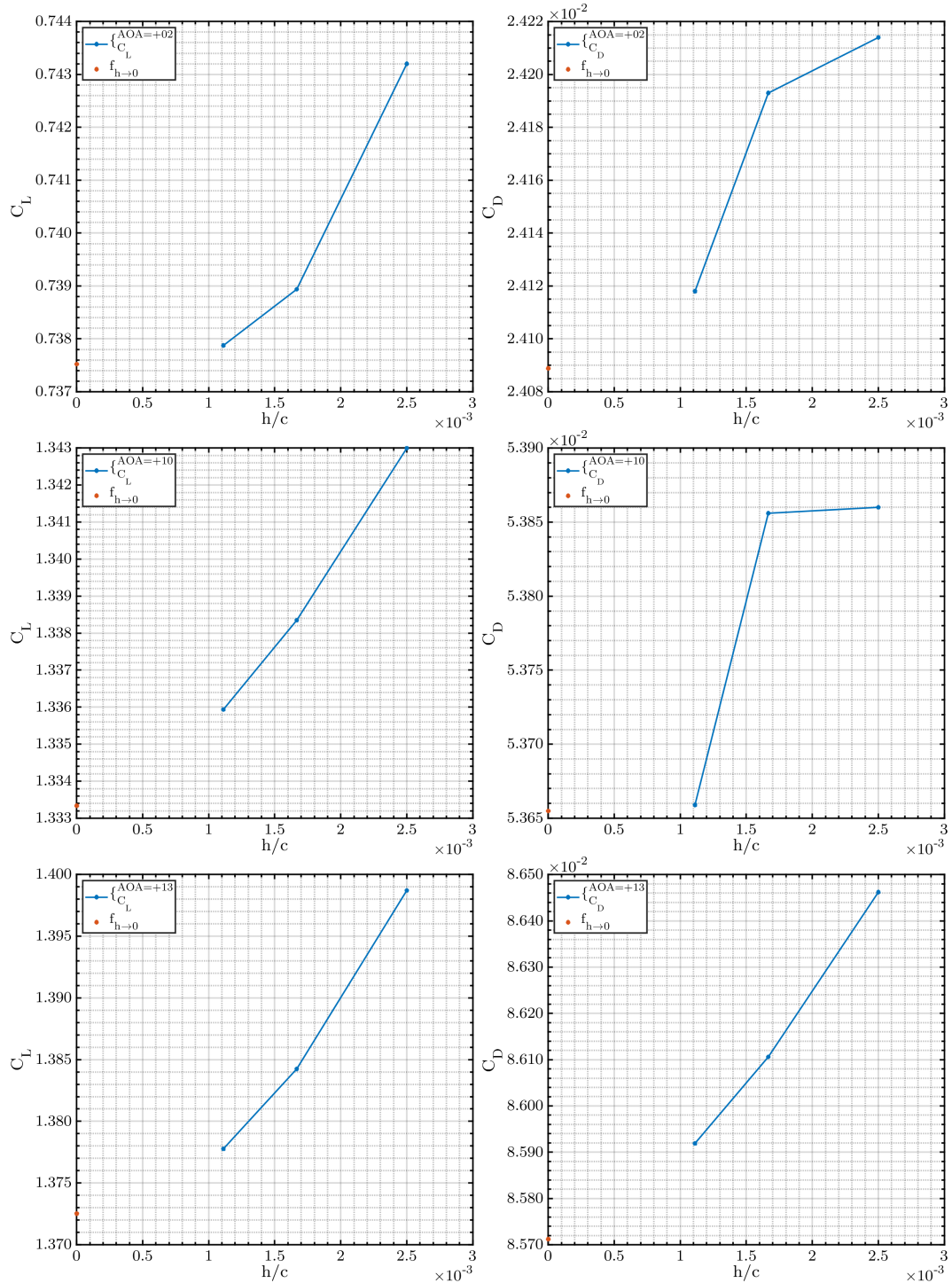
Figure 7.17: Respective C_L (left) and C_D (right) against three resolutions of grid spacing, normalised to the chord length, and the Richardson Extrapolate $(f_{h \to 0})$ prediction.

Table 7.6: The Order of accuracy and Grid Convergence Index (GCI) of three critical global variables accounting for the C_L across three angles of attack. Subscripts denote the cases of 900, 600 and 400 foil surface cells, respective to ascending order.

α	ε_{12}/f_1 [%]	ε_{23}/f_2 [%]	**R**	**p**	$\mathbf{f}_{h=0}$ [%]	**E1** [%]	**E2** [%]	**E3** [%]	**GCI**$_{12}$ [%]	**GCI**$_{23}$ [%]	**GCI**$_{AR}$ [%]
+02	0.14	0.58	0.2	3.4	0.7375	0.05	0.19	0.77	0.06	0.24	0.9986
+10	0.18	0.35	0.5	1.6	1.3333	0.19	0.38	0.72	0.24	0.47	0.9982
+13	0.47	1.04	0.4	2.0	1.3725	0.38	0.85	1.91	0.48	1.06	0.9953

Table 7.7: The Order of accuracy and Grid Convergence Index (GCI) of three critical global variables accounting for the C_L across three angles of attack. Subscripts denote the cases of 900, 600 and 400 foil surface cells, respective to ascending order.

α	ε_{12}/f_1 [%]	ε_{23}/f_2 [%]	**R**	**p**	$\mathbf{f}_{h=0}$ [%]	**E1** [%]	**E2** [%]	**E3** [%]	**GCI**$_{12}$ [%]	**GCI**$_{23}$ [%]	**GCI**$_{AR}$ [%]
+02	0.31	0.09	3.6	3.1	0.0241	0.05	0.19	0.77	0.15	0.04	0.0782
+10	0.37	0.01	49.3	9.6	0.0537	0.19	0.38	0.72	0.01	0.00	0.0004
+13	0.22	0.41	0.5	1.6	0.0857	0.38	0.85	1.91	0.30	0.57	0.9978

Surface Cell Height Dependence   The surface-cell height, perpendicular to the SG6043 foil section surface is generated through initial application of equations 2.73:**??**. With respect to research hindsight, the skin friction equation 2.73 should have been interpreted as equation 7.10.

$$C_f = 0.0576 Re_x^{-0.2} \tag{7.10}$$

Where the Reynolds number is relative to the downstream distance. Instead, the
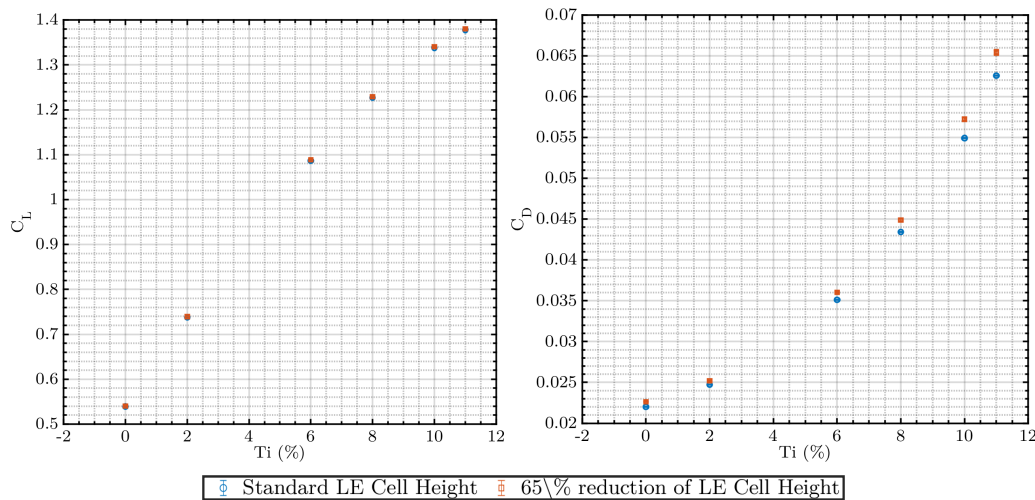
Figure 7.18: Comparison of both C_L (left) and C_D (right) with the LE surface cell height mesh parameter reduced by 65%.

reference length was taken as the chord length. The mesh generation tool detailed in Appendix E, did take into account the inevitability of flow acceleration near the leading edge. The cell height along the LE section was reduced through the application of a constant, in addition to decreasing the cell width intervals.

Post simulation processing revealed the y^+ along the upper surface of the LE, from the LEP to $0.1c$ to was > 1 for all cases simulated. However, the y^+ did not exceed 5 for all cases, which is within the viscous sub-layer. Though outside of the $y^+ < 1$ recommendation for a fully resolved boundary layer. The remainder of both the upper and lower surfaces successfully met the $y^+ < 1$ condition.

This creates a predicament where it is unknown to what extent the boundary layer was correctly modelled. The initial concern is that if the initial propagation was incorrect, there would effectively be a subsequent knock-on effect along the upper surface. The degree of which is difficult to attain without additional testing.

The LE minimum cell height parameter δ_o was thus reduced by 65% to gauge the possible degree of error. The flow-field from a previous simulation with conditions set for a $Re = 63k$ and a $Ti = 2.2\%$, was mapped for initial conditions suitable for the $k - \omega$ SST model to be initiated without the substantial stabilisation period. Figure 7.18 presents the findings for the the case. A high degree of similarity between the C_L exists with the greatest percentage difference between the sets being that of 0.25%. The C_D exhibits a greater degree of separation with increasing α. Initially at an $\alpha = \pm 00^o$ the difference is 2.5%. Approaching the stall point, the percentage difference increases to 4.5% - which can be of some degree of significance when compared to system dependence on other parameters.

What should also be taken of consequential note was the substantial 245$ mark-up of computational cost required. Considering the research objective relates to computational efficient approaches to simulating HATT arrays, there is a corresponding departure away from exact precision for a reasonable solution at a modest computational cost. When balanced against other sources of error within the collective GAD model system a difference in C_D of 4.5% might well be inconsequential.

Omega Corrections   The selection of ω on the domain wall surfaces is covered in section 7.3. However, initial misconception lead to an understanding that equation 2.75, which shows $\omega \to \infty$ as $y \to 0$, indicated that no distinct ω value was required and could be semi-arbitrarily set as long as the value was very large.

A comparative case using both the Wilcox' and Hellsten corrections for a flow field of $Re = 53k$ and $Ti = 2.2\%$ is presented in Figure 7.19. The initial set boundary condition was $\omega = 1 \times 10^{15}$ as presented in table 7.4. The corrected ω value is $1.32E + 04$. Comparatively, the corrected ω case under-predicts C_L at lower α and over-predicts C_D. For the approach to stall at $\alpha = 10^o$, there is over-prediction for the lower $T_i = 2.2\%$ but under-predicts at the higher $T_i = 12.6\%$. There is constant over-prediction for C_D. All the $\alpha = +02^o$ cases reached an oscillatory convergence. For such convergence type, the median average reduces possible imbalances that the mean could create. The error bars present the amplitude of the oscillations. Quick reference reveals that the corrected case exhibits considerably larger oscillation. Referring to Figure 7.20, it can be seen that the eddy-shedding phenomenon is cause. Both the pressure and the velocity flow-field along the majority of the foil present very little variance. However, the pressure gradient fluctuation around the sharp TE forces flow streamlines from the lower surface around the TE and become entrained

in the TE re-circulatory region.

7.4.2 Dependence on Reynolds Number & Turbulence Intensity

The results in this section are comparisons of an 2D SG6043 foil profile within a scaled flume as described in section 7.1. Computational experimental results are evaluated with respect lift (C_L) and drag (C_D) coefficient curves at Reynolds numbers of 73k, 63k and 43k and Ti equivalent to Lehigh University's flume experiment.

Each foil was set to have a completely smooth surface ($K_s = 0\mu m$) and a consistent 1m chord length with no alterations to the foil profile coordinates from [68]. The Summarised parameters for all cases under review within this section can be found consolidated in Table **??**.

The simulations were carried out with consistent flow input boundaries with input velocities consistent with the case Reynolds number. For each flow condition, the foil position rotated from -08° to $+18^o$ degrees to replicate the impact across an equivalent α sweep. Each instance, simulated was conducted under transient conditions for 200 seconds - allowing the model to have completely flushed through and entered developed flow conditions.

Figure 7.23 demonstrates the performance of the SG6043 foil in terms of C_L (C_L) and C_D (drag coefficient) and α.
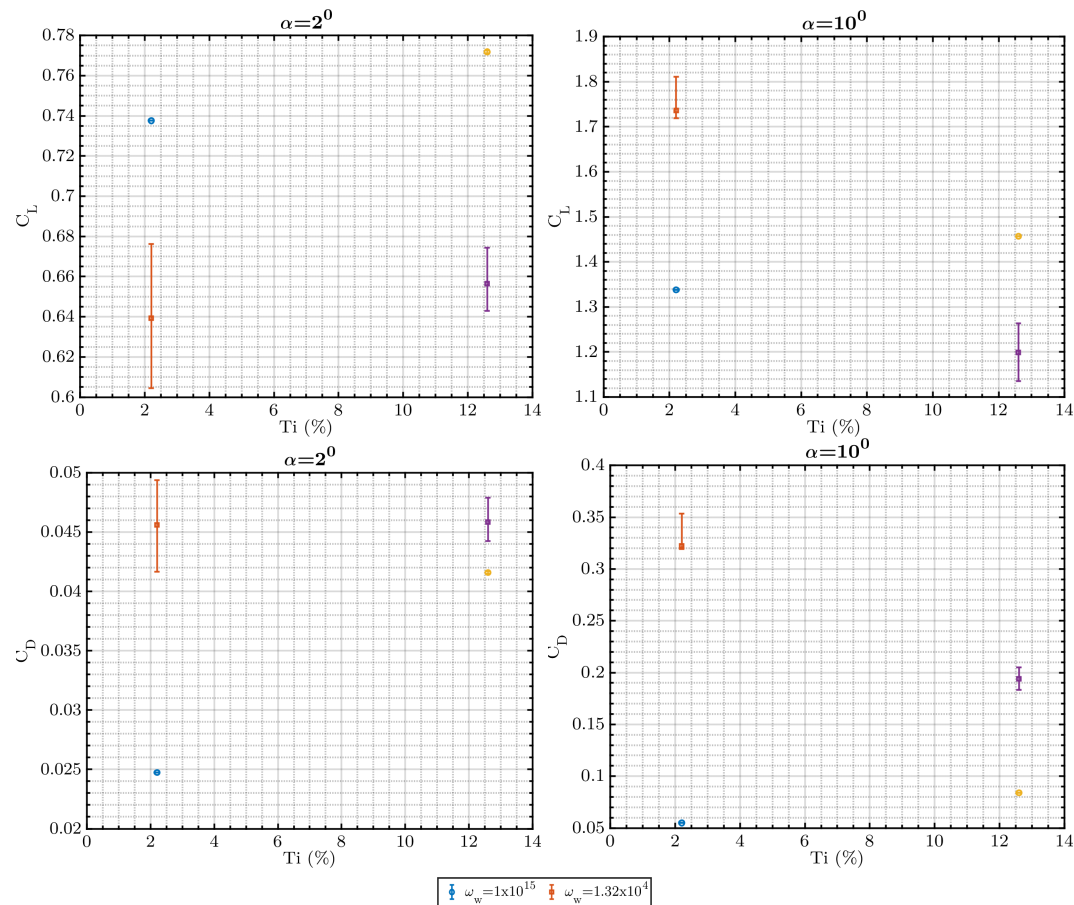
Figure 7.19: Comparison between respective ω_w fixed values of 1×10^{15} and 1.32×10^4 for Respective C_L (top) and C_D (bottom) and $\alpha = 2^o$ and $\alpha = 10^o$

The system has shown consistent reaction to changes in system variables; Increasing the turbulence intensity leads to increases in both the C_L and C_D and increasingly delayed stall. Increasing Reynolds number also leads to increases in C_L,
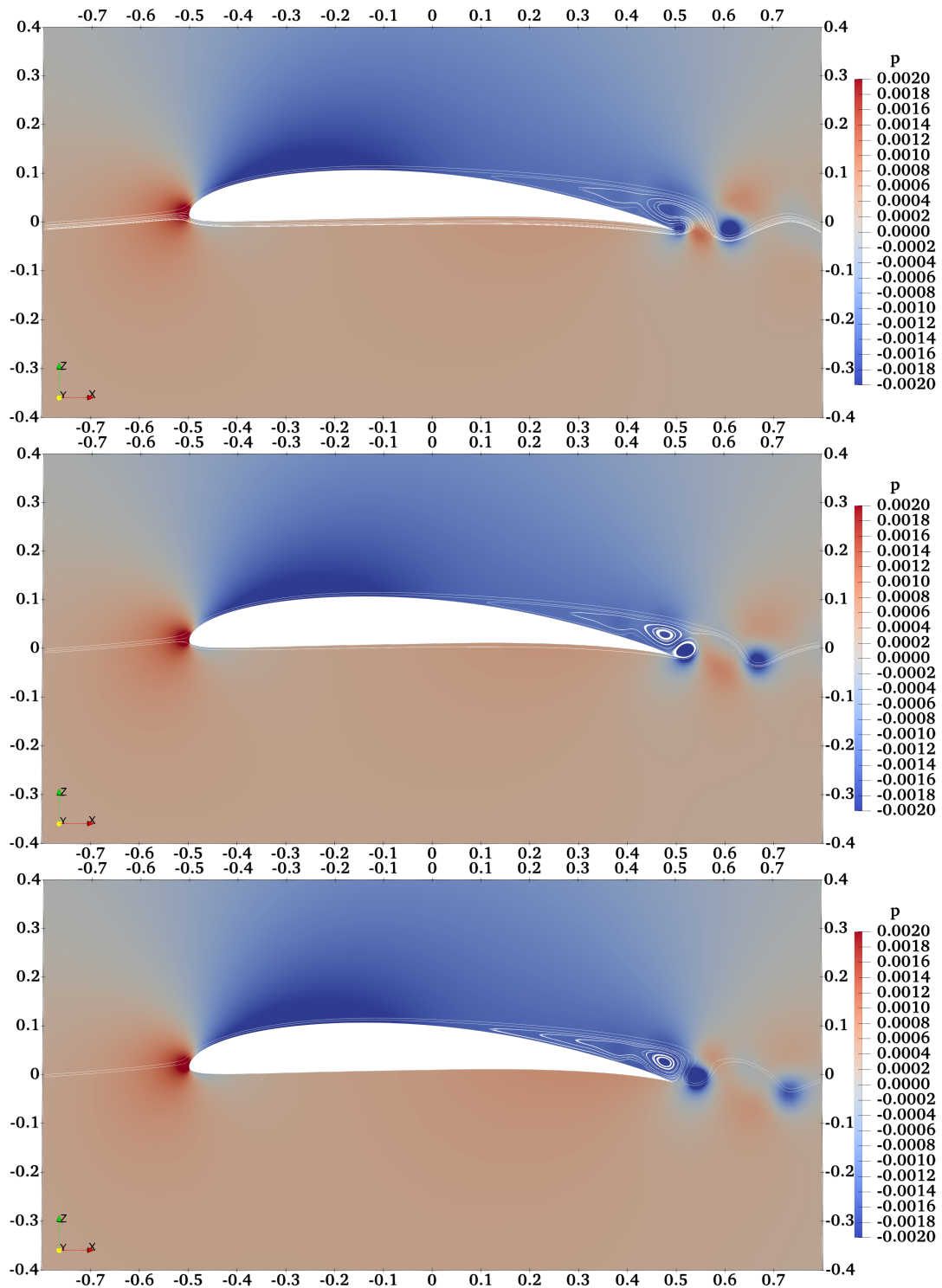
Figure 7.20: Velocity streamline and pressure contour plots displaying the eddy-shedding phenomenon. The top image presents the pressure flow-field just before the trough of the C_L oscillation. The middle image sequentially after. The bottom image shows the flow-field at the peak C_L.
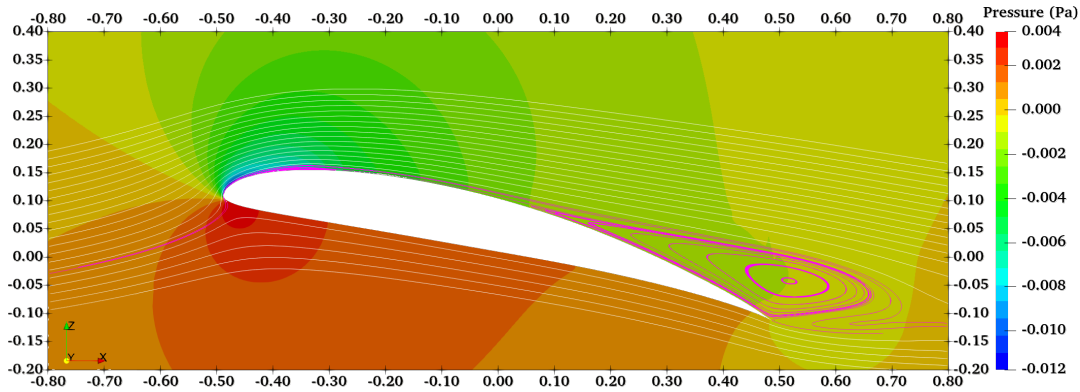
Figure 7.21: Pressure (Pa) contours complimented with flow direction streamlines around the SG6043 geometry at a α position of +13 degrees. Flow phenomena of LEB and complete boundary flow separation are highlighted with pink streamlines. Flow conditions were of a Reynolds Number of 63K.
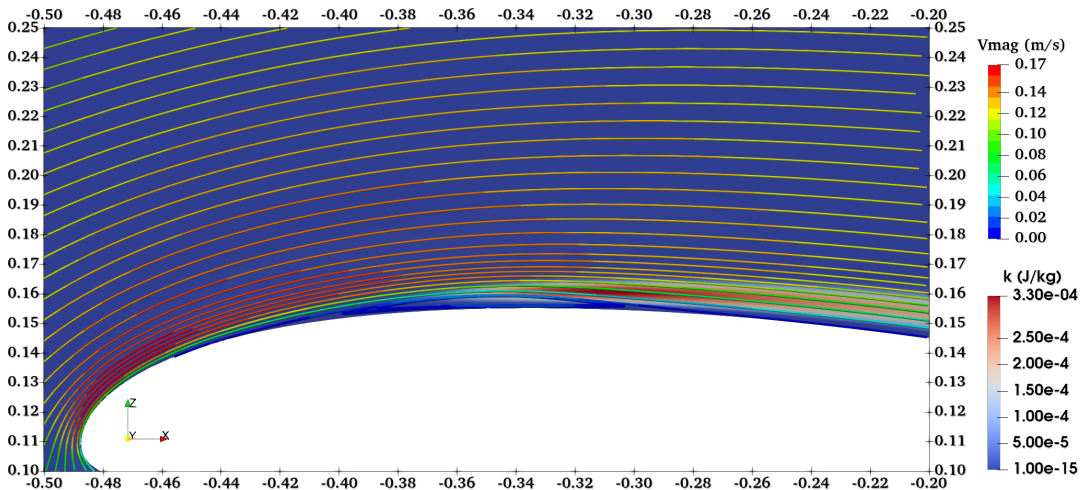
Figure 7.22: Turbulent Kinetic Energy (κ) contours complimented with velocity magnitude streamlines around the SG6043's frontal section of the upper surface. The flow conditions were instigated at a Reynolds number of 63K and an α of +13 degrees.

but reduction in the drag coefficient. When increasing C_L/C_D ratio also increases.

The highest C_L/C_D ratio was 34 for Re=73K and $T_i = 2.2\%$ and a α position of 4°. However, under those conditions the performance characteristic is sensitive to change with α - displaying a Mesokuretic characteristic. Conversely, the lowest C_L/C_D ratio was 18 for Re=43K and $T_i = 12.5\%$ and a α position between 4 and 5 degrees - displaying a more platykurtic nature.

The sensitivity to Reynolds number decreases with increasing T_i. Contrasting the Re=73K, series against the Re=63K; the C_L/C_D ratio drops by approximately 2 when $T_i = 1.5\%$. In comparison, a drop of < 1 is observed when $T_i = 12.5\%$

Conclusion

An computational fluid dynamics study into the effects of wall functions with surface roughness features on the SG6043 foil operating under a Reynolds number of
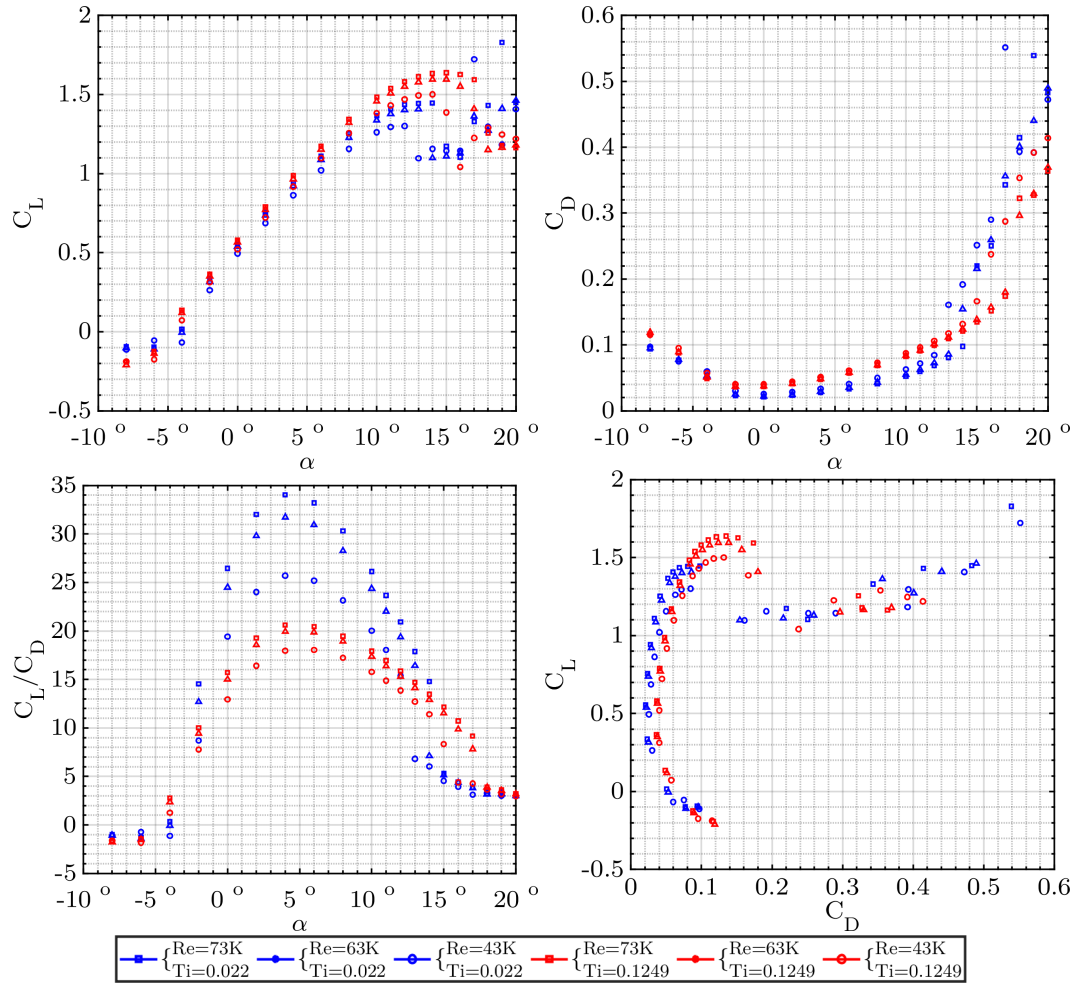
Figure 7.23: Details a combined Figure plot of C_L and C_D predicted over α sweep range -08 to$+18$ degrees and in polar configuration. Series present comparisons between $Re = [73k, 63k, 43k]$ and $Ti = [02.20\%, 12.49\%]$; Each foil has a smooth '$no-slip'$ boundary condition and fixed ω_w value of 1×10^{15}.

63,000 was under taken. The investigation used the simulated measurements of the lift and drag forces to formulate the respective lift and drag coefficients to be used as the comparative matrix. Seven parameter variations were simulated with intention to cover an envelope of equivalent roughness to the physical experimental foil against a smooth-wall representation, with additional scope to cover up to N.A.C.A standard surface roughness values; which act as a representation of the maximum surface roughness likely to be encountered with a turbine blade operation *in situ*. The results attained do not show surface roughness to be a considerable factor for foil performance across the parametrisation that fell under the current investigation. All cases showed high similarity across the full α sweep. Albeit greater difference past the estimated stall point, where simulated predictions show a high tendency for a considerable range of coefficient values. While the high similarity is suggestive of a convergence, the absence of a stall point, which can typically be witnessed with the SG6043's lift and drag plots, is absent. This causes some concern for the reliability of the results present. Despite the high similarity, the greatest difference is seen with the high surface roughness N.A.C.A standard series. While there is no consistent trend observed, the series shows a proclivity to be more volatile for α past the stall

point that is usually typical for the SG6043 foil. The series covering surface roughness values around those of Lehigh's experimental SG6043 blade so no concernable separation of data points.

Therefore, consideration into surface roughness, of the typical "polished" surface, is not of reasonable concern to progress further and spend future computational resources.

Consideration must however be brought to the C_L trend observed. The continual increase in lift beyond stall is not consistent with previous datasets of the SG6043 profile. Typical simulations of the SG6043 profile operating at similar α show evidence of flow separation and adverse velocity gradients. The continual increase in lift despite said features likely forming, heavily indicates that the boundary layer flow is not accurately being simulated. As the mechanism of how surface roughness will interact with the foil performance is through alterations to the boundary layer flow. It could be strongly argued that the results are not dependable, and that further consideration into how the boundary layer is simulated will be required.

Further Considerations

As mentioned in the Conclusion section of this chapter; how the selected wall function is able to predict the boundary layer needs to be investigated for credible results to be attained.

The degree of which surface roughness has on the boundary layer flow over the SG6043 foil may be a function of the roughness location. Literature often mentions the leading edge roughness in particular. Additionally, when operating *in situ*, the leading edge is the blade area that is most likely to come into hard contact with a foreign body. Thus, it can be understood why particular attention could be seen towards the leading edge. There is a method available where a non-uniform roughness can be implemented - as can be seen in the OpenFoam's user guide.

The location that the FST was measured was the same position as the hydrofoil before being placed in situ. The active grid turbulence generator was tweaked until the ADV would output the required FST level. The ADV was then swapped for the hydrofoil in situ. Hence the FST value was at the location of the hydrofoil. This presents a difference in model characteristic between the CFD simulation and the physical experiment as the CFD FST turbulence condition was imposed on the inlet Patch. Therefore to properly compare results, the FST depreciation rate must be predicted so that the same FST levels will be applied to both cases.

The Surface Roughness (R_a) measurements along the SG6043 hydrofoil blade are also due to be sent from the Lehigh University Team. This will further reduce the current unknowns between the CFD models and the physical experiments conducted at Lehigh University.

7.4.3   Validation

The coefficient data is validated against experimental flume data provided by Lehigh University. Which ran the flume at a Reynolds number of 73k,63k and 43k and Ti of 2.2% and 12.6%. The data that was received is thought to have been out of phase by four degrees, which has been corrected in the data presented. The original form of the data is displayed in Figure 7.2,7.3 and 7.4 in section 7.1.2 There is a consistent

over-prediction of lift approaching the stall point, and a sharper stall characteristic. However, the point of maximum lift shows greater similarity. There is an under prediction of drag for lower $Ti = 2.2\%$.

At the lower $Ti = 2.2\%$ of the CFD cases present a substantially superior C_L/C_D ratio and a more leptokurtic-shaped profile, whereas the higher $Ti = 12.6\%$ is more comparable. The Lehigh presents a more general platykurtic-shaped profile.

There is a current question to the influence that the skin friction will have on the system. With consideration to results attained from section 7.4.1 and Figure 7.19. Particularly with the low $\alpha = +2^o$,

A point to possibly note is a possible limitation with the foils construction method. Typically Aluminium sheets are folded to form the TE. However, manufacturing in such a way can prevent supporting ribs inside the TE. Without such support the integrity of the foil cross-sectional profile can become compromised should structural flexion occur - effectively modifying the foil profile [104, 142].

7.4.4 Conclusion

- The higher T_i cases are shown to perform to a higher degree than the lower T_i counterparts with respect to C_L.

- Possible confirmation that the SG6043 foil produces a delayed stall when operating under set conditions.

- initial increases in T_i are shown to have a greater bearing than subsequent increases.

- Lower T_i have a greater initial gain, though plateau at lower α.

- The performance is not possible to fully gauge at higher α due to the non-converged α case continuous across all series. However, within the near-linear region, there is a consistent trend where the higher the T_i, the higher the drag coefficient and lower the C_L.

- higher α points largely have not yet appeared to have converged.
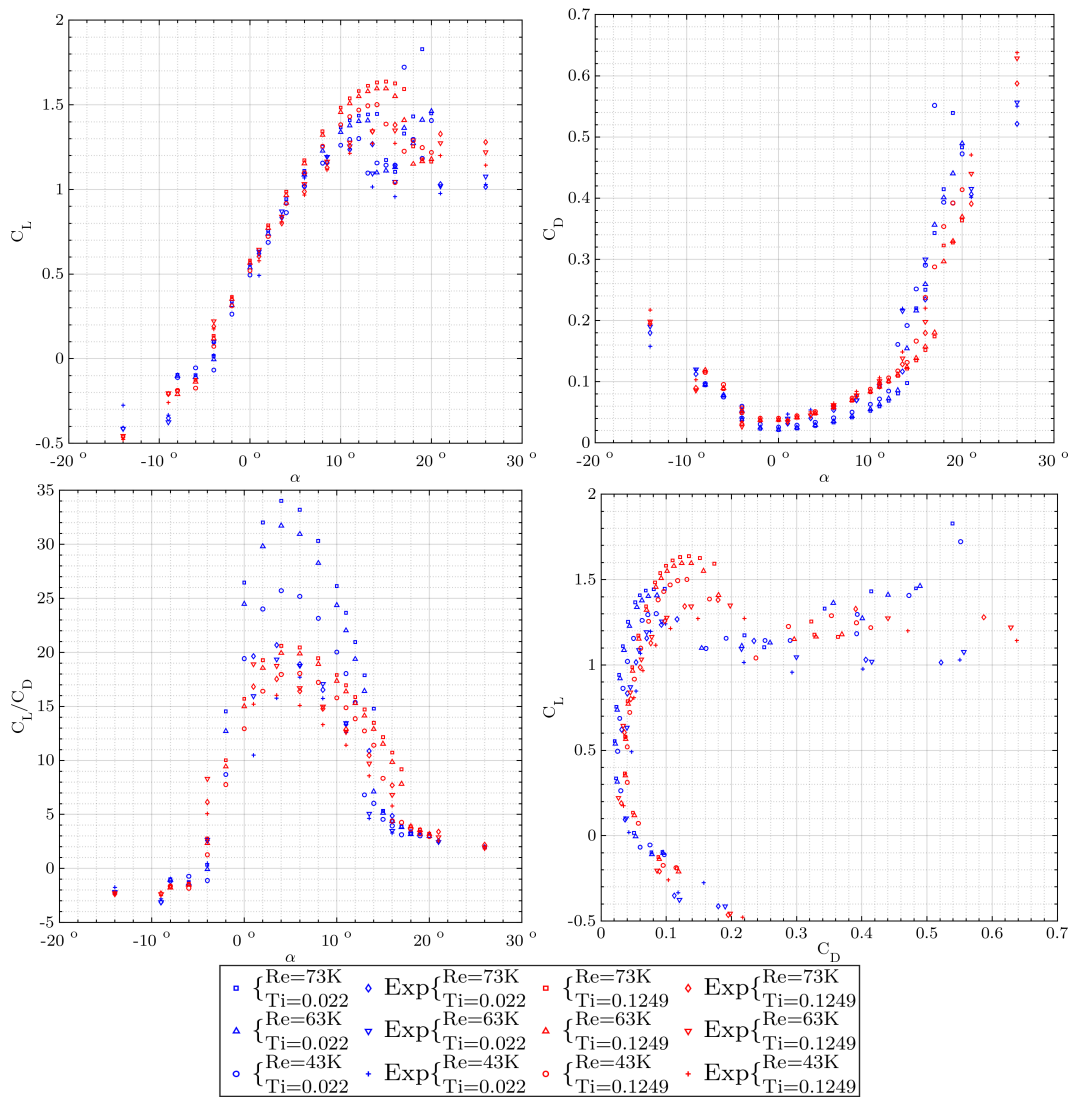
Figure 7.24: Details a combined Figure plot of C_L and C_D predicted over α sweep range -08 to $+18$ degrees and in polar configuration. Series present comparisons between $Re = [73k, 63k, 43k]$ and $Ti = [02.20\%, 12.49\%]$; Each foil has a smooth '$no-slip$' boundary condition and fixed ω_w value of 1×10^{15}.
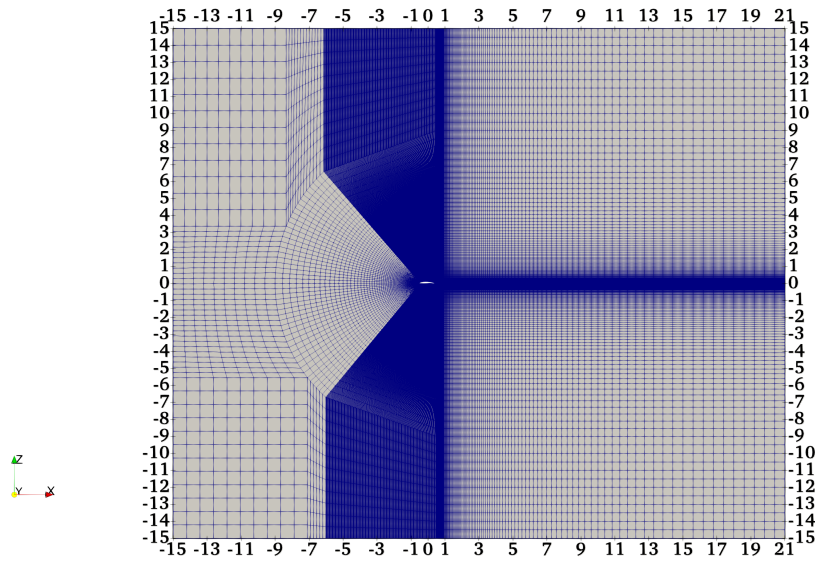
Figure 7.25: First Angle view of the Open-Flow mesh domain. The SG6043 foil is set at two degrees α with its centre-point set as the model origin. The mesh was generated through a in-house mesh parameter generation tool and OpenFOAM's 'blockMesh' utility. The mesh was refined so that there would be a $y^+ < 1$ for the first surface cell-centre - OpenFOAM solver via a cell-center approach.

7.5 Open-Flow Parametrisation

A 2D open-flow parametrisation of the SG6043 foil profile is required to remove any boundary dependant C_L or C_D characteristics, such as blockage effects, as a direct result of the relative close proximity of the flume walls.

7.5.1 Open-flow model Description

As mentioned in section 7.4.1, an independent performance parametrisation of the SG6043 foil would necessitate, an external flow regime without there being any question of reactionary flow dynamics from adjacent surfaces - which would interact with the formation of the boundary layer over the foil surfaces. Based on the simulation data provided in the Flume-flow parametrisation in section 7.4, the extent that the flume walls influence the performance parametrisation can be ascertained.

The domains defining geometric entity is kept as the normalised SG6043 foil cross-section, which is positioned centrally at the domains point of origin. Thus exists at the furthest extend from the domain boundaries, which are shown in Figure 7.25. The domain boundaries can be seen to be of dimensions 36*m* X 30*m*.

In total, within the confines of the domain boundaries, a single rectangular block of maximum and minimum bounding coordinate points of $[-15, -5.4 \times 10^{-05}, -15]$ to $[21, 5.4 \times 10^{-05}, 15]$.

All geometric entities set for the SG6043 foil profile were set in accordance to those defined under they 'Forward-most' edge definition outlines in section 7.2.2 as they were in section 7.4.

217

Initial & Boundary Conditions

The initial fluid state is set with a kinematic viscosity (ν) equal $1.3065 \times^{-06}$ $m^2 s^{-1}$, which is approximately equivalent to air temperatures of 281 degrees Kelvin [9]. The boundary conditions imposed throughout the domain on all patch surfaces were set in accordance to those specified in Table 7.8.

With respect to the domains initial condition state, the fluid was forced to be consistent with parameters specified on the inlet boundary. Thus, the fluid is injected as a uniform plug velocity flow condition at said boundary, with continuity being preserved with flow exiting out of the domain through the 'Outlet' patch.

The κ and ω are set similarly, with values according to case profile as stipulated in Table7.3. The flume walls from the equivalent flume-flow domain altered to be represented through '*inletOutlet*' patches and the flow velocity set likewise to the other '*inletOutlet*' boundary patches. The XZ-Boundary planes existing at both the maximum and minimum Y-axis values was set as empty which represent directions that are not solved during said cases. The Courant number is set to dynamically change with the simulation requirements but is limited to not exceed 0.9. The mesh is configured likewise to what is described in section **??**, though there is a departure from the specific cell height implemented in the flume-flow parametrisation, to account for the use of wall functions.

7.5.2 Boundary Independent Characterisation

The same flow condition parameters that were implemented in the section 7.4 were repeated with the Open-flow grid domain. Comparisons with the flow conditions of $Re = 63k$ and $Ti = 2.2\% \& 12.5\%$ are presented in figure 7.26 against equivalent flow parameters in the Flume-flow case.

In general the C_L and C_D performance characteristics possess a high degree of similarity between respective flow domains. However, the characteristic blockage effects resulting from increased flow velocities are plainly observed with C_L and C_D in the lower $Ti + 2.2\%$ case - with the increasing departure of coefficient values at higher α when such effects are increasingly influential with increasing blockage. Interestingly, no consistent trend is observed in higher $Ti = 12.5\%$ flow conditions with approximately consistent separation between for the α range. With the evidence at hand, the likely reason is down to the higher Ti reducing the Laminar flow layer length.

The sudden sharpness of the C_L drop in for the flume-flow case at $TI = 2.2\%$ is typically indicative of what is commonly referred to as the LE short bubble stall. Figure 7.27 confirms the existence of which through presenting the flow-field at an $\alpha = +13^o$, which coincides with the point of maximum lift. The presence of the LE bubble is indicated along the upper surface adjacent to the LE between approximately $0.05X'/c$ and $0.2X'/c$. After which the flow reattaches until the point of flow separation at approximately $0.5X'/c$. At an α between $+13^o$ and $+14^o$, flow attachment fails to take place resulting in the completely de-attached flow observed at $\alpha = +14^o$.

Table 7.8: This table displays a summary of each boundary condition specified of every boundary within the 2D flume model.

Field		Velocity (m/s)	κ (J/kg)	ω (J/kgs)	nut (Pas)	Pressure (Pa)
Initial State	Value:	uniform (* 0 0)	uniform **	uniform ***	uniform 0	uniform 0
SG6043	Type:	FixedValue	FixedValue	FixedValue	calculated	zeroGradient
	Value:	uniform (0 0 0)	uniform 1e-15	uniform 1e15	uniform 0	-
topAndBottom	Type:	inletOutlet	inletOutlet	inletOutlet	calculated	outletInlet
	Value:	uniform (* 0 0)	uniform **/0	uniform ***/0	uniform 0	uniform 0/0
Inlet	Type:	inletOutlet	inletOutlet	inletOutlet	calculated	outletInlet
	Value:	uniform (* 0 0)	uniform **/0	uniform ***/0	uniform 0	uniform 0/0
Outlet	Type:	inletOutlet	inletOutlet	inletOutlet	calculated	outletInlet
	Value:	uniform (* 0 0)	uniform **/0	uniform ***/0	uniform 0	uniform 0/0
XZ-Boundary Planes	Type:	empty	empty	empty	empty	empty

* : Denotes case dependant velocity value which can be looked up in table 7.3

** : Denotes case dependant κ value.

*** : Denotes case dependant ω value.

Figure 7.26: Details a combined Figure plot of C_L and C_D predicted over α sweep range -08 to$+18$ degrees and in polar configuration. Series present comparisons between $Re = [73k, 63k, 43k]$ and $Ti = [02.20\%, 12.49\%]$; Each foil has a smooth '$no - slip$' boundary condition and fixed ω_w value of 1×10^{15}.

7.5.3 Behaviour Under High Reynolds Number Flow Conditions

The data from this is to be compared against the SG6043 performance data presented in [145], and displayed in the previous chapters Appendix: Figure **??** and **??**.

Figure **??** shows the C_L predicted over a sweeping range of α over a range of -18° to $+18^o$, for flow conditions of $Re = 500k$ and $Ti = 3.65 \times 10^{-05}$. Additionally, comparative SG6043 experimental data procured from from [145] is included. Generally, as the α increases in a positive direction away from the neutral, a general increase in C_L is observed. The opposite is true for minus α. From -18° to -10°, there is a general increase in C_L, though the error bars show that the data points had not completely converged and there is still a substantial degree of variance. Between -10° to -4°, a plateau trend is observed where there is minimal variation in the C_Ls produced. From that point until the stalling region, a general near-linear trend is observed. Additionally, the data-points have little variance as the simulation did converge towards a small value. Within the stall region, there is a clear indication of a stall point at $+12^o$ as the series hits a maximum before the C_L decreases at an increasing rate. The data points past $+16^o$ show an increase in variance again which
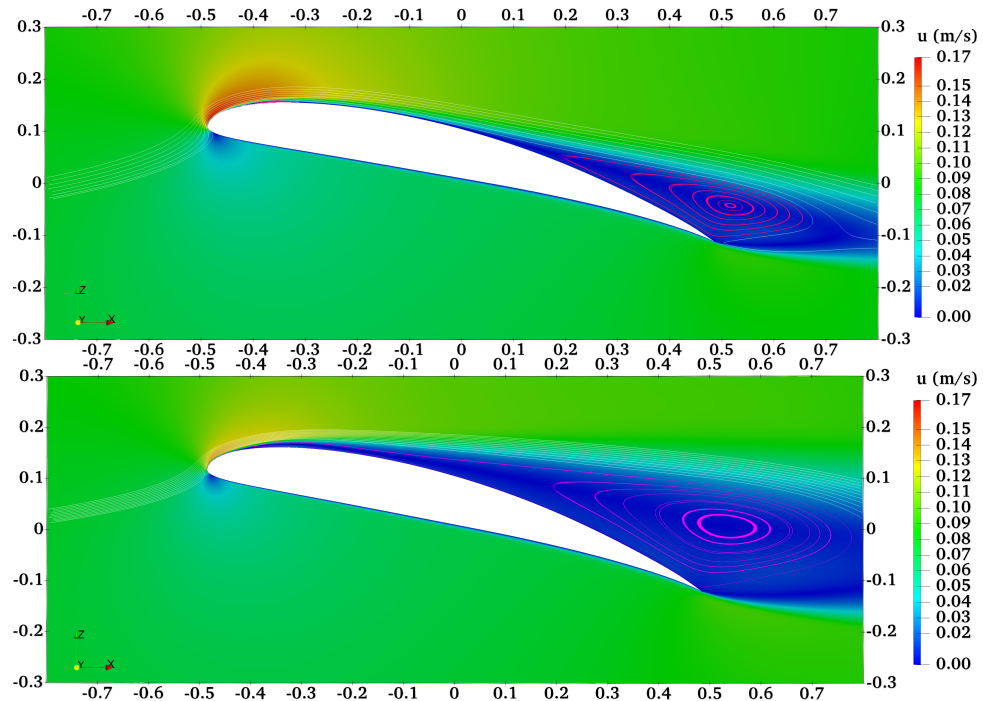
Figure 7.27: Presents an example of the LE
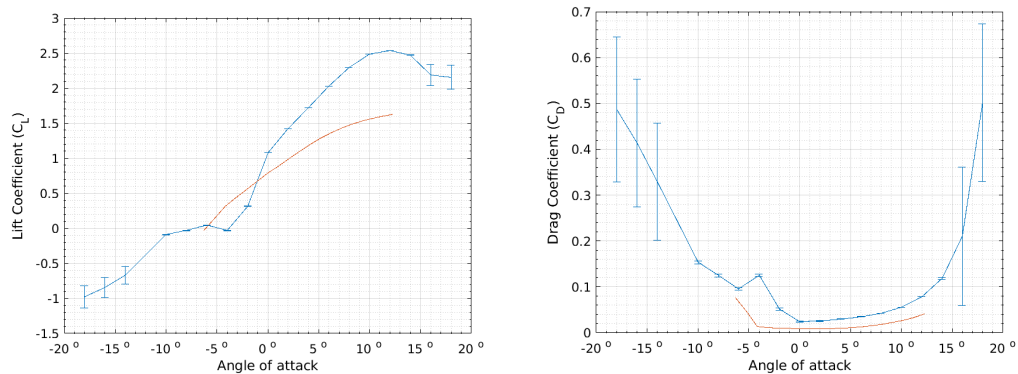
Figure 7.28: Details a series plot of C_L and C_D predicted over a sweeping range of α over a range of -18° to $+18^o$. Experimental results from [145] are included for validation purposes. The experimental data were taken with Turbulence Intensity less than 1% in a wind tunnel, has a polished fibreglass finish and collected at a Reynolds Number of 500K.

is likely produce of the increased turbulence produced from the stall characteristics.

When comparing the experimental data, there is a general over-estimation of the C_L. Though there is underestimation for the minus α. Additionally, the experimental data has a smaller positive gradient than the CFD result. As experimental data was not provided past $+12^o$, it is unclear if the stall point has been reached. However, there is a plateau trend towards that point, which could indicate that there is a similarity in the stall points. A limitation in comparing the two data sets is that there will be differences between the near 2D Open-Flow of the CFD experiment and the enclosed wind tunnel results of the experimental data. Although the experimental data was said to be corrected for blockage losses.

221

Interestingly, similar differences between the experimental data and the CFD model occurred with the validation case presented in section 7.4.3. The CFD C_L consistently and substantially over-predicts at higher α. Additionally, the aspect appears to differ with the CFD data appearing comparably squished together.

The predicted Drag Coefficients are shown in Figure **??**. Like the C_L data points, higher α has lead to un-converged data. Though the range of data points for the Drag Coefficient is far greater than for the C_L. Concerning the converged data points, past the $\pm 0^o$ α point, the series follows a largely smooth exponential increase. There is an outlying data point for the -04° data point, where the point seems to break the trend and produce higher Drag that the surrounding α until -08°. An interesting observation is that at the same point of -04°, the experimental data also exhibits a stark change in character; where there is a large gradient for increasing the minus α, and a plateau for increasing positive α before looking like it would exhibit the typical exponential growth in Drag Coefficient. From the $\pm 0^o$ α mark, there is a similarity between the CFD simulation series data and the experimental series data, though the CFD data series consistently over-predicts the Drag coefficient by 0.02 at $\pm 0^o$ to approximately 0.04 at $+12^o$. The two data-sets loose the comparative similarity for α below $\pm 0^o$. The CFD data series shows a substantial increase in drag after instantly passing the $\pm 0^o$ in the minus direction and hence the two data-sets loose the comparitive similarity as the Drag Coefficient in the experimental data series does not start to increase until the -04° point.

Section Conclusion

A comparative study of the sensitivity of the SG6043 foil profile under 2D-flow conditions and operating under near zero turbulence intensity and a Reynolds Number of 500K has been performed. The data series was then compared with experimental data from a wind tunnel operating between α of -6° and $+12^o$. Several conclusions can be drawn from the comparative results:

- The $Re = 500k$ and $Ti = 3.65 \times 10^{-05}$ case was able to produce results which on the surface appear to look as though they are correct. Albeit there are high data ranges at higher α due to un-converged results.

- When comparing the CFD and the experimental series, there is mostly an over prediction of results, albeit between -01° and -06° where the experimental series gave higher C_Ls than the CFD series.

- There was a higher similarity between the CFD and experimental results, with a similar trend to α above $\pm 0^o$. However the experimental showed a delay in the increasing Drag when operation with increasing minus α.

- increasing the T_i appears to have a diminishing influence on the performance characteristic of the C_L as it's increased since the data series converge. However, there is separation with the Drag Coefficient which would indicate that the overall performance will decrease with increasing T_i.

Validation

To validate the lift and drag coefficient dataset, a comparison is made with the experimental results published in [220, 96].

Selig *et al*. SG6043 Aerofoil data

The experimental coefficient of lift C_L and coefficient of drag C_D data was recorded in the University of Illinois at the Urbana-Champaign low-turbulence subsonic wind tunnel [96]. The tunnel test section had dimensions of 0.857m high and 1.219m wide. The turbulence intensity of the tunnel was reported to be less than 0.1% for the test Reynolds numbers. The foils tested were each 0.305m chord with a foam core and a fibreglass surface finish. The lift was measured using a strain-gauge load cell and the drag was predicted from the average of four different span-wise wake surveys. Both measurements were estimated to have 1.5% uncertainty. The measurements were also corrected for the wind-tunnel interference through validating against data collected from NASA Langley low turbulence pressure tunnel [156, 98]. Zig-zag trips were used to simulate the leading edge roughness effects.

The numeric data was attained for uses of validation against equivalent Reynolds Numbers in the current CFD experimentation. Tabulated results can be seen in Appendix **??**, Figure D.1. The Drag polar and C_L plots of the data-sets are presented in Figure **??**. The Reynolds Number's stipulated in the data-set does not have an the exact match with that presented in the Figure - which were rounded.

7.5.4 Coefficient Surface Mapping

In relation to the *Raison D'etre* of this investigation. The primary motivation behind the project is to develop numerically efficient approaches to simulating HATT. The GAD system requires accurate foil coefficient data with respect to flow conditions to functionally perform. A significant drawback becomes apparent with the additional computational cost, that comes with generating a coefficient library for a particular foil section; that is robust enough to cater for the various flow-conditions that a HATT will encounter while $in-situ$.

A computationally cost effective approach to the matter could be to form a coefficient surface map, where a select number of 2D flow parametrisation simulations provide anchors for interpolation of points to produce a surface. Figure 7.29 presents a coefficient surface generated for a $Re = 63k$ and $Ti = 1.05\% : 20\%$.

7.5.5 Conclusion

A parametric study of the sensitivity of the SG6043 foil profile under various 2D-flow conditions has been performed to date. Several general conclusions can be drawn from the CFD predictive results: for the investigation going forward:

- There was a consistent series of un-converged results outside the -2° to $+10^o$ α case range. This is due to the slow convergence rate of cases with higher α with respect to the internal simulation time.
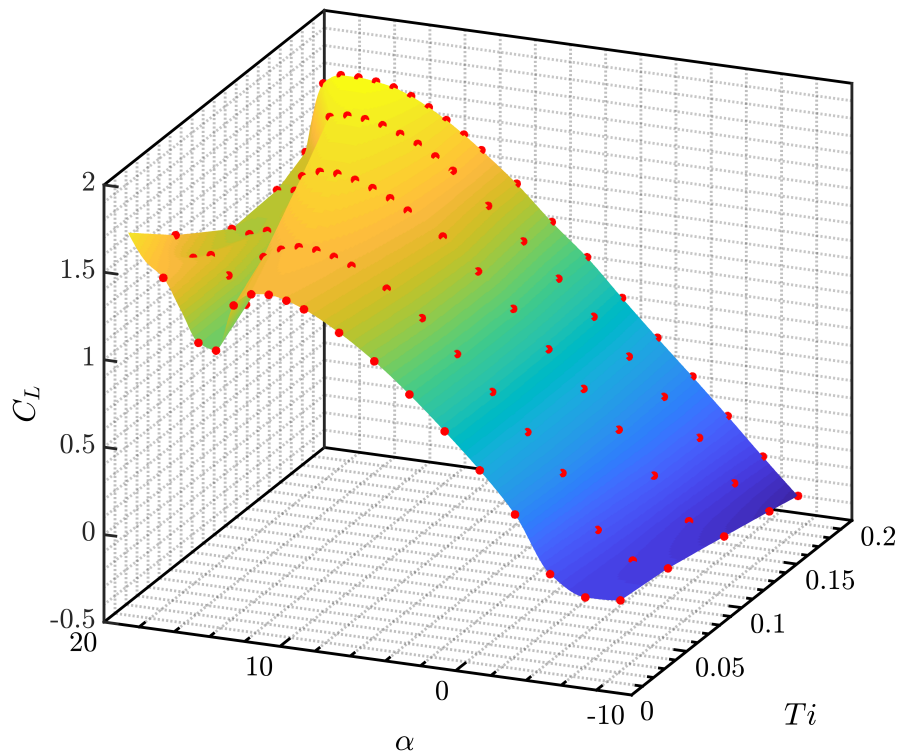
Figure 7.29: Presents an example of the coefficient surface generated for the Re=63k. Special weighting was applied to account for the stall delay characteristics.

- The slower convergence rate when operating at higher α is compounded with the simulations also having a considerably longer clock time for the same simulation time.

- Higher α cases do look like convergence could be reached, or the variance to considerably reduce. However, as the α deviates away from the neutral, the likelihood of convergence being reached diminishes.

- Higher Reynolds Numbers results in a consistent increase in simulation times.

- The lower Reynolds Number cases do not appear to have as much C_L drop-off past the stall region.

Chapter 8

3D Flume-GAD Implementation

8.1 Summary

This Chapter covers the implementation and current results of the GAD (Generalised Actuator Disk) plug-in used in conjunction with OpenFoam's SimpleFoam solver for a 3D HATT (Horizontal Axis Tidal Turbine) case.

Firstly the an overview of the GAD Plug-in and how it is implemented, then the CFD model characteristics are described. The succeeding sections cover the mesh sensitivity, comparisons to previous plug-in versions such as BEAD, then finally the 2D lift/drag coefficient data from the 2D flume cases and comparisons to those with the BEMT data.

8.2 Introduction

The purpose of GAD is to seek to accurately represent the dynamic interaction between the fluid and the turbine while being computationally cost effective. This includes accurate turbine performance data etc, and downstream wake representation for array comparison case studies. Thus, areas adjacent to and within the blade-box and the downstream wake, require adequate refinement to meet the level of accuracy necessary for the GAD method to be feasible for the proposed research purposes.

The case study can briefly be described as a independent replicate of the experimental flume model presented in [73], albeit replacing the Blade Element Momentum CFD (BEM-CFD) turbine representation with the GAD system.

The objective of this case study is to correlate the implemented GAD system with experimental results from the laboratory flume at Lehigh University; Additionally, to compare with previous BEM-CFD results and evaluate the extend to which the GAD system addresses previous BEM-CFD model limitations.

8.3 GAD Test Case study: Lehigh Flume

8.3.1 Experimental Basis

The comparative basis for this study can be seen in the paper by A.Vinod and A.Banerjee [255] where their experiment is discussed in further detail that the content below.

The turbine is classified as a three-blade tidal turbine model of 1:20 scale, with a sweep area of 0.2794m.

The blades were constructed from corrosion resistant Aluminium alloy, which was machined to the shape of the SG6043 foil with a chord length of 0.0165m.

8.3.2 Model Description

The case study computational model comprises of external fluid dynamic flow around representational features of a HATT turbine and nacelle body; which itself exists as internal flow domain, within the confines of representational flume walls defined within a single rectangular block with maximum and minimum bounding coordinate points of [-0.908, -0.3048, -0.2499] : [1.073, 0.3048, 0.2499]. Thus, replicates a total domain volume of 1.981m x 0.6096m x 0.4998m respectively to the x,y and z Cartesian coordinate system.

The blade-box, is positioned centrally within the domain, where the mid-point of the central axis intersects domain point of origin. The blade box is not representative of a solid geometric surface, but a conceptual sectioned area spanning a radial sweep of 0.14m and thickness of 0.04m. The GAD operates through the sweep area
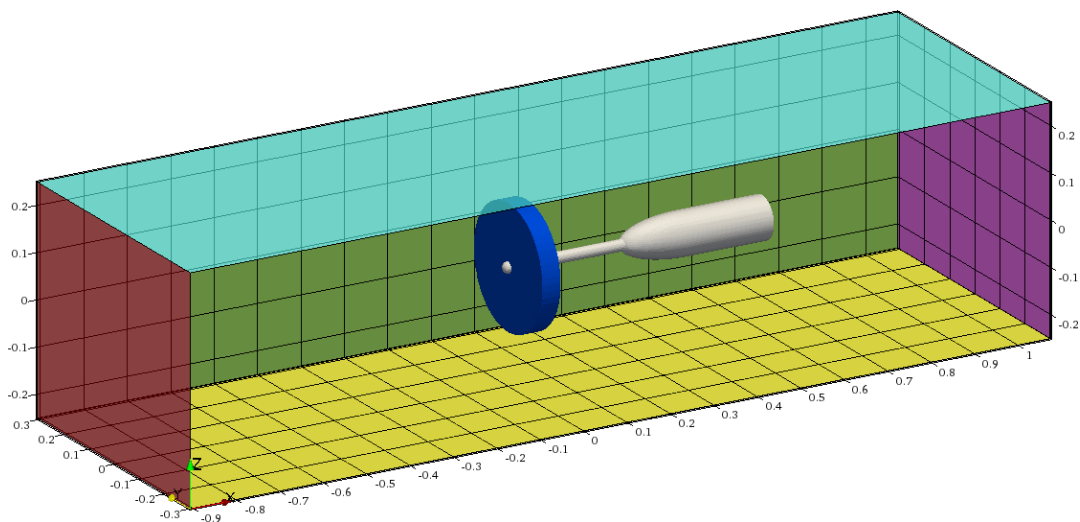
Figure 8.1: An image coordinating each boundary surface with an associated colour for the 3D GAD-Flume model. The Blade box (dark blue) is placed with its centre as the model origin point across all x,y and z axis. Unlike the other surfaces, the blade box is not representative of a surface but an source term. The nacelle (white) is a solid wall that is positioned without accompanying supporting tower. The Inlet (red) and Outlet (purple) are diametrically opposed along the X-axis. The flume walls (Green, yellow & transparent). The upper surface (light blue).

interacting with the incident flow as a source term.

The defining geometric body is that of a combined and simplified nacelle and protruding shaft of 0.6m length and symmetrical around its central axis - which runs parallel to the domain's X-axis and positioned at the origin points of th Z and Y-axis. The shaft protrudes 0.012m in-front of the blade-box area and is rounded to form a rotor hub. The shaft extends 0.24m downstream from the blade-box to the nacelle. At which point, the shaft radius of 0.0125m is filleted to the nacelle radius of 0.095m. The nacelle exists without the supporting tower structure. The absence of which limits the presence of additional turbulent hydraulic features within the domain; which only initiates additional complexity, rather than contribute to the assessment of the GAD model operating under CFD generated foil coefficient data. A to-scale, colour coordinated schematic presentation of the domain is shown in Figure 8.1.

Initial & Boundary Conditions

The domain's initial fluid state is set with a kinematic viscosity equal to $1.4 \times^{-06}$ m^2s^{-1} and set to a velocity of $0.84ms^{-1}$ in the X-axis direction. The boundary conditions imposed of all domain patch surfaces were set to accordance to those specified in Table 8.1.

The fluid through the domain was forced to be consistent with the initial conditions. Thus, fluid is injected as a uniform plug velocity at the 'Inlet' boundary and exits at the 'Outlet' patch through a 'zero-gradient' condition.

The kinetic energy (κ) and the turbulence dissipation rate (ε) are set similarly at $9.375 \times 10^{-04}m^2s^{-2}$ and $9.8 \times 10^{-05}m^2s^{-3}$ respectively. The conditions described contribute to a turbulence intensity (Ti) of 3% at the inlet, which drops to approximately 1% at the blade box section.

The flume walls are represented through solid wall patches listed as the 'Bottom', 'Y-plus', 'Y-minus' and are set as 'noSlip', fixing the flow velocity at $0.0ms^{-1}$. Wall functions are also employed to estimate a un-resolved boundary layer. The nacelle and shaft surfaces are set likewise, albeit differing in wall-functions; since the surface cell sizes are below appropriate y^+ for standard wall-function implementation criteria of $30 < y^+ < 200$. The alternative Spaldings wall-function can be used to predict the boundary layer through all regions existing $y^+ < 300$; providing equivalent representation across the viscous sub-layer, small under prediction within the buffer layer, and a small over prediction in log-law region.

The experimental flume had a free-surface, which is modelled through the 'Upper' patch surface being set to a slip condition - acting to be approximately equatable, though without the additional computational intensity that is synonymous with a free-surface.

Mesh Configuration

The mesh was constructed with a combination of OpenFoam's built in blockMesh and snappyHexMe through sequentialsh utilities. The mesh is configured as being of the hierarchical hexahedral type - structured to be refined through levelled subdivisions of the domain towards areas interest, notably being the blade box, nacelle and

Table 8.1: This table displays a summary of each boundary condition specified of every boundary within the model.

Field		Velocity (m/s)	κ (J/kg)	ε (J/kgs)	nut (Pas)	Pressure (Pa)	Force Field (N)
Initial State	Value:	uniform (0.84 0 0)	uniform 2.3814E-04	uniform 8.626E-06	uniform 0	uniform 0	uniform (0 0 0)
Nacelle	Type:	noSlip	zeroGradient	epsilonWallFunction	nutUSpaldingWallFunction	zeroGradient	slip
	Value:	-	-	uniform 0	uniform 0	-	-
Flume-wall	Type:	noSlip	kqRWallFunction	epsilonWallFunction	nutkWallFunction	zeroGradient	slip
	Value:	-	uniform 0	uniform 0	uniform 0	-	-
Inlet	Type:	fixedValue	fixedValue	fixedValue	calculated	zeroGradient	slip
	Value:	uniform (0.84 0 0)	uniform 2.3814E-04	uniform 8.626E-06	uniform 0	-	-
Outlet	Type:	zeroGradient	zeroGradient	zeroGradient	calculated	fixedValue	slip
	Value:	-	-	-	uniform 0	uniform 0	-
Ceiling	Type:	slip	slip	slip	slip	slip	slip

228
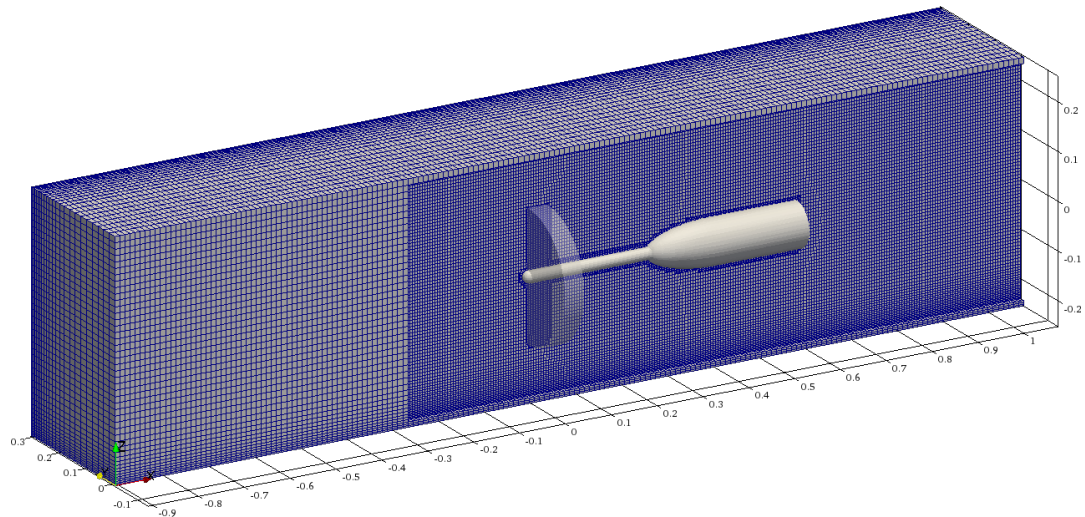
Figure 8.2: An image of the 3D GAD-Flume model sectioned across the X-Z plane. The nacelle body is shown in solid white with the blade box shown similarly albeit with a degree of transparency. The mesh grading within the model domain is featured. The base mesh division is shown between coordinate points of [-0.908, -0.175, -0.175] : [-0.3, 0.175, 0.175]. Outside which and towards the flume edges the mesh is graded to account for boundary layer formation. The mesh is not graded towards the upper surface. The approach to the blade box and the downstream section are shown with level 2 grading. The mesh is refined to level 3 around the blade box and the nacelle body. The mesh is again further refined within the blade box area to level 4.

the downstream wake region. The mesh cells was also graded towards the Flume-Wall surfaces to account for boundary layer formation along the solid wall. Initial cell heights are set to be within the non-dimensional $30 < y^+ < 200$ range.

Where a transient simulation would instigate characteristically volatile turbulent wake features, steady-state averaging does not require equivalent cell refinement. Though considering computational simulation optimisation, refinement with respect to the base cell size is still required downstream, since the consistently straight flow of the upstream ambient fluid requires little refinement with respect to the fluctuating velocity field within the downstream wake. The downstream wake region is encapsulated within a cylindrical area of 0.24m radius, and extends to the Outlet boundary. Cells are also refined 0.27m in front of the 'blade-box' to capture the changes in the velocity field induced through blockage effects.

The wake region is refined by a factor of two from the base cell size. The adjacent cells of three layers thick to the nacelle and shaft are further refined through a divisional factor of four of the base mesh. Within the blade-box, the cells are subdivided a divisional factor of six, with a intermediary layer of two cells thickness and a divisional factor of four. The structured mesh grading is shown in Figure 8.2.
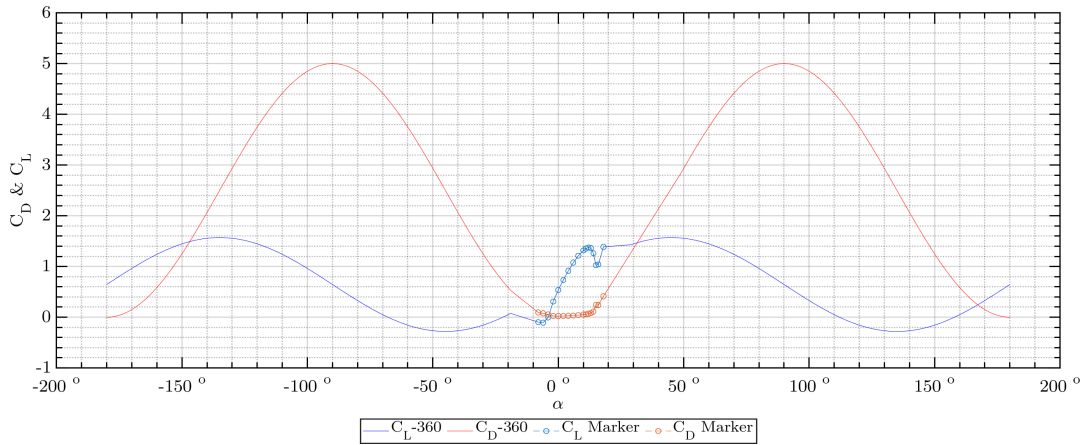
Figure 8.3: A combined C_L and C_D plot of the SG6043 foil through the full 360 degrees α. The Solid colour lines represent the predicted coefficient values. The data is constricted with 2D CFD simulation anchor points for both the C_L and C_D shown through circular markers.
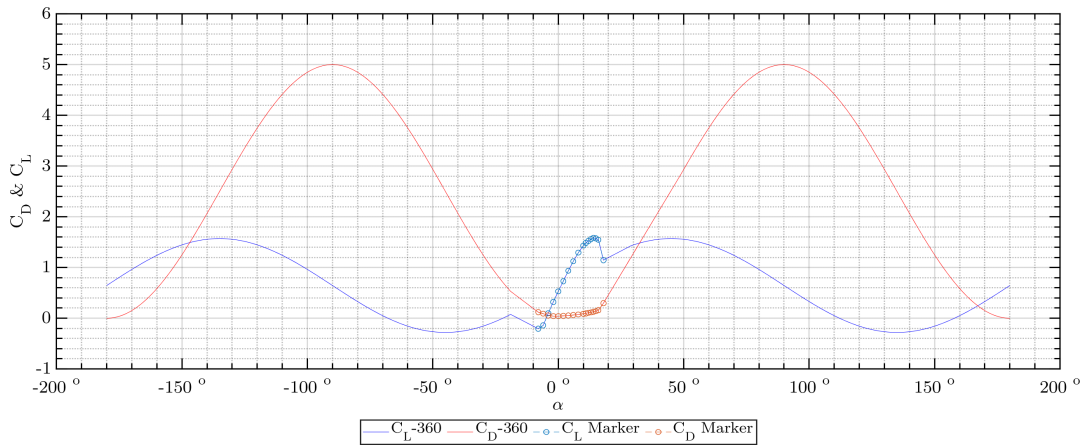
Figure 8.4: A combined C_L and C_D plot of the SG6043 foil through the full 360 degrees α. The Solid colour lines represent the predicted coefficient values. The data is constricted with 2D CFD simulation anchor points for both the C_L and C_D shown through circular markers.

360 Data Collection

Mesh Sensitivity

Confidence in the mesh refinement was demonstrated in attained results from an mesh dependence study. While it was reported in [72, 73] that a mesh sensitivity study has previously been carried out with the flume model of identical parameters, with the additional application of a new plug-in, it of good practice to carry out an independent mesh sensitivity study to validate the claim. The mesh was varied through incremental differences of [36 9 9] base divisions in the x,y and z respective directions. The summative mesh characteristics for each mesh are presented in Table 8.2. Each of the mesh cases are generated using identical structuring as set out in Section 8.3.2.

The first attributes to be considered are coefficients related to turbine perfor-

Table 8.2: Summary table of the mesh sensitivity base mesh divisions.

Mesh	Base Divisions	Total Number of cells
Mesh 1	[36 9 9]	9134
Mesh 2	[72 18 18]	78552
Mesh 3	[108 27 27]	242901
Mesh 4	[144 36 36]	559124
Mesh 5	[180 45 45]	1071408
Mesh 6	[216 54 54]	1935440
Mesh 7	[252 63 63]	3022348
Mesh 8	[288 72 72]	4441908

mance under set operational criteria. With the objective of HATT being to extract energy from flowing water, the coefficients of power (C_P) and thrust (C_T) are relevant measures of the efficiency of such.

With respect to both power (C_P) and thrust (C_T); across the operational conditions tested, a coefficient convergence of $< 1\%$ percentage error was achieved with Mesh Base Divisions (MBD) greater than 144 (Figure8.5).

The limiting factor with respect to performance coefficients, is shown to be C_P when operating at higher TSR conditions, notably beyond the associated peak-performance. Thus, should be the first point of consideration to validate the mesh under a given operating condition.

The question of optimum mesh density with respect to computational cost, is not particularly relevant. All meshes featured produced a converged result within the set iteration limit of 3000, with the finest doing so in little over an hour and the 144 MBD in 0.05 hr's.

The second attribute for consideration is that of the velocity variation around the blade-box near-field and downstream length. Figure 8.6 illustrates the location of select positions detailed in Table 8.3 within the domain; where velocities under the TSR conditions of 3,4,5,6, and 7 are extracted (Figure 8.7).

The velocities at the specified points show various degrees of convergence. However, several points did not meet criteria across all meshes. With respect to velocity points with convergence, the highest BMD was 216.

Convergence was attained across all meshes with respect to P1, which showed a velocity drop of approximately 0.8 (m/s) from the input flow velocity of 0.84 m/s - a likely function of the rotors blockage effect. Positions P2:P6 had show a general negative trend with increasing TSR. At a TSR of 3, no discernible velocity trend with respect to down stream position is shown. With an increasing TSR of 4 and 5, a trend of positive increase emerges with downstream distance with greater dispersion between positions. With a TSR of 6, P4 is shown to have undergone a greater velocity decrease. Antithetically, P2 showed a smaller velocity decrease; resulting in the positions amalgamating. Large velocity drops across all positions are shown for a TSR of 7.

P8 and P9 did not attain convergence, with both positions exhibiting a negative gradient as mesh density increased. P7 reached convergence for TSR of 5 and lower.

When comparing against mesh sensitivity studies completed in [72, 71], similar

convergence profiles can be between the two both studies.
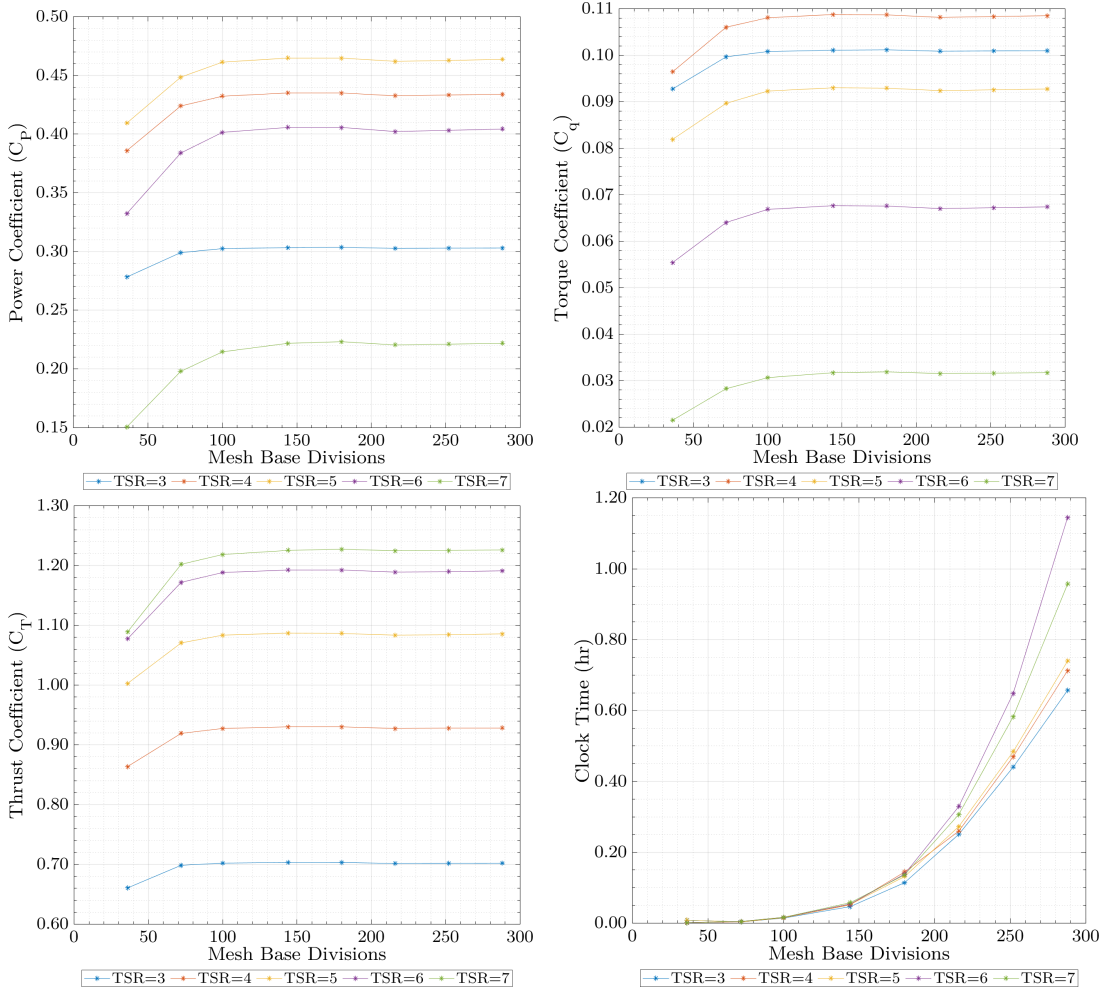
Figure 8.5: Coefficients of power (C_P) and thrust(C_T) against the base mesh divisions along the domain's X-axis, for a range of TSR operational conditions. Additionally, simulation clock time with respect to the mesh base divisions.
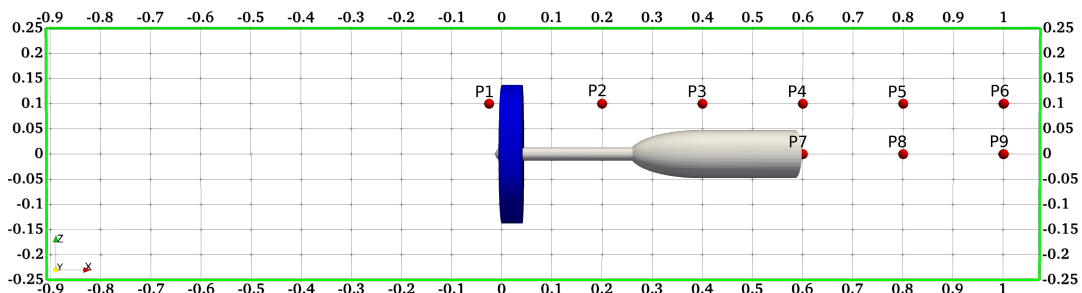
Figure 8.6: This schematic figure shows the position of the velocity points relative to the blade-box, nacelle and the model domain with respect to the ZX plane. Coordinate positions of each point can be seen in Table8.3.

Table 8.3: Cartesian coordinate position of the velocity reference points, with meter unit lengths.

Axes	P1	P2	P3	P4	P5	P6	P7	P8	P9
X	-0.025	0.2	0.4	0.6	0.8	1.0	0.6	0.8	1.0
Y	0.0	0.0	0.0	0.0	0.0	0.0	0.0	0.0	0.0
Z	0.1	0.1	0.1	0.1	0.1	0.1	0.0	0.0	0.0

8.3.3   Results & Discussion

8.3.4   Conclusion

8.4   Further Considerations
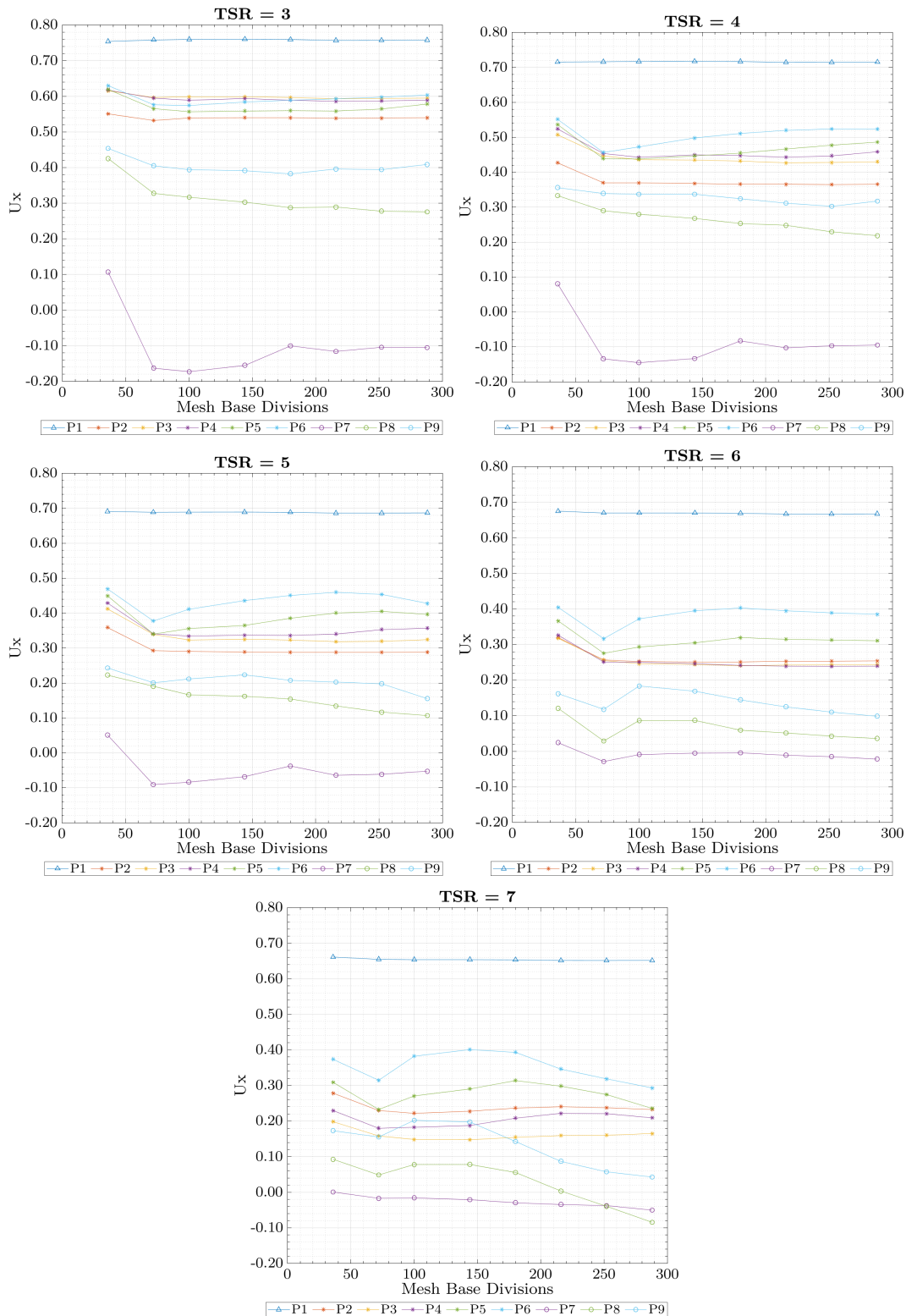
Figure 8.7: Point velocity (U_X) at set locations specified in Table 8.3, against the base mesh divisions along the domain's X-axis, for a range of TSR operational conditions.

Part IV

Conclusions

Chapter 9

Synthesis

Technological development, as a concept is near infinite in capacity.

Each objective outlined within this thesis, acts as an individual part of a complex whole - being the development of tidal range and tidal stream schemes analysis through CFD methods.

This thesis contains research work from two distinct streams as outlined in Part I, Section **??**.

The fundamental aim of the research involving the proposed Swansea Bay Tidal Lagoon, Part II, was to improve the representation of tidal range schemes when utilizing current CFD modelling methods. In striving towards that goal, several objectives were set out to be achieved during the research process that went into the production of this thesis document.

The main objectives of Part II :

- Model the far-field tidal forcings around the United Kingdoms, welsh and English coastlines.

- Coastal for accurate spatial velocity vector application on coastal models with smaller length scales.

9.1   Swansea Bay Tidal Lagoon Conclusion

9.1.1   Main outcomes

The tidal regime over the North West Continental Shelf was simulated over a period of 22 days. The simulation took approximately 14 days until visible instabilities ceased from being present within the measured sections of the model. There was good agreement between the simulated water levels and those recorded at six location or the UK's National Tide Gauge Network, with respect to measured level and tidal forcing phase. However, the hydrographic model does appear to under predict the maximum tidal level. There are several possible hypothesised reasons as to why this is relating to either the mesh coarseness or wetting and drying functions. Since this feature has only currently been observed over two sites, further investigation could reveal if its an artefact of the two sites or a continuous issue within the model. In summary, further measurements and a fully post-processed dataset would act to

clarify the current situation within the model. However, the general high agreement with measured data provides confidence that only several small tweaks would be required to solve any issues.

The tidal regime over the North West Continental Shelf was simulated over a period of 22 days. The simulation took approximately 14 days until visible instabilities ceased from being present within the measured sections of the model. There was good agreement between the simulated water levels and those recorded at six location or the UK's National Tide Gauge Network, with respect to measured level and tidal forcing phase. However, the hydrographic model does appear to under predict the maximum tidal level. There are several possible hypothesised reasons as to why this is relating to either the mesh coarseness or wetting and drying functions. Since this feature has only currently been observed over two sites, further investigation could reveal if its an artefact of the two sites or a continuous issue within the model. In summary, further measurements and a fully post-processed dataset would act to clarify the current situation within the model. However, the general high agreement with measured data provides confidence that only several small tweaks would be required to solve any issues.

9.1.2 Future Research Work

The next stage in the process would be too further the progress with the nested models. The higher resolution mesh could possibly rectify the under prediction or the high tide currently observed with in the model, while also not significantly increasing the computational expense. After such, Lagoon or barrage representations could be implemented and tested to provide a bench mark for future development when incorporating the CFD parametrised sub-grid.

The next stage in the process would be too further the progress with the nested models. The higher resolution mesh could possibly rectify the under prediction or the high tide currently observed with in the model, while also not significantly increasing the computational expense. After such, Lagoon or barrage representations could be implemented and tested to provide a bench mark for future development when incorporating the CFD parametrised sub-grid.

9.2 SG6043 Aerofoil 2D Performance

9.2.1 Main outcomes

An computational fluid dynamics study into the effects of wall functions with surface roughness features on the SG6043 foil operating under a Reynolds number of 63,000 was under taken. The investigation used the simulated measurements of the lift and drag forces to formulate the respective lift and drag coefficients to be used as the comparative matrix. Seven parameter variations were simulated with intention to cover an envelope of equivalent roughness to the physical experimental foil against a smooth-wall representation, with additional scope to cover up to N.A.C.A standard surface roughness values; which act as a representation of the maximum surface roughness likely to be encountered with a turbine blade operation $in - situ$. The results attained do not show surface roughness to be a considerable factor for aerofoil

performance across the parametrisation that fell under the current investigation. All cases showed high similarity across the full AOA sweep. Albeit greater difference past the estimated stall point, where simulated predictions show a high tendency for a considerable range of coefficient values. While the high similarity is suggestive of a convergence, the absence of a stall point, which can typically be witnessed with the SG6043's lift and drag plots, is absent. This causes some concern for the reliability of the results present. Despite the high similarity, the greatest difference is seen with the high surface roughness N.A.C.A standard series. While there is no consistent trend observed, the series shows a proclivity to be more volatile for AOA past the stall point that is usually typical for the SG6043 foil. The series covering surface roughness values around those of Lehigh's experimental SG6043 blade so no concernable separation of data points.

Therefore, consideration into surface roughness, of the typical "polished" surface, is not of reasonable concern to progress further and spend future computational resources.

Consideration must however be brought to the lift coefficient trend observed. The continual increase in lift beyond stall is not consistent with previous datasets of the SG6043 profile. Typical simulations of the SG6043 profile operating at similar AOA show evidence of flow separation and adverse velocity gradients. The continual increase in lift despite said features likely forming, heavily indicates that the boundary layer flow is not accurately being simulated. As the mechanism of how surface roughness will interact with the foil performance is through alterations to the boundary layer flow. It could be strongly argued that the results are not dependable, and that further consideration into how the boundary layer is simulated will be required.

A parametric study of the sensitivity of the SG6043 foil profile under various 2D-flow conditions has been performed to date. Several general conclusions can be drawn from the CFD predictive results for the investigation going forward. There was a consistent series of un-converged results outside the -2° to $+10^o$ AOA case range. This is due to the slow convergence rate of cases with higher angles of attack with respect to the internal simulation time. The slower convergence rate when operating at higher angles of attack is compounded with the simulations also having a considerably longer clock time for the same simulation time. Higher AOA cases do look like convergence could be reached, or the variance to considerably reduce. However, as the AOA deviates away from the neutral, the likelihood of convergence being reached diminishes. Higher Reynolds Numbers results in a consistent increase in simulation times.

9.2.2 Future Research Work

As mentioned in the Conclusion section of this chapter; how the selected wall function is able to predict the boundary layer needs to be investigated for credible results to be attained.

The degree of which surface roughness has on the boundary layer flow over the SG6043 foil may be a function of the roughness location. Literature often mentions the leading edge roughness in particular. Additionally, when operating $in-situ$, the leading edge is the blade area that is most likely to come into hard contact with a foreign body. Thus, it can be understood why particular attention could be seen to-

wards the leading edge. There is a method available where a non-uniform roughness can be implemented - as can be seen in the OpenFoam's user guide.

9.3 3D Flume Model

9.3.1 Main outcomes

9.3.2 Future Research Work

Appendices

Appendix A

Coordinate Systems

There are several geographic coordinate systems in use to define global position:

- Spherical coordinate system - Latitude,Longitude and Elevation

- Cartesian coordinate system - x,y & z

- Orthometric height

- Mean Sea Level

- Easting and Northings

While the Earth is typically thought of as a sphere, it's actual shape is a more complex entity. For the purposes of geo-positioning, the Earth's shape is often simplified to the closest geometric shape - biaxial ellipsoid. But since it's an approximation, there are multiple geometric ellipsoids that have been implemented, some for the best fit globally, others for regional. There has been effort to create a standard for cross-national compatibility. However, many nations have previously developed their own mapping coordinate systems which are still in use today.

Latitude, Longitude and Ellipsoid Height is the most common coordinate system utilized. A point on Earths surface is defined through two angles of latitude and longitude which describe a ellipsoid that has been approximately fitted to the Earth. As mentioned before, multiple earth-fitted ellipsoids exist, so the spherical coordinates must be matched with the correct ellipsoid. The lines of latitude and longitude are also referred to as parallels and meridians respectfully. The system is based of the prime meridian, also called the Greenwich meridian, which acts as the longitudinal origin. Points within 0-180 degrees either side are divided into either eastern or western hemispheres. The latitudinal origin is the equator. Likewise, points are divided based on the side of the equator; either 0-90 North or 0-90 South. Elevation is simply perpendicularly referenced from the ellipsoid surface. Though since the reference ellipsoid can both be above or below the actual surface, ellipsoid height is distinct from surface elevation.

The Cartesian coordinate coordinate system conveys the same position using three spatial dimensions of x,y and z perpendicular axes. The origin of which is at the centre of the ellipsoid.

As with the spherical coordinate system, the Cartesian coordinates are ellipsoid specific. Equivalent coordinates can be calculated between the two systems. If different coordinate data is based from different ellipsoids, equivalents can be determined through applying a transformation.

When considering how to determine altitude or Orthometric height, a single point position is referenced against an geometric entity - from which all measurements are based off throughout the world. The shape would be similar to that of an ellipsoid, but defined by being perpendicular to the direction of gravity, rather than geometrics resulting in the Geoid. The reason for this is because the gravitational direction varies at both global and local scales, rather than simply being directly towards the Earth's centre. Like the various ellipsoids used for coordinate reference systems, there are several geoids' that are used globally as height references; again due to independent development and the arbitrary nature of selecting a singular energy level of the gravitational field. A common choice is that of the mean sea-level (MSL) as being the reference. Despite being difficult to measure with the fluctuating water levels of the worlds oceans, it is the best fit for global compatibility.

Local maps are based of the MSL taken from local tidal gauges rather than the global average ocean level. The local references are considered to be parallel to the global geoid, just varyingly offset from it. The UK uses such a system with select locations shown in Figure 3.4. The local systems are referred to as Chart datum. Newlyns MSL is used as a standard called Ordnance Datum Newlyn (ODN) vertical coordinate system; which is essentially a local geoid that the Chart datums are relative to.

Eastings and Northings, also called the plane coordinate system and the grid coordinates; are coordinates based on map projection - a 2D surface of a 3D object. This coordinate system is most often applied alongside the Ordnance Survey National Grid and the Universal Transverse Mercator (UTM); both of which use the Mercator projection. There are always inherent distortions when projecting a 3D curved surface onto a 2D plane that are unique to each projection. Thus the projection type must always accompany the Easting and Northing coordinates.

A.1   Conversion of Coordinate Type

The frame of reference is a pivotal aspect when comparing datasets from various geographical locale. The two principle coordinate systems encountered are that of latitude and longitude, and the Universal Transverse Mercator (UTM); based on ellipsoidal and cylindrical coordinates systems respectfully.

A.1.1   Converting between 3D Cartesian and Spherical coordinates

3D Cartesian coordinates can be converted to equivalent latitude, longitude and ellipsoidal height coordinates through the following equations:

With the ellipsoid constants, the semi-major axis length a and semi-minor axis length b, the eccentricity squared e^2 can be calculated by:
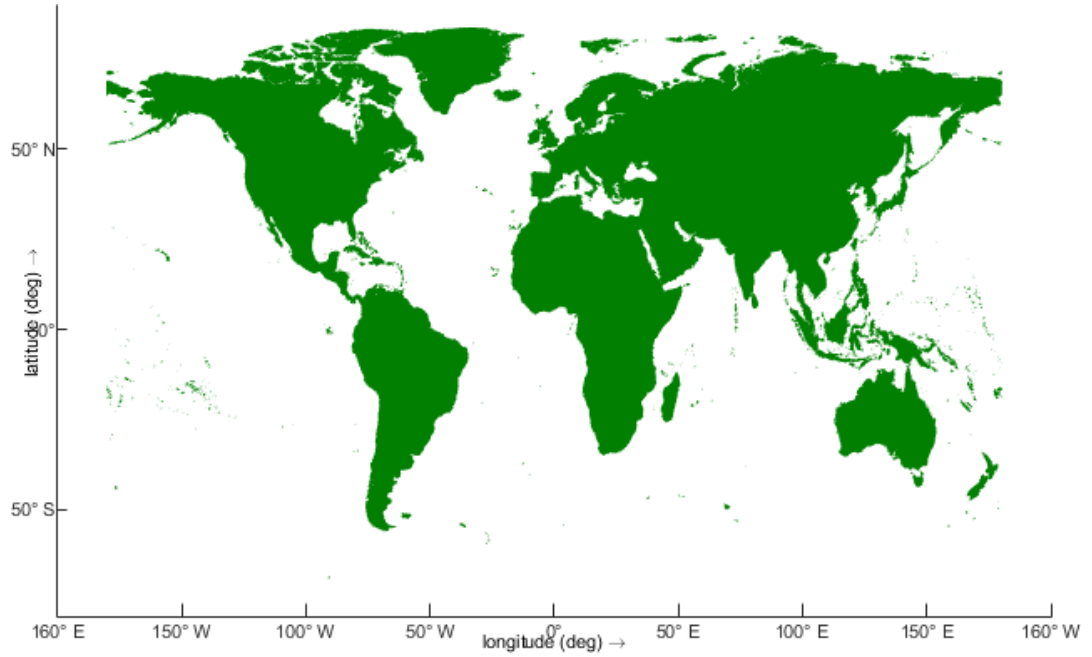
Figure A.1: Complete High-resolution World Vector Shoreline (WVS) polygon data set.

$$e^2 = \frac{(a^2 - b^2)}{(a^2)} = 2f - f^2 \tag{A.1}$$

The Cartesian coordinates x,y and z through:

$$\nu = \frac{a}{\sqrt{1 - e^2 sin^2 \varphi}} \tag{A.2}$$

$$x = (\nu + H)cos\varphi cos\lambda \tag{A.3}$$

$$x = (\nu + H)cos\varphi sin\lambda \tag{A.4}$$

$$z = ((1 - e^2)\nu + H)sin\varphi \tag{A.5}$$

Latitude, longitude and ellipsoidal height coordinates can be converted to equivalent 3D Cartesian coordinates through the following equations:

$$\lambda = arctan\left(\frac{y}{x}\right) \tag{A.6}$$

$$\varphi = arctan\left(\frac{z}{(x^2 + y^2)^{0.5}(1 - e^2)}\right) \tag{A.7}$$

φ is continually iterated by through substituting Equation A.8 into Equation A.2, then:

$$\varphi = arctan\left(\frac{z + e^2 \nu sin\varphi}{(x^2 + y^2)^{0.5}}\right) \tag{A.8}$$

until the change in φ is smaller than the intended precision of the spherical coordinates. Ellipsoid height can then be calculated by:

$$H = \frac{(x^2 + y^2)^{0.5}}{cos\varphi} - v \tag{A.9}$$

A.1.2 Conversion of Easting and Northing coordinates and ellipsoidal latitude and longitude

Conversion of a coordinate position given from latitude and longitude coordinates (φ, λ) to easting and northing coordinates (E, N) of Mercator projection can be done through the following equations:

With the ellipsoid constants, the semi-major axis length a, semi-minor axis length b and eccentricity squared e^2; and the projection constants of Northing of true origin N_0, Easting of true origin E_0, scale factor on central meridian F_0, latitude of true origin φ_0 and longitude of true origin and central meridian λ.

$$n = \frac{(a-b)}{(a+b)} \tag{A.10}$$

$$v = aF_0(1 - e^2 sin^2\varphi)^{-0.5} \tag{A.11}$$

$$\rho = aF_0(1 - e^2)(1 - e^2 sin^2\varphi)^{-1.5} \tag{A.12}$$

$$\eta^2 = \frac{v}{\rho} - 1 \tag{A.13}$$

$$M = bF_0 \begin{pmatrix} \left(1 + n + \frac{5}{4}n^2 + \frac{5}{4}n^3\right)(\varphi - \varphi_0) \\ -\left(3n + 3n^2 + \frac{21}{8}n^3\right)sin(\varphi - \varphi_0)cos(\varphi + \varphi_0) \\ +\left(\frac{15}{8}n^2 + \frac{15}{8}n^3\right)sin(2(\varphi - \varphi_0))cos(2(\varphi + \varphi_0)) \\ -\frac{35}{24}n^3 sin(2(\varphi - \varphi_0))cos(2(\varphi + \varphi_0)) \end{pmatrix} \tag{A.14}$$

$$I = M + N_0 \tag{A.15}$$

$$II = \frac{v}{2}sin\varphi cos\varphi \tag{A.16}$$

$$III = \frac{v}{24}sin\varphi cos^3\varphi(5 - tan^2\varphi + 9\eta^2) \tag{A.17}$$

$$IIIA = \frac{v}{720}sin\varphi cos^5\varphi(61 - 58tan^2\varphi + tan^4\varphi) \tag{A.18}$$

$$IV = v\cos\varphi \tag{A.19}$$

$$V = \frac{v}{6}\cos^3\varphi \left(\frac{v}{\rho} - \tan^2\varphi\right) \tag{A.20}$$

$$VI = \frac{v}{120}\cos^5\varphi \left(5 - 18\tan^2\varphi + \tan^4\varphi + 14\eta^2 - 58(\tan^2\varphi)\eta^2\right) \tag{A.21}$$

$$N = I + II(\lambda - \lambda_0)^2 + III(\lambda - \lambda_0)^4 + IIIA(\lambda - \lambda_0)^6 \tag{A.22}$$

$$E = E_0 + IV(\lambda - \lambda_0) + V(\lambda - \lambda_0)^3 + V(\lambda - \lambda_0)^5 \tag{A.23}$$

$$e^2 = \frac{((a^2) - (b^2))}{(a^2)} \tag{A.24}$$

Converting easting and northing (E, N) coordinates with the Mercator projection to latitude and longitude (φ, λ) coordinates:

$$\phi' = \frac{(N - N_0)}{(aF_0)} + \phi_0 \tag{A.25}$$

Then M from equation A.14, though substitute φ' for φ. Should the absolute value of $N - N_0 - M > 0.01$, then:

$$\phi'_{new} = \frac{(N - N_0 - M)}{(aF_0)} + \phi_0 \tag{A.26}$$

Then continually iterate M by substituting φ' in for φ until the absolute value of $N - N_0 - M < 0.01$. Compute ρ, v and η^2 using equations A.11, A.12 and A.13.

$$VII = \frac{\tan\varphi'}{2\rho v} \tag{A.27}$$

$$VIII = \frac{\tan\varphi'}{24\rho v^3}(5 + 3\tan^2\varphi' + \eta^2 - 9(\tan^2\varphi')\eta^2) \tag{A.28}$$

$$IX = \frac{\tan\varphi'}{720\rho v^5}(61 + 90\tan^2\varphi' + 45\tan^4\varphi') \tag{A.29}$$

$$X = \frac{\sec\varphi'}{v} \tag{A.30}$$

$$XI = \frac{\sec\varphi'}{6v^3}\left(\frac{v}{\rho} + 2\tan^2\varphi'\right) \tag{A.31}$$

$$XII = \frac{\sec\varphi'}{120v^5}(5 + 28\tan^2\varphi' + 24\tan^4\varphi') \tag{A.32}$$

$$XIIA = \frac{sec\varphi'}{5040v^7} \left(61 + 662tan^2\varphi' + 1320tan^4\varphi' + 720tan^4\varphi'\right) \qquad (A.33)$$

$$\varphi = \varphi' - VII(E - E_0)^2 + VIII(E - E_0)^4 - IX(E - E_0)^6 \qquad (A.34)$$

$$\lambda = \lambda' + X(E - E_0) - XI(E - E_0)^3 + XII(E - E_0)^5 - XIIA(E - E_0)^7 \qquad (A.35)$$

There are limitations of simple datum transformations. The methodology used does not take into account the local distortions present in coordinate reference frames.

A.2   Determination of Coordinate system

The point referencing system is based on the World Geodetic system of 1984 (WGS 84). WGS 84 consists of a 3D Cartesian coordinate system with a reference ellipsoid, altitude data and a geoid. The parameters of the reference ellipsoid (Table A.1) list the semi-major axis ellipsoid, the flattening factor, the nominal mean angular velocity and the geocentric gravitational constant. The WGS 84 system is aligned with that of the International Reference Terrestrial System (ITRF2008), which helps ensure unity for scientific comparison.

The coordinate system was set to spherical (decimal degrees) coordinates as the model covers large regional scales rendering the Cartesian coordinate system ineffective as neither the curvature of the earth or the Coriolis force is not taken into account.

The British National Grid (BNG) is a system of geographic grid references that encompasses the UK

The Universal Transverse Mercator coordinate system (UTM)

Table A.1: The defining parameters of the WGS 84 ellipsoid[169, 166, 167].

Parameter	Notation	Value
Semi-major Axis	a	6378137 m
Flattening Factor	1/f	298.257223563
Nominal Mean Angular Velocity	ω	$7292115x10^{-11}$ rad/sec
Geocentric Gravitational Constant	GM	$3.986004418x10^{14}$ m^3/sec

Appendix B

Lagoon Geometry

All lagoon geometry is based from to-scale representation from engineering drawings available to the public at the National Infrastructure Planning website [242, 241, 240, 189]. Specific examples are displayed in Figure B.1 and B.2 for both the internal and external geometries respectfully.

The dimensions were conveyed through the application of the image processing tool ImageJ [200], which can be used to attain dimensions to the nearest scale pixel of the image. Thus dimensions can be taken from drawings with limited length quantifications and then used to construct representative models through Solidworks CAD software.

Said models were then held as .stl files to be used in conjunction with Open-FOAM's internal tools BlockMesh and SnappyHexMesh to construct the simulation domains.

Figure B.1: Cross-sectional cut of the Turbine housing along the draft tube length
[241].
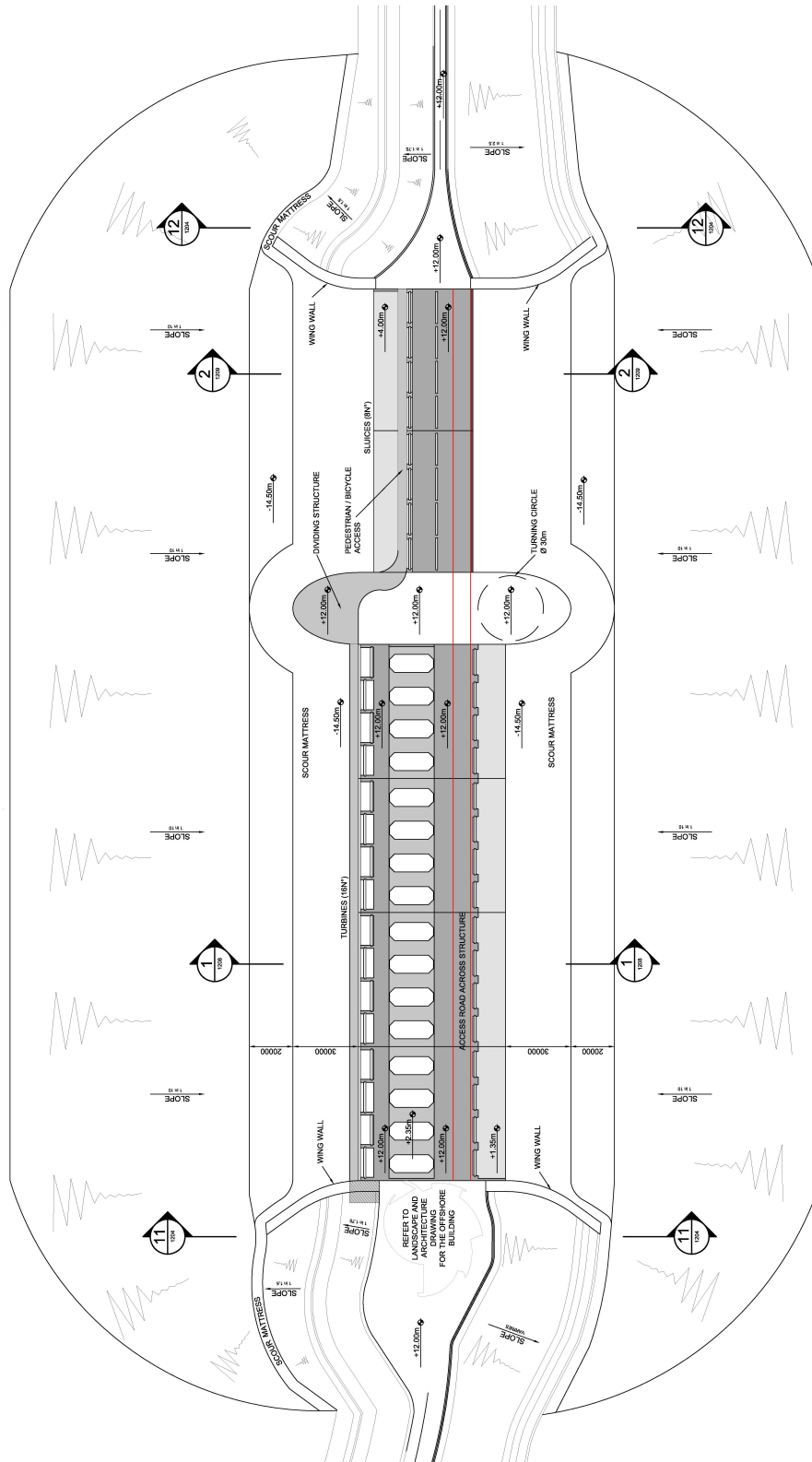
Figure B.2: Top-down view of the turbine housing and surrounding scour mattress [240].

Appendix C

Core Computation Test

Parallel computing can be described as a type of computation process where calculations are carried out simultaneously in discrete but interacting cores. Large problems are essentially divided up into several smaller problems and simultaneously solved. This contrasts with the more traditional computing which can be referred to as series computing; a problem is discretised and processed through a single CPU unit, where one task is executed before the next task in a sequential manner until the entire complex system is calculated. Computational intensity is a crucial factor in numerical analysis. Modern projects require high computational performance to carry out increasingly intensive tasks. Without parallelisation, high performance computing is near impossible at the rates demanded by the academic and commercial world [33].

The fundamental aim of parallel processing is to decrease the computation clock time through spreading the computational load as efficiently as possible across as many cores as possible; hence the "speed-up" is a common measure of the parallel processing performance over the original Computation. It is measured as a ratio between the clock times using a single processor and the clock times of simulations with N processors [33, 57]. In an idealised scenario, the computation speed-up would be linear. Double the allocated CPU's, half the computation time. This idealised scenario is often not realised when the discretised sections are not equally assigned, or communication delays/disruption between cores exchanging information [57]. The speedup algorithm for a computing system is given through Amdahl's law. The core function of which is to show that the parallel computation does not run at 100% efficiency. In summary, the more cores that are used the lower the effectiveness that each core computes at. Eventually, a plateau point is reached. Increasing the number of cores past which will have no effect on computational speedup. The STDT model was ran on Swansea universities HPC cluster with varying number of cores (Table 3). The computation clock times for each case were then used to calculate speed-up and the percentage time reduction for each case.

Figure (C.1) shows a combined comparison plot of the calculated speed-up factors for both the actual measured speed-up and the calculated Amdahls Law speed-up:

$$S_A = \frac{1}{(1 - P_E) + P_E / C_n} \tag{C.1}$$

Where S_A = Amdahls speedup, P_E=Parallel efficiency and C_N= number of cores.
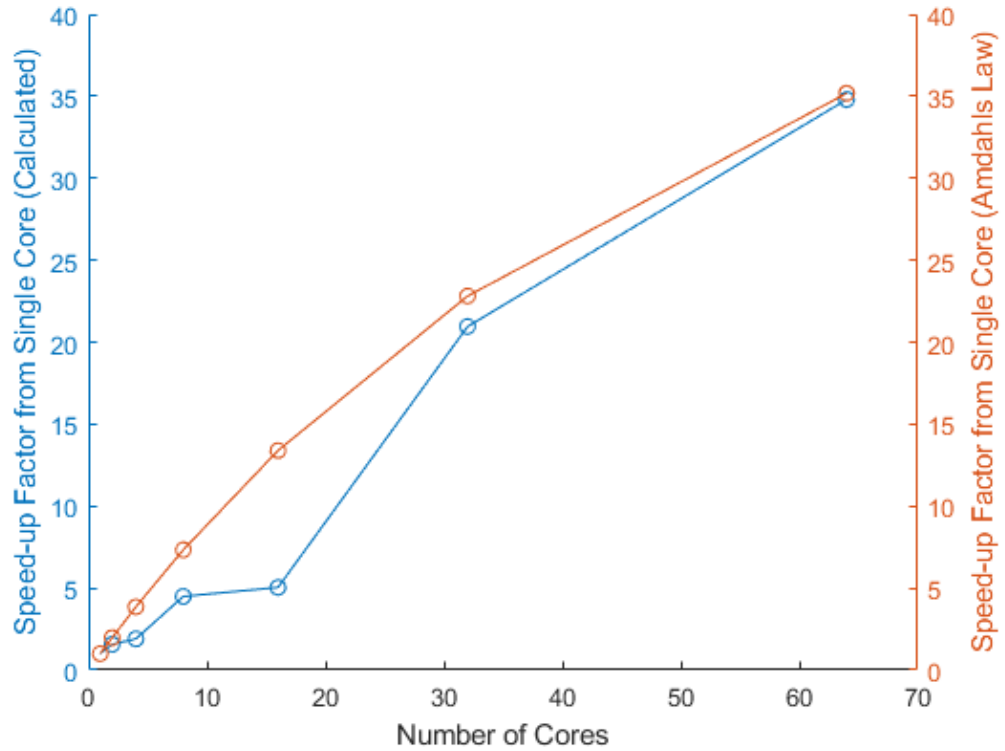
Figure C.1: Parallel speed-up factors relative to a single core for both the measured speedup (blue) and a curve fitting based on Amdahl's Law with a parallel efficiency of 0.987 (orange).

Table C.1: Table showing relation between the Number of computational cores and the simulation Clock Times

Number of Cores	1	2	4	8	16	32	64
Clock Time (hrs)	19.02	12.15	10.02	4.23	3.78	0.91	0.55

Parallel efficiency values were selected on a trial and error basis, through subbing the estimated values into Equation (4). Then a Amhdals speed-up vs core number graph curve was plotted against the measured speed-up curve. The Parallel Efficiency value found to plot a curve closest to that of the measured speed-up was selected to be Swansea Universities HPC cluster parallel efficiency. The parallel efficiently of the system used with the STDT model was calculated to be 0.987 (3.dp). The speed-up investigation did not extend to the point where a clear plateau is seen, however substituting values into the equation can be an effective method for gauging the optimum number of cores to use to reduce computation times. The measured speed-up line deviates away from the predictive Amhdals speed-up line with 16 cores. The operating hardware details have not been made available, however, the deviation in the trend could be down to the breaching the total number of cores in a single processor. Forcing the cluster system to spread the computational load over multiple systems, which could introduce extra communication delays. A possible reason that the effect was less pronounced as the number of cores increased could
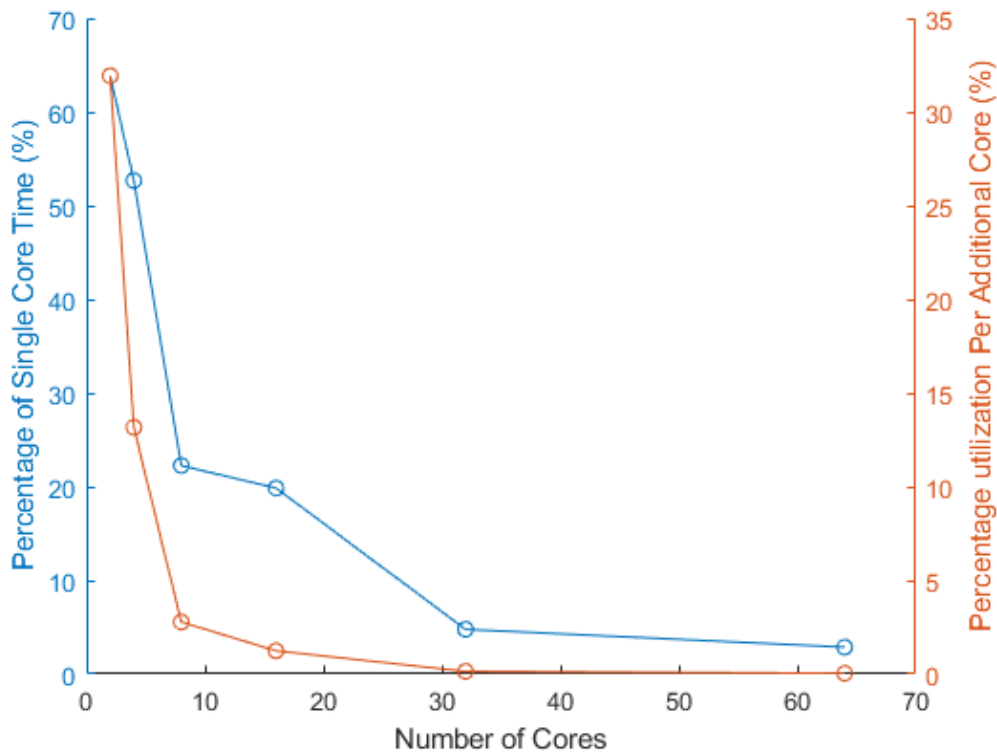
Figure C.2: Shows a combined plot of the percentage of the single core processing time and the percentage utilisation per additional core.

also be put down to the smaller, spread-out load each core had to compute. This allowed the 'scotch' mesh tool more freedom to intelligently spread the work load, so that effective computation sequencing could be achieved. Essentially reducing the possibility for the computation process to be held up by dependencies.

Figure (C.2) shows the percentage of the single core with increasing number of computation cores, as well as the percentage utilisation per additional core. The graph indicates the intuitive notion that as the number of active computational cores increase, the computation time reduces. The effect of diminishing returns can also clearly be seen as the rate of percentage reduction is not linear to the increase in number of computing cores. While applying Amdhals law did converge in a plateau and therefore reveal the ideal trade off point. The Percentage reduction does however show a clear convergence. From the graph, there is no reason why a greater number of cores than 32 cores should be used for the computation of the STDT model. However, the STDT model consists of the fewest elements out of the models tested during this study. This aspect could mean that the optimum number of cores could be higher for models with a greater number of elements. A counter perspective could be that the small difference between 32 and 8 core computational times, would mean there is little point with being pedantic while choosing an optimum number of cores based on the computational time alone. A greater problem could arise with the HPC cluster system being overloaded with simulation applications from numerous models and running out of memory, either booting the model or refusing to initiate. Selecting a smaller number of cores could decrease this chance and potentially save research time in the long run.

Appendix D

SG6043 Coefficient Data

??

Table D.1: Tabulated Lift & Drag coefficient data operating at a **Reynolds Number of 6.3X10^4** and an **Turbulence intensity of 1.5%**. The experimental foil used for this data collection had a chord length of 0.0762m and the flume flow velocity was 0.82m/s.

AOA	CL	CD	CL/CD
-20	-0.5106	0.2687	-1.9003
-15	-0.4144	0.1678	-2.47
-10	-0.2597	0.0916	-2.835
-5	0.3532	0.0464	7.6146
0	1.036	0.0495	20.9198
5	1.5613	0.0707	22.0743
7.5	1.6538	0.0915	18.077
9	1.731	0.1119	15.4754
10	1.7346	0.1303	13.3117
11	1.5301	0.2542	6.0192
12.5	1.5069	0.3955	3.8097
15	1.4864	0.4444	3.3452
20	1.4497	0.6039	2.4007

α	C_l	C_d
1.68	0.661	0.0086
3.22	0.795	0.0120
4.72	0.904	0.0165
6.36	1.054	0.0189
7.96	1.184	0.0221
9.50	1.293	0.0262
11.02	1.369	0.0326
12.28	1.406	0.0431

Run: PG02653
Re = 299228

α	C_l	C_d
-6.14	-0.279	0.0693
-4.53	-0.015	0.0185
-2.91	0.188	0.0135
-1.39	0.353	0.0114
0.13	0.497	0.0112
1.60	0.617	0.0142
3.28	0.764	0.0171
4.80	0.900	0.0184
6.24	1.026	0.0199
8.16	1.174	0.0243
9.63	1.266	0.0293
10.92	1.320	0.0365
12.43	1.357	0.0533

Run: PG02655
Re = 299932

α	C_l	C_d
-6.13	-0.273	0.0678
-4.78	-0.047	0.0196
-3.03	0.173	0.0142
-1.36	0.340	0.0118
0.25	0.475	0.0133
1.93	0.631	0.0162
3.13	0.742	0.0177
4.84	0.896	0.0201
6.35	1.025	0.0229
8.08	1.127	0.0266
9.55	1.226	0.0326
11.12	1.281	0.0434
12.36	1.300	0.0592

Run: PG02552
Re = 299566

α	C_l	C_d
-6.14	-0.279	0.0699
-4.50	-0.005	0.0175
-2.79	0.175	0.0125
-1.32	0.308	0.0135
0.07	0.443	0.0148
1.71	0.602	0.0168
3.41	0.761	0.0191
4.56	0.860	0.0207
6.69	1.036	0.0252
8.11	1.128	0.0293
9.19	1.187	0.0340
10.77	1.240	0.0436
12.38	1.267	0.0624

Run: PG02553
Re = 298975

α	C_l	C_d
-5.37	-0.133	0.0420
-3.76	0.090	0.0140

SG6042
Fig. 5.199

Run: PG02695
Re = 299822

α	C_l	C_d
-6.15	-0.292	0.0736
-4.56	-0.020	0.0227
-2.96	0.178	0.0139
-1.41	0.346	0.0114
0.13	0.495	0.0092
1.92	0.677	0.0086
3.17	0.805	0.0096
4.66	0.940	0.0118
6.35	1.087	0.0151
7.98	1.209	0.0192
9.53	1.310	0.0241
11.07	1.392	0.0303
12.51	1.432	0.0418

SG6043
Fig. 5.203

Run: PG02385
Re = 99681

α	C_l	C_d
-4.32	-0.278	0.0888
-3.07	0.047	0.0428
-1.89	0.190	0.0332
-0.87	0.300	0.0338
0.10	0.379	0.0330
1.13	0.483	0.0383
2.25	0.616	0.0428
2.95	0.708	0.0427
4.20	0.961	0.0359
5.10	1.095	0.0298
6.08	1.203	0.0235
7.27	1.285	0.0218
8.39	1.366	0.0230
9.35	1.413	0.0257
10.33	1.424	0.0295
11.30	1.432	0.0364

Run: PG02500
Re = 149877

α	C_l	C_d
-4.01	-0.071	0.0623
-3.18	0.141	0.0391
-2.22	0.269	0.0308
-0.69	0.466	0.0276
0.37	0.601	0.0247
1.34	0.745	0.0236
2.33	0.873	0.0216
2.95	0.946	0.0206
4.56	1.110	0.0182
5.43	1.192	0.0173
6.72	1.313	0.0177
7.12	1.348	0.0184
8.51	1.438	0.0212
9.40	1.473	0.0252
10.41	1.490	0.0339
11.58	1.521	0.0408

α	C_l	C_d
12.43	1.538	0.0483

Run: PG02387
Re = 199784

α	C_l	C_d
-4.95	-0.122	0.0750
-3.91	0.142	0.0395
-2.93	0.303	0.0257
-1.85	0.454	0.0210
-0.97	0.570	0.0186
0.08	0.682	0.0162
1.07	0.793	0.0154
2.20	0.915	0.0148
3.36	1.038	0.0145
3.97	1.095	0.0143
5.32	1.228	0.0143
6.46	1.325	0.0153
7.55	1.403	0.0172
8.59	1.458	0.0201
9.56	1.493	0.0245
10.20	1.507	0.0285
11.44	1.542	0.0352

Run: PG02388
Re = 199052

α	C_l	C_d
12.28	1.563	0.0404
13.61	1.576	0.0507

Run: PG02390
Re = 299102

α	C_l	C_d
-6.23	-0.124	0.0864
-5.20	0.052	0.0583
-4.13	0.271	0.0240
-3.05	0.401	0.0158
-2.05	0.517	0.0136
-1.02	0.631	0.0121
-0.02	0.733	0.0109
1.05	0.840	0.0106
2.17	0.958	0.0108
3.12	1.053	0.0108
4.17	1.158	0.0110
5.18	1.249	0.0119
6.35	1.349	0.0135
7.19	1.410	0.0154
8.25	1.467	0.0187
9.34	1.511	0.0230
10.31	1.540	0.0282
11.33	1.570	0.0343
12.32	1.592	0.0408
13.30	1.607	0.0519

Run: PG02391
Re = 302510

α	C_l	C_d
-5.73	-0.051	0.0740

Run: PG02393
Re = 399643

α	C_l	C_d
-6.25	-0.051	0.0776
-5.21	0.118	0.0498
-4.11	0.305	0.0171
-3.09	0.418	0.0124
-2.02	0.539	0.0111

α	C_l	C_d
-0.96	0.656	0.0102

Run: PG02394
Re = 398416

α	C_l	C_d
-0.02	0.755	0.0095
1.04	0.858	0.0088
2.03	0.961	0.0090
3.06	1.066	0.0093
4.10	1.168	0.0099
5.13	1.261	0.0109
6.14	1.344	0.0126
7.21	1.417	0.0151
8.18	1.468	0.0182
9.27	1.516	0.0220
10.32	1.554	0.0271
11.33	1.587	0.0328
12.38	1.614	0.0419

Run: PG02397
Re = 498423

α	C_l	C_d
-6.32	-0.036	0.0763
-5.22	0.143	0.0459
-4.17	0.316	0.0134
-3.17	0.433	0.0108
-2.12	0.550	0.0098
-1.08	0.667	0.0092
-0.06	0.782	0.0085
1.00	0.883	0.0080
2.11	0.997	0.0084
3.15	1.101	0.0088
4.20	1.201	0.0096
5.20	1.288	0.0109
6.17	1.360	0.0127
7.29	1.433	0.0156
8.18	1.482	0.0183
9.22	1.530	0.0226
10.21	1.566	0.0269
11.22	1.599	0.0328
12.28	1.627	0.0409

SG6043
Fig. 5.205

Run: PG02537
Re = 138371

α	C_l	C_d
-6.20	-0.358	0.1138
-4.64	-0.255	0.0892
-2.95	0.153	0.0371
-1.33	0.369	0.0286
-0.26	0.550	0.0227
1.99	0.813	0.0183
3.23	0.900	0.0215
4.82	1.008	0.0240
6.22	1.108	0.0272
7.74	1.202	0.0335
9.28	1.268	0.0414
10.74	1.306	0.0535
6.17	1.360	0.0127

Figure D.1: A print of tabulated data showing the lift and drag curve point data for the SG6043 foil for varying Reynolds numbers [145].

Table D.2: Tabulated Lift & Drag coefficient data operating at a **Reynolds Number of 6.3X10^4** and an **Turbulence intensity of 3.74%**. The experimental foil used for this data collection had a chord length of 0.0762m and the flume flow velocity was 0.82m/s.

AOA	CL	CD	CL/CD
-20	-0.5544	0.26	-2.1483
-15	-0.4912	0.17	-2.9173
-10	-0.266	0.11	-2.4668
-5	0.6676	$4.25 \cdot 10^{-2}$	15.696
0	1.1246	$5.59 \cdot 10^{-2}$	20.1328
5	1.6307	0.11	15.3934
7.5	1.6276	0.1	16.186
9	1.6833	0.11	14.8151
10	1.7308	0.14	12.7881
11	1.7778	0.17	10.5846
12.5	1.7831	0.17	10.5339
14	1.7037	0.33	5.1117
15	1.6538	0.32	5.0954
20	1.5026	0.59	2.5317

Table D.3: Tabulated Lift & Drag coefficient data operating at a **Reynolds Number of 6.3X10^4** and an **Turbulence intensity of 9.2%**. The experimental foil used for this data collection had a chord length of 0.0762m and the flume flow velocity was 0.82m/s.

AOA	CL	CD	CL/CD
-20	-0.7721	0.35	-2.1873
-15	-0.5505	0.2	-2.7462
-10	0.1441	$6.3 \cdot 10^{-2}$	2.2856
-5	0.7951	$4.78 \cdot 10^{-2}$	16.6367
0	1.1845	$6.21 \cdot 10^{-2}$	19.0805
5	1.7311	0.11	16.2094
10	1.9906	0.16	12.3351
12.5	2.0657	0.28	7.3717
15	2.0178	0.39	5.1541
17.5	1.9953	0.52	3.8065
20	1.9351	0.74	2.6233
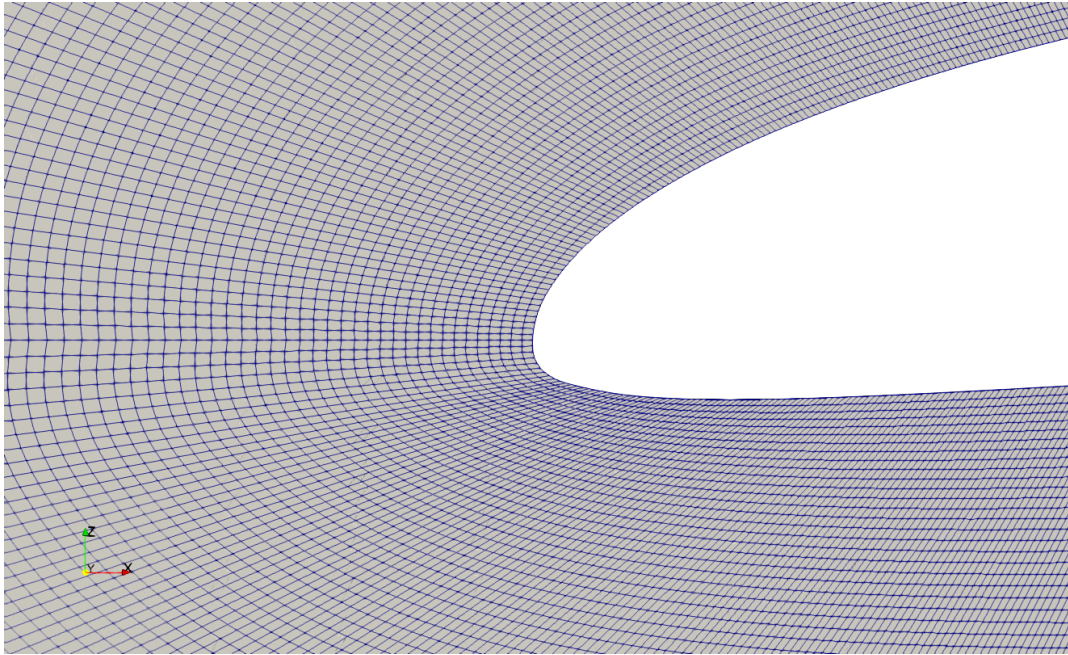
Figure E.1: An image of the Open-Flow case mesh with a focus on the skewed cells along the underside of the nose surface.

Appendix E

2D Foil mesh generation tool

E.1 Introduction

Mesh Modifications

A limitation with the Open-FLow case mesh was that it is not possible to implement solid walls into the domain without administering some change the mesh- which has been validated through convergence and for conformity should not be changed between the different test cases.

The Open-Flow case mesh had uniform outer boundary condition with acted as a constant flow velocity source. The mesh was simply rotated to effectively change the angle of attack. With sidewalls in place, it is no longer possible to simply rotate the mesh to achieve the same effect.

Thus, to achieve this, additional mesh blocks were coded into the Open-Flow
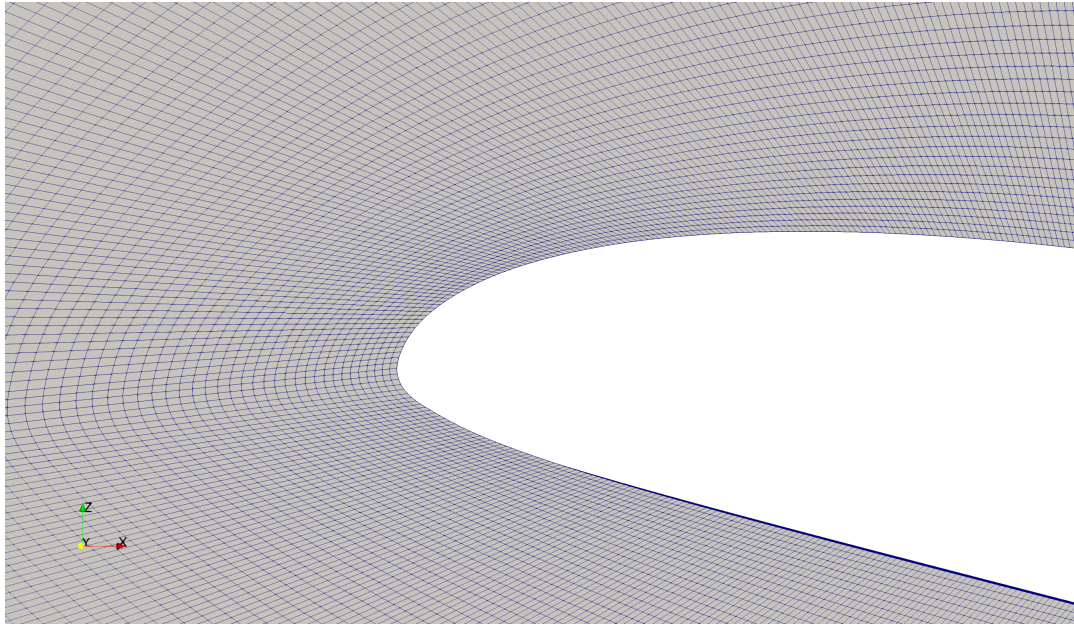
Figure E.2: An image showing the corrected cell skewness along with the skewed cells along the underside of the nose surface.

mesh structure which could act as an intermediately between the sidewalls and the C-type mesh. A schematic of the re-design Flume-Wall-Flow case mesh can be found in the appendix Figure E.5, which labels all the mesh construction parameters.

There were two original methods considered in which to adapt the mesh for various angles of attack. One was to rotate the C-type mesh within the boundary blocks - which keeps the original C-mesh intact, albeit truncated to account for the outer blocks and the sidewall. A severe limitation to the first case was that at greater angles of attack, the rotation of the C-type mesh block would cause a high degree of skewness across all the outer blocks cells.

The second was to rotate the foil surfaces within the C-type mesh blocks. In contrast to the other method, the second would lead to greater changes to the C-type and reduces the conformity to the Open-Flow case mesh. Additionally, at higher angles of attack, the cells against the foil surface would become so skewed that the mesh would also have been at too low a quality to warrant being used.

Thus a Hybridisation between the two original methods was developed which had a basis in the second method but would additionally dynamically couple the block vertices between the C-type mesh blocks and the outer blocks. So as the foil surface would be rotated, the connecting vertices would rotate to the same degree, thus reducing the impact on the C-type mesh cells while allowing greater angles of attack without distorting the mesh beyond reasonability.

The Open-flow mesh was deemed suitable to produce results within the required degree of accuracy due to the convergence of coefficient data. However, the cells along the underside of the nose exhibited skewed dimensions which could affect the results when stimulated at certain angles of attack, which inadvertently cause the area in question to exhibit more dynamic flow conditions. Figure E.1 shows the location and extent of the skewed cells along the foil nose. The skewed cells feature, concerning the location, is not expected to be pivotal. As the flow over the underside nose of the foil is not the main contributor to the foil performance concerning

the lift & drag coefficients since most lift is generated through the increased fluid velocity over the upper surface. Thus the cell skewness was previously tolerated for the duration of the Open-Flow case. With the development of the Flume-Wall-Flow case mesh, the opportunity was also taken to rectify the skewed cells by tweaking the mesh generation parameters. A further validation case could be investigated by comparing the previous mesh with the skewed nose cells against the newly tweaked mesh. Figure E.2 shows in comparison to Figure E.1 the reduced skewness of the cells around the nose section. Additionally, the improved cell quality can be compared through coloured contour plots which can give a viewer a superior perspective to the changes made Figure E.2. A potential complication that has arisen is that skewed cells are still present within the domain. However, these problem cells are located in areas of open flow and away from geometric surfaces, where dynamic flow characteristics are more likely to be present. Additionally, the C-type mesh has been significantly altered concerning the original Open-Flow case mesh 9Figure E.4, however, cells near the foil surface have been improved and the partitioning effects are not noticeable in the near-field region.

$$r = \beta^{n-1} = \frac{d_{n-1}}{d_o} \tag{E.1}$$

$$\beta = e^{\left(\frac{ln(r)}{n-1}\right)} \tag{E.2}$$

$$d_o = L \cdot \frac{(1-\beta)}{(1-\beta^{n-1})} \tag{E.3}$$
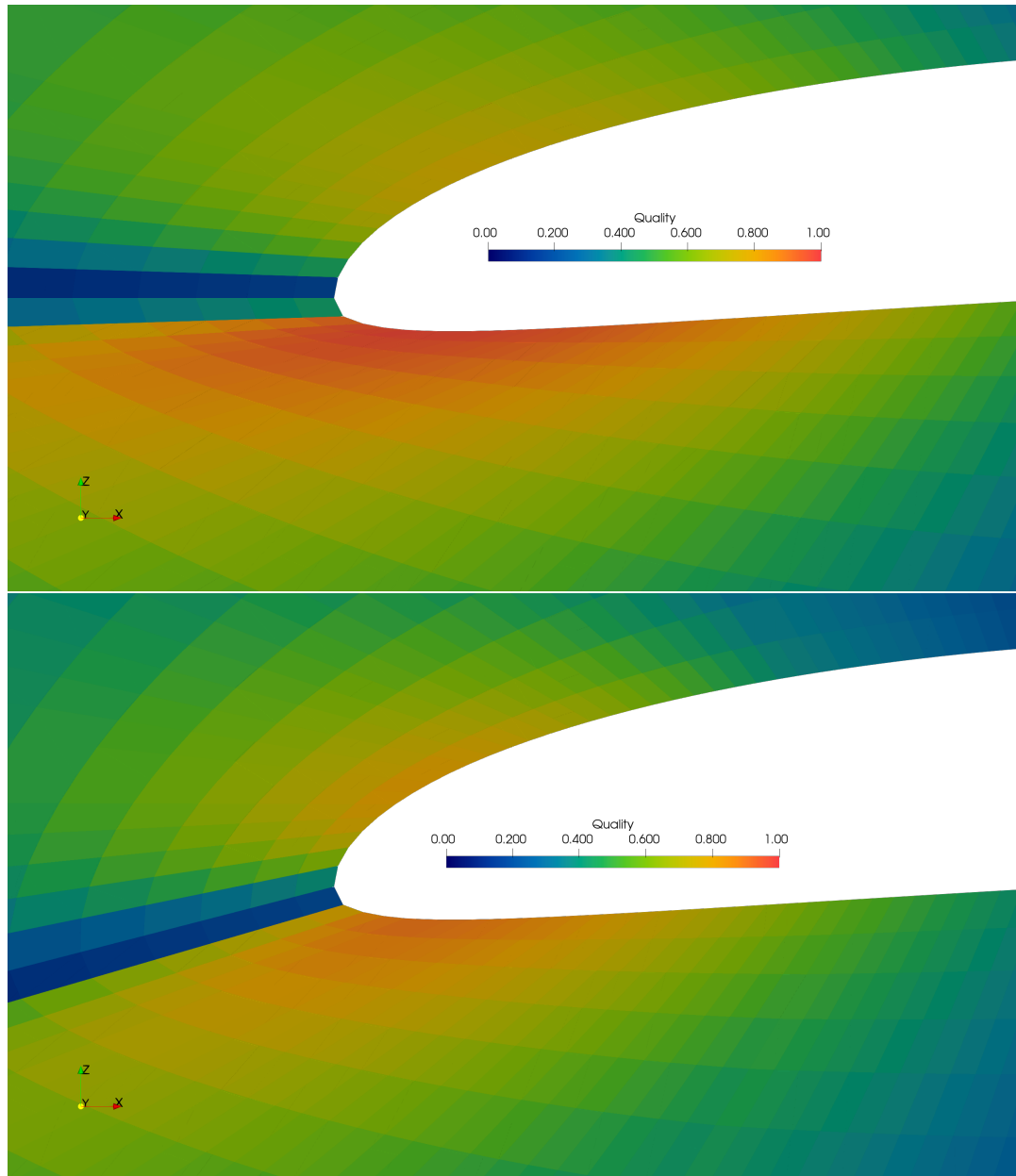
Figure E.3: A comparison contour plot highlighting the improvements to cell skewness around the foil nose. The image on the left is of the original Open-Flow case. The image on the right is after the current corrections have been implemented.
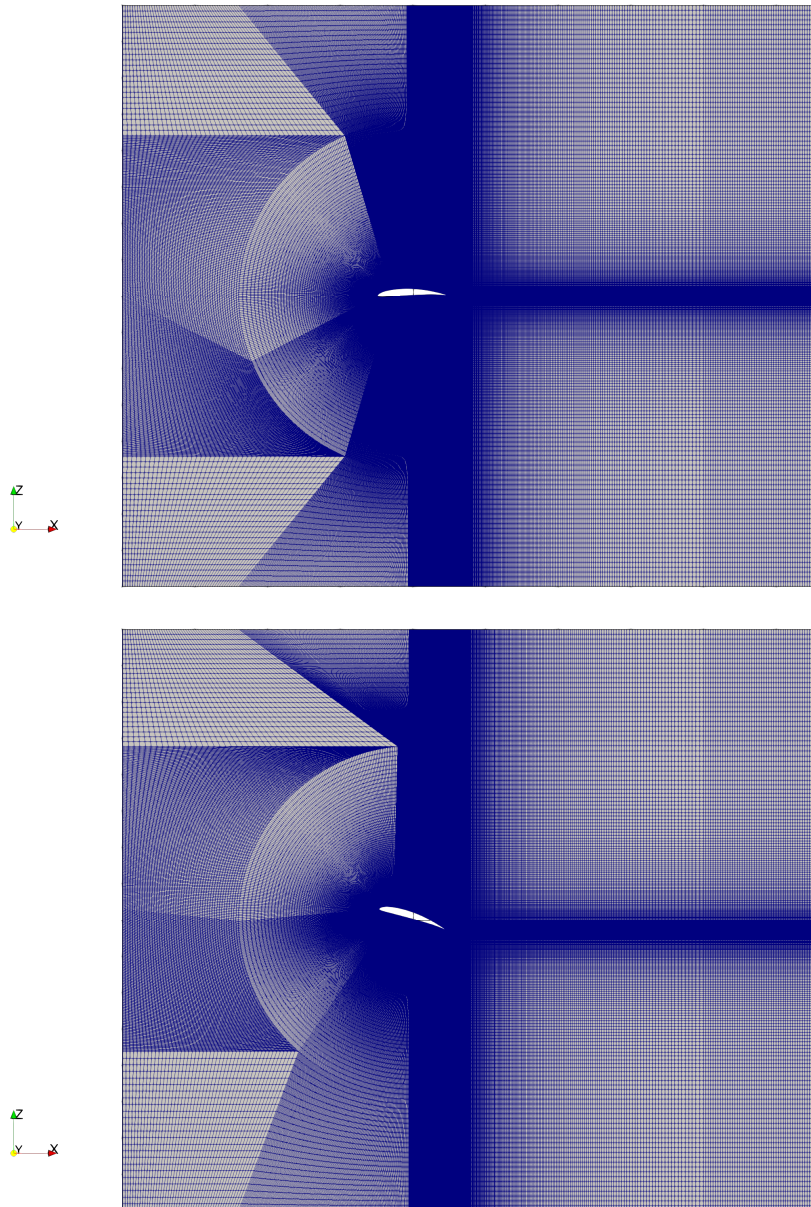
Figure E.4: This figure shows the cell layout across the whole domain. The image on the left is when the foil is at 0° AOA. The image on the right shows how the mesh dynamically moves when the foil AOA is changed to 18°.
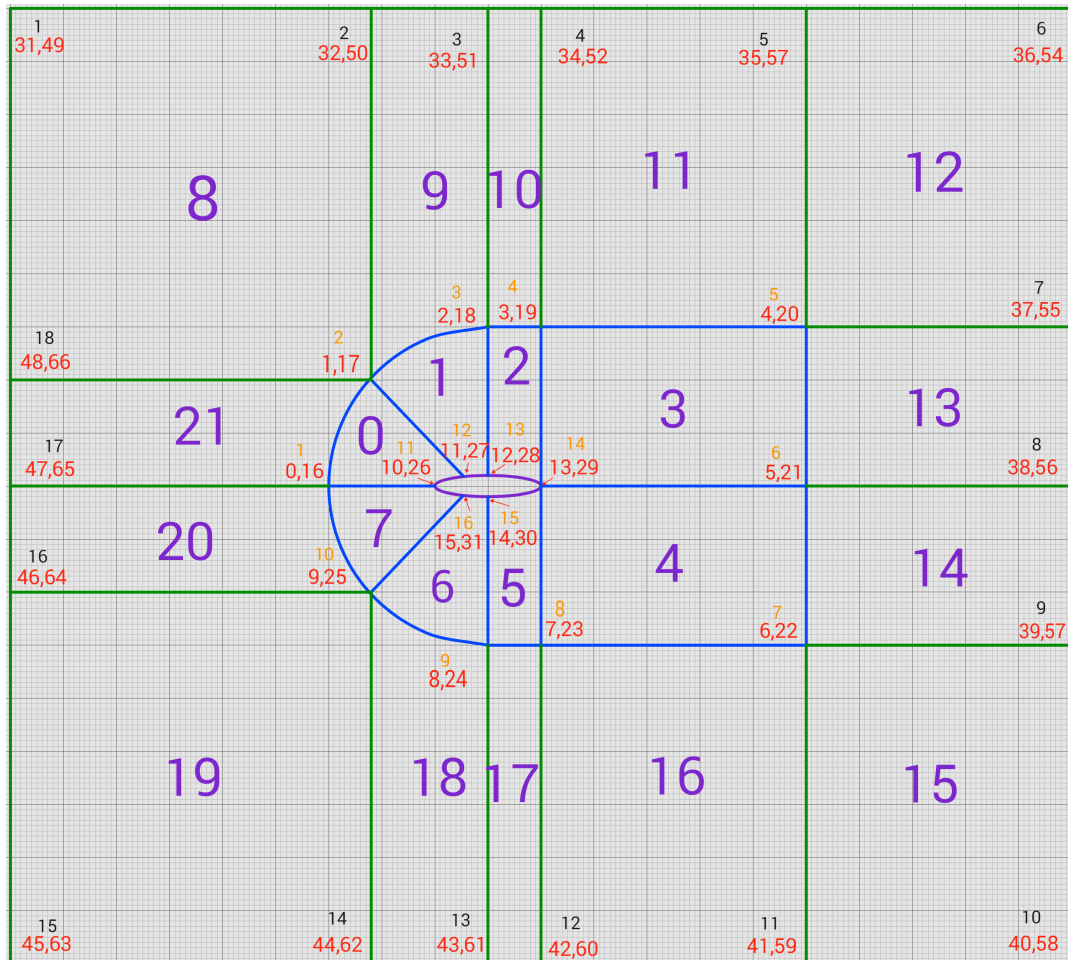
Figure E.5: A schematic detailing the construction parameters used to set up the mesh for the Flume-Wall-Flow case. The blue blocks represent the original block layout of the Open-flow case mesh. The Green blocks represent the additional blocks added so that the Flume walls could be simulated while attempting to have as little impact on the cells close to the foil surface as possible. The purple numbers list the block number. The black numbers show the vertice numbering. The red numbers show the node numbering on each end of the vertices.

Establish Fluid Flow Variables:
Re, Ti & Coordinate Position

Parameter Calculations:
-Boundary Conditions
- domain Y-Plus formulation.

Mesh Parameter Calculations.
Sorts:
- Number of Grid Cells over 3D space.
- Cell-size Expansion ratio's

Builds tailored OpenFOAM
4.1 files from name notation.
Both Steady-state and Transient files.

Meshes domain with select AOA positions

Figure E.6: Breakdown of the Boundary Condition determination process for correct sub-grid turbulence intensity.

Appendix F

Turbulence Depreciation

F.1 Turbulence Depreciation

Almost all flows that are studied under a engineering discipline have a measure of turbulence. Characteristics of turbulent flow such as the length scales and fluctuating velocity magnitudes present in turbulent fluid flow can drastically alter measured outcomes. As such, and within a CFD scope of interest, the ability to generate accurate degrees of turbulence is often pivotal to the scientific success of the research. Thus, methods that can aid in the generation of such are of vital interest.

Every CFD simulation flow domain is defined through the application of the initial and boundary conditions. Thus, it is of vital importance that the conditions are defined correctly and their role in the solver algorithm is understood.

This chapter covers the bridge between the turbulence variable of the physical experiments conducted by Lehigh University, and how the same properties were computationally modelled.

F.1.1 Turbulence Intensity

Turbulent flow is ubiquitous by nature and difficult to produce definitive numerical prediction. Despite this, statistical properties of the turbulent flow are reproducible [54]. L.F. Richardson [206] introduced the concept of an energy dissipation cascade within turbulent flow. By nature turbulent flow has various eddy length scales. The idea speculates that each eddie within the turbulent flow, independent of length scale, is in itself subjected to inertial instabilities. There condition leads to continual break-up of a larger body into smaller and smaller vortices. The hypothesis is based on viscosity playing no part. Since the Reynolds number is large, the viscous stresses within the eddies are comparatively small enough to be classified as having a negligible influence. Thus the inertia forces is the significant driving factor. The cascade continues until the Reynolds number, taken across the length of the eddy, fall to an order of unity. In contrast to flow of a high Reynolds number, the viscous forces become significant and thus dissipation becomes a dominant factor. Within CFD, Turbulence is depicted under two related categories; being sub-grid and resolved. The turbulence intensity (Ti) is defined as:

$$I \equiv \frac{u'}{U} \tag{F.1}$$

Where u' is the root-mean-square of the turbulent velocity fluctuations and U is the mean-flow velocity. The root-mean-square u' is calculated from the turbulent kinetic energy contained across each cell. The relationship is detailed as:

$$u' \equiv \underbrace{\sqrt{\frac{1}{3}(u_x'^2 + u_y'^2 + u_z'^2)}}_{l>cell} = \underbrace{\sqrt{\frac{2}{3}\kappa}}_{l<cell} \tag{F.2}$$

Where the resolved turbulence has length scales larger that the grid cells, the vector properties of eddies can be determined. The root-mean-square u' is calculated from the sum of variances of the fluid velocity components. Conversely, turbulence with length scales smaller than the grid cells cannot be fully resolved, thus the turbulence is numerical calculated within the Governing equations in the $k-\omega$ SST solver. The mean velocity U is calculated from the velocity vectors.

$$U \equiv \sqrt{U_x^2 + U_y^2 + U_z^2} \tag{F.3}$$

F.1.2   Experimental Measurement

Calculating turbulence intensity through physical experimentation revolves around measuring the fluids 3D velocity components through instrumentation. Lehigh's experiment consisted of measuring the Free-Stream Turbulence (FST) through inserting a Acoustic Doppler Velocimeter (ADV) device into the flume, downstream from the active-grid turbulence generator, and without the presence of a foil blade section. ADV's work from the principle of the Doppler shift - measuring the difference between emitted and received acoustic waves (Doppler shift). The fluid velocity is then calculated from:

$$-(U_1 - U_0) = \frac{(f_1 - f_0) \cdot C}{f_0} \tag{F.4}$$

Where U_0 is the velocity source, U_1 is the velocity received, f_1 is the received frequency and f_o is the emitted frequency. C is the speed of light in the fluid medium.

F.1.3   CFD Implementation

The turbulence characteristic of the CFD model is dictated by set boundary conditions, with only the initial conditions being independent. Consideration is often made to reduce boundary artefacts through setting considerable separation between boundaries and the are-of-interest. Therefore, consideration must be made for how the FST magnitude will depreciate downstream from the boundary to the location of interest.

Figure F.1 provides a over-view of process steps to determine correct boundary conditions so that the desired turbulence intensity is present at the area-of-interest. Initial consideration must be made to fluid flow independent variables: Re, Ti (at
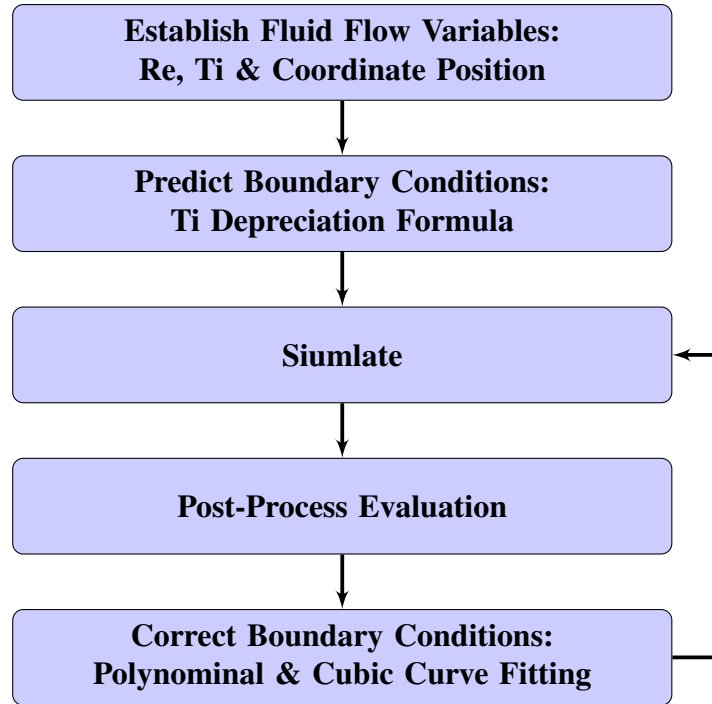
Figure F.1: Breakdown of the Boundary Condition determination process for correct sub-grid turbulence intensity.

the location) and the coordinate position within the model domain. Boundary conditions can be initially predicted through a turbulence intensity depreciation formula derived from simplified transport equations. The predicted turbulence criteria can then be simulated and then subsequently undergo a post-processing evaluation of the turbulent flow regime. Dependant on individual model characteristics, the predicted turbulence criteria should either be sufficient or be within the 'ball-park'. Should it be necessary for the turbulence criteria to be corrected; the evaluated turbulence depreciation regime of the simulated cases are polynomial curve-fitted. Intermediate polynomial coefficients can then determined through fitting a cubic spline. Thus, turbulence criteria can be further tailored to intended values. The model can then be re-simulated with the modified turbulence criteria, following a feedback loop until the desired turbulence regime has been evaluated.

F.1.4   Predicting Depreciation

The flow being considered within this thesis is a statistically steady, single phase, incompressible Newtonian fluid flow - governed by RANS turbulence model: $\kappa - \omega$ SST. Which solves the transport equations for the turbulent kinetic energy (κ), and the specific turbulence dissipation (ω). An 'eddy-viscosity' term is used to close the system. Refer to 2.3.3 for further discussion of the model.

If the flow direction is considered to be in parallel alignment with the x-axis, and the cross-diffusion term ... in ignored. The transport equations simplify to:

$$U\frac{d\kappa}{dx} = -\beta^*\omega\kappa \qquad (F.5)$$

$$U\frac{d\omega}{dx} = -\beta\omega^2 \tag{F.6}$$

Where β and β^* are constants of the same value as those specified by Menter **??** Under said constraints, the eddy-viscosity can be calculated from:

$$\nu_t = \frac{\kappa}{\omega} \tag{F.7}$$

The depreciation of the turbulent kinetic energy (κ) along downstream length (x) can be derived from solving equation F.5 & F.6 through using dimensionless variables:

$$\kappa^* = \frac{\kappa}{U_{ref}^2}, \omega^* = \frac{\omega * L_{ref}}{U_{ref}}, U^* = \frac{U}{U_{ref}}, x^* = \frac{x}{L_{ref}}, U^* = 1 \tag{F.8}$$

To be written in terms of Re, initial turbulent kinetic energy (κ_o), eddy viscosity ratio (ν_t/ν) and with independent variables from the $\kappa - \omega$ SST equation β and β^* constants.

$$\kappa^* = \kappa_o^* \left(1 + \beta(x^* - x_o)\kappa_o \left(\tfrac{\nu_t}{\nu}\right)_o^{-1} Re\right)^{-\frac{\beta^*}{\beta}} \tag{F.9}$$

Turbulence intensity can be defined in terms of turbulent kinetic energy and freestream velocity through combining equations F.1, F.2, F.3 to:

$$I = \sqrt{\frac{2\kappa}{3}} \cdot \frac{1}{U_{ref}} \tag{F.10}$$

Rearranging equation F.10 to solve for the turbulent kinetic energy κ:

$$k = \frac{3}{2}(U_{ref} \times I)^2 \tag{F.11}$$

Then subbing equation F.11 into F.9 to solve for Turbulence Intensity (I)

$$I = \left(I_o^2 \left[1 + \tfrac{3}{2}\beta(x^* - x_o)I_o^2 \left(\tfrac{\nu_t}{\nu}\right)_o^{-1} Re\right]^{-\frac{\beta^*}{\beta}}\right)^{\frac{1}{2}} \tag{F.12}$$

Thus, it can be observed that the turbulence intensity can be predicted along the downstream length from the initial conditions imposed in the Boundary Condition.

F.1.5   Evaluating Turbulence Depreciation

As discussed in Section 2.1.2, models require modes of validation to ensure reliability in the results being generated. One method of such is setting up a feedback loop to evaluate the outcome of the turbulence criteria and match against the theoretical hypothesis.

Figure F.2 depicts the variation of downstream turbulence regime aligned to the x-axis with vertical distance from the foil centre-point. The zero point along the x-axis coincides with the respective centre-point position of the aerofoil.
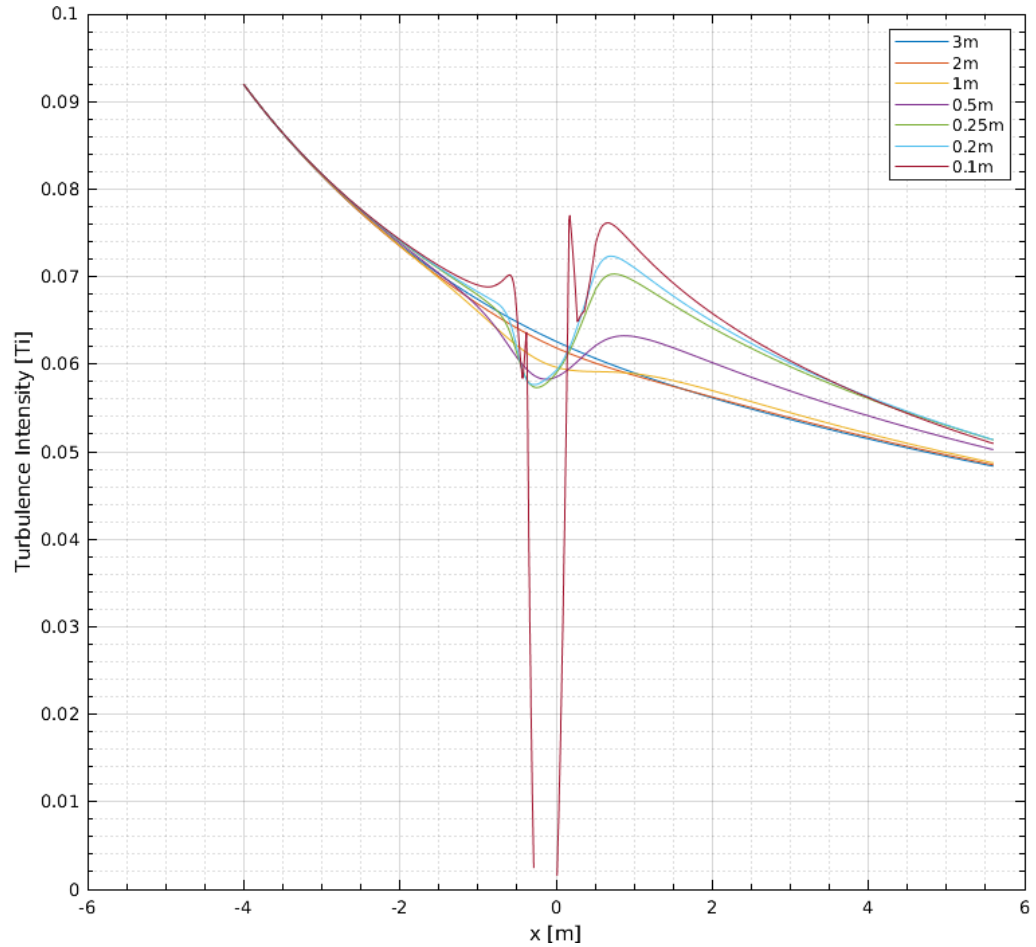
Figure F.2: How Turbulence Intensity varies across the vertical span and down-stream length of the model. This case had an AOA of 2 degrees and an inlet boundary condition that imposed a turbulence intensity of 9.2%
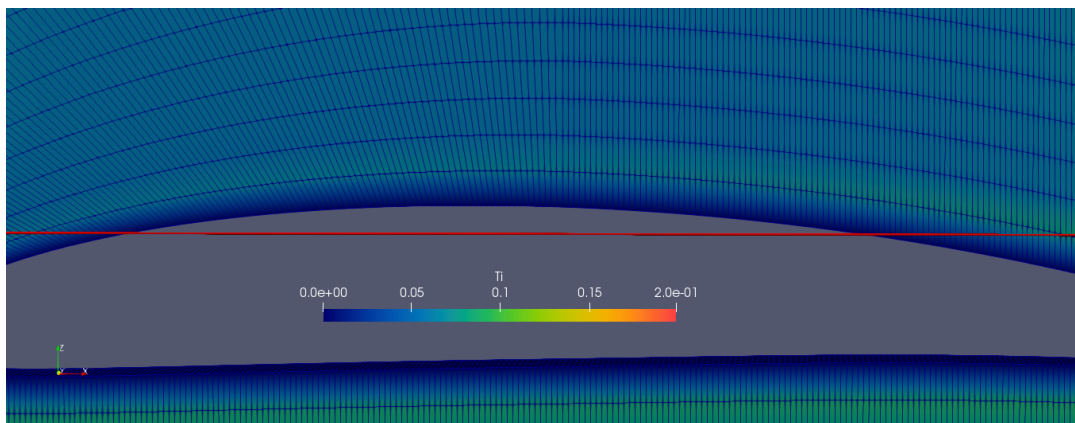
Figure F.3: A close image of the SG6043 foil with Ti contours and visible grid. The red line shown marks the extraction of turbulence data along the length for the 0.1m series shown in Figure F.2.

Series data taken incrementally closer to the aerofoil show a large disruption in the general depreciation trend. There is an initial value drop, the degree of which increases with decreasing distance from the aerofoil geometry. The trend however

is limited to where the aerofoil geometry intercepts the data line. This aspect can be be explained relating the Turbulence intensity definition in equation F.1 and the increased velocity flow over the upper surface of the aerofoil; with the trending characteristic being attributed to the dominance of of the directional flow at this point. The Turbulence intensity then increases sharply, the degree of which is again related to the horizontal distance from the aerofoil geometry, to a maximum located just after the aerofoil's tail position. The series then continue to depreciate towards convergence. An interesting observation is that a trend can be seen past the maximum point, where there is a higher depreciation rate in correlating to the higher maximum. The higher depreciation rate appears to maintain itself since there is a cross-over point at the 4m mark, where the order of magnitude is reversed and the higher depreciation rate continues. The 0.1m series has three extra peaks in comparison to the other series plotted. There is an initial peak just past the nose of the aerofoil. This could a characteristic detail of how fluid flow behaves around the blockage of the nose, where the flow is suddenly forced around the point - leading to sudden acceleration and change of direction, hence the spike in Ti values. Additionally, the feature will be more prevalent in the incompressible fluid cases such as the simulations being carried out. There is also a smaller peak located adjacent to the first, the causation of which can be attributed the turbulence attributed to the aerofoil surface cells by the wall function. The third additional peak can likely be the attributed to the same reasoning as the second additional peak. Figure F.3 corroborates this finding showing the 0.1m line through the domain at the location in question. The turbulence intensity increases sharply on across the cell adjacent to the aerofoil surface cells which operate under the wall function.

The aerofoil blockage influence on the flow body is shown to depreciate with horizontal distance until the data shows convergence at 3m, where a continuous depreciation rate is observed. It was thus determined that since convergence had been reached, blockage effects were not dominant and a model separate model was not necessary.

However, when the aerofoil is rotated to higher angles of attack, evidence of blockage existed up to the near wall area. Additionally, the Ti magnitudes present are substantially larger and depict several fluctuations along the downstream length. This is indicative of the effects past the separation point where the inverse pressure gradient has generated the existence of vortex shedding.

A comparison of Turbulence intensity depreciation rates spanning a range of inlet boundary conditions is shown in Figure **??**. The data was collected in accordance with the findings that blockage effects were no longer present past a horizontal distance of 3m from the aerofoil midpoint.

F.1.6 Polynomial & Cubic Prediction

Each of the initial datasets previously simulated were approximated using a polynomial equation as it was found to be the best for application - allowing estimations to be formed with a relatively high degree of accuracy without the need for a trial and error approach to be taken.

The general polynomial regression model; k^{th} order polynomial method (eqn:F.13), was deemed through curve fitting to be able to approximate the datasets with accept-
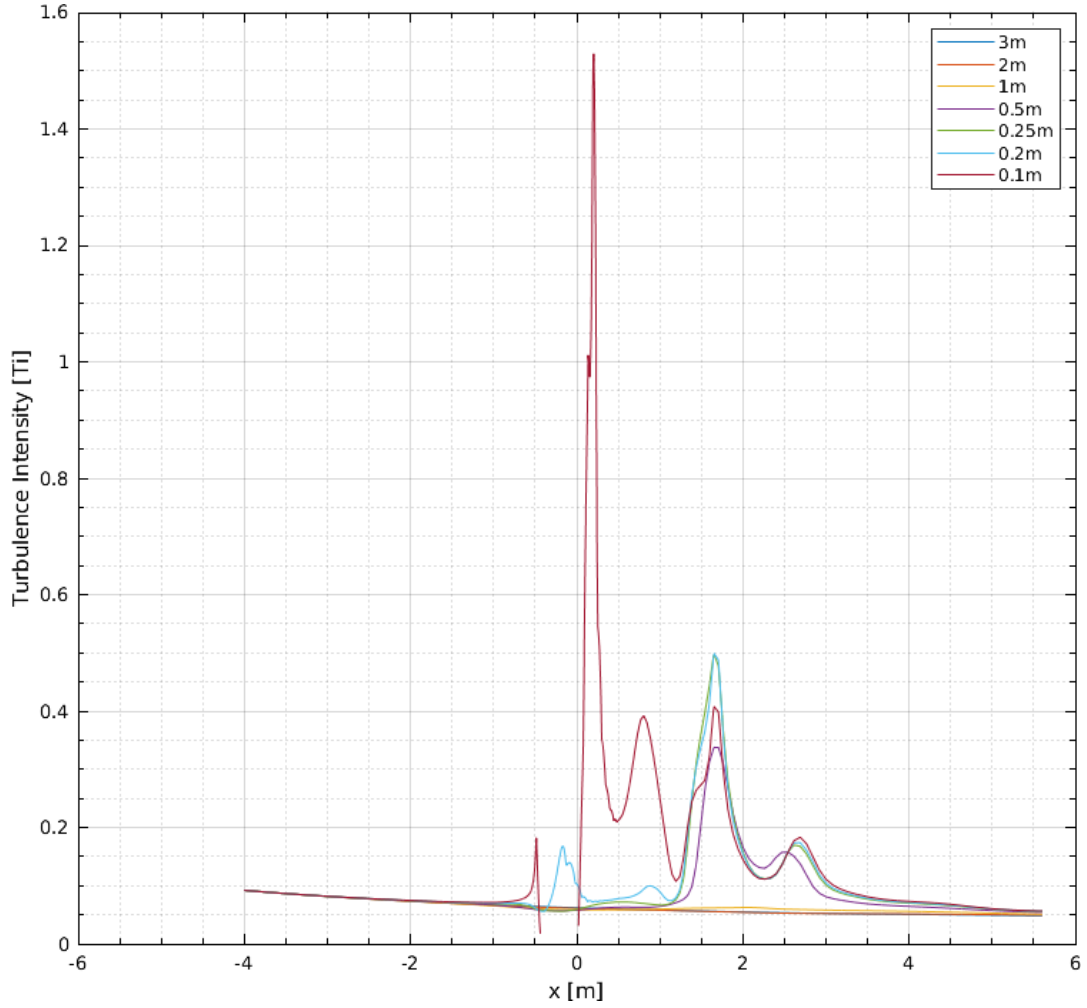
Figure F.4: This figure depicts a plot of how Turbulence intensity varies across the width and length of the model. This case had an AOA of 2 degrees and an inlet boundary condition that imposed a turbulence intensity of 9.2%

able error (ε).

$$y = a_k x^k + \longrightarrow + a_1 x + a_0 + \varepsilon \tag{F.13}$$

Each of the data-series was used to develop Polynomial equations of orders ranging from 2 to 8, through the application of the least squares method. Which numerically acts to minimise the variance between the polynomial and the data-series. The polynomial coefficients for each kth order polynomial was determined through the resolution of eqn:F.14; A derivative of the polynomial residual function, which when presented in standard form $Ma = b$.

$$
\begin{bmatrix}
N & \Sigma_{i=1}^{N} x_i & \longrightarrow & \Sigma_{i=1}^{N} x_i^k \\
\Sigma_{i=1}^{N} x_i & \Sigma_{i=1}^{N} x_i^2 & \longrightarrow & \Sigma_{i=1}^{N} x_i^{k+1} \\
\downarrow & \downarrow & \downarrow & \downarrow \\
\Sigma_{i=1}^{N} x_i^k & \Sigma_{i=1}^{N} x_i^{k+1} & \longrightarrow & \Sigma_{i=1}^{N} x_i^{2k}
\end{bmatrix}
\begin{bmatrix}
a_0 \\
a_1 \\
\downarrow \\
a_k
\end{bmatrix}
=
\begin{bmatrix}
\Sigma_{i=1}^{N} y_i \\
\Sigma_{i=1}^{N} x_i y_i \\
\downarrow \\
\Sigma_{i=1}^{N} x_i^k y_i
\end{bmatrix}
\tag{F.14}
$$

Cramer's Rule (Eqn:F.15) was used to solve for the coefficients through the determinants of M. M_i is formed from substituting the column vector listed as b into

M's i^{th} column.

$$a_k = \frac{det(M_i)}{det(M)} \tag{F.15}$$

The polynomial curves of orders 2 to 8 was curve fitted to the data-series. An initial observation was taken for each kth term polynomial series fit, to provide a quick visual gauge of fit across all series. Additionally, observations of the fitted curve allow for any erratic polynomial fluctuation from Runge's phenomenon to be easily identified. With polynomial orders of 5 to 8, the visual difference became indistinct. So a statistical analysis of each curve fit was used to provide a direct numerical comparison between the polynomial orders. The Goodness-of-fit statistical analysis methods of the sum of squares due to error (eqn:F.16), R-square (eqn:F.19), Adjusted R-square (eqn:F.20) and the Root mean squared error (eqn:F.21).

$$SSE = \Sigma_{i=1}^{N} w_i (y_i - \hat{y}_i)^2 \tag{F.16}$$

$$SSR = \Sigma_{i=1}^{N} w_i (\hat{y}_i - \bar{y})^2 \tag{F.17}$$

$$SST = \Sigma_{i=1}^{N} w_i (y_i - \bar{y})^2 \tag{F.18}$$

$$R_{sq} = \frac{SSR}{SST} = 1 - \frac{SSE}{SST} \tag{F.19}$$

$$adjustedR_{sq} = 1 - \frac{SSE(n-1)}{SST(v)} \tag{F.20}$$

$$RootMeanSquareError = \sqrt{\frac{SSE}{v}} \tag{F.21}$$

It was found that the 8th order polynomial provided the best fit to the dataset with an $SSE : 9.425e - 08$, an $R_{sq} : 1$, Adjusted $R_{sq} : 1$ and an $RMSE : 9.748e - 06$. The 8th term polynomial curve fit of the data-series is shown in Figure F.5.

The 8th term polynomial coefficients were plotted against the inlet boundary turbulence intensity for the respective data-series (Figure F.6). All the coefficient series had a cubic relationship with The inlet boundary turbulence intensity value, except the coefficient series notated as a_0 which had a linear.

Thus, each coefficient series provided the 'markers' for a cubic spline interpolation series, which would allow for the determination of appropriate coefficients for an 8th term polynomial predicting the turbulence intensity depreciation for any given turbulence intensity inlet boundary condition. Thus the appropriate boundary conditions could be imposed on the model for any value of turbulence over the foil.

$$f(x) = a(x - x_1)^3 + b(x - x_1)^2 + c(x - x_1) + d \tag{F.22}$$

The Not-a-Knot cubic spline interpolation, proposed by De Boor [27], was used as the type does not exert 'super-convergence' at the knot points. This is achieved through setting a boundary condition where two points either-side of the interval are set to be equal (eqn:F.23).
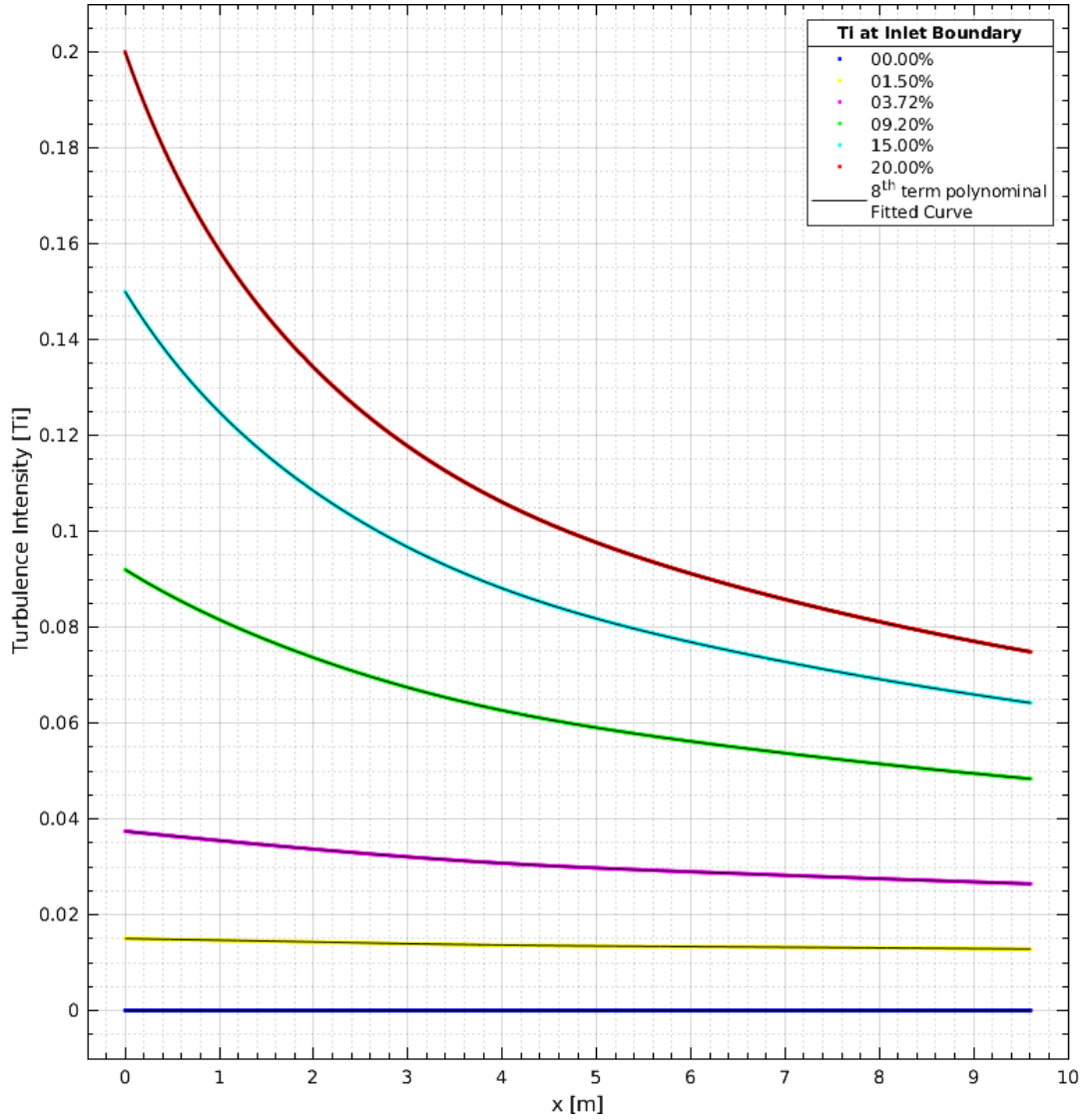
Figure F.5: 8th term polynomial curve fitting for data-series with boundary conditions correlating to an input turbulence intensity of $00.00\%, 01.50\%, 03.72\%, 09.20\%, 15.00\%, 20.00\%$. The polynomial fit for each series is over laying the parent data-series.

$$S_0(x) \equiv S_1(x), \quad and \quad S_{n-2}(x) \equiv S_{n-1}(x) \tag{F.23}$$

Which is enacted by (eqn:F.23)

$$S_0'''(x) = S_1'''(x), \quad and \quad S_{n-2}'''(x) = S_{n-1}'''(x) \tag{F.24}$$

The method was validated through an initial test to predict existing reference data-series through the method. A second guaranty validation test is to extract the turbulence intensity data points from a simulation with boundary conditions determined from this method, then compare the predicted to the simulated values.

When predicting existing data-series, shown in Figure F.7, The reference data-series provided an initial validated through applying it to already simulated cases shown in Figure F.7. The original simulated data series are shown in solid colour.
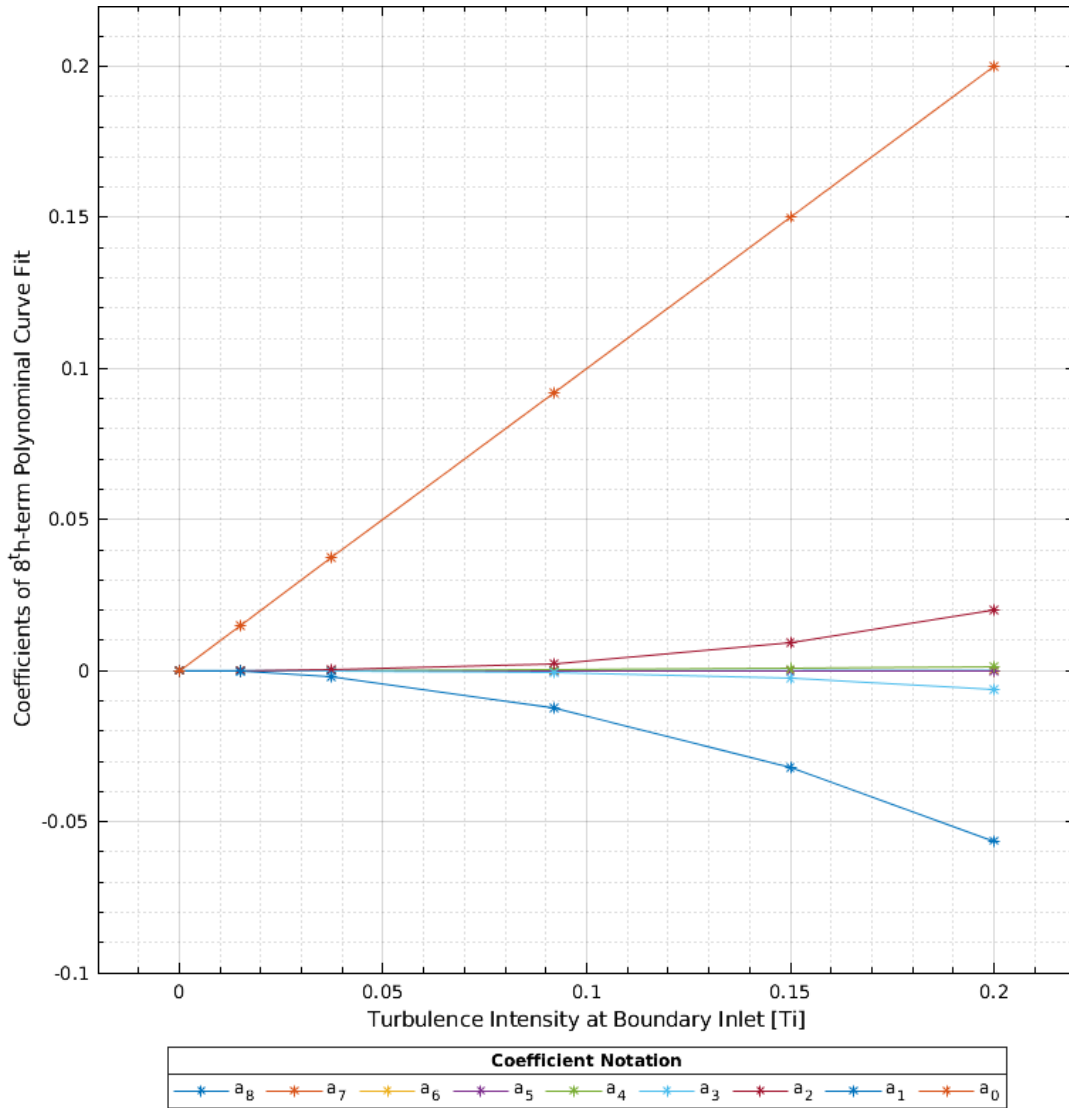
Figure F.6: Cubic

The predicted turbulence intensity boundary values are denoted through a star marker, and the predicted depreciation curve is presented as a dashed line. The colour scheme was kept consistent for both.

The results generated showed a high degree of similarity to the original values with percentage errors being 0.0316% 0.0305% 0.0273% 0.0516% 0.0614% for the 1.5%, 3.73%, 9.2%,15% and the 20% series respectfully.Thus, a percentage decrease of 76.24% 88.58% 94.6575% & 81.56% from the reducing balance method has been achieved. The cause of the errors in itself is likely down to Runge's phenomenon. A feature of high degree polynomials which leads to oscillations of increasing magnitude along a fitted series.

The larger percentage error seen with the predictions of the higher turbulence intensity values is likely down to the increasing difference between the downstream turbulence intensity and that at the boundary. However, the prediction errors are uniformly diminutive, thus the method can be considered a reliable way of determining the appropriate inlet boundary conditions for specific turbulence cases.

It should be noted that the error will continue to increase, if turbulence intensities
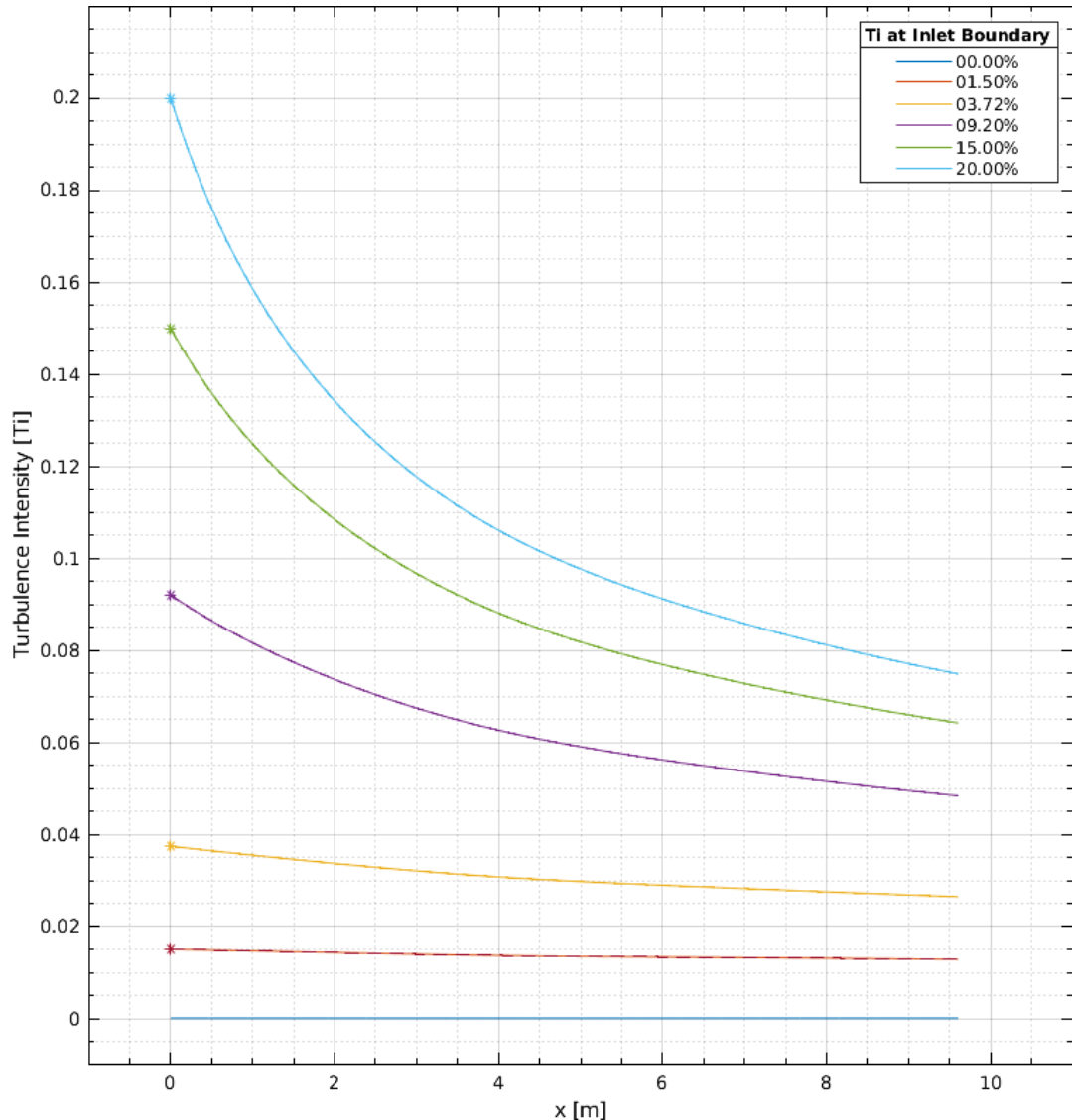
Figure F.7: Cubic

are selected that are far greater that those which currently act as markers for the cubic spline.

F.1.7 Conclusion

An investigation into how Turbulence intensity depreciates and potential methodologies to estimate the turbulence conditions at the boundary for correct depreciative conditions to be present over the simulated aerofoil. Firstly a examination of flow across the horizontal span was conducted and it was deduced that when the AOA is small; definitively ¡2 degrees, there is no evidence of aerofoil induced blockage spanning the horizontal width to the wall. The conclusion is based on convergence of depreciation rates with horizontal distance from the midpoint. Additionally looking into the behaviour of how turbulence intensity depreciated with respect to downstream distance, it was found that the turbulence depreciation rates are conserved over the downstream length unless acted upon by an additional factor. An additional finding is that the turbulence intensity increases sharply on across the cell adjacent

to the aerofoil surface cells which operate under the wall function. whether this is an expected outcome or a model artefact has yet to be determined at the time of writing.

A secondary examination was then conducted which addressed the question as to how the depreciation rate changed with respect to different turbulence intensity inlet values. Where it was confirmed that the depreciation rate was conserved along the downstream length, and the depreciation fits the Reducing Balance Method of Depreciation. Thus, it could be possible to form approximation estimates for intermediary cases, and develop a methodology. The method was then internally validated to which the method validation test provided very small errors. It should also be noted that further predictions would be based of reference data with a smaller separation between points thus further reduction in error. The methodology can thus be considered sound and will not require further validation through implemented testing.

A downside to the method presented in this section is that additional simulations are required to provide reference series to act as reference for the predicted value. This obviously is not a perfect scenario as it requires additional project time. It is not yet known how the material properties and the flow velocity will exactly change the depreciation rates, therefore further investigation is required to determine whether the rates calculated for the above cases could be more universally applied.

F.1.8   Further Work

As discussed before, the error will continually increase with increasing turbulence intensity. Should this become a problem in the future, two steps could be taken to reduce the possible errors in th methodical system. Firstly, Runge's phenomenon could be addressed by fitting the reference series with a cubic spline method - which is a trait of high degree polynomials. Secondly, if simulation cases were run with sequential increases in the turbulence intensity, and the simulation turbulence depreciation data was added to the initial reference datasets, the new 'markers' will contribute to pining the cubic splines. Thus, will allow an continually iterative prediction with ever increasing accuracy of high turbulence intensity prediction.

Bibliography

[1]   A. A. Abdel-Rahman and W. M. Chakroun. "Surface roughness effects on flow over aerofoils". In: *Wind Engineering* 21.3 (1997), pp. 125–137. ISSN: 0309524X.

[2]   T. a. Adcock, S. Draper, and T. Nishino. "Tidal power generation - A review of hydrodynamic modelling". In: *Proceedings of the Institution of Mechanical Engineers, Part A: Journal of Power and Energy* 229.7 (2015), pp. 755–771. ISSN: 0957-6509. DOI: 10.1177/0957650915570349. URL: http://pia.sagepub.com/lookup/doi/10.1177/0957650915570349.

[3]   Taa Adcock et al. "The available power from tidal stream turbines in the Pentland Firth". In: *Proceedings of the Royal Society A: Mathematical, Physical and Engineering Science* 469.2157 (2013), pp. 1471–2946. ISSN: 1364-5021. DOI: 10.1098/rspa.2013.0072. URL: http://rspa.royalsocietypublishing.org/content/469/2157/20130072.short.

[4]   G A Aggidis and D S Benzon. "Operational optimisation of a tidal barrage across the Mersey estuary using 0-D modelling". In: *Ocean Engineering* 66 (2013), pp. 69–81. ISSN: 0029-8018. DOI: 10.1016/j.oceaneng.2013.03.019. URL: http://dx.doi.org/10.1016/j.oceaneng.2013.03.019.

[5]   G A Aggidis and O Feather. "Tidal range turbines and generation on the Solway Firth". In: *Renewable Energy* 43 (2012), pp. 9–17. ISSN: 0960-1481. DOI: 10.1016/j.renene.2011.11.045. URL: http://dx.doi.org/10.1016/j.renene.2011.11.045.

[6]   Arman Aghahosseini and Christian Breyer. "From hot rock to useful energy: A global estimate of enhanced geothermal systems potential". In: *Applied Energy* 279 (Dec. 2020), p. 115769. ISSN: 03062619. DOI: 10.1016/j.apenergy.2020.115769.

[7]   Reza Ahmadian and Roger A. Falconer. "Assessment of array shape of tidal stream turbines on hydro-environmental impacts and power output". In: *Renewable Energy* 44 (2012), pp. 318–327. ISSN: 09601481. DOI: 10.1016/

j.renene.2012.01.106. URL: http://dx.doi.org/10.1016/j.renene.2012.01.106.

[8] S R Ahmed, G Ramm, and G Faltin. "Some Salient Features of the Time -Averaged Ground". In: *SAE Transactions* 93.1984 (1984), pp. 473–503. URL: http://courses.me.metu.edu.tr/courses/me485/files/Ahmed%201984.pdf.

[9] *Air-Dynamic and Kinematic Viscosity*. 2019. URL: https://www.engineeringtoolbox.com/air-absolute-kinematic-viscosity-d%7B%5C_%7D601.html.

[10] *Airfoil Tools SG6043 (sg6043-il)*. 2021. URL: http://airfoiltools.com/airfoil/details?airfoil=sg6043-il (visited on 09/08/2021).

[11] Dale A. Anderson et al. *Computational Fluid Mechanics and Heat Transfer*. Fourth edi. CRC Press, Dec. 2020, p. 974. ISBN: 9781351124027. DOI: 10.1201/9781351124027. URL: https://www.taylorfrancis.com/books/9781351124010.

[12] John David Anderson. *Fundamentals of Aerodynamics*. Fifth Edit. McGraw-Hill, 2011. URL: https://books.google.co.uk/books/about/Fundamentals%7B%5C_%7Dof%7B%5C_%7DAerodynamics.html?id=993HMgEACAAJ%7B%5C&%7Dredir%7B%5C_%7Desc=y.

[13] H Andre. "Operating experiance with bulb units at the Rance Tidal Power Plant and other French hydro-power sites". In: *IEE Transactions on Power Apparatus and Systems* 95.4 (1976), pp. 1038–1044. URL: http://ieeexplore.ieee.org/stamp/stamp.jsp?arnumber=1601796.

[14] Athanasios Angeloudis and Roger A. Falconer. "Sensitivity of tidal lagoon and barrage hydrodynamic impacts and energy outputs to operational characteristics". In: *Renewable Energy* (2016), pp. 1–15. ISSN: 18790682. DOI: 10.1016/j.renene.2016.08.033. URL: http://dx.doi.org/10.1016/j.renene.2016.08.033.

[15] Athanasios Angeloudis et al. "Comparison of 0-D, 1-D and 2-D model capabilities for tidal range energy resource assessments". In: *proceedings of the 12th European Wave and Tidal Energy Conference (EWTEC)*. 2017.

[16] Athanasios Angeloudis et al. "Numerical model simulations for optimisation of tidal lagoon schemes". In: *Applied Energy* 165 (2016), pp. 522–536. ISSN: 03062619. DOI: 10.1016/j.apenergy.2015.12.079. URL: http://dx.doi.org/10.1016/j.apenergy.2015.12.079.

[17] Athanasios Angeloudis et al. "Representation and operation of tidal energy impoundments in a coastal hydrodynamic model". In: *Renewable Energy* 99 (2016), pp. 1103–1115. ISSN: 18790682. DOI: 10.1016/j.renene.2016.08.004. URL: http://dx.doi.org/10.1016/j.renene.2016.08.004.

[18] F Antonio and O Falcao. "Wave energy utilization: A review of the technologies". In: *Renewable and Sustainable Energy Reviews* 14.3 (2010), pp. 899–918. ISSN: 13640321. DOI: 10.1016/j.rser.2009.11.003. URL: http://ac.els-cdn.com/S1364032109002652/1-s2.0-S1364032109002652-main.pdf?%7B%5C_%7Dtid=661ae596-a09f-11e4-9982-00000aacb361%7B%5C&%7Dacdnat=1421756900%7B%5C_%7De92c82c056901aca9435c3e4d5dfdcd0.

[19] Aquaret. *Case Study - Annapolis Royal Technology Type Project Type / Phase*. Tech. rep. December 2008. 2008, pp. 1–2. URL: http://www.aquaret.com/images/stories/aquaret/pdf/cstidalbarrageannapolisroyal.pdf.

[20] Brian K. Arbic et al. "The accuracy of surface elevations in forward global barotropic and baroclinic tide models". In: *Deep-Sea Research Part II: Topical Studies in Oceanography* 51.25-26 SPEC. ISS. (2004), pp. 3069–3101. ISSN: 09670645. DOI: 10.1016/j.dsr2.2004.09.014.

[21] B Aupoix. "Wall Roughness Modelling with k-w SST Model". In: *10th International ERCOFTAC Sym-posium on Engineering Turbulence Modelling and Measurement*. MARBELLA, Spain: hal-01071701, 2014. URL: https://hal-onera.archives-ouvertes.fr/hal-01071701.

[22] S. Avinash, K. Tinesh, and B. T. Kannan. "Preliminary Studies of Compressible Jet Flow from a Pipe with Hexagonal Cross-section". In: *International Conference on Advances in Mechanical Engineering* 912.4 (Sept. 2020). ISSN: 1757899X. DOI: 10.1088/1757-899X/912/4/042057.

[23] Young Ho Bae, Kyeong Ok Kim, and Byung Ho Choi. "Lake Sihwa tidal power plant project". In: *Ocean Engineering* 37.5-6 (2010), pp. 454–463. ISSN: 00298018. DOI: 10.1016/j.oceaneng.2010.01.015. URL: http://dx.doi.org/10.1016/j.oceaneng.2010.01.015.

[24] Clive Baker and Peter Leach. "Tidal Lagoon Power Generation Scheme in Swansea Bay". In: April (2006).

[25] Rayhaneh Banyassady and Ugo Piomelli. "Turbulent plane wall jets over smooth and rough surfaces". In: *Journal of Turbulence* 15.3 (2014), pp. 186–207. DOI: 10.1080/14685248.2014.888492. URL: http://www.tandfonline.com/action/journalInformation?journalCode=tjot20.

[26] G K Batchelor and A E Gill. "Analysis of the stability of axisymmetric jets". In: *Journal of Fluid Mechanics* 14.4 (1962), pp. 529–551. DOI: 10.1017/ S0022112062001421. URL: https://www.cambridge.org/core..

[27] G. Behforooz. "The not-a-knot piecewise interpolatory cubic polynomial". In: *Applied Mathematics and Computation* 52.1 (1992), pp. 29–35. ISSN: 00963003. DOI: 10.1016/0096-3003(92)90096-J.

[28] Lev B. Bernshtein. "Tidal power development - a realistic, justifiable and topical problem of today". In: *IEEE Transactions on Energy Conversion* 10.3 (1995), pp. 591–599. ISSN: 15580059. DOI: 10.1109/60.464887. URL: http://ieeexplore.ieee.org/stamp/stamp.jsp?arnumber=464887.

[29] Tom Blackmore, Luke E. Myers, and Abubakr S. Bahaj. "Effects of turbulence on tidal turbines: Implications to performance, blade loads, and condition monitoring". In: *International Journal of Marine Energy* 14 (2016), pp. 1–26. ISSN: 22141669. DOI: 10.1016/j.ijome.2016.04.017.

[30] Tom Blackmore et al. *The Effect of Freestream Turbulence on Tidal Turbines Marine Growth on Offshore Structures: assessment and modeling View project Energy, Cities and Infrastructure View project The Effect of Freestream Turbulence on Tidal Turbines*. Tech. rep. 2015. URL: https://www.researchgate. net/publication/282807576.

[31] Mircea Boşcoianu, Vasile Prisecariu, and Ionică Cîrciu. "APPLICATIONS AND COMPUTATIONAL ASPECTS REGARDING THE COANDĂ EFFECT". In: *Science & Military* 5.1 (2010), pp. 26–30. URL: https:// search.proquest.com/docview/607934022/fulltextPDF/3253636E81D84E2CPQ/ 1?accountid=14680.

[32] R. J. Boyle and M. Stripf. "Simplified approach to predicting rough surface transition". In: *Journal of Turbomachinery* 131.4 (Oct. 2009), pp. 1–11. ISSN: 0889504X. DOI: 10.1115/1.3072521.

[33] Charles-Henri Bruneau and Khodor Khadra. "Highly parallel computing of a multigrid solver for 3D Navier–Stokes equations". In: *Journal of Computational Science* 17 (2016), pp. 35–46. DOI: 10.1016/j.jocs.2016.09.005. URL: https://ac.els-cdn.com/S1877750316301478/1-s2.0- S1877750316301478-main.pdf?%7B%5C_%7Dtid=931a8ff6-f952- 11e7-8185-00000aab0f6c%7B%5C&%7Dacdnat=1515952051%7B%5C_ %7D355a83f19460a3c88a8261b999b9b434.

[34] Mikhail Pavlovich Bulat and Pavel Victorovich Bulat. "Comparison of turbulence models in the calculation of supersonic separated flows". In: *World Applied Sciences Journal* 27.10 (2013), pp. 1263–1266. ISSN: 18184952. DOI: 10.5829/idosi.wasj.2013.27.10.13715. URL: https://www.researchgate.net/profile/Pavel%7B%5C_%7DBulat/publication/260045559%7B%5C_%7DComparison%7B%5C_%7Dof%7B%5C_%7DTurbulence%7B%5C_%7DModels%7B%5C_%7Din%7B%5C_%7Dthe%7B%5C_%7DCalculation%7B%5C_%7Dof%7B%5C_%7DSupersonic%7B%5C_%7DSeparated%7B%5C_%7DFlows/links/0deec52f354e263c3c000000/Comparison-of-Turbulence-Models-in-the-Calculation-of-Supersonic-Separat.

[35] Tony Burton et al. *Wind Energy Handbook*. first. Chichester: John Wiley & Sons, 2001.

[36] Tony Burton et al. *Wind Energy Handbook*. second. John Wiley & Sons, 2011. URL: https://www.wiley.com/en-gb/Wind+Energy+Handbook%7B%5C%7D2C+2nd+Edition-p-9780470699751.

[37] Ruth Callaway and Claudio Fuentes Grünewald. *WP8 . 3 – Strategic Report for the combination of Tidal Lagoons , Aquaculture and Tourism*. Tech. rep. 652629. Blue Growth, 2011, pp. 1–15. URL: file:///C:/Users/Ross/Downloads/c3-aquaculture-and-tourism-tidal-lagoon-report.pdf.

[38] a Cazenave and Rs Nerem. "Present day sea level change: observations and causes". In: *Reviews of Geophysics* 42.2003 (2004), pp. 1–20. ISSN: 8755-1209. DOI: 10.1029/2003RG000139.1.INTRODUCTION.

[39] Ismail B Celik et al. "Editorial Policy Statement on the Control of Numerical Accuracy". In: *Journal of Fluids Engineering* 130.7 (2008). URL: https://www.asme.org/wwwasmeorg/media/resourcefiles/shop/journals/jfenumaccuracy.pdf?%7B%5C_%7Dga=2.185666281.174714773.1520931292-2045150241.1520931292.

[40] *CFD: PIMPLE Algorithm*. URL: https://www.simscale.com/forum/t/cfd-pimple-algorithm/81418 (visited on 09/27/2021).

[41] Walid Chakroun, Issa Al-Mesri, and Sami Al-Fahad. "Effect of Surface Roughness on the Aerodynamic Characteristics of a Symmetrical Airfoil". In: *Wind Engineering* 28.5 (Sept. 2004), pp. 547–564. ISSN: 0309-524X. DOI: 10.1260/0309524043028136. URL: http://journals.sagepub.com/doi/10.1260/0309524043028136.

[42] Walid Chakroun and Robert P. Taylor. "Heat transfer and fluid dynamics measurements in accelerated rough-wall boundary layer". In: *ASME 1993 International Gas Turbine and Aeroengine Congress and Exposition, GT 1993*. Vol. 2. American Society of Mechanical Engineers, Feb. 1993. ISBN: 9780791878897. DOI: 10.1115/93-GT-078.

[43] C H C Chan and K M Lam. "Centerline velocity decay of a circular jet in a counterflowing stream". In: *Physics of Fluids* 10.3 (1998), pp. 637–644. DOI: 10.1063/1.869589. URL: https://www.researchgate.net/publication/253660085.

[44] J. C. Chapman et al. "The Buhl correction factor applied to high induction conditions for tidal stream turbines". In: *Renewable Energy* 60 (Dec. 2013), pp. 472–480. ISSN: 09601481. DOI: 10.1016/j.renene.2013.05.018.

[45] Roger H Charlier et al. "Power from Arctic waters". In: *International Congress of Polar Science* 42 (2012), pp. 93–102. URL: http://www.rmri.ro/Home/Downloads/Publications.RecherchesMarines/2012/paper02.pdf.

[46] Roger H. Charlier. "Sustainable co-generation from the tides: A review". In: *Renewable and Sustainable Energy Reviews* 7.6 (2003), pp. 187–213. ISSN: 13640321. DOI: 10.1016/S1364-0321(03)00096-0. URL: file:///C:/Users/Ross/Downloads/Sustainable%7B%5C_%7Dco-generation%7B%5C_%7Dfrom%7B%5C_%7Dthe%7B%5C_%7Dtides%7B%5C_%7DA%7B%5C_%7Dreview.pdf.

[47] Wei Hsin Chen et al. "Power output analysis and optimization of two straight-bladed vertical-axis wind turbines". In: *Applied Energy* 185 (Jan. 2017), pp. 223–232. ISSN: 03062619. DOI: 10.1016/j.apenergy.2016.10.076.

[48] P Y Chou. "ON VELOCITY CORRELATIONS AND THE SOLUTIONS OF THE EQUATIONS OF TURBULENT FLUCTUATION*". In: *Quarterly of Applied Mathematics* 3.1 (1945), pp. 38–54. URL: http://www.ams.org/journals/qam/1945-03-01/S0033-569X-1945-11999-0/S0033-569X-1945-11999-0.pdf.

[49] C.F. Colebrook and C.M. White. "Experiments with Fluid Friction in Roughened Pipes". In: *Laws offlows in rough pipes, 1937. Technical Memorandum 129*. Royal Society, 1937, pp. 367–381. URL: https://royalsocietypublishing.org/.

[50] Andrew Cornett, Julien Cousineau, and Ioan Nistor. "Assessment of hydrodynamic impacts from tidal power lagoons in the Bay of Fundy". In: *International Journal of Marine Energy* 1 (2013), pp. 33–54. ISSN: 22141669.

DOI: `10.1016/j.ijome.2013.05.006`. URL: `http://dx.doi.org/10.1016/j.ijome.2013.05.006`.

[51] Fiona Crichton et al. "The link between health complaints and wind turbines: Support for the nocebo expectations hypothesis". In: *Frontiers in Public Health* 2.NOV (Nov. 2014), p. 220. ISSN: 22962565. DOI: `10.3389/fpubh.2014.00220`. URL: `www.frontiersin.org`.

[52] Thomas Nicholas Croft. *Unstructured Mesh - Finite VolumeAlgorithms for Swirling, Turbulent, Reacting Flows*. Tech. rep. London: university of Greenwich, 1998.

[53] Gordon Dalton et al. "Feasibility of investment in Blue Growth multiple-use of space and multi-use platform projects; results of a novel assessment approach and case studies". In: *Renewable and Sustainable Energy Reviews* 107 (June 2019), pp. 338–359. ISSN: 18790690. DOI: `10.1016/j.rser.2019.01.060`.

[54] P.A. Davidson. *Turbulence, An introduction for scientists and engineers*. Oxford University Press, 2007.

[55] Alan M. Davies and Simon C.M. Kwong. "Tidal energy fluxes and dissipation on the European continental shelf". In: *Journal of Geophysical Research: Oceans* 105.C9 (Sept. 2000), pp. 21969–21989. ISSN: 21699291. DOI: `10.1029/2000jc900078`. URL: `https://agupubs.onlinelibrary.wiley.com/doi/full/10.1029/2000JC900078%20https://agupubs.onlinelibrary.wiley.com/doi/abs/10.1029/2000JC900078%20https://agupubs.onlinelibrary.wiley.com/doi/10.1029/2000JC900078`.

[56] A. Dejoan and M. A. Leschziner. "Large eddy simulation of a plane turbulent wall jet". In: *Physics of Fluids* 17.2 (Feb. 2005), p. 025102. ISSN: 1070-6631. DOI: `10.1063/1.1833413`. URL: `http://aip.scitation.org/doi/10.1063/1.1833413`.

[57] Peter J Denning and Walter F Tichy. "Highly Parallel Computation". In: *Science* 250.4985 (1990), pp. 1217–1222. URL: `https://search-proquest-com.openathens-proxy.swan.ac.uk/docview/213540889/fulltextPDF/466422D63B1A4215PQ/1?accountid=14680`.

[58] Department for Business Energy & Industrial Strategy. *Energy Consumption in the UK (ECUK) 1970 to 2020*. 2021. URL: `www.gov.uk/beis`.

[59]   Department of Energy & Climate Change. *A 2030 framework for climate and energy policies; UK Government response to Commission Green Paper COM(2013) 169 final*. Tech. rep. July. 2013, pp. 1–32. URL: `https://www.gov.uk/government/uploads/system/uploads/attachment%7B%5C_%7Ddata/file/210659/130703%7B%5C_%7Dresponse%7B%5C_%7Dfor%7B%5C_%7Dpublication.pdf`.

[60]   Manhar Dhanak et al. *Effects of EMF Emissions from Cables and Junction Boxes on Marine Species*. Tech. rep. Golden, CO (United States): Golden Field Office, Sept. 2016. DOI: `10.2172/1357262`. URL: `http://www.osti.gov/servlets/purl/1357262/`.

[61]   Manuela Di Mauro and Darren Lumbroso. "Hydrodynamic and loss of life modelling for the 1953 Canvey Island flood". In: *Flood Risk Management: Research and Practice* October (2008), pp. 1117–1126. DOI: `10.1201/9780203883020.ch131`. URL: `https://eprints.hrwallingford.com/689/`.

[62]   Frederic Dias, Alan R Elcrat, and Lloyd N Trefethen. "Ideal jet flow in two dimensions". In: *J. Fluid Mech* 185 (1987), pp. 275–288. DOI: `10.1017/S0022112087003173`. URL: `https://doi.org/10.1017/S0022112087003173`.

[63]   Frank Dimroth et al. "Four-Junction Wafer-Bonded Concentrator Solar Cells". In: *Ieee Journal of Photovoltaics* 6.1 (2016), pp. 343–349. ISSN: 2156-3381. DOI: `10.1109/JPHOTOV.2015.2501729`. URL: `http://www.ekoconception.eu/en/wp-content/uploads/2016/04/Four-junction-wafer-bonded-concentrator-solar-cells%7B%5C_%7DIEEE-journal.pdf`.

[64]   Ibrahim Dincer. "Renewable energy and sustainable development: a crucial review". In: *Renewable and Sustainable Energy Reviews* 4.2 (2000), pp. 157–175. ISSN: 13640321. DOI: `10.1016/S1364-0321(99)00011-8`. URL: `http://www.sciencedirect.com/science/article/pii/S1364032199000118`.

[65]   R. DIRLING, JR. "A method for computing roughwall heat transfer rates on reentry nosetips". In: American Institute of Aeronautics and Astronautics (AIAA), July 1973. DOI: `10.2514/6.1973-763`. URL: `https://arc.aiaa.org/doi/abs/10.2514/6.1973-763`.

[66]   S. Dixon and Cesare Hall. *Fluid Mechanics and Thermodynamics of Turbomachinery*. Sixth. Elsevier Ltd, 2010. ISBN: 9781856177931. DOI: `10.1016/C2009-0-20205-4`.

[67] S.L. Dixon and Cesare Hall. *Fluid Mechanics and Thermodynamics of Turbomachinery*. Seventh. Butterworth-Heinemann, 2014. ISBN: 0123914108, 9780123914101.

[68] *DIY wind turbine, boat and weather resourses*. 2019. URL: `http://windandwet.com/` (visited on 01/15/2019).

[69] C A Douglas, G P Harrison, and J P Chick. "Life cycle assessment of the Seagen marine current turbine". In: *Proc. Inst. Mech. Eng. Part M J. Eng. Marit. Environ.* 222.1 (2008), pp. 1–12. ISSN: 1475-0902. DOI: `10.1243/14750902JEME94`. URL: `http://pim.sagepub.com/lookup/doi/10.1243/14750902JEME94`.

[70] S. Draper, A G L Borthwick, and G T Houlsby. "Energy Potential of a Tidal Fence Deployed Near a Coastal Headland". In: *Philosophical Transactions of the Royal Society* 371.1985 (2013), pp. 1–16. URL: `file:///C:/Users/Ross/Downloads/20120176.full.pdf`.

[71] Matt Edmunds et al. "A Spatially Nonlinear Generalised Actuator Disk Model for the Simulation of Horizontal Axis Wind and Tidal Turbines". In: (2018).

[72] Matt Edmunds et al. "An enhanced disk averaged CFD model for the simulation of horizontal axis tidal turbines". In: *Renewable Energy* 101 (2017), pp. 67–81. ISSN: 18790682. DOI: `10.1016/j.renene.2016.08.007`. URL: `http://dx.doi.org/10.1016/j.renene.2016.08.007`.

[73] Matt Edmunds et al. "Aspects of small scale flume correlation with a BEM-CFD Model". In: *EWTEC*. Cork, 2017, (1154)1–9. URL: `https://www.researchgate.net/publication/319311308`.

[74] Gary D. Egbert and Richard D. Ray. "Significant Dissipation of Tidal Energy in the Deep Ocean Inferred from Satellite Altimeter Data". In: *Nature* 405.1993 (2000), pp. 775–778. ISSN: 1476-4687. DOI: `10.1038/35015531`.

[75] Gary D. Egbert et al. "Efficient Inverse Modeling of Barotropic Ocean Tides". In: *Journal of Atmospheric and Oceanic Technology* 19.2 (Feb. 2002), pp. 183–204. ISSN: 0739-0572. DOI: `10.1175/1520-0426(2002)019<0183:EIMOBO>2.0.CO;2`. URL: `http://journals.ametsoc.org/doi/abs/10.1175/1520-0426%7B%5C%%7D282002%7B%5C%%7D29019%7B%5C%%7D3C0183%7B%5C%%7D3AEIMOBO%7B%5C%%7D3E2.0.CO%7B%5C%%7D3B2`.

[76] Electrical Line. "Nova Scotia Power ... A Tidal Power Pioneer". In: *Electrical Line* (2002), pp. 28–30.

[77] J G Eriksson, R I Karlsson, and J Persson. "An experimental study of a two-dimensional plane turbulent wall jet". In: *Experiments in Fluids* 25.1 (1998), pp. 50–60. URL: https://link.springer.com/content/pdf/10.1007%7B%5C%%7D2Fs003480050207.pdf.

[78] Ahmad Etemadi et al. "Electricity generation by the tidal barrages". In: *Energy Procedia* 12 (2011), pp. 928–935. ISSN: 18766102. DOI: 10.1016/j.egypro.2011.10.122. URL: http://dx.doi.org/10.1016/j.egypro.2011.10.122.

[79] I. Fairley, I. Masters, and H. Karunarathna. "The cumulative impact of tidal stream turbine arrays on sediment transport in the Pentland Firth". In: *Renewable Energy* 80 (2015), pp. 755–769. ISSN: 18790682. DOI: 10.1016/j.renene.2015.03.004. URL: http://dx.doi.org/10.1016/j.renene.2015.03.004.

[80] Iain Fairley et al. "Evaluation of tidal stream resource in a potential array area via direct measurements". In: *Renewable Energy* 57 (2013), pp. 70–78. ISSN: 09601481. DOI: 10.1016/j.renene.2013.01.024. URL: http://dx.doi.org/10.1016/j.renene.2013.01.024.

[81] Roger A Falconer et al. "The Severn Barrage and other tidal energy options : Hydrodynamic and power output modelling". In: 52.11 (2009), pp. 3413–3424. DOI: 10.1007/s11431-009-0366-z. URL: https://link.springer.com/content/pdf/10.1007%7B%5C%%7D2Fs11431-009-0366-z.pdf.

[82] Seth Finnegan et al. "Climate change and the selective signature of the Late Ordovician mass extinction". In: *Proceedings of the National Academy of Sciences of the United States of America* 109.18 (May 2012), pp. 6829–6834. ISSN: 00278424. DOI: 10.1073/pnas.1117039109.

[83] Hugo B. Fischer et al. *Mixing in Inland and Coastal Waters*. New York: Academic press, 1979, p. 500. URL: https://books.google.co.uk/books?hl=en%7B%5C&%7Dlr=%7B%5C&%7Did=ki9wPH2j1EcC%7B%5C&%7Doi=fnd%7B%5C&%7Dpg=PR11%7B%5C&%7Ddq=Fischer+et+al.+1979%7B%5C&%7Dots=Y1IyyR-etC%7B%5C&%7Dsig=k%7B%5C_%7D-Iu%7B%5C_%7Dk7tSVXetv1xtaIqAiDzsY%7B%5C#%7Dv=snippet%7B%5C&%7Dq=jet%7B%5C&%7Df=false.

[84] Karen A. Flack and Michael P. Schultz. *Review of hydraulic roughness scales in the fully rough regime*. Apr. 2010. DOI: 10.1115/1.4001492.

[85] Karen A. Flack and Michael P. Schultz. "Roughness effects on wall-bounded turbulent flows". In: *Physics of Fluids* 26.10 (Oct. 2014), p. 101305. ISSN: 1070-6631. DOI: 10.1063/1.4896280. URL: http://aip.scitation.org/doi/10.1063/1.4896280.

[86] Fluent. *Modelling Turbulent Flows- Introductory FLUENT Traing*. Tech. rep. 2006, pp. 1–49. URL: https://www.southampton.ac.uk/%7B~%7Dnwb/lectures/GoodPracticeCFD/Articles/Turbulence%7B%5C_%7DNotes%7B%5C_%7DFluent-v6.3.06.pdf.

[87] Witold Fraczek. *Mean Sea Level, GPS, and the Geoid*. 2003. URL: http://www.esri.com/news/arcuser/0703/geoid1of3.html (visited on 12/12/2018).

[88] P L Fraenkel. "Marine current turbines: pioneering the development of marine kinetic energy converters". In: *Proceedings of the Institution of Mechanical Engineers, Part A: Journal of Power and Energy* 221.2 (2007), pp. 159–169. ISSN: 0957-6509. DOI: 10.1243/09576509JPE307.

[89] Siegfried Franck et al. "Long-term evolution of the global carbon cycle: historic minimum of global surface temperature at presen". In: *Tellus B: Chemical and Physical Meteorology* 54.4 (Sept. 2002), pp. 325–343. DOI: 10.3402/tellusb.v54i4.16669. URL: https://www.tandfonline.com/doi/abs/10.3402/tellusb.v54i4.16669.

[90] Jean Pierre Frau. "Tidal energy: Promising projects la rance, a succesful Industrial-scale experiment". In: *IEEE Transactions on Energy Conversion* 8.3 (1993), pp. 552–558. ISSN: 15580059. DOI: 10.1109/60.257073. URL: http://ieeexplore.ieee.org/stamp/stamp.jsp?arnumber=257073.

[91] Luc Gagnon and Joop F. Van De Vate. "Greenhouse gas emissions from hydropower: The state of research in 1996". In: *Energy Policy* 25.1 (Jan. 1997), pp. 7–13. ISSN: 03014215. DOI: 10.1016/s0301-4215(96)00125-5.

[92] James W. Gauntner, John N. B. Livingood, and Peter Hrycuk. "SURVEY OF LITERATURE ON FLOW CHARACTERISTICS OF A SINGLE TURBULENT JET IMPINGING ON A FLAT'PLATE SURVEY OF LITERATURE ON FLOW CHARACTERISTICS OF A SINGLE TURBULENT JET IMPINGING ON A FLAT PLATE Literature survey Impinging jet Flat plate Flow characteristi". In: *NASA TECHNICAL NOTE* (1970). URL: https://ntrs.nasa.gov/archive/nasa/casi.ntrs.nasa.gov/19700009658.pdf.

[93] Benoît Gaurier et al. "Flume tank characterization of marine current turbine blade behaviour under current and wave loading". In: *Renewable Energy* 59 (Nov. 2013), pp. 1–12. ISSN: 09601481. DOI: 10.1016/j.renene.2013.02.026.

[94] Nicholas J Georgiadis and Dimitri Papamoschou. "Computational Investigations of High Speed Dual Stream Jets Computational Investigations of High-Speed Dual-Stream Jets". In: *9th AIAA/CEAS Aeroacoustics Conference and Exhibit*. 2003. DOI: 10.2514/6.2003-3311. URL: https://www.researchgate.net/publication/255668009.

[95] Nicholas J. Georgiadis and Dimitri Papamoschou. "Computational investigations of high-speed dual-stream jets". In: *9th AIAA/CEAS Aeroacoustics Conference and Exhibit*. American Institute of Aeronautics and Astronautics Inc., 2003. ISBN: 9781624101021. DOI: 10.2514/6.2003-3311.

[96] P. Giguère and M. S. Selig. "New Airfoils for Small Horizontal Axis Wind Turbines". In: *Journal of Solar Energy Engineering* 120.2 (1998), pp. 108–113. ISSN: 01996231. DOI: 10.1115/1.2888052.

[97] Tuhfe Göçmen and Bariş Özerdem. "Airfoil optimization for noise emission problem and aerodynamic performance criterion on small scale wind turbines". In: *Energy* 46.1 (Oct. 2012), pp. 62–71. ISSN: 03605442. DOI: 10.1016/j.energy.2012.05.036.

[98] Ashok Gopalarathnam et al. "Design of Low Reynolds Number Airfoils with Trips". In: *Journal of Aircraft* 40.4 (July 2003), pp. 768–775. ISSN: 0021-8669. DOI: 10.2514/2.3157. URL: http://arc.aiaa.org/doi/10.2514/2.3157.

[99] W J Graham. *ThePressure-Drag due to Blunt Leading Edges on Two-Dimensional Aerofoils, at Transonic and Low-Supersonic Speeds Pressure-Drag due to Blunt Leading Edges Two-Dimensional Aerofoils, at Transonic and Low-Supersonic Speeds*. Tech. rep. Ministry of Technology, 1965.

[100] Joe Green and Hance D Smith. *Across the waters: The Severn Estuary and Bristol Channel*. Tech. rep. December. Cardiff: Cardiff University, 2009, pp. 1–12. URL: http://www.wcl.org.uk/docs/2009/Joint%7B%5C_%7DLinks%7B%5C_%7DAcrosstheWaters%7B%5C_%7DSevernEstuary%7B%5C_%7DBristolChannel%7B%5C_%7DDec09.pdf.

[101] C.J. Greenshields and H.G. Weller. *Notes on Computational Fluid Dynamics: General Principles*. CFD Direct Limited, 2022. ISBN: 978-1-3999-2078-0.

[102]   Greenshields, Christopher J, and CFD Direct Ltd. "OpenFOAM v4 User Guide". In: *OpenFOAM Foundation Ltd* June (2016). URL: https://cfd.direct/openfoam/user-guide-v4/.

[103]   UIUC Applied Aerodynamics Group. *UIUC Airfoil Data Site*. URL: https://m-selig.ae.illinois.edu/ads.html%7B%5C#%7D:%7B~%7D:text=Selig%20are%20in%20an%20x%7B%5C%%7D2Cy%20format%20starting%20from,edge%20to%20trailing%20edge%20and%20then%20lower%20surface (visited on 09/12/2021).

[104]   Snorri Gudmundsson. "The Anatomy of the Airfoil". In: *General Aviation Aircraft Design: Applied Methods and Procedures*. Elsevier Science $ Technology, 2013. Chap. 8, pp. 235–298. ISBN: 9780123973085.

[105]   John S. Guilliver and Roger E.A. Arndt. *Hydropower Engineering Handbook*. McGraw-Hill, Inc., 1991. URL: https://conservancy.umn.edu/handle/11299/195476.

[106]   Onur Günel, Emre Koç, and Tahir Yavuz. "CFD vs. XFOIL of airfoil analysis at low reynolds numbers". In: *2016 IEEE International Conference on Renewable Energy Research and Applications, ICRERA 2016* 5 (2016), pp. 628–632. DOI: 10.1109/ICRERA.2016.7884411.

[107]   Kevin Harris. *Digest of UK Energy Statistics (DUKES) Chapter 1: Energy*. Tech. rep. UK GOV, 2021.

[108]   A Hashiehbaf and G P Romano. "Particle image velocimetry investigation on mixing enhancement of non-circular sharp edge nozzles". In: *Article in International Journal of Heat and Fluid Flow* 44 (2013), pp. 208–221. DOI: 10.1016/j.ijheatfluidflow.2013.05.017. URL: http://dx.doi.org/10.1016/j.ijheatfluidflow.2013.05.017.

[109]   Wei He et al. "Effect of the Trailing Edge Geometryon the Unsteadiness of the Flow Arounda Stalled NACA 0015 Airfoil". In: *Fluid Mechanics and its Applications*. Ed. by Theofilis Vassilis and Soria Julio. Instabilit. Vol. 107. January. Springer, 2015, pp. 45–50. ISBN: 978-3-319-06259-4. DOI: 10.1007/978-3-319-06260-0. URL: http://link.springer.com/10.1007/978-3-319-06260-0.

[110]   Antti Hellsten. "Some improvements in Menter's k-omega SST turbulence model". In: *29th AIAA, Fluid Dynamics Conference*. Reston, Virigina: American Institute of Aeronautics and Astronautics, June 1998, pp. 1–11. DOI: 10.2514/6.1998-2554. URL: https://arc.aiaa.org/doi/10.2514/6.1998-2554.

[111] Antti Hellsten and Seppo Laine. "Extension of the k-omega-SST turbulence model for flows over rough surfaces". In: *22nd Atmospheric Flight Mechanics Conference*. Reston, Virigina: American Institute of Aeronautics and Astronautics, Aug. 1997, pp. 252–260. DOI: `10.2514/6.1997-3577`. URL: `https://arc.aiaa.org/doi/10.2514/6.1997-3577`.

[112] Weston A. Hermann. "Quantifying global exergy resources". In: *Energy* 31.12 (2006), pp. 1685–1702. ISSN: 03605442. DOI: `10.1016/j.energy.2005.09.006`. URL: `http://ac.els-cdn.com/S0360544205001805/1-s2.0-S0360544205001805-main.pdf?%7B%5C_%7Dtid=416f6bac-3a73-11e7-ae06-00000aacb362%7B%5C&%7Dacdnat=1494965415%7B%5C_%7Dfb4f1c7ef21bdd64afb5d202ec13e284`.

[113] A Trevor Hodge. "Ancient Technology". In: *The Oxford Handbook of Engineering and Technology in the Classical World*. Ed. by John Peter Oleson. Vol. 59. 2. New York: New York: Oxford University Press, 2008, pp. 604–606. ISBN: 978-0-19-518731-1. DOI: `10.1017/s0009840x09001322`. URL: `https://www.cambridge.org/core/services/aop-cambridge-core/content/view/S0009840X09001322`.

[114] Yi Hu and Singiresu S. Rao. "Robust design of horizontal axis wind turbines using Taguchi method". In: *Journal of Mechanical Design, Transactions of the ASME* 133.11 (Nov. 2011). ISSN: 10500472. DOI: `10.1115/1.4004989`.

[115] J. Hussein Hussein, Steven P Capp, and William K George. "Velocity measurements in a high-Reynolds-number, momentum-conserving, axisymmetric, turbulent jet". In: *J. Fluid Mech* 258 (1994), pp. 31–75. DOI: `10.1017/S002211209400323X`. URL: `https://doi.org/10.1017/S002211209400323X`.

[116] *In-Flight Icing*. 2020. URL: `https://www.skybrary.aero/index.php/In-Flight%7B%5C_%7DIcing` (visited on 10/13/2020).

[117] R. I. Issa. "Solution of the implicitly discretised fluid flow equations by operator-splitting". In: *Journal of Computational Physics* 62.1 (Jan. 1986), pp. 40–65. ISSN: 10902716. DOI: `10.1016/0021-9991(86)90099-9`.

[118] D. S. Jang, R. Jetli, and S. Acharya. "Comparison of the piso, simpler, and simplec algorithms for the treatment of the pressure-velocity coupling in steady flow problems". In: *Numerical Heat Transfer* 10.3 (1986), pp. 209–228. ISSN: 01495720. DOI: `10.1080/10407788608913517`. URL: `https://www.tandfonline.com/doi/abs/10.1080/10407788608913517`.

[119]   Penelope Jeffcoate, Peter Stansby, and David Apsley. "Flow Due to Multiple Jets Downstream of a Barrage: Experiments, 3D Computational Fluid Dynamics, and Depth-Averaged Modeling". In: *Journal of Hydraulic Engineering* 139.7 (2013), pp. 754–762. ISSN: 0733-9429. DOI: 10.1061/(ASCE)HY.1943-7900.0000729. URL: http://ascelibrary.org/doi/abs/10.1061/%7B%5C%7D2528ASCE%7B%5C%7D2529HY.1943-7900.0000729%7B%5C%7D5Cnhttp://ascelibrary.org/doi/abs/10.1061/%7B%5C%7D7B%7B%5C%7D25%7B%5C%7D7D28ASCE%7B%5C%%7D7B%7B%5C%7D25%7B%5C%7D7D29HY.1943-7900.0000729.

[120]   Penelope Jeffcoate, Peter.K Stansby, and David .D Apsley. "Near-field flow downstream of a barrage: Experiments and 3-D modelling". In: *Oxford Tidal Energy Workshop* March (2012).

[121]   Penny Jeffcoate, Peter Stansby, and David Apsley. "Flow and bed-shear magnification downstream of a barrage with swirl generated in ducts by stators and rotors". In: *Journal of Hydraulic Engineering* 143.2 (2017), pp. 1–20. DOI: 10.1061/(ASCE)HY.1943-7900.0001228. URL: https://www.research.manchester.ac.uk/portal/files/45867197/final.19.09.2016pdf.pdf.

[122]   MI Jianchun, Graham J Nathan, and · P Kalt. "On Turbulent Jets Issuing from Notched-Rectangular and Circular Orifice Plates". In: *Flow Turbulence Combust* 84 (2010), pp. 565–582. DOI: 10.1007/978-3-540-75995-9_41. URL: https://www.researchgate.net/publication/226157899.

[123]   D. Juncu et al. "Injection-induced surface deformation and seismicity at the Hellisheidi geothermal field, Iceland". In: *Journal of Volcanology and Geothermal Research* 391 (Feb. 2020), p. 106337. ISSN: 03770273. DOI: 10.1016/j.jvolgeores.2018.03.019.

[124]   Margaret Kadiri et al. "A review of the potential water quality impacts of tidal renewable energy systems". In: *Renewable and Sustainable Energy Reviews* 16.1 (2012), pp. 329–341. ISSN: 13640321. DOI: 10.1016/j.rser.2011.07.160. URL: http://dx.doi.org/10.1016/j.rser.2011.07.160.

[125]   Mohammadreza Kadivar, David Tormey, and Gerard McGranaghan. "A review on turbulent flow over rough surfaces: Fundamentals and theories". In: *International Journal of Thermofluids* 10 (May 2021), p. 100077. ISSN: 26662027. DOI: 10.1016/j.ijft.2021.100077.

[126] Marta R. Karlsdottir et al. "Life cycle assessment of a geothermal combined heat and power plant based on high temperature utilization". In: *Geothermics* 84 (Mar. 2020), p. 101727. ISSN: 03756505. DOI: 10.1016/j.geothermics.2019.101727.

[127] Mrinal Kaushik, Rakesh Kumar, and G Humrutha. "Review of Computational Fluid Dynamics Studies on Jets". In: *American Journal of Fluid Dynamics* 5.3A (2015), pp. 1–11. DOI: 10.5923/s.ajfd.201501.01.

[128] S. W. Kim and T. J. Benson. "Comparison of the SMAC, PISO and iterative time-advancing schemes for unsteady flows". In: *Computers and Fluids* 21.3 (July 1992), pp. 435–454. ISSN: 00457930. DOI: 10.1016/0045-7930(92)90048-Z.

[129] Jan Kleissl. *Solar Energy Forecasting and Resource Assessment*. 2013, pp. 2–8. URL: https://books.google.co.uk/books?hl=en%7B%5C&%7Dlr=%7B%5C&%7Did=94KI0%7B%5C_%7DSPwW8C%7B%5C&%7Doi=fnd%7B%5C&%7Dpg=PP1%7B%5C&%7Ddq=Solar+energy+summary%7B%5C&%7Dots=Hb-kQDR7Uu%7B%5C&%7Dsig=XVjyy4nkXYKkCFh7Pg8PBI9ESl8%7B%5C#%7Dv=onepage%7B%5C&%7Dq=Solar%20energy%20summary%7B%5C&%7Df=false.

[130] Elizabeth Knowles. *The Oxford Dictionary of Phrase and Fable*. 2nd ed. Oxford University Press, Jan. 2005. DOI: 10.1093/acref/9780198609810.001.0001.

[131] A. Kolmogorov. "The local structure of turbulence in incompressible viscous fluid for very large Reynolds numbers". In: *Proc. USSR Academy of Sciences* 30 (1941), pp. 301–305.

[132] A. Kolmogorov. "The local structure of turbulence in incompressible viscous fluid for very large Reynolds numbers". In: *Proceedings of the Royal Society of London. Series A: Mathematical and Physical Sciences* 434.1890 (July 1991), pp. 9–13. ISSN: 0962-8444. DOI: 10.1098/rspa.1991.0075. URL: https://royalsocietypublishing.org/doi/epdf/10.1098/rspa.1991.0075.

[133] A Krothapalli and D K Karamcheti. "On the mixing of a rectangular jet". In: *J. Fluid Mmh* 107 (1981), pp. 201–220. DOI: 10.1017/S0022112081001730. URL: https://doi.org/10.1017/S0022112081001730.

[134] Vincent De Laleu. "La Rance Tidal Power Plant, 40-year operation feedback". In: *British Hydropower Association Annual Conference*. October. Liverpool: BHA Annual Conference, 2009, pp. 1–40. URL: http://www.british-hydro.org/downloads/La%20Rance-BHA-Oct%202009.pdf.

[135] Francesco Lalli et al. "Coanda effect in coastal flows". In: *Coastal Engineering* 57.3 (), pp. 278–289. DOI: 10.1016/j.coastaleng.2009.10.015. URL: https://ac.els-cdn.com/S0378383909001653/1-s2.0-S0378383909001653-main.pdf?%7B%5C_%7Dtid=01ef676a-fa27-11e7-beb5-00000aab0f27%7B%5C&%7Dacdnat=1516043298%7B%5C_%7Da07fcede6932886eb7e0962c38a8be77.

[136] B. E. Launder and D. B. Spalding. "The numerical computation of turbulent flows". In: *Computer Methods in Applied Mechanics and Engineering* 3.2 (Mar. 1974), pp. 269–289. ISSN: 00457825. DOI: 10.1016/0045-7825(74)90029-2.

[137] A Lawrence, A Vinod, and A Banerjee. "Effects of Free Stream Turbulence on Tidal Turbines. Part Ii – Turbine Performance and Near Wake Characteristics". In: *Proceedings of the Twelfth European Wave and Tidal Energy Conference* (2017), pp. 1–10.

[138] Angela Marie Lawrence. "Effects of Free-stream Turbulence on Tidal Turbine Blade Performance and Wake". PhD thesis. Bethlehem: Lehigh University, 2018.

[139] Chang-Hee Lee et al. "Environmental and ecological effects of Lake Shihwa reclamation project in South Korea: A review". In: *Ocean and Coastal Management* 102.PB (2014), pp. 545–558. ISSN: 09645691. DOI: 10.1016/j.ocecoaman.2013.12.018. URL: http://dx.doi.org/10.1016/j.ocecoaman.2013.12.018.

[140] H Lienhart, S Toots, and S Becker. "Flow and Turbulence Structures in the Wake of a Simplified Car Model (Ahmed Model)". In: *Notes on Numerical Fluid Mechanics and Multidisciplinary Design* 77.January (2015), pp. 323–330. DOI: 10.1007/978-3-540-45466-3.

[141] William Llovel and Tong Lee. "Importance and origin of halosteric contribution to sea level change in the southeast Indian Ocean during 2005–2013". In: *AGU .Publications* 42.4 (2015), pp. 1148–1157. URL: http://onlinelibrary.wiley.com/doi/10.1002/2014GL062611/full.

[142] Laurence K. Jr Loftin. *Theoretical and experimental data for a number of NACA 6A-series airfoil sections*. Tech. rep. National Advisory Commitee For Aeronautics, 1948.

[143] R. A. Luettich, J. J. Westerink, and N. W. Scheffner. *ADCIRC: An Advanced Three-Dimensional Circulation Model for Shelves Coasts and Estuaries, Report 1: Theory and Methodology of ADCIRC-2DDI and ADCIRC-3DL, Dredging Research Program Technical Report DRP-92-6*. Tech. rep.

32466. University of North Carolina at Chapel Hill. Insitute of Marine Sciences, University of Notre Dame. Department of Civil Engineering., 1992, pp. 1–137. URL: https://erdc-library.erdc.dren.mil/jspui/handle/11681/4618.

[144] Anthony Lydall, Laura Nesbitt, and Dan Thorley. *Swansea Visitor Survey 2015*. Tech. rep. Swansea: City and County of Swansea, 2015. URL: http://www.swansea.gov.uk/article/6406/tourism-research-and-statistics.

[145] Christopher A Lyon et al. *Summary of Low-Speed Airfoil Data, Vol. 3*. 3rd ed. Virginia Beach, Virginia: SoarTech Publications, 1997, p. 454. URL: https://m-selig.ae.illinois.edu/uiuc%7B%5C_%7Dlsat.html.

[146] Ennio Macchi and Marco Astolfi. *organic Rankine Cycle (ORC) Power Systems: Technology and Applications*. Woodhead Publishing, 2016, pp. 299–300. URL: //books.google.co.uk/books?hl=en%7B%5C&%7Dlr=%7B%5C&%7Did=SoZ4CgAAQBAJ%7B%5C&%7Doi=fnd%7B%5C&%7Dpg=PA299%7B%5C&%7Ddq=Axial-flow+turbines%7B%5C&%7Dots=7mgttIkqlA%7B%5C&%7Dsig=2blAqF2KRr5afTiROVfM3Gxg7C4%7B%5C#%7Dv=onepage%7B%5C&%7Dq=kaplan%7B%5C&%7Df=false.

[147] R Manohara, Mr A Harinath, and P G Scholar. "Application of Taguchi Method for Optimization of Process Parameters in Drilling Operation". In: *International Journal of Trend in Scientific Research and Developement* 3.4 (2019). ISSN: 24456-6470. URL: http://creativecommons.org/licenses/by/4.0.

[148] J.F. Manwell, J.G. McGowan, and A.L. Rogers. *Wind Energy Explained: Theory, Design and Application*. John Wiley & Sons Ltd., 2009. ISBN: 978-0-470-01500-1.

[149] R. Martin-Short et al. "Tidal resource extraction in the Pentland Firth, UK: Potential impacts on flow regime and sediment transport in the Inner Sound of Stroma". In: *Renewable Energy* 76 (2015), pp. 596–607. ISSN: 18790682. DOI: 10.1016/j.renene.2014.11.079. URL: http://dx.doi.org/10.1016/j.renene.2014.11.079.

[150] B.s. Massey. *Mechanics Of Fluids*. Sixth. London: Chapmaqn & Hall, 1989. ISBN: 0 412 34280 4.

[151] I. Masters et al. "A robust blade element momentum theory model for tidal stream turbines including tip and hub loss corrections". In: *Journal of Marine Engineering and Technology* 10.1 (2011), pp. 25–35. ISSN: 20568487. DOI:

10.1080/20464177.2011.11020241. URL: `https://www.tandfonline.com/action/journalInformation?journalCode=tmar20`.

[152] Ian Masters et al. "A Comparison of Numerical Modelling Techniques for Tidal Stream Turbine Analysis". In: *Energies* 8.8 (2015), pp. 7833–7853. DOI: `10.3390/en8087833`.

[153] Ian Masters et al. "The influence of flow acceleration on tidal stream turbine wake dynamics: A numerical study using a coupled BEM-CFD model". In: *Applied Mathematical Modelling* 37.16-17 (2013), pp. 7905–7918. ISSN: 0307904X. DOI: `10.1016/j.apm.2013.06.004`. URL: `http://dx.doi.org/10.1016/j.apm.2013.06.004`.

[154] Clifford Matthews. *Engineers' data book*. 4th. John Wiley & Sons Ltd., 2012. ISBN: 978-1-119-97622-6.

[155] Graeme Mccann. "Implications of Site-Specific Conditions on the Prediction of Loading and Power Performance of a Tidal Stream Device". In: 2008. URL: `https://www.researchgate.net/publication/228402190`.

[156] Robert J. Mcghee, Betty S. Walker, and Betty F. Millard. *Experimental results for the Eppler 387 airfoil at low Reynolds numbers in the Langley low-turbulence pressure tunnel*. Tech. rep. Hampton: NASA Langley Research Center, Oct. 1988. URL: `https://ntrs.nasa.gov/search.jsp?R=19890001471`.

[157] F R Menter, M Kuntz, and R Langtry. "Ten Years of Industrial Experience with the SST Turbulence Model". In: *Turbulence, heat and mass transfer* 4.1 (2003), pp. 625–632. URL: `http://aaac.larc.nasa.gov/tsab/cfdlarc/aiaa-dpw/`.

[158] F. R. Menter. "Performance of popular turbulence model for attached and separated adverse pressure gradient flows". In: *AIAA Journal* 30.8 (Aug. 1992), pp. 2066–2072. ISSN: 0001-1452. DOI: `10.2514/3.11180`. URL: `https://arc.aiaa.org/doi/10.2514/3.11180`.

[159] Florian R Menter. "Zonal Two Equation kappa-omega Turbulence Models for Aerodynamic Flows." In: *AIAA Fluid Dynamics Conferences*. Orlando: Eloret Corp, 1993.

[160] Metoffice.gov. *What is climate change?* 2020. URL: `https://www.metoffice.gov.uk/weather/climate-change/what-is-climate-change` (visited on 11/26/2020).

[161] I. A. Milne et al. "Characteristics of the turbulence in the flow at a tidal stream power site". In: *Philosophical Transactions of the Royal Society A: Mathematical, Physical and Engineering Sciences* 371.1985 (Feb. 2013). ISSN: 1364503X. DOI: 10.1098/rsta.2012.0196.

[162] MixIT. *MRF versus Sliding Mesh - Mixing Solution*. 2016. URL: `https://mixing-solution.com/2012/07/31/mrf-versus-sliding-mesh/` (visited on 08/25/2021).

[163] Scott E Munro and K K Ahuja. "APPENDIX D Fluid Dynamics of a High Aspect-Ratio Jet". In: *9th AIAA/CEAS Aeroacoustics Conference and Exhibit*. 2003. DOI: `https://doi.org/10.2514/6.2003-3129`.

[164] Paul Mycek et al. "Experimental study of the turbulence intensity effects on marine current turbines behaviour . Part I : One single turbine". In: *Renewable Energy* 66 (2014), pp. 729–746. ISSN: 0960-1481. DOI: `10.1016/j.renene.2013.12.036`. URL: `http://dx.doi.org/10.1016/j.renene.2013.12.036`.

[165] *NAFEMS - The Importance of Mesh Convergence - Part 1*. URL: `https://www.nafems.org/publications/knowledge-base/the-importance-of-mesh-convergence-part-1/` (visited on 07/02/2020).

[166] National GeoSpatial-Intelligiance Agency. *Addendum to NIMA TR 8350.2: Implementation of the World Geodetic System 1984 (WGS 84) Reference Frame G1150*. Tech. rep. NIMA. URL: `http://igscb.jpl.nasa.gov.`.

[167] National Imagery and Mapping Agency. *DEPARTMENT OF DEFENSE WORLD GEODETIC SYSTEM 1984 Its Definition and Relationships with Local Geodetic Systems*. Tech. rep. NIMA, 2000, p. 175. URL: `moz-extension://7e11865f-fd5f-4cbf-959b-65ca6503e1b3/enhanced-reader.html?openApp%7B%5C&%7Dpdf=https%7B%5C%%7D3A%7B%5C%%7D2F%7B%5C%%7D2Fearth-info.nga.mil%7B%5C%%7D2FGandG%7B%5C%%7D2Fpublications%7B%5C%%7D2Ftr8350.2%7B%5C%%7D2Fwgs84fin.pdf`.

[168] *National Oceanography Centre British Oceanographic Data Centre (BODC)*. 2017. URL: `https://www.bodc.ac.uk` (visited on 05/04/2017).

[169] NAVSTAR. *NAVSTAR GLOBAL POSITIONING SYSTEM INTERFACE SPECIFICATION IS-GPS-200 Revision D Navstar GPS Space Segment/Navigation User Interfaces*. Tech. rep. El Segundo: NAVSTAR, 2006, p. 221. URL: `moz-extension://7e11865f-fd5f-4cbf-959b-65ca6503e1b3/enhanced-reader.html?openApp%7B%5C&%7Dpdf=https%7B%5C%`

%7D3A%7B%5C%%7D2F%7B%5C%%7D2Fwww.gps.gov%7B%5C%%7D2Ftechnical%
7B%5C%%7D2Ficwg%7B%5C%%7D2FIS-GPS-200D.pdf.

[170] Simon P. Neill, James R. Jordan, and Scott J. Couch. "Impact of tidal energy converter (TEC) arrays on the dynamics of headland sand banks". In: *Renewable Energy* 37.1 (2012), pp. 387–397. ISSN: 09601481. DOI: 10.1016/j.renene.2011.07.003. URL: http://dx.doi.org/10.1016/j.renene.2011.07.003.

[171] Simon P. Neill et al. "The impact of tidal stream turbines on large-scale sediment dynamics". In: *Renewable Energy* 34.12 (Dec. 2009), pp. 2803–2812. ISSN: 0960-1481. DOI: 10.1016/J.RENENE.2009.06.015.

[172] Simon P. Neill et al. "Tidal range energy resource and optimization – Past perspectives and future challenges". In: *Renewable Energy* 127 (Nov. 2018), pp. 763–778. ISSN: 18790682. DOI: 10.1016/j.renene.2018.05.007.

[173] Kai Wern Ng, Wei Haur Lam, and Khai Ching Ng. "2002-2012: 10 Years of Research Progress in Horizontal-Axis Marine Current Turbines". In: *Energies* 6.3 (2013), pp. 1497–1526. ISSN: 19961073. DOI: 10.3390/en6031497.

[174] J Nikuradse. *NATIONAL ADVISORY COMMITTEE FOR AERONAUTICS - LAWS OF FLOW IN ROUGH PIPES*. Tech. rep. Washington, 1950.

[175] William L Oberkampf. *Verification and Validation in Computational Fluid Dynamics 1*. Tech. rep. 2002.

[176] John Peter Oleson. *The Oxford Handbook of Engineering and Technology in the Classical World*. Ed. by John Peter Oleson. New York: Oxford University Press, 2008, pp. 1–896. ISBN: 9780199734856. DOI: 10.1093/oxfordhb/9780199734856.001.0001. URL: https://books.google.co.uk/books?hl=en%7B%5C&%7Dlr=%7B%5C&%7Did=jrsVDAAAQBAJ%7B%5C&%7Doi=fnd%7B%5C&%7Dpg=PR9%7B%5C&%7Ddq=The+Oxford+Handbook+of+Engineering+and+Technology+in+the+Classical+World%7B%5C&%7Dots=uclMwPNrDD%7B%5C&%7Dsig=eHa2YgNTw15ym3QDCkswsDHXhYo%7B%5C#%7Dv=onepage%7B%5C&%7Dq=The%20Oxford%20Handbook%20of%20Engineering%20and%20Technolo.

[177] Richard C Olsen. *Remote Sensing from Air and Space -*. illustrate. Bellingham, Washington: The International Society for optical Engineering, 2007, p. 255. URL: https://books.google.co.uk/books?hl=en%7B%5C&%7Dlr=%7B%5C&%7Did=887dWbdO7FYC%7B%5C&%7Doi=fnd%7B%5C&%7Dpg=PR13%7B%5C&%7Ddq=Remote+Sensing+from+Air+and+Space%7B%5C&%7Dots=V4wIB-nSIM%7B%5C&%7Dsig=IJSnlc-PHNgMiWVQmFULn28L9Nc%7B%5C#%7Dv=onepage%7B%5C&%7Dq=bathymetry%7B%5C&%7Df=false.

[178] *OpenFOAM: User Guide: PIMPLE algorithm.* 2018. URL: `https://www.openfoam.com/documentation/guides/latest/doc/guide-applications-solvers-pimple.html` (visited on 06/07/2022).

[179] *OpenFOAM: User Guide: SIMPLE algorithm.* 2018. URL: `https://www.openfoam.com/documentation/guides/latest/doc/guide-applications-solvers-simple.html` (visited on 06/07/2022).

[180] C M Or, K M Lam, and P Liu. "Potential Core Lengths of Round Jets in Stagnant and Moving Environments". In: *Journal of Hydro-Enviroment Research* (2010). URL: `https://hub.hku.hk/bitstream/10722/137248/1/Content.pdf`.

[181] Mehmet Özger, Abdüsselam Altunkaynak, and Zekai Şen. "Statistical investigation of expected wave energy and its reliability". In: *Energy Conversion and Management* 45.13-14 (2004), pp. 2173–2185. ISSN: 01968904. DOI: `10.1016/j.enconman.2003.10.015`. URL: `http://www.sciencedirect.com/science/article/pii/S0196890403003212`.

[182] Steven G. Parkinson and William J. Collier. "Model validation of hydrodynamic loads and performance of a full-scale tidal turbine using Tidal Bladed". In: *International Journal of Marine Energy* 16 (Dec. 2016), pp. 279–297. ISSN: 22141669. DOI: `10.1016/j.ijome.2016.08.001`. URL: `http://dx.doi.org/10.1016/j.ijome.2016.08.001`.

[183] S V Patankar and D B Spalding. "A CALCULATION PROCEDURE FOR HEAT, MASS AND MOMENTUM TRANSFER IN THREE-DIMENSIONAL PARABOLIC FLOWS". In: *International Journal of Heat and Mass Transfer* 15 (1972), pp. 1787–1806. URL: `http://dns2.asia.edu.tw/%7B~%7Dysho/YSHO-English/2000%20Engineering/PDF/Int%20J%20Hea%20Mas%20Tra15,%201787.pdf`.

[184] Suhas V. Patankar. "A calculation procedure for two-dimensional elliptic situations". In: *Numerical Heat Transfer* 4.4 (1981), pp. 409–425. ISSN: 01495720. DOI: `10.1080/01495728108961801`. URL: `https://www.tandfonline.com/doi/abs/10.1080/01495728108961801`.

[185] Suhas V. Patankar. *Numerical Heat Transfer and Fluid Flow*. 1st. CRC Press, Oct. 1980, p. 214. ISBN: 9781315275130. DOI: `10.1201/9781482234213`. URL: `https://www.taylorfrancis.com/books/9781482234213`.

[186] Madhav S. Phadke. *Quality Engineering Using Robust Design*. Prentice Hall PTR, 1989. ISBN: #0137451679.

[187] David R. Plew and Craig L. Stevens. "Numerical modelling of the effect of turbines on currents in a tidal channel - Tory Channel, New Zealand". In: *Renewable Energy* 57 (2013), pp. 269–282. ISSN: 09601481. DOI: 10.1016/j.renene.2013.02.001. URL: http://dx.doi.org/10.1016/j.renene.2013.02.001.

[188] David R. Plew and Craig L. Stevens. "Numerical modelling of the effect of turbines on currents in a tidal channel - Tory Channel, New Zealand". In: *Renewable Energy* 57 (Sept. 2013), pp. 269–282. ISSN: 09601481. DOI: 10.1016/j.renene.2013.02.001.

[189] Tidal Lagoon Power. *The Project*. 2013.

[190] D Prandle. "Comparing environmental effects of Rance and Severn barrages". In: *Proceedings of the Institution of Civil Engineers: Maritime Engineering* 162.4 (2009), pp. 147–153. ISSN: 17417597. DOI: 10.1680/maen.2009.162. URL: http://www.scopus.com/inward/record.url?eid=2-s2.0-77956410019%7B%5C&%7DpartnerID=40%7B%5C&%7Dmd5=3cc1eb1047daab0afef16492d7f3b9cb.

[191] D Prandle. "Design of tidal barrage power schemes". In: *Proceedings of the Institution of Civil Engineers: Maritime Engineering* 162.4 (2009), pp. 147–153. ISSN: 17417597. DOI: 10.1680/maen.2009.162. URL: http://www.scopus.com/inward/record.url?eid=2-s2.0-77956410019%7B%5C&%7DpartnerID=40%7B%5C&%7Dmd5=3cc1eb1047daab0afef16492d7f3b9cb.

[192] David Prandle. "Simple theory for designing tidal power schemes Simple theory for designing tidal power schemes". In: *Advances in Water Resources* 6.1 (1984), pp. 21–27. DOI: 10.1016/0309-1708(84)90026-5.

[193] James F Price. *Lagrangian and Eulerian Representations of Fluid Flow: Kinematics and the Equations of Motion*. Tech. rep. 2006. URL: http://www.whoi.edu/science/PO/people/jprice.

[194] *Profili 2 - wing airfoils managing, printing and analysis software*. URL: http://www.profili2.com/eng/default.asp (visited on 09/13/2021).

[195] K Prudhvi Raj, K Santosh Kumar, and S Ajay Kumar. "CFD ANALYSIS OF NACA 0015 AEROFOIL". In: *International Journal of Application or Innovation in Engineering & Management (IJAIEM)* 7.3 (2018). URL: www.ijaiem.org.

[196] V. Ramos et al. "Assessment of the impacts of tidal stream energy through high-resolution numerical modeling". In: *Energy* 61 (Nov. 2013), pp. 541–554. ISSN: 03605442. DOI: 10.1016/j.energy.2013.08.051.

[197] Michael R. Raupach, Robert Anthony Antonia, and S. Rajagopalan. "Rough-wall turbulent boundary layers". In: *Applied Mechanics Reviews* 44.1 (Jan. 1991), pp. 1–26. ISSN: 00036900. DOI: 10.1115/1.3119492.

[198] R. D. Ray, R. J. Eanes, and B. F. Chao. "Detection of tidal dissipation in the solid Earth by satellite tracking and altimetry". In: *Nature* 381.6583 (1996), pp. 595–597. ISSN: 0028-0836. DOI: 10.1038/381595a0. URL: http://www.nature.com/doifinder/10.1038/381595a0.

[199] A. J. Read and A. J. Westgate. "Monitoring the movements of harbour porpoises (Phocoena phocoena) with satellite telemetry". In: *Marine Biology* 130.2 (Dec. 1997), pp. 315–322. ISSN: 00253162. DOI: 10.1007/s002270050251. URL: https://link.springer.com/article/10.1007/s002270050251.

[200] Larry Reinking. "ImageJ Basics". Millersville, 2007. URL: https://imagej.nih.gov/ij/docs/pdfs/ImageJ.pdf.

[201] REN21. *Renewables 2016 Global Status Report*. Tech. rep. 2016, p. 272. DOI: ISBN978-3-9818107-0-7. URL: http://www.ren21.net/status-of-renewables/global-status-report/.

[202] REN21. *RENEWABLES 2018 GLOBAL STATUS REPORT*. Tech. rep. 2018. URL: https://www.ren21.net/gsr-2018/.

[203] Renewable Energy Policy Network for the 21st Century. *Renewables 2020 Global Status Report*. Tech. rep. 2020, p. 367. URL: http://www.ren21.net/resources/publications/.

[204] Lewis Fry Richardson. *Weather Prediction by Numerical Process*. 1922.

[205] Lewis. Fry. Richardson. "The approximate arithmetical solution by finite differences of physical problems involving differential equations, with an application to the stresses in a masonry dam". In: *Philosophical Transactions of the Royal Society of London. Series A, Containing Papers of a Mathematical or Physical Character* 210.459-470 (Jan. 1911), pp. 307–357. ISSN: 0264-3952. DOI: 10.1098/rsta.1911.0009. URL: https://royalsocietypublishing.org/.

[206] Lewis. Fry. Richardson. *Weather Prediction by Numerical Process*. 2nd ed. Cambridge Mathematical Libary, 2007.

[207] Alexander Richter. *Global geothermal capacity reaches 14,900 MW - new Top 10 ranking of geothermal countries — Think GeoEnergy - Geothermal Energy News*. 2019. URL: https://www.thinkgeoenergy.com/global-geothermal-capacity-reaches-14900-mw-new-top10-ranking/ (visited on 12/01/2020).

[208] P J Roache. *QUANTIFICATION OF UNCERTAINTY IN COMPUTATIONAL FLUID DYNAMICS*. Tech. rep. 1997, pp. 123–60.

[209] P. J. Roache. "Perspective: A method for uniform reporting of grid refinement studies". In: *ASME. Journal of Fluids Engineering* 116.3 (Sept. 1994), pp. 405–413. ISSN: 1528901X. DOI: 10.1115/1.2910291.

[210] A. Roberts et al. "Current tidal power technologies and their suitability for applications in coastal and marine areas". In: *Journal of Ocean Engineering and Marine Energy* 2.2 (2016), pp. 227–245. ISSN: 2198-6444. DOI: 10.1007/s40722-016-0044-8. URL: http://link.springer.com/10.1007/s40722-016-0044-8.

[211] Peter E. Robins, Simon P. Neill, and Matt J. Lewis. "Impact of tidal-stream arrays in relation to the natural variability of sedimentary processes". In: *Renewable Energy* 72 (2014), pp. 311–321. ISSN: 09601481. DOI: 10.1016/j.renene.2014.07.037. URL: http://dx.doi.org/10.1016/j.renene.2014.07.037.

[212] P. A.Costa Rocha et al. "A case study on the calibration of the k-ω SST (shear stress transport) turbulence model for small scale wind turbines designed with cambered and symmetrical airfoils". In: *Energy* 97 (2016), pp. 144–150. ISSN: 03605442. DOI: 10.1016/j.energy.2015.12.081.

[213] W. Rodi. "Turbulence Models and Their Application in Hydraulics". In: *J. Fluid Mech.* 131 (1983), p. 471. DOI: 10.1017/S002211208321141X. URL: https://doi.org/10.1017/S002211208321141X.

[214] E W E Rogers et al. *A Study of the Effect of Leading-Edge Modifications on the Flow over a 50-deg Sweptback Wing at Transonic Speeds*. Tech. rep. Ministry of Aviation, 1962.

[215] Wilko Rohlfs et al. "Flow structures and heat transfer in submerged laminar jet impingement". In: *Proceedings of the Thermal and Fluids Engineering Summer Conference*. New York, 2015, pp. 1011–1020. ISBN: 9781567004311. DOI: 10.1615/tfesc1.fnd.012816. URL: https://www.researchgate.net/publication/280777134%7B%5C_%7DFlow%7B%5C_%7Dstructures%7B%5C_%7Dand%7B%5C_%7Dheat%7B%5C_%7Dtransfer%7B%5C_%7Din%7B%5C_%7Dsubmerged%7B%5C_%7Dlaminar%7B%5C_%7Djet%7B%5C_%7Dimpingement.

[216] Fergal O. Rourke, Fergal Boyle, and Anthony Reynolds. "Tidal energy update 2009". In: *Applied Energy* 87.2 (2010), pp. 398–409. ISSN: 03062619. DOI: 10.1016/j.apenergy.2009.08.014. URL: http://arrow.

dit.ie/cgi/viewcontent.cgi?article=1015%7B%5C&%7Dcontext=
engschmecart.

[217] Ali Sayigh. *Renewable Energy a Status Quo*. Ed. by Eric Johnson. 1st ed. River Publishers, 2016.

[218] Hermann Schlichting and Klaus Gersten. *Boundary-Layer Theory*. Ninth. Heidelberg: Springer, 2017. ISBN: 9783662529171. DOI: 10.1007/978-3-662-52919-5.

[219] Michael Selig. *UIUC Airfoil Coordinates Database*. 2021. URL: https://m-selig.ae.illinois.edu/ads/coord/sg6043.dat (visited on 09/08/2021).

[220] Michael S. Selig. "Low Reynolds Number Airfoil Design Lecture Notes". In: *VKI Lecture Series* November (2003), pp. 24–28.

[221] M. Shives and C. Crawford. "Developing an empirical model for ducted tidal turbine performance using numerical simulation results". In: *Proceedings of the Institution of Mechanical Engineers, Part A: Journal of Power and Energy* 226.1 (2012), pp. 112–125. ISSN: 0957-6509. DOI: 10.1177/0957650911417958. URL: http://pia.sagepub.com/content/226/1/112.abstract.

[222] D. B. Sims-Williams and R. G. Dominy. "Experimental Investigation into Unsteadiness and Instability in Passenger Car Aerodynamics". 1998. URL: http://tdl.libra.titech.ac.jp/journaldocs/en/recordID/article.bib-02/ZR000000019629?hit=-1%7B%5C&%7Dcaller=xc-search.

[223] John W. Slater. *Examining Spatial (Grid) Convergence*. 2021. URL: https://www.grc.nasa.gov/WWW/wind/valid/tutorial/spatconv.html (visited on 09/15/2021).

[224] EA Solur and VA Woodson. "WORLD VECTOR SHORELINE". In: *International Hydrographic Review*. Monaco, 1990. URL: https://journals.lib.unb.ca/index.php/ihr/article/view/23315.

[225] Robert Spain. "A possible Roman tide mill". In: *Paper submitted to the Kent Archaeological Society* 005 (2002), pp. 1–64. URL: http://www.kentarchaeology.ac/authors/005.pdf.

[226] A Spohn and P Gillieron. "Flow Separations Generated by a Simplified Geometry of an Automotive Vehicle, IUTAM Symp". In: *Unsteady Separated Flows* (2002). URL: http://citeseerx.ist.psu.edu/viewdoc/download?doi=10.1.1.475.4666%7B%5C&%7Drep=rep1%7B%5C&%7Dtype=pdf.

[227] Mohamed. Mat. Ali. Sukri, Con. J. Doolan, and Vincent Wheatley. "GRID CONVERGENCE STUDY FOR A TWO-DIMENSIONAL SIMULATION OF FLOW AROUND A SQUARE CYLINDER AT A LOW REYNOLDS NUMBER". In: *Seventh International Conference on CFD in the Minerals and Process Industries*. The University of Adelaide, The University of Queensland. Melbourne: CSIRO, 2009. URL: `moz-extension://7e11865f-fd5f-4cbf-959b-65ca6503e1b3/enhanced-reader.html?openApp%7B%5C&%7Dpdf=https%7B%5C%%7D3A%7B%5C%%7D2F%7B%5C%%7D2Fwww.cfd.com.au%7B%5C%%7D2Fcfd%7B%5C_%7Dconf09%7B%5C%%7D2FPDFs%7B%5C%%7D2F136ALI.pdf`.

[228] Deltares systems. *Delft3D-FLOW, User Manual*. User Manua. Rotterdam, 2014, pp. 1–684. URL: `www.deltaressystems.nl`.

[229] James L. Tangler. "The nebulous art of using wind-tunnel airfoil data for predicting rotor performance". In: *ASME 2002 Wind Energy Symposium, WIND2002*. American Society of Mechanical Engineers, Feb. 2002, pp. 190–196. ISBN: 156347476X. DOI: `10.1115/wind2002-40`.

[230] *The Art and Science of Meshing Airfoils - GridPro Blog*. 2017. URL: `https://blog.gridpro.com/the-art-and-science-of-meshing-airfoils/` (visited on 09/26/2019).

[231] The Crown Estate. *UK Wave and Tidal Key Resource Areas Project - Summary Report*. Tech. rep. October. 2012, pp. 1–10. URL: `http://www.thecrownestate.co.uk/media/5478/uk-wave-and-tidal-key-resource-areas-technological-report.pdf`.

[232] Douglas M Thompson, D M Thompson, and C R Mccarrick. "A flume experiment on the effect of constriction shape on the formation of forced pools Spatial heterogeneity of buried soils and post-settlement legacy sediments in the Christiana River Basin View project Hydrology and Earth System Sciences A flume exper". In: *Hydrol. Earth Syst. Sci* 14 (2010), pp. 1321–1330. DOI: `10.5194/hessd-7-1945-2010`. URL: `www.hydrol-earth-syst-sci.net/14/1321/2010/`.

[233] Douglas M. Thompson, Jonathan M. Nelson, and Ellen E. Wohl. "Interactions between pool geometry and hydraulics". In: *Water Resources Research* 34.12 (1998), pp. 3673–3681. ISSN: 00431397. DOI: `10.1029/1998WR900004`.

[234] Camilla Thomson, Gareth P Harrison, and John P Chick. "Life Cycle Assessment in the Marine Renewable Energy Sector". In: *LCA report - Instruments for Green Futures Markets*. Edingburgh, 2011, pp. 4–6. URL: `https://www.research.ed.ac.uk/portal/en/publications/life-cycle-`

assessment-in-the-marine-renewable-energy-sector(c7a1a262-
91e1-4b38-b7af-cb2090ece5a6).html.

[235] Jim Thomson et al. "Measurements of turbulence at two tidal energy sites in puget sound, WA". In: *IEEE Journal of Oceanic Engineering* 37.3 (2012), pp. 363–374. ISSN: 03649059. DOI: 10.1109/JOE.2012.2191656.

[236] Tidal Lagoon Power. *Coastal Protection - Tidal Lagoon*. 2018. URL: http://www.tidallagoonpower.com/tidal-technology/coastal-protection/ (visited on 06/24/2018).

[237] Tidal Lagoon Power. *Film & 3D Model*. 2017. URL: http://www.tidallagoonpower.com/projects/swansea-bay/3d-model/ (visited on 04/12/2017).

[238] Tidal Lagoon Power. *The New Power Cost League: A clear view of the consumer cost of new build power stations*. Tech. rep. July. 2016, p. 18.

[239] Tidal Lagoon Power. *Tidal Lagoon Swansea Bay plc Appendix 5.1 Sustainability: Carbon Balance Tidal Lagoon Swansea Bay plc Appendix: Sustainability: Carbon Balance*. Tech. rep. Gloucester: Tidal Lagoon Power Ltd, 2018. URL: http://www.tidallagoonpower.com/wp-content/uploads/2018/02/App-5.1-Sustainability-%E2%80%93-Carbon-Balance.pdf.

[240] Tidal Lagoon Power. *Turbine House GA*. 2014. URL: https://infrastructure.planninginspectorate.gov.uk/wp-content/ipc/uploads/projects/EN010049/EN010049-000286-2.4.24%20Turbine%20House%20GA.pdf.

[241] Tidal Lagoon Power. *Turbine House Section*. 2014. URL: https://infrastructure.planninginspectorate.gov.uk/wp-content/ipc/uploads/projects/EN010049/EN010049-000287-2.4.25%20Turbine%20House%20Section.pdf.

[242] *Tidal Lagoon Swansea Bay*. 2018. URL: https://infrastructure.planninginspectorate.gov.uk/projects/wales/tidal-lagoon-swansea-bay/ (visited on 09/23/2018).

[243] Phil N. Trathan et al. "Pollution, habitat loss, fishing, and climate change as critical threats to penguins". In: *Conservation Biology* 29.1 (2015), pp. 31–41. ISSN: 15231739. DOI: 10.1111/cobi.12349. URL: https://conbio.onlinelibrary.wiley.com/doi/full/10.1111/cobi.12349.

[244] Ben Trettel and Ofodike A Ezekoye. "THEORETICAL RANGE AND TRAJECTORY OF A WATER JET". In: *International Mechanical Engineering Congress and Exposition*. 2015.

[245] D.J Tritton. *Physical Fluid Dynamics*. Van Nostrand Reinhold Company Ltd., 1977, p. 284. URL: `https://books.google.co.uk/books?id=mrLvCAAAQBAJ%7B%5C&%7Dpg=PR3%7B%5C&%7Ddq=coanda+effect+tritton+book%7B%5C&%7Dlr=%7B%5C&%7Dsource=gbs%7B%5C_%7Dselected%7B%5C_%7Dpages%7B%5C&%7Dcad=2%7B%5C#%7Dv=onepage%7B%5C&%7Dq%7B%5C&%7Df=false`.

[246] *turbulentMixingLengthFrequencyInletFvPatchScalarField Class Reference*. URL: `https://www.openfoam.com/documentation/guides/latest/api/classFoam%7B%5C_%7D1%7B%5C_%7D1turbulentMixingLengthFrequencyInletF html%7B%5C#%7Ddetails` (visited on 03/28/2020).

[247] John Twidell and Tony Weir. *Renewable Energy Resourses*. Second Edi. London & New York: Taylor & Francis, 2006, pp. 429–450.

[248] Ucsusa.org. *How Geothermal Energy Works — Union of Concerned Scientists*. 2014. URL: `https://www.ucsusa.org/resources/how-geothermal-energy-works` (visited on 12/01/2020).

[249] UK Enviroment Agency. *Real-time data – UK National Tide Gauge Network — National Tidal and Sea Level Facility*. 2017. URL: `https://www.ntslf.org/data/uk-network-real-time` (visited on 01/07/2021).

[250] Dogancan Uzun et al. "Effect of biofouling roughness on the full-scale powering performance of a submarine". In: *Ocean Engineering* 238 (Oct. 2021), p. 109773. ISSN: 00298018. DOI: `10.1016/j.oceaneng.2021.109773`. URL: `https://linkinghub.elsevier.com/retrieve/pii/S0029801821011392`.

[251] Joop F. Van De Vate. "Comparison of energy sources in terms of their full energy chain emission factors of greenhouse gases". In: *Energy Policy* 25.1 (Jan. 1997), pp. 1–6. ISSN: 03014215. DOI: `10.1016/S0301-4215(96)00111-5`.

[252] J. P. Van Doormaal and G. D. Raithby. "Enhancements of the simple method for predicting incompressible fluid flows". In: *Numerical Heat Transfer* 7.2 (1984), pp. 147–163. ISSN: 01495720. DOI: `10.1080/01495728408961817`. URL: `https://www.tandfonline.com/doi/abs/10.1080/01495728408961817`.

[253] Varios. *A Dictionary of Physics*. 6th ed. Oxford University Press, Jan. 2009. DOI: `10.1093/acref/9780199233991.001.0001`.

[254] H K Versteeg and W Malalasekera. *An Introduction to COMPUTATIONAL FLUID DYNAMICS*. Second Edi. Pearson Education Limited, 2007.

[255] Ashwin Vinod and Arindam Banerjee. "Performance and near-wake characterization of a tidal current turbine in elevated levels of free stream turbulence". In: *Applied Energy* 254.July (2019), p. 113639. ISSN: 03062619. DOI: 10.1016/j.apenergy.2019.113639. URL: https://doi.org/10.1016/j.apenergy.2019.113639.

[256] Peter M Vitousek et al. "Human Domination of Earth' s Ecosystems". In: *Science* 277.5325 (1997), pp. 494–499. ISSN: 00368075. DOI: 10.1126/science.277.5325.494. arXiv: arXiv:1011.1669v3.

[257] Shujie Wang et al. "An overview of ocean renewable energy in China". In: *Renewable and Sustainable Energy Reviews* 15.1 (2011), pp. 91–111. ISSN: 13640321. DOI: 10.1016/j.rser.2010.09.040. URL: http://dx.doi.org/10.1016/j.rser.2010.09.040.

[258] Wei Wang and Rui Xin Huang. "Wind energy input to the surface waves". In: *Journal of Physical Oceanography* 34.5 (2004), pp. 1276–1280. ISSN: 0022-3670. URL: http://www.scopus.com/scopus/inward/record.url?eid=2-s2.0-2942604193%7B%5C&%7DpartnerID=40%7B%5C&%7Drel=R5.6.0.

[259] Zhenyu Wang, Yuchen Wang, and Mei Zhuang. "Improvement of the aerodynamic performance of vertical axis wind turbines with leading-edge serrations and helical blades using CFD and Taguchi method". In: *Energy Conversion and Management* 177 (Dec. 2018), pp. 107–121. ISSN: 01968904. DOI: 10.1016/j.enconman.2018.09.028.

[260] Tomoaki Watanabe et al. "Large eddy simulation study of turbulent kinetic energy and scalar variance budgets and turbulent/non-turbulent interface in planar jets". In: *The Japan Society of Fluid Mechanics Fluid Dynamics Research* 48 (2016), p. 19. DOI: 10.1088/0169-5983/48/2/021407.

[261] Shaun Waters and George Aggidis. "Tidal range technologies and state of the art in review". In: *Renewable and Sustainable Energy Reviews* 59 (2016), pp. 514–529. ISSN: 18790690. DOI: 10.1016/j.rser.2015.12.347. URL: http://dx.doi.org/10.1016/j.rser.2015.12.347.

[262] Daniel Weisser. "A guide to life-cycle greenhouse gas (GHG) emissions from electric supply technologies". In: *Energy* 32.9 (Sept. 2007), pp. 1543–1559. ISSN: 03605442. DOI: 10.1016/j.energy.2007.01.008.

[263] Örjan Wikander. *Handbook of ancient water technology*. Vol. 2. Leiden ;;Boston: Brill, 2000. ISBN: 9789004111233.

[264] David C. Wilcox. "Comparison of two-equation turbulence models for boundary layers with pressure gradient". In: *AIAA Journal* 31.8 (May 1993), pp. 1414–1421. ISSN: 00011452. DOI: 10.2514/3.11790. URL: https://arc.aiaa.org/doi/abs/10.2514/3.11790.

[265] David C. Wilcox. "Reassessment of the scale-determining equation for advanced turbulence models". In: *AIAA Journal* 26.11 (May 1988), pp. 1299–1310. ISSN: 00011452. DOI: 10.2514/3.10041. URL: https://arc.aiaa.org/doi/abs/10.2514/3.10041.

[266] David C. Wilcox. "Simulation of transition with a two-equation turbulence model". In: *AIAA Journal* 32.2 (May 1994), pp. 247–255. ISSN: 00011452. DOI: 10.2514/3.59994. URL: https://arc.aiaa.org/doi/abs/10.2514/3.59994.

[267] David C. Wilcox. *Turbulence Modeling for CFD, Volume 1*. Third. DCW Industries, 2006, p. 522. ISBN: 1928729088. URL: https://books.google.com/books?id=tFNNPgAACAAJ%7B%5C%&%7Dpgis=1.

[268] J. Wolf et al. "Environmental impacts of tidal power schemes". In: *Proceedings of the Institution of Civil Engineers - Maritime Engineering* 162.4 (Dec. 2009), pp. 165–177. ISSN: 1741-7597. DOI: 10.1680/maen.2009.162.4.165. URL: http://www.icevirtuallibrary.com/doi/10.1680/maen.2009.162.4.165.

[269] Edgar W. Woolard. "L. F. RICHARDSON ON WEATHER PREDICTION BY NUMERICAL PROCESS". In: *Monthly Weather Review* 50.2 (Feb. 1922), pp. 72–74. ISSN: 0027-0644. DOI: 10.1175/1520-0493(1922)50<72:lfrowp>2.0.co;2. URL: https://journals.ametsoc.org/view/journals/mwre/50/2/1520-0493%7B%5C_%7D1922%7B%5C_%7D50%7B%5C_%7D72%7B%5C_%7Dlfrowp%7B%5C_%7D2%7B%5C_%7D0%7B%5C_%7Dco%7B%5C_%7D2.xml.

[270] World Vector Shorelines. *Shoreline/Coastline Resourses*. 2018. URL: https://www.ngdc.noaa.gov/mgg/shorelines/.

[271] Donald J. Wuebbles and Atul K. Jain. "Concerns about climate change and the role of fossil fuel use". In: *Fuel Processing Technology* 71.1-3 (2001), pp. 99–119. ISSN: 03783820. DOI: 10.1016/S0378-3820(01)00139-4.

[272] Junqiang Xia, Roger A. Falconer, and Binliang Lin. "Hydrodynamic impact of a tidal barrage in the Severn Estuary, UK". In: *Renewable Energy* 35.7 (2010), pp. 1455–1468. ISSN: 09601481. DOI: 10.1016/j.renene.2009.12.009. URL: http://dx.doi.org/10.1016/j.renene.2009.12.009.

[273] L P Xia and K M Lam. "Velocity and Concentration Measurements in Initial Region of Submerged Round Jets in Stagnant Environment and in Coflow". In: *Journal of Hydro-enviroment Research* 3.1 (2009), pp. 21–34.

[274] Nicholas Yates et al. *STUDIES ON TIDAL POWER FROM THE ESTUAR-IES OF NORTH-WEST ENGLAND*. Tech. rep. Liverpool: University of Liverpool, 2010. URL: www.liv.ac.uk/engdept/tidalpower.

[275] Yin Yin Htay Aung, Myat Myat Soe, and Aung Myat Thu. "Effect of Attack angle on Aerodynamics Analysis of Different Wind Turbine Wings using Numerical Simulation". In: *American Scientific Research Journal for Engineering* 26.4 (Dec. 2016), pp. 319–329. ISSN: 2313-4402. URL: http://asrjetsjournal.org/.

[276] Enayatollah Zangiabadi. "Using 3D-CFD Methods to Investigate Hydrology of Oceans and Fish Passage through Tidal Stream Turbines". PhD thesis. Swansea University, 2014.